



**Stanley Udochukwu
Ofoegbu**

**Corrosão e inibição de corrosão em combinações
multi-materiais**

**Corrosion and corrosion inhibition in multi-material
combinations**



**Stanley Udochukwu
Ofoegbu**

**Corrosão e inibição de corrosão em combinações
multi-materiais**

**Corrosion and corrosion inhibition in multi-material
combinations**

Tese apresentada à Universidade de Aveiro para cumprimento dos requisitos necessários à obtenção do grau de Doutor em Ciência e Engenharia de Materiais, realizada sob a orientação científica do Professor Mikhail Zheludkevich, Professor e Investigador Principal Convidado da Departamento de Engenharia de Materiais e Cerâmica da Universidade de Aveiro, e do Doutor Mário Guerreiro Silva Ferreira, Professor Catedrático do Departamento de Engenharia de Materiais e Cerâmica da Universidade de Aveiro.

Apoio financeiro da FCT, referência SFRH/BD/75167/2010, e do FSE no âmbito do III Quadro Comunitário de Apoio.

This work is dedicated to the blessed memory of my parents, Benjamin and Joyce Ofoegbu who taught me quite early that I can be whatever I choose to be.

o júri

presidente

Prof. Doutora Maria Ana Dias Monteiro Santos
Professora Catedrática, Universidade de Aveiro

Prof. Doutor Christopher Michael Ashton Brett
Professor Catedrático, Faculdade de Ciências e Tecnologia, Universidade de Coimbra

Prof. Doutor Jorge Ribeiro Frade
Professor Catedrático, Universidade de Aveiro

Doutora Alda Maria Pereira Simões
Professora associada com agregação, Universidade Técnica de Lisboa

Doutor Mikhail Larionovich Zheludkevich
Investigador Principal Convidado, Universidade de Aveiro (Orientador)

Doutor Jorge Manuel Palma Correia
Investigador Auxiliar, Faculdade de ciências da Universidade de Lisboa

agradecimentos

Gostaria de agradecer aos meus orientadores, Prof. Mikhail L. Zheludkevich e Prof. Doutor Mário Guerreiro Silva Ferreira pela orientação, encorajamento e análise crítica durante todo o trabalho. Gostaria também de agradecer aos Doutores Silvar Kallip, Alexandre Bastos e Marcela Quevedo Reyes, pelo apoio em algumas partes do trabalho experimental e pelas frutuosas e interessantes discussões.

Agradeço à Prof. Helena I.S. Nogueira do Departamento de Química da Universidade de Aveiro pela ajuda com as medições de Microscopia Confocal de Raman. Agradeço também ao Prof. José António Paixão e ao Dr. Pedro Sidónio do Departamento de Física da Universidade de Coimbra pela possibilidade de utilizar o espectrómetro de fluorescência de raios-X e pela ajuda nas medições experimentais.

Não posso deixar de agradecer aos colegas do meu grupo, Olga Karavai, Jorge Carneiro, Maksim Starykevich, André Oliveira e Marco Oliveira. O meu agradecimento estende-se ao pessoal técnico e administrativo do Departamento de Engenharia de Materiais e Cerâmica da Universidade de Aveiro.

Agradeço à Fundação para a Ciência e a Tecnologia pela bolsa de doutoramento SFRH/BD/75167/2010 a qual permitiu a conclusão deste trabalho.

Finalmente, expresso reconhecimento à minha família, pelo encorajamento, compreensão e apoio durante todo o tempo que despendi nas longas horas de trabalho no laboratório.

palavras-chave

corrosão galvânica, eficiência de inibição, multi-materiais, polímeros reforçado com fibra de carbono, impedância, alumínio, cobre, zinco, ferro, SVET, SIET.

resumo

Os projectos mais recentes de veículos usados pelas indústrias aeronáutica e dos transportes combinam alta resistência, baixo peso, consumo eficiente de combustível e reduzido impacto ambiental, para o que juntam no mesmo desenho materiais muito diversos. A corrosão destas combinações multi-materiais pode ser acelerada quando se unem materiais com propriedades químicas e electroquímicas bastante diferentes. Como as estratégias actuais de mitigação da corrosão não focam sistemas multi-materiais, há a necessidade urgente em caracterizar os mecanismos da corrosão nestes novos sistemas a fim de desenvolver soluções eficazes para a sua prevenção. Este trabalho centrou-se na compreensão dos mecanismos da corrosão de dois sistemas multimateriais com relevância para as indústrias aeronáutica e dos transportes: Al - Cu - CFRP (polímeros reforçado com fibra de carbono) e Zn - Fe - CFRP, respectivamente. Com base nos resultados obtidos procurou-se identificar, à escala laboratorial, inibidores de corrosão eficazes. Começou-se por estudar separadamente cada um dos cinco materiais constituintes das combinações multi-materiais, em solução aquosa NaCl 50 mM com e sem inibidores de corrosão. O CFRP, o único material não metálico, foi estudado extensivamente para caracterizar a sua acção electroquímica como cátodo, pois esta torna-se prejudicial quando o CFRP está ligado a metais. Estudou-se também formas de minimizar a reacção catódica no CFRP e a corrosão dos outros metais. O passo seguinte foi o estudo de pares desses materiais à micro e macro-escala admitindo que os inibidores de corrosão capazes de reduzir a corrosão galvânica nestes sistemas simples (Al - CFRP, Al - Cu, e Cu - CFRP para o sistema galvânico Al - Cu - CFRP) e (Fe - CFRP, Zn - CFRP, e Zn - Fe para o sistema Zn - Fe - CFRP) serão também eficazes na protecção da estrutura multi-material real. Por fim os inibidores mais eficientes foram testados para as combinações multi-materiais completas, Al - Cu - CFRP e Zn - Fe - CFRP. Os resultados obtidos trazem uma melhor compreensão do comportamento electroquímico do CFRP quando sujeito a polarização catódica ou quando ligado galvanicamente a vários metais. Os resultados apresentam também estratégias possíveis para impedir o processo catódico à superfície do CFRP. Identificou-se ainda vários compostos com a capacidade de inibir a corrosão nos sistemas Al - Cu - CFRP e Zn - Fe - CFRP. Como resultado do trabalho realizado para esta Tese, desenvolveu-se um procedimento para monitorização da degradação do "plástico" reforçado com fibra de carbono (CFRP). Propõem-se também mecanismos para a corrosão e inibição em sistemas multi-material como por exemplo, Al - Cu - CFRP e Zn - Fe - CFRP.

keywords

galvanic corrosion, inhibition efficiency, multi-material, carbon fiber reinforced polymers, impedance, aluminium, copper, zinc, iron, SVET, SIET.

abstract

Modern high-strength but environmentally friendly, fuel-efficient and weight-optimized designs vital to the aeronautical and transport industries have resulted in the multi-material concept in which a wide range of materials are employed to exploit the various desirable mechanical and physical properties. These multi-material design concepts are susceptible to corrosion as the chemical and electrochemical properties of their constituent materials can vary widely. Since current corrosion mitigation strategies are not focused on these multi-material systems, there is an urgent need to understand the mechanism of the corrosion processes operative in these multi-material assemblies and develop suitable multi-material corrosion mitigation solutions in tandem with the increasing design trend towards multi-material structures.

This work has focused on understanding the mechanism of multi-material corrosion in two multi-material systems that are of relevance to the aeronautical and transport industries; Al - Cu - CFRP (carbon fiber reinforced polymers) and Zn - Fe - CFRP galvanic systems respectively. On the basis of the insights obtained, appropriate multi-material corrosion mitigation options using inhibitors are to be identified and verified at the laboratory scale.

The thesis objectives have been pursued by an incremental escalation technique in which the five individual materials constituting the two multi-material galvanic systems were first studied at the macro-scale in quiescent 50 mM NaCl solutions with and without inhibitors. Particularly, CFRP the only non-metallic material used was extensively studied with a view to understanding its deleterious electrochemical action as an efficient cathode when coupled to metals and how to mitigate it. Next technologically relevant dual material couples most relevant to the two galvanic systems were studied at the macro- and micro-scales, on the premise that inhibitors efficient at mitigating galvanic corrosion in these simpler components (Al - CFRP, Al - Cu, and Cu - CFRP for the Al - Cu - CFRP galvanic system) and (Fe - CFRP, Zn - CFRP, and Zn - Fe for the Zn - Fe - CFRP galvanic system) are prone to be effective for an entire multi-material system. Finally, promising inhibitors identified from dual material galvanic studies are tested on the multi-material combinations leading to identification of efficient multi-material corrosion inhibitors for both the Al - Cu - CFRP and Zn - Fe - CFRP multi-material combinations.

The results demonstrate better understanding of the electrochemical behaviour of CFRP under cathodic polarization on galvanic coupling with metals and potential strategies to suppressing its ability to support cathodic reactions, and successful identification of potential inhibitors for mitigating multi-material corrosion in both systems. On the basis of results obtained in this work a scheme for monitoring degradation of CFRP was postulated as well as plausible mechanism(s) of multi-material corrosion and multi-material corrosion inhibition in Al - Cu - CFRP and Zn - Fe - CFRP multi-material galvanic systems, respectively.

Table of Contents

	Page
Title page.....	ii
Dedication.....	iii
Jury list.....	iv
Agradecimentos.....	v
Resumo.....	vi
Abstract.....	vii
Table of Contents.....	viii
Abbreviations.....	xiii
List of Figures.....	xv
List of Tables.....	xxii
Chapter 1	
Introduction.....	1
1.1. Background to Research.....	1
1.2. Significance of Study.....	2
1.3. Study Objectives.....	3
1.4. Research Strategy.....	3
Chapter 2	
LITERATURE REVIEW.....	5
2.0 Introduction.....	5
2.1 What is corrosion?.....	8
2.2. Thermodynamics of Corrosion/Electrochemical Processes.....	11
2.3. Equilibrium (Pourbaix) Diagrams.....	12
2.4. Kinetics of Corrosion processes.....	13
2.4.1. Polarization.....	14
2.5. The Mixed Potential Theory.....	14
2.6. Corrosion Measurement/Evaluation.....	16
2.7 Forms of corrosion.....	17
2.7.1. Galvanic Corrosion.....	17
2.8. Corrosion of Metals.....	20
2. 8.1. Corrosion of Aluminium.....	21
2. 8.1.1. Corrosion of Aluminium in Near-Neutral Media.....	23
2. 8.1.2. Corrosion of Aluminium in Alkaline Media.....	25
2. 8.2. Corrosion of Copper.....	27
2. 8.2.1. Corrosion of Copper in Neutral and Near-Neutral Media.....	29
2. 8.2.2. Corrosion of Copper in Alkaline Media.....	32
2. 8.3. Corrosion of Iron.....	33
2. 8.3.1. Corrosion of Iron in Neutral and Near-Neutral Media.....	35
2. 8.3.2. Corrosion of Iron in Alkaline Media.....	36
2. 8.4. Corrosion of Zinc.....	38
2. 8.4.1. Corrosion of Zinc in Neutral and Near-Neutral Media.....	42
2. 8.4.2. Corrosion of Zinc in Alkaline Media.....	43
2. 9. "Corrosion" (Degradation) of Carbon Fiber Reinforced Polymers (CFRPs).....	44
2.9.1. The Surface Chemistry of a Carbon	44
2. 9.2. Oxygen reduction on carbon electrodes.....	46

2.9. 3. Effect of Polarization on Carbon Fiber.....	49
2.9.4. CFRP Degradation under Cathodic Polarization.....	49
2.9.5. CFRP Degradation under Anodic Polarization.....	53
2.10. Corrosion Inhibitors and Corrosion Inhibition.....	54
2.10.1. Corrosion Inhibitors.....	54
2.10.2 Classification of Corrosion Inhibitors and Factors Affecting Corrosion Inhibitor(s)/ Corrosion Inhibition Mechanisms.....	56
2.10.3 Organic Corrosion Inhibitors.....	58
2.10.4 Physical Adsorption of Corrosion Inhibitors.....	60
2.10.5 Chemisorption of Corrosion Inhibitors.....	61
2.10.6 Anodic (Passivation and Passivating) Corrosion Inhibitors.....	63
2.10.7. Cathodic Corrosion Inhibitors.....	66
2.10.8 Mixed Corrosion Inhibitors.....	68
2.10.9. Corrosion Inhibitors in Localized corrosion (Galvanic Corrosion).....	68
2.10.10. Synergism in Corrosion Inhibition (Combination of Inhibitors).....	71
2.10.10.1. Synergistic Corrosion Inhibition with Organic Inhibitor/Metallic Ion Inhibitor Combination.....	72
2.10.10.2. Synergistic Corrosion Inhibition of Galvanic Couples and Multi-material Combinations.....	73
2.10.10.3. Evaluation of Synergistic Corrosion Inhibition	74
2.11. Inhibiting the Electrochemical Reactivity of Carbon/CFRP Surface	74
2.11. Chapter Concluding Remarks	75
 Chapter 3	
Principles of Experimental Techniques.....	77
3.0. Principles of the Experimental Techniques.....	77
3.1. Chronopotentiometry (OCP Measurements).....	77
3.2. Potentiodynamic Polarization Technique.....	78
3.2.1. Potentiodynamic Polarization Test.....	79
3.2.2. The Linear Polarization Resistance Technique.....	80
3.3. Cyclic Voltammetry.....	81
3.4. ZRA Measurements for (Galvanic Couples).....	84
3.5. Electrochemical Impedance Spectroscopy (EIS).....	85
3.5.1. Basic Concepts Related to EIS.....	85
3.5.2. Interpretation of EIS Data : Equivalent Circuits.....	88
3.5.3. Combination of Circuit Elements to form Equivalent Circuits and Effect on Spectra.....	91
3.5.4. Validity of EIS data (Validating Impedance Data with Kramers-Kronig Transforms).....	92
3.6. Scanning Vibrating Electrode Technique (SVET).....	93
3.6.1. Operating Principle of SVET.....	93
3.6.2. Application of SVET to Corrosion Studies.....	95
3.6.3. Use of SVET in Corrosion Inhibition Studies.....	96
3.7. pH Measurements (micro-potentiometry).....	97
3.7.1. Use of Ion-Selective Electrodes for Local pH Measurement.....	98
3.7.2. Importance of local (micro) pH measurements in Corrosion.....	98
3.7.4. Presentation of local pH Measurements.....	98
3.8. Oxygen Concentration Measurements (Micro-amperometry).....	99
3.9. Raman Spectroscopy.....	100

3.9.1. Basic Principles of Raman Spectroscopy.....	101
3.9.2. Confocal Raman Spectroscopy and Imaging.....	102
3.10. Glow Discharge Optical Emission Spectroscopy (GD-OES).....	103
3.10.1 Working Principle of GD-OES.....	104
3.10.2. GD-OES in Corrosion and Corrosion Inhibition Studies.....	105
3.11. Scanning Kelvin Probe Microscopy (SKPFM).....	106
3.13.1. Basic Principles of Scanning Kelvin Probe Microscopy (SKPFM).....	107
3.13.2. Importance and Application of Scanning Kelvin Probe Microscopy (SKPFM).....	108

Chapter 4

Experimental Procedures.....	109
4.0. Experimental Procedures	109
4.1. Specimens.....	109
4.2. Specimen Preparation.....	109
4.2. Reagents.....	110
4.3. Solution Preparation.....	110
4.4. Techniques and Equipments Used.....	110
4.4.1. Open Circuit Potential Measurement.....	111
4.4.2. Potentiodynamic Polarization.....	111
4.4.3. Cyclic Voltammetry.....	111
4.4.4. Electrochemical Impedance Spectroscopy (EIS).....	111
4.2.5. Galvanic Current Measurement with Zero Resistance Ammeter (ZRA).....	112
4.2.6. pH Measurements.....	112
4.2.7. Oxygen Concentration Measurements/Mapping.....	113
4.4.8. Scanning Vibrating Electrode Technique (SVET).....	114
4.4.9. Scanning Kelvin Probe Force Microscopy.....	115
4.4.10. X-ray Fluorescence Spectroscopy and Mapping.....	115
4.4.11. Raman Spectroscopy and Mapping.....	115
4.4.12. Scanning Electron Microscopy.....	115
4.4.13. Glow Discharge Optical Emission Spectroscopy (GD-OES).....	116
4.4.14. X-ray Diffraction.....	116

Chapter 5

RESULTS OF TESTS ON INDIVIDUAL MATERIALS.....	117
5. Results of Tests on Individual Materials.....	117
5.1.0 Results from General Tests on Single Materials.....	117
5.1.1. Open Circuit Potential Measurement Results.....	117
5.1.2. Potentiodynamic Polarization Results for 5 Test Materials.....	118
5.1.3. Electrochemical Impedance Spectroscopy Results for 5 Test Materials.....	120
5.2.0. Results of Tests on carbon fiber reinforced plastic (CFRP).....	120
5.2.1. Electrochemical and Chemical Characterization of Components of the CFRP Composites..	121
5.2.1.1. CFRP Characterization by Scanning Kelvin Probe Force Microscopy (SKPFM).....	121
5.2.1.2 CFRP Characterization by Confocal Raman Spectroscopy/Microscopy.....	122
5.2.2. Effect of Polarization on the local environment near CFRP in 50 mM NaCl.....	123
5.2.2.1. Results of Step Chrono-amperometric Measurements and Potentiodynamic Polarization Scan on CFRP in 50 mM NaCl with Simultaneous Localized pH Measurements.....	123
5.2.3. Effect of pH on Carbon Fiber Reinforced Plastic (CFRP).....	125

5.2.3.1. Effect of Bulk pH on OCP of CFRP in Chloride Solutions.....	125
5.2.3.2. Effect of Bulk pH on the Cathodic Polarization Curve of CFRP in Chloride Solutions.....	126
5.2.3.3. Effect of Bulk pH on the Cyclic Voltammetric Response of CFRP in Chloride Solutions.....	127
5.2.3.4. Evolution of CFRP Impedance Spectra during Immersion in 50 mM NaCl (pH≈ 6.8).....	129
5.2.3.5. Effect of Bulk pH on Impedance Spectra of CFRP in Unbuffered Chloride Solutions.....	132
5.2.3.6. Effect of Bulk pH on degradation of CFRP: SEM and Raman images of CFRP.....	140
5.2.4. Effect of Cathodic Polarization on Impedance Spectra of CFRP in Chloride Solutions.....	143
5.2.4.1. Effect of Polarization on CFRP with Respect to Oxygen Diffusion.....	144
5.2.4.2. Surface Analysis: Effect of Polarization on Raman Spectra, Raman and SEM Images of CFRP.....	148
5.2.5. Scheme for Using EIS Parameters to Monitor Changes in CFRP.....	150
5.2.6. Effect of a Combination of Polarization and pH on CFRP.....	151
5.2.7. Degradative Processes of CFRP Under Cathodic Polarization and Alkaline pH.....	153
5.2.8. Choosing Inhibitors for Mitigating Electrochemical Activity of CFRP and Its Consequent Degradation.....	154
5.2.8.1. Effect of Combination of Inhibitors and Polarization at -1000 mV SCE on Carbon Fiber Reinforced Polymer (CFRP).....	155
5.2.8.2. Effect of a surfactant; Sodium Dodecyl Sulphate (SDS).....	158
5.2.8.3. Effect of Azoles (BIA, BTA, 1,2,3- triazole and 1,2,4- triazole).....	164
5.2.8.4. Effect of Nitrates and Nitrite.....	166
5.2.8.5. Effect of Acetates and Rare Earth Cations.....	169
5.2.8.6. Effect of Phosphates (Na ₃ PO ₄ and NaH ₂ PO ₄ , NaH ₂ P ₂ O ₇) and Molybdate (Na ₂ MoO ₄)...	171
5.2.9.0. Effect of a Combination of Inhibitors.....	173
5.2.4.9.1. Effect of Combination of Polarization and Inhibitor Combination Containing Nitrates...	173
5.2.4.9.2. Effect of Combination of Polarization and Inhibitor Combination Containing Acetates and BTA.....	175
5.3. Chapter Summary.....	176

Chapter 6

Multi-material Corrosion Inhibition of Galvanic Couples in the Al - Cu - CFRP Multi-material Galvanic System.....	179
6.0. Results of Tests on Galvanic Couples in the Al - Cu - CFRP Galvanic System.....	179
6.1. Overview of the Galvanic Behaviour of Galvanic Couples in 50 mM NaCl.....	180
6.2. Overview of the Multi-material Corrosion Inhibition in the Al-Cu-CFRP Galvanic System and the Galvanic Behaviour of Galvanic Couples in the System in the Presence of Inhibitors in 50 mM NaCl based Solutions.....	184
6.2.1. Effect of Selected Combinations of Inhibitors on the Galvanic Corrosion of Al - CFRP, Al - Cu, and Cu - CFRP Galvanic Couples.....	188
6.3.0. Effect of Selected Single of Inhibitors on the Galvanic Corrosion of Al - CFRP, Al - Cu, and Cu - CFRP Galvanic Couples.....	194
6.3.1. Effect of Azoles (Single of Inhibitors) on the Galvanic Corrosion of Al - CFRP, Al - Cu, and Cu - CFRP Galvanic Couples.....	194
6.3.2. Effect of Rare Earth Cations (Single of Inhibitors) on the Galvanic Corrosion of Al - CFRP, Al - Cu, and Cu - CFRP Galvanic Couples.....	198
6.3.3. Effect of Conjugate Ions of Rare-earth Metal Cations on the Galvanic Corrosion of Al - CFRP , Al - Cu, and Cu - CFRP Galvanic Couples.....	205
6.4.0. Unveiling the Mechanism of Multi-material Corrosion Inhibition	

in the Al - Cu - CFRP Galvanic system.....	211
6.4.1. Multimaterial Corrosion Inhibition in the Al - Cu - CFRP Galvanic system: Insight into the Changes in the Local pH around Constituent Materials on Galvanic Coupling.....	212
6.4.2. Multimaterial Corrosion Inhibition in the Al - Cu - CFRP Galvanic system: Insight into the Electrochemical Response of the Cathodes to Changes in Local pH.....	214
6.4.3. Multimaterial Corrosion Inhibition in the Al - Cu - CFRP Galvanic system: Insight into Significant Changes in Test Solution Composition.....	216
6.4.4. Multimaterial Corrosion Inhibition in the Al - Cu - CFRP Galvanic system: Insight into Significant Changes in Oxygen Concentration Near Component Materials.....	218
6.4.5. Multi-material Corrosion Inhibition in the Al - Cu - CFRP Galvanic system: Effect of Inhibitor Combinations (Ce(NO ₃) ₃ + BTA) on the Al - Cu - CFRP Galvanic Couple.....	219
6.4.6. Proposed Mechanism(s) of Multi-material Corrosion Inhibition in the Al - Cu - CFRP Galvanic system.....	222
6.5. Chapter Summary.....	225

Chapter 7

Multi-material Corrosion Inhibition in the Zn - Fe - CFRP Galvanic system.....	229
7.0. Results of Tests on Galvanic Couples in the Zn - Fe - CFRP Galvanic System.....	229
7.1.0. Overview of Macro Studies of Multi-material Corrosion Inhibition in the Zn - Fe - CFRP Galvanic system: Effect of Inhibitors on the Zn -Fe - CFRP Galvanic System.....	229
7.2.0. Overview of Macro Studies of Multi-material Corrosion Inhibition in the Zn - Fe - CFRP Galvanic system: Effect of Selected Inhibitor Combinations on Galvanic Corrosion of Dual Galvanic Couples in the Zn -Fe - CFRP Galvanic System.....	233
7.3.0 Effect of Single Inhibitors on the Galvanic Corrosion of Zn - Fe, Zn - CFRP, and Fe - CFRP Dual Material Galvanic Couples.....	237
7.3.1. Effect of Azoles on the Galvanic Corrosion of Zn - Fe, Zn - CFRP, and Fe - CFRP Galvanic Couples.....	238
7.3.2. Effect of Rare-Earth Cations on the Galvanic Corrosion of Zn - Fe, Zn - CFRP, and Fe - CFRP Galvanic Couples.....	241
7.3.3. Effect of Conjugate ion of Rare earths on the Galvanic Corrosion of Zn - Fe, Zn - CFRP, and Fe - CFRP Galvanic Couples.....	250
7.4. The Nature and Changes in the Local Environment Near Constituent Materials of the Zn - Fe - CFRP Multi-material Galvanic System.....	255
7.5. Proposed Mechanism(s) of Multi-material Corrosion and Multi-material Corrosion Inhibition in the Zn - Fe - CFRP Multi-Material Combination.....	259
7.5. Chapter Summary.....	266

Chapter 8

Conclusions and Future Outlook.....	269
8.0. Conclusions and Recommendations.....	269
8.1. Conclusions.....	269
8.2. Recommendations/Future Outlook.....	272
References.....	275

Abbreviations

General symbols and abbreviation

A	Surface area
C	Capacitor in equivalent circuits
C_{ads}	Adsorbed layer capacitance
C_{dl}	Double layer capacitance
C, C_{ox}, C_{red}	Concentration, Concentration of oxidative and reductive species
CFRP	Carbon fiber reinforced polymers
CE	Counter electrode
CPE	Constant phase element
D_{ox}, D_{red}	Diffusion coefficient of oxidative and reductive species
E	Electrode potential
E_{corr}	Corrosion potential
E_o/E_{eq}	Equilibrium potential
E_{pit}	Pitting potential
ΔG	Free energy
i_{corr}	Corrosion current density
j	Current density
i_L	Limiting current density
i_0	Exchange current density
I_0	Current amplitude
F	Faraday constant
f	Frequency
L	Inductor in equivalent circuits
n	Number of electrons involved in electrochemical process
nA	NanoAmperes
nm	Nanometer
ORR	Oxygen reduction reaction
Q	Fitting parameter of equivalent circuit with capacitor
r_f, r_b	Rates of forward and backward reaction
R	Resistor in equivalent circuits
R	Universal gas constant
RE	Reference electrode
Rads	Resistance of inhibitive layer
Rct	Charge transfer resistance
$R_p / R_p^{\#}$	Polarization resistance / pseudo-polarization resistance
Rsol	Solution resistance
s	Seconds
SCC	Stress corrosion cracking
SCE	Saturated calomel electrode
SHE	Standard Hydrogen Electrode
t	Time
T	Temperature
V0	Voltage amplitude
W, Z_w	Warburg impedance
WE	Working electrode
Y_0	Admittance
Z, $Z_0, Z(\omega)$	Impedance

Z', Z''	Real and imaginary part of impedance
β_a, β_c	Cathodic and anodic Tafel constant
V	Potential
δ	Diffusion layer thickness
ϵ	Dielectric permittivity
ϵ_0	Dielectric permittivity of vacuum
η	Polarization
η_a	Cathodic polarization
η_c	Anodic polarization
η_{act}, η_{conc}	Activation and concentration polarization
μm	Micrometer/micron
ρ	Specific resistance/density
σ	Warburg coefficient
τ	Time constant
ϕ	Phase shift
ω	Angular frequency
φ	Galvani potential
ψ	Volta potential
χ	Surface potential

Experimental techniques

DC-polarization	Direct current polarization
EDS	Energy Dispersive Spectroscopy
EIS	Electrochemical impedance spectroscopy
SEM	Scanning Electron Microscopy
SIET	Scanning Ion-Selective Electrode Technique
SKPFM	Scanning Kelvin Probe Microscopy
SVET	Scanning Vibrating Electrode Technique
TOF-SIMS	Time of flight Secondary Ions Mass Spectroscopy
XPS	X-ray Photoelectron Spectroscopy

Inhibitors

BIA	Benzimidazole
BTA	Benzotriazole
RE	Rare-earth

List of Figures

	Page
Fig. 2.1. Illustration of the multi-material design concept as employed in the “Superlight car”	6
Fig. 2.2. Illustration of Multi-Material design concepts.....	6
Fig. 2.3. Illustration of extensive use of composites in a multi-material design concept in the Boeing 787.....	6
Fig. 2.4. Equilibrium diagram for Aluminium E-pH diagram for pure Al at 25°C in aqueous solution (adapted from Pourbaix 1974).....	13
Fig. 2.5. Illustration of mixed-potential theory for zinc corrosion in de-aerated acid.....	15
Fig. 2.6. The corrosion rate of Aluminium as a function of pH.....	22
Fig. 2.7. The composite potentiodynamic polarization of aluminium polarized in the anodic and cathodic direction from E_{corr} in 0.05 M Na_2SO_4 adjusted to (a) pH 2, (b) pH 7 and (c) pH 10...	22
Fig. 2.8. Effect of addition of impurities ($FeCl_3$ and $CuCl_2$) on the dissolution of Aluminium in 0.30 N sodium hydroxide at 23°C.....	27
Fig. 2.9. Pourbaix diagrams for Cu - Cl- H_2O system for various chloride concentrations. (a) 10^{-3} M, (b) 10^{-2} M, (c) 0.1 M, and (d) 1.0 M.....	29
Fig. 2.10. Schematic illustration showing the possible passive layer structures on copper at different constant potential (E_s) values.....	33
Fig. 2.11. Pourbaix diagram for Fe-Cl- H_2O at 25°C.....	35
Fig. 2.12. Potential-pH equilibrium diagram for the zinc-water system at 25°C.....	39
Fig. 2.13. Plot of E_{corr} vs. i_{corr} for zinc at different pH in 0.1 M NaCl.....	39
Fig. 2.14. Regions of existence of zinc corrosion products in aqueous media as a function of pH and Cl^- concentration.....	40
Fig. 2.15. Functional groups on carbon surfaces.....	45
Fig. 2.16. Illustration of edge and basal plane sites on carbon materials and their different electrochemical response.....	48
Fig. 2.17. Schematic illustration of proposed model for the origin of the porous electrode effect in cathodically polarized CFRP samples (a) Intact CFRP sample (b) Degraded CFFRP.....	51
Fig. 2.18. Schematic illustration of how the surface charge relative to $E_{q=0}$ affects the adsorption mechanism of aniline onto mild steel surface in HCl solution.....	60
Fig. 2.19. Schematic illustration of the mechanism of anodic and cathodic inhibitors.....	67
Fig. 2.20. Schematic illustration of aniline adsorption on Zn and Fe galvanically coupled and uncoupled.....	70
Fig. 3.1. Schematic illustration of typical OCP - time profiles and their indications.....	78
Fig. 3.2. Potential time dependence in cyclic voltammetry.....	82
Fig. 3.3. Schematic illustration of the voltammogram of a reversible couple.....	84
Fig. 3.4. Sinusoidal current response in a linear system to a sinusoidal applied voltage.....	86
Fig. 3.5. Illustration of Nyquist plot.....	87
Fig. 3.6. Illustration of Bode plot.....	88
Fig. 3.7. Schematic representation of the basic components of a SVET equipment with the components of the electrochemical cell.....	94
Fig. 3.8. Schematic illustration of the general principle of pH measurement.....	97
Fig. 3.9. The three different types of light scattering.....	100
Fig. 3.10. Illustration of cathodic sputtering process in glow discharge.....	105
Fig. 4.1. Schematic illustration of epoxy mounted specimens for a triple system.....	110
Fig. 4.2. Schematic illustration of arrangement of dual galvanic couples.....	112
Fig. 4.3. Schematic illustration of the scanning sequence for dissolved oxygen spatial	

measurements.....	114
Fig. 5.1. Open circuit evolution for materials in 50 mM NaCl solution.....	118
Fig. 5.2. Potentiodynamic polarization scan for five materials in 50 mM NaCl solution after 1 hour immersion (a) scan from cathodic to anodic potentials (b) merged cathodic anodic scans 10 mV from OCP values.....	119
Fig. 5.3. Bode plots for the 5 materials after 1 hour immersion in 50 mM NaCl solution.....	120
Fig. 5.4. SKPFM measured topography (a) and (b) Volta potential profiles for polished CFRP sample.....	121
Fig. 5.5. Confocal Raman spectra of components of CFRP (Inset is the combined image generated).....	122
Fig. 5.6. Simultaneous chronoamperometric and local pH measurements on CFRP in 50 mM NaCl.....	124
Fig. 5.7. Simultaneous potentiodynamic polarization and local pH measurements on CFRP in 50 mM NaCl.....	124
Fig. 5.8. Open circuit evolution for CFRP in chloride solutions of varying pH.....	126
Fig. 5.9. Cathodic potentiodynamic polarization curves for CFRP in chloride solutions of varying pH at scan rate of 1 mV s^{-1}	127
Fig. 5.10. Cyclic voltammogram of CFRP at a scan rate of 50 mV s^{-1} in chloride solutions at (a) 50 mM HCl at pH 1, at (b) 50 mM NaCl at pH 3, (c) 50 mM NaCl at pH 7, (d) 50 mM NaCl at pH 10, (e) 50 mM NaCl at pH 12, and (f) comparison of the second scans at different pH.	128
Fig. 5.11. Cyclic voltammogram of CFRP in 50 mM NaCl at a scan rate of 50 mV s^{-1}	129
Fig. 5.12. Equivalent circuits used to fit impedance spectra.....	130
Fig. 5.13. Nyquist and Bode plots for CFRP at OCP after immersion in 50 mM NaCl solutions for different time durations.....	130
Fig. 5.14. Evolution of (a) low frequency impedance ($ Z _{0.01} \text{ Hz}$) and charge transfer resistance (R_{ct}), and (b) double layer capacitance with time for CFRP immersed in 50 mM NaCl at OCP.....	131
Fig. 5.15. Nyquist and Bode plots for CFRP at open circuit potential in un-buffered chloride solutions at different pH after 2 hours of immersion.....	132
Fig. 5.16. Evolution of (a) low frequency impedance ($ Z _{0.01} \text{ Hz}$) and charge transfer resistance (R_{ct}), and (b) double layer capacitance and open circuit potential with pH for CFRP immersed in un-buffered chloride solutions after 2 hours of immersion.....	133
Fig. 5.17. Bode plots for CFRP after immersion in buffer solutions for 20 and 120 hours and then tested after 2 hours immersion in 50 mM NaCl solution.....	134
Fig. 5.18. Evolution of low frequency impedance ($ Z _{0.01} \text{ Hz}$) with pH of buffer solutions after 20 and 120 hours immersion.....	134
Fig. 5.19. Evolution of (a) double layer capacitance and (b) charge transfer resistance for CFRP as a function of pH of buffer solution at different exposure times.....	135
Fig. 5.20. Nyquist and Bode plots for CFRP after 20 hours immersion in pH 10 buffer solution and sequential testing in NaCl and HCl solutions (a-c) tests started in HCl solution and (d-f) tests started in 50 mM NaCl (symbols are measured data while lines are fitted data using equivalent circuit of Fig. 5.12).....	137
Fig. 5.21. Extracted EIS parameters from sequential testing of CFRP in NaCl-HCl-NaCl- and HCl-NaCl-HCl- sequence in 2 hour intervals after immersion in pH 10 buffer solution for 20 hours.....	138
Fig. 5.22. Nyquist and Bode plots for CFRP after 20 hours immersion in pH 12 buffer solution and sequential testing in NaCl and HCl solutions (a-c) tests started in HCl solution and (d-f) tests started in 50 mM NaCl (symbols are measured data while lines are fitted data using equivalent circuit of Fig. 5.12).....	139

Fig. 5.23. Extracted EIS parameters from sequential testing of CFRP in NaCl-HCl-NaCl- and HCl-NaCl-HCl- sequence in 2 hour intervals after immersion in pH 12 buffer solution for 20 hours.....	140
Fig. 5.24. SEM images of CFRP after immersion in solutions of varying pH.....	141
Fig. 5.25. Raman Spectra of CFRP components after immersion in solutions of varying pH, (a) for carbon fibers and (b) for the epoxy matrix.....	142
Fig. 5.26. Raman images of CFRP after immersion in solutions of varying pH.....	143
Fig. 5.27. Selected Bode plots of EIS spectra of CFRP in 50 mM NaCl at 0 mV, -100 mV, -250 mV, 300 mV, -375 mV, and -500 mV _{SCE} to monitor diffusion effects.....	144
Fig. 5.28. Bode plot of EIS spectra of CFRP in 50 mM NaCl at different polarizations between +250 and -500 mV _{SCE} to monitor diffusion effects.....	145
Fig. 5.29. Parameters extracted from the EIS spectra as a function of potential around the diffusion limited potential ranges for CFRP in 50 mM NaCl, (a) low frequency impedance at 10 ⁻² Hz, (b) calculated double layer capacitances, (c) evolution of polarization or charge transfer resistance (R _p or R _{ct}), and the resistive component of Warburg impedance (W _{S-R}), and (d) the diffusion layer thickness estimated from EIS data.....	146
Fig. 5.30. SEM images of CFRP as received (a), and after immersion in 50 mM NaCl for 2 hours at (b) +1000 mV and (c) -1000 mV _{SCE} respectively.....	148
Fig. 5.31. Raman spectra of CFRP components (a) carbon fibers and (b) the epoxy matrix in the as received condition, and after immersion in 50 mM NaCl for 2 hours at +1000 mV and -1000 mV _{SCE} respectively.....	149
Fig. 5.32. Raman mapping of CFRP as received (a), and after immersion in 50 mM NaCl for 2 hours at (b) +1000 mV and (c) -1000 mV _{SCE} respectively.....	150
Fig. 5.33. Postulated scheme for using trends of EIS parameter to monitor degradation in CFRP.....	150
Fig. 5.34. Nyquist plot for CFRP after 2 hours immersion in 50 mM NaCl solution adjusted to pH 10.5 at different polarizations.....	152
Fig. 5.35. Bode plot for CFRP after 2 hours immersion in 50 mM NaCl solution adjusted to pH 10.5 at different polarizations.....	152
Fig. 5.36. Plots of (a) low frequency impedance at 0.01 Hz (IZI0.01 Hz) and (b) "pseudo polarization resistance" (Rp#) evolution for CFRP after immersion for 2 hours in chloride solutions of different pH and at different applied potentials.....	153
Fig. 5.37. Cathodic Potentiodynamic polarization scans of CFRP in different inhibitor solutions..	156
Fig. 5.38. Zoomed section of cathodic potentiodynamic polarization scans of CFRP in different inhibitor solutions.....	157
Fig. 5.39. Cathodic potentiodynamic polarization scans on CFRP in 50 mM NaCl with different concentrations of sodium dodecyl sulphate (SDS).....	158
Fig. 5.40. Extracted EIS fit parameters for CFRP in 50 mM NaCl without cathodic polarization in the absence and presence of 5 mM SDS, (a) low frequency impedance at 10 ⁻² Hz, (b) resistance polarization, (c) double layer capacitance, (d) inset of capacitive section of impedance spectra, (e) Phase angle plot, and (e) impedance spectra (full range).....	159
Fig. 5.41. Extracted EIS fit parameters for CFRP in 50 mM NaCl with applied cathodic polarization of -1000 mV in the presence of 5 mM SDS, (a) low frequency impedance at 10 ⁻² Hz, (b) polarization resistance, (c) double layer capacitance, and (d) the bode plot.....	160
Fig. 5.42. Extracted EIS fit parameters for sequential tests on CFRP, (a) low frequency impedance at 10 ⁻² Hz, (b) resistance polarization, (c) double layer capacitance, (d) section of impedance spectra (e) phase angle, and (f) full range of impedance spectra.....	162
Fig. 5.43. Cathodic potentiodynamic polarization scans on CFRP in different	

concentrations of (a) 1,2,3 - triazole and (b) 1,2,4 - triazole.....	164
Fig. 5.44. Cathodic potentiodynamic polarization scans on CFRP in different concentrations of (a) benzimidazole (BIA) and (b) benzotriazole (BTA).....	165
Fig. 5.45. Extracted EIS fit parameters for CFRP in 50 mM NaCl with applied cathodic polarization of -1000 mV in the presence of different azoles compounds, (a) low frequency impedance at 10^{-2} Hz, (b) polarization resistance, (c) double layer capacitance and (d) the Bode plot of the measured spectra.....	166
Fig. 5.46. Cathodic potentiodynamic polarization scans on CFRP in 50 mM NaCl with different concentrations of (a) lanthanum nitrate and (b) cerium nitrate.....	166
Fig. 5.47. Cathodic potentiodynamic polarization scans on CFRP in 50 mM NaCl with different concentrations of cerium chloride.....	167
Fig. 5.48. Extracted EIS fit parameters for CFRP in 50 mM NaCl with applied cathodic polarization of -1000 mV in the presence of different nitrate and nitrite based solutions, (a) low frequency impedance at 10^{-2} Hz, (b) polarization resistance, (c) double layer capacitance, and (d) the bode plot of the measured spectra.....	168
Fig. 5.49. Cathodic potentiodynamic polarization scans on CFRP in 50 mM NaCl with different concentrations of lanthanum acetate.....	169
Fig. 5.50. Extracted EIS fit parameters for CFRP in 50 mM NaCl with applied cathodic polarization of -1000 mV in the presence of different acetate based solutions, (a) low frequency impedance at 10^{-2} Hz, (b) polarization resistance, (c) double layer capacitance, and (d) the Bode plot of the measured spectra.....	170
Fig. 5.51. Cathodic potentiodynamic polarization scans on CFRP in 50 mM NaCl with different concentrations of Na_3PO_4 and NaH_2PO_4	171
Fig. 5.52. Cathodic potentiodynamic polarization scans on CFRP in 50 mM NaCl with different concentrations of sodium molybdate.....	172
Fig. 5.53. Plots of (a) low frequency impedance (IZI), (b) polarization resistance (R_p), and (c) double layer capacitance for CFRP under -1000 mV SCE cathodic polarization in different phosphate and molybdate based solutions.....	173
Fig. 5.54. Cathodic potentiodynamic polarization scans on CFRP in 50 mM NaCl with different concentrations of the combination of cerium nitrate and benzotriazole.....	174
Fig. 5.55. Plots of (a) low frequency impedance (IZI), (b) polarization resistance (R_p), (c) double layer capacitance, and (d) measured EIS spectra for CFRP under -1000 mV SCE cathodic polarization in 50 mM NaCl containing different combinations of nitrates and benzotriazole.....	175
Fig. 5.56. Plots of (a) low frequency impedance (IZI), (b) polarization resistance (R_p), (c) double layer capacitance, and (d) measured EIS spectra for CFRP under -1000 mV SCE cathodic polarization in 50 mM NaCl containing different combinations of acetates and benzotriazole.....	176
Fig. 6.1. ZRA results for 9 dual galvanic couples in 50 mM NaCl (a and c) galvanic current density evolution with time, and (b and d) potential evolution with time.....	181
Fig. 6.2. Potentiodynamic polarization scans for 9 dual galvanic couples after 1 hour immersion in 50 mM NaCl.....	182
Fig. 6.3. Nyquist and Bode plots for 9 dual galvanic couples after 1 hour immersion in 50 mM NaCl.....	183
Fig. 6.4. Effect of selected combination of inhibitors on evolution of (a) galvanic current density and (b) for Al - Cu - CFRP galvanic couple in 50 mM NaCl.....	187
Fig. 6.5. Effect of selected combination of inhibitors on the potentiodynamic polarization curves for Al - Cu - CFRP in 50 mM NaCl (b) is magnified section of the potentiodynamic curves..	188

Fig. 6.6. Effect of selected combination of inhibitors on evolution of galvanic current densities and potentials for (a-b) Al - CFRP, (c-d) Al - Cu, and (e-f) Cu - CFRP galvanic couples in 50 mM NaCl based inhibitor solutions.....	190
Fig. 6.7. Effect of selected combination of inhibitors on the potentiodynamic curves of (a) Al - CFRP, (b) Al - Cu, and (c) Cu - CFRP galvanic couples in 50 mM NaCl based inhibitor solutions after 1 hour immersion.....	193
Fig. 6.8. Effect of azole inhibitors on evolution of galvanic current densities and potentials for (a-b) Al - CFRP, (c-d) Al - Cu, and (e-f) Cu - CFRP galvanic couples in 50 mM NaCl based inhibitor solutions.....	195
Fig. 6.9. Effect of azole inhibitors on the potentiodynamic curves of (a) Al - CFRP, (b) Al - Cu, and (c) Cu - CFRP galvanic couples, and (d) aluminium, (e) copper, and (f) CFRP in 50 mM NaCl based inhibitor solutions after 1 hour immersion.....	196
Fig. 6.10. Effect of rare-earth nitrate inhibitors on evolution of galvanic current densities and potentials for (a-b) Al - CFRP, (c-d) Al - Cu, and (e-f) Cu - CFRP galvanic couples in 50 mM NaCl based inhibitor solutions.....	198
Fig. 6.11. Effect of nitrate inhibitors on the potentiodynamic curves of (a) Al - CFRP, (b) Al - Cu, and (c) Cu - CFRP galvanic couples, and (d) aluminium, (e) copper, and (f) CFRP in 50 mM NaCl based inhibitor solutions after 1 hour immersion.....	200
Fig. 6.12. Effect of rare-earth acetate inhibitors on evolution of galvanic current densities and potentials for (a-b) Al - CFRP, (c-d) Al - Cu, and (e-f) Cu - CFRP galvanic couples in 50 mM NaCl based inhibitor solutions.....	202
Fig. 6.13. Effect of acetate inhibitors on the potentiodynamic curves of (a) Al - CFRP, (b) Al - Cu, and (c) Cu - CFRP galvanic couples, and (d) aluminium, (e) copper, and (f) CFRP in 50 mM NaCl based inhibitor solutions after 1 hour immersion.....	203
Fig. 6.14. Effect of conjugate anion of rare-earth metal salts on the galvanic current density and (b) potential evolution of (a-b) Al - CFRP, (c-d) Al - Cu, and (e-f) Cu - CFRP galvanic couples in 50 mM NaCl based inhibitor solutions.....	207
Fig. 6.15. Effect of conjugate anion of rare-earth metal salts on the potentiodynamic polarization curves of (a) Al - CFRP, (b) Al - Cu, and (c) Cu - CFRP, (d) Al, (e) Cu, and (f) CFRP in 50 mM NaCl based inhibitor solutions after 1 hour immersion.....	208
Fig. 6.16. pH profile in 50 mM NaCl 12 μ m above (a-b) galvanically coupled and uncoupled Al - CFRP and (c-d) 40 μ m above galvanically coupled Al - Cu - CFRP "triplet" couple.....	213
Fig. 6.17. Cyclic voltammogram of copper after 1 hour immersion in quiescent 50 mM NaCl adjusted to different pH and testing under quiescent conditions and anoxic conditions respectively by purging with argon for 15 minutes prior to and during testing.....	215
Fig. 6.18. Time evolution of copper concentration in 50 mM NaCl solution for (a) Al - Cu galvanically coupled and uncoupled (surface area of Cu and Al was 0.5 cm ² and volume of test solution = 100 ml).....	216
Fig. 6.19. Measured cathodic currents due to oxygen reduction \approx 100 μ m above components of the Al-Cu-CFRP system (a) galvanically coupled, and (b) uncoupled indicative of O ₂ distribution..	218
Fig. 6.20. Measured cathodic currents due to O ₂ reduction \approx 100 μ m above galvanically coupled components of the Al-Cu-CFRP system (a) 30 min after immersion in 50 mM NaCl containing 2.5 mM each of Ce(NO ₃) ₃ and BTA after prior immersion in 50 mM NaCl solution for 150 mins, (b) 30 mins after polishing and immersion in same inhibitor solution indicative of the oxygen distribution.....	220
Fig. 6.21. Measured cathodic currents due to O ₂ reduction \approx 100 μ m above non-galvanically coupled components of the Al-Cu-CFRP system 60 mins after immersion in 50 mM NaCl containing 2.5 mM each of Ce(NO ₃) ₃ and BTA indicative of oxygen distribution.....	220

Fig. 6.22. X-ray fluorescence mapping of surfaces of aluminium and copper of coupled Al - Cu galvanic couple after exposure 50 mM NaCl containing 2.5 mM (Ce(NO ₃) ₃ + BTA).....	221
Fig. 6.23. Illustration of plausible mechanism of multi-material corrosion in the Al - Cu - CFRP multi-material galvanic system.....	222
Fig. 6.24. Illustration of the different plausible scenarios in the mechanism of multi-material corrosion inhibition in the Al - Cu - CFRP multi-material system (wavy arrows denote adsorption based inhibitors while the straight arrows denote precipitation based inhibitors).....	224
Fig. 7.1. Effect of selected inhibitor combinations on the time evolution of galvanic current densities of Zn - Fe - CFRP "triplet" galvanic couple in 50 mM NaCl (Zn - Fe was coupled together with galvanic currents measured between Zn - Fe and CFRP).....	231
Fig. 7.2. Effect of selected inhibitor combinations on the potentiodynamic polarization curves for Zn - Fe - CFRP in 50 mM NaCl after 1 hour immersion.....	232
Fig. 7.3. Effect of selected inhibitor combinations on the time evolution of galvanic current densities of (a) Zn - Fe, (b) Zn - CFRP, and (c) Fe - CFRP couples of the Zn - Fe - CFRP galvanic system couple in 50 mM NaCl.....	234
Fig. 7.4. Effect of selected inhibitor combinations on potentiodynamic polarization curves of (a) Zn - Fe, (b) Zn - CFRP, and (c) Fe - CFRP couples of the Zn-Fe-CFRP galvanic system couple in 50 mM NaCl.....	236
Fig. 7.5. Effect ofazole inhibitors on the time evolution of galvanic current densities and galvanic potential respectively of (a-b) Zn - Fe, (c-d) Zn - CFRP, and (e-f) Fe - CFRP couples of the Zn-Fe-CFRP galvanic system couple in 50 mM NaCl.....	239
Fig. 7.6. Effect ofazole inhibitors on the potentiodynamic polarization curves of (a) Zn - Fe, (b) Zn ,(c) Zn - CFRP, (d) Fe, (e) Fe - CFRP, and (f) CFRP after 1 hour immersion in different azoles in 50 mM NaCl.....	240
Fig. 7.7. Effect of nitrate inhibitors on the time evolution of galvanic current densities and galvanic potential repectively of (a-b) Zn - Fe, (c-d) Zn - CFRP, and (e-f) Fe - CFRP couples of the Zn - Fe - CFRP galvanic system couple in 50 mM NaCl.....	243
Fig. 7.8. Effect of nitrate inhibitors on the potentiodynamic polarization curves of (a) Zn - Fe, (b) Zn ,(c) Zn - CFRP, (d) Fe, (e) Fe - CFRP, and (f) CFRP after 1 hour immersion in different azoles in 50 mM NaCl.....	245
Fig. 7.9. Effect of acetate inhibitors on the time evolution of galvanic current densities and galvanic potential repectively of (a-b) Zn - Fe, (c-d) Zn - CFRP, and (e-f) Fe - CFRP couples of the Zn-Fe-CFRP galvanic system couple in 50 mM NaCl.....	247
Fig. 7.10. Effect of acetate inhibitors on the potentiodynamic polarization curves of (a) Zn - Fe, (b) Zn - CFRP, and (c) Fe - CFRP after 1 hour immersion in different acetates in 50 mM NaCl.....	248
Fig. 7.11. Effect of acetates on the potentiodynamic polarization curves of (a) zinc, (b) iron and (c) CFRP in 50 mM NaCl based solutions after 1 hour immersion.....	249
Fig. 7.12. Effect of conjugate anion of rare-earth metal salts on the time evolution of galvanic current densities and galvanic potential respectively of (a-b) Zn - Fe, (c-d) Zn - CFRP, and (e-f) Fe - CFRP couples of the Zn - Fe - CFRP galvanic system couple in 50 mM NaCl.....	251
Fig. 7.13. Effect of conjugate anion of rare-earth metal salts on the potentiodynamic polarization curves of (a) Zn - Fe, (b) Zn - CFRP, and (c) Fe - CFRP, (d) Zn, (e) Fe, and (f) CFRP in 50 mM NaCl based inhibitor solutions after 1 hour immersion.....	254
Fig. 7.14. pH profile across connected Zn - Fe - CFRP in 50 mM NaCl solution.....	255
Fig. 7.15. X-ray fluorescence mapping of surfaces of Zinc and Iron of coupled Zn - Fe galvanic couple after exposure 50 mM NaCl containing 2.5 mM (Ce(NO ₃) ₃ + BTA).....	257

Fig. 7.16. X-ray fluorescence mapping of surfaces of Zinc and Iron of uncoupled Zn - Fe galvanic couple after exposure 50 mM NaCl containing 2.5 mM (Ce(NO ₃) ₃ + BTA).....	258
Fig. 7.17. Illustration of the mechanism of multi-material corrosion in the Zn -Fe - CFRP multi-material system.....	259
Fig. 7.18. Changes in Fe concentrations in 50 mM NaCl solution as a function of time for galvanically coupled and uncoupled Zn - Fe.....	261
Fig. 7.19. Illustration of the different plausible scenarios in the mechanism of multi-material corrosion inhibition in the Zn - Fe - CFRP multi-material system (wavy arrows denote adsorption based inhibitors while the straight arrows denote precipitation based inhibitors).....	262

List of Tables

	Page
Table 3.1. Circuit elements.....	89
Table 6.1. Shortlist of potential multi-material corrosion inhibitors for the Al-Cu-CFRP galvanic system on the basis of measured galvanic current densities in $\mu\text{A cm}^{-2}$ after 150,000 seconds immersion (figures in parentheses are calculated inhibition efficiencies).....	186
Table 7.1. Shortlist of potential multi-material corrosion inhibitors for the Zn-Fe-CFRP galvanic system on the basis of measured galvanic current densities in $\mu\text{A cm}^{-2}$ after 150,000 seconds immersion (figures in parentheses are calculated inhibition efficiencies).....	230
Table 7.2. Precipitation pH Values of Rare Earth Hydroxides at Precipitation Incidence.....	265

CHAPTER 1

INTRODUCTION

1.1. Background to Research

Corrosion which is the loss or degradation of a material or its functional properties due to interaction with environment [1] has been calculated to cost between 3.5 to 5 % of an industrialized nation's Gross National Product (GNP) out of which about 10 to 45 % can be prevented [2,3]. The cost of corrosion is composed of direct costs due to the cost of protection and replacement of corroded equipment, and indirect costs due to plant shutdown, over-design to hedge against corrosion, corrosion related explosions and accidents, loss of efficiency and/or products, cost of environmental pollution and/or product contamination and the associated remediation cost [4]. The "preventable corrosion costs" are costs that can be avoided by more efficient utilization of currently available corrosion mitigation technologies coupled with greater corrosion education and awareness, while the "unavoidable corrosion costs" arise from the nature of the corrosion process [5], and the limitations of available corrosion mitigation technologies. However, through research and development of new and improved corrosion mitigation strategies, the possibility of reducing the currently high percentage of "unavoidable corrosion costs" can be achieved. The achievement of this goal is however greatly dependent on better understanding of the corrosion mechanisms in applications of interest.

The trend towards complex design in engineering structure, is prevalent today and has resulted in the emergence of multi-material combinations with attendant corrosion implications. This multi-material design trend is driven by new design demands and concepts. For instance in the transport industry the demand and concepts of "light car" and "green aircraft" which requires significant weight reduction aimed at reducing fuel consumption and CO₂ emissions, have resulted in the use of new material combinations for increased strengths at reduced weights. Efforts at such weight optimized structures predominant in the aeronautical and aerospace industries results in the use of hybrid structures composed of multi-material combinations. The most technologically relevant of these multi-material combinations to the transport industry involves the use of carbon fibre reinforced composites together with high strength but low density metals and alloys, a combination that yields composite structures with spectacular mechanical properties and light weight. Success with these multi-material combinations have led to progressive increase in percentage of the non-metallic constituents in transport vessels, the development of super-light cars and the emergence of the more technologically advanced and environmentally benign class of aircrafts such as Boeing 787

Dreamliner, with ≈ 50 % composite content in the airframe [6], Airbus's A350 XWB with 52 % composite content in the airframe [7], and 90% composite content in the experimental aircraft Voyager [8,9].

However, these multi-material combinations are particularly susceptible to galvanic corrosion. For multi-material combinations composed exclusively of metals and alloys several corrosion mitigation strategies initially developed for individual metals and alloys involving smart usage of corrosion inhibitors such as active corrosion protection [10-13], self-healing coatings [12,14-17], sol-gel coatings [18], use of single inhibitor with mixed inhibition capability [19] and use of synergistic mixture of corrosion inhibitors [20,21] were reported.

Galvanic corrosion in multi-material combinations incorporating carbon fibre reinforced polymers is favoured by the carbon's well known ability to support cathodic reactions [22-30] that makes galvanic corrosion mitigation in such assemblies a difficult task. The carbon in the carbon fibre reinforced polymers (CFRP) not being metallic, is not very receptive to corrosion mitigation strategies employed for metals acting as cathodes, creating a need for application-sensitive galvanic corrosion protection solutions. To develop such corrosion mitigation strategies targeted at multi-material assemblies incorporating carbon fibre reinforced polymers (CFRP), it is necessary to understand the electrochemical behaviour of CFRP under a wide range of cathodic polarizations it can be polarized to in its different applications with a variety of metals and alloys. Hence, for those multi-material combinations incorporating carbon fibre reinforced polymers, there is a need for sufficient understanding of the corrosion mechanisms involved, and development of appropriate corrosion mitigation solutions that can potentially enhance the safety and service life of such hybrid structures. This thesis is therefore, the product of an effort to meet this technological need.

1.2. Significance of Study

The main aim of this work is to achieve a better understanding of the corrosion mechanism(s) due to galvanic coupling in different multi-material combinations of metals incorporating carbon fiber reinforced polymers (CFRP), and based on these findings recommend possible multi-material corrosion inhibition strategies.

Deeper understanding of the corrosion issues and mechanism in such complex material combinations is vital to the development of corrosion mitigation (inhibition) solutions capable of multiple or simultaneous protection of the various materials employed in complex structures. A lack of this knowledge can be a limiting factor to the application of the multi-material design

concept in a variety of applications or a significant reduction in the service life of such structures. Since the current anti-corrosion approaches are mainly suitable for single material structures and to a smaller degree multi-metal/alloy structures, it is a crucial need to develop new strategies of active and passive corrosion protection for multi-material applications. This is not possible in the absence of a detailed knowledge of the mechanisms of the corrosion processes. Though lighter metals (aluminium, magnesium) and alloys are widely used in such combinations, multi-material combinations involving carbon fiber reinforced plastics (CFRP) continue to gain acceptance. The knowledge of galvanic corrosion of multi-material combinations, especially in the case of new alloys and CFRPs, is limited and scarce in published literature. The situation is much more difficult in the case of triple or more combinations.

1.3. Study Objectives

The objective of this thesis is to investigate the mechanism of corrosion processes caused by galvanic coupling effects in a variety of multi-material systems employed particularly in the transport industry incorporating and not incorporating CFRP and then;

- (a) Based on the insight obtained from the above step(s), to develop the basic strategies for active corrosion protection in multi-material structures.
- (b) Undertake a multi-scale study of the kinetics and corrosion mechanisms present.
- (c) To screen and select potential corrosion inhibitors suitable to selected multi-material combinations.
- (d) Make recommendations on possible practical multi-material combinations from the corrosion point of view.

1.4. Research Strategy

To achieve the study objectives stated above, it was necessary to;

- (a) Develop macro-/micro-cells for evaluating galvanic corrosion in combinations of two and more materials.
- (b) Conduct tests at the macro-level using conventional electrochemical techniques (potentiodynamic polarization tests, open circuit potential measurements, galvanic current density measurements and electrochemical impedance spectroscopy).
- (c) Test at the micro-level using localized methods such as Scanning Vibrating Electrode Technique (SVET), and Scanning Ion-selective Electrode Technique (SIET).

This thesis is divided into eight chapters. Chapter 1 introduces the work, its objectives and significance. Chapter 2 is a review of scientific literature relevant to the understanding of the present work with emphasis on galvanic corrosion and the corrosion/degradation of the constituents of the multi-material combinations (aluminium, copper, iron, zinc, and carbon fibre reinforced polymer (CFRP)). Chapter 3 describes the principles of the experimental techniques employed in the study. Chapter 4 presents the actual experimental procedures employed and chapter 5 is a presentation and comparison of results of the electrochemical tests on the individual materials constituting the multi-material combinations, and the results and discussions of results of detailed study on CFRP. Chapter 6 presents the results and discussion of results from tests on the Al-Cu-CFRP multi-material system and its constituent dual galvanic couples while chapter 7 presents and discusses the results of tests on the Zn-Fe-CFRP multi-material system and its constituent dual galvanic couples. Chapter 8 is a presentation of conclusions drawn from the results and suggestions for further work.

CHAPTER 2

LITERATURE REVIEW

2.0 Introduction

Corrosion cost more than 3% of world GDP (1.17-1.56 € trillion), and is in excess of 200€ billion annually [31]. Galvanic corrosion is a major cause of corrosion damage in multi-material combinations. It can be defined as the accelerated corrosion of a metal due to electrical contact with a more noble metal or non-metallic conductor in a corrosive electrolyte [32]. In spite of galvanic corrosion effects, multi-material combinations are becoming more attractive for different applications especially in applications in which high mechanical properties and reduction in weight are simultaneously desirable as in the automotive and aerospace industries. The superlight car program launched by European car producers is one of such initiatives devoted to the development of new approaches for the design of cars using new and lighter materials [33], with the automotive industry aiming to reduce car body weight by around 35% [34]. The multi-material concept for automotive applications is being actively developed under the framework of European projects, Superlight Car [33-39] and NADIA European Project - New Automotive components Designed for and manufactured by Intelligent processing of light Alloys (NADIA) [40] aiming at weight reduction by using Al and Mg alloys together with composite materials. Multi-material design is probably quite common in the electronics industry. This multi-material design concept is most likely to be embraced in more sectors. However, the challenge of galvanic corrosion in multi-material combinations is crucial, hence the need for this study.

Among the materials increasingly employed in these multi-material (composite) design concepts aimed at weight reduction is carbon fiber reinforced plastics (CFRP). It is obvious that if carbon fiber reinforced plastic (CFRP) is brought into contact with for instance, aluminium alloy a strong galvanic couple is created due to difference in the electrochemical potential between the composite (cathode) and aluminium (anode). This is corroborated by a report [41] citing galvanic corrosion as one of the major challenges to the development of the multi-material automobiles. This problem of multi-material combinations is not restricted to the automobile industry, as the program of "green aircraft" promoted by Airbus aims at the reduction of aircraft weight by more extensive use of composite materials including CFRPs. Composite materials account for about 22% of the total weight of the A380 Airbus [42], while the content of composites in the Boeing 787 is roughly 50% [43,44].

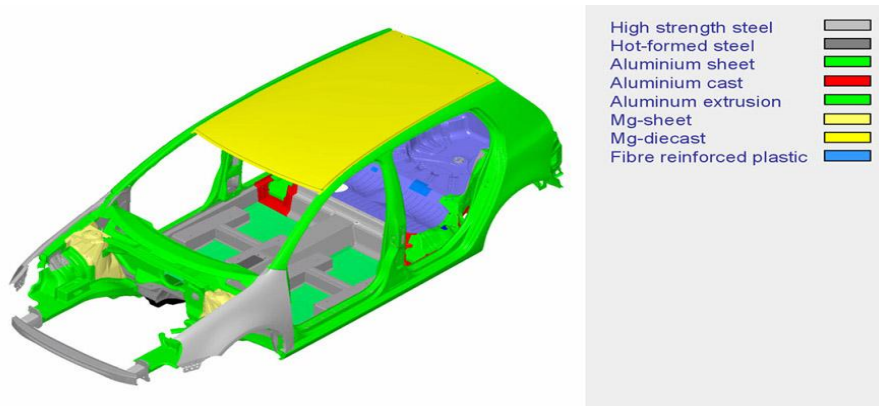


Fig. 2.1. Illustration of the multi-material design concept as employed in the “Superlight car” [39].

This multi-material design concept can be optimized with respect to production cost of an item or with respect to weight reduction as is predominant in the transport industry. With reference to Fig. 2.2 below, it can be inferred that galvanic corrosion challenges are more likely in the weight-optimized multi-material designs.

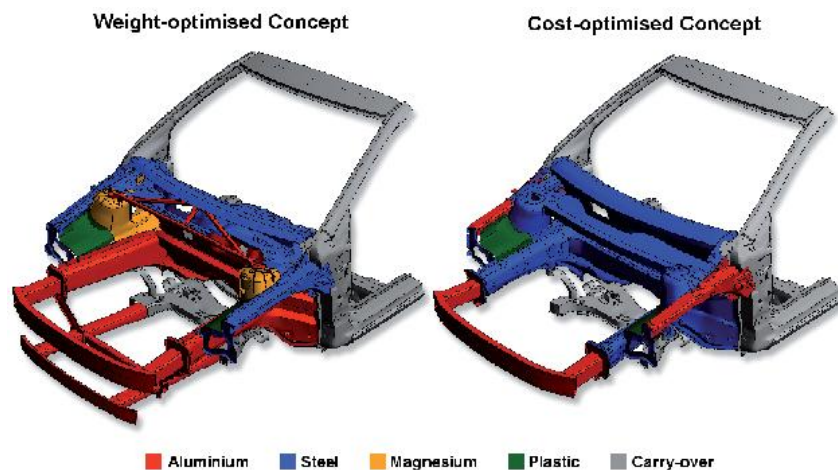


Fig. 2.2. Illustration of Multi-Material design concepts [45].

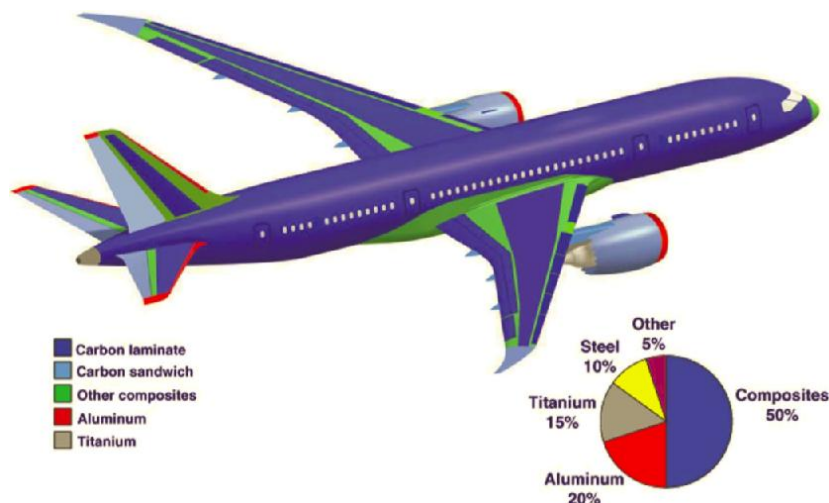


Fig. 2.3. Illustration of extensive use of composites in a multi-material design concept in the Boeing 787 [46].

In these applications carbon fiber reinforced plastic (CFRP) is introduced as a novel material component of composite and/or hybrid multi-material structures. Consequently knowledge of the galvanic compatibility of the electrically conductive CFRP with the different metallic constituents of such structures in possible operating environments is of utmost importance. However, reports in literature on galvanic compatibility of CFRP with several metals for other applications are limited. Brown and Coomber [47] reported a serious risk of galvanic corrosion at electrically connected graphite-epoxy composite materials (GECM)-aluminum joints and graphite-epoxy composite materials (GECM)-cadmium plated mild steel joints, but no risk for graphite-epoxy composite materials (GECM)-stainless steel or graphite-epoxy composite materials (GECM)-Ti-6Al-4V couples in aqueous 5% NaCl solutions. Johnston et al. [48], reported significant galvanic corrosion on coupling steel, aluminum and titanium with graphite-epoxy composite materials (GECM) in 1 M air saturated NaCl solution. Miller and Lee [49,50] measured the corrosion rates of selected aerospace alloys coupled to graphite-epoxy composite materials (GECM) in aerated neutral 3.5% NaCl solution (pH = 7) and determined acceptable galvanic compatibility only with Ti-6Al-4V, Ti-6Al-2Sn-4Zr-2Mo, Rene' 41, Inconel X, Inconel, AFC-77, PH 17-7, SS304, Be-Cu, SS301. Fischer and DeLuccia [51] confirmed Ti-6Al-4V alloy's superior galvanic corrosion resistance on coupling with graphite-epoxy composite materials (GECM) in neutral NaCl solution. Mueller et al., [52] reported remarkable localized corrosion on the stainless steel in contact with CFRP when immersed in simulated body fluid and corrosion induced delamination of carbon fibers in the composite. Danford and Higginns [53] working on effects of galvanic coupling between D6AC steel, 6061-T6 aluminum, Inconel 718, and Graphite-Epoxy Composite Material (GECM) in 3.5% NaCl reported severe galvanic corrosion occurring when bare 6061-T6 Al and D6AC steel are coupled to graphite-epoxy composite materials (GECM), while bare Inconel 718 is relatively unaffected and is compatible with graphite-epoxy composite materials (GECM). It has been reported also that CFRPs accelerate corrosion of reinforcing steel bars in concrete [54]. From the above reports, the galvanic corrosion challenge of galvanic coupling of CFRP/GECM to most metals and alloys with the exception of Ti-6Al-4V and stainless steel and a few specialty alloys, is obvious.

Reports in the scientific literature on multi-material corrosion have been scarce as most research reported has been limited to dual material corrosion or galvanic couples. The earliest and very significant work on multi-material corrosion was probably by Danford and Higginns [53] who reported that in a triple material galvanic couple comprising 6061-T6 Al - D6AC steel - Graphite-Epoxy Composite Material (GECM) that 6061-T6 Al act as an effective sacrificial anode,

providing cathodic protection to D6AC steel. Ambat and Per Møller with respect to corrosion in the electronic industry reported [55] the corrosion of the multi-material combinations in a mobile phone dome–key pad system consisting of Ag, AISI 202 steel in the dome and Au/Ni/Cu on the pad. Corrosion challenges in the electronic industry are promoted by the multi-material design and increasing miniaturization which reduces the electron path in the presence of an electrolyte [56].

Corrosion mitigation efforts in tandem with this emergent multi-material design concept is necessary to maintain and extend the integrity and service life of structures from this design concept. Corrosion mitigation efforts in this regard seem to lag the multi-material design concept.

One of the ways of mitigating corrosion is by the use of corrosion inhibitors, hence in this work the use of corrosion inhibitors on multi-material combinations have been attempted in a bid to obtain information that will be vital to the development of multi-material mitigation solutions employing inhibitors. Generally research on the use of inhibitors is presently leaning towards active corrosion protection as evidenced by many reports [11-13,15,18,57-60], with interesting results on the testing and characterization of new corrosion inhibitors [59,60]. Furthermore current corrosion research is also focusing on investigation of intimate details of corrosion mechanisms down to the micro and nano-scale in attempts to acquire better understanding of corrosion mechanism(s) that is/are vital to the development of corrosion inhibition solutions [61-64], self-healing coating effects [15,65-66], and the development of a multi-electrode method for the rapid screening and evaluation of corrosion inhibitors [67-68]. It is hoped that this thesis based on experimental studies, can be a source of important data and information for the development of multi-material corrosion inhibition strategies.

In this review of literature a brief overview of corrosion, its types with emphasis on galvanic corrosion which is the most relevant to this work, contributing factors and mechanisms are presented, with a robust discussion of the corrosion/degradation of each of the five materials employed in this study (aluminium, copper, iron, zinc and CFRP), oxygen reduction on carbon electrodes, galvanic corrosion in near neutral aqueous chloride media, corrosion inhibition and corrosion inhibitors.

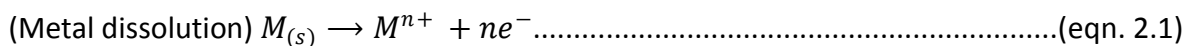
2.1 What is corrosion?

Corrosion is a degradative process which has been defined as the "physicochemical interaction between a metal and its environment which results in changes in the properties of

the metal and which may often lead to impairment of the function of the metal, the environment, or the technical system of which these form a part" [69]. The corrosion process results in degradation or deterioration of a material on interaction with its environment, and since this is not peculiar to metals alone a more encompassing definition of corrosion by (IUPAC) defines corrosion as, " an irreversible interfacial reaction of a material (metal, ceramic, polymer) with its environment which results in consumption of the material or in dissolution into the material of a component of the environment". Often, but not necessarily, corrosion results in effects detrimental to the usage of the material considered. Exclusively physical or mechanical processes such as melting or evaporation, abrasion or mechanical fracture are not included in the term corrosion" [70]. Generally, the corrosion process has an electrochemical nature meaning spatially separated oxidation and reduction processes with electron transfer ensured by an electronic conductor. For the corrosion process to be initiated, three conditions must be present: an anode, a cathode and an electrolyte. In the corrosion process, two types of reactions occur simultaneously; an oxidation reaction at the anode and at least a reduction reaction at the cathode.

The sole anodic reaction in a corroding system is metal oxidation/dissolution by electron loss.

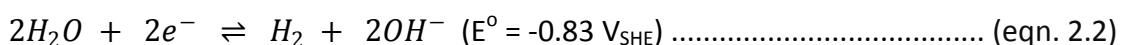
Anodic Reaction:



The possible cathodic reaction(s) can be many and diverse depending on the metal, the pH, the oxygen concentration, the nature of electrode surface, and the ions (mainly cations) present in the solution. However, there is usually a dominant cathodic reaction. Possible cathodic reactions in a corroding system include: water splitting into hydrogen and OH⁻ leading to local alkalization (eqn 2.2). This cathodic reaction is feasible for metals like Mg, Al, and Zn with high enough electronegative potentials for hydrogen evolution [71]. Other cathodic reactions include oxygen reduction with water formation (eqn. 2.3), oxygen reduction with OH⁻ formation (eqn. 2.4), hydrogen evolution by proton reduction (eqn. 2.5), metal ion reduction (eqn. 2.6), with possible metal deposition/redeposition (eqn. 2.7).

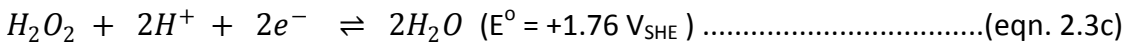
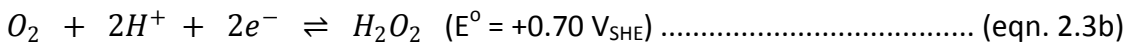
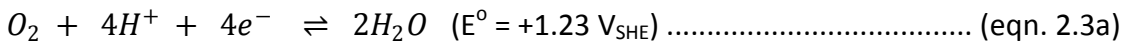
Cathodic Reactions:

(a) At nearly neutral pH and in the absence of oxygen water splitting reaction is possible (eqn. 2.2), and is so thermodynamically favoured ($E^{\circ} = -830 \text{ mV}_{\text{SHE}} \approx -1074 \text{ mV}_{\text{SCE}}$) that it can take place on metals like aluminium, zinc and magnesium:

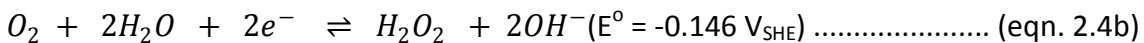
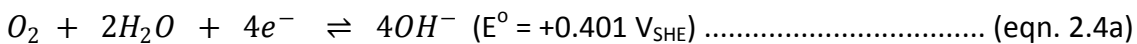


(b) In aerated acid solutions: In aerated acid solutions, due to the presence of oxygen in the

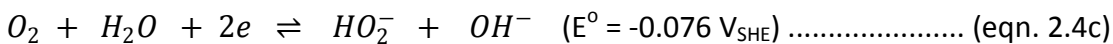
solution another possible cathodic reactions is oxygen reduction to water either through a 4 electron step (eqn. 2.3a) [72] or a 2-step 2 electron process (eqn. 2.3b and 2.3c);



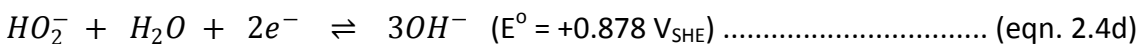
(c) In aerated neutral and basic solutions, having a dearth of protons (H^+), oxygen can be reduced to hydroxyl ions via either the 2 electron or 4 electron pathway as in equations 2.4a and 2.4b below, the main pathway for O_2 reduction being dependent on the electrode [73]:



and also via the 2 step oxygen reduction to HO_2^- and then to OH^- thus:

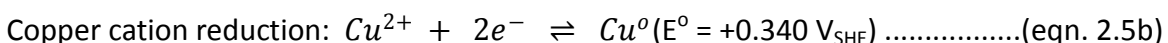
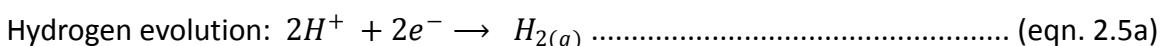
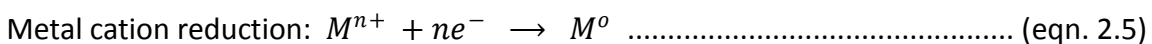


which undergoes further reaction to yield OH^- thus:

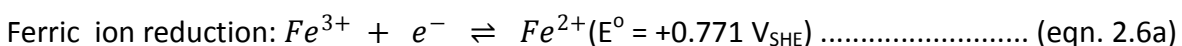


Other possible cathodic reactions in a corroding system are metal deposition and metal cation reduction under which hydrogen ion reduction or hydrogen evolution can be classified.

(d) Metal deposition occurs if there is present in the solution near the electrode, cations of a metal more noble than the corroding metal. The less noble and corroding metal acts as an reducing agent, entering into solution by forcing the cations of the nobler metal to accept electrons and be reduced thus;



(e) Metal ion reduction can occur when there is a metal ion with multiple oxidation states and thus able to accept electron(s) without being reduced to the metallic state thus:



It can be observed from the above (eqn. 2.2 to 2.6a) that with the exception of metal deposition and metal ion reduction reactions, most of the cathodic reactions result in the production of OH^- near the electrode surface. This is exploited in the use of precipitating corrosion inhibitors in which cations capable of forming insoluble hydroxides/oxides (such as rare-earths, calcium, zinc and magnesium) are introduced in a corroding system as a salt; the cation precipitating on active cathodic sites as a very thin layer of the corresponding insoluble

hydroxide/oxide inhibits the cathodic reaction by retarding the mass transport of oxygen to the metal surface [74-76].

2.2. Thermodynamics of Corrosion/ Electrochemical Processes

The corrosion of metals can be seen as an energy minimization process in which the metals seek to reduce the energy injected in transforming them from their native states. For this reason, metals requiring large input of energy in transformation from the native state do have the greater tendency to revert to the native state via the corrosion process. Besides energy minimization certain conditions (e.g. presence of an oxidant, an electrolyte, the correct pH, etc.) are necessary for corrosion to take place. Thermodynamics gives information on the possibility of a corrosion reaction taking place under conditions of interest. Corrosion involves electrode processes composed of anodic and cathodic reactions with their respective equilibrium potentials and associated free energies (ΔG°). The summation of these respective equilibrium potentials yields the measurable equilibrium potential (E_{eq}) of the electrode process.

Since corrosion processes involve chemical reactions, the thermodynamic principles applied to chemical reactions are applicable to corrosion processes as well, and enable prediction of which reactions and hence reaction schemes/mechanisms are feasible or not, under defined prevailing conditions (e.g. temperature, concentration or pressure etc.). The free energy change (ΔG) associated with corrosion reaction is related to the equilibrium potential (E_o) by eqn. 2.7:

$$\Delta G^\circ = -n F E_{eq} \dots \dots \dots \text{(eqn. 2.7)}$$

where ΔG° is the free energy change, n is the number of electrons involved in the electrode reaction, F is Faraday's constant (96487 C mol^{-1}), and E_{eq} is the equilibrium potential.

$$\Delta G^\circ = -RT \ln K \dots \dots \dots \text{(eqn. 2.8)}$$

where R is the gas constant, T is the absolute temperature and K is the equilibrium constant.

Combining equations (2.7) and (2.8) which are different expressions of the free energy change, and expressing in terms of the potential;

$$E_{eq} = \frac{RT}{-n F} \ln K \dots \dots \dots \text{(eqn. 2.9)}$$

Equation (2.9) is of great importance as it links the potential to important experimental parameters such as temperature, pressure and partial pressure of active species, and the concentration and activities of relevant species.

On the basis of this (eqn. 2.9), it is possible to construct a thermodynamic map; the Pourbaix diagram which gives information on the regions of thermodynamic stability for any metal/electrolyte systems and the possibility of corrosion under different conditions.

2.3. Equilibrium (Pourbaix) Diagrams

Pourbaix diagrams are electrochemical maps indicating the domain of stability of ions, oxides and hydroxides [77]. The Pourbaix diagram or equilibrium diagram is a vital tool in corrosion research. It is based on thermodynamics, and expresses feasible reactions but provides no information on the kinetics. This important diagram lists all the thermodynamically possible chemical and electrochemical reactions that can take place between a metal and water and defines the domains of "stability" for each chemical species. For corrosion studies 10^{-6} M concentration is usually used as the boundary and as a practical indication of the corrosion stability of a metal and its solid products, as a function of the pH for chemical reactions and as a function of the potential for electrochemical reactions [78,79]. Equilibrium diagrams are very important in corrosion and corrosion mitigation studies as it gives the ability to predict the possibility of corrosion occurring, estimate the composition of corrosion products and predict environmental changes (e.g. pH) that might be necessary to prevent or mitigate corrosion [79]. In spite of the usefulness of equilibrium diagram, they are limited by the lack of kinetic information, the assumption of equilibrium conditions, being specific to metals and not alloys, assumption of passivity for all oxides and hydroxides irrespective of actual protective properties [80].

The equilibrium diagram for aluminium below (Fig. 2.4), will be used herein to demonstrate the use of equilibrium diagrams in corrosion studies without discussion of the procedure for creating the equilibrium diagrams. The two parallel lines marked "a" and "b" between them delineate the region of stability of water. Above the line marked "a" water is unstable and liable to be oxidized to oxygen while below the line marked "b" it can be reduced to hydrogen gas. The hatched area (in grey colour) is used herein to indicate the range of potentials (-0.55 to -1.50 V_{SCE}) measured on aluminium samples in this work. Since the work was done with test solutions with bulk pH in the near-neutral pH range (based on 50 mM NaCl with and without inhibitors), it is obvious from Fig. 2.4, that this work was carried out at potentials and pH ranges in which aluminium is most likely to be passivated due to stability of Al_2O_3 in these potential and pH ranges. In addition, it can be observed that within these ranges and at potentials lower than -0.7 V_{SCE} water is unstable and liable to be reduced to hydrogen gas on aluminium surfaces.

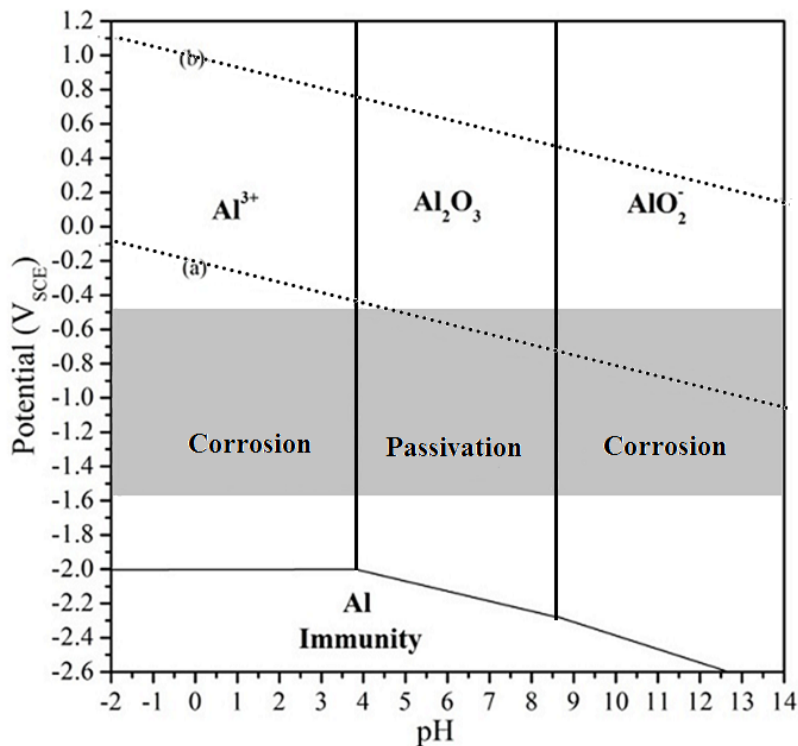


Fig. 2.4. E-pH diagram for pure Al at 25°C in aqueous solution for activities of ionic species $\approx 10^{-6}$ (adapted from Pourbaix 1974 [77]) [81].

Hence under the test conditions employed in this work both passivation of aluminium surface and hydrogen evolution reactions are predicted to be feasible from the Pourbaix diagram, but without information on their kinetics, which have to be evaluated experimentally. It must be emphasized that, due to localized electrochemical processes, the local pH can vary widely from the bulk pH employed resulting to variations in trends predicted on the basis of the bulk solution. In such localised areas with pH significantly different from the bulk, the trends will be based on the effective local pH and potentials rather than the bulk pH values. From this brief excursion through the aluminium equilibrium diagram it is obvious that aluminium is susceptible to acid and alkaline corrosion, and that the corrosion of aluminium structures can be mitigated where possible by pH control to the passivity range.

2.4. Kinetics of Corrosion processes

Thermodynamics and particularly the Pourbaix diagram gives information on the possible reactions under specified conditions, but not the possible reaction rates (kinetics) which is of vital importance for corrosion mitigation and management. Since corrosion is electrochemical in nature it involves the flow of current (charges), and thus the measurement of the rate of passage of these charges will give information on the kinetics of the corrosion process(es). Furthermore, factors that seek to impede the passage of charges exert influence on

the kinetics of corrosion processes. These factors that affect the flow of current and hence the kinetics of corrosion are discussed below.

2.4.1. Polarization

An electrode at the equilibrium potential experiences no net current flow, as reduction reactions are counter-balanced by oxidation processes. Polarization occurs in non-equilibrium conditions as a result of a net flow of current to or from an electrode, manifesting as a shift in potential from equilibrium values.

$$\eta = E - E_o \dots \dots \dots \text{(eqn. 2.10)}$$

where η is the polarization or overvoltage, E is the actual potential, and E_o is the equilibrium potential.

The factors influencing polarization also have the capacity to affect (impede) the rates of electrochemical reactions/processes, and thus related to the kinetics of corrosion processes. The three main factors capable of retarding the rates of electrochemical reaction are ; the presence of an energy barrier to the process(es) (activation polarization), mass transport constraints on reactive species at reaction sites (concentration polarization), and the presence of resistance to the flow of electrons between the cathode and anode (ohmic polarization). Hence the total polarization on an electrode is the sum of these three;

$$\eta_{total} = \eta_{conc} + \eta_{act} + iR \dots \dots \dots \text{(eqn. 2.11)}$$

where η_{total} is the total or summation of the different constituent polarizations, η_{conc} is the concentration polarization, η_{act} is the activation polarization, and iR is the ohmic drop.

2.5. The Mixed Potential Theory

The mixed potential theory, a concept put forward by Wagner and Traud [82] is an important tool in analysing the electrochemistry of corrosion processes. It can be useful in the treatment of galvanic corrosion. The mixed potential theory is based on two assumptions; (a) that every electrochemical process can be decomposed into two or more partial oxidation and reduction reactions, and (b) that charges are conserved in the course of an electrochemical reaction, hence with no net accumulation of charges. With respect to the first assumption, the mixed potential theory sees a corroding metal surface in contact with an electrolyte as if it were made up of two or more electrodes. On the basis of these assumptions, it follows that in a freely corroding system (without impressed current or voltage), the total rate of oxidation must equal the total rate of reduction reactions, or expressed in electrochemical terms, the sum of anodic

currents must equal the sum of cathodic currents. The classification of the possible reactions in a corroding system into oxidation (anodic) and reduction (cathodic) reactions permits the identification of the complementary half-cell reactions or redox couple. From the mixed potential theory, it follows and has been proven experimentally [82-84] that the rate of partial electrode reactions (faradaic processes) on an electrode solely depends on the electrode potential and is independent of the rates of other partial electrode (faradaic processes) taking place simultaneously. This deduction from the mixed potential theory permits the prediction of the over-all rates and potentials existing when more than one reaction occur simultaneously on an electrode surface by a combination of the polarization curves for the independent oxidation and reduction processes [85]. From the mixed potential theory the existence of two or more independent electrochemical reactions on a metal surface undergoing dissolution related only by the operative potential difference between the metal and solution was concluded [84]. The mixed potential theory is usually illustrated in an Evans diagram as in Fig. 2.5 for zinc in de-aerated acid. In the diagram the two relevant half-cell reactions; the cathodic hydrogen evolution reaction (upper descending line), and zinc oxidation to yield Zn^{2+} (lower ascending line) cross each other at a point denoted as i_{corr} on the current axis and E_{corr} on the potential axis. E_{corr} is the mixed potential due to the two afore-mentioned half-cell reactions. At this potential the rates at which electrons are produced and consumed due to anodic and cathodic half-cell reactions are equal, so that no net current flows in the absence of impressed voltage.

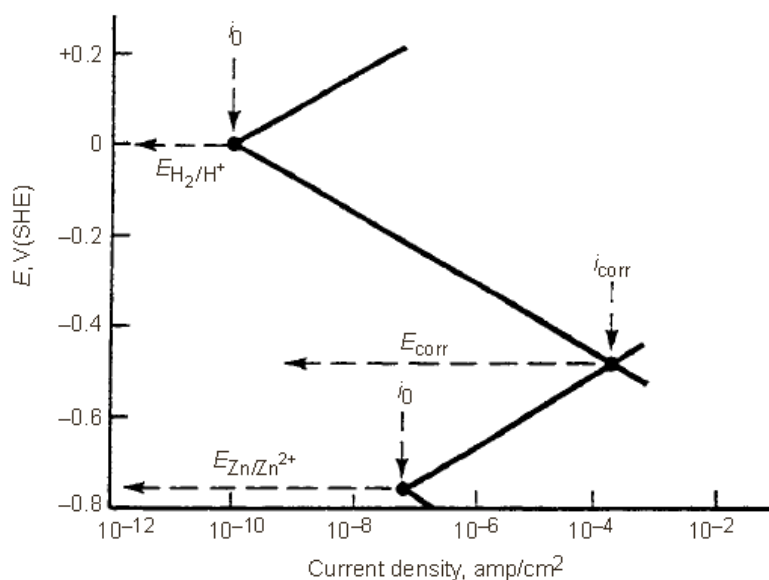


Fig. 2.5. Illustration of mixed-potential theory for zinc corrosion in de-aerated acid [86].

The mixed potential theory is applied in corrosion studies as a valuable tool in predicting corrosion phenomena from the polarization curves for the partial processes, identification of the rate-determining processes, and thus in suggesting corrosion mitigation solutions [85]. The

mixed potential theory is of great importance in studies of galvanically coupled metals [87], and is fundamental to electrochemical techniques for predicting galvanic corrosion [88]. However, it should be noted that construction of mixed-potential diagrams for modelling corrosion scenarios, requires prior knowledge of the activation overpotential for each relevant process, and information relating to processes that are sensitive to concentration polarization [89].

2.6. Corrosion Measurement/Evaluation

Generally, the extent of corrosion is measured as the rate of material loss from the metal/alloy per unit time. In principle any parameter that is linked to metal loss (like hydrogen evolution in metal corrosion in acidic media) can be used to monitor corrosion by appropriate conversion to material loss per unit time. This method of evaluating corrosion assumes uniform material loss across the metal surface and gives rise to diverse corrosion rate expressions. For localized corrosion like pitting, the assumption of uniform material loss does not hold and material failure is possible with little material loss. For pitting corrosion, corrosion rate is evaluated as pit depth per unit time. Corrosion rates are therefore expressed in many ways and different units such as; in terms of the corrosion current density in milliamperes per square centimetre (mA cm^{-2}) in electrochemical tests, in terms of penetration rates per unit time in millimetre per year (mm y^{-1}) and milli-inch per year (mpy), and in terms of mass loss per unit area per unit time in gramme per square metre per day ($\text{g m}^{-2} \text{day}^{-1}$). Measurements in terms of current density as in this work are convertible to other units if the corrosion is uniform [90-91]. From Faraday's law the measured corrosion current density, i_{corr} , from electrochemical tests can be related to corrosion rate (CR) in mil per year (mpy) as:

$$\text{CR} = \frac{i_{\text{corr}} A_w}{F n \rho} \dots\dots\dots(\text{eqn. 2.11})$$

where CR is the corrosion rate in mils per year (mpy), i_{corr} is corrosion current density (A.cm^{-2}), A_w is atomic weight (g.mole^{-1}), F is Faraday's constant ($96487 \text{ C.mole}^{-1}$), ρ is density of metal (g.cm^{-3}), and n is number of electrons involved in the reaction.

Furthermore measurements of corrosion rates in mA cm^{-2} are convertible to other units using the following relations;

$$1 \text{ mA cm}^{-2} = \left(\frac{3.28 A_w}{n \rho} \right) \text{mmy}^{-1} \dots\dots\dots(\text{eqn. 2.12})$$

$$1 \text{ mA cm}^{-2} = \left(\frac{129 A_w}{n \rho} \right) \text{mpy} \dots\dots\dots(\text{eqn. 2.13})$$

$$1 \text{ mA cm}^{-2} = \left(\frac{8.95 A_w}{n \rho} \right) \text{gm}^{-2} \text{day}^{-1} \dots\dots\dots(\text{eqn. 2.14})$$

where A_w is atomic weight (g.mole^{-1}), ρ is density of metal (g.cm^{-3}), and n is number of electrons

involved in the reaction.

2.7 Forms of corrosion

Corrosion can be classified into different forms/types on the basis of its presentation or effect of the corrosion on surface morphology, e.g., general corrosion and pitting corrosion, or the nature of the corrosion, e.g., galvanic corrosion and crevice corrosion, or on the basis of its effect on bulk material properties, e.g., intergranular corrosion and stress corrosion cracking [92]. The corrosion of metals manifest in different forms and can be classified into many forms such as uniform or general corrosion, pitting corrosion, crevice corrosion, filiform corrosion, erosion corrosion, cavitation corrosion, fretting corrosion, dealloying/selective leaching, galvanic corrosion, intergranular corrosion, and environmentally induced corrosion under which stress corrosion cracking, hydrogen embrittlement/hydrogen induced cracking, and corrosion induced fatigue may be listed. Since the present work deals more with galvanic corrosion scenarios, emphasis is placed on galvanic corrosion.

2.7.1. Galvanic Corrosion

Galvanic corrosion is the accelerated corrosion of a metal immersed in a corrosive media and electrically coupled to a more noble metal. The above definition seems to be based on the assumption that it can only be observed when two metals are galvanically coupled. However galvanic corrosion have been reported when a conductor is coupled to a metal in an electrolyte irrespective of whether the second component is a metal [93,94]. In cognisance of these observations, galvanic corrosion is herein defined in a broader concept as the accelerated deterioration of the more active metal (material) observed when two dissimilar (materials) are immersed in an electrolyte while they are electrically connected. In galvanic corrosion the corrosion rate of the more anodic component is enhanced and that of the cathodic component reduced. In galvanically coupled systems the bulk of anodic reactions (metal dissolution) take place on the more active metal while the bulk of the cathodic reactions (hydrogen evolution or oxygen reduction) occur on the nobler member (the cathode). According to Mansfeld et al., [95] the magnitude of galvanic corrosion is not always dependent on the potential difference of uncoupled dissimilar metals, but the relative values of the corrosion potentials of uncoupled materials is in most cases a good predictor of the direction of current flow.

In electrochemical measurement of galvanic corrosion, it is reported [96] that if the magnitudes of the current produced by the couples are insufficient to repress local cell activity completely,

the measured galvanic current may not be representative of the total corrosion, instead the current becomes a function of the accelerated attack of the anodic member as a result of the galvanic coupling, which is more likely in low conductance test electrolytes. In galvanically coupled metals, kinetic parameters such as corrosion rates of the uncoupled materials, Tafel slopes and area ratios are reportedly important determinants of the observed galvanic corrosion rate. The often observed decrease in galvanic current with time, has been linked to changes in the rates of the electrochemical reactions on the coupled metals which itself is linked to changes in properties of the oxides and the coating on the alloys and, also from changes in the electrolyte [97]. The measured galvanic corrosion rate from galvanic current measurements often differs from real metal dissolution rates evaluated from weight loss measurements on the anode [98]. With respect to this observation, Mansfeld and Parry proposed three scenarios. In the first case (Case I), three assumptions were made; (1) that the process is under diffusion control, (2) that there is an equal rate of depolarizer (oxygen) reduction on the anode and cathode, and (3) that the only significant process on the cathode is the reduction of the depolarizer (most of the time oxygen reduction in the absence of added inhibitors). Under these 3 assumptions, the measured galvanic current equals the limiting diffusion current (of oxygen reduction) and thus the anode dissolution current is related to the measured galvanic current. If in addition to these 3 assumptions, the cathodic and anodic areas are equal (Case 1a), the anode dissolution current (real dissolution rate) is twice as large as the measured galvanic current. However, in the absence of assumption 2 (Case 1b), where the rate of oxygen reduction on the anode and cathode are unequal for instance due to oxide film formation on the anode, then the measured galvanic current equals the limiting diffusion current of the uncoupled anode or cathode or the limiting currents on the cathode if the oxygen diffusion currents on anode and cathode are unequal [97,98]. In the second case (Case II), three assumptions were also made, (1) that the only significant process taking place on the anode on galvanic coupling is metal oxidation (anodic dissolution), (2) that the only significant process on the cathode is the reduction of the oxidizer, and (3) that Tafel behaviour is operative for these reactions at the galvanic potential. Under the conditions of these 3 assumptions, the measured galvanic current equals the true anodic dissolution current. In the third case (Case III), the galvanic potential of the coupled metals is located very close to the corrosion potential of the uncoupled anode that both anodic and cathodic reaction(s) occur at significant rate at the anode, and thus, Tafel behavior is not observed for the dissolution reaction on the anode. Under these conditions, the actual dissolution current of the anode will be somewhere between the measured galvanic

current and the measured galvanic current plus the corrosion current measured on the uncoupled anode [97-99].

There is an area effect in galvanic corrosion [100] in which the galvanic current has been shown to be independent of the anode area but directly proportional to the cathode area while the galvanic current density with respect to the anode is directly proportional to the ratio of the cathode and anode areas. Since there is electro-neutrality criterion in corrosion and hence no net accumulation of charges on a corroding system, the total anodic current equals the total cathodic current. However, the values of the anodic and cathodic current densities can vary based on the ratios of their areas.

$$I_{anodic} = I_{cathodic} \dots\dots\dots(\text{eqn. 2.15})$$

Introducing the surface areas of the cathode (S_C) and the anode (S_A) into the equation (2.15) yields:

$$i_{anodic} \times S_A = i_{cathodic} \times S_C \dots\dots\dots(\text{eqn. 2.16})$$

where i_{anodic} and $i_{cathodic}$ are the anodic and cathodic current densities respectively, measured in mA cm^{-2} or $\mu\text{A cm}^{-2}$ and of practical relevance.

From equation (2.16) above it is obvious that knowledge of the value of the cathodic and anodic surface areas and any of the cathodic or anodic current densities enables the calculation of the other;

$$i_{anodic} = i_{cathodic} \times \frac{S_C}{S_A} \dots\dots\dots(\text{eqn. 2.17})$$

From equation (2.25) above it is evident the magnitude of anodic current (which correlates to the corrosion rate) is very sensitive to the ratio of the surface area of the cathode (S_C) to that of the anode (S_A). This is of great importance in engineering design of systems with possibilities of localized and/or galvanic corrosion, in which smaller values for the ratio (i.e a higher anodic surface area relative to the cathodic surface area) is desirable to ensure reduced corrosion rates. Ratios of $S_C/S_A \gg 1$ are regarded as amplifying factor with respect to the anodic current, while values $\ll 1$ are regarded as a stifling factor [101]. The galvanic corrosion of the anode is enhanced as the ratio of the area of the cathode to anode is increased. However, there can exist local anodic and cathodic activities on each of the components of the galvanic couple. Thus accurate evaluation of the component of the corrosion of the anodic member due to galvanic corrosion requires a knowledge of its corrosion rates without galvanic coupling in the test media. This is very important in galvanic corrosion rates evaluated by weight loss methods but of little consequence in electrochemical galvanic measurements (ZRA), which measures the net electron flow from the anode to the cathode thus discriminating the self corrosion effects in the system.

Galvanic corrosion mechanisms are obviously more complex than single metal corrosion as the species resulting from interaction of one metal (usually the nobler) can affect reactions on the other (mostly less noble) in the solution. For instance the presence of Cu^{2+} , Fe^{2+} , Sn^{2+} , Ni^{2+} , As^{3+} , and Sb^{3+} ions have been reported to enhance hydrogen evolution on zinc [102-106], as these elements having more positive reversible potentials and lower hydrogen over-potentials than zinc, on precipitating on zinc surface any of these elements enhance the rate of hydrogen evolution. Conversely, Pb^{2+} ions in alkaline solution (6N KOH) have been reported to inhibit hydrogen evolution [102-106]. In acid solutions also, the presence of a trace quantities of lead in zinc have been reported to cause significant reduction in the hydrogen evolution kinetics [107].

The galvanic corrosion phenomenon is exploited in the cathodic protection of metal structures in which the more active metal is designed to sacrificially corrode and protect the more cathodic metal. However, the galvanic corrosion of an anode does not always translate to cathodic protection of the cathode. For instance, though zinc can be anodic to aluminum in some instances (.e.g. due to passivation of aluminium surface), it has been reported that aluminum corrosion was enhanced on coupling to zinc in 3.5% NaCl solution compared to the corrosion rate in the uncoupled state [100]. Mansfeld et al., [95,108] attributed the enhanced aluminium dissolution rate on coupling with zinc to increase in alkalinity on the aluminium alloy surface due to enhanced cathodic reaction on the aluminium on coupling to zinc, as the aluminium corrosion products are unstable at the prevalent high pH.

2.8. Corrosion of Metals

Metals are mostly employed in engineering applications as alloys in which form a lot of metal become more susceptible to corrosion. A metal/alloy in contact with an electrolyte has a unique potential (electrode potential). The value of this potential is dependent on (a) the nature of the metal, (b) the chemical nature of the aqueous solution (e.g. pH and chemical species present), (c) the presence of oxide films on the metal surface, (d) the presence of adsorbed gases on the metal surface, and (e) the presence of mechanical stresses on the metal [109]. Corrosion resistance may be defined as the ability of a metal to withstand deterioration due to oxidative or other chemical reactions in an environment. This is usually expressed as corrosion rate with respect to the test environment. The lower the measured corrosion rate, the higher is the corrosion resistance of the metal or alloy. The corrosion resistance of a metal is often linked to its ability to form a protective film with good barrier properties against aggressive ions coupled with a good resistance to transport of electronic and ionic species

across it. For brevity, review of the corrosion of each of the metals (aluminium, copper, iron, and zinc) will be mainly focused on works carried out at neutral and near-neutral pH, and consistent with the bulk solution pH employed in this work.

2. 8.1. Corrosion of Aluminium

Aluminium is mostly used in alloy form as the use of pure aluminium accounts for not more than 10% of the annual worldwide consumption [78]. There are significant similarities and differences in the corrosion behaviour of pure aluminium, aluminium alloys, and aluminium alloys of different series. Aluminium has been reported to maintain its passivity in neutral solutions if it contains some dissolved oxygen and activating anions or noble metal cations are absent [110]. Aluminium is very reactive in acidic and alkaline solutions as its protective oxide film being unstable at these pH ranges dissolves, exposing bare aluminium surface to attack by the aggressive electrolyte. In less pure grades of aluminium (commercial alloys), pitting under immersion is very common behaviour and thought to be due to probable incomplete passivation of weak spots in the amorphous film which result from the impurities concentrated beneath them on the metal surface [111]. It has also been suggested that impurities in the aluminium solid solution may increase the film's electrical conductivity, so that the film becomes able to function as a more efficient cathode towards the metal exposed at gaps than the pure oxide formed on high grade metal [112].

The corrosion rate of aluminium was found to depend logarithmically on the pH, with different dependencies on either side of the pH value (close to 6) at which the corrosion rate is a minimum reported by Chatalov [113], and pH greater than 7 reported by Vujičić and Lovreček [110]. Interestingly these pH values fall within the range for the minimum solubilities of hydrated alumina compounds (e.g. pH 5.5 - 7.8 for $\text{Al}(\text{OH})_3$ as reported by Deltombe and Pourbaix [77,114] which can compose the corrosion products. The thermodynamic prediction of this dependency is illustrated in the Pourbaix diagram for aluminium above (Fig 2.4 ; section 2.3) [77,81,114], showing the regions of stability of aluminium and pH ranges in which it is susceptible to corrosion.

Fig 2.6 is a plot of corrosion rate of aluminium as a function of pH illustrating how pH affects aluminium corrosion kinetics. By comparison of Fig. 2.4 (the predicted) and Fig. 2.6 (the actual), the good correlation between the thermodynamically predicted behaviour of aluminium as a function of pH and the actual kinetics is obvious.

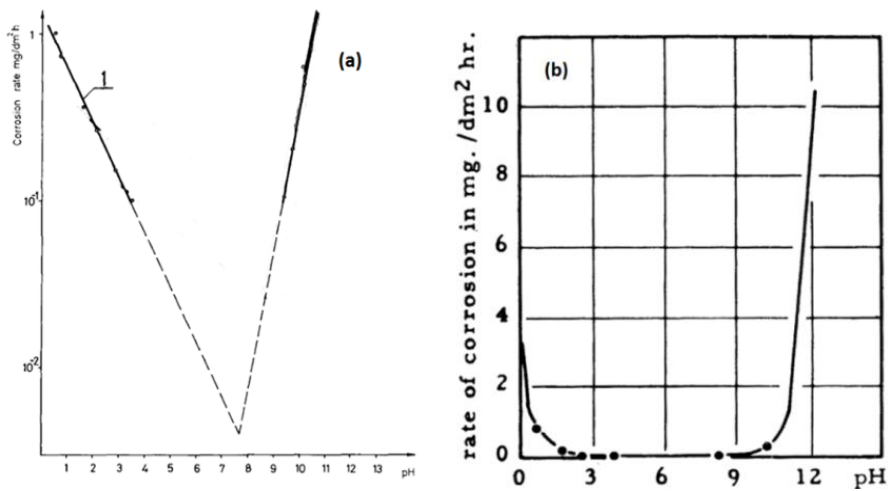


Fig. 2.6. The corrosion rate of Aluminium as a function of pH, (2.6a) [Adapted from ref: 110], and (2.6b) [Adapted from ref: 113].

Nguyen and Foley [115] in their studies of the chemical nature of aluminium corrosion and dissolution mechanism of aluminium oxide concluded that the corrosion behaviour of aluminium in a given environment is dependent on the stability of the complex species formed on the film, and on the affinity of the anion present to react with the exposed metal. In their explanation the observed reduction in aggressiveness of the nitrate ion (in some cases even inhibiting) which is normally very reactive towards elemental aluminium to produce ammonia is attributed to the ability of the complex species formed on the oxide film to remain attached to the oxide surface. Aluminium and its alloys are susceptible to a variety of forms of corrosion such as; alkaline corrosion [116], exfoliation corrosion [117], crevice corrosion and pitting corrosion [118], intergranular corrosion [119], stress corrosion cracking [120], and filiform corrosion [121].

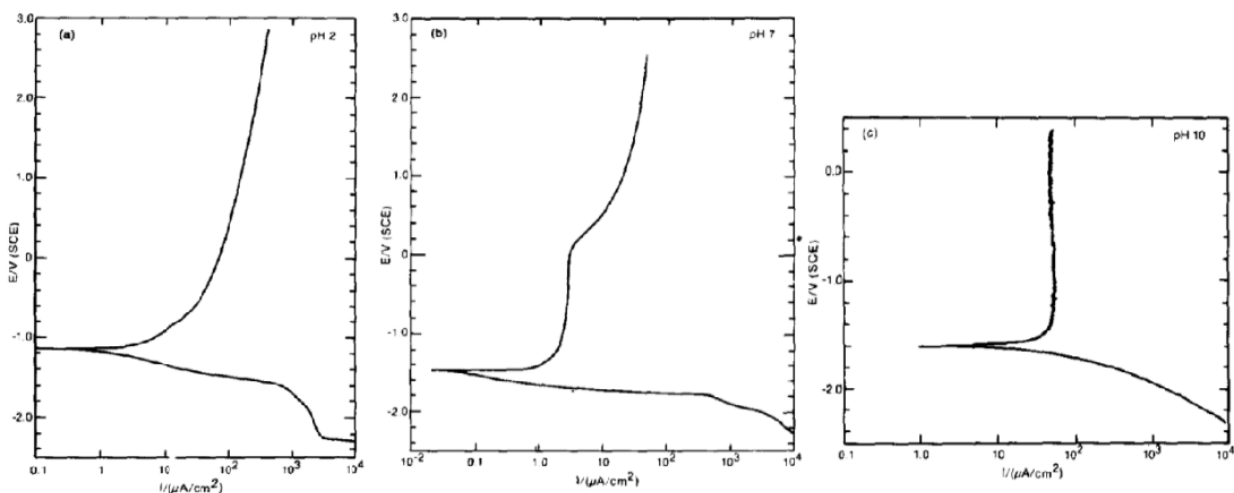
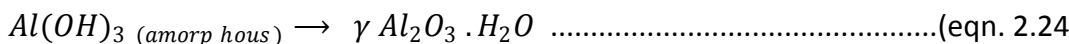
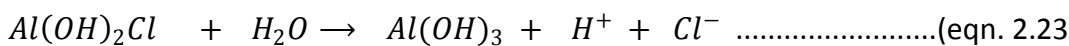
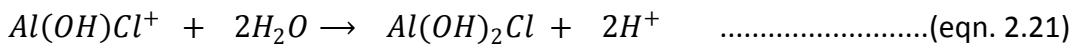
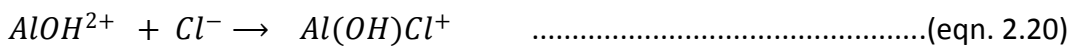
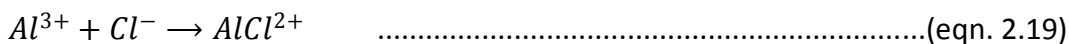
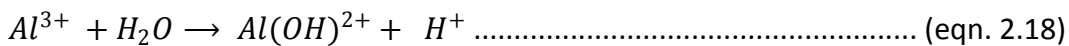


Fig. 2.7. The composite potentiodynamic polarization of aluminum polarized in the anodic and cathodic direction from E_{corr} in 0.05 M Na_2SO_4 adjusted to (a) pH 2, (b) pH 7 and (c) pH 10. [Adapted from ref: 122]

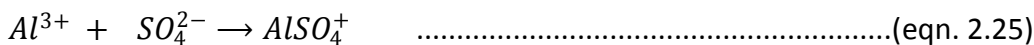
From Fig. 2.7 above it can be observed that aluminum responds to the anodic polarization in

acidic solution (pH 2) by dissolving, at neutral and near-neutral (pH 7) by forming a passive film to limit attack, and in alkaline media (pH 10) by formation of a film that does not protect the substrate from attack as deduced from the considerable amount of persistent higher frequency noise, indicating an instability in the surface film [122]. Although the differences in the electrochemical response of aluminium as a function of the solution pH is obvious, the ensuing discussion of aluminium corrosion in aqueous media is limited to the neutral and/or near-neutral pH ranges for brevity.

Some of the possible reactions on aluminium immersed in chloride media are [123,124]:



And in sulphate solutions the reactions in addition to aluminium hydroxylation reactions are [124]:



It is observed from the equations above that the cathodic reactions involving hydroxylation lead to production of H⁺ which can cause local acidification. This local acidification has been postulated to be the factor responsible for pit initiation in metals [125]. Diverse mechanisms have been proposed to explain the breakdown of the passive film on aluminium [126], but general opinion seem to favour the mechanism in which the chloride do not enter the oxide film but are chemisorbed onto the oxide surface, and by acting as a reaction partner, aids dissolution via the formation of oxide-chloride complexes [127].

2. 8.1.1. Corrosion of Aluminium in Near-Neutral Media

Aluminium exhibits its lowest corrosion rates in neutral and near neutral solutions because its thin protective oxide film is most stable in this pH range and has a low permeability for ions, electrons, or molecules (H₂O) [128]. Consequently the mechanism of aluminium corrosion in this range is dependent on the enhancement of the barrier properties of this layer by the formation of additional adherent hydrated aluminium oxides on the metal surface, hence its excellent

corrosion resistance in this pH range (Figs. 2.4 and 2.6). In order to build up this extra protective passive layer the presence of some dissolved oxygen in the solution is beneficial, with the corrosion rates tending to be highest soon after immersion as a thicker corrosion product layer is built up [129]. Consequently corrosion kinetics for aluminium in near-neutral solutions is mainly dependent on the solubility of the corrosion products in the test solution and its barrier properties.

The corrosion behaviour of aluminium in aerated near-neutral solutions is observed to vary significantly depending on the temperature range, exposure time, and concentration of the solution. Khairy and Hussein [130] working with aluminium in solutions of varying chloride concentrations in a pH range 4-8 that is consistent with near-neutral pH reported that the electrode potential is not sensitive to variations of pH, but changes linearly with the logarithm of the chloride concentration, and yielding a fairly constant potential, E_o of ≈ 546 mV. Studies [131,132] on aluminium corrosion kinetics at near-neutral pH shows that in quiescent solutions with access to air in this pH range and at low temperatures ($\leq 25^\circ\text{C}$) aluminium corrosion is slow even in the presence of significant concentrations of chloride (as KCl) in the solution, following a linear law with a rate constant that is sensitive to/dependent on the chloride concentration. The observed linear relation is explained to arise from the fact that, during the observation time range (up to 360 - 720 hours) the process takes place on an unbroken primary film, in the presence of a small but constant quantity of secondary corrosion products (amorphous aluminium hydroxides) [133] that are not firmly attached to the surface [128]. In this region in which the linear law describes the corrosion kinetics, a relationship has been reported [128] between the electrode potential of the aluminium and the KCl concentrations (equation 2.27), in which the electrode potential of aluminium increases with KCl concentrations, with the rate constants in the linear equations going through a maximum as the chloride concentration changes; the position of this maximum being dependent on the temperature such that at 20 - 25°C it lies between 1.4 - 2.0 N ($\approx 1.4 - 2.0$ M), and at 28°C shifts sharply to 0.1 N (≈ 0.1 M) (much lower chloride concentrations).

$$E = E_o + k \log C_{KCl} \dots\dots\dots(\text{eqn. 2.27})$$

where $E_o \approx 500$ mV at 20°C and 520 mV at 30°C and $k \approx 60-70$ mV.

These values of E_o obtained by Lepin and Kadev [128] are similar to the 546 mV reported by Khairy and Hussein [130]. This concentration dependence was taken by Lepin and Kadev [128] as proof that at the temperatures and timescales concerned, the aluminium electrode functions as a complex electrode with an intact primary film that is partly transformed in its

surface layer to a complex oxychloride.

In dilute solutions at higher temperatures in the range 25-35°C the trend undergoes a sharp change with increased corrosion rates that follow a power law (equation 2.28) [128].

$$\Delta w = kt^2 \dots\dots\dots \text{(eqn. 2.28)}$$

where Δw is the weight loss, k a constant and t the time.

This power law relationship is explained to be directly associated with the fact that the process takes place in the kinetic region of heterogeneous reactions, on a metal surface devoid of its primary film [134].

With the formation of new films the corrosion rate is retarded with the process following a logarithmic law (equation 2.29) [128].

$$\Delta w = k_1 \log t + k_2 \dots\dots\dots \text{(eqn. 2.29)}$$

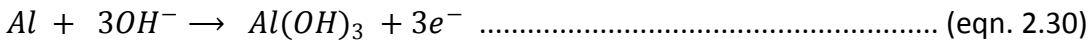
In concentrated solutions with the chloride concentration measured in normality less than 2 ($N < 2$ which is equivalent to $M < 2$), these transitions were not observed as a linear law is maintained throughout the exposure duration [128].

2. 8.1.2. Corrosion of Aluminium in Alkaline Media

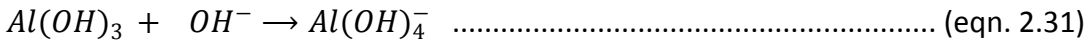
Macdonald et al., [135] proposed a model for anodic aluminium dissolution in strongly alkaline solutions involving stepwise addition of hydroxide ions to surface aluminium atoms leading to the formation of $\text{Al}(\text{OH})_4^-$. Pyun and Moon [136] studied the corrosion mechanism of pure aluminium in aqueous alkaline media (0.01 M, 0.1 M and 1 M NaOH) and reported that the steady-state value of the open circuit potential of pure aluminium in alkaline solution decreased with increasing rotation speed of the specimen, attributing this to enhanced anodic reaction and growth of a surface oxide film, and greater anodic polarization at the steady-state value open circuit potential compared to the cathodic polarization, and concluded that this was indicative that the rate of corrosion of pure aluminium is predominantly determined by the anodic reaction in alkaline solution. On the basis of their result a mechanism for the corrosion of pure aluminium in alkaline solution in the presence of the native surface oxide involving consecutive oxide formation and dissolution with simultaneous water reduction was proposed. In this proposed mechanism the anodic partial reaction on pure aluminium in alkaline solution consists of sequential electrochemical film formation at the aluminium/film interface due to the movement of OH^- through the film towards the aluminium, and chemical film dissolution due to OH^- attack at the film/solution interface (equations 2.30 and 2.31), while the coupled major cathodic partial reaction is water reduction (equation 2.32) [136].

Anodic Reactions:

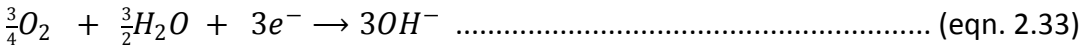
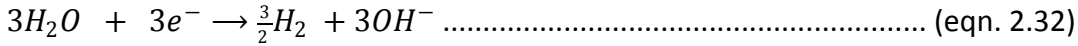
Electrochemical film formation



Chemical attack of film

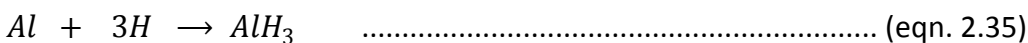


Cathodic Reactions:

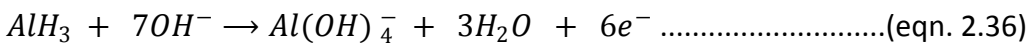


Based on their observation of gas bubbles on the aluminium surface, the water reduction reaction (equation 2.44) was concluded to be the dominant cathodic reaction [136].

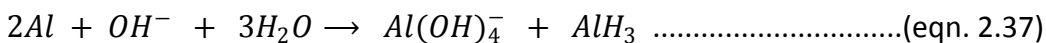
Adhikari and Hebert [137] studied open circuit corrosion of aluminium in alkaline solutions and attributed the long term anodic polarization changes to surface enrichment by impurities, and short term polarization changes to accumulation of AlH₃ corrosion products. On the basis of their detection of particles of AlH₃ using secondary ion mass spectrometry (SIMS) [138] during the open circuit potential dissolution of aluminium in 1M NaOH solution a mechanism was proposed [137-140] for alkaline dissolution of aluminium involving surface hydride species. In this proposed mechanism cathodically formed hydrogen reacts with aluminium to form a hydride thus (equations 2.34 and 2.35):



The cathodically formed hydride being unstable in the high pH environment reacts anodically to yield aluminate ions which are the stable form in the alkaline pH thus:



The overall reaction (combining the anodic and cathodic reactions) resulting in formation of the hydride and aluminate ions was presented as (equation 2.37 below) indicating that during its alkaline dissolution the aluminium surface is in direct contact with a layer of AlH₃ [136];



This proposed mechanism is supported by recent work [138] that indicates that the potential at the aluminium interface during anodic alkaline dissolution near the open circuit potential is close to the equilibrium Nernst potential of the proposed hydride anodic reaction (equation 2.37) [136]. The formation of interfacial AlH₃ is reported [138] to occur readily at the higher pH values, but stifled as the pH tends to neutral.

The corrosion rate of aluminium in alkaline solutions is dependent on the operating

conditions such as temperature, solution properties, fluid dynamics, pH, and particularly strongly dependent on the exposure time, with corrosion rate decreasing with increasing exposure time. This strong dependence of aluminium corrosion rate in quiescent alkaline solutions on the exposure time is thought [141] to account for the wide differences in reported [77,110,113,129,141-142] corrosion rates with variations of up to 50%. This trend of decreasing corrosion rate with increasing exposure time for aluminium in quiescent alkaline solutions is due to increasing aluminate ion concentration with time, the rate of which is determined by the ratio of the sample surface to volume of solution [141].

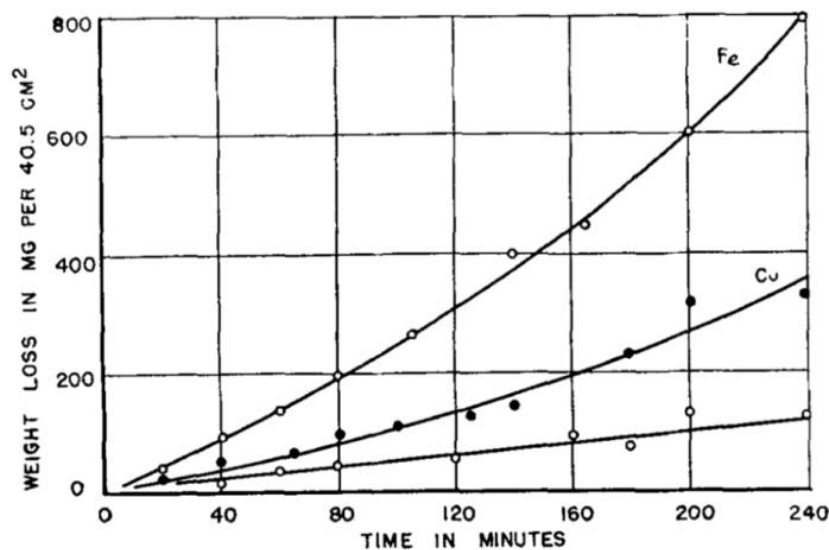


Fig. 2.8. Effect of addition of impurities (FeCl_3 and CuCl_2) on the dissolution of Aluminium in 0.30 N sodium hydroxide at 23°C [Adapted from ref: 129].

The presence of metal cations can affect aluminium dissolution kinetics in alkaline solutions as illustrated by Fig. 2.8 [129] above for a high purity aluminium sample (Al = 99.998%, Fe = 0.0005%, Cu = 0.0005%, Si = 0.001%) immersed in 0.30N sodium hydroxide at 23°C to which Fe^{3+} and Cu^{2+} ions are added to respectively as FeCl_3 and CuCl_2 . It can be seen that the presence of these cations in solution accelerated the dissolution rate of aluminium in the alkaline solution with the presence of iron ions enhancing the dissolution rates by a factor of 8, and more deleterious than copper ions [129].

2. 8.2. Corrosion of Copper

The corrosion resistance of copper is attributable to its noble potential and the formation of a protective oxide/hydroxide film under exposure conditions. From the potential-pH diagram (Fig. 2.12) for the Cu-Cl- H_2O ternary system, at 25°C Cu_2O and CuO are stable in the alkaline region; Cu_2O , CuCl , and $\text{Cu}_2(\text{OH})_3\text{Cl}$ are stable in the acidic region [143], and the presence of

CuCl, Cu₂O, and Cu₂(OH)₃Cl has been confirmed on copper and copper alloys in slightly acidic or neutral solutions with NaCl during their electrochemical oxidation [144-147]. These oxides are capable of strongly catalyzing the O₂ reduction reaction on oxide/metal interfaces with mixed oxidation states [148]. Copper is cathodic to most metals except titanium, gold, silver, platinum, and palladium and the non-metallic carbon fiber reinforced polymer (CFRP) in near neutral chloride media. Hence on galvanic coupling to most materials copper acts as the cathode, except titanium, gold, silver, platinum, palladium, and CFRP to which it is anodic and thus undergoes enhanced dissolution. There is general agreement that copper dissolution is not activation-controlled, but a diffusion controlled process [149-151]. The mechanism of the electro-dissolution of copper and copper based alloys in chloride media has been the subject of much investigation [151-158], and a mechanism proposed. In this mechanism the first step in the anodic dissolution of copper in chloride solution is thought to be the formation of the complex CuCl₂⁻ like species, with the dissolution rate controlled by its diffusion from the metal surface to the bulk of the solution [150,159-160], or by the diffusion of Cl⁻ ions from the solution to the copper surface [151]. Chemical precipitation of CuCl from the saturated solution leads to formation of a thin loose and porous film on the metal. The loose and porous nature of this film enables the continuation of the reaction by Cl⁻ diffusion through the porous layer with the rate of this step being controlled by the resistance of the electrolyte in the pores of the film [153]. Depending on the Cl⁻ concentration in the bulk solution these complexes may be involved: CuCl, CuCl₂⁻, and CuCl₃²⁻. However for chloride concentrations less than 2 M, CuCl₃²⁻ formation is considered negligible [151].

Copper dissolves anodically in Cl⁻ media to yield mainly a complex anion CuCl, [161] but the stability of the oxide layers on copper of which Cu(I)oxide is the main component under open-circuit potential conditions is significantly lowered by the presence of Cl⁻ ions in the solution [150,152]. The surface oxide layer on copper under these conditions is said to be partly formed by the hydrolysis of CuCl within the diffusion layer [150]. Since the corrosion of copper in chloride environments can be very sensitive to the chloride concentration irrespective of pH, Fig. 2.13 is presented below illustrating how changes in chloride concentrations (a) 10⁻³ M, (b) 10⁻² M, (c) 0.1 M, and (d) 1.0 M, affect the regions of stabilities of species in the Pourbaix diagrams for Cu - Cl⁻ - H₂O system [162,163].

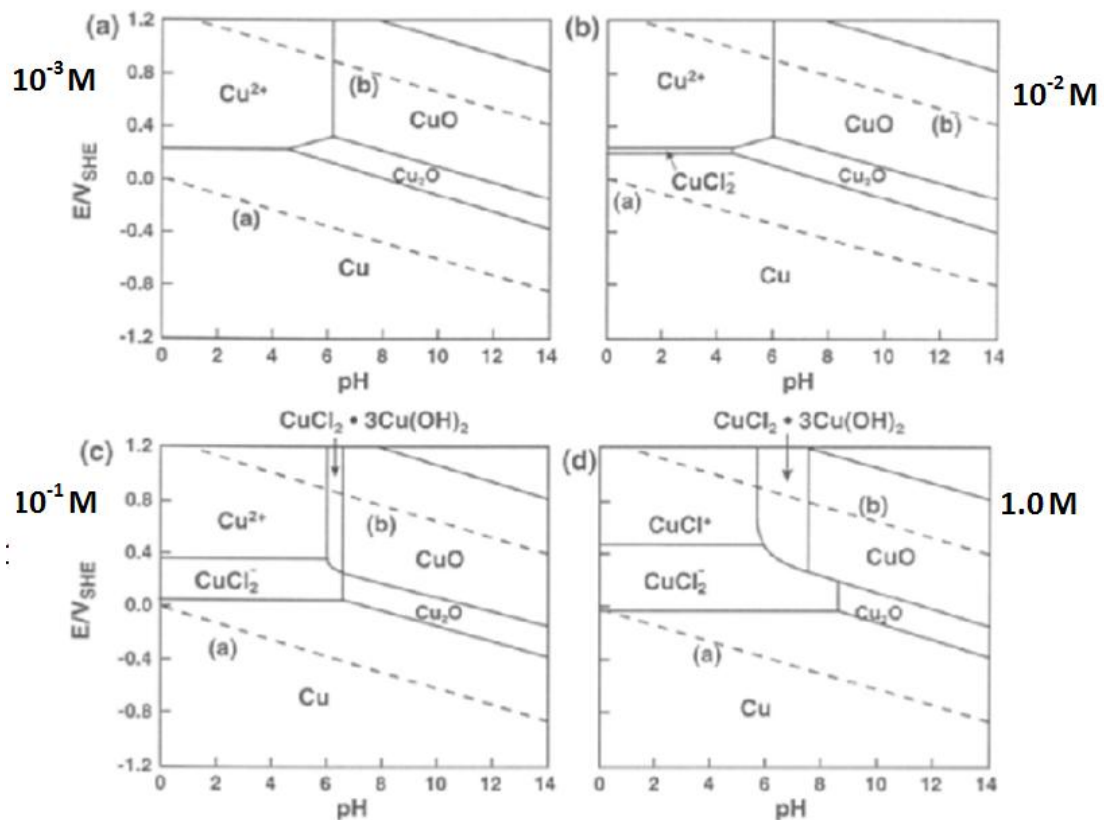


Fig. 2.9. Pourbaix diagrams for Cu - Cl⁻ - H₂O system for various chloride concentrations. (a) 10⁻³ M, (b) 10⁻² M, (c) 0.1 M, and (d) 1.0 M. [Adapted from ref: 162,163]

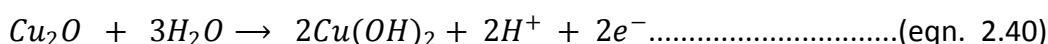
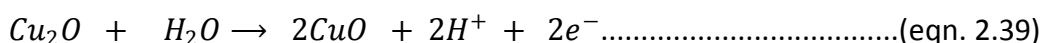
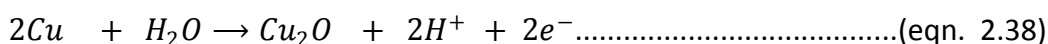
2. 8.2.1. Corrosion of Copper in Neutral and Near-Neutral Media.

There have been several reports on the neutral or near-neutral chloride solutions [164-166]. The corrosion resistance of copper alloys in seawater and chloride containing solutions has been linked to the inhibition of oxygen reduction on the oxide film formed under corroding conditions [145,146,167-169]. Regarding the effect of chloride concentration on copper corrosion, Tourky and El Wakkad [170] have suggested that the presence of chloride ions in high concentrations trigger dissolution of the oxide layer so that the electrode behaves as it would in hydrochloric acid solutions [164].

Feng et al., [171] studied the corrosion behaviour of copper in neutral aerated simulated tap water and reported increases in the very low frequency polarization resistance (R_p) with immersion time, attributed this to the growth of oxide film composed mainly of cuprous oxide on copper, that had little effect on the cathodic process but considerably reduced the anodic dissolution current. They concluded that the overall corrosion rate is controlled by the diffusion of copper ions in the oxide film and that thickening of the oxide film with immersion time increased the diffusional resistance of copper ions in the oxide film. They also reported a pH dependence of the diffusion effects, with the corrosion process controlled by the mixed

diffusion of copper ions in both solution and oxide film at a low pH of 5, disappearance of the solution diffusion phenomenon and dominance of the diffusion of copper ions in the oxide film at pH of 7.6. leading to a conclusion of a more protective oxide layer at pH of 7.6, and the displacement of diffusion effects by passivation at a high pH of 10.

Chloride ions accelerate copper corrosion by complexing Cu(I) ions in solution [163]. In alkaline solutions [77] and even in the presence of up to 1 mole per liter Cl^- which reduces the region of stability of the copper oxides [162,163], the formation of Cu (I) oxide films equation (2.38), and its subsequent oxidation to Cu(II) films equation (2.39) and equation (2.40) at higher potentials is favoured, and proceeds with the generation of protons at the electrode/electrolyte interface. The generation of these protons lead to a local decrease in pH that promotes disintegration of the passive film as the film is thermodynamically unstable at acidic pH. This can only be averted in buffered solutions in which the bulk solution has the ability to maintain the high pH at the interface [172]. Thus local acidification leads to a breakdown of the passive layer on copper even in unbuffered alkaline solutions.



From the Pourbaix diagram for copper in chloride solution [162,163,173], formation of Cu_2O is feasible in neutral solutions, and Desilovis et al., [155,156] and Otmačić et al., [174] have demonstrated that this occurs after long immersion times of about 3 hours by CuCl hydrolysis. Millet et al., [161] reported Cu_2O reduction peak near $-650 \text{ mV}_{\text{SHE}}$ ($\approx -894 \text{ mV}_{\text{SCE}}$), which shifted towards more negative values with longer immersion times and with the addition of benzotriazole respectively. In oxide layers formed under open circuit or non-anodic conditions displacement of the reduction peak of Cu_2O may be attributed to the thickening of the oxide layer [161]. However for anodically grown oxides films this correlation of Cu_2O peak displacement to oxide layer thickness does not apply as the peak displacement can also be related with ageing processes of Cu (I) oxide in anodically grown oxides [175-177]. This observation of Cu_2O reduction peak close to -900 mV SCE is of some concern in the Al-Cu galvanic couple as the aluminum can cathodically polarize copper to such potentials, and thus initiate Cu_2O dissolution and enhanced copper dissolution with respect to open circuit dissolution rates. At longer immersion times a basic cupric hydroxychloride $\text{Cu}_2(\text{OH})_3\text{Cl}$ was reportedly formed on top of Cu_2O [178,179] in 0.5M NaCl after 72 hour immersion.

The cathodic reaction of oxygen reduction is of great significance in corrosion processes

since in neutral solutions and in the absence of any other depolarizer the corrosion rate is controlled by the kinetics of oxygen reduction reaction [169]. Regarding the cathodic behaviour of copper, King et al., [180] reported cathodic oxygen reduction peaks between -0.3 and -0.4 V_{SCE} in 1 M NaCl solution and that the reaction was dominated by a four electron oxygen reduction to OH^- with the formation of small quantities of peroxide. They proposed that the mechanism involved oxygen reduction on two types of surface sites with different reactivities; the less catalytic site consisting of Cu(o) only, and the more catalytic site thought to consist of Cu(o) and Cu(I) sites, on which Cu(I) species are stabilized as $Cu(OH)_{ads}$ and or sub monolayer Cu_2O . They hinted that the observed differences in site reactivities might also be linked to difference in reactivities of different copper crystal planes, a position supported by Brisard et al's [181] report that the oxygen reduction reaction on Cu(111) and Cu(100) surfaces in sulfuric acid are structure-sensitive processes, and Jiang and Brisard's [182] report on variation in the activity and reaction pathway for oxygen reduction on crystal faces in different electrolytes which they related to the surface characteristics of Cu(*h k l*) and the structure-sensitive inhibiting effect of the adsorbed anions on their surfaces.

About the actual mechanism, King et al., [180] posited that oxygen reduction on copper in neutral NaCl solution involves molecular oxygen adsorption onto copper surface and not dissociative adsorption based on several observations; the observed reaction order ($m \geq 1$), the existence of at least two types of adsorption sites, that the surface coverage of the more active site increases with oxygen concentration, that the more catalytic surface sites unambiguously involve Cu (I) species and may also involve Cu(o) while the less catalytic surface involves Cu(o) only, that the formation of Cu(o)/ Cu(I) sites is favoured by high local pH and a more positive potential, that oxygen reduction occurs in a four electron process via a series pathway involving an adsorbed peroxide intermediate, that the rate determining step is the first electron transfer, and two possible pathways for oxygen reduction. Correlating the surface coverage of Cu_2O to increased peroxide release in solution they considered this to indicate that Cu_2O sites (i.e. Cu(I) sites) might be good catalysts for O_2 reduction to HO_2^- , but less efficient for HO_2^- reduction to OH^- , while Cu(o) sites, are more effective at reducing HO_2^- to OH^- since at more negative and/or lower oxygen concentration in solution, fast peroxide reduction before its desorption from the surface ensures increased difficulty in its detection in solution [180]. Cyclic voltammograms of copper in near neutral chloride solutions have been reported to present several anodic peaks and always only one cathodic peak [153,174]. This observation was explained according to the generally accepted mechanism of copper dissolution in chloride media (at the $[Cl^-] < 1M$)

[152,155,156,173,183] in which the first anodic peak is attributed to the formation of a porous CuCl precipitate on the electrode surface through which species can pass through, enabling the continuation of the electrochemical reaction. A second anodic peak is observed and followed by a current plateau whose intensity indicates the existence of a poorly protective film [153].

2. 8.2.2. Corrosion of Copper in Alkaline Media

The corrosion of copper in alkaline solution has received much research attention [176,184-188]. Since copper is cathodic to other metals of interest in this work (aluminum, zinc, and iron), and on galvanic coupling to these other metals a higher pH is expected in the electrolyte above the copper surface, more emphasis will be on copper corrosion in alkaline chloride media. Depending on the electrolyte composition and electrochemical conditions the anodic behaviour of copper in alkaline environments is reported to lead to the formation of an oxide film consisting of either Cu₂O or a duplex layer of Cu₂O and CuO [189-191]. The formation of Cu₂O in the course of copper dissolution in alkaline solutions have been severally reported [184,186,188].

Droog et al., [189] studied the initial stages of anodic oxidation of polycrystalline copper electrodes in alkaline solution and concluded that the first stage in the anodic oxidation of polycrystalline copper electrodes in NaOH solutions is the electrosorption of oxygen species in a process that occur in two successive stages. Drogowska et al., [147] studied copper dissolution in an alkaline aqueous solution at pH 12 (0.01 M NaOH) containing up to 1 M NaCl at 25°C using cyclic voltammetry and demonstrated the existence of two electrochemically different, oxidized species identified as Cu₂O and CuO [192] on the electrode surface. In the presence of NaCl in solution a third cathodic peak corresponding to the reduction of CuCl was observed, the presence of which was suggested to indicate that the copper oxides/solution interface becomes acidic during the dissolution. Furthermore the morphology of the accumulated CuCl and the presence of holes in it reportedly suggest that the corrosion product is non-protective, and on detaching from the electrode surface into the alkaline solution, reacts with the electrolyte forms a final product that is a mixture of (Cu₂O), (CuCl₂)·3Cu(OH)₂, and (CuCl₂·3Cu(OH)₂·3H₂O) [147]. Antonijevic et al., [193] studied the influence of pH on electrochemical behaviour of copper in presence of chloride ions and reported that chloride ions have smaller effect at higher pH, and that the presence of chloride ions renders the open circuit potentials more negative. Becerra et al., [176] studied the influence of slow Cu(OH)₂ phase formation on the electrochemical behaviour of copper in (in 0.1 M NaOH) alkaline solutions and reported that the complex

electrochemical behaviour of copper in alkaline solutions involves the electroformation and electroreduction of different oxides or hydroxides layers accompanied by the formation of Cu(I) and Cu(II) soluble species depending on the potential and time windows used in the electrochemical measurements, and evidences of a slow $\text{Cu}(\text{OH})_2$ phase formation, explained by proposing the existence of two limiting complex structures of the anodic layers namely $\text{Cu}/\text{Cu}_2\text{O}$ (porous inner layer)/ CuO (outer layer) and $\text{Cu}/\text{Cu}_2\text{O}$ (porous inner layer)/ $\text{CuO}/\text{Cu}(\text{OH})_2$, (outer layer).

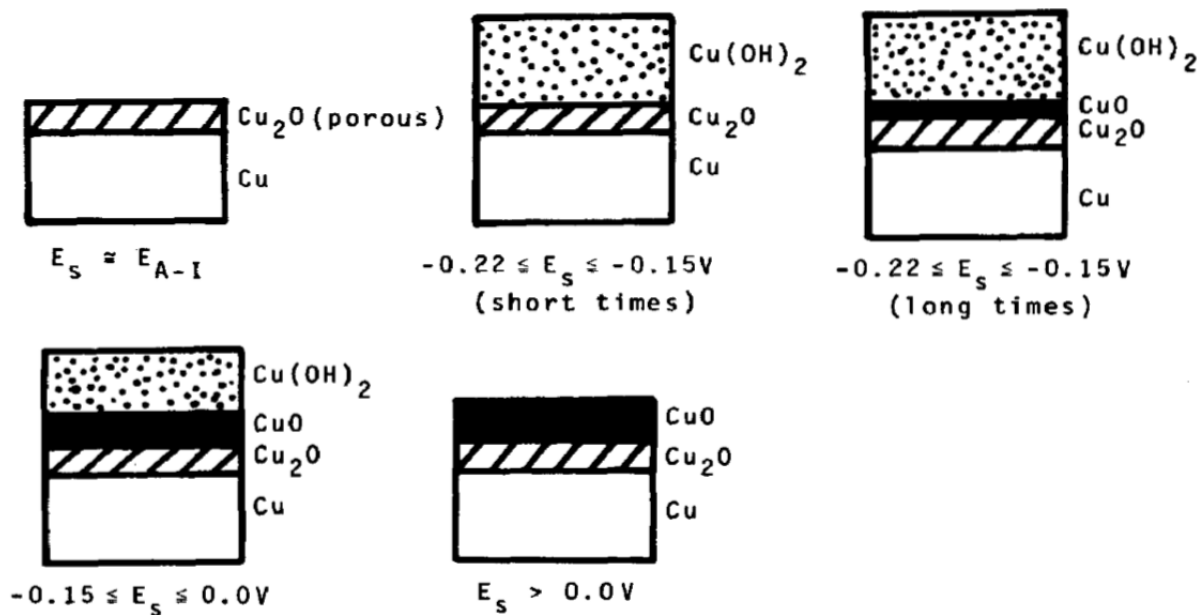


Fig. 2.10. Schematic illustration showing the possible passive layer structures on copper at different constant potential (E_s) values. [Adapted from ref: 176]

Fig. 2.10. above adapted from Becerra et al., [176] shows that the composition and structure of the film formed on copper in alkaline media can vary significantly depending on the polarization applied and the duration of the polarization. These have important implications in galvanic couples of copper with other metals such as aluminium, zinc and iron, which will place the copper under significant cathodic polarization with possible effects on the mechanism of the cathodic activities on copper.

2. 8.3. Corrosion of Iron

Without the use of inhibitors and with respect to pH, iron is best employed in the pH range $\geq 4 \leq 9$, as from pH 4 to 9 its corrosion rate is practically independent of pH, forms protective films of corrosion products at higher pH values, and undergoes rapid dissolution with hydrogen evolution at pH less than 4 [194]. The corrosion rate of steel is reported to increase with aeration of the water, and that oxygen is five to ten times more aggressive than carbonic

acid [195]. The corrosion of iron proceeds in almost all environments with the production of a noticeable corrosion product layer; the rust layer. The rust layer formed on iron decreases the corrosion rate, the effectiveness of this inhibiting effect being dependent on the film's specific resistance to oxygen diffusion and to its uniformity over the metal surface. The specific resistance of films is determined by its composition and the distribution of the constituents from the metal-oxide interface surfaces outwards, while the uniformity of the film is dependent on a variety of factors the most of which are the original condition of the metals, the local distribution of dissolved oxygen and hydrogen ions (pH) [196]. The corrosion products formed on iron can also interfere with the corrosion mechanism. Forrest et al., [196] have established the corrosion products formed in iron immersed in water, deduced the mechanism of their formation and using the then available literature data on chemical equilibria, solubilities, thermal properties, and the free-energy contents, calculated the free-energy decreases accompanying reactions involved in the formation of corrosion products that can constitute the corrosion product film/layer(s) on iron. The corrosion product on iron (rust) is composed of a variety of iron oxides and oxyhydroxides, the particular composition being dependent on the physico-chemical conditions near the immersed iron surface and usually exhibits increasing iron to oxygen ratios from the metal oxide interface towards the oxide water interface.

An increase in the OH^- concentration near the iron surface and reduced oxygen supply are reported as the most important factors favouring the precipitation of ferrous hydroxide ($\text{Fe}(\text{OH})_2$) while a low pH in the solution near the iron surface coupled with plentiful oxygen supply favours the precipitation of ferric oxide ($\text{Fe}(\text{OH})_3$) [196]. In iron immersed in distilled water magnetic iron oxide (Fe_3O_4), which is not very resistant to ionic and oxygen diffusion towards the metal, is the predominant component of the rust layer formed when the diffusion of ions from the diffusion layer to the bulk solution proceeds slowly or non-uniformly [196]. Diverse mechanisms have been advanced to explain the dissolution kinetics of iron in aqueous solutions [197].

Since the corrosion resistance of iron is related to the properties of the corrosion product layer on it, and the nature of this layer dependent on pH, the Pourbaix diagram for iron (Fig 2.11) illustrates the thermodynamically determined dissolution behaviour of iron as a function of pH at 25°C for an Fe-Cl- H_2O system since all tests in the present work was done in the presence of chloride ions. Lines (a) and (b) represent the equilibrium potentials for the hydrogen evolution and the oxygen reduction reactions in aqueous solutions, respectively, the

dotted lines correspond to the equilibria involving ionic species only, while the solid lines correspond to equilibria between the different solid and ionic species considered.

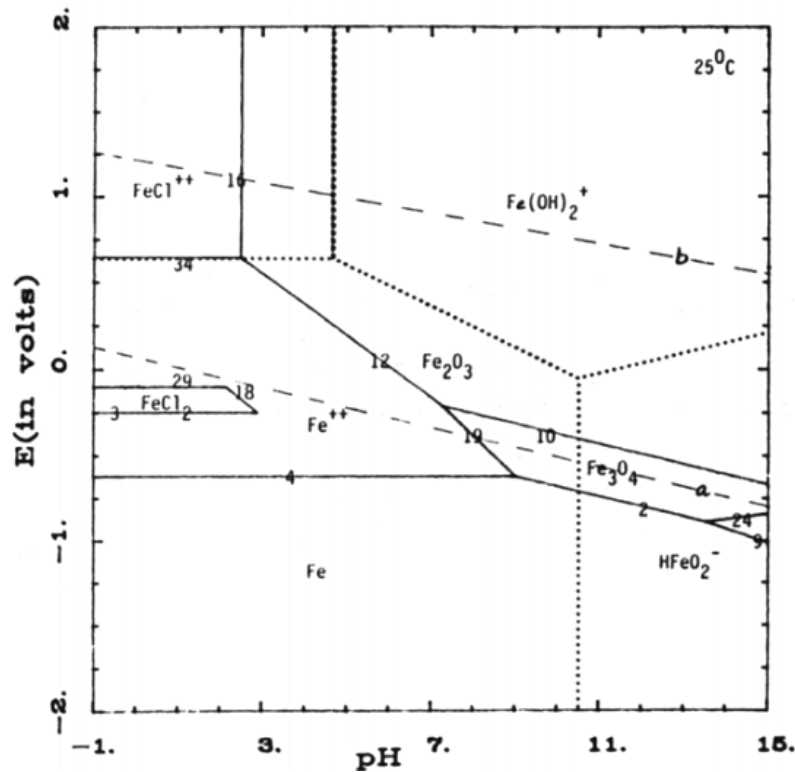


Fig. 2.11. Pourbaix diagram for Fe-Cl- H₂O at 25°C. [Adapted from ref: 198]

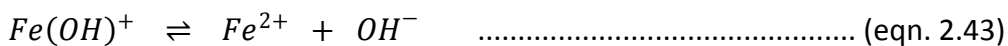
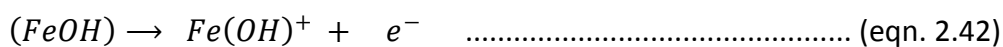
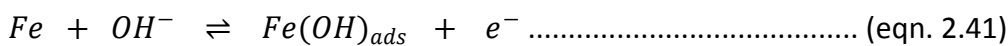
2. 8.3.1. Corrosion of Iron in Neutral and Near-Neutral Media

Stratman and Müller [199] reported significant increase in oxygen reduction on iron electrodes on formation of rust. This was linked to an increase in the effective surface area on rust formation, and more importantly on the presence of Fe₂O₃ an n-type semiconductor in the rust, which enhances cathodic reactions while suppressing anodic reactions [199,200]. They established that for iron in near neutral aqueous solutions, the electron transfer reaction (of oxygen reduction) takes place within the oxide scale on reduced (Fe²⁺ states) and thus electron conducting iron oxides and not on the metal/oxide interface, with the rate strongly dependent on the electronic properties of the oxide [199]. Oxygen reduction on iron is reported to occur through two different pathways and at different rates depending on the nature of the electrode [201]. Oxygen reduction proceeds through 4e⁻ pathways on bare iron with very little H₂O₂ formation as an intermediate, but proceeds at a greater rate through a 2e⁻ pathway with the formation of hydrogen peroxide as a reaction product on passive iron. According to Jovancicevic and Bockris, [201] the rate determining step involves O₂ formation on bare iron but is O₂⁻ chemisorption on passive layer. You et al., [202] concluded that in neutral chloride solutions, iron corrosion is initiated in pits that quickly become blocked by corrosion products causing

propagation around pits and the formation of passive layers. They observed a time dependent corrosion process in which for very short immersion times before the formation of the porous layer, the cathodic reaction of dissolved oxygen reduction proceeds on a bare surface, while anodic reaction proceeds on a very small area, while at longer immersion times, the anodic sites (pits) become less active with oxygen reduction taking places through the porous layer, the area of the bare metal thus decreased, corrosion becomes generalized.

Bonnel et al., [203], demonstrated that at the corrosion potential the oxygen reduction reaction on iron in neutral chloride solution is under diffusional or mixed (activation + diffusion) control depending on test conditions, that oxygen transport takes place in the liquid phase and also through a porous layer of corrosion products, and that the oxygen consumption occurs not only by electrochemical reduction but also by chemical oxidation of ferrous to ferric ions. The corrosion rate of carbon steel in aerated sodium chloride solution is reported to be controlled by the reduction of dissolved oxygen [204].

For iron dissolution in neutral aqueous media, the mechanisms based on that proposed by Bockris et al., [197] have been employed in which the rate determining step is equation 2.42.

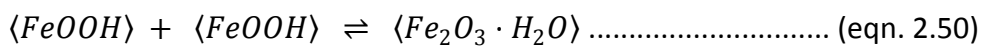
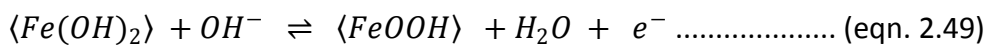
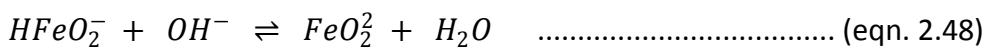
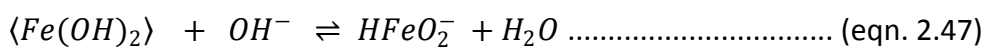
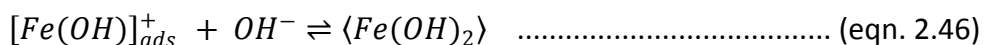
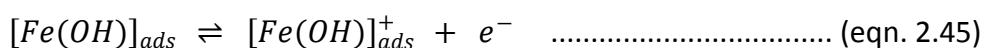
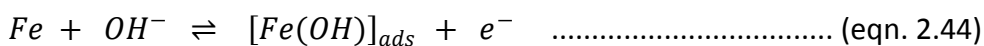


2. 8.3.2. Corrosion of Iron in Alkaline Media

Due to challenges with steady state measurements on iron in alkaline solutions [205], most investigations have been carried out in non-steady state conditions. Asakura and Nobe [206] have noted that the mechanism of iron dissolution in chloride containing alkaline solution differs from that in neutral solutions in three ways; (a) due to the high concentration of OH⁻ the surface coverage of the reaction intermediate Fe(OH) is considerably larger, (b) pH changes at the electrode surface is not significant, and (c) the nature of the hydroxochloro-iron complex complex $[Fe(OH)_m(Cl)_n]^{2m-n}$, in alkaline solutions is different from that in neutral solutions. In alkaline solutions iron exists predominantly in the form of HFeO₂⁻ ions [207]. Kabanov et al., [208] showed that at equal potentials the anodic dissolution of iron in chloride free alkaline solutions proceeds about 10⁴ times as fast as in acids, but slows down drastically with time and finally completely ceases due to passivation; a phenomenon not observed in acid solutions. These observations of greater dissolution rate and passivation in alkalis were attributed to anodic deposition of oxygen on the iron surface, which in alkaline solutions is triggered by the

large concentration of hydroxyl ions, so that the oxygen on the iron surface plays a dual role of accelerating dissolution, and passivating the iron to stop iron dissolution. In chloride containing alkaline solutions passivation was not observed especially at significant chloride concentrations leading to a conclusion that the accelerating effect of Cl^- ions on the corrosion of iron is due it hindering the passivation of iron by adsorbed oxygen, which otherwise would put an end to the dissolution of the iron. In the light of experimental observations, they [208] suggested the formation of $\text{Fe}(\text{OH})_2$ and $\text{Fe}(\text{OH})_3$ and proposed a mechanism of anodic dissolution of iron in alkaline solutions that occur not by direct transition of hydrated metal ions into the solution, but by formation of intermediate surface iron-hydroxyl complex(es).

Guzman et al., [209] studied the potentiodynamic behaviour of iron in alkaline solutions and reported that the electrochemical characteristics of the systems can be explained through a series of successive conjugated redox couples principally involving $\text{Fe}(\text{OH})$, $\text{Fe}(\text{OH})_2$, and FeOOH as limiting stoichiometric species with the yield of soluble species such as either FeO_2^{2-} or HFeO_2^- increasing with increase in the pH of the solution. They put forward a mechanism for iron corrosion and passivation in KOH solutions under the potentiodynamic conditions in terms of a reaction sequence containing only hydroxo- and oxo-species participating in different proton transfer processes (equation 2.76 to 2.81). The square brackets denote reaction intermediates whose surface coverage is of the order of a fraction of the monolayer and the angle brackets indicate species eventually related to the formation of new phases and which may undergo ageing in the equations below [209].

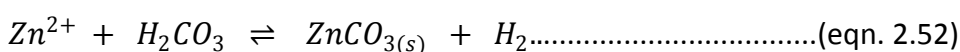
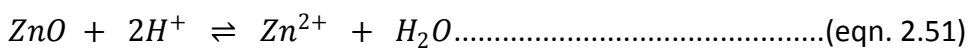


Zou and Chin [210] studied the anodic behaviour of carbon steel in deaerated concentrated (1-19 N) NaOH solutions at 25-80°C over a range of potentials from the active to transpassive regimes and reported that in the active dissolution potential regime, steel dissolution occur primarily via a two-electron transfer reaction to HFeO_2^- ion, and as the potential approaches the active-passive transition potential, a parallel reaction occur, which produces the soluble trivalent iron species; FeO_2^- ion. The formation of this species was

attributed to the oxidation of an intermediate $\text{Fe}(\text{OH})_2$ surface species in the active dissolution reaction. At the active-passive transition potential, the $\text{Fe}(\text{OH})_2$ intermediate was reportedly further oxidized to a passive Fe_3O_4 film, leading to reduction in the current with further increase in potential, and its further oxidation to a Fe_2O_3 film in the the course of the current drop from the active to passive state that presents as a small second current peak on the anodic polarization curves [210].

2. 8.5. Corrosion of Zinc

Zinc is reported to be divalent in all its compounds, as compounds of $\text{Zn}(\text{I})$ are not existent in nature [211]. Temperature and crystal orientation have been reported to have little effect on the zinc potential, as the equilibrium potential difference measured between different crystal surfaces of a zinc single crystal and polycrystalline zinc was less than 10 mV [212]. Zinc in aqueous media can form insoluble compounds like zinc carbonate, sulphate, and phosphate which are commonly found in corrosion products particularly zinc carbonate. As a consequence these compounds enhance the corrosion resistance of zinc in diverse environments [213]. The enhanced atmospheric corrosion resistance of zinc and its corrosion resistance in aqueous media rich in dissolved carbon dioxide is linked to the formation of insoluble and protective layer of zinc carbonate. The two-step mechanism of the formation of zinc carbonate in aqueous solutions containing carbonates and bicarbonates can be expressed by the following reactions (equation. 2.51 and 2.52) below [214,215]:



From Fig. 2.12, it is evident that zinc is thermodynamically unstable in water and aqueous solutions being prone to dissolution with hydrogen evolution over the entire pH range. If the solutions pH falls between about 8.5 and 12, zinc can be covered with a hydroxide film, with a resultant inhibition of zinc dissolution rates. This is the principle of one of the corrosion mitigation strategies employed in corrosion inhibition of metals in aqueous media wherein the local change in pH due to metal dissolution reactions is used as a trigger to effect the deposition of insoluble species on the metal surface either from the system itself or from interaction of added chemical species (corrosion inhibitors). While the Pourbaix diagram below (Fig. 2.12) gives information of equilibrium behaviour of zinc as a function of pH, it gives no information on the rate of zinc dissolution in real systems as a fuction of pH.

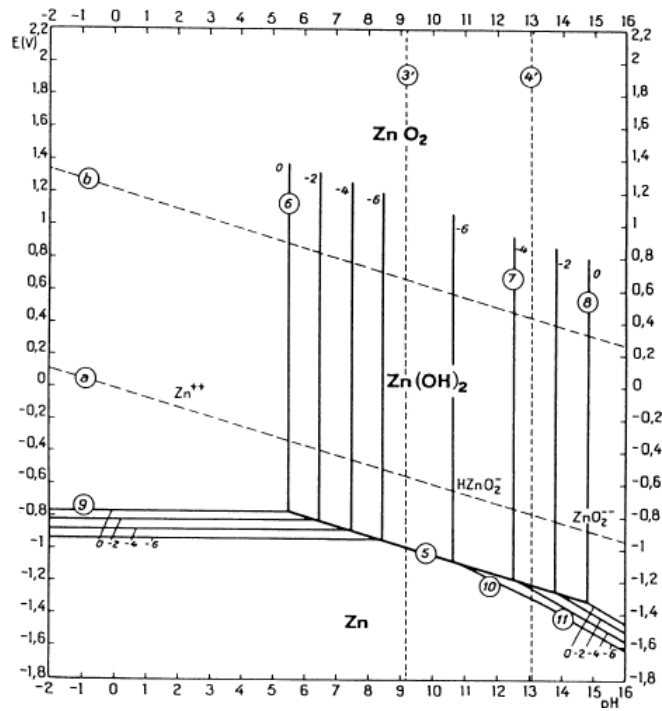


Fig. 2.12. Potential-pH equilibrium diagram for the zinc-water system at 25°C [Adapted from ref: 77].

For an insight into the kinetics of zinc dissolution as a function of pH, the fairly recent work by Thomas et al., [216] is a good resource. Fig 2.13 below, adapted from a unique recent report [216] illustrates the combination of electrochemically acquired thermodynamic (E_{corr}) and kinetic (i_{corr}) information for zinc as a function of pH. It is obvious from the plot that the corrosion rate of zinc is pH dependent, with the lowest corrosion rates at very alkaline potential, and that the corrosion rate is under cathodic control in acidic pH region evidenced by decreasing E_{corr} with decreasing i_{corr} , but under anodic control at alkaline pH as observed from decrease in E_{corr} with increase in i_{corr} .

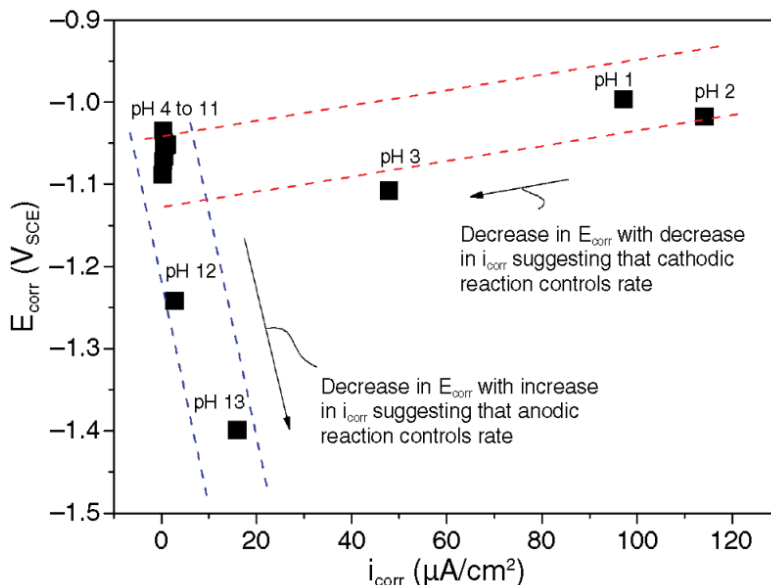


Fig. 2.13. Plot of E_{corr} vs. i_{corr} for zinc at different pH in 0.1 M NaCl [Adapted from ref: 216].

Other important factors that influence zinc corrosion rates are temperature and chloride content of the aqueous media. Increase in temperature in aqueous media is reported to enhance the dissolution of zinc up to 60°C after which dissolution rate decreases at higher temperatures [217]. The chloride ion is the most corrosive to zinc in aqueous media, especially if present in amounts in excess of 50 mg/l (50 ppm), the effect being enhanced in soft waters with low carbonate content [218]. On the contrary the presence of carbonates, silicates, alkali and alkaline earth compounds, and free carbon dioxide have a tendency to inhibit zinc corrosion in aqueous media [219]. Since chlorides have such deleterious effects on zinc corrosion rates in aqueous media, and the corrosion resistance of zinc is based on the nature and type of corrosion product formed on its surface. Fig 2.14 below [220] is used to illustrate how variations of the chloride content and pH influence the corrosion product formed in aqueous media.

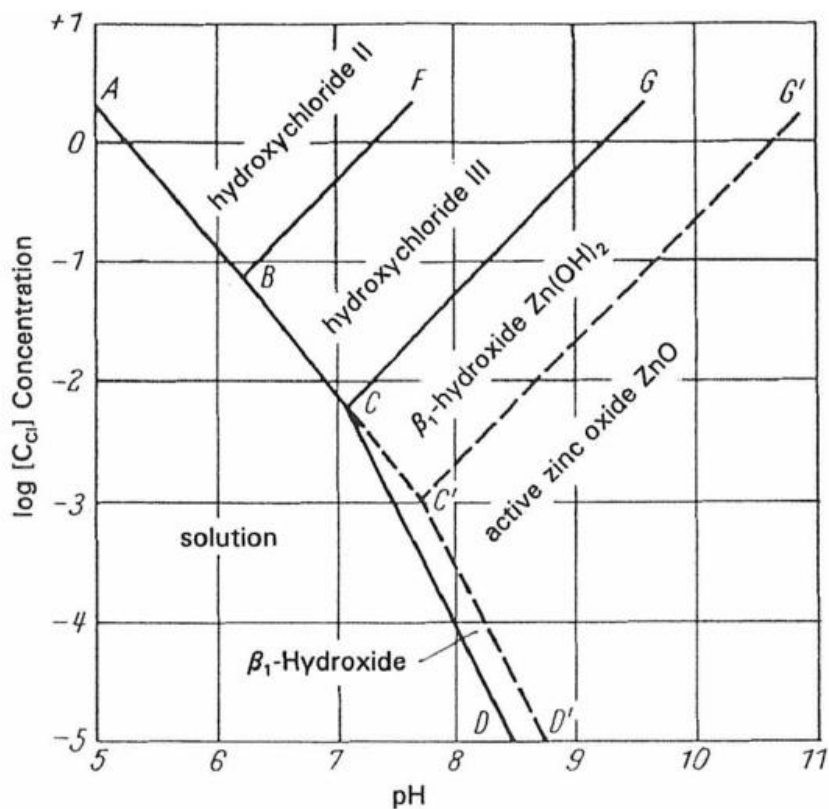


Fig. 2.14. Regions of existence of zinc corrosion products in aqueous media as a function of pH and Cl⁻ concentration [Adapted from ref: 220].

Roetheli et al., [221], investigating zinc corrosion in HCl and NaOH of varying pH reported that no corrosion films are formed on zinc samples at pH lower than 5 or higher than 13.5 even after 30 days immersion and that films observed at pH between 6 and 12.5 were not adherent. Baugh [222] reported the formation of a porous non-passivating oxide film in the pH range 3.8 - 5.8 in slightly acidic solutions of NaCl, NaClO₄, and Na₂SO₄. Boto and Williams [223]

observed that buffering sulphate solution in the pH range 5.6 to 6.2 yielded no corrosion products whereas corrosion products were formed in unbuffered solution in the same pH range. In explaining this observation, it was remarked that a higher bulk pH than the surface pH is necessary for hydroxide formation and this being absent in the buffered solution due to the buffering effect no corrosion products are formed in contrast to unbuffered solution [223,224].

Macias and Andrade [225] investigating corrosion products on zinc surfaces in alkaline solutions reported that in KOH solutions of varying concentrations the initial corrosion product was ZnO but became mainly Zn(OH)₂ after about 30 days immersion, with the rate of transformation from ZnO to Zn(OH)₂ increasing with increasing pH. The morphology of the corrosion products was also reported to be dependent on pH with the zinc oxide formed between pH 11-12 porous and non-adherent but porous and a continuous layer at pH greater than 13.4. However, between pH 12 and 12.8 they reported a thin and compact ZnO layer, and a layer of well-packed Zn(OH)₂ crystals at pH 12.8 to 13.4.

Since the morphology and type of zinc corrosion products from the reports above are sensitive to pH, the dependence of zinc corrosion rates on pH is obvious. Although slight differences are observed in literature [221,226,227,228] on the pH ranges for formation and nature of zinc corrosion products, most probably due to slight differences in test conditions, Zhang [224] had summarized that, in general at pH values lower than 5, zinc corrosion rate is high as no corrosion product is formed on zinc surface and consequently the corrosion of zinc in this region is solely dependent on the cathodic reaction rates. Between pH 5 and 9, zinc corrosion rate is reduced by the formation of bulky but porous corrosion products, and least in the pH range 9 to 12 due to formation of a passive thin and compact corrosion product layer. In contrast at pH higher than 13, the corrosion rate rises sharply due to difficulty in maintaining a stable corrosion product layer [224]. Reduction in corrosion rate of zinc at pH close to 14 had been attributed to decreased solubility of oxygen in strongly alkaline solutions [221].

The formation of corrosion products on zinc immersed in aqueous solutions can manifest in changes in measured double layer capacitances. The measured capacitance value on zinc is a function of the potential, solution concentration, and also the pH as strong interaction with OH⁻ have been reported at pH greater than 3.8 [228]. Prominent values of double layer capacitance on zinc electrode immersed in aqueous media around its reversible potential have been reported to be in the range of 16 to 20 μF cm⁻² [212,230-232]. Higher measured values of capacitance on zinc in neutral and alkaline solutions with prolonged immersion time may be due to slow formation of a solid film on the electrode surface [233]. In addition measured

capacitance values higher than $20 \mu\text{F cm}^{-2}$ have been attributed to faradaic and specific adsorption processes [234]. However, capacitance values up to $600 \mu\text{F cm}^{-2}$ have been reported in KOH solutions as a result of OH^- adsorption [235-237].

2. 8.4.1. Corrosion of Zinc in Neutral and Near-Neutral Media

The mechanism of zinc corrosion in aerated neutral and near neutral solutions can be complex due to the formation of a wide range of compounds in the corrosion product layer on the metal [238], mainly composed of zinc oxide, zinc hydroxide and zinc hydroxide chloride or simonkolleite ($\text{Zn}_5(\text{OH})_8\text{Cl}_2 \cdot 2\text{H}_2\text{O}$). The zinc hydroxide chloride and zinc oxide are the dominant corrosion products [239]. There have been slight variations in the compounds detected on corrosion product layers formed on zinc in aerated near neutral solutions [239-241]. At ambient CO_2 levels, zinc hydroxide carbonate ($\text{Zn}_5(\text{OH})_6(\text{CO}_3)_2 \cdot \text{H}_2\text{O}$) have been an additional observation in the corrosion product layer on zinc [238,240].

Mouanga et al., [238] in studies on the corrosion product layer formed on zinc in aerated 0.6M NaCl (pH = 6.5) and 0.5M NaOH (pH = 13.69) solutions at ambient reported a less compact corrosion product layer in NaCl and the presence of zinc oxide (ZnO), zinc chloride (ZnCl_2), zinc hydroxide ($\text{Zn}(\text{OH})_2$), zinc hydroxide chloride ($\text{Zn}_5(\text{OH})_8\text{Cl}_2 \cdot 2\text{H}_2\text{O}$) and zinc hydroxide carbonate ($\text{Zn}_5(\text{OH})_6(\text{CO}_3)_2$) and proposed a mechanism for their formation. Their proposed mechanism for zinc corrosion in near neutral NaCl at ambient is composed of two partial reactions; the anodic dissolution of zinc (equation 2.53) and the cathodic reduction of oxygen to yield hydroxide ions (equation 2.54). Further reaction of the products of these partial electrode reactions (Zn^{2+} and OH^-) with other species in the solution depending on the local pH and concentration of species yields the observed constituents of the corrosion product layer(s) on zinc.



The zinc hydroxide is formed by the reaction of the zinc cations and the hydroxide ions (eqn. 2.55).

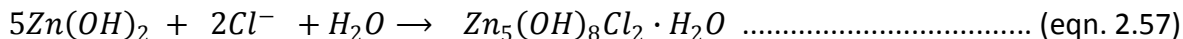


At very active cathodic sites with high enough local pH values the formation of zincate ions ($\text{Zn}(\text{OH})_4^{2-}$) may occur according to equation 2.96, by further reaction of zinc hydroxide with the excess hydroxide ions.

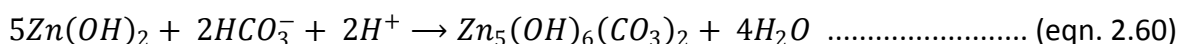
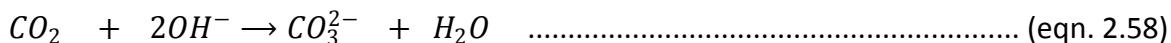


By the migration of chloride ions to the anodic sites rich in zinc ions, zinc hydroxide chloride is

formed (equation 2.57).



The absorption of atmospheric carbon dioxide by the test electrolyte leads to the formation of carbonate (equation 2.58) and bicarbonate ions (equation 2.59), which leads ultimately to the formation of zinc hydroxide carbonate by the reaction of zinc hydroxide and hydrogen carbonate ions (equation 2.60).

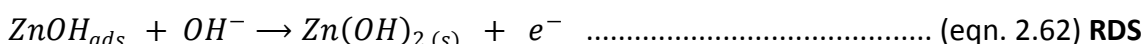


Based on the above proposed mechanism of Mouanga et al., [238] it is obvious that formation of Zn(OH)₂ is the pivotal step on which the formation of the more complex corrosion products depend.

2. 8.4.2. Corrosion of Zinc in Alkaline Media

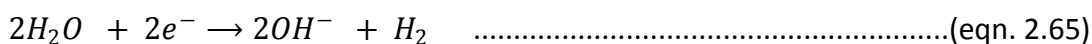
Mokaddem et al., [227] studied anodic dissolution of zinc and zinc alloys in alkaline solution and by independently measuring the oxidation rate of zinc (electrical current) and the rate of Zn²⁺ dissolution (partial elemental current) calculated the amount of insoluble zinc cations produced at any time, and by assuming that the insoluble cations are present as a zinc oxide film, determined the growth of the oxide film as a function of potential and time. Based on their results they concluded that at least three forms of zinc based oxide/hydroxide films form during the anodic polarization; Type I oxide which is formed when the metal/electrolyte interface becomes locally saturated with Zn²⁺ ions, Type II oxide which forms on the metal surface underneath the film of Type I oxide but has little inhibiting effect on zinc dissolution, and Type III oxide which is produced in much smaller quantity and result in a transition to the passive state, possibly by a potential induced transition of Type II to Type III oxide.

They proposed a mechanism to match their observations which involves the sequential addition of OH⁻ to Zn (equation 2.61 to 2.64):



In another instance, Mouanga et al., [238] in studies on the corrosion product layer formed on zinc in aerated 0.6M NaCl (pH = 6.5) and 0.5M NaOH (pH = 13.69) solutions at

ambient reported a more compact corrosion product layer in NaOH and the presence of zinc oxide (ZnO), zinc hydroxide (Zn(OH)₂), and zinc hydroxide carbonate (Zn₅(OH)₆(CO₃)₂) and proposed a mechanism for their formation. In their proposed mechanism the main cathodic reaction (equation 2.65) is hydrogen evolution by water reduction while zinc dissolution is via "alkaline attack" to yield zincate ion in a reaction (equation 2.66) earlier proposed by Youssef et al., [242], with the production of zinc oxide and hydroxide involving the afore produced zincate ions according to equations 2.67 and 2.68 respectively, and that of zinc hydroxide carbonate following the same scheme as in NaCl above (equations 2.58, 2.59 and 2.60).



2. 9. "Corrosion" (Degradation) of Carbon Fiber Reinforced Plastics (CFRPs)

Carbon fiber reinforced polymers being a composite material are capable of exhibiting at least two and practically three forms of degradation, related to the degradation of the matrix, the carbon fibers, and the interface between them. Degradation of carbon fiber reinforced polymers can be accelerated under polarization (either cathodic and anodic polarization) [243]. However in this work, the degradation of CFRP under cathodic polarization is of much greater relevance as the CFRP is cathodically polarized on galvanic coupling with metals used. Carbon fibers for structural material applications are designed to have the graphitic a-axis oriented along the fiber length in order to maximize the tensile strength [244].

2.9.1. The Surface Chemistry of Carbon

A review of literature reveals that the carbon fiber surface composition under the test conditions employed in this work is bound to be complex and dynamic, as carbon is capable of forming "surface oxides" of oxygen containing and even nitrogen containing functional groups [245-248] which affect surface reactivity. These "surface oxides" have been classified as basic [249] or acidic [250] depending on the acidity of the functional group.

The introduction of oxidizing agents to carbon materials under wet or dry conditions can lead to the formation of either of three types of oxygen containing surface groups; acidic, basic, and neutral [251-253]. Gas phase oxidation of the carbon is reported to lead mainly to increase in the concentration of hydroxyl and carbonyl surface groups, while oxidations in an electrolyte

predominantly increases the concentration of carboxylic acid groups [254]. The application of electrochemical polarization as employed in this work is capable of changing the type of surface groups [255]. Anodic oxidation of graphitic materials in aqueous solutions reportedly leads to formation of surface oxides predominantly composed of carboxylic and phenolic groups [256-258]. Cathodic polarization of carbon surfaces containing "surface oxides" is likely to result in some reduction of these oxides [259-262]. The specific capacitance of carbon is reportedly structure sensitive [263] and increases with formation of carboxyl groups on the surface during anodic oxidation [264-266]. Without special pretreatments almost all carbon surfaces are prone to reactions with oxygen and water, resulting in the formation of oxygen-containing functional groups on the carbon surfaces. Hence the exposed surfaces of carbon fibers in the carbon fiber reinforced polymers, used in this work were most probably oxygen terminated. This can result in information of "surface oxides" or oxygen-containing functional groups on the carbon fiber surfaces on interaction with air and moisture during polishing, and also on immersion in aqueous media whilst galvanically coupled to metals which leads to a high pH environment near the CFRP. These surface oxide species can have effects on the general electrochemical behaviour of the carbon fibers, and on specific processes such as adsorption, electron transfer kinetics, electrocatalysis, etc. For instance, negative surface charge due to carboxylates as surface oxides on carbon, have been reported to exert marked electrochemical effects on adsorption and electron transfer rates [267-269]. Though the presence of these surface oxides are almost inevitable and undesirable, it is possible in some situations to manipulate them for beneficial electrochemical performance [244].

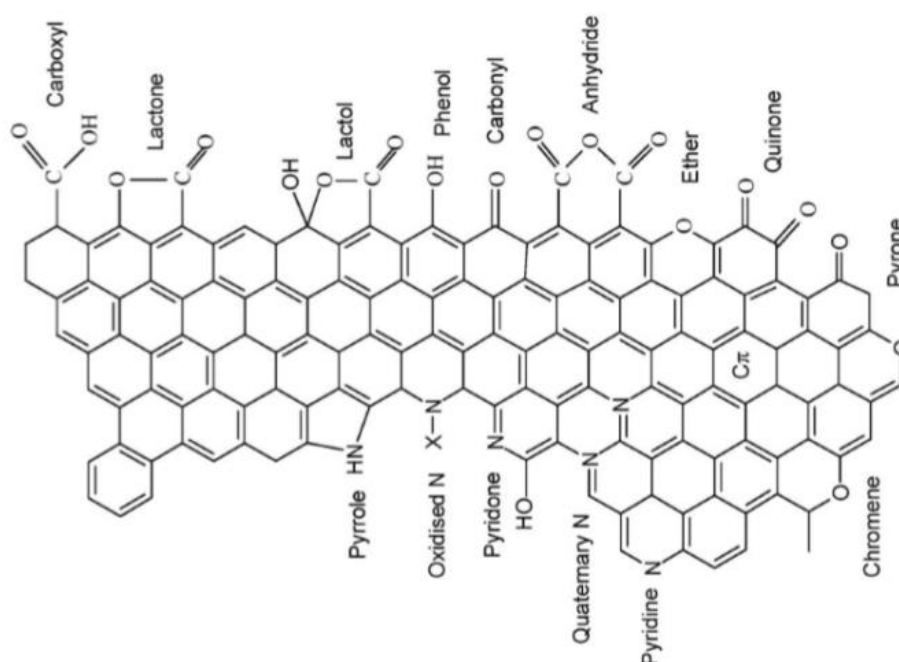


Fig. 2.15. Functional groups on carbon surfaces [Adapted from ref: 248].

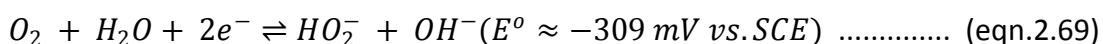
Graphitic materials are regarded to be composed of at least two well defined surface sites; the edge plane sites perceived to be the active sites for electrochemical reactions, and the basal plane sites regarded as relatively inactive electrochemically, as improvements in electrochemical behaviour have been reported by increasing the edge sites [29]. The application of a high current density through carbon fibers in an electrolyte solution is reported to have extraordinary effects on the fiber morphology, by the generation of a very high surface area with an apparent capacitance up to $4000 \mu\text{F cm}^{-2}$, which is more than two orders of magnitude higher than the typical values for glassy carbon and carbon fibers [244,270-273]. Generally the double layer capacitance of carbon materials is reported to be about $20 \mu\text{F cm}^{-2}$ or less [274]. However, marked differences have been reported in the double layer capacitances of the basal and edge sites of graphite with capacitance values of $3\text{-}16 \mu\text{F cm}^{-2}$ reported for the basal sites, and $50\text{-}70 \mu\text{F cm}^{-2}$ for the edge sites respectively in 0.9 M NaF solutions [275]. Chu and Kinoshita [29] have suggested that such marked differences in the double layer capacitance of basal and edge plane sites can be exploited as a convenient diagnostic tool to monitor changes to the carbon surface, and anticipated that modifications to the carbon surface that increase the concentration of exposed edge sites on the basal plane surface will result in higher values of double layer capacitance. Conversely, it is anticipated in this work that surface modifications to the carbon surface that result in decrease in the concentration of exposed edge sites on the basal plane surface is likely to result in lower double layer capacitances.

In energy research pertaining to fuel cells and batteries, iron, platinum, and nitrogen are incorporated into carbon electrode materials to provide catalytic sites for electrocatalysis of O_2 reduction to both hydrogen peroxide and water [244,276-278]. This is interesting with respect to the present work as it reveals the possibility of enhanced cathodic activity on CFRP galvanically coupled to metals, if metal cations precipitate from solution onto carbon surfaces in the local high pH zones (as observed in Fig. 6.5) around galvanically coupled CFRP surface as a film of metal oxide(s)/hydroxide(s). Since the main cathodic reaction on CFRP used in this work is oxygen reduction by the carbon fibres, oxygen reduction on carbon electrodes is discussed before CFRP degradation.

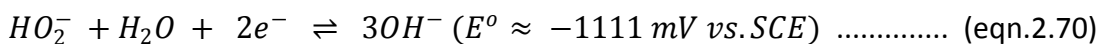
2. 9.2. Oxygen reduction on carbon electrodes

Oxygen reduction on carbon and graphite electrodes reportedly proceeds mainly through the peroxide pathway [22,25,279]. The general mechanism of oxygen reduction on ordinary

graphitic electrode in the absence of added catalysts involves two successive oxygen reduction processes (eqns. 2.69 and 2.70) [22-25,27,276,280];



The reaction of equation (2.69) is either followed by another 2-electron (electrochemical) reduction of the hydroperoxyl (HO_2^-) ion to hydroxyl ion (OH^-), expressed in equation (2.70);



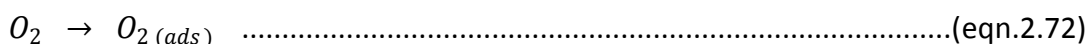
or by a fast chemical decomposition of the hydroperoxyl (HO_2^-) ion that leads to regenerative production of oxygen (eqn 2.71);



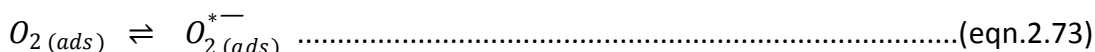
The rate of the chemical decomposition of the hydroperoxyl (HO_2^-) ion (equation 2.71) relative to its consumption rate in the 2-electron electrochemical reduction process (equation 2.70) is a factor in detection of a second peak in cyclic voltammograms attributable to the electrochemical reduction of the hydroperoxyl (HO_2^-) ion to hydroxyl ion (OH^-) [276].

In spite of the fact that a full-scale mechanistic analysis of the oxygen reduction reaction is inexpedient [276], there appears to be a general consensus [25,281-283] that the process starts with or involves surface adsorption of oxygen on metal-free carbon surfaces (equation2.72), followed by an initial electron-transfer step leading to O_2 reduction to superoxide (equation 2.73), a protonation step leading to formation of hydroperoxide radical (equation 2.74), and its subsequent reduction to hydroperoxide (equation 2.75) [276]. This treatment is equivalent to considering the first 2-electron reaction (equation 2.69) to take place as a four-step 2-electron process expressed in (equation 2.72 to 2.75) below.

An adsorption step:



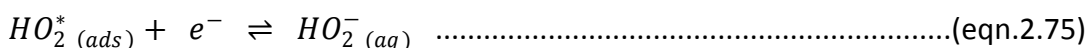
An electron-transfer step which is reportedly [23,283] the likely rate determining step at pH < 10 while surface migration of O_{2^-} ions to active sites on the electrode surface is reported to be the rate determining step at pH > 10 [24].



A proton-transfer step



and then another electron transfer process



For a single layer graphene sheet much larger specific capacitance, faster electron transfer rate and stronger electrocatalytic activity have been reported for the graphene edge compared to the basal plane [284]. Recently direct evidence of the greater electrochemical activity of graphite edge sites towards the oxygen reduction reaction has been demonstrated [285].

In addition, the type of surface functional group on the carbon surface can affect the kinetics of oxygen reduction on carbon electrodes. Rao et al., [287], reported best ORR performance from vertically aligned carbon nanotubes (VA-CNTs) with a nitrogen concentration of 8.4 atom % and ascribed it to a greater number of pyridinic-type nitrogen sites. Maldonado and Stevenson [276], using electrochemical methods studied the influence of nitrogen doping on the oxygen reduction reaction (ORR) on carbon nanofiber (CNF) electrodes in aqueous KNO_3 solutions at neutral to basic pH, and reported differences in the mechanism of oxygen reduction in which ORR proceeds by the peroxide pathway via two successive two-electron reductions but for N-doped CNF electrodes, proceeds as a catalytic regenerative process in which the intermediate hydroperoxide (HO_2^-) is chemically decomposed to regenerate oxygen, with a spectacular ≈ 100 fold enhancement of hydroperoxide decomposition process. This observed enhanced activity was attributed to the presence of edge plane defects and nitrogen functionalities within the carbon nanofiber (CNF) structure.

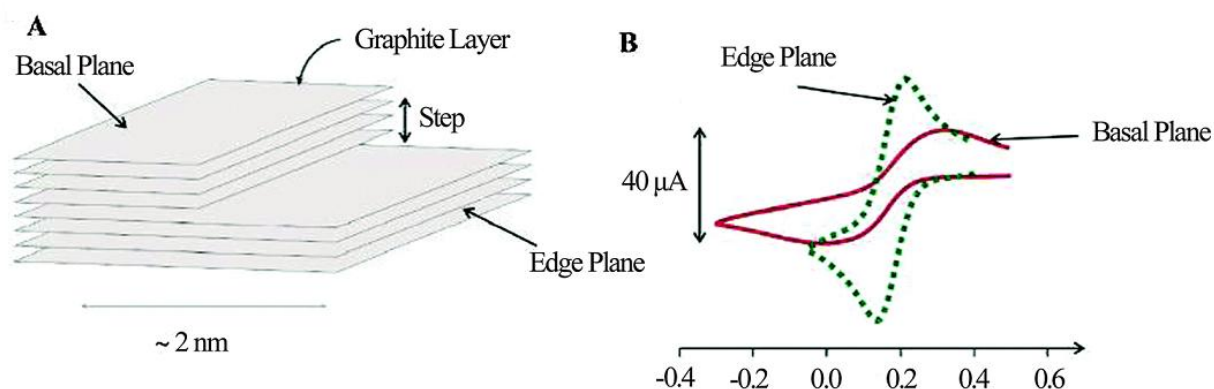


Fig.2.16. Illustration of edge and basal plane sites on carbon materials and their different electrochemical response, [Adapted from ref: 286].

Working with un-doped and nitrogen doped carbon nanotubes, Wiggins-Camacho and Stevenson [288], established a positive correlation between nitrogen content and ORR activities in which the ORR at undoped CNTs proceeds via two successive two-electron processes with hydroperoxide (HO_2^-) as the intermediate, but proceeds via a “pseudo” four-electron pathway involving a catalytic regenerative process in which hydroperoxide is chemically decomposed to form hydroxide (OH^-) and molecular oxygen (O_2) at nitrogen-doped carbon

nanotubes, and reported an even better >1000-fold enhancement for hydroperoxide disproportionation. By analysis of observed charge-transfer coefficients, α_{obs} in an earlier article [276] they had concluded that for N-doped CNFs the charge-transfer coefficient, was consistent with a strongly adsorptive pathway while that of the nondoped CNFs being invariant to solution pH, was suggestive of the absence of strongly adsorbed O_2 at the undoped CNFs in the studied pH range. Furthermore, they [276] concluded that the absence of the second reduction peak in the N-doped CNF electrode in contrast to its presence in the un-doped CNF electrode was suggestive of faster rate of chemical decomposition of the electrochemically generated hydroperoxide to oxygen compared to the rate at which it is electrochemically reduced to OH^- .

2.9. 3. Effect of Polarization on Carbon Fiber

Uvarov et al., [289] studied the effect of electrochemical treatment (cathodic, anodic, and combination of these) on the morphology and surface chemical composition of carbon fiber materials and reported that whereas anodic polarization resulted in a marked decrease in conductivity with significant weight gain, a single cathodic polarization had no effect on specific conductivity but resulted in slight reduction in weight due to 'degradation of fiber surface and the attendant loss of material.

2.9.4. CFRP Degradation under Cathodic Polarization

As on most metals [223,290-292], the reduction of oxygen on CFRP, especially when under cathodic polarization on coupling with most metals, most probably occur in two well-defined steps. Tucker et al., [293] studied the behaviour of graphite/epoxy composites galvanically coupled to a range of metals in seawater and reported degradation in form of blisters on the composite when active corrosion of aluminum occurred which is not observed without galvanic coupling and hence linked to enhanced cathodic chemical reactions associated with galvanic corrosion of the metal.

Sloan [294] studied the degradation of graphite/epoxy composites (with the matrix composed of tetraglycidyl diaminodiphenyl methane (TGDDM) epoxy systems cross-linked with the use of the bifunctional cross-linking agent diaminodiphenylsulfone (DDS)), after long-term environmental exposure (one year) in 5 % solutions of H_2O_2 at pH values of 6, 10 and 12 for a period of one year using scanning electron microscopy and FT-IR analysis, and reported based on the spectroscopic results that hydrogen peroxide electrophilically attacks the secondary

amines in the cured epoxy structure with SEM images showing general decomposition of the matrix, but found no evidence of attack by the high pH solutions. On the mechanism of this degradation, Sloan [294] proposed a mechanism in which the hydrogen peroxide would first form the amine hydroxide, which under mildly acidic conditions undergoes hydrolysis (dilute solutions of H₂O₂ being mildly acidic [295]), followed by an H₂O addition reaction and finally the formation of an aldehyde.

Sloan and Talbot [296] in a later study on the evolution of perhydroxyl ions on graphite/epoxy cathodes demonstrated clearly that both hydroxyl and perhydroxyl ions are evolved during cathodic polarization of graphite/epoxy, and concluded that the earlier mechanism explaining the degradation of polymeric matrix materials in carbon fiber reinforced polymer (CFRP) composites, in which damage is attributed to nucleophilic attack of hydrolyzable polymer linkages (e.g., esters, imides, etc.) by hydroxyl ions (OH⁻) evolved at the cathode. Though seemingly plausible for damage to the hydrolyzable polymers this postulation is insufficient to explain the damage observed in non-hydrolyzable polymers. On the basis of their experimental observations they proposed a new mechanism accounting for the degradation of both hydrolyzable and non-hydrolyzable polymers in which degradation is attributed to the build up of deleterious concentrations of highly reactive perhydroxyl ions (HO₂⁻) in occluded regions of the composite with high pH solutions, in which the evolved perhydroxyl ion is both stable and highly reactive as these are strongly dependent on solution pH.

Taylor et al., [297] studied electrochemical damage in bismaleimide/graphite fiber composites in aerated 0.6 M NaCl and 0.1, 1.0, and 2.0 M NaOH solutions using mainly electrochemical impedance spectroscopy and reported that cathodic polarization of graphite fiber composites produced porous electrode behaviour which was attributed to breakdown of the fiber/matrix interface and subsequent moisture intrusion whereas exposure to caustic solutions yielded no porous electrode response leading them to conclude that the reaction intermediates generated during the oxygen reduction reaction, such as peroxide and superoxide radicals, are the main species responsible for degradation and not OH⁻ ions. Their conclusion of fiber/matrix breakdown was based on the observations of increase in capacitance with time coupled with a decrease in impedance with time, consistent with an increasing electrochemically active area, absence of fiber surface roughening and the presence of small gaps between fiber and matrix (both observed from scanning electron microscopy), and decreasing slope of the impedance magnitude plot coupled with decreasing phase angle peak which are indicative of the "squaring effect" that is characteristic of porous electrodes [298-

300]. Based on their analysis of impedance spectroscopy data, they [297,301] concluded that the phase angle was the most sensitive indicator of changes (damage) in the composite, and employed "delta phase angle" plots to compare interfacial changes (or material damage) as a function of exposure conditions (exposure time and cathodic polarization) with interesting results. The delta phase angle plot is a frequency by frequency subtraction of the phase angle value at an exposure condition (e.g. an exposure time ($t=t_1$) or polarization ($\eta = \eta_1$)) from a baseline exposure condition (exposure time ($t=t_0$) or polarization ($\eta = \eta_0$)); smaller values of the output tending to zero being indicative of smaller interfacial changes from initial conditions and higher values suggesting more profound changes. A time based "delta phase angle" plot may be calculated or expressed thus [297]:

$$\Delta\theta_{(\omega_{t=t_1})} = \theta_{(\omega_{t=t_0})} - \theta_{(\omega_{t=t_1})} \dots\dots\dots(\text{eqn.2.76})$$

where θ is the phase angle, ω is the frequency and t is time.

Their delta phase angle plots showed that cathodic polarization produces a delta-phase angle plot with characteristic peak between 10 and 100 Hz and a gradually increasing value below 1 Hz referred to as a low frequency "tail". The peak was attributed to parallel shift of the phase angle response to lower frequencies with increasing damage (increasing time or potential), and the tail to decreased impedance and accompanying phase angles at lower frequencies. On the strength of experimental evidence of the absence of these "tails" in tests in caustic solutions (with abundance of OH^-) and their emergence in same solutions on addition of H_2O_2 without cathodic polarization, these tails were associated to the accumulation of cathodically produced electroactive species which are most probably electrochemically generated peroxide and peroxide intermediates (e.g. superoxide radicals) which were not present in the caustic solutions [297].

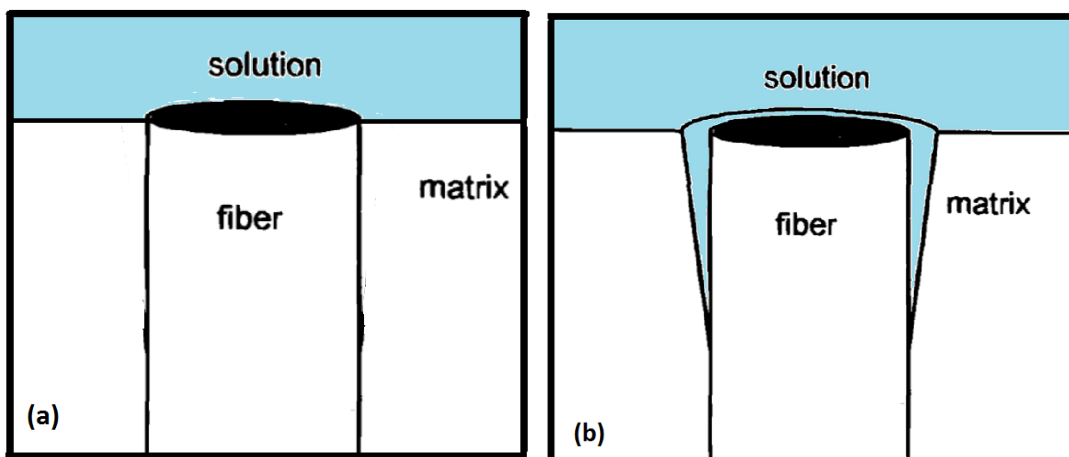


Fig. 2.17. Schematic illustration of proposed model for the origin of the porous electrode effect in cathodically polarized CFRP samples (a) Intact CFRP sample (b) Degraded CFRP sample [Adapted from ref: 297].

Pauly et al., [302] in the section of their work on effect of cathodic polarization on the durability of pultruded graphite/epoxy composites in aerated 0.6 M NaCl, concluded that the high pH environment generated during the oxygen reduction reaction was a necessary but not a sufficient condition for composite degradation because unpolarized specimens exposed to a pH 13 environment exhibited no degradation, and postulated that cathodic polarization of a magnitude achievable by galvanic coupling to steel or aluminum is needed, and that degradation of the fiber/matrix interface is most probably due to the intermediates (peroxide (HO_2^-) and long-lived super oxide species) generated during the oxygen reduction reaction and not the OH^- that are final reaction products. They [302] emphasized a damage mechanism for CFRP degradation under cathodic polarization proposed by earlier authors [243,297,303] based on the premise that the two-electron pathway capable of producing deleterious intermediate species that are able to interact with certain polymer bonds in the matrix and in a lot of cases degrade it is the favoured mechanism for oxygen reduction on carbon. In this proposed mechanism, oxygen is reduced to hydroxyl ions at the surface of the graphite fibers leading to the generation of local areas of high pH which in occluded areas near the fibers is even higher promoting the build-up of peroxide radicals. These reactive peroxide radicals then attack and degrade the polymer matrix in close proximity to the graphite fiber, leading to a break-down of the fiber/matrix interface; a process which continues until solution ingress occurs along the fiber causing an increase in the active surface area of the electrode and inducing a porous electrode response. In addition to the mechanism summarized above, Taylor et al., [297] have postulated from their results that, although hydroxyl ions were regarded to be the damaging species, the superoxide radicals produced during homogeneous peroxide decomposition can be the major deleterious species owing to their ability to react with labile hydrogens on the polymer surface to produce the even more highly reactive hydroperoxyl radical (HOO^*) which being hydrocarbon soluble can readily diffuse through the polymer matrix in which its further reaction with labile hydrogens produces peroxide [304].

Tang et al., [305] studied the degradation of carbon/vinyl ester composites under cathodic polarization in seawater and reported that both the flexural modulus and flexural strength decreased with the increase in cathodic polarization, with the scanning electron micrographs showing that under cathodic polarization the polymer matrix was locally detached and some carbon fibers released from the specimens.

2.9.5. CFRP Degradation under Anodic Polarization

Also under anodic polarization in aqueous electrolytes, which can arise in practice from stray currents, CFRP can be susceptible to degradation. Sloan and Talbot [306] have reported that anodic polarization of graphite/epoxy composites at applied current densities as low as $1 \mu\text{A cm}^{-2}$ are capable of causing rapid and substantial corrosion damage, with the graphite-reinforcing fibers attacked by atomic oxygen that is produced as an intermediate in the oxygen evolution reaction. However unlike metals that degrade under anodic polarization by electrochemical dissolution, CFRP degradation under this condition is due to secondary chemical reactions involving electrochemically evolved species which have been linked to oxygen evolution at the (CFRP) anode. The mechanism of CFRP degradation under anodic polarization is perceived to involve attack by adsorbed atomic oxygen; an intermediate in the oxygen evolution reaction. [306].

Stafford et al., [307] studied electrochemical stability of graphite fiber - polymer matrix composites as electrolysis electrodes in simulated seawater electrolyte, and reported electrochemical and mechanical stability as a cathode, but significant interfacial attack directed toward the fiber/resin interface with about 15% reduction in the average fiber diameter as an anode. This interfacial loss was attributed to a combination of chemical and electrochemical graphite oxidation and cavitation, due to the evolution of oxygen and chlorine, and almost entirely to oxidation by active chlorine in acidic chloride solutions at moderate current densities, since the current efficiency for chlorine evolution is close to 100% under these conditions. According to Stafford et al., [307] increased graphite oxidation is generally observed at pH greater than 4 depending on the temperature and chloride concentration of the electrolyte. Furthermore they [307] reported initial capacitance increases (during the first few hours) of immersion for graphite fiber - polymer matrix composites under anodic polarization after which the capacitance tended towards initial values and ultimately decreased, and attributed the initial increase to a combination of fiber roughening and surface oxidation.

Bismarck et al., [308] studied the surface properties of PAN-based carbon fibers after anodic oxidation by cyclic voltammetry in different alkaline electrolyte systems, and reported increased fiber surface tension due to increased number of oxygen containing surface groups and roughening of the fiber surfaces as a result of their anodic oxidation. Anodic oxidation of fiber surface is one of the methods used to improve the fiber-matrix adhesion for improved load transfer from the matrix to the fibers [309]. Basova et al., [310] studied how the surface modification of carbon fiber composites by oxidation–reduction cycles affected their

electrochemical behaviour towards oxygen evolution and concluded that the presence of acidic functional groups (such as $-\text{COH}$, $-\text{COOH}$) on the carbon fiber surface enhances the electrochemical interaction between the oxidized carbon fiber surface and electrolyte, while the presence of phenolic, hydroxy, and quinone groups inhibit this interaction.

Taylor and Humffray [24] working on oxygen reduction in solutions of high pH ($\text{pH} > 10$) on glassy carbon electrodes, reported effects on the mechanism based on the treatment (cathodic or anodic) given to the glassy carbon electrodes; with the major difference between polished cathodically treated glassy carbon electrodes and anodically treated ones being that oxygen reduction to OH^- rather than to peroxide is boosted at all potentials by the anodization process.

In summary, from the literature it seems that while anodic polarization of CFRP leads to degradation of the carbon fibers (the reinforcing phase) by adsorbed atomic oxygen; an intermediate in the oxygen evolution reaction [306], cathodic polarization ensures composite degradation by attack on the epoxy of the matrix phase most probably due to nucleophilic attack by hydroxyl and perhydroxyl ions, formed as a result of the oxygen reduction reaction on carbon fiber [305].

2.10. Corrosion Inhibitors and Corrosion Inhibition

Corrosion can be mitigated by coating metals to avoid an electrical path, excluding electrolytes and when these are not feasible, controlling the prevalent potential to a region of stability for the metal. In addition species can be introduced (inhibitors) which can act by modifying the local environment, and/or the type and nature of corrosion products to become protective.

2.10.1. Corrosion Inhibitors

Corrosion inhibitors are chemical compounds or mixtures of compounds which when introduced in small concentrations into corrosion systems impede the kinetics of the corrosion processes and hence significantly reduce the corrosion rates. The actual choice of compound as a corrosion inhibitor is usually dependent on the properties (chemical and physical) of the compound with regard to the application and intended operating conditions. For instance, whereas an inhibitor with a high solubility might be compatible in acid pickling baths, such will be undesirable for incorporation in coating systems where the high solubility could lead to fast and or premature leaching, and risk of formation of osmotic blisters. Corrosion inhibitors can be

classified based on different criteria. On the basis of its effect on the two types of electrode reactions observed in corrosion to reduce corrosion rates, an inhibitor is classified as a cathodic inhibitor if it acts predominantly on the cathodic reactions, an anodic inhibitor if it mainly acts on the anodic reaction, and a mixed inhibitor if it suppresses both cathodic and anodic reactions. According to Riggs [311], designation of a compound as a cathodic or anodic inhibitor can be made if the open circuit potential (OCP) measured in its presence is displaced at least 85 mV from values measured in the absence of inhibitor. On the basis of their chemical nature or elemental constitution inhibitors are classified as organic or inorganic inhibitors [312]. On the basis of corrosion component (metal, electrolyte) on which the inhibitor acts on, inhibitors can be classified as environmental conditioners and interface inhibitors [313]. The environmental conditioners (scavengers) include all the inhibitors that effect reduction in corrosion rates by removing the corrosive species in the medium such as hydrazine that scavenges oxygen [314,315], while all other inhibitors that act on the metal are classified as interface inhibitors. On the basis of their effects on the chemical reactivity of the metal inhibitors are classified as passivating or non-passivating inhibitors, and on the basis of the chemical action by which passivation of metal surface is achieved, passivating inhibitors can be further classified as oxidizing or non-oxidizing [316]. Since many corrosion inhibitors dissociate, hydrolyse or become protonated in solution, so that the active form is usually not neutral but charged, corrosion inhibitors can be classified on the basis of the charge on these species, as cationic and anionic inhibitors for possessing positive and negative charge(s) respectively.

Corrosion inhibitors can act by increasing cathodic and anodic overpotentials on metal surfaces or by changing the slopes of the partial reaction curves or both [317]. Generally anionic inhibitors, such as chromates and nitrites usually inhibit corrosion by aiding formation of passive films on metal surface which leads to passivation [318,319]. Cationic inhibitors such as Al^{3+} , Ce^{3+} , La^{3+} , Pr^{3+} , Nd^{3+} , and Ni^{3+} and Zn^{2+} act by precipitating insoluble oxides and hydroxides films on metal surface which have been reported to inhibit corrosion by suppression of the kinetics of oxygen reduction reaction at cathodic sites on the metal surface [320,321].

In the ensuing sub-sections the factors affecting corrosion inhibitors and corrosion inhibition mechanism, and four of the classifications of corrosion inhibitors (anodic, cathodic, mixed and organic corrosion inhibitors) that are most relevant to the present work are discussed in more detail.

2.10.2 Classification of Corrosion Inhibitors and Factors Affecting Corrosion Inhibitor(s)/ Corrosion Inhibition Mechanisms

The corrosion inhibition mechanism can vary with the pH of the environment. In acidic solutions the natural oxide film present on the metal surfaces are dissolved, thus providing the inhibitors direct access to the metal surface. In near neutral solutions, the mechanism can be more complex, as the native oxide films being more stable are usually present, so that inhibitors not having direct access to the metal surface are most likely to interact with the metal surface through the native film [322]. Based on the locality where inhibition of electrode reactions occur corrosion inhibition and inhibitors have been classified into three modes of inhibition and inhibitors; interface inhibition (inhibitors), electrolyte-layer inhibition (inhibitors) and membrane inhibition (inhibitors) [323,324]. Mansfeld and Lorenz [325] made further segregation of interface and interphase inhibition as different corrosion inhibition modes.

Interface inhibition is a predominant occurrence in corroding system in which bare (oxide free) metal surface is in contact with the corrosive media as is the case in active metal dissolution in acid solutions [325]. Interface inhibition occurs in the region spanning both sides of the compact Helmholtz-double-layer [326,327]. Interface inhibition is caused by the assemblage of substances (interface inhibitors) staying within this layer that simultaneously cover the interface as they displace from the interface other less interfacially active substances such as water molecules and species involved in electrode reactions [328]. These inhibiting substances are called interface inhibitors and most of them are organic compounds [329]. Interface inhibition is effected by reduction in the rate of physical, electrochemical and/or chemical partial processes of electrode reactions that take place at the electrode-electrolyte interface [323]. The partial electrode reaction steps that may be affected include; charging and discharge of the double layer resulting in change in the capacitance, and deposition or dissolution of metal crystals which may involve entry and exit of adatoms from lattice positions such as kinks, surface diffusion, development of crystal or etch nuclei [330], charge transfer involving electrons or metal ions [331], heterogenous chemical reactions at the electrode side of the interface [332].

Interface inhibition is supposedly characterized by the formation of a 2-dimensional potential dependent layer due to strong interaction between corroding metal surface and inhibitor that involves specific adsorption, and potential dependent adsorption of inhibitor to metal surface [323,325,333]. The inhibitor thus adsorbed can retard corrosion reactions via three distinct routes; (a) by geometric blocking effect, in which inhibition is effected by relatively

high surface coverage on electrode surface by adsorbed inhibitor, (b) by deactivating coverage involving blockage of active surface sites at low surface coverage by an inert adsorbate, and (c) by reactive coverage of metal surface in chemical or electrochemical reactions that occur after inhibitor adsorption to electrode surface which may result in primary and/or secondary inhibition [325]. On the premise of strong interaction between the corroding electrode and the inhibitor and potential dependent adsorption of inhibitor, the inhibition efficiency in this scenario is most likely to be dependent on the electrode potential, the inhibitor concentration, and the exposure time to the corroding electrode [325].

Interphase inhibition is a predominant feature in neutral and near-neutral electrolytes in which direct contact of metal surface with corrosive media is hampered by the presence of porous or non-porous layers of corrosion products on electrode surface. As a consequence interphase inhibition is characterized by the formation of a 3-dimensional layer consisting of both the corrosion products and the inhibitor between the metal and electrolyte [334,335]. In interphase inhibition, the inhibition efficiency is strongly dependent on the time for formation of the 3-D layer, and on the properties of this layer particularly its porosity and stability [325]. Many interface inhibitors exhibit lowered or loss of inhibition efficiency in the presence of surface layers obviously due to weaker interaction between the inhibitor species and the electrode surface in the presence of a 3-D coverage [325], which can explain why a lot of corrosion inhibitors manifesting high inhibition efficiencies in acidic solutions are unable to replicate such high efficiencies in similar but near-neutral electrolytes.

Electrolyte layer inhibition [331,336] can lead to a reduction in the rate of physical and chemical partial electrode processes/reactions which take place in the thin electrolyte-layer adhering to the interface that is mainly composed of the diffuse part of the double layer, the Nernst diffusion layer and the Prandtl flow boundary layer [337]. Electrolyte layer inhibition is in most cases caused by species dispersed or dissolved in the afore described electrolyte layer [323], and can be divided into two types; mechanical and electrochemical electrolyte layer inhibition [338]. Partial electrode processes/reaction steps that may be retarded in electrolyte layer inhibition include transport of components (by diffusion and/or migration and/or convection) to or from the interface, and partial steps of homogenous chemical reactions within the electrolyte layer [323]. It has been reported that in the case of strong electrolyte layer inhibition even the natural convection at the submicroscopical profile of the interface may cease [339].

Membrane inhibition results from the covering of the electrode interface by a porous but

coherent polymolecular or polymeric layer, and may even be considered a type of interface inhibition covering the interface of the electrode. However, it is distinguished from interface inhibition by having thicker layers, of thickness in the order of microns, with narrow pores that extend into the electrolyte layer whilst still extending up to the electrode surface so that transport of species to the electrode surface is restricted, unlike in pure interface inhibition which involves at most a mono-molecular coverage of the interface by a much thinner and monomeric layer [323]. Membrane inhibition may result either by formation of adherent precipitates of metal hydroxides, phosphates, carbonates, and silicates on the interface when these anions interact with cations from the electrode surface [340], or by chemical reaction of complexing substances in the electrolyte with the metal at the interface to form layers of organo-metallic complexes [329]. Membrane inhibition is reported to be able to retard every kind of the partial electrode reaction steps [323].

On the basis of the origin of the inhibiting specie(s) corrosion inhibition (inhibitors) can be classified into two modes; primary inhibition (inhibitors) and secondary inhibition (inhibitors) [329,336,341-345]. Primary inhibition occurs when inhibition is effected by the originally added compound without a change of its initial stoichiometric composition, while secondary inhibition occurs when inhibition is not due to the initial added compound, but due to species (intermediates) which are generated from the initial compound either by a chemical or electrochemical reaction, and competing with the basic corrosion process(es) or reactions in such a manner that the corrosion rate of the system is retarded [322,323]. In fact secondary inhibition is more frequent as it is really difficult to find compounds that do not undergo any chemical change in solution during the course of a corrosion process [346].

2.10.3. Organic Corrosion Inhibitors

An organic inhibitor can be defined as an organic compound which when introduced to a corroding system is able to reduce the corrosion rate by interactions of the added organic molecule, its product(s) or ions, with the metal surface, its ions and/or other species in the environment. The potential of an organic compound to be an effective organic corrosion inhibitor is dependent on many factors which include; the size of the organic molecule, the presence of aromaticity and/or conjugated bonding, the type and number of bonding atoms or groups in the molecule particularly the presence of hetero-atoms or polar groups containing either π or σ bonding electrons, the length of the carbon (aliphatic) chain, the ability to form on the metal surface a compact or cross-linked layer, the strength of its bonds with the metal

substrate, the ability to form an adherent complex with the metal atom, and sufficient solubility in the electrolyte [347]. Organic inhibitors are reported to act mainly by adsorption at the metal-solution interface [311,329,348] mainly either by physisorption, or chemisorption [349-351]. Insights from studies in the course of this thesis on copper inhibition with triazoles (1 H-1, 2, 3-triazole and 1, 2, 4-triazole), indicate that very small changes in molecular structure can affect the mechanism of inhibitor adsorption on metal surface and consequently inhibition efficiencies [352].

According to Riggs [311,353], the mode of adsorption of a molecule to a metal is dependent on the chemical nature of the inhibitor molecule, the nature of the metal surface, the environment, and the electrochemical potential at the metal-solution interface, and adsorption classified into three types; π bond orbital adsorption, electrostatic adsorption, and chemisorption.

Furthermore, Riggs [311,353] proposed that the adsorption phenomena involves either of three types of species; proton acceptors, electron acceptors, and ambiodic or mixed molecules. This leads to the three known types of corrosion inhibitors on the basis of the electrochemical nature of corrosion. The proton acceptors being species that are most likely to act at cathodic sites by accepting hydrogen ion or protons and migrating to cathodic samples. Examples include acid inhibitors such as anilines, quinolines, ureas and aliphatic amines [311,347]. The electron acceptors are species such as organic peroxides, thiols, and selenols that adsorb at anodic sites due to their ability to accept electrons. The ambiodic species or mixed molecules are able to adsorb to both anodic and cathodic sites due to the possession of more than one orienting functional group. This characteristic may be due to a basic molecule containing two orienting groups (e.g. $-\text{NH}_2$, and $-\text{SH}$) as in aminobenzenethiol, salts composed of proton and electron acceptors from two separate molecules as in benzenethiol and aniline, or due to reaction products of organic species that are able to form 'organic ions' in acidic system as in pyridinium benzylbromide [311,347]. The actual performance of an organic compound as an organic corrosion inhibitor is dependent on a variety of factors such as; its chemical structure and physicochemical properties, the ability of its molecules or their ions to adsorb on anodic and/or cathodic sites on the metal surface, the ability of its interaction with the metal surface to result in an increase in the cathodic and/or anodic over-voltage, and the formation of protective barrier films composed of complexes or insoluble films, from the interactions of the organic inhibitor molecule and/or its ions, and the metal, its ions, and the ions available in the surroundings [347].

2.10.4. Physical Adsorption of Corrosion Inhibitors

Physical adsorption of corrosion inhibitors to metal surface is due to electrostatic interactions between the inhibiting organic ions or dipoles and the electrically charged metal surface [354]. Physical adsorption is characterized by a relative non-dependence on temperature and low activation energy [355], an apparent dependence on the type of adsorbable anions present in the solution, the sign of the surface charge on the metal, and the electrical characteristics of the organic inhibitor [356].

Metals immersed in solutions possess surface charge due to the electric field in the outer Helmholtz plane (OHP) of the electric double layer at the metal-electrolyte interface. Depending on the position of the metal potential (E_{corr}) relative to its potential of zero charge ($E_{q=0}$), the surface charge can be positive or negative [346,357,358].

$$E_{corr} - E_{q=0} = \varphi \dots\dots\dots \text{(eqn. 2.77)}$$

where E_{corr} is the electrode potential, $E_{q=0}$ is the potential of zero charge.

For this class of inhibitors their inhibition efficiency is determined by their adsorption which is itself strongly dependent on the surface charge and, consequently, on the position of the steady-state corrosion potential (E_{corr}), relative to the potential of zero-charge point ($E_{q=0}$) [359-362].

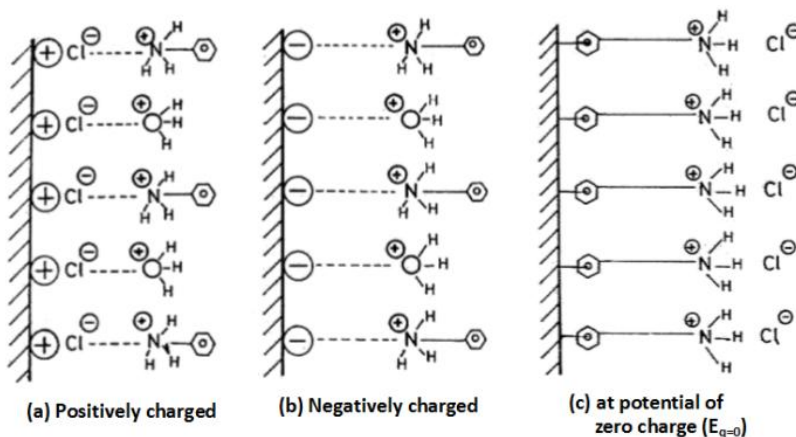


Fig. 2.18. Schematic illustration of how the surface charge relative to $E_{q=0}$ affects the adsorption mechanism of aniline onto mild steel surface in HCl solution [Adapted from ref: 363].

When $E_{corr} - E_{q=0}$ is negative, the surface charge on the metal is negative, and aids cation adsorption, and when this is positive the surface charge is positive and supports anion adsorption [364]. The potential of an immersed metal surface relative to its potential of zero charge in the solution is of great importance in determining the possibility of corrosion inhibition by adsorption of inhibitive ions, as a positive surface potential relative to the potential of zero charge is crucial for anion adsorption. Similar effects on inhibiting species by different metals with similar values of φ - potential have been predicted in similar environments [346]. The

factors influencing this potential reportedly includes; the surface condition of the metal, the presence of oxygen or other cathodic depolarizers, the concentration of aggressive ions in the electrolyte, contact with other metals (galvanic coupling) or the passage of current [365]. De [366], proposed that in neutral and acidic solutions inhibitive anions are preferentially adsorbed on the metal-electrolyte interfaces at sites that are more positive than the potential of zero charge of the metal. In neutral solutions, such sites are consistent with cathodic sites on the metal surface [365]. This preferential adsorption have been severally reported in acidic media [352,367], and also in neutral solutions [365]. According to Brasher [365], the major function of oxygen in solutions containing non-oxidizing inhibitors is to maintain the potential of the electrode surface above that of the potential of zero charge for sufficient time to enable adsorption of inhibitive anions onto metal surface.

2.10.5. Chemisorption of Corrosion Inhibitors

Chemisorption of corrosion inhibitors onto metal surfaces unlike physisorption involves charge transfer or sharing between the inhibitor molecule/ion and metal surface which leads to the formation of co-ordinate type bonds [354]. Compared to physisorption it is a slower process and is characterized by a higher activation energy, a temperature dependence, enhanced adsorption and hence better inhibition at higher temperatures, specificity to certain metals, and better stability as it is not easily reversible [355]. This type of inhibitor bonding to metal surface by electron transfer is frequent in compounds containing relatively loosely bound electrons usually from heteroatoms, multiple bonds or aromatic rings with π -electrons [312]. Functional groups rich in these features act as reaction centres for chemisorption. The strength of such adsorption bond is determined by the heteroatom electron density and the polarizability of the functional group [312].

For a homologous series of organic compounds with the different heteroatoms inhibition efficiency has been reported to follow in this order $P > Se > S > N > O$ and the order explained to result from the ease of polarizability and the lower electronegativity, moving from P to O [355]. Furthermore, the chemisorption of anions onto metal surfaces is reportedly [368] influenced by electronic and chemical forces, with the degree of specific adsorption on metal surfaces increasing as follows; $F^- < ClO_4^- < SO_4^{2-} < Cl^- < Br^- < I^-$, in accordance with decreasing solvation energy of the species. Thus as seen from the sequence, the strongly solvated F^- and ClO_4^- are either non-specifically or just weakly adsorbed while the other weakly solvated species (SO_4^{2-} , Cl^- , Br^- , and I^-) are able to establish direct chemical bonds with metal surfaces.

Anion adsorption (by chemisorption) on electrode surface is reportedly capable of affecting electrochemical processes in a variety of ways which includes; by blocking of active sites on which other reactants and/or intermediates could be adsorbed; by modification of the adsorption energy for sites adjacent to adsorbed anions; by changes in the potential distribution across the interface; and by restructuring the surface [368,369]. The presence of a polar groups and heteroatoms (such as sulfur, nitrogen, amines, phosphorous) in the molecular structure, through which the molecules can adsorb to the metal surface enhances chemisorption. The molecular structure and size of the organic compound influence their inhibitive action as primary amines become more effective inhibitors as their chain length increases; an effect that is attributed to the steric effect provided by long chains creating diffusion barriers, though mercaptans and aldehydes are exceptions [354]. Credible explanation for observed inhibitive effects of organic compounds on metals was found in Maxted's [370-373] connection of catalytic poisoning of metallic hydrogenation catalysts by adsorbed species to the formation of a dative bond with metal, in which the "electron rich" adsorbate acts as the donor and the metal the acceptor, as both processes (catalytic poisoning and corrosion inhibition by organic compounds) involved adsorption of "electron rich" species onto metal surfaces. The resultant hypothesis that the electron donation involved the d-shell of the metal was confirmed by decrease in magnetic susceptibility measurements by Dilke et al., [374] on palladium due to adsorption of dimethyl sulphide, which they concluded to be consistent with the entrance of one electron from the dimethyl sulphide (specifically from the sulphur atom) into the d-shell of the palladium. This linkage and better understanding of the mechanism of the interaction of organic inhibitors has directed the search for organic corrosion inhibitors towards "electron rich" compounds and the use of the electron density of candidate compounds as an inhibition modelling parameter.

The most critical factors affecting the degree of chemisorption are the nature of the metal and the electronic structure of the adsorbent. In chemisorption, bonding usually involves electron transfer, and hence is favoured in metals having low energy vacant atomic orbitals and organic compounds containing moieties that are "electron rich" (containing lone pair electrons, double bonds) and/ or aromatic rings with π -electrons. In chemisorption the functional group(s) are regarded as the reaction center(s) for the chemisorption process and the strength of the adsorption bond related to the heteroatom electron density and to the functional group polarizability [354]. On these basis Hackerman and Makrides [350], rightly postulated as confirmed in the course of this work that such chemisorbing organic inhibitors should be more effective for iron with electron configuration $1s^2 2s^2 2p^6 3s^2 3p^6 4s^2 3d^6$ (an electron deficit in its

outermost shell) than for zinc with electron configuration $1s^2 2s^2 2p^6 3s^2 3p^6 3d^{10} 4s^2$. In addition to the electronic structure [375], the molecular structure and size [376,377,378] of the organic compound influence their inhibitive action, while the strength of the bond is dependent on the metal due to its relation to the residual valence orbitals existing at the metal surface [350], which varying for different metals contributes to the differences in bond strength of an inhibitor to different metal surfaces.

2.10.6 Anodic (Passivation and Passivating) Corrosion Inhibitors

Anodic inhibitors mostly act by promoting the formation of a protective oxide film on the metal surface of the metal causing a large anodic shift of the corrosion potential (E_{corr}) into the passivation region. Passivation is a term used to describe the transition of a metal surface from the active state in which metal dissolution rate increases with increasing polarization, to the passive state in which the rate of metal dissolution suddenly decreases and loses its dependency on the applied potential. A passivating film is formed on a metal surface at electrode potentials more positive than the equilibrium potential of formation of the oxide(s) constituting the film by reaction between a metal or an alloy and an electrolyte, with the compound (oxide, etc.) possessing the most negative potential of formation usually innermost and in contact with the metallic phase [379]. Metals in the passive state (passive/passivated metals) have a thin protective (often non-porous) oxide layer of typical thickness around 1-3 nm on their surface called the passive film, that acts as a barrier separating the metal from its environment [380]. It has been demonstrated that passive films formed on a metal or alloy do not possess a specific structure, thickness and composition, and that these parameters are dependent on a variety of factors such as; the prevailing environmental conditions which includes, pH of the electrolyte, the chemical composition of the electrolyte, applied potential, exposure time, and the composition of the metal/alloy [379-387]. Due to the presence of this passive film, the dissolution rate of a passive metal at a given potential is much lower than that of an active metal, and depends mainly on the properties of the passive film and its solubility in the environment [379]. For a metal to become passive its potential must exceed its passivation potential in the environment. This can be achieved either by anodic polarization (anodic passivation) or by reaction with an oxidizing agent (spontaneous passivation) [380]. In this section discussion will be limited to mitigation of metal corrosion by use of inhibitors to achieve spontaneous passivation. A passivating-type inhibitor functions by producing local-action current that anodically polarizes the metal into the passive potential region and thus provides

the means for obtaining a noble mixed potential [388]. These passivating inhibitors or passivators are divided into two classes [389] depending on their ability to passivate in the presence or absence of oxygen as oxidizing and non-oxidizing anodic corrosion inhibitors.

The oxidizing inhibitors include oxidizing anions such as chromates, nitrites and nitrates that are able to passivate (for instance steel) in the absence of oxygen, often by modification of the oxide film on the metal by their incorporation into the film. These inorganic inhibitors (oxidizing anodic inhibitors) like chromates according to Evans [390,391] in studies on chromate inhibition of iron corroding in neutral salt solutions inhibit by a mechanism that involves the oxidation and reduction of the initial corrosion product; ferrous ion (Fe^{2+}), to the ferric state (Fe^{3+}), and then co-precipitation of ferric and chromic oxides, respectively, which are the oxidation and reduction products in the conversion of the initial corrosion product, ferrous ion, to the ferric state. This proposed mechanism demands that such inhibitors be oxidizing agents capable of oxidizing ferrous ions in neutral solutions. Based on observations that the ratio of chromic oxide in passive films stripped from the metal, after exposure to inhibited solutions, varied with the duration and conditions before exposure of the abraded iron to atmospheric oxidation, Evans proposed the pore repair /plugging theory that the inhibitive effect is most probably due to the co-precipitated oxides (mixture of ferric and chromic oxides) repairing the original air-formed oxide films at discontinuities and weak points [392].

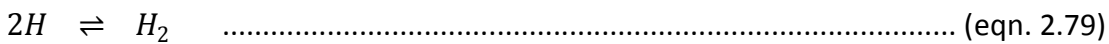
The second class of anodic inhibitors, the non-oxidizing inhibitors include non-oxidizing anions such as tungstates and molybdates [393,394], benzoates [395], and phosphates [396,397] that are only able to exert passivating effects in the presence of oxygen [398]. Since non-oxidizing corrosion inhibitors such as molybdates and tungstates are not oxidizing agents (at least) with respect to ferrous ion, and their oxides are not stable in neutral or alkaline solutions [399], the mechanism of their observed inhibitive effect is bound to be different. According to Robertson [400] the mechanism of corrosion inhibition by non-oxidizing anions such as molybdate and tungstate is related to their availability and adsorption at the metal surface and not co-precipitation (as for the oxidizing inhibitors), since these ions are not capable of oxidizing ferrous ions (corroding metal ions) even in acid solutions like chromates and to a smaller extent nitrites. The quantity of oxygen necessary to ensure passivation by non-oxidizing inhibitors can be really small. Gilroy and Mayne [401], demonstrated with iron in 0.1 M sodium benzoate solution of pH =7, that oxygen concentrations necessary for passivation can be much less than the saturated oxygen concentration (≈ 8 ppm) as they obtained passivation with oxygen concentrations as low as ≈ 0.3 ppm which is more than 25 times lower than the saturated

oxygen concentration. Passivation is favoured by high pH values (alkaline) [401], with a critical pH value below which passivation does not take place dependent on the type of inhibitive anion, its concentration and the dissolved oxygen concentration; the oxygen concentration required for passivation increasing as the solution becomes more acidic [402]. From the literature, the critical pH values for passivation of iron in air-saturated 0.1 M solutions of different anions are; 7.25 for phosphates [403], 6.1 for benzoates with the critical pH value increasing with benzoate concentration [404,405], 5.0-5.5 for nitrates [406,407], 4.5 for azelates [408], but as low as 1.0 for chromates [409,410]. Nitrites reportedly inhibit only above a $\text{pH} \approx 6.0$, tending to decompose in more acidic environments into the volatile nitric oxide and nitrogen peroxide [354]. The detection of iron (III) phosphate [411,412] and chromium [391,413] in oxide films stripped from iron electrodes after passivation in phosphate and chromate respectively have led to linking of passivation with interaction of anions with the oxide film on the metal, with different mechanisms suggested to explain observations. The main theories advanced to explain interaction of anions with the surface film include the adsorption/ion exchange theory [414] of inhibitive ions assimilation into the oxide film, in which the anions replace oxide ions as they leave the oxide lattice to enter solution. There is however a lack of consensus on the anion adsorption being a surface phenomena or the anions entering the oxide layer [382,425-417]. It has even been suggested [418,419] that incorporated anions might be able to exert influence on barrier properties of the passive film, inhibiting ionic transport of OH^- anions, and impart selectivity on transport of ionic species, with passive films on iron in phosphate solution (pH 8.4) being cation selective, and those in borate solution anion selective [417]. The second theory is the film repair theory [388,420], in which passivation is ensured by repair of the oxide film via a chemical or pore plugging effect, in which the inhibitive anions react with metal cations leaving metal/metal oxide surface at discontinuities precipitating insoluble products; the precipitation being favoured by a local non-acidic pH [410].

Caution is advised in the use of anodic/passivating corrosion inhibitors as they are capable of stimulating pitting and enhancement in corrosion rates at insufficient concentrations, as (the smaller) uncovered areas become anodic to a larger protected area. Anodic corrosion inhibitors are characterized by a large shift in the corrosion potential (E_{corr}) to more positive (anodic) values; a feature that is exploited in monitoring their effectiveness in practical applications [421], especially as close monitoring to ensure sufficient concentration to maintain inhibition effects is vital.

2.10.7. Cathodic Corrosion Inhibitors

Cathodic corrosion inhibitors are substances that cause reduction in corrosion rates by acting on the cathodic reactions. Substances that cause high overpotential for hydrogen and those that form precipitates at the cathode are effective as cathodic inhibitors in acid and neutral/alkaline solutions respectively. On the basis of their inhibition mechanism, cathodic inhibitors are classified into three groups as; cathodic poisons, cathodic precipitates, and oxygen scavengers [422]. In corroding systems there can be a variety of cathodic reactions, the possible and dominant reactions being dependent on the pH, the presence or absence of oxygen or other oxidants, the impressed potential or corrosion potential of the metal/alloy, and the presence of reducible metal cations. In principle, corrosion can be inhibited by reduction in the rates of these cathodic reactions. In acidic solutions the dominant cathodic reaction is the reduction of hydrogen ions to hydrogen atoms, which then combine to form hydrogen molecules as illustrated in equations (2.78 and 2.79) below:

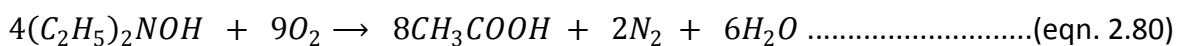


This cathodic process can be inhibited by the use of a cathodic inhibitors that can inhibit any or both of the steps involved in the hydrogen evolution above. The electron transfer reaction (eqn. 2.78) can be inhibited by increasing the activation energy for the electron transfer step, in other words increasing the overvoltage for the electron transfer required for hydrogen ion reduction, while the second step in the process (eqn. 2.79) can be inhibited by the use of cathodic poisons. Cathodic poisons such as (sulphides, bismuth, antimony, selenides, and arsenates (As_2O_3 or Na_3AsO_4) adsorb or deposit on the metal surface to reduce the rate of the hydrogen evolution reaction. Selenides and sulphides adsorb on the metal surface while compounds of bismuth, antimony, and arsenic are reduced at the cathode and form a metallic layer [313]. These cathodic poisons are usually employed in acidic media [423]. However, there is a risk of blistering and hydrogen embrittlement with the use of cathodic poisons, as the hydrogen atoms prevented from recombining to form molecular hydrogen and leaving the metal surface, diffuse into the metal.

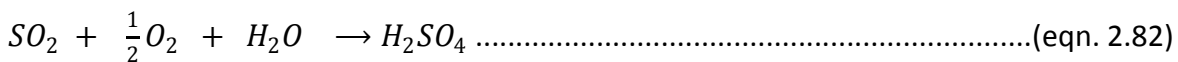
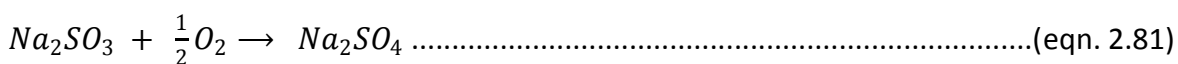
Oxygen is a cathodic depolarizer that promotes corrosion processes by influencing cathodic reactions in reacting and removing hydrogen atoms from the electrode surface. Since dissolved oxygen in the electrolyte is a participant in many of the cathodic processes, its absence is bound to reduce the rate of cathodic reactions. Oxygen scavengers are substances introduced into the electrolyte that are capable of trapping and deactivating the excess dissolved oxygen and thus

make it unavailable to participate in cathodic reactions at the electrode surface, and thus inhibit cathodic reactions. Typical substances used as aqueous oxygen scavengers include hydrazine, sodium nitrite, sodium sulphite, sulphur dioxide [424], erythorbic acid (C₆H₈O₆) or its salt (C₆H₇NaO₆) [425] and Diethylhydroxylamine (DEHA) [426,427]. Other compounds that are used as oxygen scavengers include tannins, hydroxylamine, carbonylhydrazides and quinolines [428].

For instance the oxygen scavenging activity of DEHA and its subsequent oxidation though a complex process involving several reactions steps, that are dependent on temperature, pH, and the concentrations of both DEHA and oxygen [426,429] can be summarized in equation 2.80 below as;



For oxygen scavengers like sodium sulphite (Na₂SO₃), sulphur dioxide (SO₂), and hydrazine (N₂H₄), the oxygen scavenging reactions can be expressed respectively as in equations 2.81 to 2.84 below:



From the equations above it is observed that stoichiometrically, for the removal of 1 ppm of oxygen from water, 7.9 ppm of Na₂SO₃, 4 ppm of SO₂, 1.2 ppm of DEHA ((C₂H₅)₂NOH), and 1 ppm of hydrazine (N₂H₄) is required. In practice however, overages in excess of these stoichiometric quantities are used in addition to catalysts to hasten the rates of the oxygen scavenging reactions [424,427].

Analytically, cathodic action of an inhibitor can be observed or established by significant shift in the open circuit potential measurements and the corrosion potential E_{corr} in polarization tests to more negative (cathodic) values compared to that observed in uninhibited solutions.

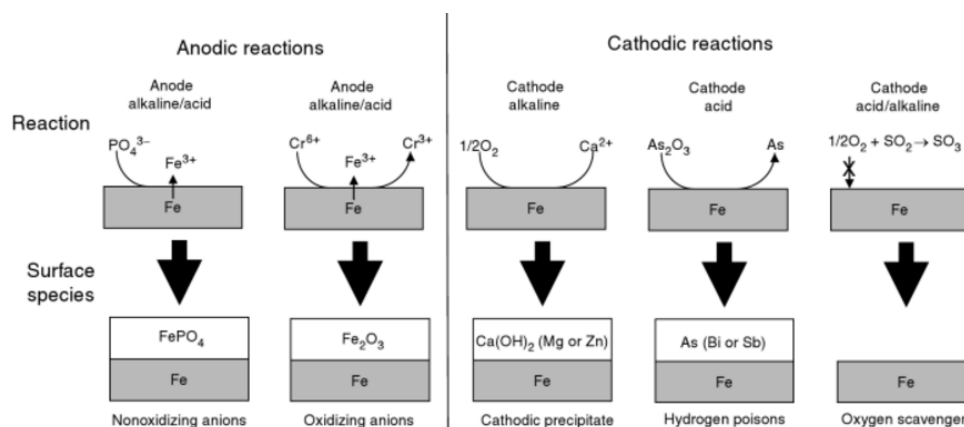


Fig. 2.19. Schematic illustration of the mechanism of anodic and cathodic inhibitors [Adapted from ref: 423] .

2.10.8 Mixed Corrosion Inhibitors

Mixed corrosion inhibitors are compounds that are able to significantly and simultaneously inhibit cathodic and anodic processes in a corroding metal/alloy. They are mostly organic compounds and their efficiency is linked to their adsorption and coverage of the electrode surface. Like other organic inhibitors their inhibitive action is effected by either, physisorption, chemisorption, or film formation on the electrode surface [430]. Ma et al., [431] studied the inhibitive action of the four surfactants, cetyltrimethylammonium bromide (CTAB), sodium dodecyl sulfate, sodium oleate and polyoxyethylene sorbitan monooleate (TWEEN-80), on the corrosion of copper in aerated $0.5 \text{ mol dm}^{-3} \text{ H}_2\text{SO}_4$ solutions and reported mixed corrosion inhibition effect for all four surfactants attributed to their blocking of the copper surface by electrostatic adsorption or chemisorption. Khaled and Hackerman [432], studied inhibitory activity of some *o*-substituted anilines (comprising 2-chloroaniline, 2-fluoroaniline, 2-aminophenetole, 2-ethylaniline, *o*-aminoanisole and *o*-toluidine) on iron corrosion in 1 M hydrochloric acid and reported no change in the anodic and cathodic Tafel slopes in the presence of these inhibitors and concluded that the inhibitive effect was due to blocking of the reaction sites on iron surface on adsorption to the iron surface with no effect on the anodic and cathodic reaction mechanism [433]. They suggested a credible but experimentally unverified possibility of multi-mode adsorption of the *o*-substituted anilines onto the iron surface as (a) a neutral molecule via chemisorption mechanism [434] involving electron sharing between the nitrogen atom and iron, (b) π electron interactions between the benzene ring of the molecule and the metal surface, and (c) adsorption in the the cationic form in which the positively charged part of the molecule (ammonium- NH_3^+) is oriented towards the negatively charged iron surface with chloride ions pre-adsorbed unto the iron surface acting as bridges between the cationic form of *o*-substituted aniline molecule and the iron surface [432]. There is need for better understanding of the mechanism of action of mixed type corrosion inhibitors. Future developments in corrosion inhibition may be towards tailored use of multifunctional compounds that contain at least two functional groups that are able to selectively act on each of the half-cell corrosion reactions, and hence mixed-type inhibitors. An example of such mixed corrosion inhibitor is *p*-aminobenzoic acid which contains the $-\text{NH}_2$ and $-\text{COOH}$ groups that act and inhibit cathodic and anodic reactions respectively [435].

2.10.9. Corrosion Inhibition/Inhibitors in Localized corrosion (Galvanic Corrosion)

Success with the use of corrosion inhibitors to mitigate localized corrosion processes like

galvanic corrosion is limited by the specific action of inhibitors to specific metals, the need for higher concentrations than that required to combat general and single metal corrosion [354], and the fact that surface properties (like the sign of the surface charge) of a metal can change on galvanic coupling with another metal thus affecting its interaction with inhibitors in comparison to that observed without coupling. In spite of these challenges some reports have been made of the inhibition of galvanically coupled metals. Hatch [96] reported glass phosphates to be a very effective inhibitor of steel-copper, and zinc-copper and zinc-steel galvanic couples in quiescent and aerated Pittsburgh tap water of pH between 6.5 and 7 at 35°C and 80°C. The inhibitive effect on galvanic corrosion of steel coupled to the copper was attributed to a marked enhancement of the cathodic polarization due to the formation of a glass phosphate film on the copper (the cathode). This conclusion from such an early report gives a hint that the suppression of the cathodic reactions is most probably a key factor in mitigating galvanic corrosion by the use of inhibitors. For uninhibited couples containing zinc and markedly in the zinc-copper couple, Hatch [96] had observed an initial drop in the galvanic current followed by an increase and attributed this to the inhibitive action of the initial zinc corrosion products [436], while the initial current rise for the uninhibited copper-steel system was attributed to the breakdown of the initial air-formed oxide film present on the steel surface.

Ai et al., [437] studied the inhibition of galvanic corrosion of carbon steel (N80) - stainless steel (S31803) couple with dodecanoic acid and its sodium salt (an anionic inhibitor) in 1% NaCl at pH = 4 and observed that uncoupled, the inhibitor inhibited cathodic processes on stainless steel (the would be cathode on coupling) and anodic processes on the carbon steel, significant reduction of the galvanic current density on galvanic coupling which they linked to favourable surface charge conditions on the carbon steel and stainless steel surfaces at their mixed potential.

Ai et al, [438] also studied the synergistic inhibition effect of KI and an imidazoline derivative as a cationic inhibitor for galvanic corrosion of carbon steel - stainless steel couple in NaCl and reported formation of a more compact inhibitor film on the anode of the galvanic couple and synergistic effects attributed to modification of the surface charge by I⁻ pre-adsorption on electrode surface.

From this brief review of attempts at inhibition of galvanic corrosion of coupled metals and corrosion inhibition with inhibitors generally, it can be deciphered that some of the important parameters for mitigating galvanic corrosion with inhibitors might include; temperature, pH, dissolved oxygen concentration, presence and type of corrosion products

formed on each of the metals in the couple, the surface charge of the individual metal components of the galvanic couple in the test electrolyte at their mixed potential, the type of inhibitor (anionic or cationic), and the presence of species that can act as bridges for inhibitor species unto metal surface (e.g. I^-).

Reports from investigations on inhibition of iron corrosion in acid solutions by aniline and its derivatives indicate that aniline or anilinium ion due to interaction between its π -electrons of the benzene ring and iron are adsorbed on the iron surface in parallel with the iron surface [439,440]. In a later work, aniline has been reported [441] to adsorb as the aniline molecule on the silver and iron surfaces in 0.1 M KCl and most probably as anilinium ion on the silver and iron surfaces in acidic chloride media (0.5 M HCl) containing 0.2 M aniline in a joint adsorption of the cation with the chloride ion, with a predominantly perpendicular orientation and very little parallel orientation. The authors [441] concluded that aniline molecule may be adsorbed on the silver and iron surfaces in 0.1 M KCl by the formation of a δ -bond in the perpendicular orientation and partly via the π -electron interaction in the parallel orientation. The difference between this work (predominance of perpendicular orientation of aniline/anilinium ion) and earlier works was attributed to the higher concentration of aniline (0.2 M) used, in contrast to lower concentrations usually used in corrosion inhibition in the range of 10^{-3} or 10^{-2} M since the orientation of an adsorbed molecule can be dependent on the coverage which itself affected by concentration [442,443].

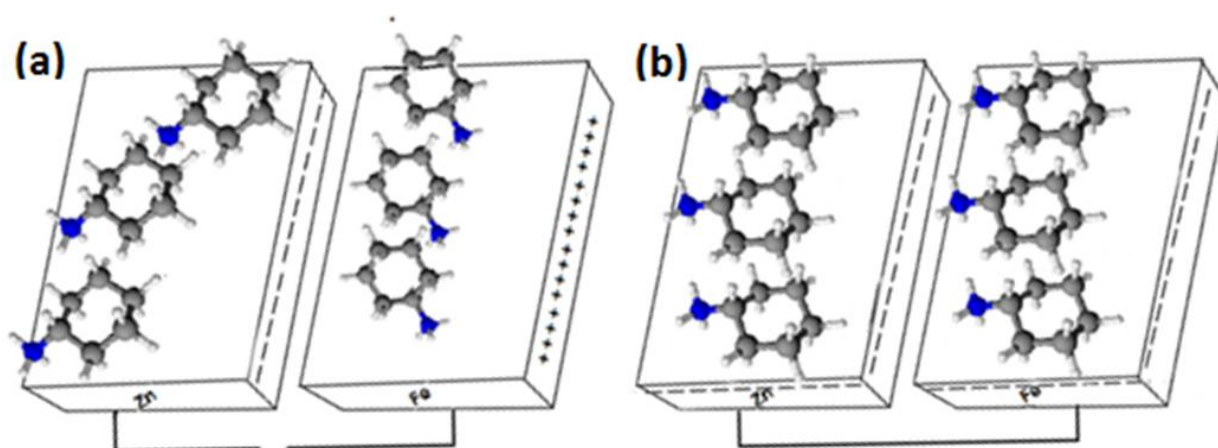


Fig. 2.20. Schematic illustration of aniline adsorption on Zn and Fe galvanically coupled and uncoupled.

On the basis of literature reports on aniline adsorption on iron and zinc in acidic media [348,363,444], their potentials of zero charge in acidic media [445-447], the range of their mixed corrosion potential in acid media, and their respective surface charges at such potentials, the possible scenarios of aniline adsorption on iron and zinc respectively and on galvanic coupling in

acidic media is schematically illustrated in Fig. 2.20 above, to depict possible favourable changes in adsorption mechanism that might be necessary for a single inhibitor to act as a galvanic and/or multi-material corrosion inhibitor.

Fig 2.20 above illustrates the challenge encountered in the use of a single organic inhibitor to inhibit galvanic corrosion systems. For instance for the Zn-Fe galvanic couple the mechanism of the iron interaction with aniline (as the anilinium ion in acidic media) will most likely change from that illustrated in (a) with a positively charged surface on iron, to (b) in which the iron surface becomes negatively charged on coupling to zinc, as it becomes the cathode in the galvanic couple. At near neutral and alkaline solutions the situation on immersed metal surfaces are most likely to change as the oxides and hydroxides formed change the properties of the metal surface.

2.10.10. Synergism in Corrosion Inhibition (Combination of Inhibitors)

Synergism has reportedly become one of the most important phenomena in corrosion inhibition processes, serving as the basis for most modern corrosion inhibitor formulations [448,449]. Synergism in corrosion inhibition is the combined use of two inhibitors to attain inhibition efficiencies greater than the sum of that obtained from each inhibitor when used separately. Synergism of corrosion inhibitors reportedly results from either interaction between the individual components of the inhibitor composition or due to interactions between the inhibitor and one of the ions present in the aqueous solution [450]. Lazarides et al., [451] in the late 1970's reported their observation of synergism using two commercial inhibitors, having obtained better inhibition efficiencies from the mixture than from the individual inhibitors with a caveat that the ratios of the inhibitors employed was a critical factor. For the observed synergistic corrosion inhibition effect of some anions and organic compounds three possible mechanisms have been advanced; (a) passivating potentials imposed by redox couples [452], (b) mixed oxide formation [453], and (c) strong anion adsorption on metal surfaces; which has been acclaimed to best explain the observed synergistic effects between anions and organic inhibitors and inhibition in the absence of alternate redox couples and/or bulk oxide formation [454]. Hosseini et al., [455] demonstrated how critical a factor, the concentrations of two inhibitors can be as they reported antagonism on mixing sodium dodecylbenzenesulphonate (SDBS) and hexamethylenetetramine (HA) when one of the components was in concentrations less than 75 ppm but moderate synergism at higher concentrations. It is important to note that the observation of an increase of inhibition efficiency does not necessarily translate to

synergism as the observed increase might be additive.

Buck and Leidheiser [456] in reporting the results of a broad survey on the effect of 35 different metallic cations at concentrations ranging from 10^{-7} to 10^{-3} M on the corrosion of 15 metals (aluminum, copper, iron, zinc, magnesium, manganese, molybdenum, nickel, cadmium, tin, silver, titanium, tungsten, gold, and zirconium) in different boiling media, concluded that as a general rule, cations of the elements in groups II to V in the periodic table showed the highest tendency to inhibiting corrosion while the transition elements exhibited the greatest tendency to accelerating corrosion. This ability to inhibit or accelerate corrosion rate was reportedly possible even at cation concentrations as low as 10^{-7} to 10^{-5} M which is equivalent to 0.1 to 10 atomic layers of the added metal on the assumption that all the ions added into the solution adhered to the metal surface. Furthermore, they reported that in all the metallic ions exerting influence on the corrosion rate a plating out mechanism of the ion onto the metal surface was involved.

The most reported synergistic combinations have been with combinations of organic compounds and halide ions [449,457,458]. In the search for the synergistic corrosion inhibition effect, much work have been carried out on metals in acidic and near neutral media with diverse combinations of different inhibitor types and ion types. These inhibitor combinations can be classified as; organic inhibitor/metallic ion mixture [459], inorganic inhibitor/metallic ion mixture [460], organic inhibitor/metallic ion mixture [461], organic inhibitor/organic inhibitor mixture [462], metallic ion/metallic ion inhibitor mixture [463], organic/organic inhibitor mixture [464,465]. For brevity a detailed review of only the synergistic corrosion inhibition with organic inhibitor/metallic ion mixture on primarily galvanic couples which is most relevant to the present work (due to much better inhibition efficiencies) is presented below.

2.10.10.1. Synergistic Corrosion Inhibition with organic inhibitor/metallic ion inhibitor combinations.

Hackerman et al. [454] reported the following order for the degree of adsorption of anions on mild steel in acidic media; $I^- > Br^- > Cl^-$. From their results they concluded that since the observed synergism of inhibitor efficiency between these anions and organic cations is greater than can be accounted solely by a shift in the metal surface potential due to anion adsorption, a component of it must be attributable to stabilization of the adsorbed anion layer by organic cations. Consequently, the molecular structure of the organic compound was suggested as a dominant factor in the degree of enhancement of (synergistic) inhibition by a

foreign anion, with the greatest enhancement most probable when both the anion and cation exhibit a tendency toward covalent bonding. Iofa et al, [359] observed that chemisorption of halogen anions from H₂SO₄ solutions on cobalt and iron, led to increase in the overvoltage of both the cathodic hydrogen-ion discharge reaction and the anodic metal ionization reaction. They posited that due to the positive charge of the cobalt surface in H₂SO₄ solutions, organic cations are poorly adsorbed and hence ineffective as inhibitors for cobalt and iron in the test media, but in the presence of halogen anions their adsorption increases leading to the observed synergistic effect though this effect was reportedly less pronounced with iron. In essence the adsorption of halogen anions altered the surface states of the metal shifting its potential of zero charge to positive values, so that the metal surface becoming negatively charged after halogen ion adsorption interacts with much ease with the organic cations from organic inhibitors [359].

Mu et al., [466] studied the effect of the metallic cations Cu²⁺, Ni²⁺, and La³⁺ on corrosion inhibition of the anionic surfactant sodium dodecyl sulfonate (SDS) on cold-rolled mild steel in 2M hydrochloric acid and reported marked inhibition synergism of Cu²⁺ and SDS, accelerated corrosion with a lower concentration range of La³⁺, but a powerful synergistic inhibition at certain higher concentration range for the mixture of La³⁺ and SDS, and a minor (additive) effect with Ni²⁺. They attributed the marked synergistic effect with Cu²⁺ to steel surface electrode potential modification by adsorption of Cu²⁺ and copper deposition on steel via the oxidation-reduction reaction of eqn. 2.84, and easier adsorption of SDS to steel through the deposited fine copper film.



Li et al., [467] reported strong synergistic inhibition effect of Ce⁴⁺ ion and iso-vanillin (3-hydroxy-4-methoxy-benzaldehyde) on the corrosion of cold rolled steel in 1.0 M H₂SO₄ solution over a wide range of concentrations of both components. The observed synergistic effect was attributed to formation of iso-vanillin-Ce⁴⁺ complex which precipitate on anodic sites while the iso-vanillin adsorbs on cathodic sites.

2.10.10.2. Synergistic Corrosion Inhibition of Galvanic Couples and Multi-material Combinations.

There seems to be a dearth of information on synergistic corrosion inhibition of galvanic and multi-material couples as most of the published literature on the synergistic use of corrosion inhibitors have been focused on individual metal or alloy [458,449,463,468,469]. However, Ai et al., [438] reported synergistic effect of KI and an imidazoline derivative on a carbon steel-

stainless steel galvanic couple in 1% NaCl, and attributed the synergistic effect to the I⁻ ion changing the excess surface charge distribution on the coupled electrodes thus promoting the adsorption of the cationic inhibitor to both cathodic and anodic areas. Musa et al., [470] reported synergistic inhibition of galvanic corrosion of aluminum-mild steel couple in 1 M HCl by iodide ion and 1-(2H)-Phthalazinone and suggested that stabilization of adsorbed iodide ions by the 1-(2H)-Phthalazinone as a possible mechanism for the observed synergistic inhibition of galvanic corrosion. Kallip et al., [21] investigated synergistic activity of 1,2,3-benzotriazole (BTA) and cerium nitrate on Zn–Fe galvanic couple using the scanning vibrating electrode technique among other electrochemical test methods and reported synergistic effect with specific activities of BTA at anodic and Ce(NO₃)₃ at cathodic sites of the Zn-Fe couple respectively. On the use of synergistic corrosion inhibitors on more than two coupled metals (multi-material combinations) or on a dual material corrosion system composed of even a metal and a non-metal no published literature is yet available.

2.10.10.3. Evaluation of Synergistic Corrosion Inhibition

To establish synergism, the synergistic parameter originally hinted by Murakawa et al [317] and developed by Aramaki and Hackerman [471] need to be evaluated. For interaction between two inhibitors A and B, the synergism parameter, *s* can be expressed thus;

$$s = \frac{1 - \eta_A - \eta_B + \eta_A \eta_B}{1 - \eta_{AB}} \dots\dots\dots \text{(eqn. 2.85)}$$

where *s* is the synergistic parameter, η_A and η_B are the inhibition efficiencies observed with only compound A, and B acting alone respectively, and η_{AB} is the observed inhibition efficiency for the mixture of the two compounds. When $s < 1$, there is antagonism and if $s > 1$ there is synergism. It is good to note that when two corrosion inhibitors are mixed and targeted at a material the concentrations notwithstanding, three principal possible outcomes are possibilities; synergistic action, additive action or antagonistic action.

2.11. Inhibiting the Electrochemical Reactivity of Carbon/CFRP Surfaces

Since carbon fibre reinforced polymers (CFRPs) are components of the multi-material combinations studied in this work, in which its electrochemical reactivity exerts on deleterious effects to the corrosion resistance of multi-material combinations, a review on any attempts at inhibiting electrochemical reactivity of carbon materials would be desirable. Unfortunately, due to the fact that in other applications of carbon fibres and carbon materials such as in catalysis, sensors, energy applications etc., electrochemical reactivity is a desirable quality, most reports

in the literature have been on improvements of the electrochemical reactivity of carbon materials/surfaces. Electrochemical based methods that have been employed to modify carbon surface include, mainly electrochemical oxidation [473-475] and covalent modification by aryl radicals generated from the electrochemical reduction of diazonium salts [476-478].

Hoekstra and Bein [479] using $\text{Fe}(\text{CN})_6^{3-}$ (in 0.1M KCl) reported marked decrease in electron transfer kinetics with a large overpotential, (across the carbon surface-solution interface) after electrooxidation of decylamine or octadecylamine on glassy carbon surface compared to unmodified glassy carbon. Increased barrier properties and reduced electron transfer kinetics have been reported [480,481] for glassy carbon surfaces modified with 4-nitrophenyl using the reduction of aryl diazonium cation method, and the decreased electron transfer kinetics proposed to be most probably due to changes in the electronic properties of glassy carbon due to the surface modification [481]. Surface modification of glassy carbon surface with a nitrophenyl monolayer have been reported [283] to decrease electron transfer kinetics compared to unmodified glassy carbon, and the changes in electron transfer kinetics were postulated to be suggestive of increase in the distance over which electron transfer needs to occur [282,283]. In the light of these, it is plausible that the electrochemical reactivity of carbon surfaces might be suppressed by surface modification(s) that tunes the composition of the surface functional groups present on carbon surfaces, and increases the path for electron transport across the interface between carbon surface and solution.

2.12. Chapter Concluding Remarks

In this chapter (Chapter 2), the corrosion of the metals employed in the work (Al, Cu, Fe and Zn) have been reviewed as well as the methods and mechanism(s) of corrosion inhibition for metals and galvanic-systems to aid appreciation of the current work. The degradation of carbon fibre reinforced polymers, the surface chemistry of carbon and its electrochemical reactivity have been reviewed along with attempts at surface modification of carbon surfaces for increased surface reactivity from which insights have been drawn on possible means of suppressing the electrochemical activity of carbon surface (particularly to oxygen reduction reactions).

CHAPTER 3

PRINCIPLES OF EXPERIMENTAL TECHNIQUES

3.0. Principles of the Experimental Techniques.

The experimental techniques employed in this work are mainly electrochemical techniques and surface analysis techniques. Electrochemical techniques have the advantage of relatively short measurement time coupled with the possibility of extracting mechanistic information from test results that are vital to the thesis objectives. Since corrosion is a surface phenomena, surface analysis provides surface compositional information that aid understanding of possible reaction pathways, mechanisms, and inhibitor interaction with metal/metal oxide surface. The electrochemical test methods employed are chronopotentiometry (open circuit potential measurements), chronoamperometry, potentiometry (for pH and oxygen measurements), potentiodynamic polarization, cyclic voltammetry, zero resistance ammeter (ZRA) measurements for (galvanic couples and galvanic triplets), electrochemical impedance spectroscopy (EIS), and Scanning Vibrating Electrode Technique (SVET). The surface analysis techniques employed are scanning electron microscopy (SEM), Scanning Kelvin Probe Force Microscopy (SKPFM), gas discharge optical emission spectroscopy (GD-OES), X-ray Fluorescence Spectroscopy (XRFS), and Raman spectroscopy. In the rest of this section the principles of each of these techniques/tests are discussed. Since the work is mainly based on electrochemistry, the major electrochemical techniques employed are discussed in greater detail.

3.1. Chronopotentiometry (OCP Measurements)

Open Circuit Potential is the potential difference measured between the working and reference electrodes in an electrochemical cell under equilibrium conditions (i.e no impressed currents or voltage) using a high impedance voltmeter. Since an electrode in a corroding system undergoes simultaneous anodic and cathodic processes, the measured open circuit potential is actually the mixed potential arising from these processes, and has a value that lies between the equilibrium potentials of these processes, and tending towards the values for the faster half-cell reaction. Open circuit potential measurements with time can be considered a type of chronopotentiometry except that in this case no current is passed between the working electrode and the reference electrode as the voltage is measured through a high impedance voltmeter against the reference electrode. This is an important difference between OCP measurements and chronopotentiometric tests.

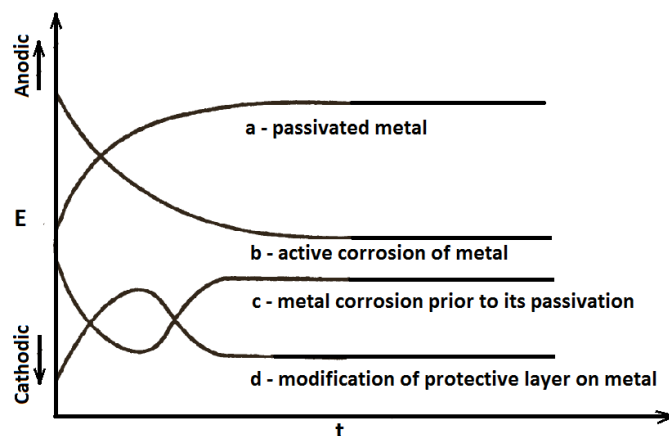


Fig. 3.1. Schematic illustration of typical OCP - time profiles and their indications [Adapted from ref: 472].

Open circuit potential measurements can give insight on what is happening on the exposed material surface in the test media, and in solutions containing inhibitors give some clues to the type of inhibitor (cathodic or anodic), which is confirmed usually by potentiodynamic tests. Measurement of open circuit potential evolution over time though a simple test, can give interesting information about the evolution of corrosion or onset/presence of passivation phenomena [482]. Secondly, measurements of OCP evolution during the immersion can be helpful in inhibition studies in the planning and determination of appropriate time scales for other electrochemical measurements/tests as it provides information on the balance of redox processes on the metal surface. Thirdly, the probable presence of pitting and metastable pitting events in an immersed sample can be observed as a "noisy" OCP-time evolution or as sharp fluctuations. Finally, observation of shifts in the OCP of a metal immersed in an inhibitor containing system in comparison to the trend in the uninhibited solution can provide first indications of the type of inhibitor (cathodic or anodic). Open-circuit potential usually increases (tending towards nobler potentials) with time for passive samples as passivity improves, and often decreases (tending towards more negative potentials) when localized corrosion begins [483]. Care must however be exercised not to make conclusions on the sole basis of OCP measurements.

3.2. Potentiodynamic Polarization Technique

The potentiodynamic polarization technique is a DC technique used to determine the corrosion properties of a metal or alloy with respect to impressed changes in its potential. It is used to obtain a quick qualitative picture or signature of an electrode in the test media. With this technique a wide range of important information such as the different regions (the active

corrosion region, the passive region, the transpassive region), and important parameters such as the potentials and currents associated with the onset of passivity, breakdown of passivity, the corrosion current density and corrosion potential, corrosion rate, pitting susceptibility, passivity range, active corrosion range and the cathodic behavior of an electrochemical system can be established [484,485], depending on the test parameters employed. In corrosion inhibition studies, comparison of the logarithm of current - voltage relationship for an electrode in the presence of inhibitors with that without inhibitors gives information on the mode of action of the inhibitor on the basis of the particular electrode half reaction (cathodic and anodic) the inhibitor influences and shifts in the corrosion potential.

3.2.1. Potentiodynamic Polarization Test

Potentiodynamic polarization is a DC test technique in the driving force for electrochemical processes to occur is supplied in the form of an impressed potential gradient with a potentiostat in a desired direction (cathodic or anodic), or a sequence of directions from a chosen potential usually the open circuit potential, or some anodic or cathodic displacements from it, depending on the test objectives, while the resultant current output is measured. The magnitude of this driving force (polarization) dictates which electrochemical processes actually take place at the anode and cathode, as well as their rates [485,486]. A potentiodynamic polarization test is a three electrode test in which potential is applied to the working electrode (the specimen), through a potentiostat and the resultant current flowing between it and the counter electrode is measured with reference to a reference electrode whose potential is invariant under the test condition. The counter electrode should be very conductive and stable under the test condition; platinum being the usual choice in aqueous corrosion studies. Additionally, it is beneficial that the surface area of the counter electrode is higher than that of the working electrode, so that the response of the system is determined solely or predominantly by the working electrode. Prior to a potentiodynamic test it is necessary to immerse the working electrode in the test solution for some time to achieve equilibrium, the actual time duration being dependent on the metal/alloy and the test solution. Depending on the desired test conditions and objective(s), temperature control by use of a water bath, pH control by use of buffered solutions, and dissolved oxygen concentration control (by oxygen, nitrogen or argon sparging before and/or during the scan) may be necessary. Since the currents measured can be very low, measurements are usually made in a Faraday cage. The scan rate (rate of change of potential) is an important variable as it determines how close to equilibrium

each point reaches before the next increment and affects the shape of the polarization curve and features that it manifests. To reduce ohmic potential drop through the test electrolyte, the working and reference electrodes are placed as close to each other as possible often by the use of a Luggin capillary.

The results from a potentiodynamic polarization test are often presented in the form of a plot of the applied potential against the logarithm of the current. From observations in the literature there appears not to be a strict rule on which of the two variables is the ordinate and the abscissa. In this work potentiodynamic results are presented with the log of current on the Y-axis and the applied potential on the X-axis. At the corrosion potential, E_{corr} , or open circuit potential the total anodic current is equivalent to the total cathodic current and the net current measured current should theoretically be zero, but practically observed to have a finite value that tends to zero. This practical observation is exploited in quick identification/estimation of the values of the corrosion potential, E_{corr} , and the corrosion current, i_{corr} , directly from the scan.

The corrosion current density (i_{corr}), and subsequently the corrosion rate, can be determined graphically from the so-called Tafel extrapolation in which the Tafel region of a polarization curve can be extrapolated back to the steady-state open-circuit corrosion potential to give the open-circuit corrosion rate provided that the following conditions are met; the branch of the polarization curve is under activation control, presence of a well-defined Tafel region, corrosion is uniform not localized corrosion, and changes in electrode potential (within the Tafel region) do not induce additional electrode reactions [487]. The Tafel region is the region of the curve in which the applied potential varies linearly with the logarithm of the current.

3.2.2. The Linear Polarization Resistance Technique

The linear polarization method is discussed herein under potentiodynamic polarization because it is a type of potentiodynamic test, and secondly and more importantly because in the course of this work a scheme was devised that enabled simultaneous acquisition of linear polarization resistance data with anodic potentiodynamic polarization data in one test. This was done during anodic potentiodynamic polarization tests by starting at potentials 10-20 mV cathodic from the open circuit potential and scanning towards the terminal anodic potential. By the time the scan has gone past 10-20 mV anodic with respect to OCP, the data for the polarization resistance is already acquired, while the rest of the data for the anodic potentiodynamic polarization is being acquired.

Linear polarization resistance technique is a potentiodynamic polarization test in which the potential excursions are limited to a small range, typically within $\pm 10\text{-}25$ mV with respect to the corrosion potential, in which range the current response to the applied potential is linear and very small. A plot of the measured current against the applied potential, gives a slope that is equal to the polarization resistance (equation 3.1).

$$R_p = \left(\frac{\partial \Delta E}{\partial i} \right)_{i=0, dE/dt \rightarrow 0} \dots\dots\dots \text{(eqn. 3.1)}$$

where R_p is the polarization resistance in ohm.cm^2 , i is the current density and E the applied potential.

With foreknowledge of the values of the Tafel constants (obtainable from potentiodynamic polarization) the polarization resistance thus obtained can be used to evaluate corrosion rates [488], as the obtained polarization resistance relates to the corrosion current density, i_{corr} , according to equation 3.2, which in turn relates to the corrosion rate according to equation 3.5.

$$i_{\text{corr}} = \frac{B}{R_p} \dots\dots\dots \text{(eqn. 3.2)}$$

where B is the Stern - Geary constant [489] and relates to the Tafel constants thus:

$$B = \frac{\beta_a \beta_c}{2.3 (\beta_a + \beta_c)} \dots\dots\dots \text{(eqn. 3.3)}$$

where β_a and β_c are the anodic and cathodic Tafel slopes

Substituting for B in equation 3.2 yields;

$$i_{\text{corr}} = \frac{\beta_a \beta_c R_p}{2.3 (\beta_a + \beta_c)} \dots\dots\dots \text{(eqn. 3.4)}$$

But from Faraday's law corrosion rate (CR) in mil per year (mpy) is expressed as:

$$CR = \frac{i_{\text{corr}} A_w}{F n \rho} \dots\dots\dots \text{(eqn. 3.5)}$$

where CR is the corrosion rate in mils per year (mpy), i_{corr} is corrosion current density (A.cm^{-2}), A_w is atomic weight (g.mol^{-1}), F is Faraday's constant ($96,487 \text{ C.mol}^{-1}$), ρ is density of metal (g.cm^{-3}), and n is number of electrons involved in the reaction.

Substituting for i_{corr} according to equation 3.4 into equation 3.5 yields;

$$CR = \frac{\beta_a \beta_c A_w}{2.3 (\beta_a + \beta_c) F n \rho} \dots\dots\dots \text{(eqn. 3.6)}$$

.

3.3. Cyclic Voltammetry

Cyclic voltammetry is a useful electrochemical technique for the study and determination of the mechanisms and rates of the redox processes (oxidation/reduction reactions), taking place on electrode surface or across the electrode/solution in an electrochemical system. Cyclic voltammetry is capable of providing thermodynamic information of redox processes, and the

kinetics of heterogenous electron transfer reactions, coupled chemical reactions, and adsorption processes taking place on or near electrode surface, which are relevant to corrosion and corrosion inhibition studies. Furthermore, the characteristic shapes of the voltammetric waves and their known position on the potential scale function virtually as fingerprint of the individual electroactive species and electrochemical properties of redox systems; the reason the cyclic voltammetry has been regarded as an “electrochemical spectroscopy” [490,491,492].

In cyclic voltammetry, the potential of a working electrode is ramped or scanned linearly between two potentials using a triangular waveform (Fig. 3.2), and the current response measured. Cyclic voltammetry is executed with a three electrode arrangement; the working electrode, the reference electrode and the counter electrode.

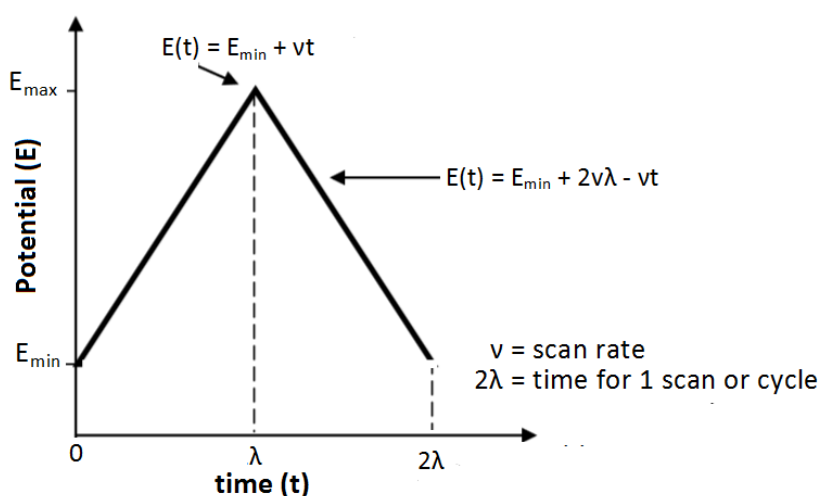


Fig. 3.2. Potential time dependence in cyclic voltammetry.

The potential can be scanned in two ways, either linearly or in a staircase manner. In the linear scan method the potential scan is accomplished by a linear increase or decrease of the potential in a sequence of small potential steps, between the vertices of the scan with the resultant current sampled at regular intervals during the scan. In the staircase method for cyclic voltammetry, the applied potential is changed in a stepwise manner with each step, ($1/N$, where N is the total number of steps), having a magnitude of ΔE and following the previous step by a time lapse of τ in seconds. Hence staircase voltammetry is a unique current-potential-time relation specified by at least three parameters; ΔE , τ , and N , while linear scan voltammetry is easily described by the scan rate.

In linear scan voltammetry since the potential change is effected at a constant rate, the charging or capacitive currents generated gravitate to a constant value given by the relation:

$$i_c = C_{dl} v \dots\dots\dots \text{(eqn. 3.8)}$$

where i_c is the charging current, C_{dl} is the double layer capacitance and v is the scan rate.

The potential is applied between the working electrode and the reference electrode while the resultant current is measured between the working electrode and the counter electrode. Often times repeated or multiple scans are employed or scan rates varied depending on the information needed. The resultant plot of current vs. potential is called a cyclic voltammogram and can be exploited to evaluate time dependent information of many physical and chemical parameters of the electrochemical system under study such as concentration of redox species, diffusion coefficients, heterogeneous rate constants and the transfer coefficient [491,493]. During a cyclic voltammetric forward scan (towards more noble potentials) in a quiescent solution, current increases as the potential is ramped due to the oxidizable species, R, near the electrode surface being oxidized to yield O species and electrons (Fig.3.3). The reducing concentration of R near the electrode surface needs to be augmented by the diffusion of R species from the bulk to the electrode surface, thus increasing diffusion layer thickness. The combined effects of a potential increment and an increasing diffusion layer thickness leads to current maximum (peak i_a). After this the current reduces as fewer R becomes available near the electrode surface with the concentration of O in this region increasing. Maintenance of high currents requires the diffusion of more R from the bulk to the electrode surface (increase of diffusion layer thickness), the rate of this process being dependent on the allowed time (scan rate), the diffusion coefficient of the R species, and its bulk concentration. Furthermore, as the concentration of O near the electrode surface increases, the zone near the electrode surface depleted of R increases, and so does the distance R needs to be transverse from the bulk to electrode surface. As a result of these, the current tends towards zero. Increasing the scan rate reduces the time available for depleted species near the electrode surface to be replenished by diffusion from the bulk, as a consequence increasing the scan rate in cyclic voltammetry yields better defined peaks. On reversing the scan direction in a reversible system (in which the O species produced in the forward scan are not converted to another specie P, or rendered electrochemically inactive), these O species near the electrode surface are reduced leading to the formation of the cathodic peak (i_c), until most of the O species near the electrode surface are consumed with more O species required to diffuse to the electrode surface from the bulk. Thus it is obvious that the measured peak currents can be related to a variety of parameter of the electroactive species present in the electrochemical system.

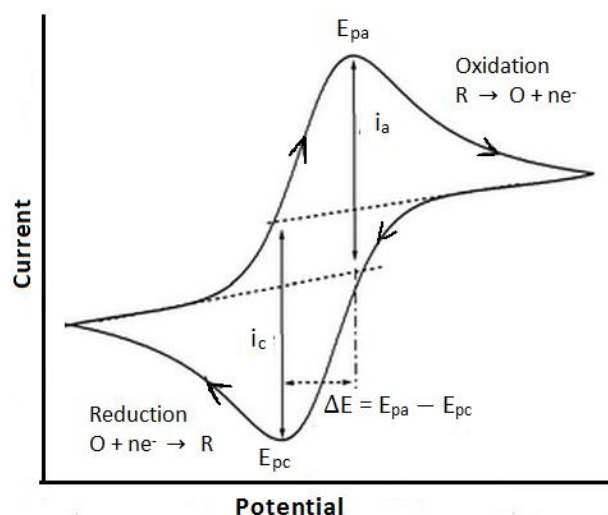


Fig. 3.3. Schematic illustration of the voltammogram of a reversible couple.

The important parameters directly obtained from a cyclic voltammogram are the magnitudes of the anodic peak current (i_a) and cathodic peak current (i_c), the anodic peak potential (E_{pa}) and the cathodic peak potential (E_{pc}). The values of these parameters, their relationships to each other and to the scanning rate (v), describes the thermodynamics and kinetics of processes taking place in the system, and the electrochemical properties of the working electrode. Other important parameters that are extracted from these four basic parameters include; the peak separation ΔE , and the mean of the peaks, $E_{1/2}$ (also referred to as E^0 , the formal reduction potential). Evaluation of the currents is done by extrapolation of the baseline (Fig. 3.3), care being taken to accurately determine the baseline. A redox couple in which both (reductant and oxidant) species rapidly exchange electrons with the working electrode as the potential is cycled is termed an electrochemically reversible couple.

3.4. ZRA Measurements for (Galvanic Couples)

When two dissimilar metals are in electrical contact and immersed in an electrolyte a voltage difference becomes operative between them which drives a current (the galvanic current). The magnitude of the galvanic current is dependent on the factors like the distance between the two metals in the galvanic series, the conductivity of the electrolyte, the kinetics of the electrode processes on each electrode, the presence of oxygen or other oxidants, the presence and nature of corrosion products on each of the metals, and the presence of inhibitors. The value of the galvanic current is measured using a zero resistance ammeter (ZRA). An ordinary ammeter can in principle be used for the same purpose but the voltage drop in the test of equipment, of the usually small galvanic current being measured will be a source of very significant error.

3.5. Electrochemical Impedance Spectroscopy (EIS)

Electrochemical impedance spectroscopy has emerged as a tool for investigating the mechanism of corrosion and its mitigation efforts with corrosion inhibitors, conversion coatings, polymer coatings, oxide layers, and cathodic protection, providing mechanistic information in situation in which traditional DC techniques are limited such as corrosion protection by polymer coatings and anodic films [494]. The increasing use of impedance techniques is due to its many advantages which include: use of very small perturbations that exert negligible effects on the electrode processes being studied, possibility of studying corrosion reactions and measuring corrosion rates in low-conductivity media, in which traditional DC methods are ineffective such as corrosion under painted or concrete structures, and the possibility of evaluating polarization resistance and double-layer capacitance data in one measurement [495]. Electrochemical impedance spectroscopy is a test method in which the impedance response of an electrochemical system is studied as a function of the frequency by application of an a.c. wave of small amplitude [496]. In electrochemical impedance spectroscopy, this impedance response from an electrochemical system is measured point by point as a function of frequency, usually from higher to lower frequencies to obtain a spectrum, on application of a sinusoidal voltage of small amplitude. The spectra thus acquired are rich in information about the system which includes at each frequency in the spectra; the Z modulus and the phase angle (between the applied potential and the resultant current), from which the imaginary and real components of the impedance are easily evaluated. Analysis of the spectra yields even more information. To interpret the spectra by relating it to physical processes taking place in the electrochemical system under study, an analog or "model" of the system (an electrical equivalent circuit), capable of producing a similar electrical response as the studied system with appropriate values of its constituent elements is employed.

3.5.1. Basic Concepts Related to EIS

The resistance, R, of a circuit to the flow of current is described by Ohm's law as a ratio of the applied voltage E, to the current, I.

$$R = \frac{E}{I} \dots\dots\dots \text{(eqn. 3.17)}$$

Ohm's law description of the relationship between voltage and current is valid at all levels of voltage and current, for ideal systems with an ideal resistor, characterized by a constant resistance independent of frequency, and a.c. current and voltage in phase. Real systems are composed of different circuit elements and exhibit a more complex behaviour than described by

Ohm's law. As a consequence the concept of impedance was introduced to accurately describe observations.

Impedance can be defined as the complex resistance (being composed of real and imaginary components) to the flow of current in a circuit comprised of resistive, capacitive, and inductive elements, on application of a potential.

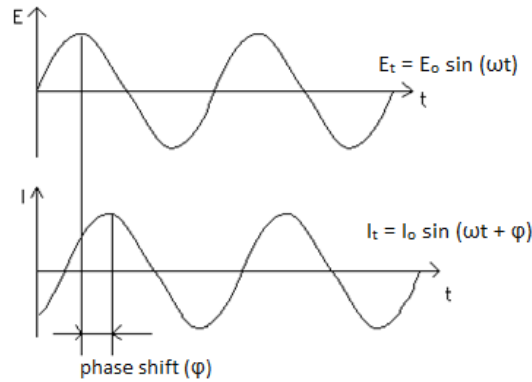


Fig. 3.4. Sinusoidal current response in a linear system to a sinusoidal applied voltage.

Assuming as in an EIS measurement a small a.c sinusoidal potential excitation E_t is applied to an electrochemical system. The response to this excitation signal is an a.c. sinusoidal signal with same frequency as the excitation signal, but phase shifted by (ϕ) as illustrated in Fig. 3.6. Since the potential excitation is sinusoidal, it changes with time and can be expressed as a function of time as:

$$E_t = E_o \sin(\omega t) \dots\dots\dots \text{(eqn. 3.18)}$$

where E_t is the potential at a time denoted by t , E_o is the amplitude of the potential, and ω is the angular frequency. The angular frequency, ω (in radians/second), is related to the frequency, f , measured in Hertz (Hz) by the relation:

$$\omega = 2\pi f \dots\dots\dots \text{(eqn. 3.19)}$$

The response signal to this applied potential in a linear system, is a current signal I_t that can be expressed as:

$$I_t = I_o \sin(\omega t + \phi) \dots\dots\dots \text{(eqn. 3.20)}$$

where I_t is the current at a time denoted by t , I_o is the amplitude of the current, ω is the angular frequency, and ϕ is the phase angle between the applied potential and the current.

Guided by Ohm's law, the impedance, Z , of such system at a time t , after application of the excitation can be expressed as:

$$Z = \frac{E_t}{I_t} = \frac{E_o \sin(\omega t)}{I_o \sin(\omega t + \phi)} \dots\dots\dots \text{(eqn. 3.21)}$$

From equation (3.21) above, eliminating the amplitudes gives:

$$Z_o = \frac{\sin(\omega t)}{\sin(\omega t + \phi)} \dots\dots\dots (\text{eqn. 3.22})$$

where Z_o is the magnitude of the impedance.

Employing Euler's relationship (equation 3.23), makes it easier to graphically present complex impedance data.

$$\exp(j\phi) = \cos \phi + j \sin \phi \dots\dots\dots (\text{eqn. 3.23})$$

Using the Eulers notation, the applied voltage is expressed as:

$$E_t = E_o \exp(j\omega t) \dots\dots\dots (\text{eqn. 3.24})$$

and the current response as:

$$I_t = I_o \exp(j\omega t - \phi) \dots\dots\dots (\text{eqn. 3.25})$$

Thus the impedance is expressed as:

$$Z(\omega) = \frac{E_t}{I_t} = Z_o \exp(j\phi) \dots\dots\dots (\text{eqn. 3.26})$$

or as:

$$Z(\omega) = Z_o \exp(\cos\phi + j \sin \phi) \dots\dots\dots (\text{eqn. 3.27})$$

where $\cos \phi$ denotes the real part (Z_{real}), and $j \sin \phi$ the imaginary part (Z_{im}) of the impedance ($Z(\omega)$)

The real part of impedance is characteristic of charge transfer processes (resistive), while the imaginary part characterizes the charge storage processes (capacitive) like polarization.

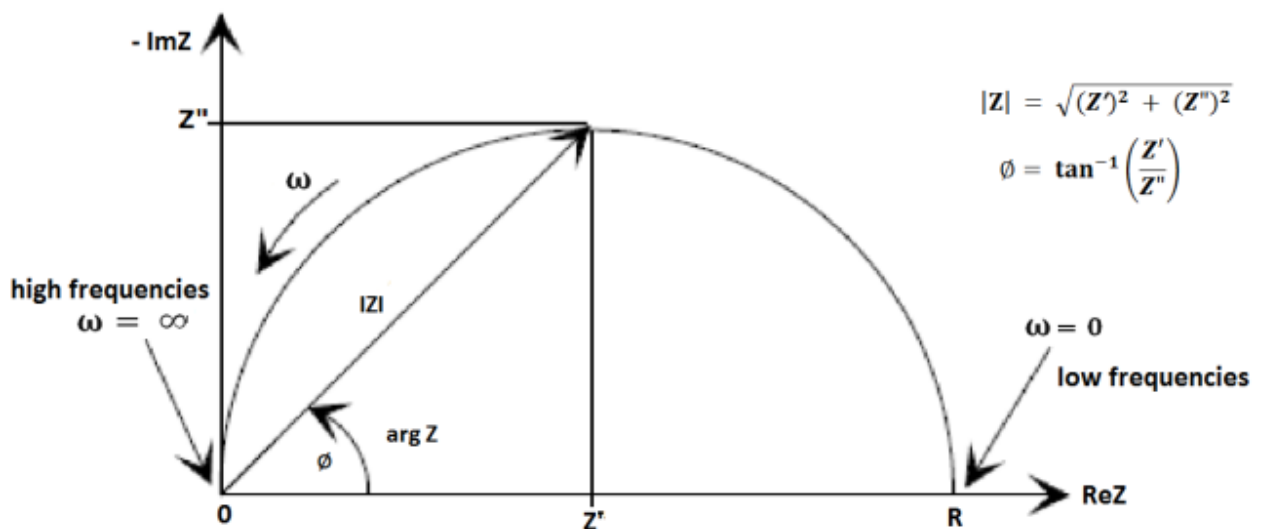


Fig. 3.5. Illustration of the Nyquist plot.

The Nyquist plot (Fig. 3.5) is presentation of impedance data obtained by plotting the impedance at each frequency as a vector of magnitude $|Z|$, the angle between the vector and the x-axis being the phase angle ϕ , with the x-axis denoting the real component (Z') and the y-axis the imaginary component (Z'') of the impedance. To convey the frequency dependence of impedance data in Nyquist plots it is necessary to label individual points of interest with frequency information.

Impedance data can also be presented as a Bode spectra or plot in which both the logarithm of the modulus of impedance, $\log |Z|$, and the phase angle, ϕ , are plotted as a function of the logarithm of frequency (Fig.3.6) [496]. The presentation of EIS data in the form of Bode plots has several advantages over the Nyquist plot, as the frequency dependence of the components of the impedance (predominantly resistive and capacitive regions) are easily distinguished and in combination with the information easily accessible from the frequency dependence of the phase angle, which is very sensitive to small changes in the spectra, enables fast analysis of impedance spectra. For instance the presence of multiple time constants is easier to detect in the evenly spaced data points and logarithmic scale of the Bode plot.

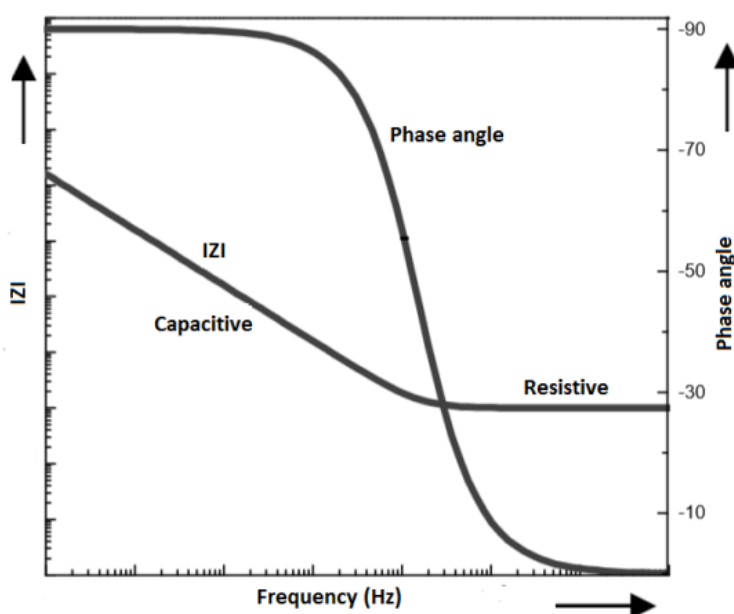


Fig. 3.6. Schematic illustration of the Bode plot.

3.5.3. Interpretation of EIS Data : Equivalent Circuits

Two tools, analogs and physical models can be used to interpret EIS data. Physical models attempt to interpret EIS data by reproducing the phenomenon of interest and also accounting for the mechanism of the processes occurring at the interface while analogs achieve same by simply reproducing the properties of the system [497]. Equivalent electrical circuits are used as "models" (but are actually analogs [497]) to explain electrochemical impedance results.


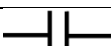
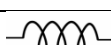
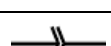
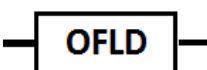
This approach is supported by the fact that impedance functions often display many of the features of passive electrical circuits [496].

These equivalent electrical circuits use diverse combinations of resistance(s), capacitance(s) or other elements such as constant phase elements (CPE) or Warburg elements [498,499], which having certain values accurately simulate the electrical equivalent of processes taking place in a system under study. For a model to achieve this, two conditions must be satisfied [500];

(a) All elements of a proposed circuit must have a clear physical meaning, each being associated to a physical property of the system that can generate same kind of electrical response, and collectively producing a combined output equivalent to that of the system being studied, and with parameter values of these elements evolving with time in a continuous and non-random manner.

(b) The equivalent electrical circuit must be as simple as possible, by elimination of elements whose absence do not invalidate previously described condition(s), and generate spectra with suitable value of the elements that vary only negligibly (error) in a non-periodic or regular manner as a function of frequency [500].

Table 3.1. Circuit elements

Circuit Elements	Symbol	Impedance Expression
Resistor, R		$Z = R$
Capacitor, C		$Z = 1/j\omega C$
Inductor, L		$Z = j\omega L$
Constant Phase Element, CPE		$Z_{(\omega)} = \sigma (j\omega)^{-\alpha}$
Warburg, W	-W-	$Z_w = \delta (1 - j) \omega^{-1/2}$
Open Boundary Finite Length Diffusion (OFLD), O		$Z_{\text{OFLD}} = \frac{[\tanh B(j\omega)^{\frac{1}{2}}]}{Y_o(j\omega)^{\frac{1}{2}}}$
Blocked Finite Length Diffusion (BFLD), T	T	$Z_{\text{BFLD}} = \frac{[\coth B(j\omega)^{\frac{1}{2}}]}{Y_o(j\omega)^{\frac{1}{2}}}$

An equivalent circuit consists of basic elements such as; a resistor, R, to represent the resistance that charge carriers encounter in a specific process or material; a capacitor, C,

representing the accumulation of charged species; and an inductor, L, representing the deposition of surface layers such as a passive layer [496]. The main constituents of equivalent circuits and their impedance expressions are presented in Table 3.1 above. A resistor, lacking in a frequency dependence of its impedance and without an imaginary impedance component is used to account for charge transfer processes and the resistance that charge carriers encounter during these processes in an electrochemical system. As a consequence current output from a resistor is in phase with and proportional to the applied voltage. A capacitor is used to represent processes that lead to charge accumulation in the electrochemical system. It only has an imaginary component, and its impedance is frequency dependent. The imaginary component of its impedance decreases with increasing frequency, and there is a phase shift between the output current and the applied voltage that is -90° for an ideal capacitor. The inductor is used to represent relaxation processes of adsorbed species on the electrode surface [501,502], and pit formation [503] in an electrochemical system, and though its impedance is frequency dependent, in contrast to the capacitor it increases with increasing frequency, and the phase shift between the output current and applied voltage is phase shifted tending towards $+90^\circ$ for an ideal inductor.

Constant phase elements are general circuit elements introduced in equivalent circuits to account for electrode surface inhomogeneities (which can arise from distributed surface reactivity, surface inhomogeneity, roughness or fractal geometry, electrode porosity, and current and potential distributions associated with electrode geometry) [504] which can cause non ideal behaviour of circuit elements, and thus can in principle stand in place of any circuit element given an appropriate exponent. Values for the exponent, n, of the constant phase element representing different circuit elements are, inductance ($n = -1$), resistance ($n = 0$), Warburg ($n = 0.5$), capacitance ($n = 1$), non-ideal dielectric behaviour ($-1 \leq n \leq 1$) resulting from a distribution of relaxation times [505] or from non-uniform diffusion whose electrical analog is an inhomogeneously distributed RC transmission line [506]. Constant-phase element or impedance can be represented in a general form, by equation(3.28) [507]:

$$Z(\omega) = \sigma (j\omega)^{-\alpha} \dots\dots\dots \text{(eqn. 3.28)}$$

where σ and α are frequency-independent real constants.

Setting α equal to $1/2$ and $1/4$ in equation (3.28) yields two of the most important constant-phase impedances in electrochemistry; semi-infinite planar diffusion and pore diffusion [507] respectively which manifests as a straight line of slope 45° ($\pi/4$) and 22.5° ($\pi/8$) in the complex plane respectively [507].

3.5.5 Combination of Circuit Elements to form Equivalent Circuits and Effect on Spectra

Commonly used equivalent circuits consist of two or more elements which may be arranged either in series or in parallel. The arrangement of circuit element in an equivalent circuit affects the total impedance of the circuit, in accordance with Kirchhoff's laws. For a series circuit, with n impedances arranged in series, the total impedance Z is given by :

$$Z = Z_1 + Z_2 + Z_3 \dots \dots \dots + Z_n \dots \dots \dots \text{ (eqn. 3.33)}$$

For a circuit, with n impedances arranged in parallel, the total impedance Z is given by:

$$\frac{1}{Z} = \frac{1}{Z_1} + \frac{1}{Z_2} + \frac{1}{Z_3} \dots \dots \dots + \frac{1}{Z_n} \dots \dots \dots \text{ (eqn. 3.34)}$$

Most equivalent circuits are often made up of different combinations/arrangements of resistors and capacitors. Table 3.1 lists the most likely circuit elements that may be encountered in corrosion, their symbols, and impedance expressions. Since the impedance response of each of these circuit elements to the change in frequency of the applied voltage is different, it is possible to use these differences to identify the dominant elements at different frequencies and thus extract mechanistic information.

The choice of amplitude of the impressed a.c. input voltage is guided by the objective of introducing voltage perturbations that are just strong enough to elicit a measurable response without much disturbance of the electrochemical system under study. For uncoated metals, signals of 5-20 mV are typical. On introduction of a perturbation to a system in a steady state, for instance by application of an a.c. voltage as in EIS, the system relaxes to a new steady state after some interval. The time duration it takes (in seconds) to establish a new steady state after perturbation is known as a time constant, τ , and defined by equation (3.35) as :

$$\tau = RC \dots \dots \dots \text{ (eqn. 3.35)}$$

where R is the resistance in ohms and C is the capacitance of the system in Farads.

Each time constant is associated with a characteristic frequency expressed by;

$$f = \frac{1}{2\pi\tau} \dots \dots \dots \text{ (eqn. 3.36)}$$

In the frequency domain, fast processes (with low τ) occur at high frequencies while slow processes (with high τ) occur at low frequencies, hence dipolar properties can be studied at high frequencies, bulk properties at intermediate frequencies and surface properties/processes at low frequencies [496]. Parameters that can be easily extracted from EIS data for a system manifesting a single time constant are; the capacitance of the double layer, C_{dl} , the polarization resistance R_p . In EIS the polarization resistance R_p , is defined as the dc limit of the impedance [508]. For more complex systems such as coated samples or samples on which a

layer(s) of corrosion products have been formed, the phase angle dependence on frequency in the Bode plot can provide a lot of mechanistically important information, as the high frequency region is reportedly determined by the coating properties, the medium frequency by the changes in the coating conductivity/barrier properties during exposure to corrosive media, and the low frequency region by the corrosion processes taking place at the coating/metal interface being studied [509].

3.5.5. Validity of EIS data (Validating Impedance Data with Kramers-Kronig Transforms)

In spite of the benefits accruable from use of EIS in studying electrochemical systems, the validity of the acquired experimental data can be a challenge as invalid impedance data may yield apparently correct kinetic parameters that fit into an equivalent circuit model [496]. To ensure the validity of EIS data and its freedom from experimental artifacts and errors, Macdonald et al. [510,511] proposed the use of a set of mathematical relationships; the Kramers-Kronig (K-K) transforms to validate impedance data. Kramers-Kronig (K-K) transforms have been acknowledged as useful tool for the evaluation and interpretation of electrochemical impedance data [512], and demonstrated as a diagnostic criteria for confirming the validity of EIS data [510,511]. The Kramers-Kronig (K-K) transforms are mathematical relationships that are able to transform the real component into the imaginary component and vice versa, thus specifying the relationship between an input voltage perturbation and the resultant current response as the impedance only when four criteria are satisfied. These four criteria are causality, linearity, stability, continuity or finiteness [513,514], and the details of these criteria are explained below;

(a) Causality implies that the response of the system is due only to the perturbation applied and lacks significant components from spurious sources.

(b) Linearity implies that the applied perturbation and resultant response of the system is describable by a set of differential laws; a condition requiring that the impedance is independent of the magnitude of the perturbation. In practice this requirement is taken into account by using a perturbation of small amplitude in the linear portion of the current-voltage curve of the sample.

(c) Stability implies that the system must be stable, returning to its original (equilibrium) state on removal of the applied perturbation. The applied perturbation must not be such that creates irreversible effects on the system.

(d) Finiteness implies that the transfer function must be finite valued as $\omega \rightarrow 0$ and $\omega \rightarrow \infty$, and

must be a continuous and finite-valued function at all intermediate frequencies. If these conditions are met, a set of transforms between the real and imaginary components have been shown to hold by Kramers [513]. This means that the experimentally observed real component can be transformed by K-K transforms, to yield the experimentally observed imaginary component and vice versa. If it does not, then the measured quantity cannot be interpreted as impedance [514-516].

In addition to validating EIS data with KKT it is necessary to be cautious in the choice of equivalent circuit to fit the data to, ensuring that the circuit and its elements are physically meaningful, have a good fit with experimental data and is confirmable by some other techniques [496,517].

3.6. Scanning Vibrating Electrode Technique (SVET)

Scanning vibrating electrode technique is one of the scanning electrochemical (probe) techniques that can be used to measure and spatially resolve corrosion activity, on the assumption that corrosion involves cathodic and anodic activities taking place on spatially separated sites. Scanning vibrating electrode technique is an AC test method that measures the flux of ions in the electrolyte over a sample from measurements of the potential difference between the two extremes (i.e vibration amplitude) of the vibrating probe, but without identification of the species creating the ionic fluxes that are measured [518-521].

3.6.1. Operating Principle of SVET

The five major components of the SVET equipment are: the electrochemical cell; the piezo-oscillator system for producing the vibration of the microelectrode; the signal processing system composed of two lock-in amplifiers that measure and filter the signal produced in the probe; the positioning system composed of tri-axial motors for precise movement and positioning of the vibrating probe; and the data management and control system composed of the computer, interface and display system. The electrochemical cell consists of the vibrating and fixed microelectrodes, the reference electrode, the sample and its electrolyte receptacle [520].

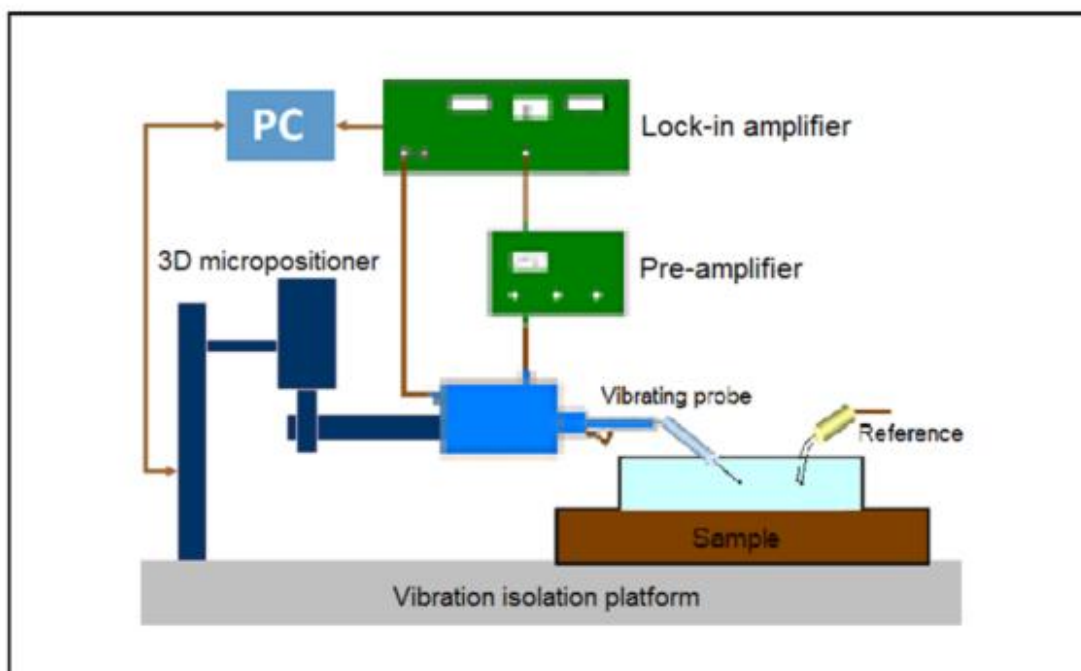


Fig. 3.7. Schematic representation of the basic components of a SVET equipment with the components of the electrochemical cell [Adapted from ref: 520].

The most critical part of SVET is the vibrating electrode which usually consists of a platinum microelectrode tip at the end of an insulated wire thinned down to a fine point [521]. The probe vibrates simultaneously in two orthogonal directions, but with a different vibration frequency in each direction [522]. The vibrations are produced either by excitation via a piezoelectric reed [523-528] or an electromagnet [529], the frequency and amplitude of the vibration both being independently adjustable. The vibration of the electrode tip within a potential field converts the DC field to an AC signal. By making the tip impedance more capacitive and tuning the vibration frequency to a suitably high and specific frequency, it becomes possible to filter out other frequencies using a lock-in amplifier, which being "locked" to the vibration frequency of the probe, filters out signals at any other frequency thereby reducing the background noise by many orders of magnitude to such negligible values that potential variations of the order of nanovolts can be measured [523,529,530]. The enhancement of sensitivity of the probe tip to make it more capacitive can be achieved by platinization to acquire a "spheric ball" of dark platinum at the tip. A "ball" with a capacitance of 2 nF is reported to be adequate [522,523]. More details of probe tip plating procedure and calibration can be seen in the report of Reid et al., [529]. SVET spatial resolution is jointly dependent on the diameter of the test electrode, vibration amplitude, and current density resolution which is mainly dependent on the probe's resistance [524-526].

In SVET measurements the vibrating probe actually measures the electrical potential gradient between the maximum and minimum position of a vibrating probe tip. The measured potential difference(s) in solution can be transferred to the ionic currents producing them either by a appropriate calibration or by employing Ohm's law. Calibration of the equipment is vital to obtaining reliable data as it enables the measured potentials to be converted into accurate current densities [523]. Employing Ohm's law the current density is calculated by relating the measured potential gradient to the electrical conductivity of the medium using equation (3.41) below [530-532] with prior knowledge of the solution conductivity.

$$i = kE = -k \frac{\Delta V}{\Delta r} \dots\dots\dots \text{(eqn. 3.41)}$$

where k is the electrolyte conductivity, E is the electric field between two points in the solution (i.e. the vibration amplitude), and Δr is the probe vibration amplitude, and ΔV is the potential difference between two points in the solution at a distance Δr apart.

Calibration involves generating a known current density near the probe in the electrolyte to be used in tests, measuring it and correlating the measured values from the probe to the expected current density. Generation of a known current density can be achieved by either passing a known current across two parallel plates or wires separated by a known distance, and calculating the current density (by dividing the current by the area between the plates), or by passing a known current through a point source for which the current density at a distance r from the source is given by equation (3.42) [532,533]:

$$i = \frac{I}{4\pi r^2} \dots\dots\dots \text{(eqn. 3.42)}$$

where i is the current density, I is the known current introduced through a point source, and r is the distance of the probe from the point source [529,530]. The calibration factor (CF) thus obtained is reportedly influenced by a number of parameters including, solution conductivity, height of probe above the surface, probe vibration amplitude, etc. [533,534].

3.6.2. Application of SVET to Corrosion Studies

Using SVET it is possible to measure currents in a solution with spatial and current density resolutions on the order of 15-20 μm and 5 nA cm⁻², respectively [523,524,529,535,536]. Such resolutions create the possibility of measuring very low corrosion currents emanating from individual local cell activity on a scale consistent with the size of microstructural features of many materials, thus enabling the probing at the micro-scale of localized corrosion phenomena such as pitting and crevice corrosion, and galvanic effects between constituents and interfaces in

composite materials [536-540]. It is possible to make SVET measurement on freely corroding sample or with some anodic/cathodic polarization [539,540]. SVET has been used in the study of localized [540-542], galvanic [542,543], and intercrystalline corrosion [544], stress corrosion cracking [545], corrosion inhibition [546], and also in studying the healing capabilities of functionalized self-healing coatings [547,548], detection of defects (inclusions) in coatings [549], and differentiation of the types of inclusions in coatings [550].

3.6.3. Use of SVET in Corrosion Inhibition Studies

In principle, it is possible to evaluate the inhibition efficiency of corrosion inhibitors by SVET in a variety of ways based on the method used to extract the currents with and without inhibitor. Bastos et al.,[551] proposed that these currents can be extracted from (a) the anodic peak maxima, (b) the cathodic peak maxima c, (c) by integration of anodic currents, (d) by integration of cathodic currents, and (e) by summation of the magnitudes of all detected electrode currents (both anodic and cathodic) and concluded from their results that the use of the anodic peak maxima, the cathodic peak maxima, and the integration of the cathodic activity yield better estimations of inhibitor efficiency. Using the summation of absolute values of cathodic and anodic ionic currents, the currents vital for estimating inhibition efficiency for samples in the presence of inhibitors from SVET data can be obtained using equation(3.43) [21,552-553] below :

$$i_{\text{int}} = \sum_{n=1}^N |i_n| \cdot S_n \dots\dots\dots \text{(eqn. 3.43)}$$

where i_n is the absolute value of SVET current density measured in point n (at 100 μm above the surface), S_n is the surface area (cm^2) corresponding to one data point and N is the number of data points considered for calculation. However, there exists a possibility of under estimation of inhibition efficiency when corrosion products are formed in the blank test solutions (without inhibitor) which are the baseline used in calculating inhibition efficiencies.

SVET data is usually presented as a map showing spatial distribution of current densities, which presented beside or superimposed over the area of sample from which the data was obtained gives an easy to comprehend perspective of corrosion activities on the microscale, and with time when data acquired at progressive time intervals are presented. Other ways of presenting SVET data include contour lines maps, contour colour maps, contour mesh maps, contour lines maps superimposed on sample image, vector maps, vector maps superimposed on sample image etc. [551-552].

3.7.0. pH Measurements (micro-potentiometry)

Electrochemical measurements of pH are basically potentiometric measurements in which the potential generated between a pH sensitive electrode and a reference electrode that is insensitive to pH changes is measured and on the basis of the Nernst equation correlated to the hydrogen ion activity.

The Nernst equation enables the correlation of the activity of a cation to the potential of its electrode. For the hydrogen cation the Nernst equation can be expressed thus:

$$E = E_o + \frac{2.303 RT}{F} * \log_{10}(a_{H^+}) \dots \dots \dots \text{(eqn. 3.48)}$$

where E is the electrode potential, E_o the standard electrode potential, R is the real gas constant = 8.314 J mol⁻¹ K⁻¹, F is the Faraday constant (96,487 C mol⁻¹), T is the temperature in the Kelvin scale, and α_{H+} is the activity of the hydrogen ion.

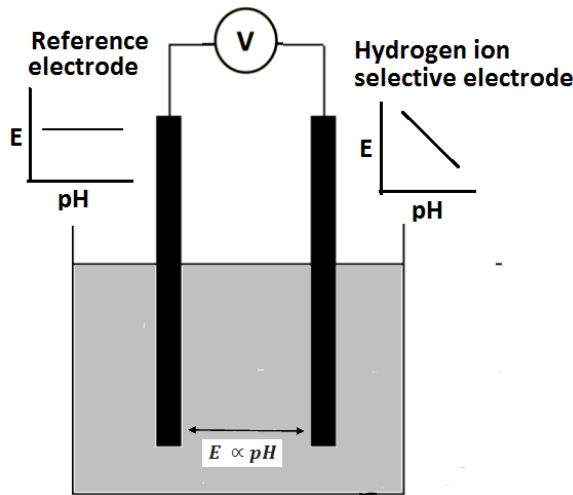


Fig. 3.8. Schematic illustration of the general principle of pH measurement.

An electrochemical system for pH measurement system is composed of a pH-sensitive electrode with a varying potential output with changing pH, a reference electrode that maintains a stable potential in the electrolyte irrespective of the changes in the activity of the hydrogen ion and consequently pH, and a high input impedance meter that enables measurement of the very small potential difference generated between the reference and measuring electrode (Fig. 3.8.). The output from a pH measurement is potential. To convert this potential to the corresponding pH value a prior calibration of the measuring system is necessary. This can be done by measuring solutions of known pH, above and below the range of pH to be determined to obtain a calibration curve relating measured potentials to pH, from which the potential measured in the solution of unknown pH is easily converted to pH values. In practice the two electrodes (the reference and pH measuring electrode) are usually combined as a single unit; the combination pH electrode. Since the hydrogen ion activity is affected by temperature it is necessary to

make temperature corrections when measurements are made at temperatures different from the standard or calibration temperatures.

3.7.1. Use of ion-selective micro-electrodes for local pH measurement

Microelectrodes are powerful analytical tools that can be employed to measure important parameters in microscale environments [518] such as pH, select ion concentrations (such as Zn^{2+} , Mg^{2+} , Na^+ , Ca^{2+}), and dissolved oxygen concentrations to get information on their spatial distribution, often times in and around features of interest [554,555]. The use of ultra-microelectrodes in this manner to create a map of spatial pH distributions have been referred to as scanning pH-microscopy [555-559], and applied in corrosion related research [547,556-557]. pH microelectrodes reported in literature include miniaturized glass electrodes [558-561], polymer coated graphite electrodes [561], and solid-state metal oxides microelectrodes [562-563].

3.7.2. Importance of local (micro) pH measurements in corrosion

Since pH exerts effects on corrosion rates [564-566], corrosion mechanisms [332,566-569], and corrosion inhibition [570] of metals in aqueous solution, access to information regarding the pH distribution/profile around a corroding metal is important to understanding corrosion mechanisms, and developing mitigation strategies. Furthermore, knowledge of the local pH around corroding metals is so important that its correlation with the potential of the metal as in the Pourbaix diagram enables the prediction of thermodynamically favoured species and corrosion possibilities such as active corrosion, immunity, and passivation. Consequently, in this work the pH profile across metal and CFRP samples and galvanically coupled materials were measured in a variety of scenarios.

3.7.3. Presentation of local pH measurements

pH data presentation is usually dependent on the mode of acquisition. For bulk or point pH measurements it is sufficient to indicate the measured pH value and the measurement temperature. For line-scans (1D micro-pH measurements along a line at a specific height from sample surface), the pH is usually presented as a profile of pH against distance. For area (2D scans in the XY-plane at a specific Z value or YZ-plane in a specified X value), data is usually presented as a contour diagram or coloured map, a presentation format that can be referred to as pH micrograph or pH microscopy image [556-559].

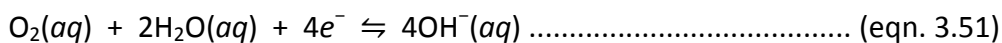
3.8. Oxygen Concentration Measurements (Micro-amperometry)

Oxygen acts as an accelerator of corrosion processes acting as a cathodic depolarizer [571-573] especially in actively corroding metals. The corrosion rate of steel in near neutral aqueous solution is reportedly dependent on the dissolved oxygen concentration at the steel surface [571]. Oxygen is found in concentrations of up to 8.26 ppm (i.e. 8.6 mgL⁻¹) in water at 25°C [573-577] with its concentration decreasing with increasing temperature [576-578]. The saturation solubility of oxygen in pure water under an oxygen pressure of 1 atm at 25°C has been reported to be 40.2 mg L⁻¹ (40.2 ppm). In aqueous electrolyte solutions (water containing salts), oxygen solubility was found to decrease with increase in the concentration of the electrolyte, but the effects of temperature and the oxygen partial pressure on oxygen solubility in the electrolyte solutions were reported to be very similar to those in pure water under same conditions [575-576]. Oxygen concentration in an aqueous media is dependent on temperature, depth, salt concentration, partial oxygen pressure, P_{O₂}, and the total pressure [574-579]. Bulk oxygen concentration in aqueous liquids are usually made with a dissolved oxygen meter, of which there are two main types; electrochemical oxygen sensors [573,579-581] based on current generated due to oxygen interaction with sensor electrodes, and optodes (optical sensors) [582-585] with its sensing ability based on the quenching of fluorescence by oxygen.

The knowledge of the micro-spatial distribution of the oxygen on and around a corroding system, and particularly a galvanic couple is vital to understanding of the mechanism of corrosion processes. Generally, oxygen is sensed in a liquid through the current generated by its reduction in the sensing device. In such devices the peak voltage position (or applied voltage) identifies the analyzed specie to be oxygen, while the magnitude of the current is correlated to the quantity of oxygen present. Macro oxygen sensors/electrodes permit bulk oxygen concentration measurements in aqueous media, but for evaluation of oxygen distribution at a micro-scale near corroding metal systems, a microelectrode capable of detecting oxygen with fidelity in the midst of many different species in solution is vital. For this purpose, a locally fabricated and validated [586,587] fluorinated boron doped diamond microelectrode was used for spatial oxygen concentration measurements.

In this work, the working electrode employed for oxygen sensing was a fluorinated boron doped diamond microelectrode. The the micro-amperometric detection of oxygen using this diamond microelectrode involved the application of a constant voltage sufficient to reduce the chemical specie of interest (dissolved O₂) but no other species in the system. This reduction yields a small but measureable current which being proportional to the

dissolved oxygen concentration in the test media (equation 3.51) becomes an indicator of the oxygen concentration.



By making measurements in test media with known dissolved oxygen content a calibration curve can be made from which current readings can be correlated to oxygen content. By making measurement point by point in a scanning pattern, the spatial oxygen distribution in the scanned area is obtained, while a line profile is obtainable by scanning along a line.

3.9 Raman Spectroscopy

Raman spectroscopy is an analytical technique that exploits the Raman effect; the inelastic scattering of monochromatic light due to changes in the frequency of photons on interaction with a sample that contain molecules with changing polarisability [588] to observe vibrational, rotational, and other low-frequency modes in a system [588-590]. It has emerged as an analytical technique of choice, employed in a variety of fields requiring non-destructive microscopic chemical analysis and imaging, due to its capability to identify chemical compounds by their chemical composition and structure, their functional groups, and the conformation of complex molecules, using samples in a variety of forms (solid, liquid, gas, gel, slurry or powder) and even with mixtures of compounds, and thus suitable for in-situ studies [590-591].

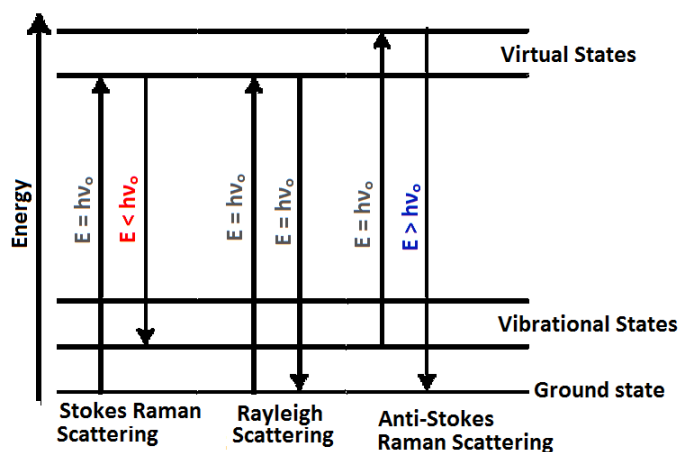


Fig. 3.9. The three different types of light scattering.

Light interacts with matter in a variety of ways creating different phenomena but in this section the focus will be on the scattering interactions of matter with light. Scattering is the change in the direction of incident light. Light being an electromagnetic wave interacts with the electrons of a compound via its electric vector resulting in scattering of the incident radiation. These interactions cause periodic vibrations in the electrons which having an electric charge

produce oscillating electric moments that emit radiation as scattered light [591-594]. The light thus scattered may either be elastically scattered having same frequency (and hence same wavelength) as the incident light and known as Rayleigh scattering, inelastically scattered with a lower frequency (and hence a longer wavelength) as the incident light which is consistent with a loss of energy and known as Stokes Raman scattering, or inelastically scattered with a higher frequency (and hence shorter wavelength) as the incident light, consistent with a gain in energy known as anti-Stokes Raman Scattering. The proportion of the incident photon scattered is very small, being about 1 in 10,000,000 incident photons undergoing stokes scattering [593-596]. As a consequence the scattered signal is generally very weak. Due to the higher intensity of Stokes inelastic scattering signals compared to anti-Stokes inelastic scattering only the Stokes scattering is mostly used in Raman spectroscopy.

3.9.1. Basic Principles of Raman Spectroscopy

The intensity of Raman scattered light is proportional to the fourth power of the scattering frequency, the square of the change in the molecules polarizability, and the square of the electric field of the incident radiation [594-596]. Hence small increases in the excitation laser frequency leads to huge enhancement in the scattered Raman signal.

$$i \propto \nu^4 \dots\dots\dots \text{(eqn. 3.52)}$$

where ν is the frequency of the exciting laser radiation and i the intensity of the scattered photons.

Since the Raman scattering intensity is proportional to both the laser power and the laser frequency, increase in either of these leads to increase in the intensity of the scattered Raman signal. To avoid sample damage an appropriate laser power which is dependent on sample properties such as absorption and thermal conductivity is needed. For instance switching from a laser excitation in the infrared region of 800 nm (frequency \approx 375 THz and $E \approx$ 1.55 eV) to one in the ultraviolet region of wavelength 400 nm (frequency \approx 750 THz and $E \approx$ 3.10 eV) leads to a 16 fold increase in the Raman signal. However, with many samples fluorescence is much increased with the use of the excitation laser signals in the ultraviolet and blue region of the spectrum while being much lower with excitations from the red or near-infrared region. Moreover, shorter excitation laser wavelengths gives higher lateral resolution (the shortest distinguishable distance between two points), equation (3.53):

$$\Delta x = 0.61 \times \frac{\lambda}{NA} \dots\dots\dots \text{(eqn. 3.53)}$$

where Δx is the lateral resolution i.e. the shortest distinguishable distance between two points, λ

the wavelength of the excitation laser, and NA the numerical aperture of the objective used which is dependent on the aperture angle and refractive index of the ambient media.

With very short wavelength (i.e. high photon energy) the likelihood of sample damage is increased while at very long wavelengths (i.e. lower photon energy) both the lateral resolution and the Raman efficiency is decreased as is the possibility of fluorescence [596]. Hence to acquire good Raman data an intelligent and informed compromise taking the above highlighted factors into cognisance is necessary to obtaining optimum performance.

In Raman spectroscopy, the incident photons (electromagnetic radiation) interact with molecules in the sample possessing polarizable electron density and bonds resulting in scattered photons of energy different from the incident radiation but very dependent on the chemical bonds and symmetry of molecules and thus can be employed as a molecular fingerprint for identifying and tracking any effects that can affect these (chemical bonds and molecular symmetry) such as; structural changes in a molecule due to chemical interactions/bonding e.g. adsorption of a molecule to a metal surface [597-603], the type of adsorption [599-600], and even the orientation of the adsorbed molecule(s) [601-603], presence of/or changes in the stresses and strains in a sample which can arise from mechanical or thermal effects (thermal expansion due to heating) [604-611], re-arrangement of molecules due to phase changes or transformations [609-612].

3.9.2. Confocal Raman Spectroscopy and Imaging

Confocal Raman spectroscopy is a novel high-resolution analytical technique arising from the fusion of confocal microscopy with its diffraction-limited resolution and Raman spectroscopy with its chemical sensitivity, that enables three-dimensional chemometric characterization of materials [613-616], with very high sensitivity, little or no sample preparation, and at ambient test conditions. Without a confocal arrangement no resolution along the optical axis can be achieved in optical microscopy, since light is collected equally from each plane in the sample [614-616]. In confocal microscopy, a point light source (usually a laser) is focused onto a spot on a sample while the image of this spot is detected through a small pinhole placed in the image plane of the microscope and in front of a suitable detector, so that light from areas around the spot are shielded from reaching the detector by the pinhole. Since the pinhole is located in the image plane of the microscope, the pinhole is confocal (common focus) with the illuminating spot, hence the name; confocal microscope/microscopy [613-616]. With this arrangement the observed signals are limited to only those emanating from a very small area being studied [615],

leading to very significant improvement in image quality at the expense of the observation area, as signals from the surrounding material are blocked. Thus with confocal microscopy only a small area of the sample is studied per time (good spatial resolution). The theoretical performance of a confocal Raman microscope is mainly dependent on the optical properties of the microscope objective (numerical aperture, magnification power, and focal length) and by the size of the pinhole placed in the back image plane of the microscope [615].

Since in confocal microscopy in a bid to improve image quality only a small area of the sample is examined (in focus at the image plane) at a time, it is necessary to scan the sample to acquire information from a significant sample area. Scanning can be achieved either by moving the light source across the sample or by moving the sample.

The potential for using Raman spectroscopy to monitor electrochemical reactions that are relevant to corrosion inhibition in-situ has been demonstrated [600,617]. Confocal Raman spectroscopy data can be presented in a variety of formats. For point analysis or single spectrums, it is normal to present it as a plot of Raman intensity against wavenumbers (cm^{-1}), often overlaid in a "water-fall" pattern if there are multiple spectra for comparison. For surface scans, the point by point acquired spectra are data-treated and usually presented as a map or maps showing the spatial distribution of intensities of peaks of interest which are often presented along with optical images of the scan area. In cases in which different phases are on the scanned area, relevant peaks of each phase are used to create a combined image of the phases present.

3.10. Glow Discharge Optical Emission Spectroscopy (GD-OES)

Glow discharge optical emission spectroscopy (GD-OES) is a very important technique for direct elemental analysis and depth profiling of bulk solids, surfaces, and coatings [618], with the capability of ppm level detection of virtually all the elements in the periodic table. Due to its high sputtering rates of more than $1 \mu\text{m min}^{-1}$, GD-OES has found much application in depth profiling analysis of relatively thick films [619-622]. Glow discharge optical emission spectroscopy has evolved from a hitherto depth profiling analysis tool for relatively thick films (in the tens of microns range) [623], to a powerful sub-nanometer analysis tool out-performing other surface analysis techniques like electron spectroscopy for chemical analysis (ESCA) [624], Auger Electron Spectroscopy (AES) [625,626], Rutherford back-scattering spectroscopy (RBS) [627,628], and Secondary Ion Mass Spectrometry (SIMS) [629,630] in different instances. Its advantages over other afore-mentioned surface analysis techniques arise from its ability to

deliver results in much shorter test times (seconds to a few minutes), with less matrix effects, on conducting and non-conducting samples (using a radio frequency source) without much surface preparation, and without a need for ultra-high vacuum through depths ranging from tens of microns to sub-nanometric dimensions [631,632]. Near atomic-scale depth resolution with rf-GD-OES has been reported by Shimizu et al., [632] in sub-nanometer depth profiling analysis of thiourea monolayer adsorbed on copper surface, thus potentially extending application of GD-OES to atomic level surface analysis of adsorbed molecules or monolayers.

Sample features like sample reflectivity has been reported to influence the sensitivity of the GD-OES technique [632]. Factors that can influence the depth resolution in the GD-OES depth profiling technique include sample roughness [633], argon pressure [634], and interfacial depth [635].

3.10.1 Working Principle of GD-OES

The working principle of GD-OES involves major mechanisms; plasma generation and material ablation by sputtering, excitation of sputtered species and their de-excitation by release of characteristic photons that are analyzed by the spectrometer to obtain elemental identification and quantification. In glow discharge, plasma is generated by the application of a potential difference (of the order of 1 kV) across two electrodes (a cathode which is usually the sample for analysis and an anode) in a cell filled with a gas at low pressure (e.g. 1 Torr) usually argon is used for analytical applications, though reactive gases like N_2 , O_2 , SiH_4 , SF_6 , etc. are frequently used for certain technological applications. The applied potential difference initiates plasma formation by "gas breakdown" as the gas is partially broken up into negatively charged electrons and positively charged ions etc. The actual composition of the species in the glow discharge can be complex but for an argon glow discharge for analytical purposes the most relevant species are electrons, argon atoms, singly charged positive argon ions, argon atoms excited to a variety of energy levels, including the metastable levels, and atoms and ions of the cathode material. The positively charged ions, under the applied potential difference are accelerated towards the cathode which they bombard releasing both secondary electrons and also atoms of the cathode material [636]. The atoms removed from the cathode (test sample) due to the bombardment of ions, enter the plasma, undergo collisions that cause the emission of characteristic photons that can be analyzed by an optical emission spectrometer for elemental identification and quantification, resulting in the surface analysis technique known as glow discharge optical emission spectroscopy (GD-OES). With a polychromatic spectrometer as

used in most commercial GD-OES equipment it is possible to simultaneously analyze the emitted photons for many elements (up to 47 with GD Profiler 2 for elements with characteristic photons between 110 and 800nm). The loss or erosion of material from the cathode due to ion bombardment is called sputtering. Using argon as the plasma gas and at typical operating parameters of 500-1500 V and 20-200 mA, the sputtering rate is reported to be in the range 10-100 nm s⁻¹; a high sputtering rate which in combination with a good time resolution (≤ 10 -ms integration times) permit fast analysis and profiling of surface layers ranging from a few nanometres to several tenths of micrometre in depth [637].

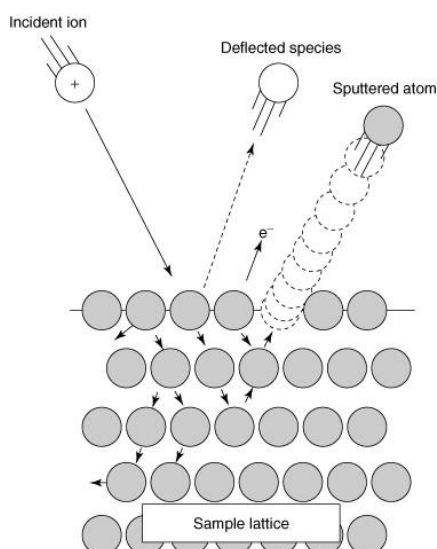


Fig. 3.10. Illustration of cathodic sputtering process in glow discharge [Adapted from ref: 638].

In glow discharge by progressive sputtering, material is released into the plasma from deeper layers in a material, thus elemental information at increasing depth is achieved to create a depth profile. For further details of the processes taking place in the plasma, analysis of possible scenarios, and the energies involved the review by Bogaert and Gijbels is recommended [636].

3.10.3. GD-OES in Corrosion and Corrosion Inhibition Studies

Since corrosion is a surface phenomenon information about the composition and changes in the composition of the surface layers on test samples is important to understanding corrosion mechanisms and development of appropriate mitigation strategies. The GD-OES surface analysis technique is vital to answering questions regarding compositions of the surfaces and interfaces, before and after metal interaction with aggressive media and inhibitors which is very useful in establishing mechanism. The main drawback of this surface analysis technique with particular respect to the thesis is that it provides elemental compositional profile of surfaces only without any molecular information.

3.11. Scanning Kelvin Probe Force Microscopy (SKPFM)

Scanning Kelvin Probe Force Microscopy (SKPFM) is a powerful technique that comes from the combination of atomic force microscopy and Kelvin probe technology and enables the acquisition of high-resolution maps of the surface potential distribution on conducting and non-conducting samples [638] based on the measured Volta potential differences. The SKPFM technique measures the Volta potential difference and changes in these differences instead of the Volta potential itself, by measuring values with respect to the cantilever tips as a reference or more accurately a pseudo-reference [639-641]. The Volta potential is defined as the work required to move a test charge from infinity (in vacuum, an inert gas, or a solution) to a point close to the surface at a distance far enough ($\approx 1 \mu\text{m}$) that chemical and image forces interactions with the surface are negligible [640]. In simpler terms the Volta potential has been defined as the minimum energy required to extract an electron from the metal surface to a point just outside the surface [642]. Volta potential is referred to also as the the outer potential, Volta potential difference, or contact potential difference.

The Volta potential difference (or contact potential difference (CPD)) between two materials is dependent on a variety of factors such as the work function, adsorption layers, oxide layers, dopant concentration in semiconductors, and temperature changes on the sample [643,644]. However, for clean surfaces bereft of surface contaminations, oxides, isolated charges, or condensed water films, the contact potential difference between two different materials is equivalent to the difference in their work functions [645]. Scanning Kelvin Probe Microscopy (SKPFM) permits the imaging of the surface electronic properties (the contact potential difference (CPD)) of a material with nanometric resolutions [646]. Initial reports on this technique demonstrated simultaneous imaging of both topography and contact potential difference with a high resolution for both the contact potential difference (better than 0.1 mV) and the lateral dimension ($< 50 \text{ nm}$) [645,647]. Jacobs et al. [638], concluded that the use of long and slender but slightly blunt tips on cantilevers of minimal width and surface area are beneficial for good resolution in potential maps. Recent reports indicate the application of SKPFM in imaging of surface potential distributions with sub-nanometer resolution [648-651]. Tanem et al, [652] have demonstrated with inclusions (MgSi, AlCuMgSi, and AlMnFeCuSi) in EN AW-6005 aluminium alloy that surface preparation techniques (ultramicrotomy, mechanical polishing, and electro-polishing) can affect the measured Volta potential, and recommended ultramicrotomy as the most reliable preparation technique among the studied techniques.

3.13.1. Basic Principles of Scanning Kelvin Probe Microscopy (SKPFM)

The potential at any charged interface can be divided into two components; the outer (or Volta potential), ψ , and the surface potential, χ , [653-655]. These two components are related to the Galvani potential, ϕ , which is the potential that is taken into account in equilibrium electrochemistry, by the relation [640];

$$\phi = \psi + \chi \dots\dots\dots (\text{eqn. 3.55})$$

where ϕ is the Galvani potential, ψ is the Volta potential, and χ is the surface potential.

From the relation above (equation 3.55), it obvious that the direct measurement of the Volta potential will require the unambiguous determination of the Galvani and surface potential, hence the easier practice of determining the Volta potential difference using the cantilever tip as a reference or pseudo-reference. The contact potential difference or Volta potential difference (V_{CPD}) between the tip and sample is defined as [656]:

$$V_{CPD} = \frac{\phi_{tip} - \phi_{sample}}{-e} \dots\dots\dots (\text{eqn. 3.56})$$

where ϕ_{tip} and ϕ_{sample} are the work functions of the tip and sample respectively, and e is the electronic charge.

Volta potential difference can be measured using either of two operational modes; the dual-pass mode and the single pass mode [657]. Measurement of Volta potential difference in Scanning Kelvin Probe Force Microscopy (SKPFM) using the dual pass mode is based on first employing the principles of atomic force microscopy (AFM) techniques to establish the topography of the sample by moving the cantilever tip in a tapping mode over the sample surface in a line. Next, using the acquired topographic information, the cantilever tip is maintained at a fixed distance (typically 50-100 nm) above the sample surface as it is moved over the sample surface in a "re-scan" of same topography, but this time an AC voltage is applied to the tip causing oscillations of the cantilever in resultant electric field. These oscillations are cancelled out (nulled) by the application of a DC voltage. The applied DC voltage that just balances the oscillations by nullifying them is equivalent to the Volta potential difference between the tip and the particular spot under the tip on the sample surface in absence of the bias but of opposite sign [656,657]. In most recent equipment the control software makes an inversion of the signal to output the appropriate polarity for the potential measurements. By making these measurement point by point as the tip moves the selected height above the pre-established topography the volta potential difference is established along a line and by repeating the whole sequence in closely packed lines, data for the Volta potential map of the scanned surface is obtained. It is necessary to note that the potential values thus

measured are obtained relative to the potential of the tip used; the tips functioning actually as pseudo-references, since their potential may be liable to change with changes in the surface oxide [658]. In the single-pass mode the electrostatic force interaction between the conducting probe and the sample is triggered by the application of an AC voltage at much lower frequency to the probe [557,659], with the measured electrostatic forces nullified with a DC voltage which gives a quantitative measure of the Volta potential difference [659]. Recent reports have claimed the achievement of higher resolution using the single-pass mode attributing this to closer proximity of the tip to the sample [659-663].

3.11.2. Importance and Application of Scanning Kelvin Probe Microscopy (SKPFM)

In certain applications (corrosion studies inclusive), the knowledge of the local electric potential distribution is of great importance as it helps in linking the structure and composition to observed function or activity [638]. Scanning Kelvin probe force microscopy (SKPFM) finds application in corrosion studies having been recognized as a powerful technique for the characterization of intermetallic compounds on alloy surfaces, tracking corrosion processes related with local inhomogeneities on passive surfaces with the capability of discriminating these features with respect to their shape, position, compositional heterogeneities and local potential values with submicrometer resolution [664-667], and validated for use in the prediction of local corrosion sites and the study of surface modification on electrodes during solution exposure [639]. In stainless steels, the Volta potential differences between phases measured have been correlated to their relative nobility and consequently their respective propensities to corrode on immersion in solution [642]. Furthermore, the volta potential has been demonstrated to be linearly correlated to the corrosion potential [668].

In this study SKPFM technique was employed to map at submicron-scales the Volta potential difference between carbon fibers and the epoxy matrix of the composite; carbon fiber reinforced plastic (CFRP) using a Digital Instruments Nanoscope III equipment.

CHAPTER 4

EXPERIMENTAL PROCEDURES

4.0. Experimental Procedures

In this chapter the particular materials used for this work and the exact experimental procedures employed in realization of the thesis objectives are presented starting with the specimens, their sources, and preparation, test media preparation, and then the experimental procedure employed for each test.

4.1. Specimens

High purity metals comprising aluminium, copper, iron and zinc of purity $\geq 99.9\%$ obtained from MaTeCK GmbH and Goodfellow UK were used in all the work the only exception being the work with chloroquine diphosphate as inhibitor in which carbon steel rods of $\varnothing 10$ mm (EN1A equivalent to EN 1.0718) used. The carbon fiber reinforced composite used was obtained in the form of 1 mm, 3 mm and 8 mm diameter solid pultruded cylindrical lengths from Modulor Material Total GmbH. This CFRP was made of carbon fibre Tenax HT 24 K with 65% fibre content, and epoxy vinyl matrix material. The tensile strength is 900 MPa, and modulus of elasticity $> 90,000$ MPa.

4.2. Specimen Preparation

For electrochemical tests, a working electrode was prepared by cutting cylindrical pieces of height 10 - 15 mm from the as-received cylindrical rods, ultrasonic cleaning in ethanol for 5-10 minutes, drying at ambient. Insulated conducting wire is attached to one of the flat ends of the cylindrical samples using a conductive silver-containing glue. After drying, the cylindrical surfaces of the samples were coated with a special varnish or wax. When the coating dries the samples were mounted in a polymeric resin (Epokwick) so that the other flat end is free of resin. After the resin is cured, samples were removed and polished with silicon carbide abrasive papers of grit sizes 220, 330, 400, 600, 800, 1200, and 2500. In between test sample surfaces were refreshed by progressively polishing with silicon carbide papers of grit size 400, 600, 800, 1200, and 2500 in that order.

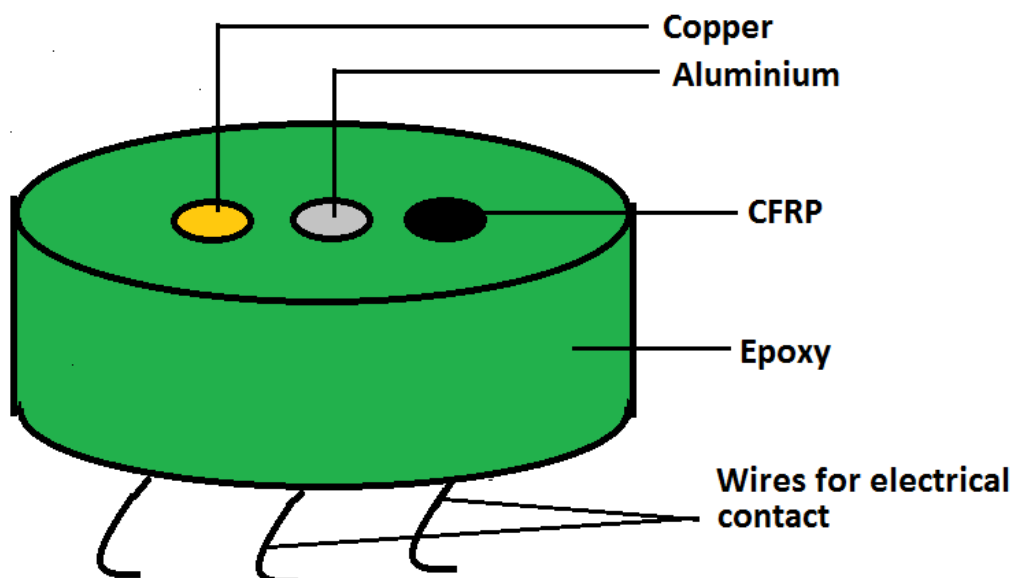


Fig. 4.1. Schematic illustration of epoxy mounted specimens for a galvanic triplet system.

For most micro-tests (such as SVET, local pH and dissolved oxygen measurements) electrodes of 1 mm diameter were used and assembled as shown in Fig 4.1 above, with a scotch tape wound around the cylindrical edges of the epoxy mounting to form a receptacle for the test electrolyte.

4.2. Reagents

Reagents were sourced from Sigma-Aldrich, of purity $\geq 98\%$ and were used without further purification.

4.3. Solution Preparation

Test solutions were prepared using Type 1 deionized water from a Millipore system (resistivity $> 18 \text{ M}\Omega\text{-cm}$) to make stock solutions of mostly 50 mM NaCl by adding 5.844 g of NaCl into a 2 litre flask and making it up with deionized water and stirring until fully dissolved. For test with HCl, stock solutions were made by diluting the as received 37% HCl with the appropriate quantity of deionized water to obtain the desired concentration.

4.4. Techniques and Equipments Used

Below is a concise description of the techniques used and the precise procedures employed in this work. All global electrochemical tests were carried out with Autolab PGSTAT302N potentiostat, using the 3-electrode method with a saturated calomel reference electrode and platinum wire as counter electrode. Galvanic (ZRA) measurements were made with Gamry PCI4 potentiostat/galvanostat.

4.4.1. Open Circuit Potential Measurement

Using the three electrode arrangement open circuit potential measurements were carried out on the metals/alloys that can form part of the multi-material systems in test solutions with and without inhibitors at 60 seconds interval immediately after immersion till 12 hours. Though simple, the results are capable of giving quick insights into the mechanism of action of selected inhibitors on the corrosion of particular materials.

4.4.2. Potentiodynamic Polarization

Potentiodynamic tests were done first from -1.6 to $0.8 V_{SCE}$ (full scans) with a step of $0.00244 V$ and a scan rate of $1 mV s^{-1}$ on samples after 60 minutes immersion in the test media, and then with $20 mV$ displacement from OCP to the cathodic ($-2.0 V_{SCE}$) and anodic ($-1.0 V_{SCE}$) potentials respectively for each concentration, using a new sample for each scan. Tafel fit parameters and polarization resistance were obtained by analyzing the polarization curves of the full scans using the General Purpose Electrochemical System software (GPES).

4.4.3. Cyclic Voltammetry

Cyclic voltammetry was much used in studies of CFRP in a bid to understand its electrochemical activity. Employing the well known ferricyanide/ferrocyanide redox couple, a cyclic voltammetry study of the electrode behaviour of CFRP in $0.1M KCl + 1mM K_4[Fe(CN)_6] + 1mM K_3[Fe(CN)_6]$ was done at different scan rates between $-0.2 V_{SCE}$ and $+0.5 V_{SCE}$, using a 3-electrode arrangement and a step size of $2 mV$. Additionally, repeated cyclic scans were made in $50mM NaCl$ over an enhanced potential window (-1.50 to $+1.50 V$).

4.4.4. Electrochemical Impedance Spectroscopy (EIS)

All EIS tests in this study were performed under potentiostatic control, in which a perturbing voltage of $10 mV$ rms vs. OCP is applied to a system and the resulting current is measured, and then the resulting impedance evaluated. For the electrochemical impedance spectroscopy, the set-up used for the polarization test was employed, using a single sine wave in the frequency range of $10 mHz$ to $100,000 Hz$ and in some instances down to $1 mHz$. Impedance measurements were taken with samples in the blank solutions (without inhibitor) and in the presence of inhibitors at different time intervals. The acquired spectra were fitted to equivalent circuits to determine the values of circuit elements. After normalization, values thus obtained are now used to obtain normalized values of circuit elements like resistances, impedances, capacitances etc, using the appropriate relations. The capacitance of the double layer was

calculated from impedance data (in systems presenting only one time constant and no diffusion effects) using the relation (eqn.4.1) proposed by Brug et al [669]:

$$C_{dl} = Y_o^n \cdot \left[\frac{1}{R_s} \right]^{\frac{n-1}{n}} \dots\dots\dots(\text{eqn. 4.1})$$

where Y_o is the fitted value of CPE element, R_s is the resistance in series with a CPE element (in the case of one time constant this was the solution resistance) and n the CPE exponent.

From the EIS spectra information on the evolution of low frequency impedance was extracted and presented graphically, while the and the evolution of polarization resistance (R_p), constant phase element CPE, low frequency impedance, and double layer capacitance were calculated from fitted EIS data and presented graphically.

4.2.5. Galvanic Current Measurement with Zero Resistance Ammeter (ZRA)

Galvanic current measurement were made using Gamry PCI4 potentiostat/galvanostat in the ZRA mode which permits simultaneous measurements of the current flowing between galvanically coupled metals and the potential across them with respect to a reference (SCE) in a three-electrode arrangement. The two metals are connected as working and counter electrodes respectively, and then a standard calomel electrode is connected as a reference electrode. Samples for galvanic current measurements were attached side by side so that the edge to edge distance between them was between 5 to 10 millimetres.

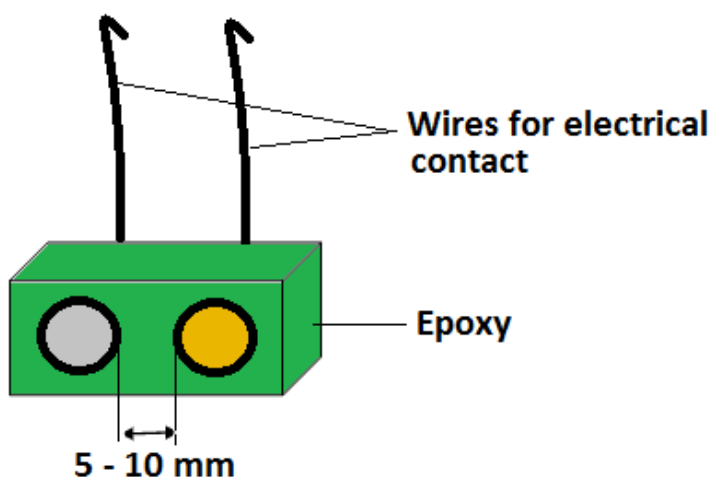


Fig. 4.2. Schematic illustration of arrangement of dual galvanic couples.

4.2.6. pH Measurements

pH values of bulk prepared test solutions were measured with Mettler Toledo Seven Multi pH meter. In the present work, local pH and the pH profile(s) above immersed metal and

galvanic couples were measured by electrochemical methods; specifically by (micro-) potentiometry using the procedure earlier reported by Bastos et al. [62] at a height of 40 microns above the surface of the immersed samples and along a straight line (for pH profile measurements). The procedure follows the principle of electrochemical pH measurement as illustrated in Fig. 3.18, except that the electrodes were miniaturized to micro-dimensions. It involved the use of an in-house fabricated "micro" Ag | AgCl reference electrode filled with 0.05M NaCl solution. The pH sensitive microelectrode was fabricated by pulling single-barrelled borosilicate glass capillaries with initial outer diameter of 1.5 mm (WPI, USA, Ref. TW150- 4) with a P97 micropipette puller (Sutter, USA) using a four step pulling protocol to obtain 2 μm tip diameter at one end. The micropipettes thus obtained were silanized for 2 hours in an oven at 200°C after injection of 200 mL of N,N-dimethyltrimethylsilylamine (Fluka, Ref. 41716). The micropipette was back-filled with an internal solution of 0.1 M KCl + 0.01 M KH_2PO_4 to a length of 5 mm from the tip and front-filled with a 20 - 30 mm column of hydrogen I cocktail B ionophore (Fluka, Ref. 95293). The filled micropipette is inserted into a half-cell plastic holder (WPI, USA, Ref. EHB1) containing a chloridised silver wire to obtain the pH measuring microelectrode assembly. The microelectrode thus fabricated were calibrated before and after measurements with commercial pH buffers (Riedel-de Haen), and a linear response in the pH range of 5 to 13 confirmed. The 3D positioning system used for SVET measurements, an IPA2 amplifier (input resistance $>10^{15} \Omega$) from Applicable Electronics Inc. and controlled by the ASET program was used to measure and record data.

Point pH measurements over immersed metal were made at 40 microns above the immersed metal or CFRP surface. For CFRP, point pH measurement was made over a 2 mm diameter CFRP rod immersed in 50 mM CFRP while simultaneously making a polarization scan from -1.5 V to 1.5 V_{SCE} at a scan rate of 1 mV s^{-1} and step size of 1 mV, and also as the potential is varied stepwise from cathodic to anodic (Figs. 5.6 and 5.7).

4.2.7. Oxygen Concentration Measurements/Mapping

Micro-spatial distribution of oxygen over coupled and uncoupled galvanic systems was performed using a novel locally fabricated fluorinated boron doped diamond microelectrode [586-687] in SPET (Scanning Polarized Electrode Technique) mode. The oxygen concentration was measured in the near surface at a height of $\approx 100 \mu\text{m}$ above two triple systems (Zn - Fe - CFRP and Al - Cu - CFRP) immersed in 50 mM NaCl in galvanically coupled and uncoupled configurations. Microamperometric measurements were performed with a boron

doped diamond microelectrode with surface modification by CF_4 plasma. The measurement scheme followed a back and forth step movement as shown in Fig. 4.3. using an IPA2 amplifier (Applicable Electronics Inc., USA) in the voltammetric/amperometric mode, a 2-electrode arrangement, with a Ag|AgCl electrode as counter and reference electrode. 2D X-Y scans were made using a microstepping motor driver (USDIGITAL, USA). The time parameters (waiting and averaging times) for the measurements are adjustable, but for these measurements a waiting and averaging time of 0.1 second each was used.

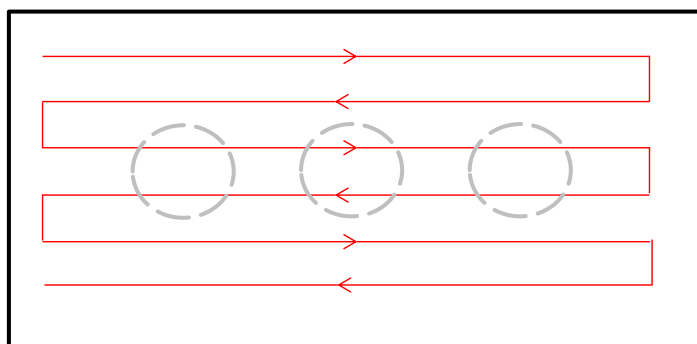


Fig. 4.3. Schematic illustration of the scanning sequence for dissolved oxygen spatial measurements.

The microelectrode polarization was adjusted between -1.0 and -1.3 V vs. Ag|AgCl, according to the limitations of each system. Examples of such limitations are the possible contamination of the electrode with ions like Zn^{2+} and Al^{3+} , if their concentration is too high. Systems containing these and pits were the most critical in terms of the risk of electrode contamination, due to the possibility of fast pit formation with attendant high acidity within the pit. Nevertheless, the behaviour of the microelectrode could be completely restored after a few voltammetric cycles when there was contamination, until the point that it was verified that by polarizing the microelectrode at -1 V, it was perfectly possible to visualize oxygen depletion over the active electrodes.

4.4.8. Scanning Vibrating Electrode Technique (SVET)

Localized electrochemical tests were done using a Scanning Vibrating Electrode Technique equipment manufactured by Applicable Electronics (USA) with a spherical probe tip of 20 μm , vibrating at 200 μm above the surface of the sample in-situ in the test media. Sample for SVET were mounted in epoxy, polished to mirror finish. Scotch-tape wound round the edges of the cylindrical epoxy mount formed a receptacle for the requisite test media. The probe was platinized in a plating solution consisting of platinum chloride (10% w/v H_2PtCl_6 in deionized H_2O) and lead acetate (1% w/v $(\text{C}_2\text{H}_3\text{O}_2)_2\text{Pb} \cdot 3\text{H}_2\text{O}$ in deionized H_2O).

4.4.9. Scanning Kelvin Probe Force Microscopy

Scanning Kelvin probe force microscopy (SKPFM) measurements were performed with a commercial AFM (Nanoscope Digital Instruments NanoScope III system) in the dual pass mode, in air to obtain Volta potential distribution maps over the composite; carbon fiber reinforced plastic (CFRP).

4.4.10. X-ray Fluorescence Spectroscopy and Mapping

X-ray fluorescence analysis and mapping of coupled and uncoupled samples before and after immersion in 50 mM NaCl with and without inhibitors was made with a Hitachi SEA6000VX x-ray fluorescence analyzer with capability of detecting elements from Mg (12) to U (92) with helium purging of the sample chamber. After test runs and optimization mapping of the Zn - Fe couple was done coupled and uncoupled, after 12 hours immersion in a mixture containing 2.5 mM cerium nitrate and 2.5mM benzotriazole in 50 mM NaCl. The test parameters used were; 40 kV voltage, 1000 μ A current with a collimator of size 0.2 x 0.2 mm and pixel size set at 50 μ m/pixel for a total acquisition time of 112.1 minutes.

4.4.11. Raman Spectroscopy and Mapping

Raman spectra of inhibitors as received was acquired using a Bruker RFS 100/S FT-Raman Spectrometer with YAG:Nd laser (1064 nm) excitation source, set to 350 mW laser power with a resolution of 4 cm^{-1} from wavenumbers 4000 to 50 (cm^{-1}) using between 500 to 1000 scans depending on the response from the sample. For confocal Raman measurements on CFRP and metals after immersion in inhibitor containing 50 mM NaCl a Witec alpha 300 Ras+ confocal Raman with a 532 nm laser was used. In some instances mapping of inhibitor interaction and adsorption on metal surface was done by selecting peaks of interest from earlier acquired Raman data.

4.4.12. Scanning Electron Microscopy

Scanning Electron Microscopy images were acquired using Hitachi S4100 scanning electron microscope with maximum accelerating voltage of 30 kV and resolution of 15 Å, and Hitachi SU-70 scanning electron microscope with resolution of 10 Å with EDS capability provided by a Bruker Quantax 400 EDS system.

4.4.13. Glow Discharge Optical Emission Spectroscopy (GD-OES)

Qualitative information on the composition of protective films and oxides formed on exposed sample surfaces were obtained using a Horiba Jobin Yvon GD-Profilier 2. The GD-Profilier 2 is an RF-GD-OES with a MARCUS GD-source and anode diameter of 4 mm and 13.56 MHz RF sputtering source with capabilities for analyses in non-pulsed or pulsed mode with a variety of duty cycle. The instrument is capable of over 40 simultaneous spectral measurements via a polychromator (110 - 620 nm) with 45 installed optical emission lines and an additional high resolution monochromator (160-500 nm). Measurement were made in rf- mode at a power of 10 W and argon pressure of 650 Pa. The following emission lines were used for identification of elements of interest; H: 122 nm, O: 130 nm, Cl: 135 nm, N: 149 nm, C: 166 nm, P: 178 nm, Cu: 325nm, Fe: 372 nm, Al: 396 nm, Ce: 413 nm, Zn: 481 nm, and Na: 590 nm. To monitor adsorption of organic inhibitors the nitrogen and carbon profiles were used as markers, while for inorganic inhibitors like phosphates and rare earths like cerium based inhibitors the phosphorus and cerium profiles were used as markers to trace precipitation on sample surface. For tests on blank solutions (containing Na, Cl, and H and O), the profiles of these 4 elements in addition to that of the metal was used to acquire insight on the nature and qualitative composition of corrosion products formed on metal surface under test conditions.

4.4.14. X-ray Diffraction

X-ray diffraction on corrosion products centrifuged from the test media and then dried to a thick paste and in some instances mechanically stripped from metal sample surfaces after immersion using a Rigaku Geigerflex X-ray Powder Diffractometer with Cu-K α radiation at a speed of 3°/min with steps of 0.2 ° from 10° to 80°.

CHAPTER 5

RESULTS OF TESTS ON INDIVIDUAL MATERIALS

5. Results of Tests on Individual Materials

Detailed results and the discussion of results obtained from tests carried out separately on each of the five materials (CFRP, aluminium, copper, iron (carbon steel), and zinc) used in this work are omitted in a bid to keep the thesis concise. Instead a compact and comparative preview of the electrochemical behaviour of the five materials in 50 mM NaCl solutions is presented and discussed in section 5.1. The rest of the chapter presents the electrochemical behaviour of the carbon fiber reinforced polymers (CFRP) under a variety of polarization, consequent changes in the local environment near the CFRP surface, and the effects of parameters (such as polarization, pH, presence inhibitors) on its response. The chapter ends with a summary of the information acquired from tests on the individual materials in section 5.3.

5.1. Results from General Tests on Single Materials

The results of general tests on the individual materials (aluminium, copper, iron, zinc, and carbon fiber reinforced plastic (CFRP)) in quiescent 50 mM NaCl solution without any inhibitors which includes open circuit potential measurements, potentiodynamic polarization test, and electrochemical impedance spectra are presented together in this section for easy appreciation and comparison of the different behaviours of these materials in similar tests and test conditions.

5.1.1. Open Circuit Potential Measurement Results

The results of the open circuit potential measurements on the four high purity metals and carbon fiber reinforced plastic (CFRP) used in this work and measured in quiescent test solution (50 mM NaCl) without inhibitors is presented in Fig. 5.1 below.

The open circuit potential measurements (Fig 5.1) for the five materials illustrates the very significant variation in open circuit potentials that ranges from -1.25 to 0 V_{SCE} at the beginning of the test to -1.1 to about 0.1 V_{SCE} after 10 hours immersion. The variations in their individual OCP values is the driving force for galvanic corrosion when any two or more of these materials are galvanically coupled.

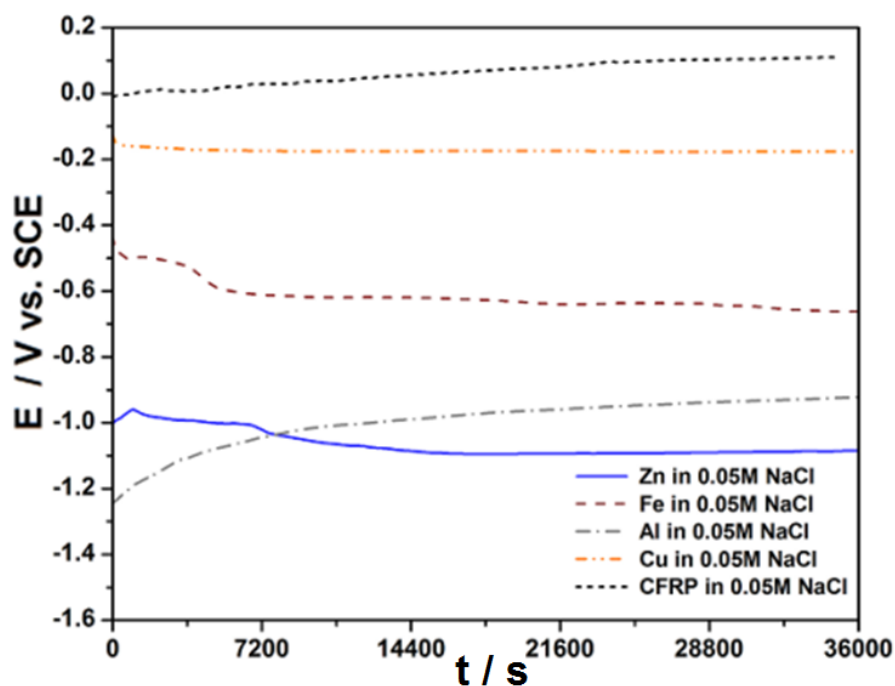


Fig. 5.1. Open circuit evolution for materials in 50 mM NaCl solution.

From this result the ranking of the materials from the most noble to the least during the first 2 hours of immersion is CFRP > Cu > Fe > Zn > Al, but changes after 2 hours immersion to CFRP > Cu > Fe > Al > Zn, due to a probable surface modification and ennoblement of aluminium with time and attack on zinc with time. Copper was stable all through the test duration but for CFRP a gradual shift of the OCP towards anodic potentials throughout the test duration was observed though the total change is very small; about 100 mV after 10 hours.

5.1.2. Potentiodynamic Polarization Results for 5 Test Materials

The potentiodynamic polarization curves for the four high purity metals and carbon fiber reinforced plastic (CFRP) used in this work were measured in quiescent test solution (50 mM NaCl) and are presented in Fig. 5.2 below. Unlike in OCP and EIS test without polarization, in which the test signals have insignificant effects on the corroding system, in potentiodynamic polarization tests the reactions taking place on the electrode surface are "forced" to proceed in a direction determined by the scan direction. Anodic scans promote oxidation while cathodic scans promote reduction processes. It is observed that the trend of open circuit potentials established with OCP measurements after 10 hours matched that obtained from the merged cathodic and anodic scans (Fig 5.2) while the trend observed at less than 2 hours immersion matched that obtained from cathodic to terminal anodic potential. From this observation, it is inferred that the potentiodynamic polarization curves of the respective materials presented in Fig. 5.2 are representative of their respective longer term corrosion behaviour.

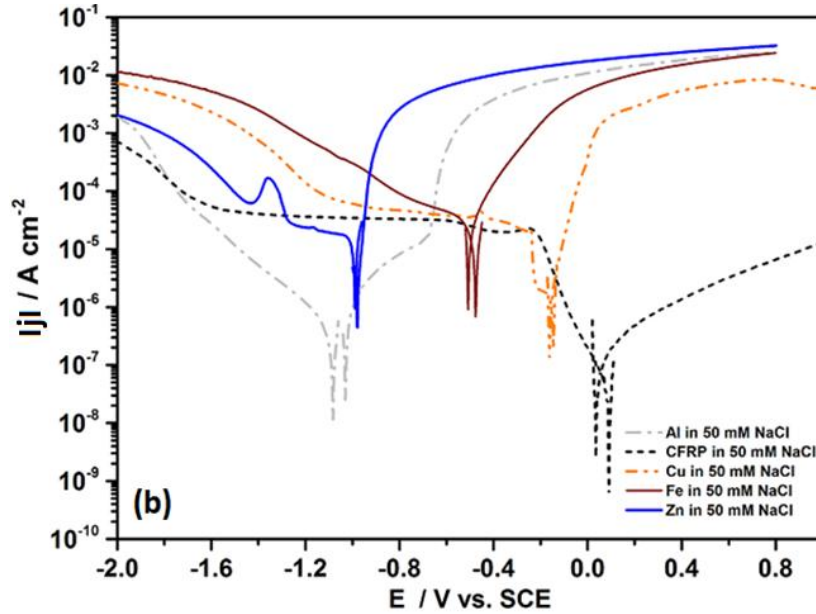


Fig. 5.2. Potentiodynamic polarization scan for five materials in 50 mM NaCl solution after 1 hour immersion (merged cathodic anodic scans 10 mV from OCP values).

A well-defined diffusion limited region is observed in the cathodic curves for copper and CFRP, with CFRP diffusion limited region extending to above $-1.4 V_{SCE}$ compared to about $-0.8 V_{SCE}$ for copper. The diffusion limited current density observed for CFRP and attributed to oxygen reduction is about $40 \mu A cm^{-2}$ and slightly higher for copper. The long range of the oxygen diffusion limited region (from about -0.2 to $> -1.4 V_{SCE}$) which incidentally falls in the range of the open circuit and corrosion potentials of aluminium, zinc and iron indicates; (a) that the main cathodic reaction on CFRP in near neutral chloride media is oxygen reduction, (b) that water-splitting reactions with hydrogen evolution is unlikely on CFRP at cathodic potentials less than $-1.4 V_{SCE}$, and (c) as a consequence galvanic corrosion of the aluminium, zinc, and iron coupled to CFRP will most likely be stifled in de-aerated near neutral solutions. A peak was observed on the cathodic curve for zinc irrespective of the scan sequence at around $\approx -1.4 V_{SCE}$, and attributed to the reduction of zinc oxide/hydroxide layer [670,671] most probably formed on the zinc surface during the 1 hour immersion period. Based on the observed limiting oxygen diffusion corrosion current density for CFRP in the test media of $\approx 40 \mu A cm^{-2}$, it is estimated that galvanic coupling of the CFRP to zinc, aluminium, and iron under the test condition will be equivalent to corrosion rates of about 0.599 , 0.436 , and $0.132 mm yr^{-1}$ respectively or mass loss rates of 11.708 , 3.223 and $2.85 gm^{-2} d^{-1}$ respectively, on the assumption that all the cathodic activity occurs on CFRP and discounting self-corrosion of the metals.

5.1.3. Electrochemical Impedance Spectroscopy Results for 5 Test Materials

The electrochemical impedance spectra for the four high purity metals and carbon fiber reinforced plastic (CFRP) used in this work and measured in quiescent test solution (50 mM NaCl) are presented in Fig. 5.3 below.

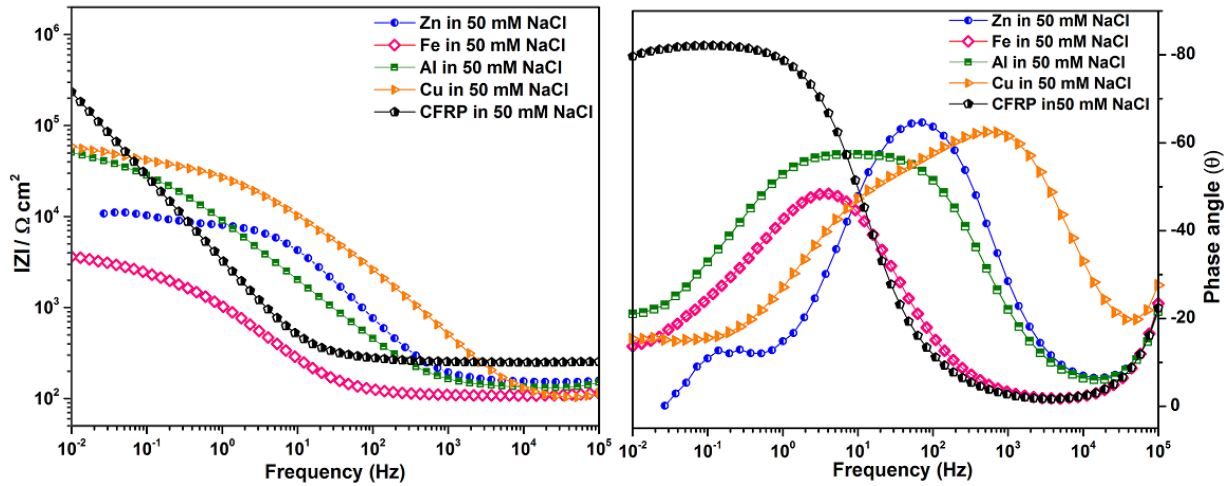


Fig. 5.3. Bode plots for the 5 materials after 1 hour immersion in 50 mM NaCl solution.

In the Bode plots above it can be observed from the impedance magnitude (|Z|) for CFRP is quite high at low frequencies and very capacitive. Furthermore, two well-defined time constants are observed for copper, aluminium and zinc, the time constant at mid-frequencies indicative of the barrier properties of corrosion product films formed on the metals. For copper the mid-frequency time constant manifests at higher frequencies while only iron displayed a single time constant suggesting that its corrosion product layer is either non-protective with very weak barrier properties or is formed much slowly under the test conditions.

5.2. Results of Tests on carbon fiber reinforced plastic (CFRP)

CFRP is unique in the ensemble of materials studied; being a non-metal and a composite material. As a consequence of this, and its reported ability to enhance anodic oxidation of galvanically coupled metals by supporting cathodic reactions, tests were carried out over a wide range of cathodic potentials covering the corrosion potentials of the metals employed in this study, and even at anodic potentials in near neutral (50 mM NaCl) and acidic (100 mM HCl) solutions. To monitor any dependence of its electrochemical and degradation behaviour on the bulk solution pH, tests were done in un-buffered 50 mM NaCl solutions adjusted to alkaline pH of 8, 9, 10.5 and 12 and buffered solutions of pH 8, 9, 10, and 12. Degradation of the CFRP under these test conditions were monitored through changes in the impedance magnitude (|Z|), changes in electrochemically active area by the capacitance, and changes in the chemistry of the

surface by the polarization resistance (R_p) or the charge transfer resistance (R_{ct}) (when a second time constant emerges) with respect to time and polarization respectively. Using localised techniques the local environment around CFRP in 50 mM NaCl as a function of polarization was monitored. Finally, the electrochemical behaviour of CFRP in the presence of a wide range of inhibitors was studied, and the results from all these tests presented herein.

5.2.1. Electrochemical and Chemical Characterization of Components of the CFRP Composites

The electrochemical and chemical behaviour of the carbon fibers and the epoxy matrix of the CFRP composite was characterized and found to be distinct using both scanning Kelvin force microscopy (SKPFM) and confocal Raman microscopy.

5.2.1.1. CFRP Characterization by Scanning Kelvin Probe Force Microscopy (SKPFM).

Scanning Kelvin Probe Force Microscopy (SKPFM) was employed to evaluate the electrical behaviour of the polished surface of the carbon fiber reinforced plastic (CFRP). The results are presented in Fig. 5.4 (b) below, confirming the manufacturer's claim of 6 μm diameter carbon fibers, and indicating differences in the Volta potential of the fiber and epoxy matrix in the CFRP.

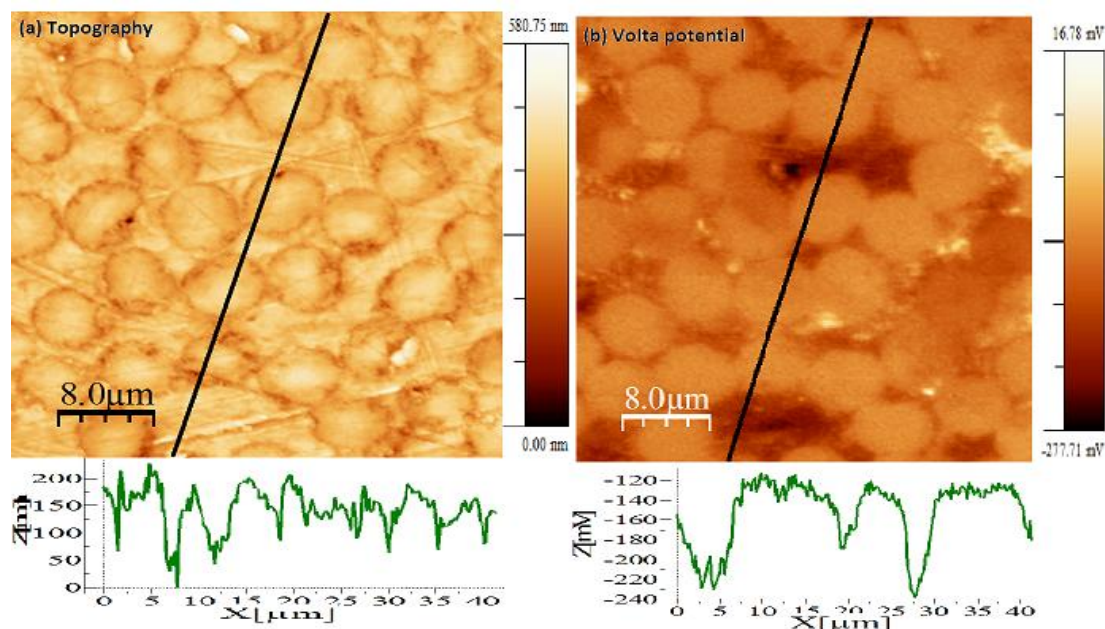


Fig. 5.4. SKPFM measured topography (a) and (b) Volta potential profiles for polished CFRP sample.

Hence the Volta potential measurements characterizes the epoxy matrix and the carbon fibers as two electrically different phases. The correlation between the Volta potential, the surface potential, χ , and the the Galvani potential, ψ , which is the potential that is taken into account in

equilibrium electrochemistry, had been illustrated earlier under the details of experimental techniques in Chapter 3 (eqn. 3.55) by the relation [640,653-655]. As a consequence of this relationship differences in measured volta potentials can be associated to differences in electrochemical properties, which would in turn have implications on electrochemical processes and inhibitor interaction with material surfaces. The topography image and profile Fig. 5.4(a) above, indicates that in the polished CFRP sample the carbon fibers are somewhat elevated above the epoxy matrix.

5.2.1.2. CFRP Characterization by Confocal Raman Spectroscopy/Microscopy.

Raman spectroscopy/microscopy is often employed in the characterization of composite materials as it can be very sensitive to differences in both the chemical composition of the individual components of the composite and also track changes in the chemistry of each of the individual components in the absence of over-lapping peaks. This ability enables the use of Raman spectroscopy in monitoring chemical degradation of both mono and multi-component systems due to either thermal, chemical or other environmental stimuli, which is vital in the present study. Hence this ability is exploited in this work in an attempt to monitor chemical changes to multi-component CFRP as a function of both exposure time and different test media and polarizations, which in combination with electrochemical test data gives a deeper perspective on the mechanism of CFRP degradation.

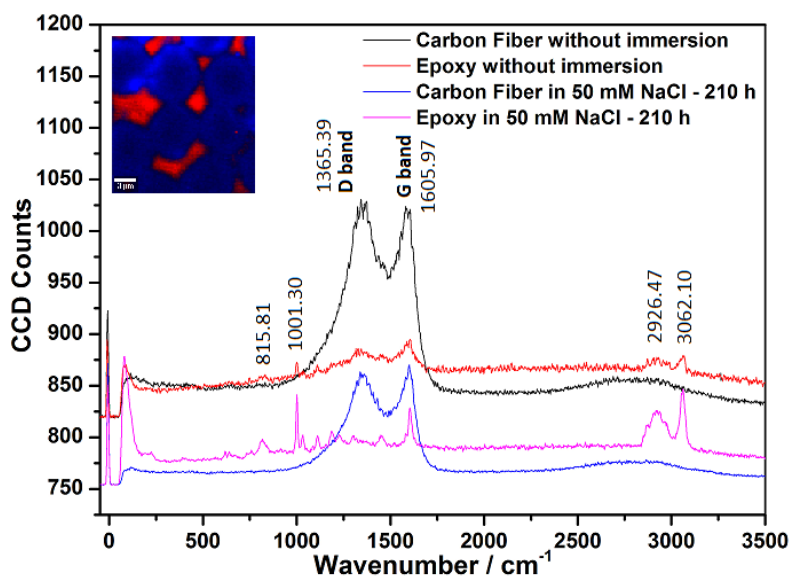


Fig 5.5. Confocal Raman spectra of components of CFRP (Inset is the combined image generated).

Chemical characterization of the carbon fiber reinforced polymer (CFRP) by confocal Raman microscopy confirms the presence of two chemically distinct phases (Fig. 5.5); the carbon fiber

characterized by its D-band (1365 cm^{-1}) and G-band (1606 cm^{-1}) and the epoxy matrix with prominent peaks at 3062 , 2926 , 1605 , 1001 , and 815 cm^{-1} . Mapping was achieved by using the carbon D-band around 1365 cm^{-1} for carbon fibers and the 3062 and 1001 cm^{-1} peaks for the epoxy matrix. The confocal Raman mapping of unexposed CFRP sample (inset in Fig. 5.5) shows carbon fibers (blue) of diameter $\approx 6\text{ }\mu\text{m}$ in the epoxy matrix (red).

5.2.2. Effect of Polarization on the local environment near CFRP in 50 mM NaCl

Since electrochemical testing of CFRP in the test media involves the application of a potential, knowledge of the effect of such polarization on the properties of the local environment such as pH, oxygen distribution, etc. is important. To monitor the effect of polarization on the local pH near CFRP, chrono-amperometric and potentiodynamic polarization tests were made with simultaneous measurement of the local pH, and the results are presented below.

5.2.2.1. Results of Step Chrono-amperometric Measurements and Potentiodynamic Polarization Scan on CFRP in 50 mM NaCl with Simultaneous Localized pH Measurements.

To monitor the pH changes in the local environment close to the CFRP surface, static measurements of the pH at a height $\approx 40\text{ }\mu\text{m}$ above the CFRP in quiescent 50 mM NaCl was made, in which the potential is progressively changed from cathodic to anodic values (-1000 , -750 , -500 , -250 , 0 , $+250$, and $+500\text{ mV}_{\text{SCE}}$) and held for about 300 seconds at each potential before the next potential change with concurrent measurement of the resultant current. This test is important as it yields information on the local pH very close to the CFRP surface as a function of polarization that will be helpful in analysis and understanding of subsequent test results particularly electrochemical impedance spectroscopy and tests on CFRP in the presence of inhibitors. The results (Fig. 5.6) indicate a marked and sustained increase in pH (> 9.5) above the CFRP surface at applied cathodic potentials greater than $-500\text{ mV}_{\text{SCE}}$, a drastic reduction in local pH at $-250\text{ mV}_{\text{SCE}}$ towards the bulk pH value (6.8) and slight acidification with local pH around 5.5 at 0 , $+250$ and $+500\text{ mV}_{\text{SCE}}$. These results indicate that at OCP ($-19\text{ mV}_{\text{SCE}}$) in 50 mM NaCl the local pH around uncoupled CFRP is similar to the bulk pH but undergoes a steep increase towards a pH of 10 as applied polarization tends towards $-1000\text{ mV}_{\text{SCE}}$. It is also observed that significant changes in the current density on application of potential is achieved at cathodic potential greater than $-250\text{ mV}_{\text{SCE}}$; having values $> 50\text{ }\mu\text{A cm}^{-2}$ at $-1000\text{ mV}_{\text{SCE}}$, $\approx 40\text{ }\mu\text{A}$

cm^{-2} at $-750 \text{ mV}_{\text{SCE}}$, and $\approx 13 \mu\text{A cm}^{-2}$ at $-500 \text{ mV}_{\text{SCE}}$, but tends towards $0 \mu\text{A cm}^{-2}$ at $-250, 0, +250,$ and $+500 \text{ mV}_{\text{SCE}}$. This coincidence of marked increase in pH with increase in cathodic current density at same potentials confirm that alkalization results from cathodic processes.

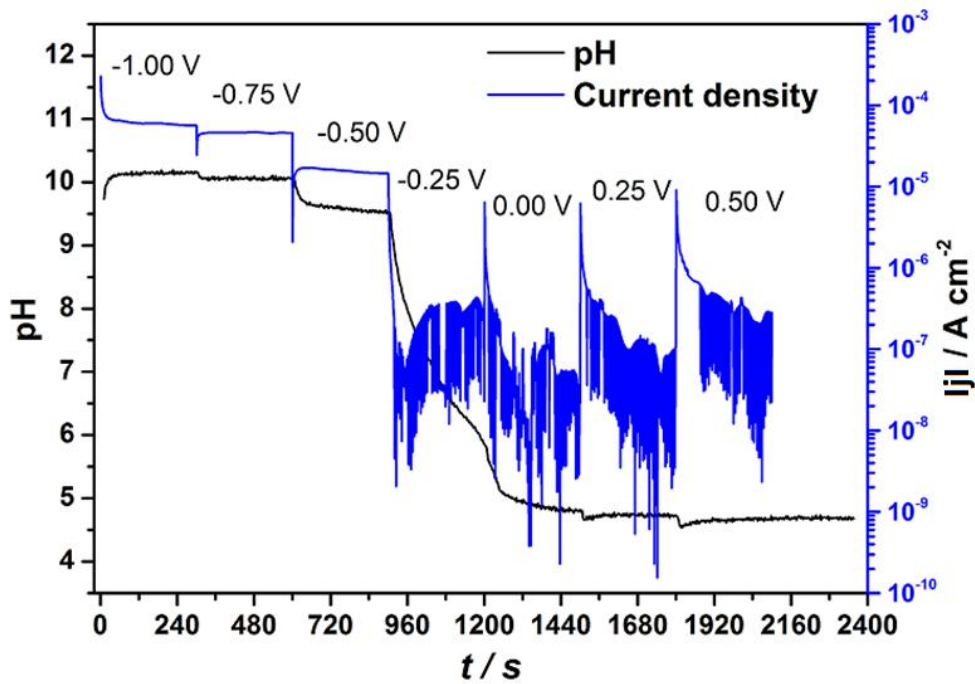


Fig. 5.6. Simultaneous chronoamperometric and local pH measurements on CFRP in 50 mM NaCl.

Further monitoring of the pH changes in the local environment close to the CFRP surface, was done by subjecting the CFRP to a potentiodynamic polarization test, ramping the applied voltage from cathodic to anodic potentials (-1.5 V to $+1.5 \text{ V}_{\text{SCE}}$) while simultaneously measuring the pH at a height $\approx 40 \mu\text{m}$ above the CFRP in quiescent 50 mM NaCl.

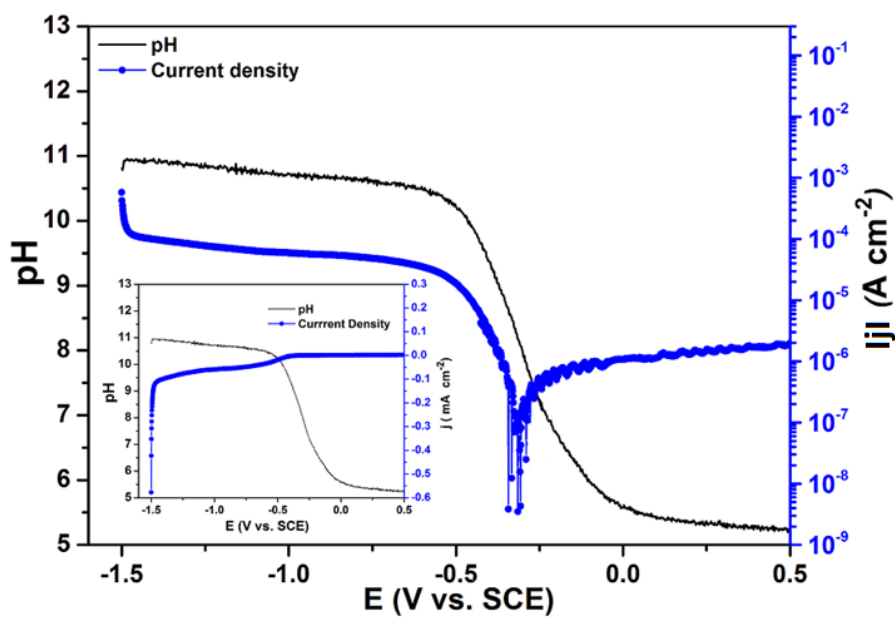


Fig. 5.7. Simultaneous potentiodynamic polarization and local pH measurements on CFRP in 50 mM NaCl.

Results of simultaneous potentiodynamic polarization measurements with localized pH measurements (Fig. 5.7.) show an instantaneous rise in the local pH to ≈ 11 from the bulk pH value of ≈ 6.8 at the commencement of the scan at a cathodic potential of $-1500 \text{ mV}_{\text{SCE}}$, a gradual decrease in local pH with decrease in applied cathodic potential to ≈ 10.5 at about $-500 \text{ mV}_{\text{SCE}}$ from which point the local pH drops sharply to around 8 at " E_{corr} " and then into the acidic range as the applied potential becomes anodic. This pH profile is comparable with that presented in Fig. 5.6 and together yield important information on the local pH values near the CFRP surface with respect to applied potentials that are vital in the choice of applied potentials and understanding of results from other tests. The slight difference in the local pH at the commencement of scan in Fig. 5.7 and the chronoamperometric test (Fig. 5.6) is attributed to the differences in the test procedures (starting potential and scan rate).

5.2.3. Effect of pH on carbon fiber reinforced plastic (CFRP)

Since the polarization of CFRP in the test media has been demonstrated above to significantly affect the local pH, knowledge of the effect of pH on the properties, degradation, and electrochemical response of CFRP is vital. The effect of pH was monitored using OCP measurements and electrochemical impedance spectroscopy, Raman spectroscopy imaging and scanning electron microscopy during and after immersion in solutions at varying bulk pH. The results of tests on effect of pH on the electrochemical behaviour and degradation of CFRP are presented below.

5.2.3.1. Effect of Bulk pH on OCP of CFRP in Chloride Solutions.

The time evolution of the open circuit potential (OCP) of CFRP in chloride solutions of varying pH is presented in Fig. 5.8 below, in which a sensitivity of the OCP to pH is observed. The OCP tends towards more cathodic values in alkaline pH and towards more anodic potentials with reduction in pH value. This observed decrease in OCP values with increase in pH might be indicative of probable Nernstian behaviour. Indeed the E-pH slope is not ideally Nernstian in all the pH range but the trend in generally is quite clear.

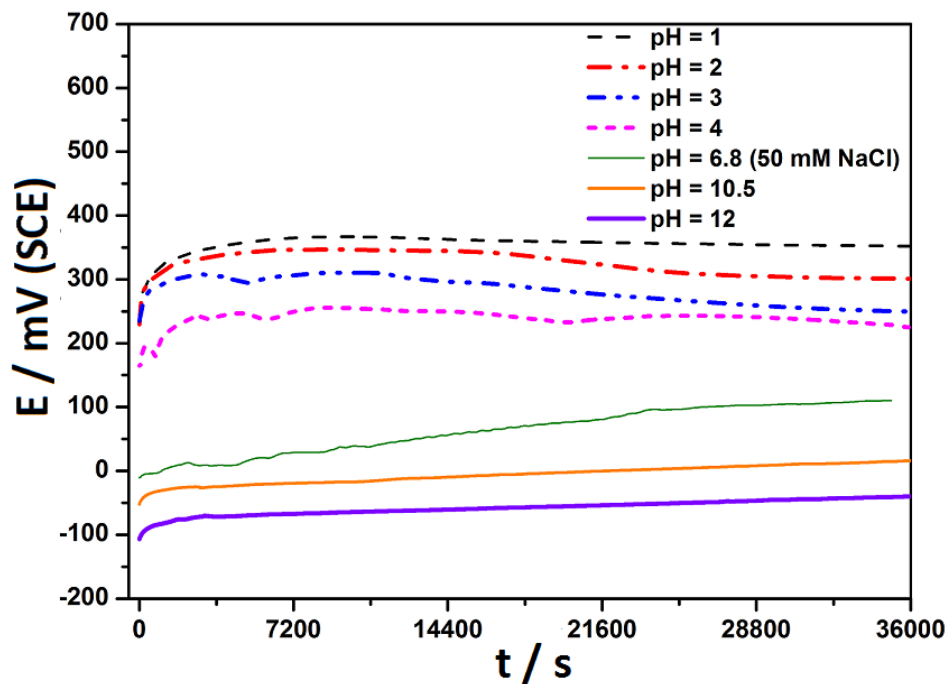


Fig. 5.8. Open circuit evolution for CFRP in chloride solutions of varying pH.

5.2.3.2. Effect of Bulk pH on the Cathodic Potentiodynamic Polarization Curve of CFRP in Chloride Solutions.

To study the effect of pH on the cathodic potentiodynamic polarization response of CFRP, potentiodynamic tests were carried out on CFRP after 1 hour immersion in unbuffered chloride solutions adjusted to pH 1, 3, 7, 10, and 12 respectively, at a scan rate of 1 mV s^{-1} starting at 20 mV anodic to OCP values, and the results presented in Fig. 5.9 below. From Fig. 5.9, it is observed that the cathodic polarization curves are marked by a Tafel region, a diffusion limited plateau region attributed to oxygen diffusion limitations, and at higher cathodic potentials, increased current densities, that have onset potentials that are more cathodic at neutral and alkaline pH. The onset of this increase in current densities is attributed to the onset of other cathodic processes such as hydrogen evolution reactions besides oxygen reduction. These potentiodynamic polarization curves show that CFRP in these test electrolyte display an "active" region between OCP and about $-200 \text{ mV}_{\text{SCE}}$ after which a diffusion limited region is observed with a current density of in the range of 30 to $40 \mu\text{A cm}^{-2}$. This value is important for processing galvanic current densities measured in galvanic couples involving CFRP, as it is the limit of expected galvanic current densities in such couples when galvanic corrosion is under diffusion control at the cathode. In addition the Tafel slopes are observed to be sensitive to the bulk solution pH, getting steeper with increasing pH. With respect to the hydrogen evolution reaction (HER), a steeper Tafel slope is indicative of enhanced kinetics while the reverse is true for oxygen reduction reaction (ORR). From these results, it is concluded that cathodic activities

on CFRP surface are more prominent at acidic pH due to the marked contribution from the hydrogen evolution reaction (HER), which appear to be much favoured in acidic media.

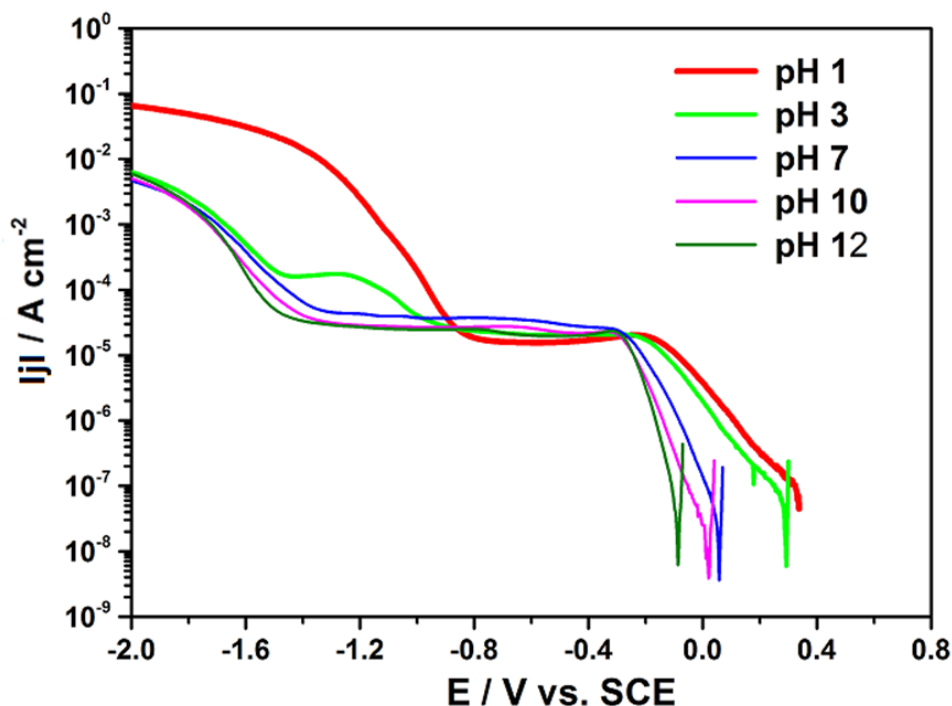


Fig. 5.9. Cathodic potentiodynamic polarization curves for CFRP in chloride solutions of varying pH at scan rate of 1 mV s^{-1} .

5.2.3.3. Effect of Bulk pH on the cyclic voltammetric response of CFRP in Chloride.

The results of cyclic voltammetric tests on CFRP in quiescent chloride solutions adjusted to pH 1, 3, 7, 10, and 12, over a potential range of -1000 to $+500 \text{ mV}_{\text{SCE}}$ at a scan rate of 50 mV s^{-1} is presented in Fig. 5.10 showing a significant and consistent cathodic peak around $-250 \text{ mV}_{\text{SCE}}$ under all test conditions employed. This cathodic peak is attributed to the 2-electron reduction of oxygen with formation of hydroxyl ions and hydrogen peroxide [672], and is consistently observed in EIS tests as a marked reduction in impedance at the observed polarization. The persistence of this cathodic peak over this wide pH range indicates that changes in bulk solution pH exerts insignificant deleterious effects on cathodic processes (the 2-electron reduction of oxygen with formation of hydroxyl ions and hydrogen peroxide) on the studied carbon fibre reinforced polymer (CFRP). From the comparison of the second scans at different pH (Fig. 5.10f), it is observed that the cathodic processes are most pronounced at pH 10, which incidentally is within the range of pH measured near CFRP sample coupled to aluminium in 50 mM NaCl solution (Fig. 6.5). These results indicate that the local pH around CFRP galvanically coupled to metals (Al and Zn) is at a pH range in which (oxygen reduction) cathodic processes are most pronounced on CFRP, and that unlike in metals cathodic processes

on CFRP are much less sensitive to changes in local pH. Consequently, it is concluded that control of bulk and/or local pH around CFRP is unlikely to be a viable option for mitigating cathodic processes on CFRP.

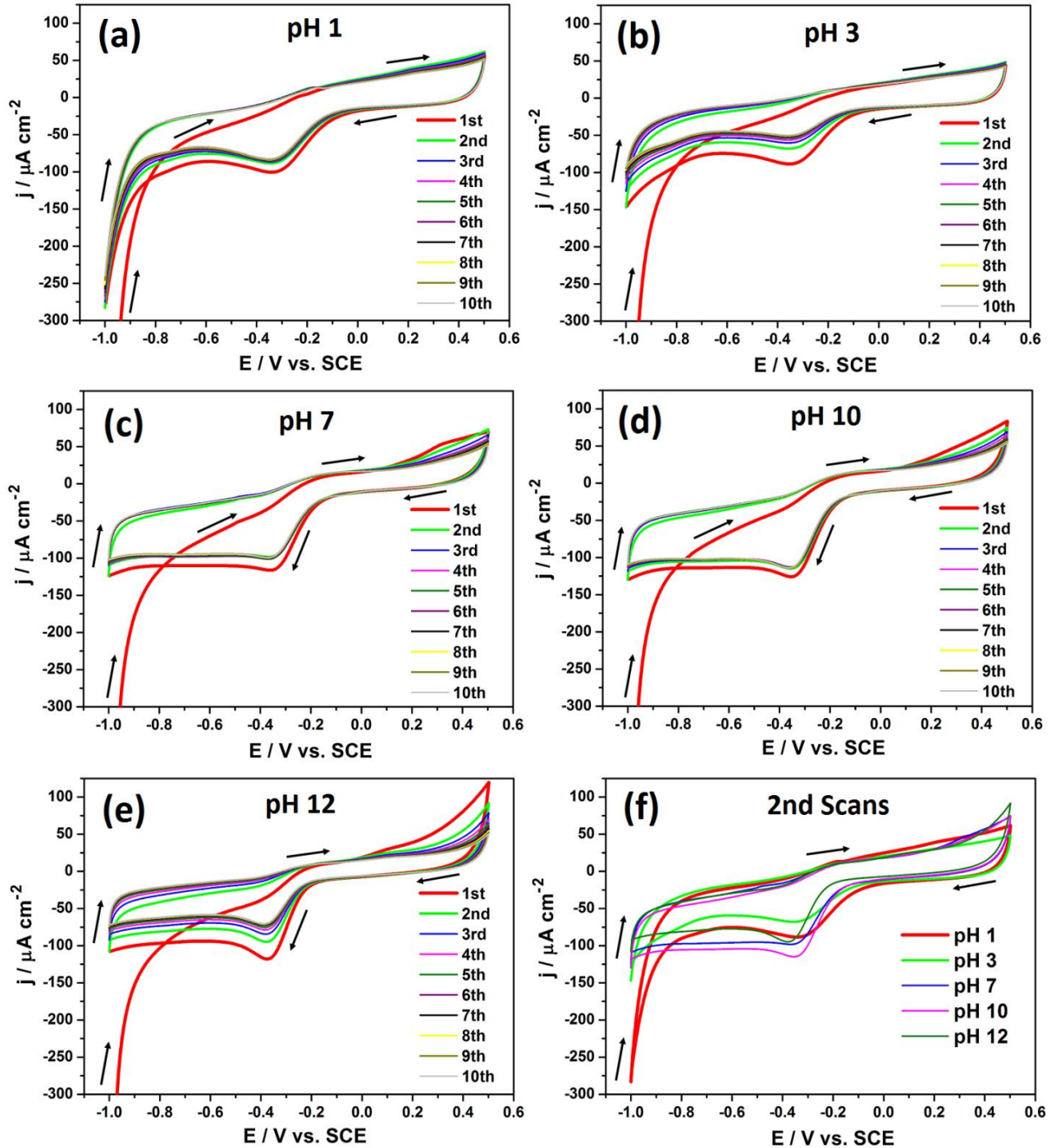


Fig. 5.10. Cyclic voltammogram of CFRP at a scan rate of 50 mV s^{-1} in chloride solutions at (a) 50 mM HCl at pH 1, at (b) 50 mM NaCl at pH 3, (c) 50 mM NaCl at pH 7, (d) 50 mM NaCl at pH 10, (e) 50 mM NaCl at pH 12, and (f) comparison of the second scans at different pH.

Cyclic voltammetric tests conducted over a wider potential range -1000 to $+1000 \text{ mV}_{\text{SCE}}$ to permit oxidative processes on CFRP surface Fig. 5.11 indicate that any changes effected on

CFRP surface by promoting oxidative processes in the studied anodic potential range (up to +1500 mV_{SCE} but CV up to +1000 mV_{SCE} shown) apparently do not have any significant effects on the 2-electron oxygen reduction process on CFRP surface.

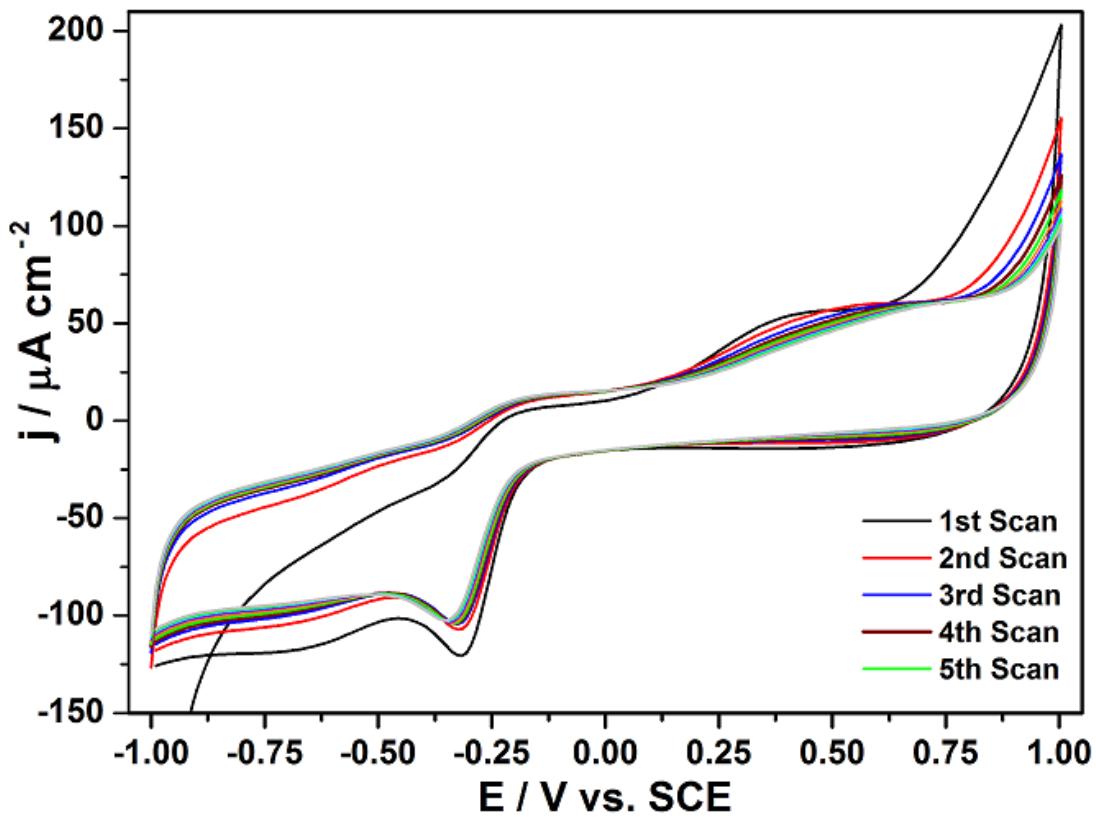
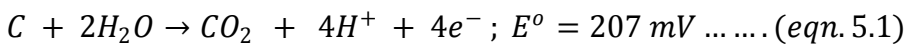


Fig.5.11. Cyclic voltammogram of CFRP in 50 mM NaCl at a scan rate of 50 mV s⁻¹.

The corrosion reaction of carbon material in aqueous acid electrolytes has been generalized to follow the scheme expressed in equation 5.1 below [280,673]; with dissolved oxygen postulated to apparently affect both the surface oxide coverage and carbon corrosion process(es) [673-675].



From equation 5.1, it is plausible that oxidation of carbon fibres of the CFRP is likely to result in local acidification due to the generation of protons. In spite of the plausible changes in the local pH and surface functional group composition on CFRP surface, the cathodic process(es) are largely insensitive to these changes even on increasing the scan potential range toward more anodic potentials (Fig. 5.11).

5.2.3.4. Evolution of CFRP Impedance Spectra during Immersion in 50 mM NaCl (pH ≈ 6.8).

In order to study the effect of possible changes in the local pH of the test solution (50 mM NaCl) on the impedance response of CFRP, electrochemical impedance spectra was first

acquired from CFRP samples immersed in the test blank solution (pH unadjusted); 50 mM NaCl of pH \approx 6.8. The electrochemical impedance spectra acquired in this and other sections of the work were normalized and fitted to equivalent circuit(s) illustrated in Fig. 5.12(a and b) below. The equivalent circuit of Fig. 5.12a was used to fit spectra manifesting only one time constant while that of Fig. 5.12b was used to fit impedance spectra presenting diffusion effects.

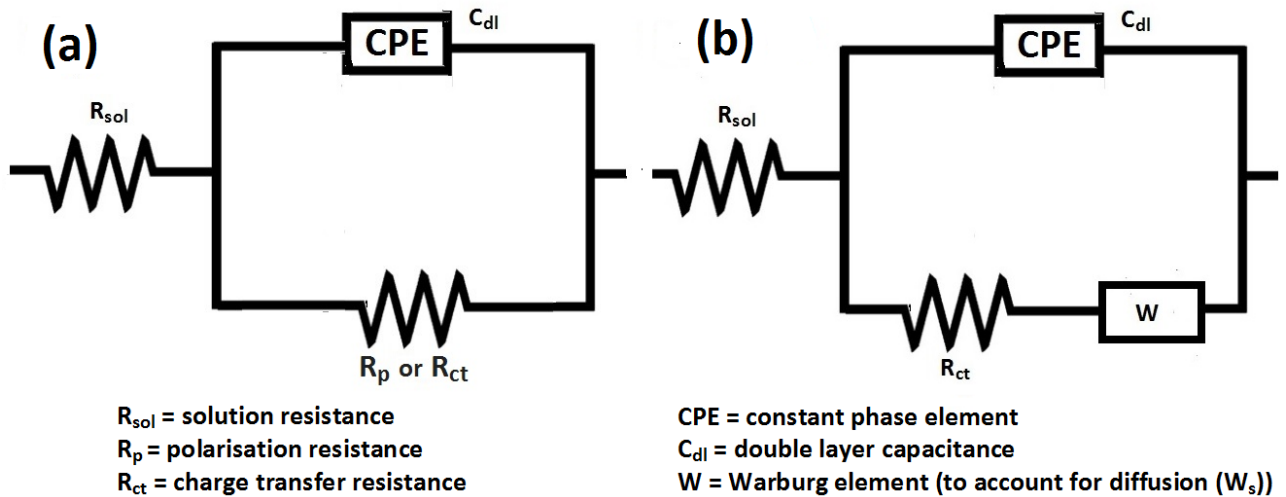


Fig. 5.12. Equivalent circuit used to fit impedance spectra

Fig. 5.13. below presents the Nyquist and Bode plots for tests on CFRP in quiescent 50 mM NaCl at OCP at immersion times ranging from 1 to 10 hours showing a marked capacitive one time constant electrochemical response. These impedance spectra were fitted to the equivalent circuit of Fig. 5.12 (a) comprising a capacitive element (CPE) which denotes the capacitance of the double layer, and parallel to a resistive element (R_p or R_{ct}) denoting the polarization resistance or the resistance to charge transfer across the CFRP-electrolyte interface, with both of these circuit elements in series with the electrolyte resistance (R_{sol}).

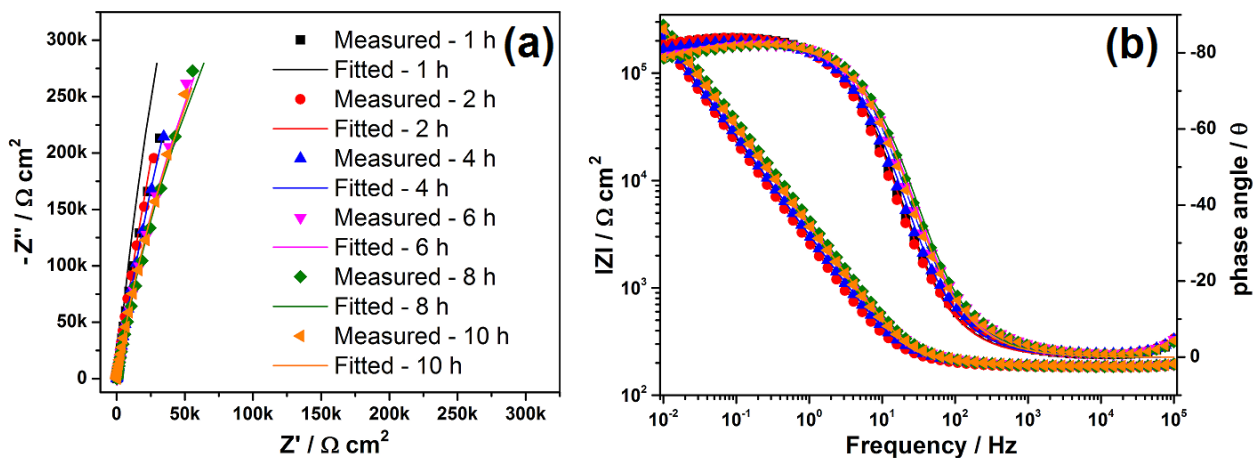


Fig. 5.13. Nyquist and Bode plots for CFRP at OCP after immersion in 50 mM NaCl solutions for different time durations (symbols are measured values and corresponding lines fitted values).

Fig. 5.14 below presents the time evolution of the measured low frequency impedance at 0.01 Hz and the extracted value of the fitted circuit elements (double layer capacitance (C_{dl}) and charge transfer resistance (R_{ct})) of the impedance spectra (Fig. 5.13) of CFRP in 50 mM NaCl at OCP using the equivalent circuit illustrated in Fig.5.12 (a) and Zview software. The indicated errors are fitting errors and have been observed to be consistently much higher for CFRP in uninhibited solutions during the first few hours of immersion reducing to more or less stable values after more than 6 hours immersion. The higher fitting errors during the first few hours of immersion is attributable to very high initial values of impedance measured for CFRP in which the error in the R_{ct} becomes high due to the greater uncertainty of the point at which the almost straight Nyquist curve would cross the X-axis.

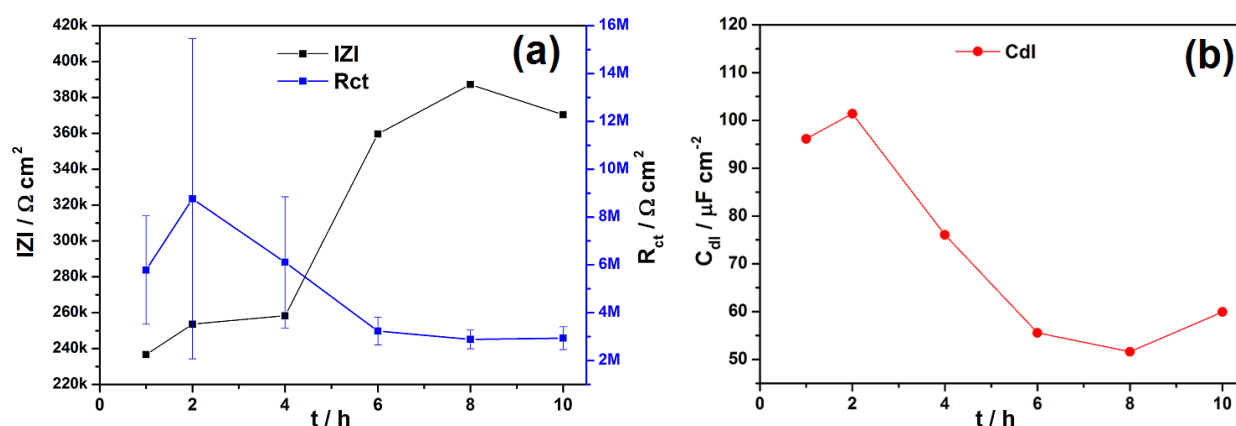


Fig. 5.14. Evolution of (a) low frequency impedance ($IZI_{0.01 \text{ Hz}}$) and charge transfer resistance (R_{ct}), and (b) double layer capacitance with time for CFRP immersed in 50 mM NaCl at OCP.

From the plots of measured (low frequency impedance) and fitted parameters (R_{ct} and C_{dl}) (Fig. 5.14), it is observed that the magnitude of the low frequency impedance is generally fairly stable, increasing slightly with time. The fact that the low frequency impedance does not decrease with immersion time in 50 mM NaCl at OCP indicates that significant changes in the electrochemical activity of the CFRP surface does not occur during the test time scale. The charge transfer resistance is observed to be relatively stable during the 10 hour period, and correlating changes in the charge transfer resistance to changes in surface chemistry this might be indicative of insignificant changes in the surface chemistry of the CFRP during the 10 hour duration in 50 mM NaCl solution without polarization. The double layer capacitance (Fig. 5.14) is observed to decrease markedly with immersion time. This general reduction of the double layer capacitance with time is inferred to result most probably from surface modification of the CFRP surface due to adsorption of species which can lead to either/both a reduction in electroactive surface area and increase in the interfacial "distance". Though this is the most

probable explanation for the observed general reduction of the double layer capacitance with time, however, cognisant of the fact that in this case the low frequency impedance is basically the reciprocal of the C_{dl} since the phase angle is very negative (close to -90°) so that the trend is that the low frequency impedance closely follows the trend for C_{dl} another possibility can be some surface modification, most probably evolution of the surface termination of the carbon fibers which is not likely to significantly affect R_{ct} values.

5.2.3.5. Effect of Bulk pH on Impedance Spectra of CFRP in Unbuffered Chloride Solutions.

Having established the electrochemical impedance response of CFRP in the absence of polarization in the blank solution (50 mM NaCl of $pH \approx 6.8$) in the preceding sub-section, the impedance response in unbuffered chloride media of different pH (1, 10.5, and 12) were evaluated and compared with that measured in 50 mM NaCl at OCP. The measured impedance spectra in unbuffered chloride solutions at these different pH values after 2 hours immersion are presented in Fig. 5.15 below.

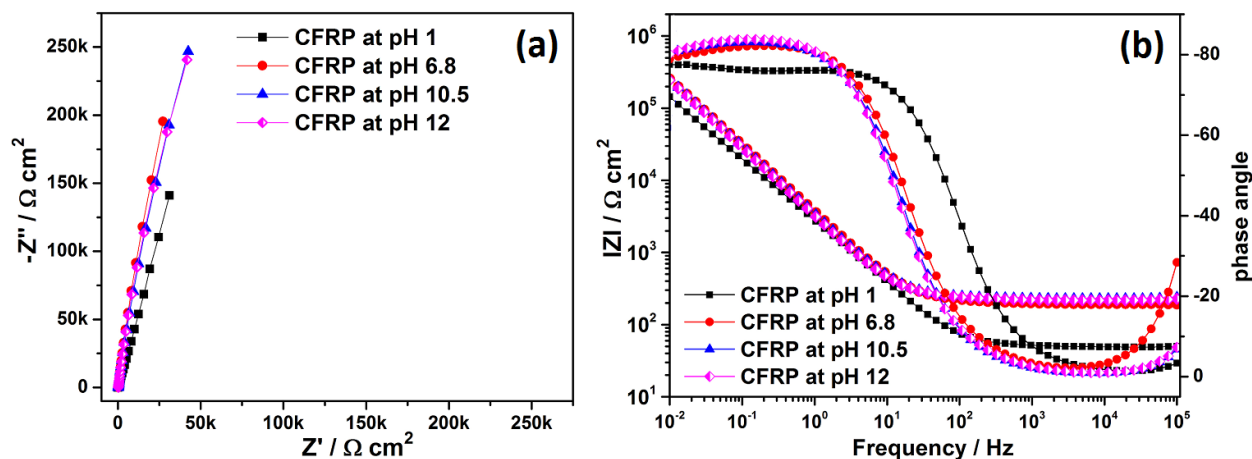


Fig. 5.15. Nyquist and Bode plots for CFRP at open circuit potential in un-buffered chloride solutions at different pH after 2 hours of immersion.

By fitting the impedance spectra above (Fig. 5.15) of CFRP in un-buffered chloride solutions at different pH after 2 hours of immersion to the one time constant equivalent circuit (Fig. 5.12a), parameters such as low frequency impedance ($|Z|_{0.01 \text{ Hz}}$), charge transfer resistance (R_{ct}), double layer capacitance were evaluated and presented in in Fig. 5.16 below as functions of pH.

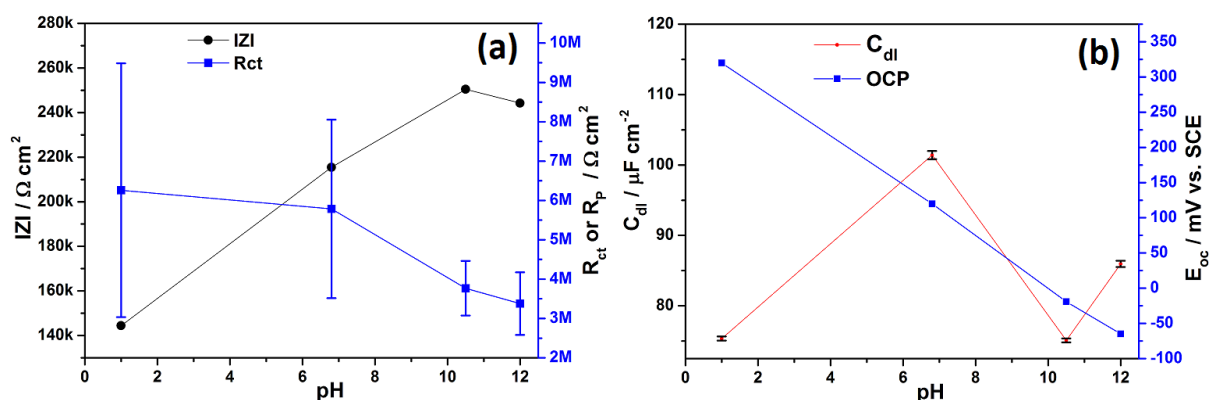


Fig. 5.16. Evolution of (a) low frequency impedance ($IZI_{0.01 \text{ Hz}}$) and charge transfer resistance (R_{ct}), and (b) double layer capacitance and open circuit potential with pH for CFRP immersed in un-buffered chloride solutions after 2 hours of immersion.

From Fig. 5.16(a) a gradual decrease in the charge transfer resistance with increasing pH is observed while the low frequency impedance increasing with increasing pH up to pH of 10.5 above which it slightly drops. Diminution in the low frequency impedance above 10.5 in tandem with reduction in capacitance is understandably because both are directly linked, since at this frequency the impedance value is dominated by the imaginary part which reflects capacitance. However by comparing the evolution of this trend as a function of pH enhanced general degradation of the CFRP at $\text{pH} > 10.5$ and/or significant changes in the surface functional group composition and coverage is suggested to possibly account for values observed at $\text{pH} \geq 10.5$. Fig. 5.16(b) reveals that the double layer capacitance is highest at a $\text{pH} \approx 6.8$ (in 50 mM NaCl solution), and a linear response of the CFRP open circuit potential to solution pH in the pH range 1 to 12 in unbuffered chloride solutions.

Having established the impedance response of CFRP in unbuffered chloride solution over a wide range of pH in the absence of polarization, and taking cognisance of earlier findings that local pH is prone to change on introduction of polarization, electrochemical impedance spectroscopy test were made on CFRP in 50 mM NaCl solution after longer term exposure (20 and 120 hours) to alkaline buffer solution of pH 8, 9, 10, and 12 respectively. The aim of these tests in pH buffered solutions was to observe the impedance response of CFRP in bulk (buffered) solutions in which the local pH near CFRP is less likely to change due to the buffering effect in order to use this as a baseline in discriminating electrochemical response due to local pH changes near CFRP surface from those due to impressed cathodic polarization (as can be seen in upcoming sub sections of this work). The impedance spectra obtained from these tests are presented in Fig. 5.17 and the parameters extracted after fitting are presented in Figs. 5.18 and 5.19 respectively below.

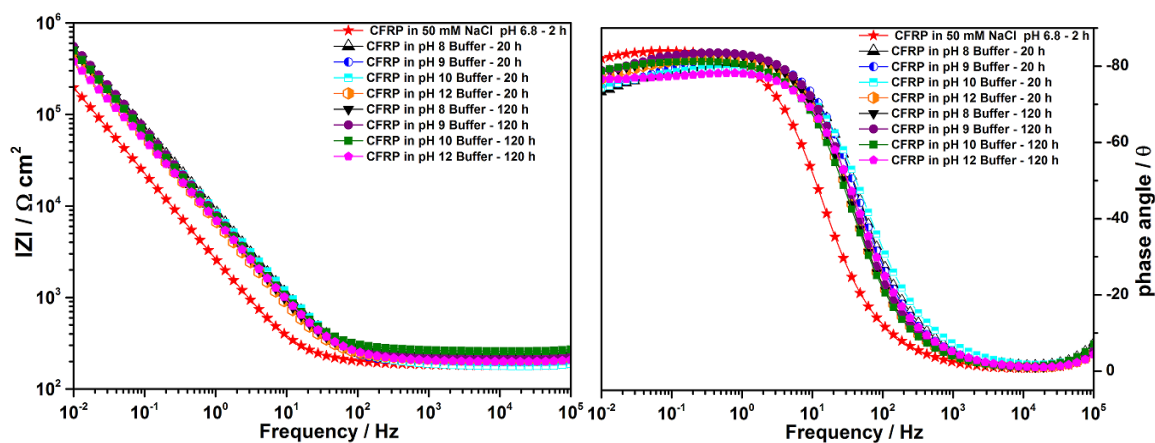


Fig. 5.17. Bode plots for CFRP after immersion in buffer solutions for 20 and 120 hours and then tested after 2 hours immersion in 50 mM NaCl solution.

The Bode plot above (Fig. 5.17) reveals a marked reduction in capacitance after long term exposure to alkaline buffer solutions in comparison to the reference spectra (in red of CFRP immersed for only 2 hours in 50 mM NaCl). Generally, such decrease in capacitance can be mainly accounted for by either a reduction in electrochemically active surface area, an increase in the interfacial distance (due for instance to adsorption of species onto the CFRP surface), or changes in surface termination. The analysis of the evolution of measured and fitted impedance parameters (low frequency impedance at 0.01 Hz ($IZI_{0.01 \text{ Hz}}$), double layer capacitance (C_{dl}), and charge transfer resistance (R_{ct})) presented in Figs. 5.18 and 5.19 below yields further information.

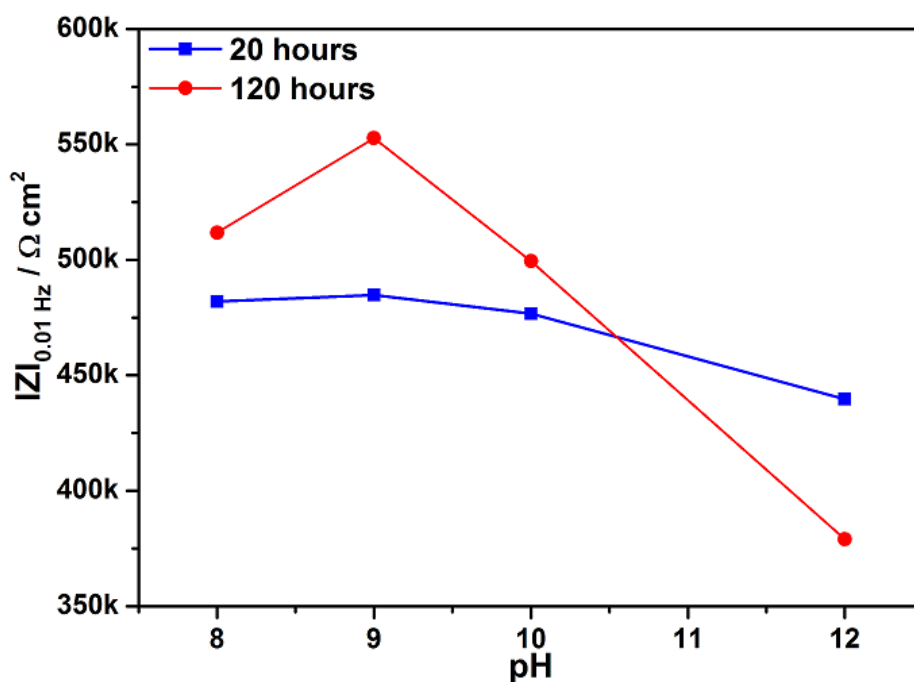


Fig. 5.18. Evolution of low frequency impedance ($IZI_{0.01 \text{ Hz}}$) with pH of buffer solutions after 20 and 120 hours immersion.

Fig. 5.18 above presents the evolution of low frequency impedance ($|Z|_{0.01 \text{ Hz}}$) with respect to the pH of buffer solutions after 20 and 120 hours immersion respectively in which similar trend of decreasing low frequency impedance with increase in pH from pH 9 for both exposure times. Considering the evolution of the low frequency impedance values with pH in the highly capacitive impedance values at 0.01 Hz in which the imaginary component predominates, reduction in low frequency impedance at pH values ≥ 9 is most likely to be linked to processes that significantly affect the capacitance at higher pH values. A clearer insight into these processes is only possible by the fitting and analysis of fitted impedance spectra parameters presented in Fig. 5.19 below.

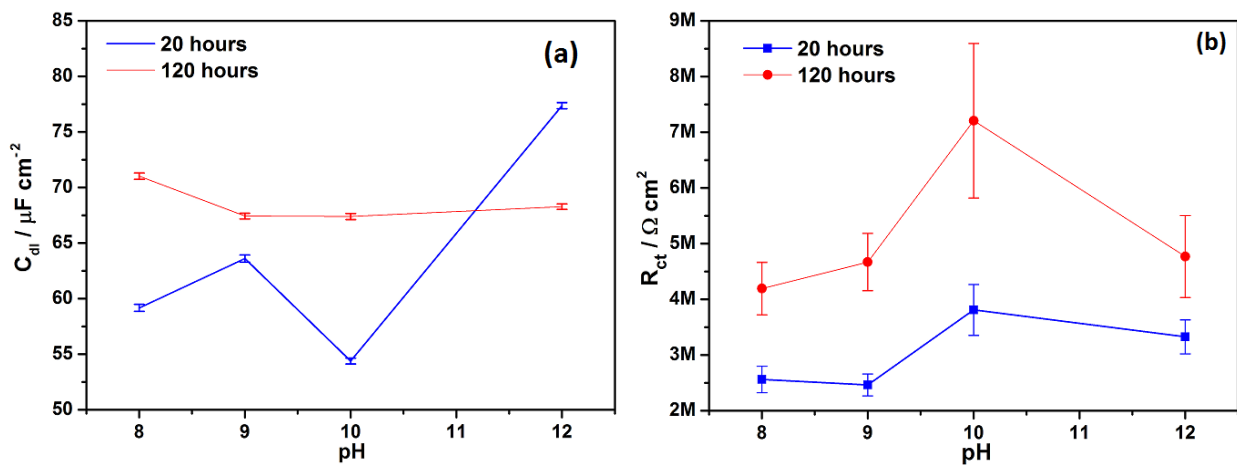


Fig. 5.19. Evolution of (a) double layer capacitance and (b) charge transfer resistance for CFRP as a function of pH of buffer solution at different exposure times.

In Fig. 5.19(a) above, the trend of the double layer capacitance observed in buffered solution is found to differ significantly from the trend observed in unbuffered chloride solutions (Fig. 5.16) with calculated capacitances generally much lower in buffered solutions. Cognisance should be taken of the fact that whereas the data obtained from tests in unbuffered chloride media, presented herein were taken after 2 hours immersion while those in buffered solutions were taken after 20 and 120 hours immersion. The idea was to use the short immersion time test data in un-buffered test media (with similar pH but apparently much less potential for degradative effects) as a baseline for longer term tests in buffered alkaline media as degradation of CFRP had been linked to the presence of OH^- ions. These differences are probably due to the interaction of the constituents of the buffer solution with the CFRP surface. From Fig. 5.19(b) above, it is observed that at pH values between 8 and 10, increase in immersion time yields an increase in the charge transfer resistance that peaks at pH 10, but appears to decrease with further increase in pH. Furthermore, a marked increase is observed in the charge transfer resistances measured between pH 9 and 10. Comparing the slopes for these

increases in charge transfer resistance after both 20 hours and 120 hours of immersion, a steeper slope is observed from data acquired after 120 hours immersion suggesting possible effects of immersion time on the kinetics of the process. Correlating the charge transfer resistance (R_{ct}) to changes in the surface chemistry of the CFRP, it is inferred that trends observed from this result might be indicative of some form of surface modification process that is apparently slow at pH 8 to 9, but faster between pH 9 and 10 and increases with increased immersion time.

Since exposure of CFRP to an alkaline pH has been demonstrated to be deleterious to the carbon fibers of CFRP, and the observed changes in capacitance can result from either changes in the surface area of the conductive carbon fibers and/or chemical modification of the carbon surface by attached functional groups, further EIS tests were made on CFRP samples after 20 hours' immersion in pH 10 and 12 buffers respectively and then measured after washing in distilled water and immersing interminently (for 2 hours prior to testing) using the sequences; HCl- NaCl-HCl-NaCl..... and NaCl-HCl-NaCl-HCl.... respectively. These sequential EIS tests after exposure in alkaline buffer solutions, are premised on the postulation that changes in capacitance due to changes in electrochemically active surface area are less likely to be affected by sequential testing in near-neutral and acidic chloride solutions, while changes due to attachment of functional groups to the carbon fiber surfaces are most likely to be affected by changes in the pH of the test solution. The measured impedance spectra was fitted using the equivalent circuit of Fig. 5.12a, and measured impedance spectra (presented as symbols) together with the fitted spectra (presented as lines), are presented in Figs. 5.20 and 5.22 below for samples immersed in pH 10 and pH 12 buffer solutions respectively. The extracted and fitted parameters from these sequential EIS tests are presented in Figs. 5.21 and 5.23 for samples immersed in pH 10 and pH 12 buffer solutions respectively.

From the Nyquist plots for the sequential EIS tests carried out on CFRP samples after 20 hours immersion in pH 10 buffer (Fig. 5.20a and 5.20d), it can be observed that whereas the measured and fitted data matched closely at high and mid-frequencies, slight deviations are observed at very low frequencies. This was thought to be possibly due to emerging but not well-defined diffusion effects. As a result the data was also fitted to the equivalent circuit of Fig. 5.12b containing a Warburg element. Fitting to this equivalent circuit (Fig. 5.12b), however resulted in higher errors in the circuit element values, hence data for the one time constant equivalent circuit (Fig. 5.12a) was upheld and presented herein. This phenomenon appears to be more prominent in sequential tests starting from acidic chloride media (100 mM HCl, Figs.

5.20a,b, and c). In contrast the measured and fitted spectra for sequential tests after exposure to pH 12 buffer irrespective of the starting test media pH fitted very well to the one time constant equivalent circuit of Fig. 5.12a at all measured frequencies (Fig. 5.22a and 5.22b).

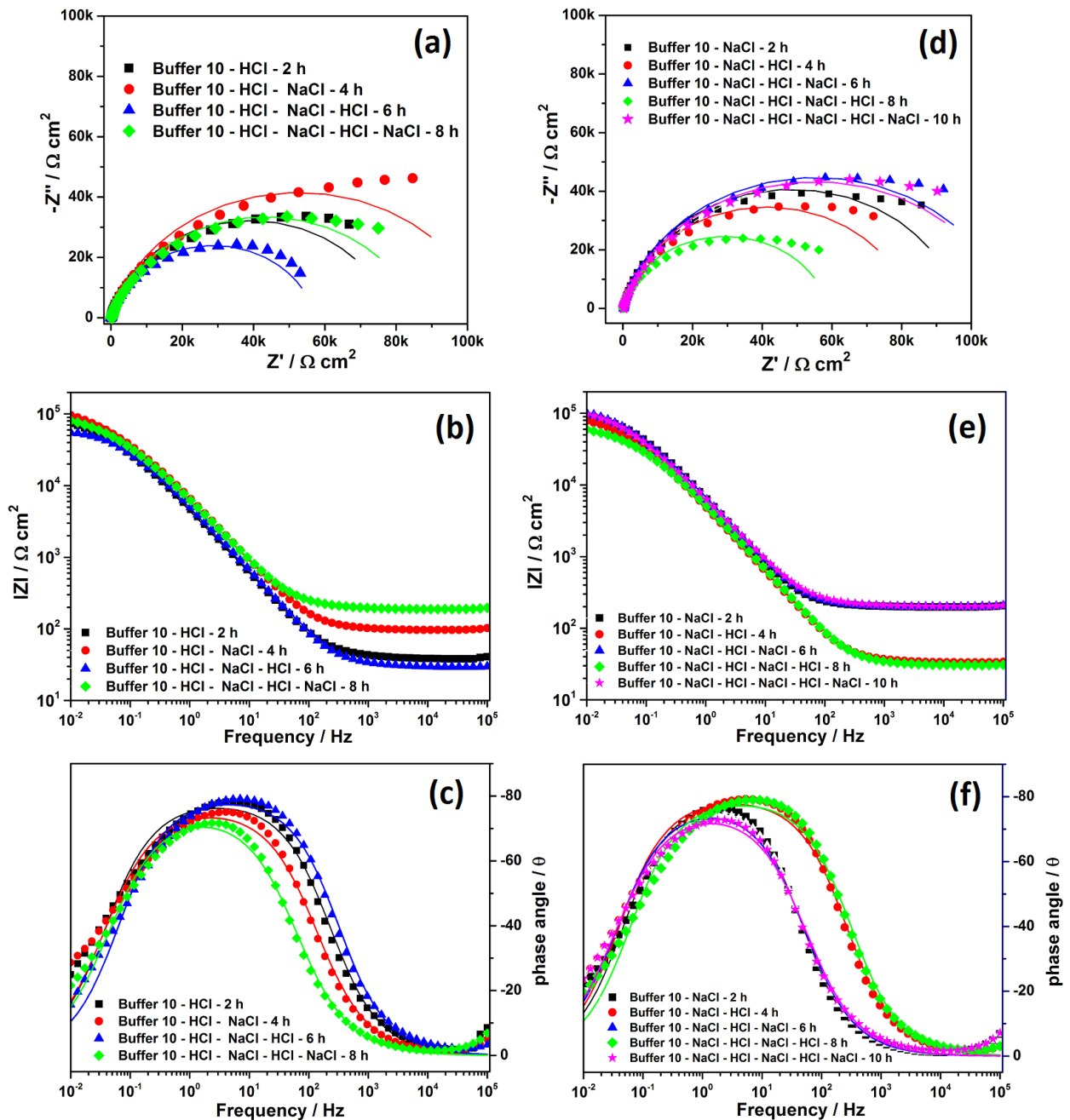


Fig. 5.20. Nyquist and Bode plots for CFRP after 20 hours immersion in pH 10 buffer solution and sequential testing in NaCl and HCl solutions (a-c) tests started in HCl solution and (d-f) tests started in 50 mM NaCl (symbols are measured data while lines are fitted data using equivalent circuit of Fig. 5.12).

From Figs. 5. 20 and 5.21 for samples tested sequentially after 20 hours immersion in pH 10 buffer solution, the test sequence (starting of testing in HCl or NaCl) is observed to affect the extracted EIS parameters (low frequency impedance, polarization resistance, and double layer capacitance) irrespective of the time scale, indicating the predominant effect of the attached

functional groups on the measured capacitance. Irrespective of the time scale and the immersion/testing sequence, the low frequency impedance and polarization resistance were observed to be consistently higher in 50 mM NaCl solution compared to values in 100 mM HCl solution, while the reverse was the case with the calculated capacitance (Fig. 5.21 c).

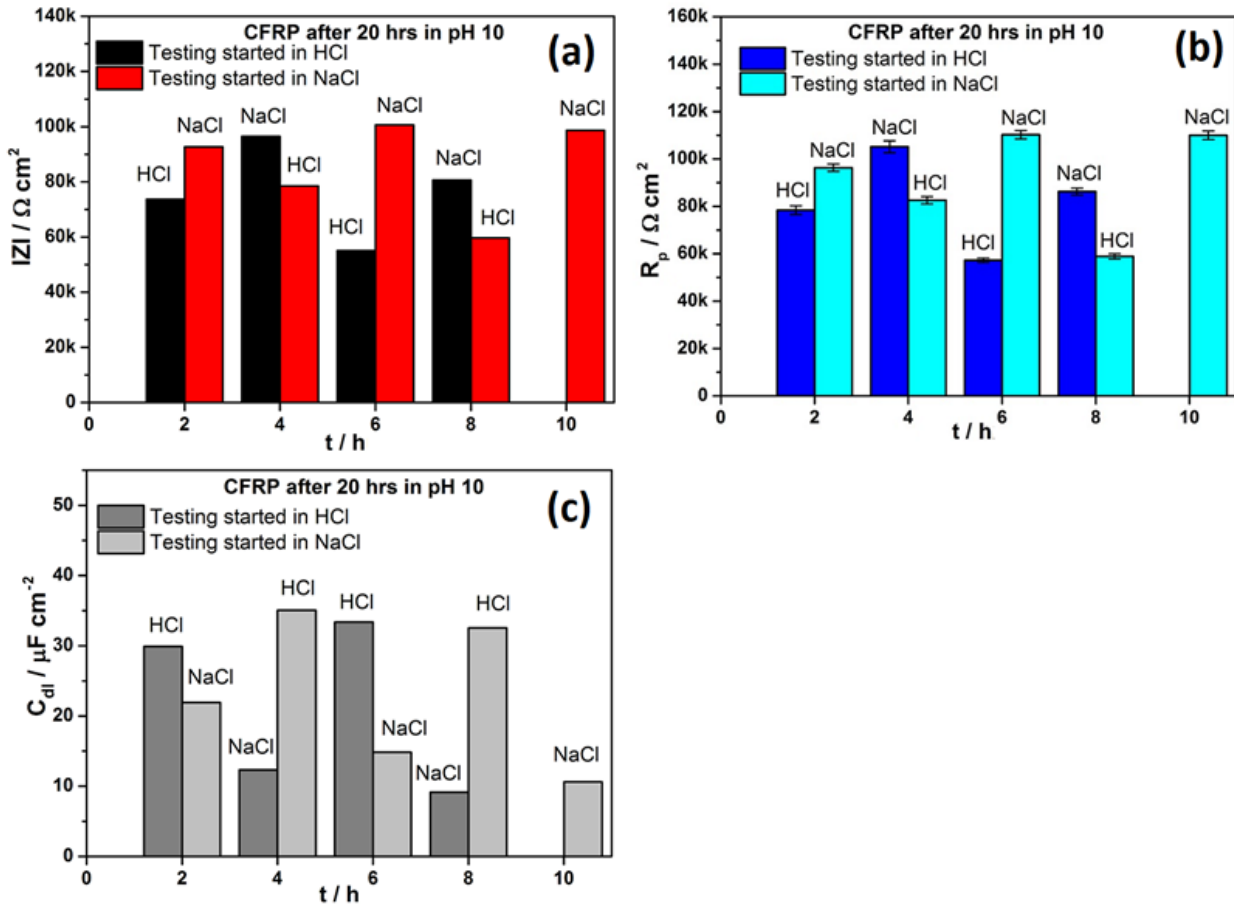


Fig.5.21. Extracted EIS parameters from sequential testing of CFRP in NaCl-HCl-NaCl- and HCl-NaCl-HCl- sequence in 2 hour intervals after immersion in pH 10 buffer solution for 20 hours.

From Fig. 5.21 (c), after immersion in pH 10 buffer solution for 20 hours, the carbon fiber surfaces were most probably rich in O and OH terminated functional groups. Immersion in HCl solution most probably "neutralized" these attached functional groups as they are likely to be less stable at such low pH causing their removal from the carbon surface. In the absence of these attached functional groups, the electrochemically active surface area is increased resulting in the very significantly higher double layer capacitances measured in HCl solutions irrespective of immersion/test sequence. Furthermore measured double layer capacitances in NaCl were observed to reduce with time irrespective of whether first immersion was in NaCl (light grey bars) or in HCl (darker grey bars).

Fig. 5.22 below presents the measured spectra (presented as symbols) and spectra acquired from fitting to the equivalent circuit of Fig. 5.12a (presented as lines) of

electrochemical impedance data for CFRP after 20 hours immersion in pH 12 buffer solution, and then sequentially and intermittently immersing for 2 hours and testing in acidic (100 mM HCl) and near-neutral (50 mM NaCl) solutions. The close agreement of the measured spectra to the fitted spectra is obvious.

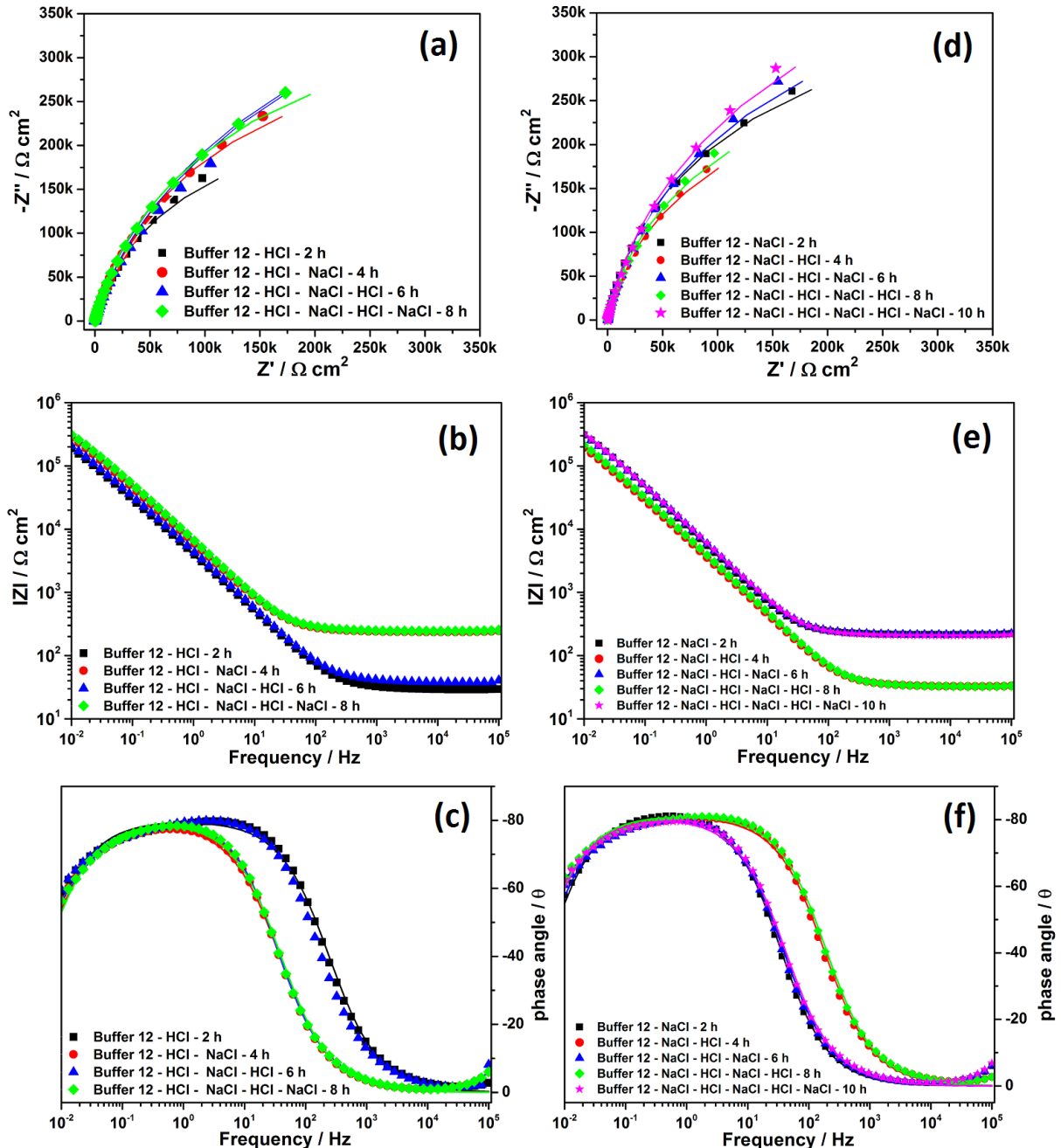


Fig. 5.22. Nyquist and Bode plots for CFRP after 20 hours immersion in pH 12 buffer solution and sequential testing in NaCl and HCl solutions (a-c) tests started in HCl solution and (d-f) tests started in 50 mM NaCl (symbols are measured data while lines are fitted data using equivalent circuit of fig. 5.12).

An interesting hysteresis phenomenon is observed in the impedance spectra of sequential tests carried out in HCl and NaCl after 20 hours prior exposure to pH 12 buffer solution irrespective of the starting media for the sequential test, in which unlike for tests after prior exposure the

impedance spectra is reproducible and strictly dependent on the test media and apparently insensitive to time and immersion sequence.

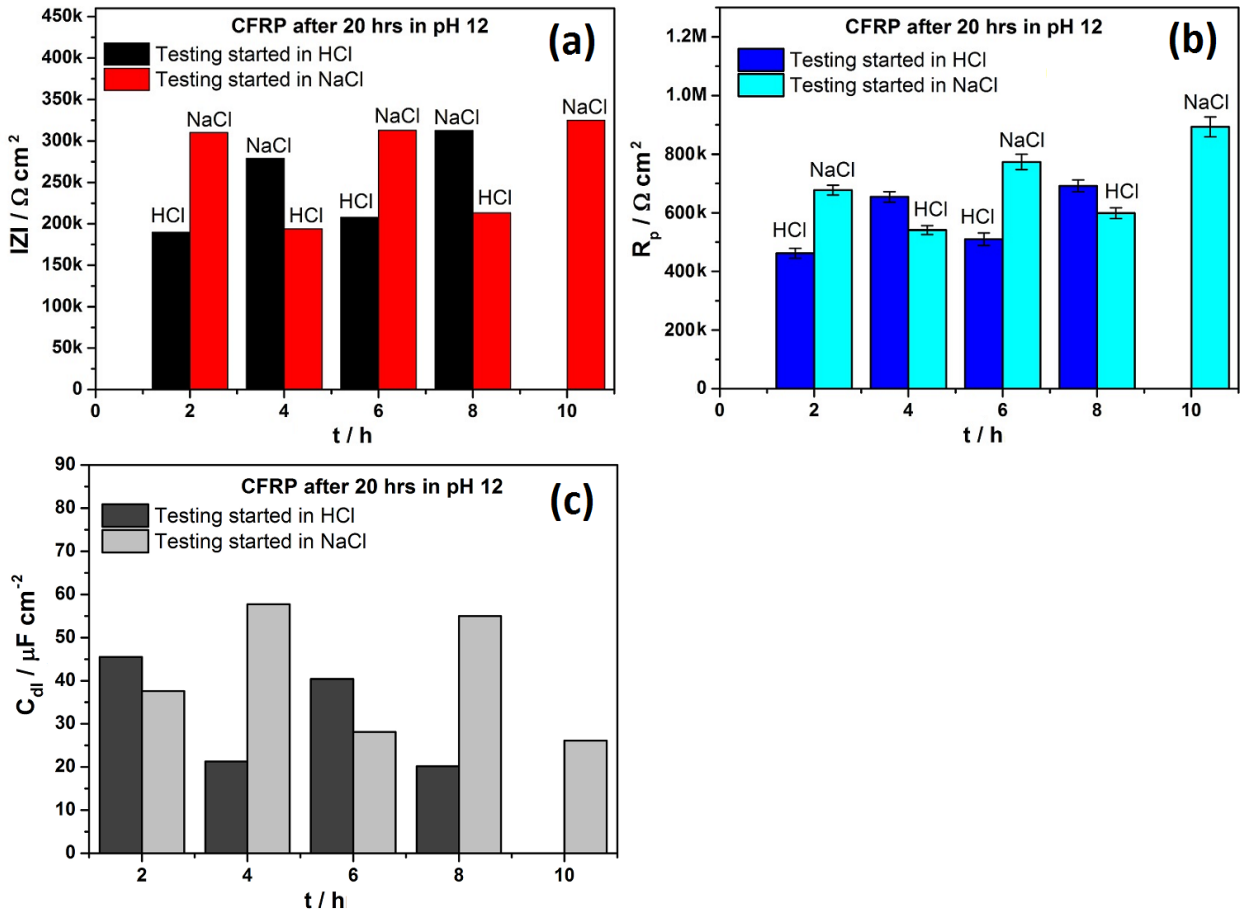


Fig.5.23. Extracted EIS parameters from sequential testing of CFRP in NaCl-HCl-NaCl- and HCl-NaCl-HCl- sequence in 2 hour intervals after immersion in pH 12 buffer solution for 20 hours.

Such high sensitivity of the capacitance changes in the pH of the test solution is attributed to very significant changes in the functional groups attached to carbon surface in test solutions of different pH.

5.2.3.6. Effect of Bulk pH on degradation of CFRP: SEM and Raman images of CFRP

The SEM images of Fig. 5.24 below show that solution pH apparently to exert a marked effect on the presentation of CFRP degradation. In very acidic (pH ≈ 1) and near neutral (pH ≈ 6.8) solutions CFRP degradation occur mainly in the epoxy matrix with the carbon fibers intact, while in alkaline solutions (pH ≥ 8) degradation manifests mainly on the carbon fibers as significant fiber erosion with limited matrix loss. In the highly alkaline solution (pH ≈ 11) damage to the carbon fibers appear less severe with the epoxy matrix virtually unaffected. This is apparently corroborated by the combined confocal Raman images of CFRP after immersion in solutions of different pH (Fig. 5.26). Figs. 5.24 and 5.26 below suggests that alkaline solutions

(pH \geq 8) promote carbon fiber degradation.

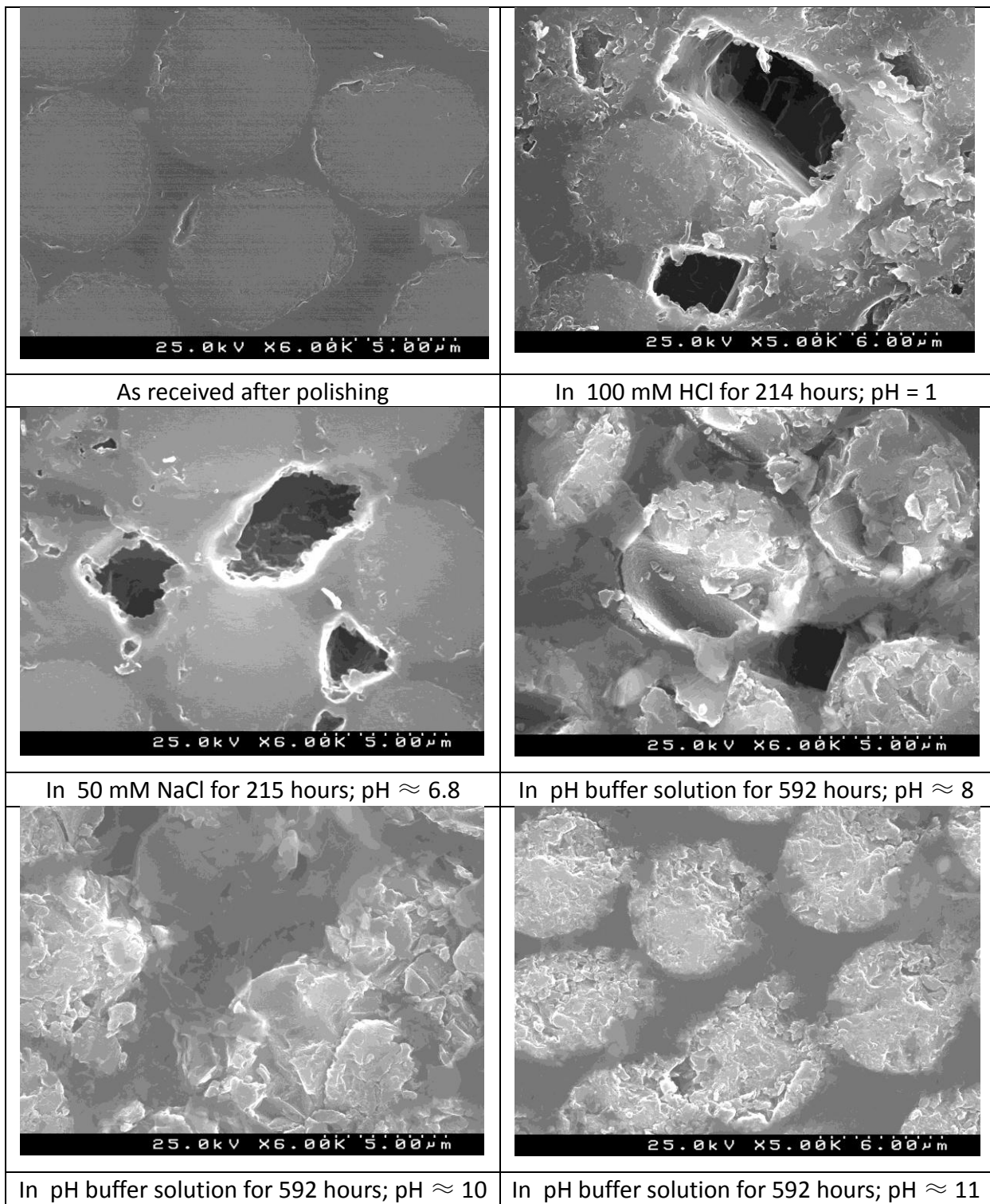


Fig. 5.24. SEM images of CFRP after immersion in solutions of varying pH.

This apparent degradative effect observed in un-polarized CFRP samples (specially the epoxy matrix) exposed to high pH solutions is in tandem with earlier reports [293,294,297] that have linked CFRP degradation to the presence of OH⁻ ions (which are in abundance in high pH

solutions) or the reactive peroxide (HO_2^-) and long-lived intermediates that are produced under cathodic polarization. In simultaneous chronoamperometric and local pH measurements on CFRP in 50 mM NaCl in this work (Fig. 5.6.), changes in local pH which could be attributed to onset and progress of significant cathodic activity was not observed at zero or positive (anodic) polarizations. Hence the apparent degradation to the epoxy matrix is thought to be an artefact developed in the low pressure vacuum conditions of the scanning electron microscope as the presence of reactive peroxide (HO_2^-) and long-lived intermediates presumed to be capable of initiating polymer degradation are not expected to be significant in the absence of impressed cathodic polarization.

In tandem with results from electron microscopy, the results from Raman spectroscopy (Figs. 5.25 and 5.26) indicate degradative features in CFRP exposed to alkaline solutions. However, the superpositioning of the characteristic broad D and G bands of carbon in the wavenumber ranges for important anticipated vibrations from the epoxy matrix limits the exploitation of acquired confocal Raman data to rigorously monitor degradation in the composite. In spite of this limitation, employing the characteristic bands for carbon and the less intense bands emanating from the epoxy outside the range of wave-numbers of the carbon peaks, Raman images (Fig. 5.26) were obtained that discriminated the carbon fibres and the epoxy matrix, while the relative sharpness of the edges of the carbon fibres with respect to un-immersed sample employed to compare apparent degradative tendencies in different test solutions.

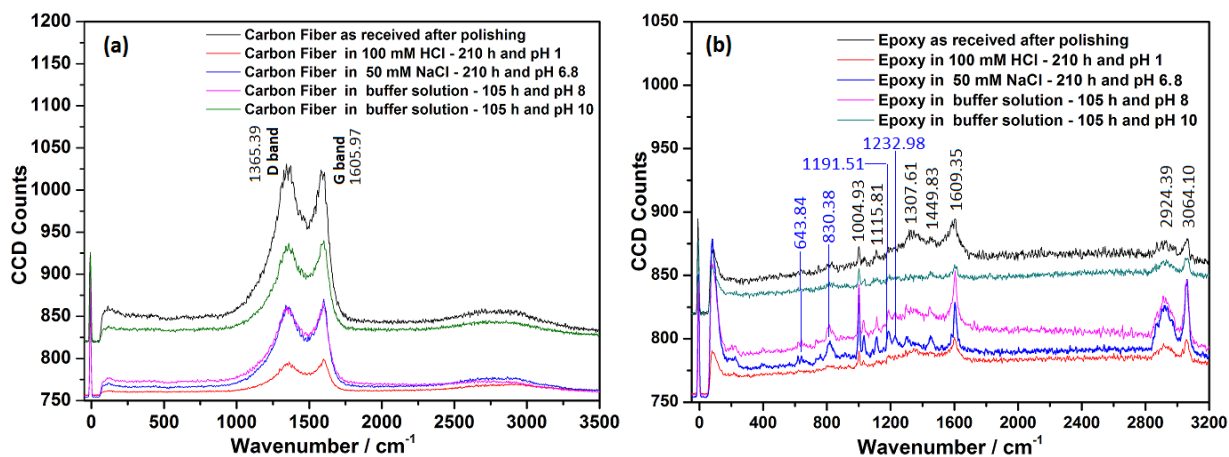


Fig. 5.25. Raman Spectra of CFRP components after immersion in solutions of varying pH, (a) for carbon fibers and (b) for the epoxy matrix.

From Fig. 5.26 below, it is observed that compared to un-immersed CFRP samples and samples immersed in acidic solution, the definition of the edges of the carbon fibres were poorest in the samples immersed in alkaline solutions. This diminution in the definition of the carbon fibre-

epoxy matrix interface after immersion in alkaline solutions is attributed to probable interfacial degradation. Though it can be argued that these differences in the definition of interfacial region between the carbon fibres and the epoxy matrix is not linked to interfacial damage, its severity after immersion in alkaline solutions links this phenomena to the higher pH of these solutions which is tantamount to higher OH^- concentrations.

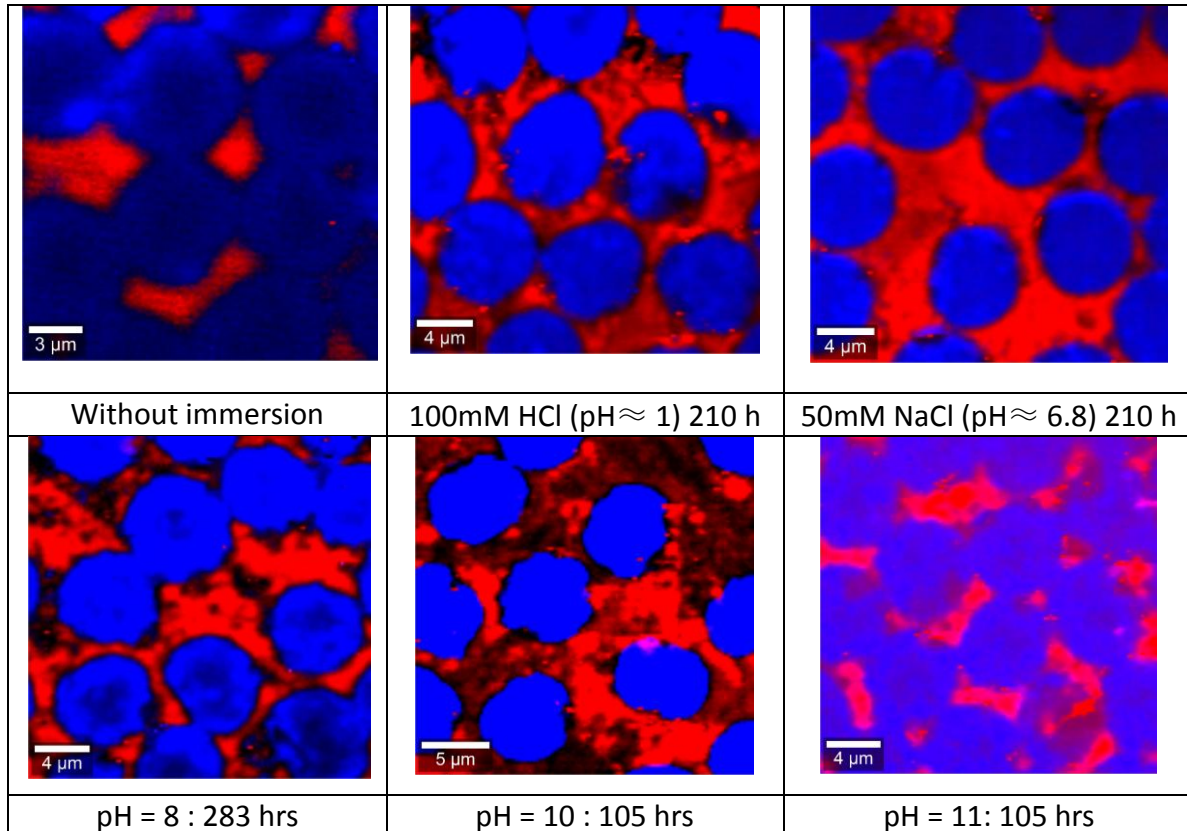


Fig. 5.26. Raman images of CFRP after immersion in solutions of varying pH.

5.2.4. Effect of cathodic polarization on Impedance Spectra of CFRP in Chloride Solutions

Having established in the preceding sub-sections (**section 5.2.3.5**) the impedance response of CFRP in near-neutral chloride solution in the absence of impressed polarization, and that the application of a potential can change the pH close to the CFRP surface in 50 mM NaCl (**section 5.2.2.1**), the effect of applied cathodic polarization on the electrochemical impedance spectra was studied. Electrochemical impedance spectroscopy was employed to study the behaviour of CFRP at different polarizations. The acquired spectra are presented in Figs. 5.27 and 5.28, while parameters extracted from the spectra post-fitting such as low frequency impedance, IZI, double layer capacitance, C_{dl} , and charge transfer resistance, R_{ct} , and diffusion resistance, W_{s-R} are presented in Fig. 5.29. Furthermore, SEM images and Raman spectra and maps of CFRP samples after immersion in 50 mM NaCl under cathodic and anodic polarization were acquired and presented in Figs. 5.30 to 5.32.

However, since some of these tests were carried out at applied potentials much higher than potentials in the cathodic "Tafel region" for CFRP (Fig. 5.9), the extracted parameters such as impedance, capacitance, and polarization resistance may not be strictly classified as such but as the respective "pseudo-parameters", as under these test conditions the linearity principle for EIS tests is not achieved. As a consequence, extracted EIS parameter for tests under significant cathodic polarizations are treated as "pseudo-parameters" and employed only for comparative purposes in the systems under study.

5.2.4.1. Effect of Polarization on carbon fiber reinforced polymer (CFRP) with respect to oxygen diffusion.

To understand effects occurring between the " E_{corr} " up to the diffusion limited regime in CFRP immersed in quiescent 50 mM NaCl solution, EIS test were done in steps of 25 mV from +250 to -500 mV_{SCE} and fitted to the equivalent circuits presented in Fig. 5.12. Figs. 5.27 and 5.28 below presents the Bode plots of CFRP in this potential range showing the emergence of a second time constant attributed to diffusion effects within a certain potential range. For clarity regarding the evolution of impedance response with changes in applied polarization, a selection of the Bode plots at 0 mV, -100 mV, -250 mV, 300 mV, -375 mV, and -500 mV_{SCE} only, are presented in Fig. 5.24 below while the Bode plots obtained in the entire range of potentials between +250 and -500 mV_{SCE} are presented in Fig. 5.28 to monitor diffusion effects.

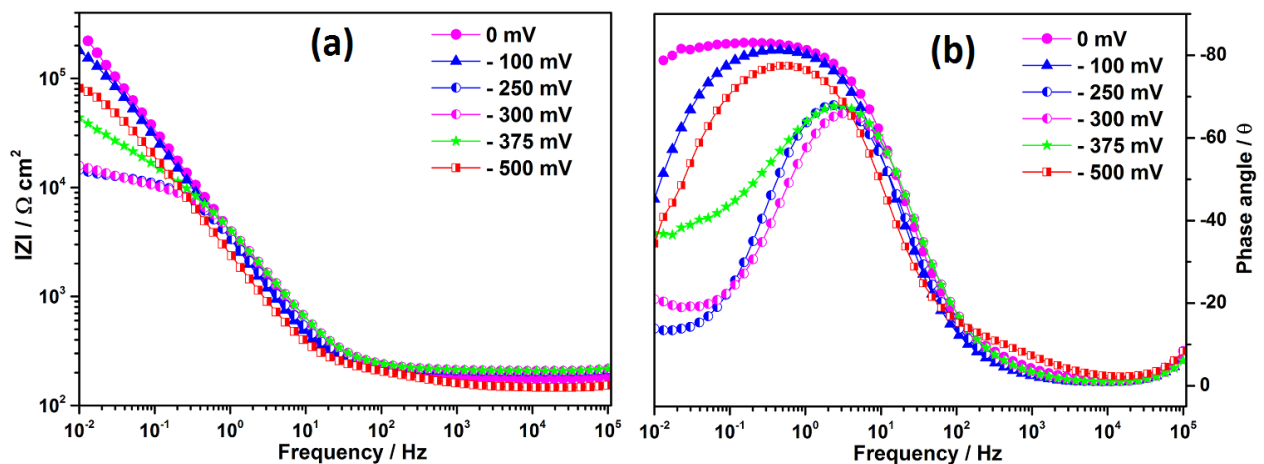


Fig. 5.27. Selected Bode plots of EIS spectra of CFRP in 50 mM NaCl at 0 mV, -100 mV, -250 mV, 300 mV, -375 mV, and -500 mV_{SCE} to monitor diffusion effects.

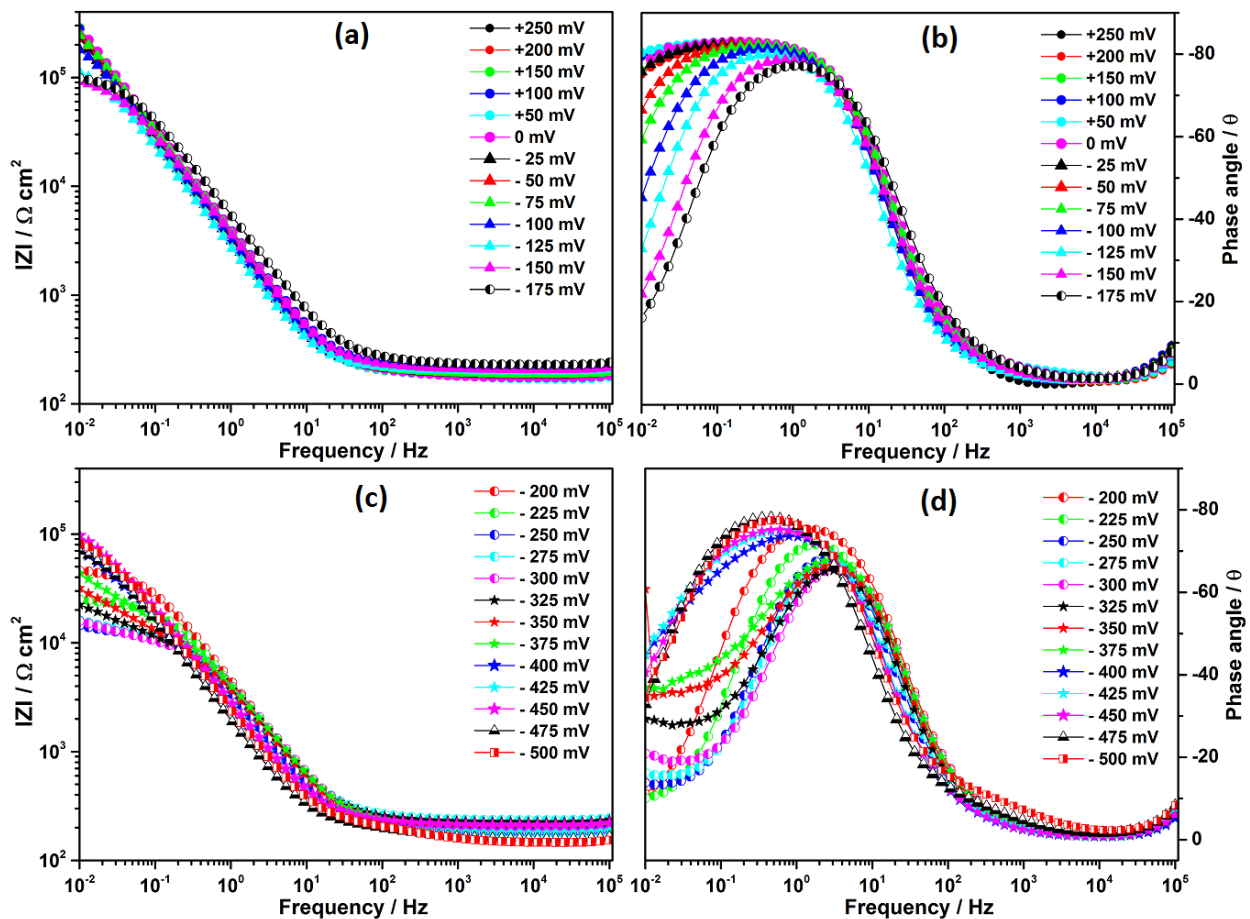


Fig. 5.28. Bode plot of EIS spectra of CFRP in 50 mM NaCl at different polarizations between +250 and -500 mV_{SCE} to monitor diffusion effects.

These EIS data were treated, analyzed and fitted to the equivalent circuits presented in Fig. 5.12. The fitted and extracted parameters from the data are presented in Fig. 5.29 below. Fig. 5.29 reveals similar trends in the low frequency/global impedance (Fig. 5.29a), the capacitance (Fig. 5.29b), and the charge transfer resistance (Fig. 5.29c). Fig. 5.26c shows that from +150 mV_{SCE} (close to the OCP value of CFRP in the test media $\approx +125 \text{ mV}_{\text{SCE}}$) the charge transfer resistance (R_{ct}) decreases steeply with increase in applied cathodic potentials until about -225 mV_{SCE} . Between -225 and -375 mV_{SCE} the charge transfer resistance (R_{ct}) is observed to be more or less stable. Interestingly, the resistive component ($W_{\text{s-R}}$ or R_{d}) of the diffusion impedance is observed to increase steeply in this same cathodic potential range (-225 to -375 mV_{SCE}) in which the charge transfer resistance (R_{ct}) appears to stabilize at its lowest values. Incidentally, this potential range (-225 to -375 mV_{SCE}) is consistent with the potential range of the cathodic peak observed in cyclic voltammetric tests (Figs. 5.10 and 5.11) attributed to the 2-electron reduction of oxygen with formation of hydroxyl ions and hydrogen peroxide [672].

This phenomenon can be explained by considering that the initial increase in the cathodic polarization stimulates easier transfer of charges across the CFRP-solution interface

causing the kinetics of the charge transfer process to be enhanced until the process comes under diffusion control. Once diffusion control becomes dominant, the charge transfer resistance (R_{ct}) becomes independent of further increase in applied cathodic potential, hence its value become lowered and stable with respect to applied potential. Similar trends are observed in the values of the global/low frequency impedance (Fig. 5.29a) and capacitance (Fig. 5.29b) in this potential range in which diffusion appears to predominate. At applied cathodic potentials > -450 mV_{SCE} the impedance spectra no longer fits o the equivalent circuit of Fig. 5.12b, which might be indicative of increased complexity in the operative electrochemical processes, as other cathodic processes besides the 2-electron oxygen reduction process apparently begin to become significant.

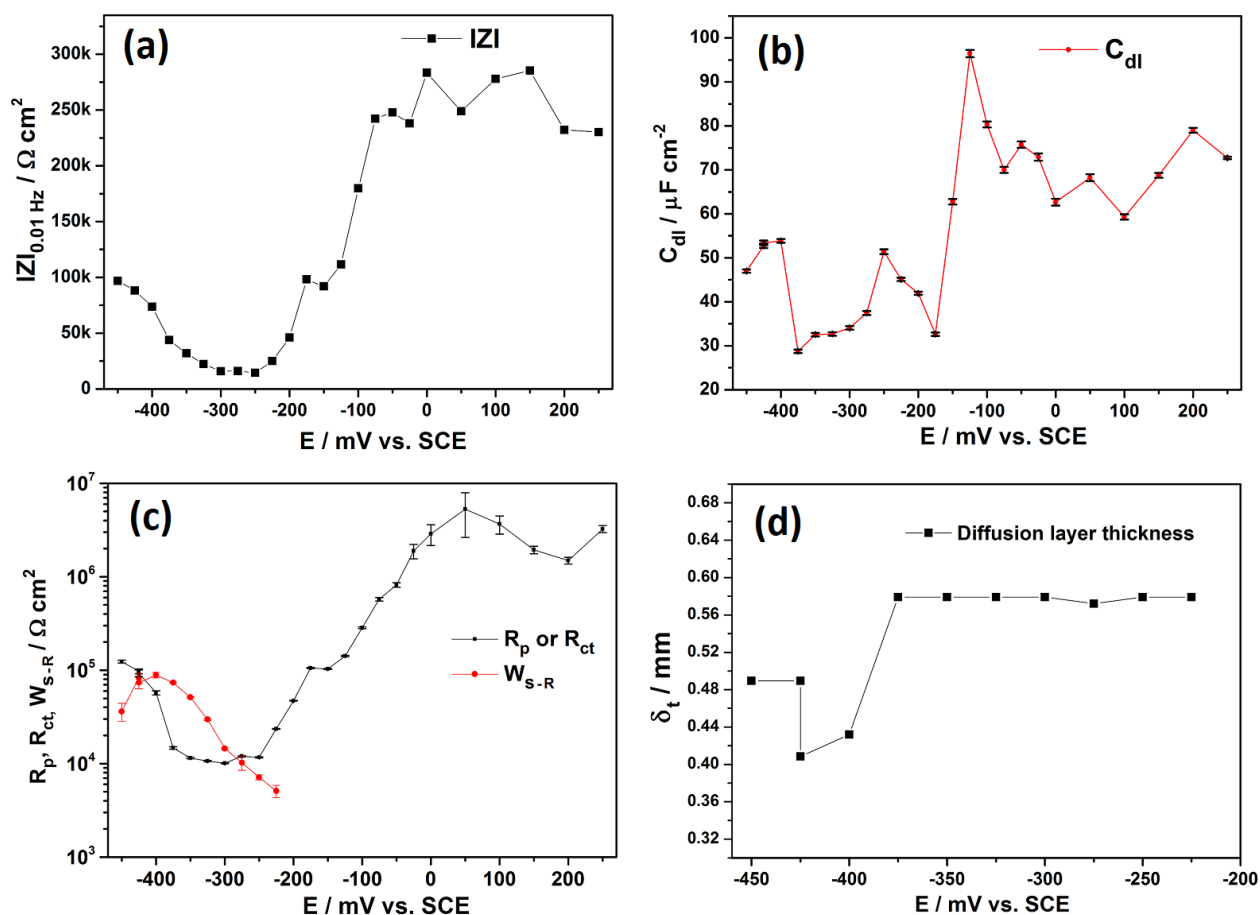


Fig. 5.29. Parameters extracted from the EIS spectra as a function of potential around the diffusion limited potential ranges for CFRP in 50 mM NaCl, (a) low frequency impedance at 10^{-2} Hz, (b) calculated double layer capacitances, (c) evolution of polarization or charge transfer resistance (R_p or R_{ct}), and the resistive component of warburg impedance (W_{s-R}), and (d) the diffusion layer thickness estimated from EIS data.

Using the value $2.41 \times 10^{-5} \text{ cm}^2 \text{ s}^{-1}$ obtained by Vivian and King [676] which had been considered by St-Denis and Fell [677,678] to be the most reliable value for oxygen diffusion coefficient in water, the length of the diffusion layer was calculated from fitting and analysis of

EIS data and presented as a function of potential in Fig 5.29d. From Fig 5.29d it is observed that the calculated length of the diffusion layer is in the range of 0.42 to 0.58 mm with the lower limit values calculated at potentials more cathodic than $-375 \text{ mV}_{\text{SCE}}$ above which other cathodic processes besides the 2-electron reduction process have been postulated earlier to very probably become significant. These calculated values from EIS data for the diffusion layer thickness (δ) compares very well with values reported in unstirred electrolytes by Gerasimov and Rozenfeld [679] at 20°C , which were 0.47 mm on platinum in $0.0047 \text{ N FeCl}_3 + 0.1 \text{ N HCl}$, 0.52 mm on iron in 1 N NaCl solution, and 0.56 mm on copper in iron in 1 N NaCl solution, placing the range of their reported values of diffusion layer thickness (δ) at 20°C at 0.47 mm to 0.56 mm. Discounting the lower values calculated for diffusion layer thickness at higher cathodic potentials where other processes besides 2-electron oxygen reduction have been explained to become significant, the value of 0.58 mm calculated repeatedly at several potentials in the potential region in which the 2-electron oxygen reduction predominates compare favourably with 0.56 mm reported on both iron and copper. The fact that the values of diffusion layer thickness (δ) calculated from treated EIS data compares so favourably with values reported from a different technique validates both the treatment of the EIS data and the inferences made earlier from Fig. 5.29c, especially regarding the potential range in which the 2-electron oxygen reduction predominates on CFRP surface. In addition, the fact that the diffusion layer thickness calculated from such a composite electrode with $6 \mu\text{m}$ diameter carbon fibres embedded in "seemingly" non-conductive epoxy matrix with the distances between neighbouring fibres seldom $> 12 \mu\text{m}$ ($= 2$ carbon fibre diameters) (see Figs. 5.4, and 5.22a for microstructure of CFRP surface) compared favourably with values measured in monolithic metal surfaces and supports the assertion in the concluding section of this chapter that the CFRP surface appears to act electrochemically as a uniform and continuous electro-active surface when the diffusion controlled processes dominate (section 5.3). This can be explained by the fact that by reason of the size of the carbon fibres ($6 \mu\text{m}$ diameter) and the distance separating each carbon fibre from the other ($\leq 12 \mu\text{m}$) being much less than the estimated length of the diffusion layer 0.58 mm ($= 580 \mu\text{m}$), the diffusion fields of adjacent carbon fibres are bound to overlap so that instead of acting as individual micro-electrodes, they apparently act as a single planar electrode.

5.2.4.4. Surface Analysis: Effect of Polarization on Raman Spectra, Raman and SEM Images of CFRP

The effect of polarization on CFRP after short term immersion in 50 mM NaCl for 2 hours was studied at cathodic (-1000 mV_{SCE}) and anodic (+1000 mV_{SCE}) potentials using scanning electron microscopy and confocal Raman spectroscopy/microscopy. The results thus obtained are compared with that obtained from unpolarized and unimmersed samples and presented in Fig. 5.30 for SEM, and Figs. 5.31 and 5.32 for confocal Raman spectroscopy.

From Fig. 5.30, it is observed that cathodic polarization appears to apparently lead to significant composite degradation characterized by carbon fiber erosion and interfacial damage in the interface between the carbon fiber and epoxy matrix. In contrast anodic polarization to +1000 mV_{SCE} results in much less damage which appears to be concentrated on the epoxy matrix. It is important to mention however that though previous authors [294,305,672] have observed similar "degradation" from SEM images, attempts to monitor this degradation after application of applied cathodic polarizations using in-situ atomic force microscopy (AFM) techniques did not show evidence of such damage. Attempts at AFM measurement under impressed cathodic polarization were not successful due to gas evolution. The non-observance of the surface damage observed with SEM in AFM tests might be suggestive that the damage might have been produced or magnified in the non-ambient test conditions of the scanning electron microscope. Another reason can be related to differences in actual test conditions when performing polarization in bulk electrolyte and in the electrochemical AFM cell.

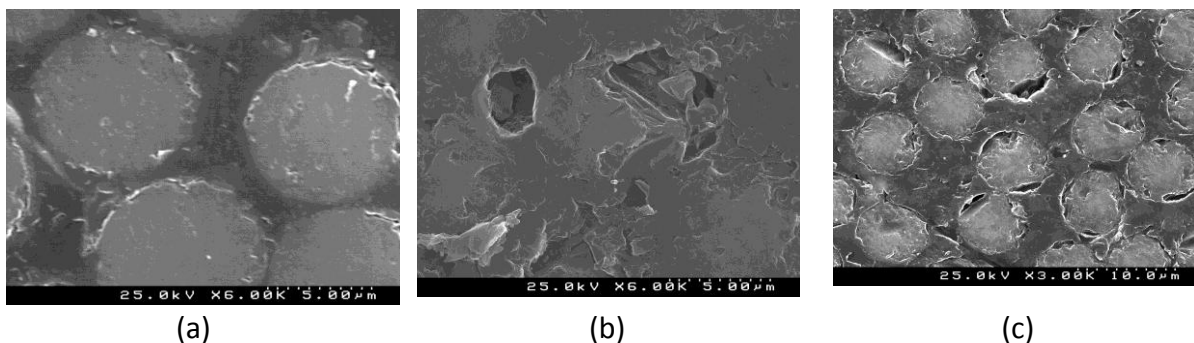


Fig 5.30. SEM images of CFRP as received (a), and after immersion in 50 mM NaCl for 2 hours at (b) +1000 mV and (c) -1000 mV_{SCE} respectively.

Fig. 5.31 below presents the Raman spectra acquired from the epoxy and carbon fiber components of the CFRP and also from the interface before and after immersion with polarization. The carbon fibers are identifiable through their D-band ($\approx 1368 \text{ cm}^{-1}$) and G-band ($\approx 1606 \text{ cm}^{-1}$) peaks but the D-band was utilized in this work since it is not superimposed on any significant peaks from the epoxy matrix. The epoxy is characterized by peaks around 816,

1001, 1036, 1115, 1296, 1459, 1616, 2924, and 3067 cm^{-1} but the peaks around 1001, 1036 and 3067 cm^{-1} were used in identifying the epoxy in this work.

In Fig. 5.32a the epoxy peak at 1004 cm^{-1} was observed on carbon fibers polarized at an anodic potential (+1000 mV_{SCE}) and at the carbon fiber-epoxy interface for samples polarized at cathodic potential (-1000 mV_{SCE}). The presence of this peak on carbon fibers in anodically polarized samples suggests deposition of some eroded epoxy matrix material on carbon fibers under anodic polarization conditions. On exposing CFRP to the cathodic polarization of -1000 mV_{SCE} , the epoxy surfaces appears to be covered by a significant layer of re-deposited carbon as evidenced by the prominence of the D- and G-band peaks of carbon on the epoxy surface (blue line in Fig. 5.32b) and the absence of even the prominent peaks associated with epoxy such as 1001, 1036, 2924, and 3067 cm^{-1} . This observation implies that under cathodic polarization the electrochemically active surface area on CFRP samples might be significantly higher than the surface area estimated on the basis of the exposed carbon fiber fraction.

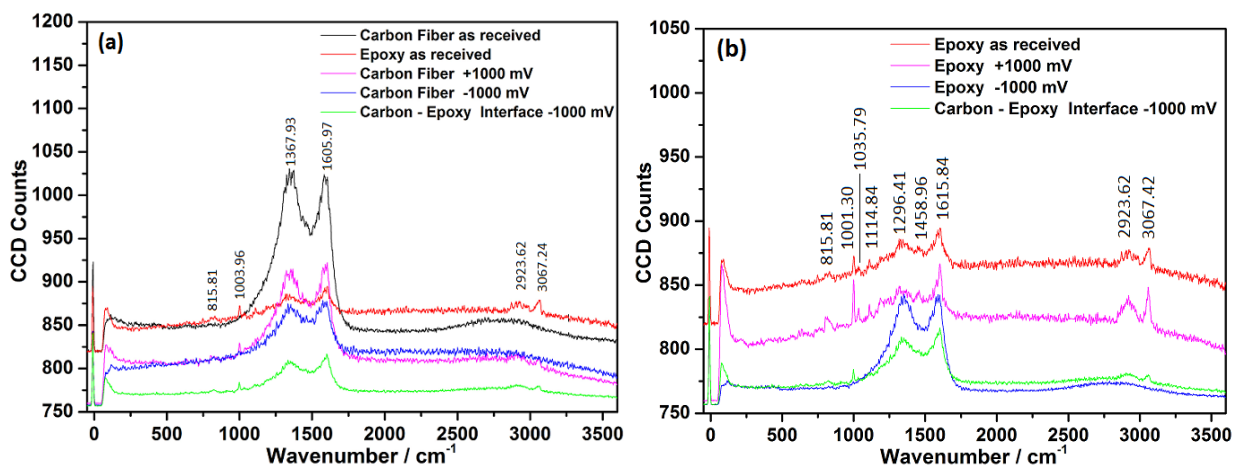


Fig 5.31. Raman spectra of CFRP components (a) carbon fibers and (b) the epoxy matrix in the as received condition, and after immersion in 50 mM NaCl for 2 hours at +1000 mV_{SCE} and -1000 mV_{SCE} respectively.

From point by point acquired spectra like those presented in Fig. 5.31 above, the confocal Raman images presented in Fig. 5.32 were generated. These Raman images (Fig. 5.32) confirm earlier observations from SEM images (Fig. 5.30) of significant interfacial damage and carbon fiber erosion in samples exposed to cathodic polarization and almost pristine carbon fibres in samples exposed to anodic polarization.

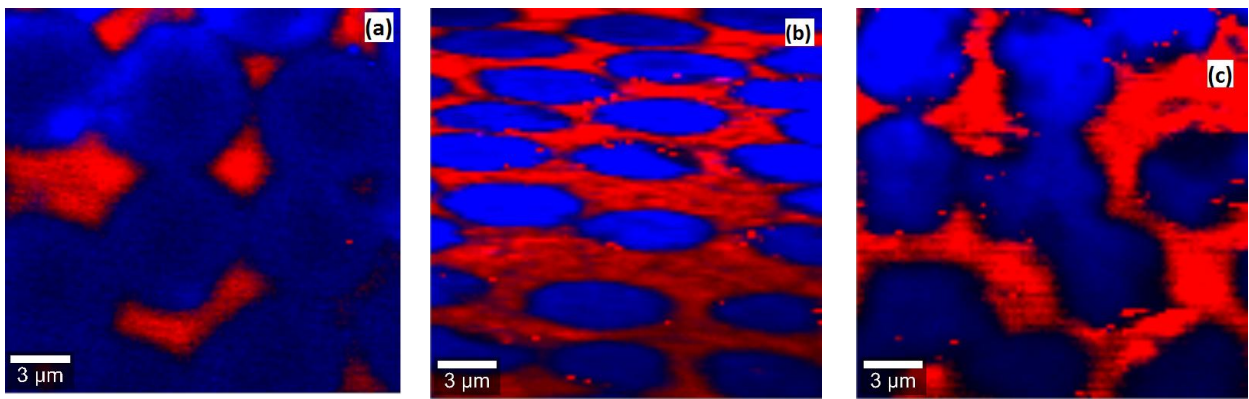


Fig. 5.32. Raman mapping of CFRP as received (a), and after immersion in 50 mM NaCl for 2 hours at (b) +1000 mV and (c) -1000 mV_{SCE} respectively.

5.2.5. Scheme for Using EIS Parameters to Monitor Changes in CFRP

From the trends observed in the electrochemical response of CFRP after exposure to solutions of varying pH without an impressed potential and those under cathodic polarization, and following the arguments and suggestions by Taylor et al., [297,301] on the use of EIS parameters to detect, monitor, and analyze damage in carbon fibre composites under aqueous and cathodic polarization conditions, it is postulated that the "degradation" trends of CFRP under these test conditions in this work might be monitored by a careful consideration of the trends of the extracted "pseudo" EIS parameters (low frequency impedance ($|Z|_{0.01 \text{ Hz}}$), charge transfer resistance (R_{ct}) and double layer capacitance (C_{dl})) post-fitting as illustrated below (Fig. 5.33):

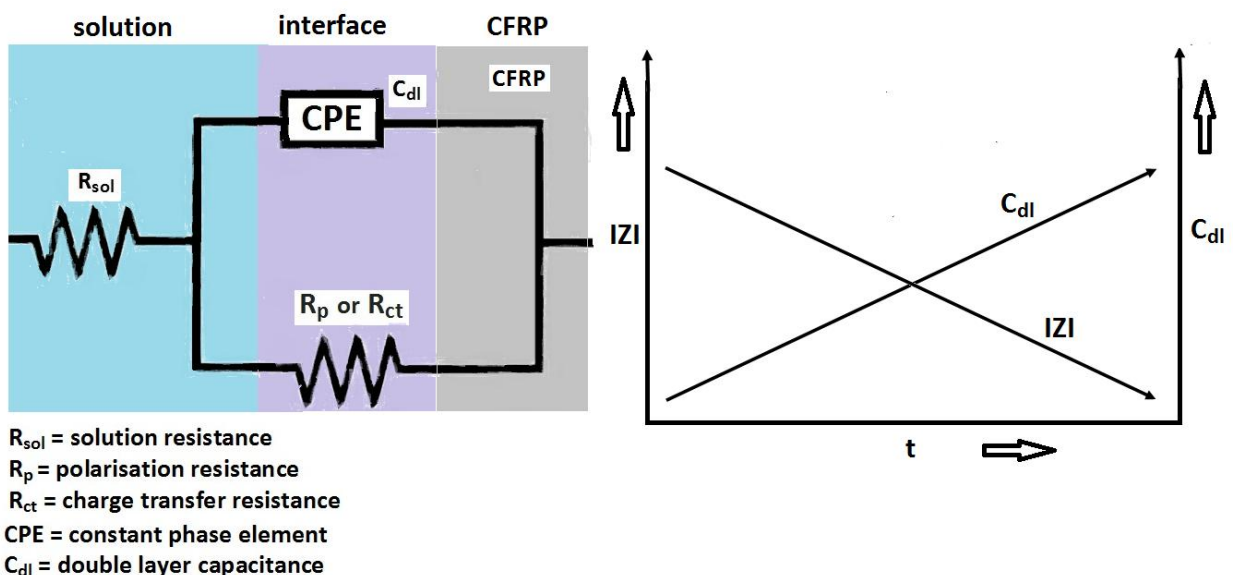


Fig. 5.33. Postulated scheme for using trends of EIS parameter to monitor degradation in CFRP.

From the equivalent circuit in Fig. 5.33 above, it can be observed that the capacitance will be higher when the charge transfer resistance is high, thus minimizing the rate of current

leakage from the interface. Changes in the surface of the electrode that make charge transfer across the interface more difficult are likely to lead to higher values of charge transfer resistance (R_{ct}) while surface modifications that promote charge transfer across the interface are likely to lead to lowered values for charge transfer resistance (R_{ct}). Consequently, charge transfer resistance (R_{ct}) being sensitive to changes in surface conditions can be used to monitor these changes. The value and trend of the low frequency impedance being the global impedance undiscriminated into its components can along with information on the values of the R_{ct} and C_{dl} provide insights on the distribution of the impedance between capacitive and resistive components and their evolution with time. Based on these, a reaction occurring across the interface is equivalent to a leaky capacitor, and thus should lead to a reduction in both the double layer capacitance and the charge transfer resistance, and even the low frequency impedance/global impedance. This postulation is validated by the observed trends in Fig. 5.29, where the 2-electron oxygen reduction reaction observed between -225 and -375 mV_{SCE} led to a reduction in all these three parameters around the potential range for the reaction. Furthermore, increase in C_{dl} coupled with decrease in the low frequency/global impedance is inferred to be consistent an increasing electroactive surface area, and thus can be used to monitor degradative processes that lead to increase in the electrochemical surface area. These arguments were employed in section 5.2.6 below to explain observed trends in EIS data for CFRP samples subjected to the combination of cathodic polarization and pH.

5.2.6. Effect of combination of Polarization and pH on carbon fiber reinforced plastic (CFRP)

Having studied the effect of polarization and bulk pH of solution separately on the electrochemical response of CFRP, the effect of a combination of these factors was studied under cathodic polarization conditions. To monitor the effect of the bulk solution pH on CFRP degradation under cathodic polarization un-buffered chloride solutions of varying pH were prepared by addition of NaOH to 50 mM NaCl solutions to achieve alkaline pH, and by use of an appropriately diluted HCl solution as bulk solution for pH 1. Using solutions of pH 1, 10, and 12, the EIS tests under cathodic polarizations were repeated, and the spectra extracted and fitted parameters compared with those obtained earlier in 50 mM NaCl solution (pH \approx 6.8). The Nyquist and Bode plot for the spectra acquired in pH 10.5 un-buffered chloride solution after 2 hours immersion are presented in Figs. 5.34 and 5.35, extracted and fitted parameters for the different pH values are presented in Figs. 5.36 and 5.37 below.

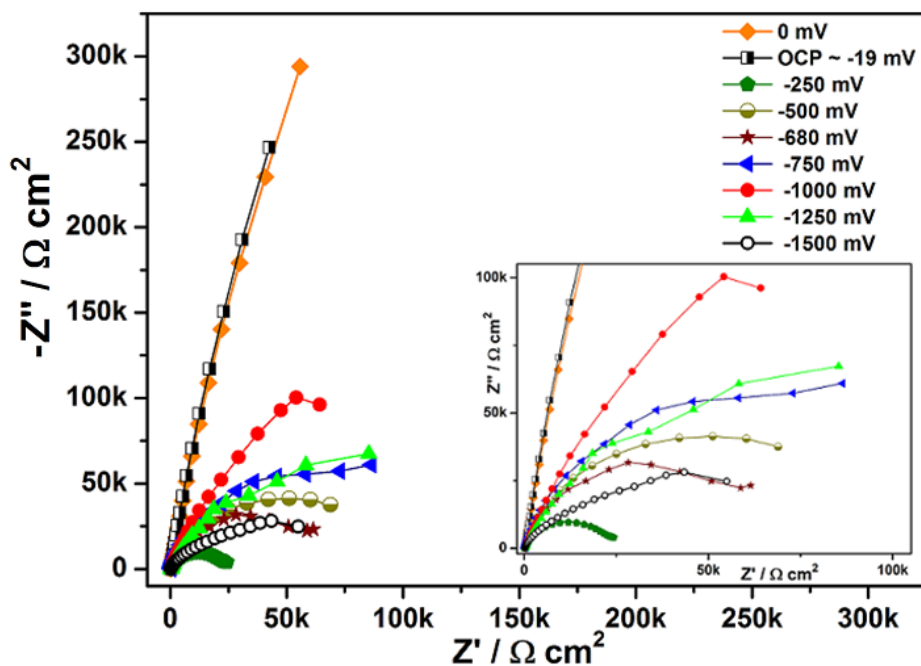


Fig. 5.34. Nyquist plot for CFRP after 2 hours immersion in 50 mM NaCl solution adjusted to pH 10.5 at different polarizations.

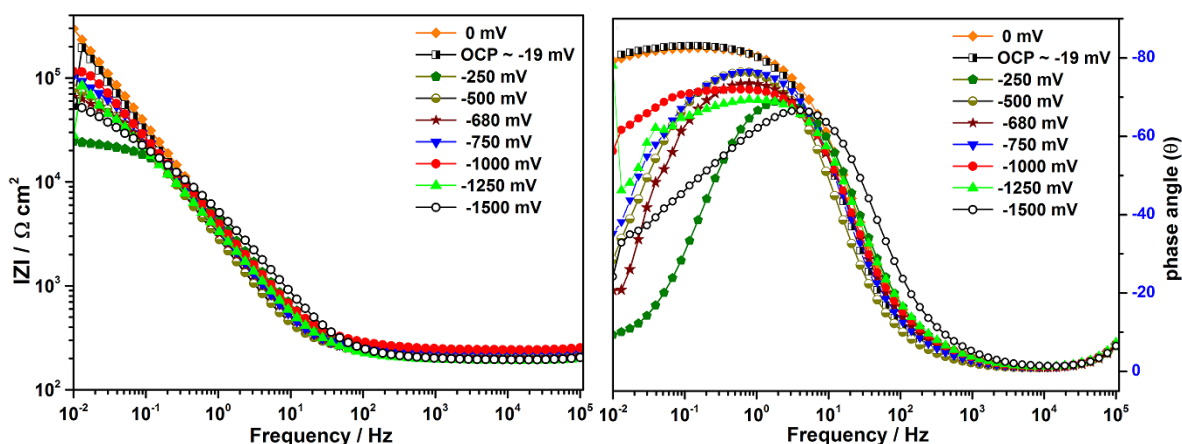


Fig. 5.35. Bode plot for CFRP after 2 hours immersion in 50 mM NaCl solution adjusted to pH 10.5 at different polarizations.

The Nyquist and Bode plot for the spectra acquired in pH 10.5 un-buffered chloride solution after 2 hours immersion (Figs. 5.34 and 5.35) generally presenting a potential dependent electrochemical response. Under no or very small cathodic polarizations a one-time constant electrochemical response is observed, but as potential are increased above $-500 \text{ mV}_{\text{SCE}}$ features of the presence of at least a second time constant attributed predominantly to diffusion effects begin to manifest. Attempts to fit the data in this higher cathodic polarization range to the equivalent circuit of Fig. 5.12 with a Warburg diffusion element produced much higher errors in the circuit elements than the simpler equivalent circuit of Fig. 5.12a. This is thought to be probably due to the presence of other processes other than diffusion effects at these higher

cathodic polarizations ($> -500 \text{ mV}_{\text{SCE}}$) or diffusion with different bonding conditions. Secondly, and very importantly, since at such high cathodic polarizations the electrode is far from its "Tafel region" and hence the linearity condition for validity of EIS data is less likely to be fulfilled, a more robust analysis of the EIS data was not done. Consequently, the simple equivalent circuit of Fig. 5.12a returning much lower errors than the circuit of Fig. 5.12b was used to fit the "impedance data". The values presented in Fig. 5.36 below (particularly at high cathodic polarizations) are considered as pseudo values and employed for comparison only. Since these features manifest at all higher cathodic polarizations in the different pH solutions, any errors are expected to cancel out to permit at least rudimentary comparison.

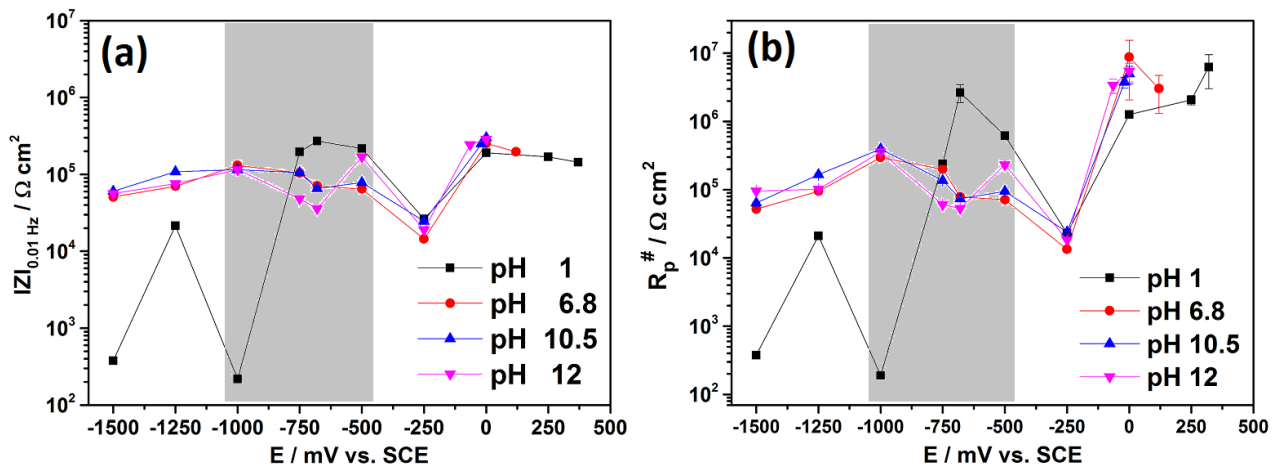


Fig. 5.36. Plots of (a) low frequency impedance at 0.01 Hz ($|Z|_{0.01 \text{ Hz}}$) and (b) "pseudo polarization resistance" ($R_p^{\#}$) evolution for CFRP after immersion for 2 hours in chloride solutions of different pH and at different applied potentials.

The approximations from fitted EIS data of low frequency impedance and the pseudo polarization resistance are presented in Fig. 5.36 above, from which it can be observed that changes in the bulk pH near CFRP surface under the cathodic potential range (hatched in grey) envisaged in this work on galvanic coupling of CFRP to metals such as aluminium, zinc, and iron respectively in this work does not exert marked differences in the electrochemical response/activity. Hence it is concluded that environmental control (pH) employed in mitigation of metallic corrosion is not a viable option for mitigating electrochemical activity of CFRP under cathodic polarizations consistent with galvanic coupling with metals of interest in multi-material assemblies.

5.2.7. Degradative processes on CFRP under cathodic polarization and alkaline pH

Results obtained from tests on CFRP in preceding sections of this work indicates changes in the electrochemical responses obtained from CFRP as pH is changed toward more alkaline

values and as a cathodic polarization is applied, which have been attributed to both changes in chemistry of the carbon surface and some degradative processes. Degradation in CFRP appears to involve the interface between the carbon fibres and the epoxy matrix, the epoxy matrix, and the carbon fibres, respectively. Interfacial degradation between the carbon fibres and epoxy matrix, besides its deleterious effects on mechanical properties is very likely to lead to increased electroactive surface area and hence enhanced electrochemical activity, as more of the carbon fibre surface (its sides) come into contact with electrolyte. Though tests under high pH conditions were carried out over longer time periods compared to tests with impressed cathodic polarizations due to obvious high resource demand of long term impressed cathodic polarization tests, the results appear to indicate that degradation is more prominent when cathodic polarization is applied to CFRP in alkaline media. Under cathodic polarization in acidic media, the production of the degradative short-lived peroxide radicals and oxo-species is apparently less favoured, as they are likely to be easily deactivated as a result of their reduction by the high proton (H^+) concentration of the bulk solution. Under alkaline pH alone these more deleterious short-lived peroxide and oxo-radicals are not likely to be significantly generated, so that degradative processes are not likely to be much accelerated. As a consequence much of the changes in electrochemical response on/after exposure to alkaline media are more probable to be due to changes in the surface chemistry of carbon through changes in the attached functional groups. In summary results obtained by exposure of CFRP to solutions of varying pH, in the absence and presence of applied cathodic potentials appear to be in agreement with the assertion of Pauly et al., [302] that the presence of a local alkaline pH (abundance of OH^-) is a necessary but not sufficient condition for CFRP degradation, as the concomitant presence of a cathodic polarization is apparently more dominant for onset and sustenance of degradative processes.

5.2.8. Choosing Inhibitors for Mitigating Electrochemical Activity of CFRP and Its Consequent Degradation.

Since the application of cathodic polarization on CFRP has been demonstrated to result in marked changes in the pH near CFRP surface to values ($pH \approx 10$) at which cathodic processes appear to be most favoured on CFRP surface, and that these cathodic processes are not significantly affected by changes in bulk pH, inhibitors were explored as a potential option for mitigating the cathodic processes and degradative processes on CFRP surface under cathodic polarization. In the light of the fact that as a component in multi-material combinations,

CFRP being very noble is most likely to be under cathodic polarization, studies with inhibitors were carried out at applied cathodic potentials consistent with the upper range of potentials, CFRP is most likely to be polarized on galvanic coupling with the metals employed in this work. This test procedure ensured that the study of CFRP interaction with inhibitors and its effects on cathodic and degradative processes are carried out under test conditions reminiscent of real conditions in galvanic systems. The use and choice of inhibitors are premised on the observed changes of the local pH around CFRP on galvanic coupling or application of cathodic polarization and the consequent onset of cathodic processes, and carbon's well known adsorbent properties which extends to both organic compounds [680,681], metal cations [682] and anions [683]. On these basis, research efforts were directed at inhibitors that can potentially precipitate onto CFRP surface on onset of cathodic processes with the precipitation prompted by increase in local pH, and adsorption based inhibitors (organic inhibitors) with the expectation that these might adsorb onto the carbon surface on the CFRP reducing the electrochemically active surface area, and as a consequence a reduction in cathodic processes.

5.2.8.1. Effect of combination of Inhibitors and Polarization at $-1000\text{ mV}_{\text{SCE}}$ on carbon fiber reinforced plastic (CFRP)

After studying the electrochemical behaviour of CFRP in solutions of varying pH, with and without polarization, tests were conducted in 50 mM NaCl based solutions containing a wide range of inhibitors and their combinations under cathodic polarization consistent with that anticipated on galvanic coupling of CFRP with the very active metals using potentiodynamic polarization and electrochemical impedance spectroscopy. The results of the tests on the effect of inhibitors on CFRP in 50 mM NaCl based solutions are presented below.

From exploratory cathodic potentiodynamic polarizations scans presented in Fig. 5.37 below, it is observed that the addition of most of the inhibitors yielded no significant reduction in cathodic activities on CFRP with increased cathodic currents significantly above that in the blank solution recorded with some inhibitors (such as cerium nitrate, cerium acetate, ethylene diaminetetraacetic acid (EDTA), dipotassium dichromate ($\text{K}_2\text{Cr}_2\text{O}_7$), and the mixture of benzotriazole and cerium nitrate) at cathodic potential $-900\text{ mV}_{\text{SCE}}$.

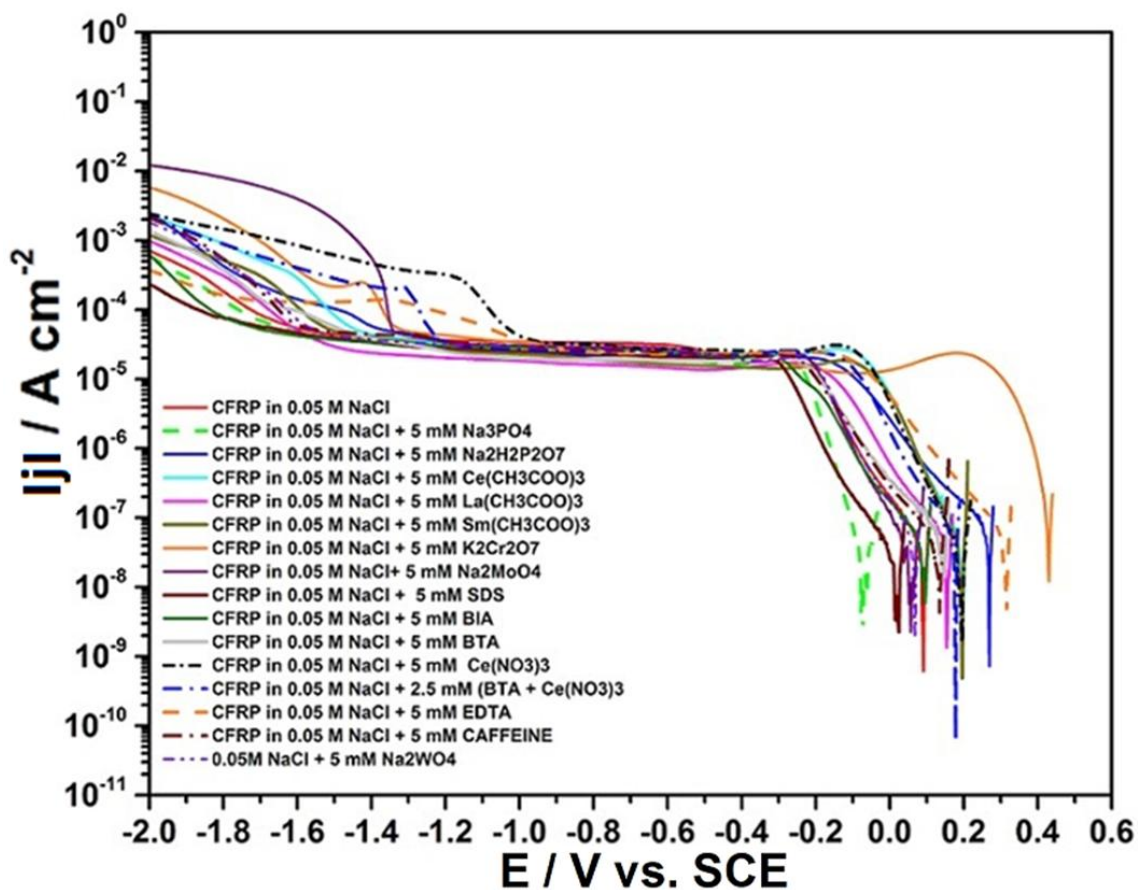


Fig. 5.37. Cathodic Potentiodynamic polarization scans of CFRP in different inhibitor solutions.

From the zoomed section of the cathodic potentiodynamic polarization scans (Fig. 5.38 below) a slight reduction in the diffusion limited cathodic current density was observed in the presence of lanthanum acetate, samarium acetate, benzotriazole (BTA), sodium dodecyl sulphate (SDS), benzimidazole (BIA), trisodium phosphohate (Na_3PO_4), and sodium tungstate (Na_2WO_4), and interestingly reduction in the cathodic current density at potentials between -1200 and -2000 mV_{SCE} that are most probably linked with water reduction reactions with hydrogen evolution in the presence of sodium dodecyl sulphate (SDS), benzimidazole (BIA), and trisodium phosphate (Na_3PO_4). These results suggest that these three inhibitors are able to inhibit cathodic activities on CFRP in the entire cathodic range studied; from OCP to -2000 mV_{SCE} . To exert such influences these three inhibitors need to be able to affect oxygen transport processes to metal surface and electron transfer across the interface.

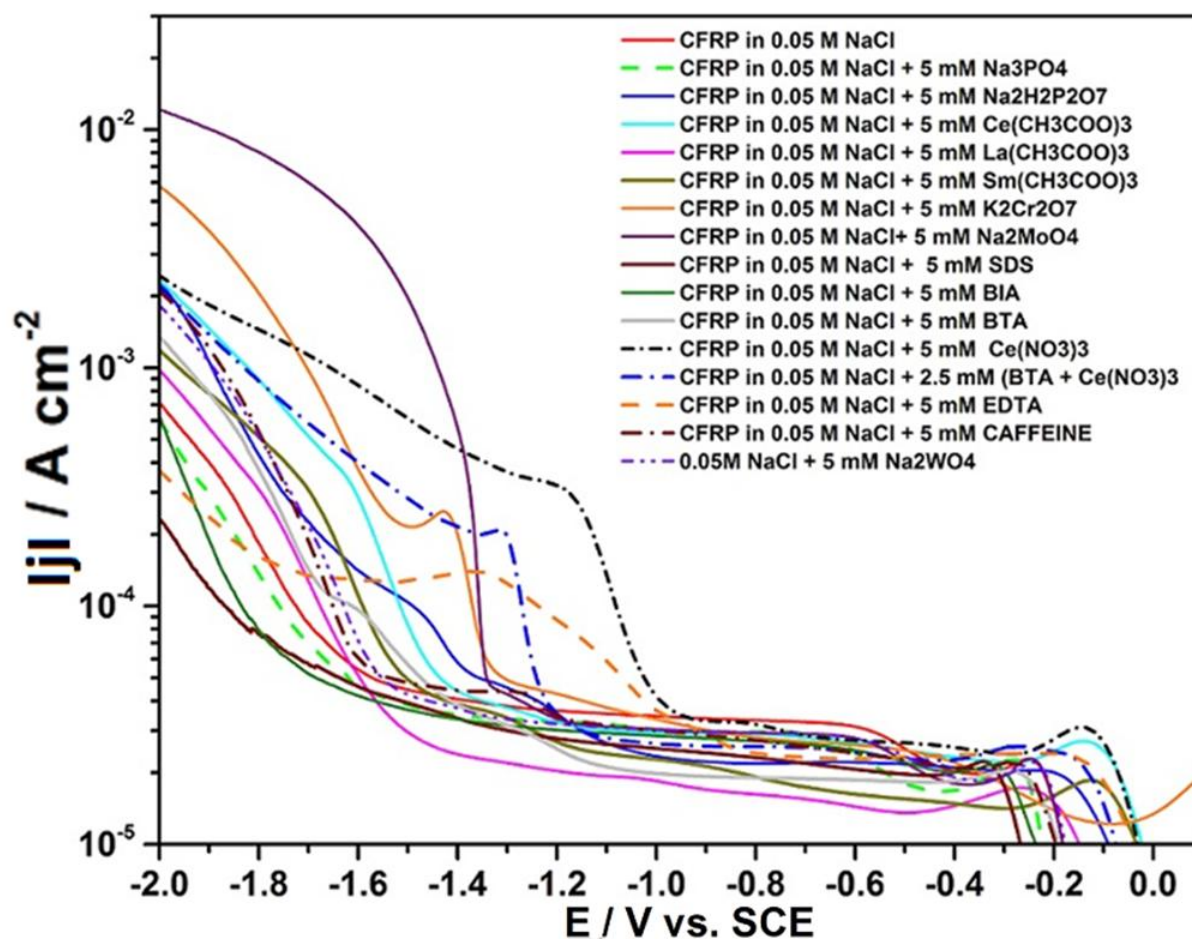


Fig. 5.38. Zoomed section of cathodic potentiodynamic polarization scans of CFRP in different inhibitor solutions.

Further test were carried out to determine if these observations were due to enhancement of cathodic activity on CFRP by the added compounds or due to other effects such as inhibitor electro-/cathodic reduction by varying the concentrations of inhibitors and monitoring the cathodic current response, potential peaks, increase and/or shifts in peaks. The results of some of these potentiodynamic tests and EIS tests are presented in the ensuing section on the basis of the type of inhibitors along with electrochemical impedance test results on CFRP in the presence of some of these inhibitors and a cathodic polarization of $-1000 \text{ mV}_{\text{SCE}}$.

5.2.8.2. Effect of a surfactant; Sodium Dodecyl Sulphate (SDS)

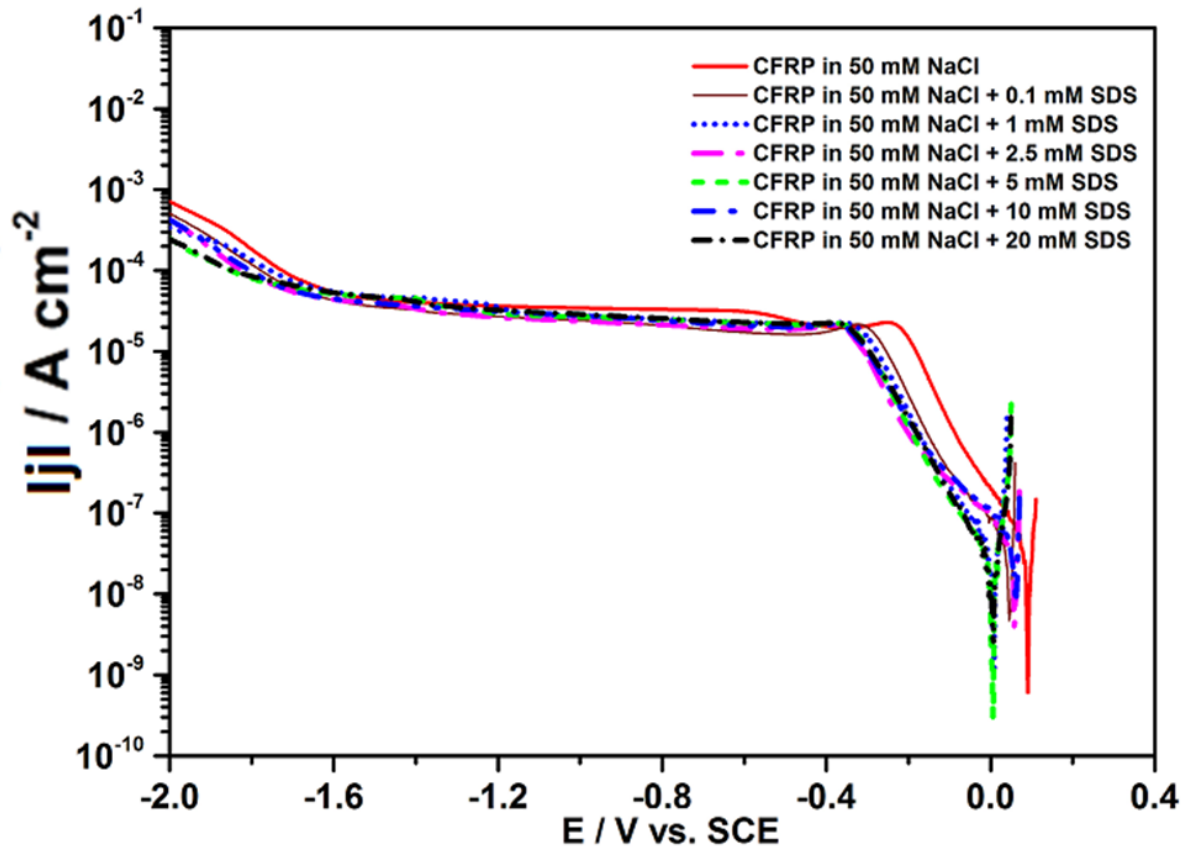


Fig. 5.39. Cathodic potentiodynamic polarization scans on CFRP in 50 mM NaCl with different concentrations of sodium dodecyl sulphate (SDS).

Fig 5.39. above presents the cathodic potentiodynamic polarization scans on CFRP in 50 mM NaCl solutions containing from 0 to 20 mM sodium dodecyl sulphate (SDS). From Fig. 5.39., the presence of SDS shifts in the OCP towards cathodic potentials. In addition a reduction in the cathodic current density in virtually the entire studied potential range (from OCP to -2000 mV_{SCE}) are observed in the presence of SDS. On the basis of these observations it is postulated that most probably due to the well known surfactant properties of SDS it is able to interact with the CFRP surface in a manner that retards oxygen transport to the surface (lower limiting diffusion current density) and electron transport across the interface that results in lower current densities above -1600 mV_{SCE} cathodic potentials for the secondary cathodic reaction of water reduction with hydrogen evolution. Additionally adsorption of SDS to the CFRP surface can suppress this cathodic reaction by inhibiting the atomic hydrogen re-combination step. However, confirmation of these postulations obviously require further tests.

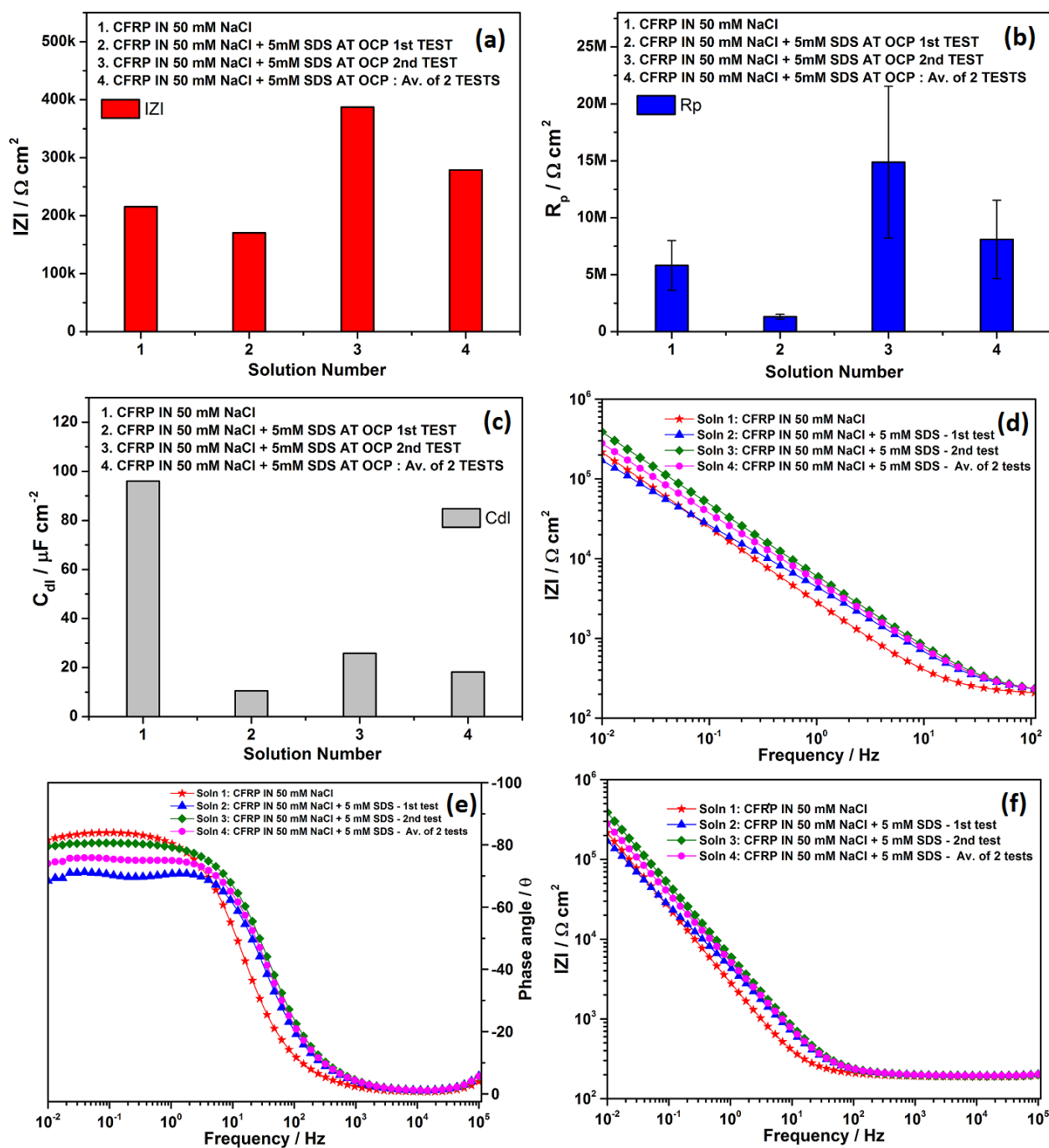


Fig. 5.40. Extracted EIS fit parameters for CFRP in 50 mM NaCl without cathodic polarization in the absence and presence of 5 mM SDS, (a) low frequency impedance at 10^{-2} Hz, (b) resistance polarization, (c) double layer capacitance, (d) inset of capacitive section of impedance spectra, (e) Phase angle plot, and (e) impedance spectra (full range).

Fig. 5.40 presents the effect of SDS on parameters such as (a) low frequency impedance at 10^{-2} Hz, (b) resistance polarization, (c) double layer capacitance, and (d) the measured impedance spectra for CFRP in quiescent 50 mM NaCl in the absence of cathodic polarization. From Fig. 5.40a it is observed that the presence of SDS markedly increased the low frequency impedance in the absence of a cathodic polarization. Correlating the enhanced impedance to the arrest of degradative processes, it is concluded that SDS in the absence of cathodic polarization inhibits

degradative processes on CFRP surface in the test media. From Fig. 5.40b increase in polarization resistance is observed in the presence of SDS indicating the presence of a greater barrier to charge and/or mass transfer processes across the CFRP-solution interface. From Fig. 5.40c about a four-fold reduction in the double layer capacitance is observed in the presence of SDS compared to values in the absence of SDS and any cathodic polarization. The observed marked reduction in double layer capacitance is inferred to arise from a decrease in the electrochemically active surface area due to adsorption of SDS to the carbon fiber surfaces in the CFRP and the retardation of degradative processes that promote the creation of more electrochemically active surface on the carbon fibers. This position is supported by the observed marked increase in the low frequency impedance values in the presence of SDS.

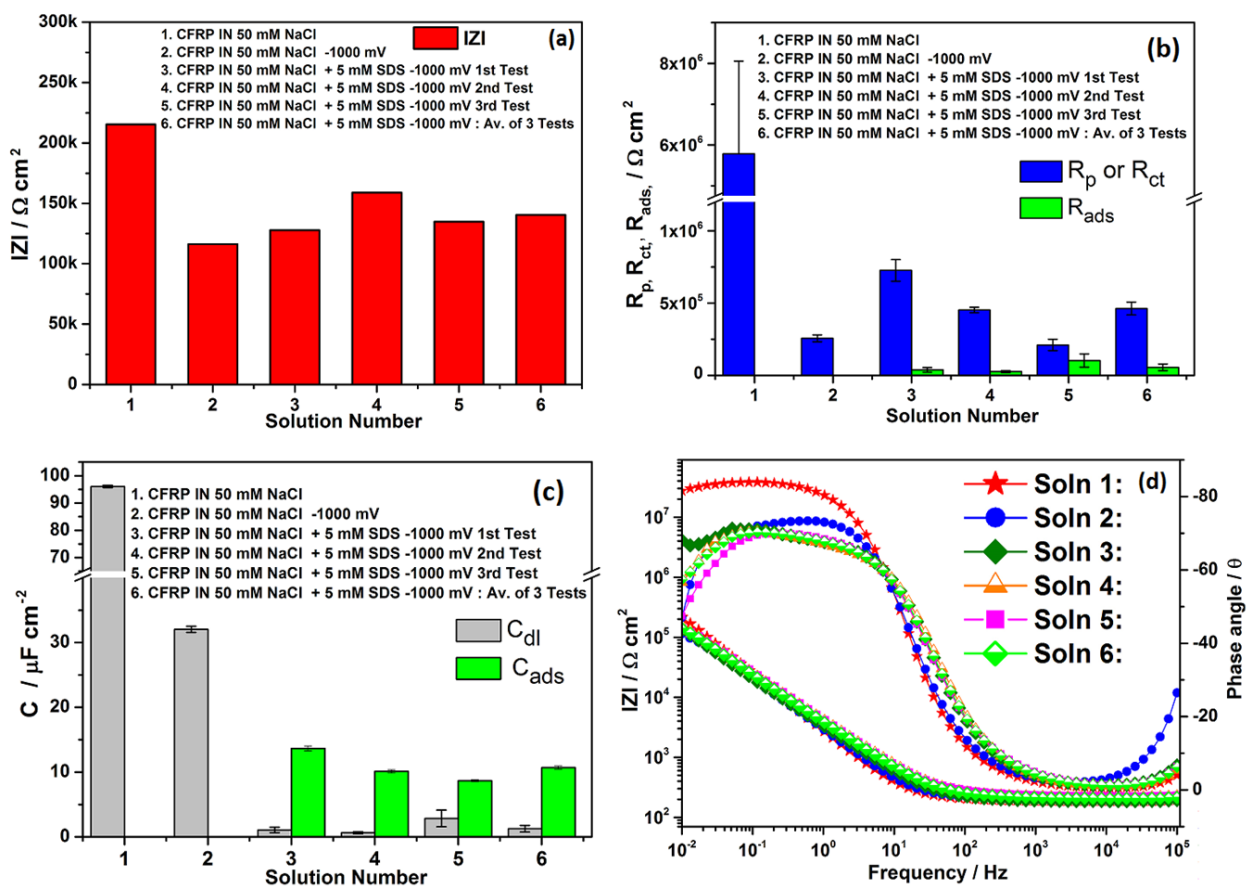


Fig. 5.41. Extracted EIS fit parameters for CFRP in 50 mM NaCl with applied cathodic polarization of $-1000 \text{ mV}_{\text{SCE}}$ in the presence of 5 mM SDS, (a) low frequency impedance at 10^{-2} Hz , (b) polarization resistance, (c) double layer capacitance, and (d) the bode plot.

In order to determine if the observed inhibitive effects are maintained under the kind of cathodic polarization the CFRP can be exposed in service on galvanic coupling with metals (such as aluminium and zinc), the EIS test are repeated in the absence and presence of 5 mM SDS and a cathodic polarization of $-1000 \text{ mV}_{\text{SCE}}$. The relevant parameters extracted from this test is presented in Fig. 5.41 above.

The results from electrochemical impedance spectroscopy on CFRP in quiescent 50 mM NaCl solution containing 5 mM SDS and under a cathodic polarization is presented in Fig. 5.42 above. The tests in the presence of SDS was done in triplicate and extracts and fitted parameters for each test presented along with the average values. From Fig. 5.41a (the low frequency impedance plot), it is observed that the low frequency impedance in the presence of SDS and cathodic polarization of $-1000 \text{ mV}_{\text{SCE}}$ is consistently slightly higher than that in the presence of cathodic polarization but without SDS, but smaller than that in the absence of both. Correlating IZI to general degradation of the CFRP, it is concluded that under the applied cathodic polarization the presence of SDS impedes composite degradation. Comparison of IZI values in the absence of a cathodic polarization, with and without SDS shows a marked increase in IZI values in the presence of SDS. From Fig. 5.41b it is observed that the polarization resistance, R_p , which is significantly diminished under cathodic polarization in SDS-free 50 mM NaCl solution is significantly increased in the presence of SDS. Such increase in R_p values is consistent with increased resistance to charge and/or mass transfer across the CFRP interface with the solution on introduction of SDS. Fig. 5.41c shows approximately 10-fold and 4-fold reduction in the double layer capacitance values with respect to values measured without and with applied cathodic polarization respectively. Such reduction in capacitance on introduction of SDS confirms that the increased R_p values in the presence of SDS (Fig. 5.41b) is definitely due to a reduction in the electrochemically active surface area by SDS adsorption on the carbon fiber surface of the CFRP.

To confirm if these observed effects can be sustained outside the SDS (inhibitor) containing solutions, 3 sets of sequential immersion and EIS tests were carried out after immersion and testing in SDS containing solutions in 50 mM NaCl. In the first sequential test the EIS spectra of CFRP is acquired in 50 mM NaCl containing 5mM SDS after 1 hour immersion without any cathodic polarization, and then in 50 mM NaCl only after another hour immersion without any cathodic polarization. The aim was to establish if inhibitive effects after immersion in SDS containing solutions at OCP is sustained in aggressive media in the absence of inhibitors. In the second sequential test, the EIS spectra of CFRP is acquired in 50 mM NaCl containing 5mM SDS after 1 hour immersion under a cathodic polarization of $-1000 \text{ mV}_{\text{SCE}}$, and again after 1 hour immersion in the same solution but without cathodic polarization. In the third sequential test the EIS spectra of CFRP is acquired in 50 mM NaCl containing 5 mM SDS after 1 hour immersion under a cathodic polarization of $-1000 \text{ mV}_{\text{SCE}}$, and then in 50 mM NaCl after another hour immersion with a sustained cathodic polarization of $-1000 \text{ mV}_{\text{SCE}}$. The aim of this sequence of

tests was to confirm if inhibitive effects in SDS containing solutions under cathodic polarization are sustained on exposure under cathodic polarization in uninhibited solutions. Prior to transfer to a new test solution the sample was washed by dipping severally in distilled water and under a jet of distilled water. The results from these sequential tests are presented in Fig. 5.42 below.

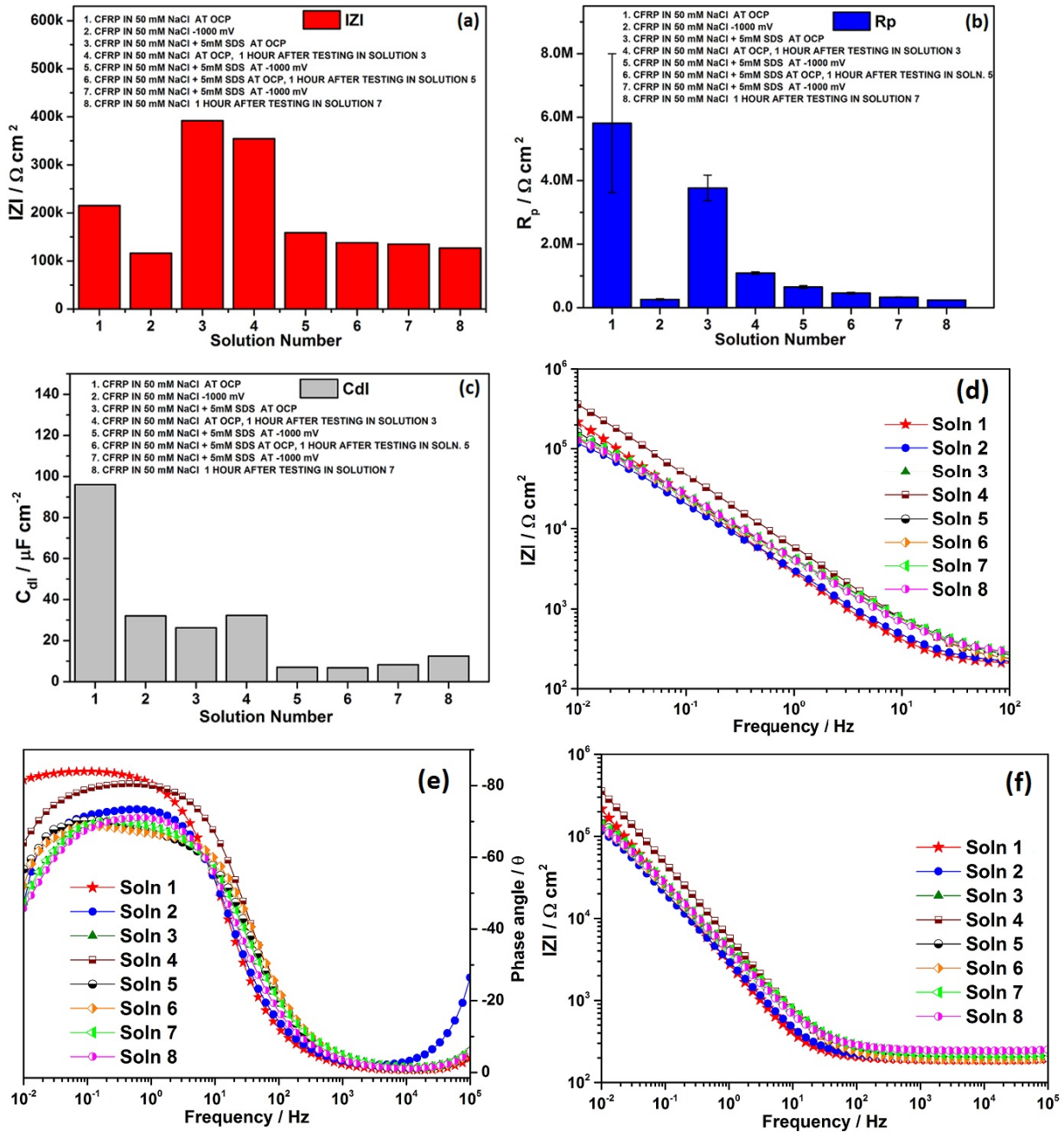


Fig. 5.42. Extracted EIS fit parameters for sequential tests on CFRP, (a) low frequency impedance at 10^{-2} Hz, (b) resistance polarization, (c) double layer capacitance, (d) section of impedance spectram (e) phase angle , and (f) full range of impedance spectra.

From Fig. 5.42a above it is observed that a marked improvement is obtained in the low frequency impedance in the presence of SDS and without any polarization (solution 3) and sustained after washing in distilled water and testing in 50 mM NaCl without applied cathodic

polarization (solution 4) compared to values obtained in 50 mM NaCl (solution 1) without prior immersion in SDS containing solution. This results indicate that the inhibitive effects obtained by immersion in SDS containing solution at OCP is sustained on removal from the inhibitor solution and on exposure to aggressive media. Comparing solutions 5 and 6 with solution 2 in Fig. 5.42a, it is observed that addition of 5 mM SDS to 50 mM NaCl causes an increase in the measured low frequency impedance even under a cathodic polarization of -1000 mV (solution 5) compared to the value obtained in uninhibited solution under cathodic polarization (solution 2). On re-testing the sample in same inhibited solution after a further 1 hour immersion but without an applied cathodic polarization (solution 6) the IZI values obtained were marginally higher than that obtained in same solution with applied cathodic polarization and in the uninhibited solution (solution 2) with cathodic polarization. Though marginal, these observations suggest that the inhibitive effect of SDS on CFRP degradation is sustained both in the presence and absence of a cathodic polarization. Comparing the sustained and higher IZI values obtained both after testing under cathodic polarization in inhibited solution (solution 7) and after washing in distilled water and testing in uninhibited solution after 1 hour immersion under cathodic polarization (solution 8) with values obtained in uninhibited solution under cathodic polarization (solution 2) confirms the stability of the inhibitive effect imparted by immersion of CFRP in SDS containing solution with or without cathodic polarization.

From Fig. 5.42b, it is observed that irrespective of the testing sequence on application of cathodic polarization and after application of a cathodic polarization the measured values of the polarization resistance (R_p) was consistently and significantly higher than values measured in uninhibited solution with cathodic polarization (solution 2). This observation is indicative of an increased and sustained resistance to charge transfer and /or mass transfer processes after exposure of CFRP to SDS laden solutions.

From Fig. 5.42c, a marginal reduction in the double layer capacitance is observed in SDS containing test media without cathodic polarization (solution 3) but was not sustained after washing in distilled water and testing in 50 mM NaCl after 1 hour immersion without cathodic polarization. However on application of and/or after application of cathodic polarization of -1000 mV_{SCE} (solutions 5,6,7, and 8) in the presence of SDS a sustained and very significant reduction in the double layer capacitance is observed even after washing in distilled water and testing in uninhibited solution and without cathodic polarization (solution 8). This observation suggests that the application of a cathodic polarization promotes a stable interaction (adsorption) of SDS with the carbon fiber surfaces on the CFRP leading to a sustained reduction

in the electrochemically active surface area. Such reduction of electrochemically active surface area on CFRP under cathodic polarization in the presence of SDS holds promise to mitigating the deleterious cathodic oxygen reduction processes that occur on CFRP when galvanically coupled to a range of metals.

5.2.8.3. Effect of Azoles (BIA, BTA, 1,2,3- triazole and 1,2,4- triazole)

Fig 5.43. below illustrates the cathodic potentiodynamic polarization scans on CFRP in 50 mM NaCl solutions containing (a) 1,2,3 - triazole and (b) 1,2,4 - triazole in varying concentrations ranging from 0 to 10 mM. It is observed that the two inhibitors are stable over the pH range from OCP to $-2000 \text{ mV}_{\text{SCE}}$. However from Fig 5.43a an apparent reduction in the limiting cathodic current density due to oxygen transport is observed in the presence of 1,2,3 - triazole.

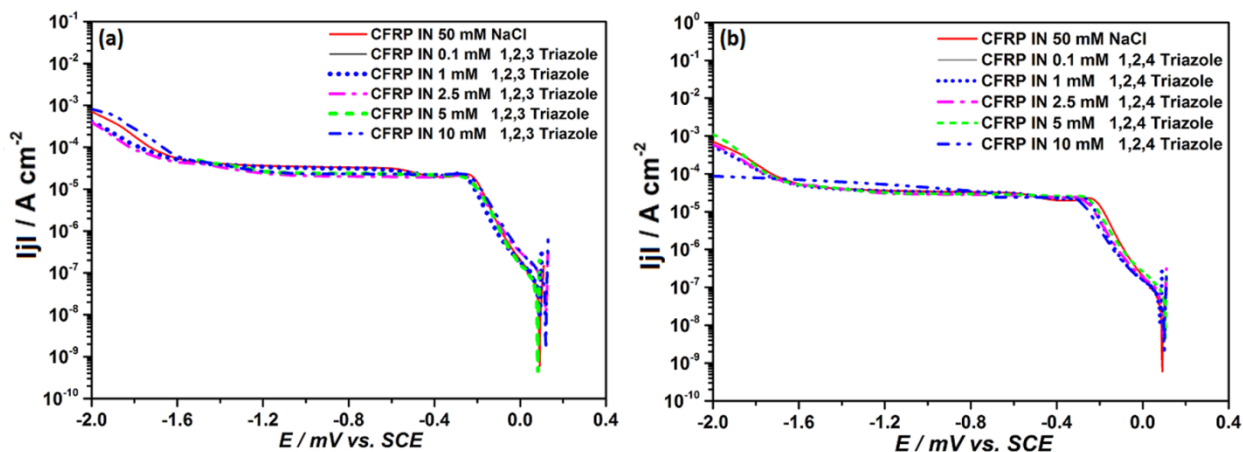


Fig. 5.43. Cathodic potentiodynamic polarization scans on CFRP in different concentrations of (a) 1,2,3 - triazole and (b) 1,2,4 - triazole.

Fig 5.44. below presents the cathodic potentiodynamic polarization scans on CFRP in 50 mM NaCl solutions containing (a) benzimidazole (BIA) and (b) benzotriazole (BTA) in varying concentrations ranging from 0 to 10 mM. From Fig 5.44(a), benzimidazole is stable over the entire cathodic potential range and does not exert any significant effects on cathodic reactions on CFRP in the studied concentration range. In contrast (Fig. 5.44(b)), benzotriazole appears to cause marginal reduction in the cathodic current densities at low concentration but appears to become reactive at cathodic potentials greater than $-1400 \text{ mV}_{\text{SCE}}$ as observed from the emergence of shoulders of higher current densities at benzotriazole concentrations of 5 mM and 10 mM. The observed increase of these shoulders with increasing benzotriazole concentration links the current source to the inhibitor and informs the conclusion that the increased current density is most probably due to benzotriazole electro-decomposition at such cathodic potentials.

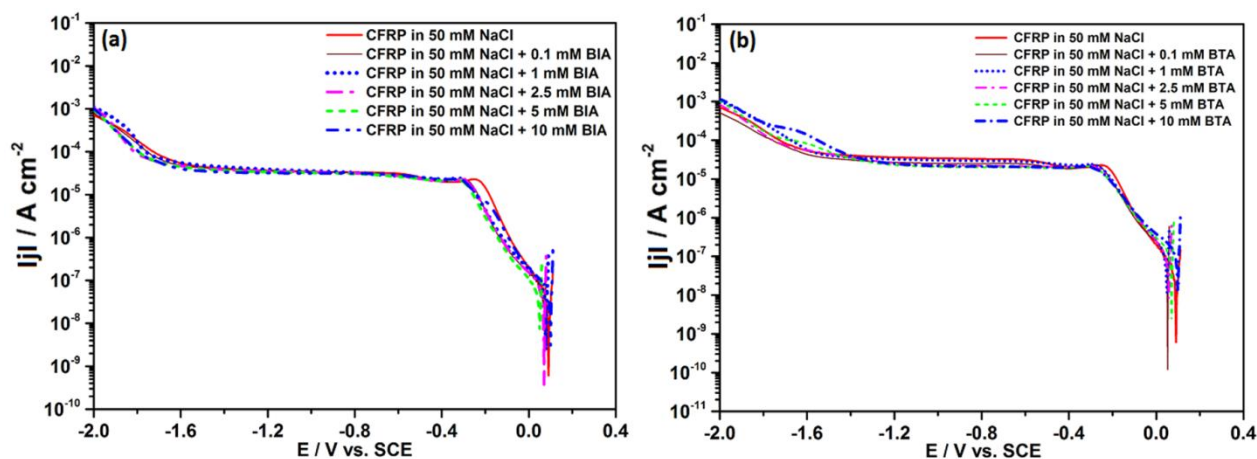


Fig. 5.44. Cathodic potentiodynamic polarization scans on CFRP in different concentrations of (a) benzimidazole (BIA) and (b) benzotriazole (BTA).

Fig. 5.45 below presents the results obtained from electrochemical impedance spectroscopy of the effect of azole type inhibitors on CFRP at a cathodic polarization of $-1000 mV_{SCE}$ from which it is observed that the low frequency impedance (Fig. 5.45a) is increased in the presence of all the azoles (benzotriazole, benzimidazole, 1,2,3-triazole and 1,2,4-triazole) studied and their mixtures (1,2,3- and 1,2,4- triazole). Correlating higher low frequency impedance values to increased resistance to CFRP degradation, it can be concluded that the presence of the azoles retard CFRP degradation under cathodic polarization conditions. This position is supported by the polarization resistance plot (Fig. 5.45b) in which at least a 20-fold increase is observed in the polarization resistance values in the presence of each of the azoles compared to values in their absence. The observed increase in polarization resistance indicates an increase in the resistance to charge and mass transfer processes which could promote degradation. From Figs. 5.45c and 5.45d, higher capacitance values are observed in the presence of 1,2,3-triazole, 1,2,4-triazole, and their combinations compared to values in the absence of azoles under cathodic polarization, while the reverse is the case in the presence of benzotriazole and benzimidazole.

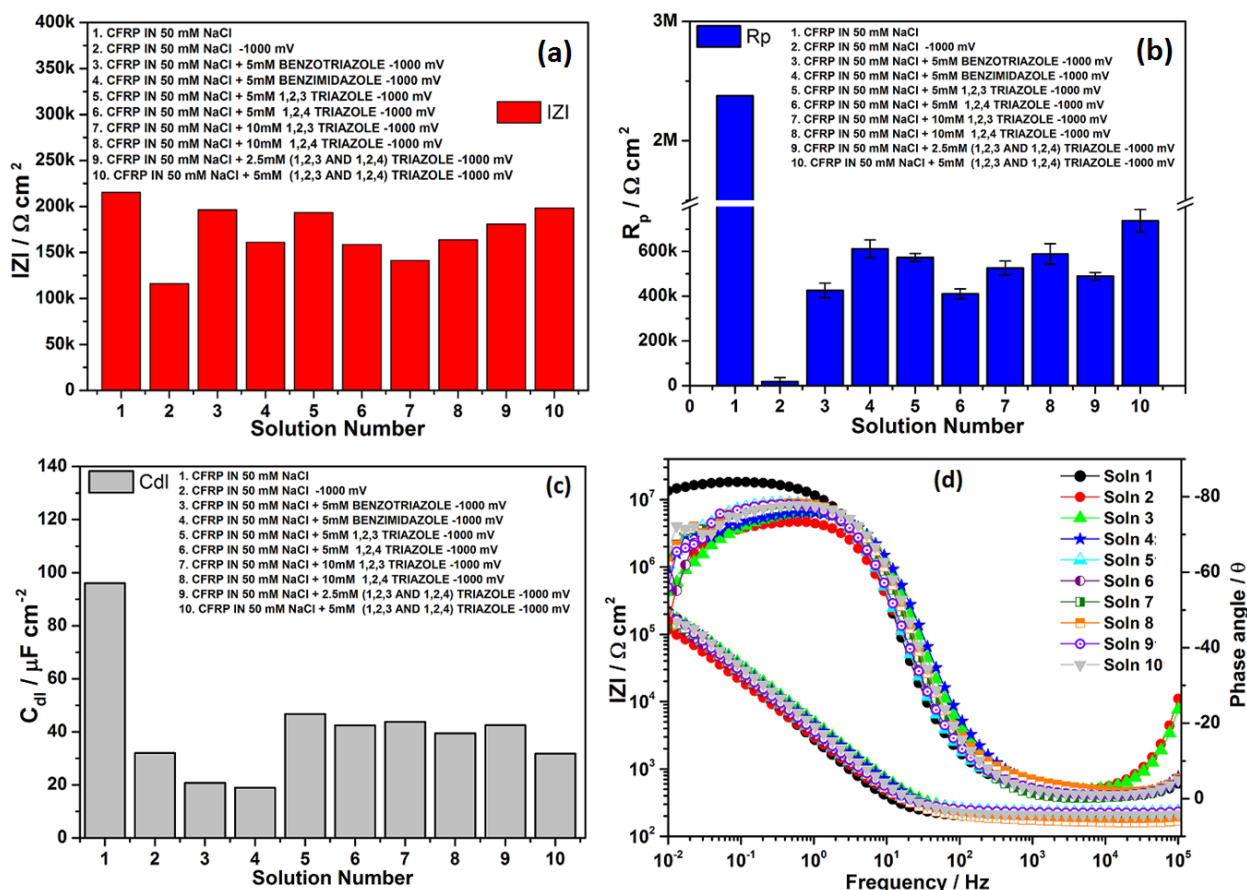


Fig. 5.45. Extracted EIS fit parameters for CFRP in 50 mM NaCl with applied cathodic polarization of -1000 mV_{SCE} in the presence of different azoles compounds, (a) low frequency impedance at 10⁻² Hz, (b) polarization resistance, (c) double layer capacitance and (d) the bode plot of the measured spectra.

5.2.8.4. Effect of Nitrates and Nitrite.

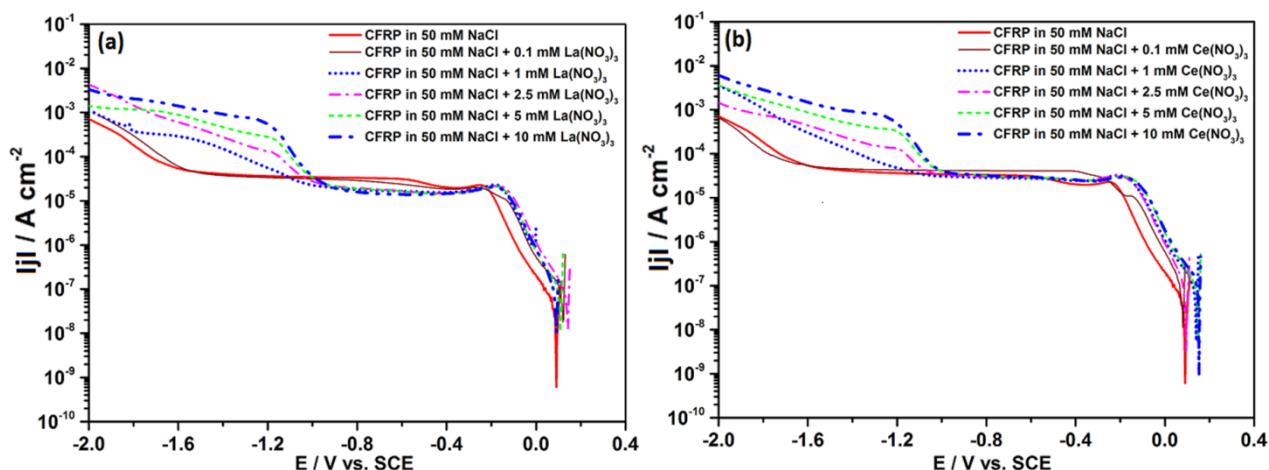


Fig. 5.46. Cathodic potentiodynamic polarization scans on CFRP in 50 mM NaCl with different concentrations of (a) lanthanum nitrate and (b) cerium nitrate.

Potentiodynamic polarization tests on CFRP in quiescent 50 mM NaCl solution yielded interesting results. Fig 5.46(a and b), above presents the cathodic potentiodynamic polarization scans on CFRP in 50 mM NaCl solutions containing from 0 to 10 mM lanthanum nitrate (a) and

(b) cerium nitrate respectively. From Fig. 5.46(a) a significant reduction in the limiting cathodic current density is observed in the presence of lanthanum nitrate but over a much shorter potential range compared to lanthanum acetate below (Fig. 5.49). At cathodic polarizations greater than $-950 \text{ mV}_{\text{SCE}}$, early onset of the increased current density shoulders that are normally attributed to the onset of the predominance of another cathodic reaction; water reduction with hydrogen evolution is observed but in this case attributed the cathodic decomposition of nitrates from the inhibitor. This attribution is based on the dependence of the increased cathodic current density in this potential range on lanthanum nitrate concentration and the almost congruent onset potential ($\approx -960 \text{ mV}_{\text{SCE}}$) which from the literature [684,685] is consistent with the potential for nitrate reduction under the test conditions. This conclusion finds further support in the observation of similar onset potential in the presence of cerium nitrate (Fig. 5.46(a)) that is coupled with an identical increased current density trend and dependence on increasing inhibitor concentration. Any suggestion that such increased current density shoulders may be due to rare-earth ion (Ce^{3+} or La^{3+}) reduction is ruled out by the absence of such in 50 mM NaCl solution containing cerium chloride (Fig. 5.47 below).

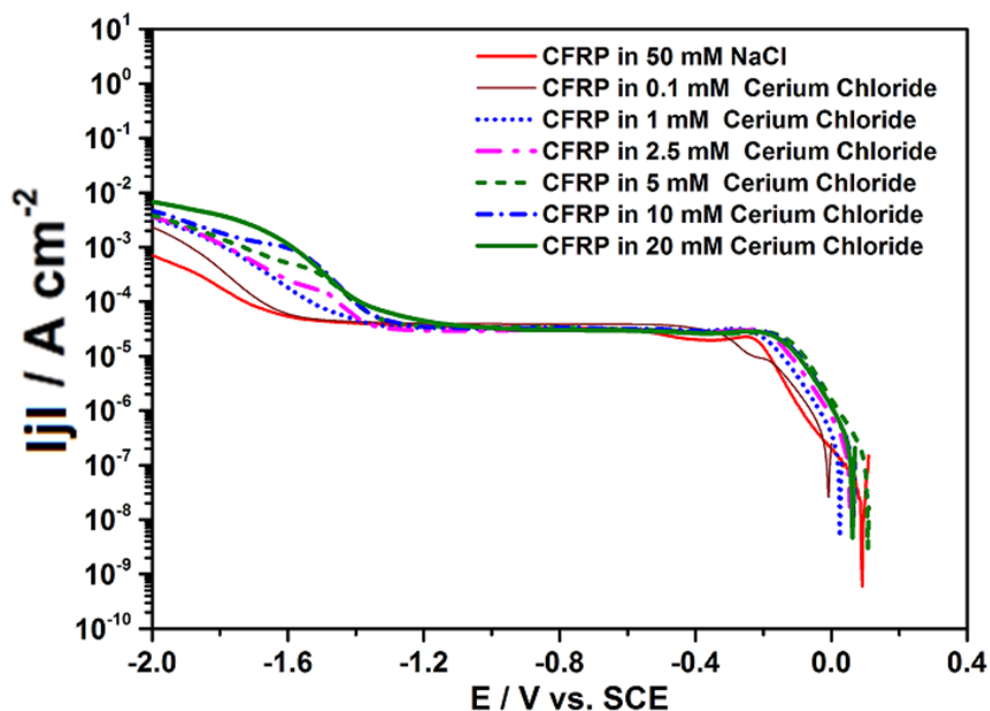


Fig. 5.47. Cathodic potentiodynamic polarization scans on CFRP in 50 mM NaCl with different concentrations of cerium chloride.

Further studies on the effect of nitrates and nitrite on CFRP in 50 mM NaCl solution under cathodic polarization was carried out using electrochemical impedance spectroscopy and a cathodic polarization of $-1000 \text{ mV}_{\text{SCE}}$, and the result presented in Fig. 5.48 below. From Fig.

5.48a and 5.48b, significantly smaller low frequency impedance values compared to that in the absence of inhibitors (solution 2) is observed in the presence of all the rare-earth nitrates and sodium nitrite. Analyzing these results in the light of earlier observations of nitrate decomposition above 950 mV_{SCE} (Fig. 5.46), these low values are attributed to nitrate decomposition. However values in the presence of sodium nitrate appears unchanged with an apparent marginal improvement in the presence of sodium nitrite. From Fig. 5.48b, very significant improvements (over 6-folds) in polarization resistance are observed in the presence of sodium nitrate and sodium nitrite. Of the rare earth nitrates studied increased polarization resistance values were observed only in the presence of cerium nitrate. Significant improvements (decrease) in capacitance was observed in the presence of sodium nitrate and praesodymium nitrate while a reduction was observed in the presence of cerium nitrate (Fig. 5.48c and d).

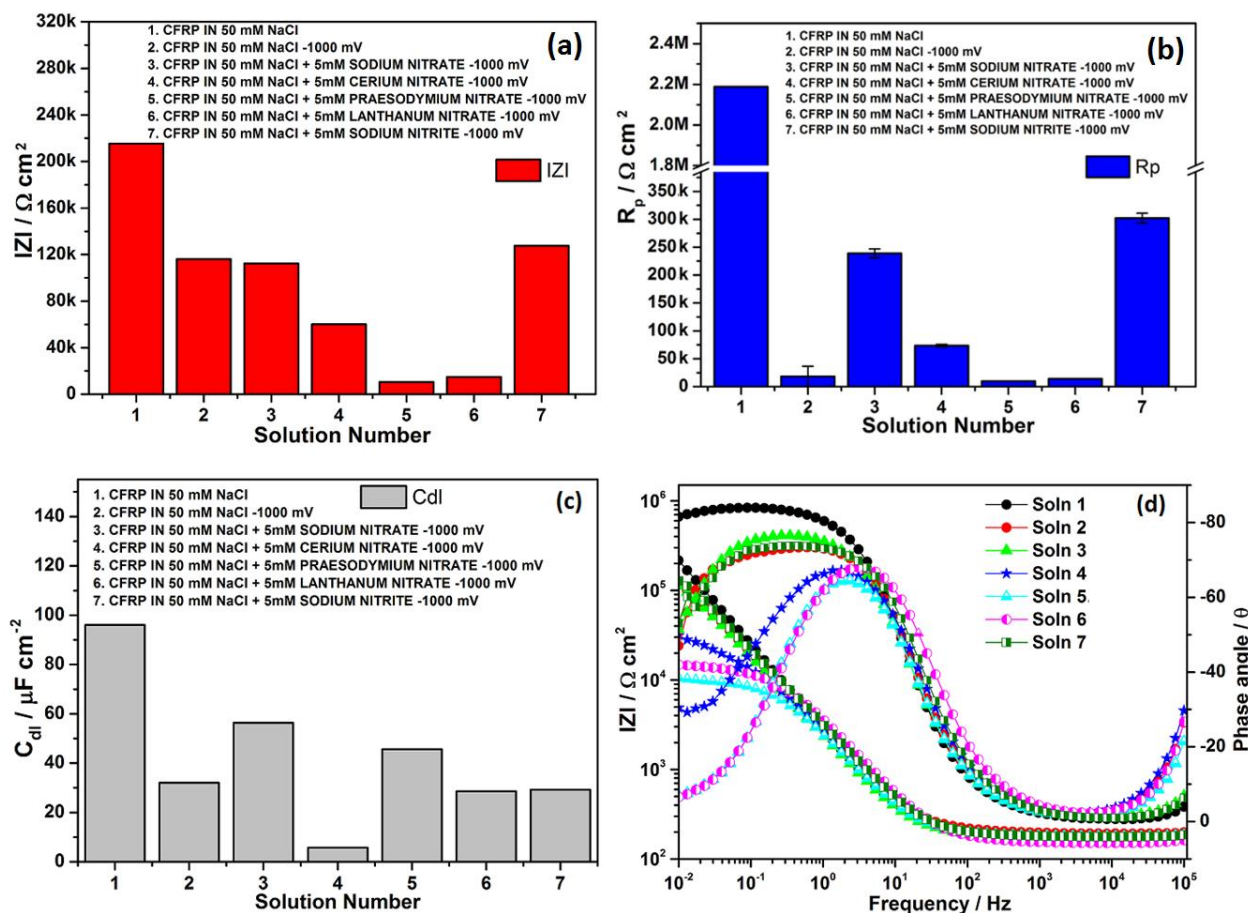


Fig. 5.48. Extracted EIS fit parameters for CFRP in 50 mM NaCl with applied cathodic polarization of -1000 mV_{SCE} in the presence of different nitrate and nitrite based solutions, (a) low frequency impedance at 10^{-2} Hz, (b) polarization resistance, (c) double layer capacitance, and (d) the bode plot of the measured spectra.

From a comparative analysis of the potentiodynamic polarization test results for CFRP in the presence of a variety of nitrates and nitrites presented above, it is concluded that the nitrates

and nitrites are not able to significantly effect a reduction in the cathodic current densities with the exception of lanthanum nitrate in which a significant reduction in the limiting cathodic current density was observed. Since a significant reduction in the limiting cathodic current density was observed only in the concomitant presence of La^{3+} ion and NO_3^- ion of all the nitrates and also observed with lanthanum acetate (Fig. 5.49), this effect is directly linked to the presence of La^{3+} ion. Hence it concluded that the presence of the rare-earth ion; La^{3+} leads to reduction in the limiting cathodic current density on CFRP in a process that is not yet understood.

5.2.8.5. Effect of Acetates and Rare Earth Cations

Fig. 5.49. below presents the cathodic potentiodynamic polarization scans on CFRP in 50 mM NaCl solutions containing from 0 to 10 mM lanthanum acetate, from which a significant reduction in the limiting cathodic current density is observed for lanthanum acetate concentrations greater than 0.1 mM with the reduction apparently reducing with increasing lanthanum acetate concentrations. However at cathodic potentials greater than $-1400 \text{ mV}_{\text{SCE}}$ the lanthanum acetate appears to promote the cathodic water reduction processes as evidenced by increased current densities above that in the blank solution, though the trend of the increase is at variance with the concentration of lanthanum acetate.

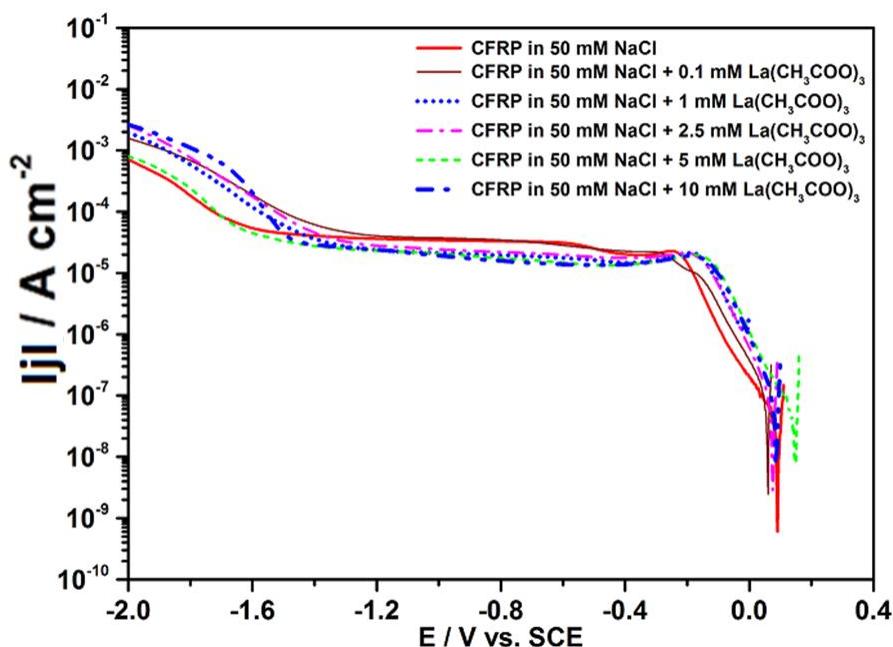


Fig. 5.49. Cathodic potentiodynamic polarization scans on CFRP in 50 mM NaCl with different concentrations of lanthanum acetate.

From the potentiodynamic polarizarion curves presented in Fig. 5.49 above for CFRP in lanthanum acetate solutions of different concentrations and comparison of similar curves in

the presence of rare-earth nitrates (Fig. 5.46) and the rare-earth (cerium) chloride (Fig. 5.47), the unique ability of the rare-earth cation; La^{3+} in suppressing the cathodic current density in the diffusion limited region is established.

Further studies were carried out using electrochemical impedance spectroscopy and four additional acetates at a cathodic potential and the results presented in Fig. 5.50 below. From Fig. 5.50, increased low frequency impedance (Fig. 5.48a), enhanced polarization resistance (Fig. 5.50b) and increase in double layer capacitance (Fig. 5.50c and d), are only observed in the presence of sodium acetate, indicating its beneficial effects under the test conditions.

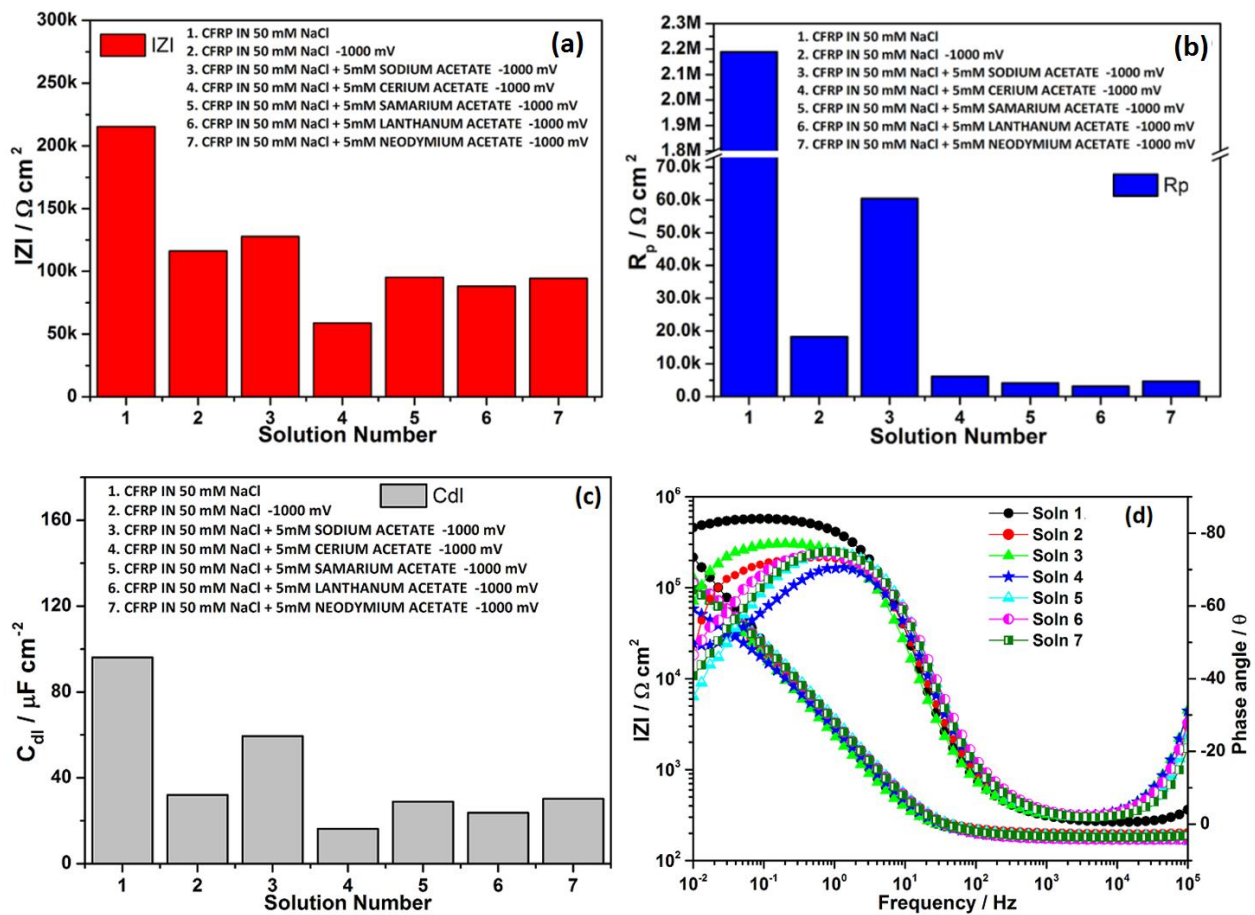


Fig. 5.50. Extracted EIS fit parameters for CFRP in 50 mM NaCl with applied cathodic polarization of $-1000 \text{ mV}_{\text{SCE}}$ in the presence of different acetate based solutions, (a) low frequency impedance at 10^{-2} Hz , (b) polarization resistance, (c) double layer capacitance, and (d) the bode plot of the measured spectra.

On the basis of these observations, it is advanced that sodium acetate is very likely to be a potential candidate in a combination of inhibitors for inhibiting cathodic reactions on CFRP on galvanic coupling with metals in a multi-material combination that does not polarize the CFRP beyond $-1400 \text{ mV}_{\text{SCE}}$ such as Al - CFRP and Zn - CFRP galvanic systems.

5.2.8.6. Effect of Phosphates (Na_3PO_4 and NaH_2PO_4 , $\text{NaH}_2\text{P}_2\text{O}_7$) and Molybdate (Na_2MoO_4)

Cathodic potentiodynamic polarization tests on phosphates (Fig.5.51) and sodium molybdate (Fig.5.52) yielded interesting results in the presence of phosphates which was further studied using electrochemical impedance spectroscopy. In Fig. 5.51(a and b) below presenting the cathodic potentiodynamic polarization scans on CFRP in 50 mM NaCl solutions containing from 0 to 10 mM Na_3PO_4 and NaH_2PO_4 interesting effects on the limiting cathodic current density which appeared reduced were observed. Such reduction in the limiting cathodic current density suggests either a reduction in oxygen transport to the electrochemically active composite surface or increased resistance to the charge transfer processes leading to their consumption. Irrespective of the cause such a phenomenon if consistent, presents the phosphates as a candidate inhibitor for suppression of cathodic processes on CFRP under cathodic polarization conditions.

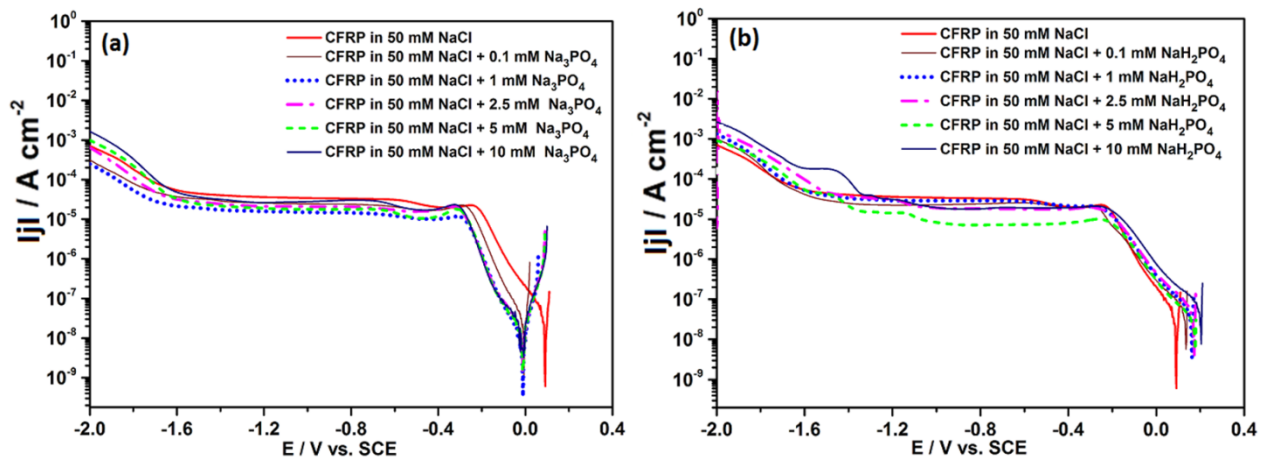


Fig. 5.51. Cathodic potentiodynamic polarization scans on CFRP in 50 mM NaCl with different concentrations of Na_3PO_4 and NaH_2PO_4 .

In Fig. 5.52. below presenting the cathodic potentiodynamic polarization scans on CFRP in 50 mM NaCl solutions containing from 0 to 10 mM sodium molybdate no effects on the limiting cathodic current density but the same early onset of increase in current density (observed with nitrates) was recorded but started at $\approx -1200 \text{ mV}_{\text{SCE}}$ in the highest molybdate concentration (10 mM) and around $-1400 \text{ mV}_{\text{SCE}}$ for other inhibitor concentrations. An increase in the current densities with increased molybdate concentration was recorded and hence the phenomenon is attributed to cathodic reduction of the molybdate.

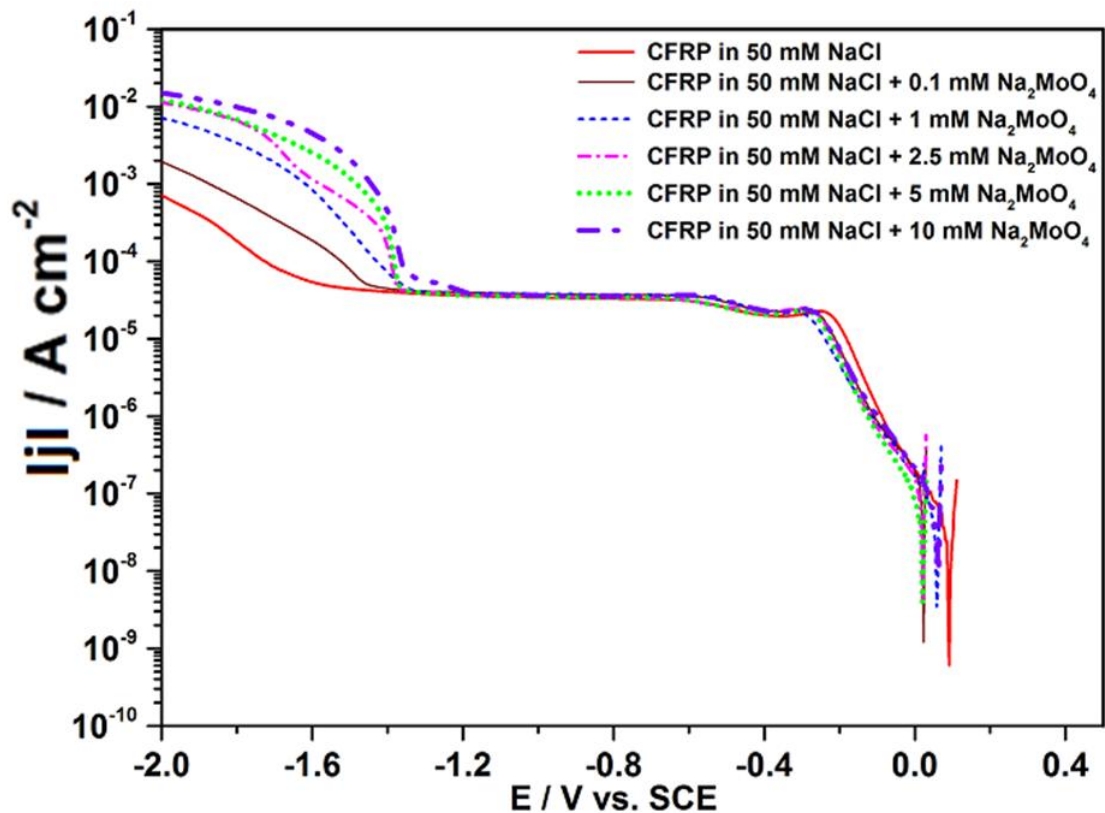


Fig. 5.52. Cathodic potentiodynamic polarization scans on CFRP in 50 mM NaCl with different concentrations of sodium molybdate.

Electrochemical impedance spectroscopy results of studies on CFRP in 50 mM NaCl in the presence of phosphates and molybdate are presented in Fig. 5.53 below. From Fig. 5.53a increase in low frequency impedance is observed in the presence of Na_3PO_4 and Na_2MoO_4 while increased polarization resistance (Fig. 5.53b) is observed in the presence of all the phosphates and molybdate tested, but very significantly in the presence of Na_3PO_4 compared to values at -1000 mV_{SCE} without inhibitors. From Figs. (Fig. 5.53c and d) very significant increase in the capacitance compared to values at -1000 mV_{SCE} without inhibitors, and similar to values obtained for CFRP in the absence of inhibitors and cathodic polarization (solution 1) is observed in the presence of Na_3PO_4 and suggestive of the presence of a layer on the CFRP surface which is inferred from earlier potentiodynamic polarization scans (Fig. 5.51a) and the significantly increased polarization resistance (Fig. 5.53b) to be protective. On the strength of these observations (Fig. 5.53b) Na_3PO_4 , is further advanced as a candidate inhibitor for suppression of cathodic processes on CFRP under cathodic conditions consistent with its galvanic coupling to active metals.

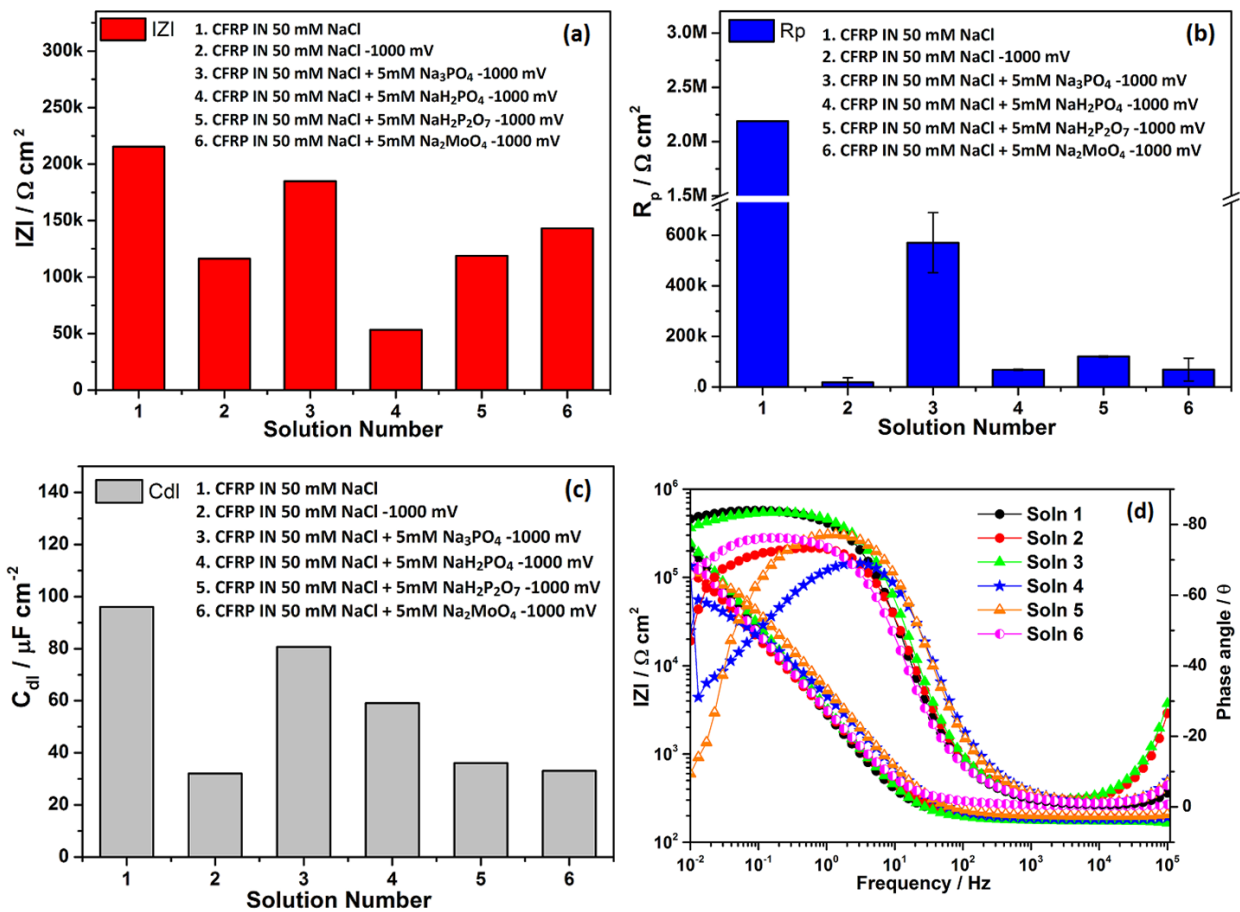


Fig. 5.53. Plots of (a) low frequency impedance (IZI), (b) polarization resistance (Rp) , and (c) double layer capacitance for CFRP under -1000 mV_{SCE} cathodic polarization in different phosphate and molybdate based solutions.

5.2.9.0. Effect of a Combination of Inhibitors

In a further bid to explore possibilities of suppressing cathodic activity on CFRP surface under cathodic polarization consistent with that anticipated in service on galvanic coupling with metals cathodic, a combination of corrosion inhibitors were studied. Results of potentiodynamic and EIS test conducted with different combinations of inhibitors are results presented below.

5.2.4.9.1. Effect of Combination of Polarization and Inhibitor Combination Containing Nitrates.

In Fig. 5.54. below, illustrating the cathodic potentiodynamic polarization scans on CFRP in 50 mM NaCl solutions containing a combination of cerium nitrate and benzotriazole in respective concentrations ranging from 0 to 10 mM, some suppression of the limiting cathodic current density is observed in addition to the concentration dependent increase in current densities at more cathodic potentials earlier observed with nitrate containing solutions, and

attributed to the electroreduction of the nitrates. However, unlike in the presence of cerium nitrate alone (Fig 5.46b) in which the onset potential was around $-1000 \text{ mV}_{\text{SCE}}$, it was recorded at a more cathodic potential, $\approx -1200 \text{ mV}_{\text{SCE}}$ with the addition of benzotriazole. Apparently the benzotriazole increases the stability range of the nitrate by about 200 mV.

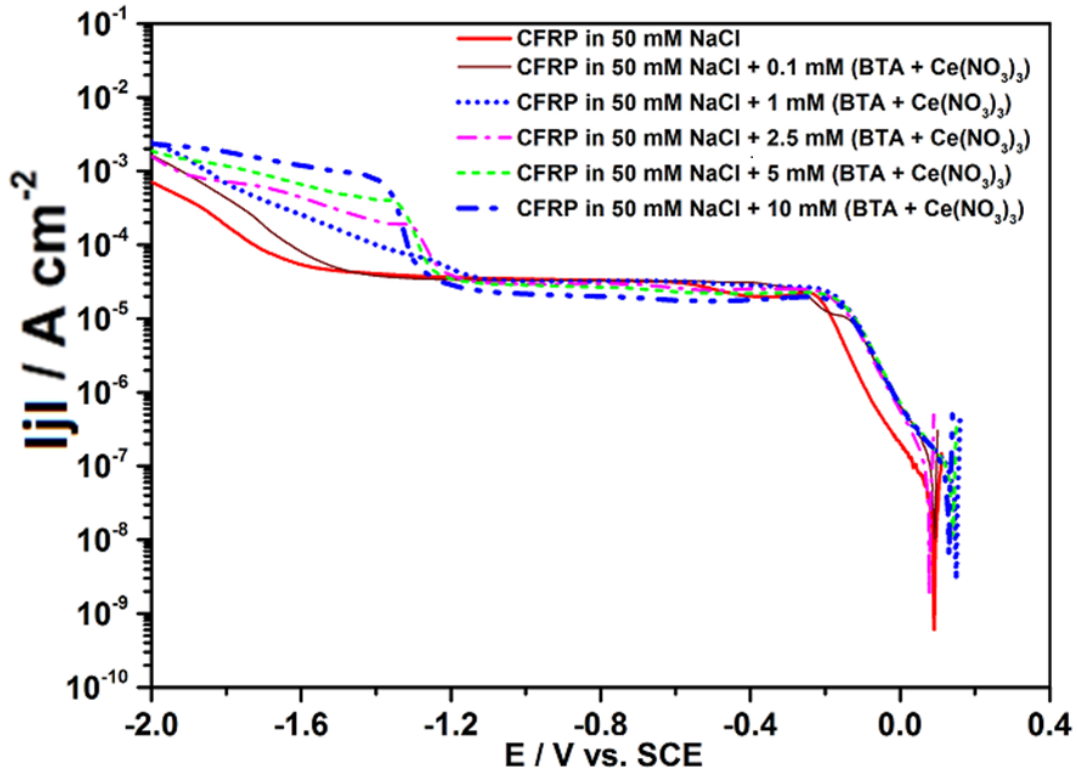


Fig. 5.54. Cathodic potentiodynamic polarization scans on CFRP in 50 mM NaCl with different concentrations of the combination of cerium nitrate and benzotriazole.

EIS test results on CFRP using combinations of inhibitors composed of nitrates and benzotriazole under cathodic polarization is presented in Fig. 5.55 below. Very spectacular increase is observed in the low frequency impedance values (Fig. 5.52a) in the presence of sodium nitrate and benzotriazole compared to values under same cathodic polarization without inhibitors (2-fold compared to solution 2) and even higher than values obtained for uninhibited and unpolarized samples. From Fig. 5.55b, very significant increase (> 10 -fold) is observed in the polarization resistance value in the presence of sodium nitrate and benzotriazole combination (solution 3) compared to values under similar cathodic polarization but without inhibitor (solution 2). The same trend of higher values can be observed for the capacitance values in the middle frequency range in the presence of sodium nitrate and benzotriazole combination. In the light of these results the sodium nitrate and benzotriazole combination is advanced as a possible synergistic inhibitor combination for suppression of cathodic processes on CFRP galvanically coupled to active metals.

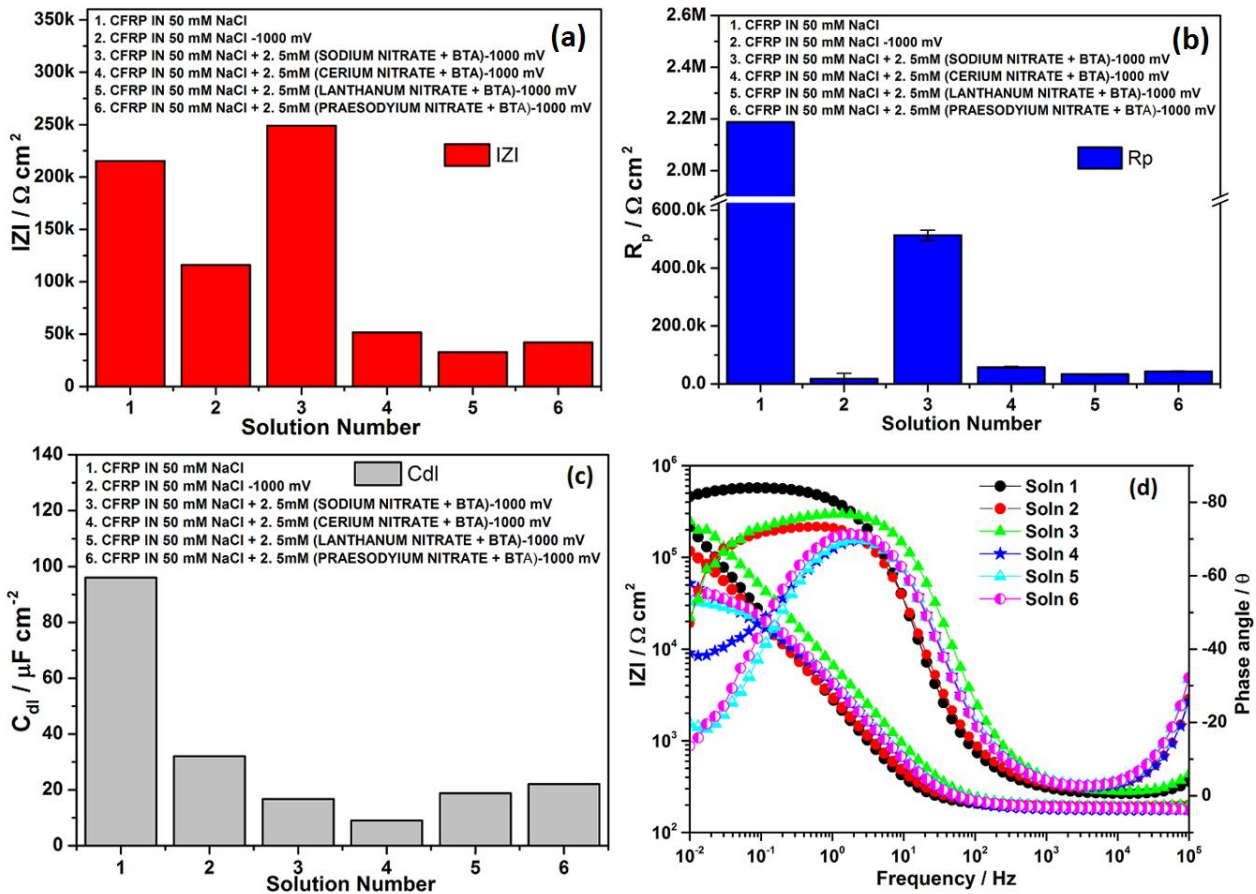


Fig. 5.55. Plots of (a) low frequency impedance (IZI), (b) polarization resistance (Rp), (c) double layer capacitance, and (d) measured EIS spectra for CFRP under -1000 mV_{SCE} cathodic polarization in 50 mM NaCl containing different combinations of nitrates and benzotriazole.

5.2.4.9.2. Effect of Combination of Polarization and Inhibitor Combination Containing Acetates and BTA.

In Fig 5.56. below, the results of electrochemical impedance spectroscopy tests on CFRP in 50 mM NaCl in the presence of combinations of inhibitors composed of acetates and benzotriazole under cathodic polarization conditions are presented.

From Fig. 5.56(a), judging from the low frequency impedance values the presence of the combination comprised of 2.5 mM cerium acetate and 2.5 mM benzotriazole appear to cancel the (degradation) effect due to the applied cathodic polarization of -1000 mV_{SCE}, as values obtained under cathodic polarization in the presence of this combination is quite similar to the high values measured in the absence of cathodic polarization. Even in the polarization resistance plot (Fig. 5.56b), the superior performance of this combination is sustained in the more than 10-fold increment in polarization resistance in the presence of the combination comprised of 2.5 mM cerium acetate and 2.5 mM benzotriazole compared to values in its absence (solution 2). It

is also observed that the polarization resistance values improved in the presence of all the studied inhibitor combinations comprised of acetates and benzotriazole. From 5.53d, higher capacitance is observed in the presence of the combination comprised of 2.5 mM cerium acetate and 2.5 mM benzotriazole compared to values in its absence (solution 2).

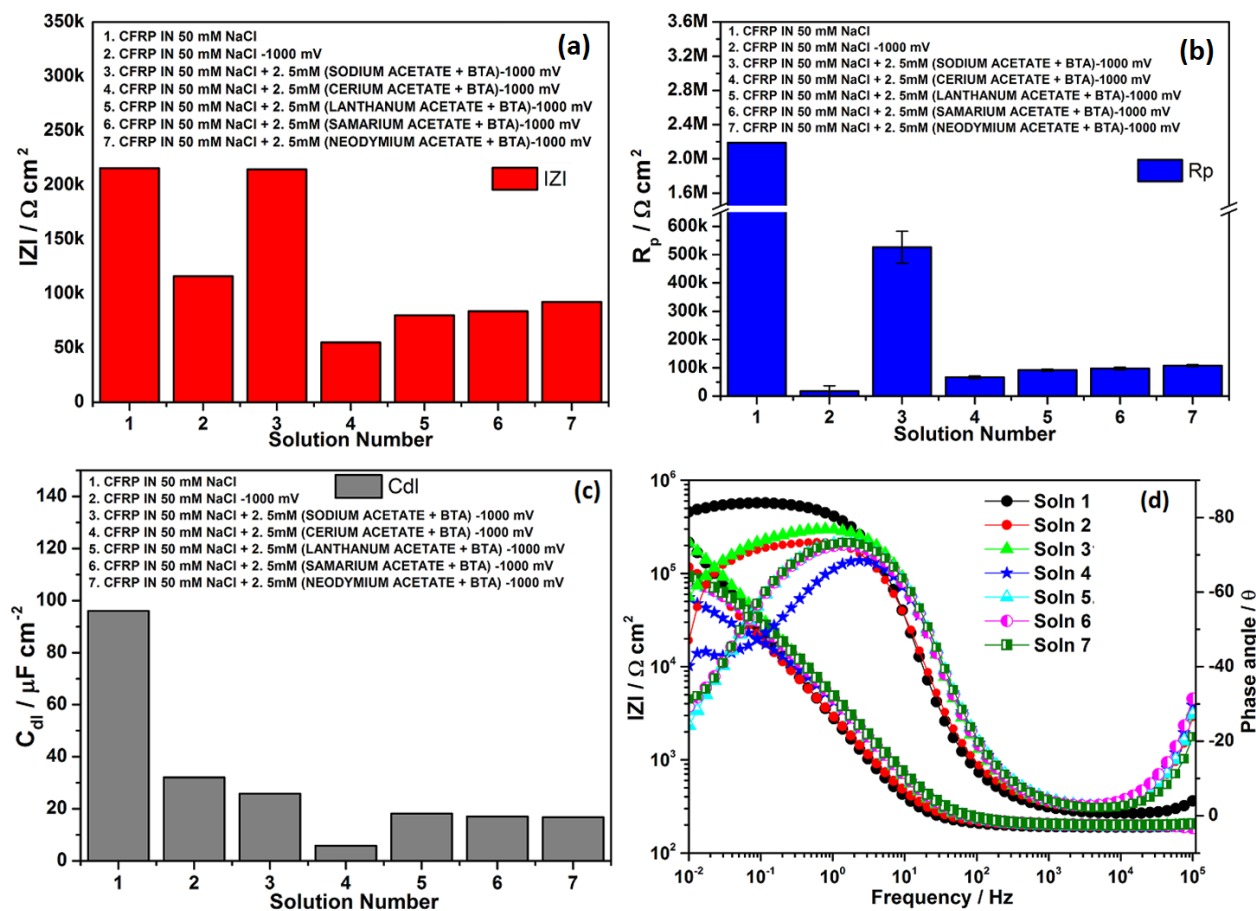


Fig. 5.56. Plots of (a) low frequency impedance (IZI), (b) polarization resistance (R_p), (c) double layer capacitance, and (d) measured EIS spectra for CFRP under $-1000 \text{ mV}_{\text{SCE}}$ cathodic polarization in 50 mM NaCl containing different combinations of acetates and benzotriazole.

5.3 Chapter Summary

In summary the results obtained from the tests on CFRP under different conditions confirm the marked electrochemical activity of CFRP at cathodic potentials. Its electrochemical activity under cathodic polarization is independent of the bulk pH and is most significant around $-250 \text{ mV}_{\text{SCE}}$ as observed from cyclic voltammograms at different pH (Fig. 5.10 and 5.11) and impedance data (Fig. 5.24 to 5.26). The marked electrochemical activity observed around $-250 \text{ mV}_{\text{SCE}}$ is attributed to the 2-electron reduction of oxygen with formation of hydroxyl ions and hydrogen peroxide on CFRP surface at this potential. This has serious implications, because

unlike previously thought an erroneously assumed mild cathodic polarization in this range can produce more deleterious effects on CFRP than much higher cathodic polarizations at which this reaction is not favoured and diffusion effects gain prominence. The danger of this cathodic process (2-electron oxygen reduction which is the favoured mechanism for oxygen reduction on carbonunlike the 4-electron process) on CFRP surface is that it leads to the production of the hydroperoxyl radical (HO_2^-) which have been reported [297] to be able to interact with certain polymer bonds in the matrix and hence lead to epoxy degradation. The present findings appear to be at variance with the report of Pauly et al., [302] who reported no degradation in unpolarized specimens exposed to a pH 13 environment and concluded that the high pH environment generated during the oxygen reduction reaction was a necessary but not a sufficient condition for composite degradation. However, results from this work indicate marked reduction in epoxy matrix degradation at $\text{pH} \approx 11$ compared to $\text{pH} \approx 8$, and suggestive of the possibility that matrix degradation might not be favoured at very high pH. In the light of the observation of enhanced cathodic activity around $-250 \text{ mV}_{\text{SCE}}$ in the present work, it is concluded that composite degradation (and enhanced anodic dissolution of galvanically coupled metal) might be possible at much lower cathodic polarizations than previously thought [302], such as cathodic polarizations of magnitudes achievable by galvanic coupling to steel or aluminum. The diffusion limited current density observed for CFRP in this work and attributed to oxygen reduction is about $40 \mu\text{A cm}^{-2}$.

On the basis of the results obtained in this chapter, it is concluded that: the carbon fiber component of CFRP is very active electrochemically in supporting cathodic reactions under cathodic polarization, and the electrochemical activity appears not to be limited to the surface area of the carbon fibers, as carbon deposition is likely to enhance the electrochemically active surface area. This position appears to be supported by the fact that selective deposition of copper onto carbon fibers was not observed in very dilute copper solutions (10 mM to 10 μM) even for shortest deposition periods (less than 1s), as copper was observed to cover both the fiber and epoxy matrix surfaces. The short current pulses and very dilute copper solutions were employed in an attempt to favour nucleation at the expense of the growth of copper crystals on the carbon fiber surface in the anticipated but unobserved selective deposition. This electrochemical activity under cathodic polarization results in composite degradation which presents predominantly as carbon fiber erosion and interfacial damage. CFRP's ability to support cathodic reaction under cathodic polarizations consistent with that anticipated on galvanic coupling with active metals can be mitigated by the use of inhibitors or combination

of inhibitors. On the strength of obtained results, Na_3PO_4 , sodium dodecyl sulphate (SDS), lanthanum acetate, combinations of sodium nitrate with benzotriazole, and cerium acetate with benzotriazole are advanced as potential inhibitors for mitigating cathodic activity on CFRP on galvanic coupling with metals. The suppression of cathodic activity on CFRP realized in this work in the presence of the above named inhibitors is proposed to arise from two mechanisms both of which results from reduction in the electrochemically active area. In the first mechanism decrease in electrochemically active area is achieved by the interaction of inhibitor molecules with CFRP surface most probably by adsorption. This mechanism is most likely with organic inhibitors and explains the reduced cathodic activity demonstrated in the presence of sodium dodecyl sulphate. In the second mechanism decrease in electrochemical area and/or oxygen diffusion to the CFRP surface is achieved by high local pH promoted precipitation of inhibitor-based compounds unto CFRP surface as with Na_3PO_4 .

Double layer capacitance (C_{dl}) values measured for CFRP in chloride solutions of different pH and at different applied potentials ranged between 4 and $100 \mu\text{F cm}^{-2}$ for all solutions, with a general trend of increasing capacitance values moving from cathodic to anodic potentials. However, in the presence of cathodic polarization of $-1000 \text{ mV}_{\text{SCE}}$ and an organic compound (SDS), that adsorbed to CFRP surface much lower double layer capacitance values ($< 4 \mu\text{F cm}^{-2}$) were calculated from fitted EIS data. Since the magnitude and changes in measured values of double layer capacitance of carbon materials can be related to changes in the proportions of the electrochemically active edge sites with respect to the electrochemically inactive basal sites [29], and double layer capacitances reported to be in the range of $50 - 70 \mu\text{F cm}^{-2}$ for edge sites and $3 - 16 \mu\text{F cm}^{-2}$ for the inactive basal sites [29,275,284,286], such diminution of measured double layer capacitance for CFRP especially in the presence of inhibitors (e.g. SDS) to values $< 4 \mu\text{F cm}^{-2}$ in this work can be indicative of the in-activation of the hitherto electrochemically active edge sites on carbon fibers by SDS adsorption to these sites.

CHAPTER 6

Multi-material Corrosion Inhibition of Galvanic Couples in the Al - Cu - CFRP Multi-material Galvanic System

6.0. Results of Tests on Galvanic Couples in the Al - Cu - CFRP Galvanic System

This chapter presents the results of some of the tests carried out on the dual galvanic couples (Al - CFRP, Al - Cu, and Cu - CFRP), and the galvanic triplet (Al - Cu - CFRP) in the Al - Cu - CFRP triplet galvanic system, in quiescent 50 mM NaCl solution with and without the addition of a wide range of inhibitors and combinations of inhibitors. On the basis of results obtained for each of the dual galvanic couples (Al - CFRP, Al - Cu, and Cu - CFRP) and mainly from the more active galvanic couples (Al - CFRP and Al - Cu) in the system, potential multi-material corrosion inhibitors for the Al - Cu - CFRP triplet galvanic ensemble were identified and tested on the triplet galvanic system, and the results presented herein.

The chapter begins with a general and brief presentation of the electrochemical properties of the 9 dual galvanic couples (Al - CFRP, Al - Cu, Al - Fe, Cu -CFRP, Fe - CFRP, Zn - Fe, Zn - Al, and Zn - Cu) from various dual galvanic combinations of the five materials employed in this work (Al, Cu, CFRP, Fe, and Zn) determined in 50 mM NaCl without inhibitors using the galvanic current density evolution with time, along with the operative potential (from ZRA measurements), potentiodynamic polarization scans, and electrochemical impedance spectroscopy as a basis for later galvanic couple specific results incorporating inhibitors. From these, the ranges and evolution(s) of the galvanic current densities of each of the couples in uninhibited solution and other important electrochemical parameters were established. Having thus established galvanic current densities in chloride solution for these couples, further tests were conducted in the presence of selected inhibitors to identify effective inhibitors for each (dual) galvanic couple and subsequently galvanic triplets of interest. In addition to ZRA measurements potentiodynamic polarization and EIS tests were employed to study the galvanic couples in the presence and absence of inhibitors. In selected cases, SVET and SIET were employed to study the galvanic systems at a micro-scale. Due to the technological importance to the aerospace and transport industries more emphasis have been placed on Al - CFRP galvanic system in this chapter.

The same sequential testing procedure employed for Al - CFRP was extended to the Al - Cu, and Cu - CFRP galvanic system, and the analysis of the test data (Table 6.1) lead to the shortlisting and ranking of potential multi-material corrosion inhibitors for the Al - Cu - CFRP

triplet galvanic system mainly based on measured galvanic current densities in $\mu\text{A cm}^{-2}$ after 150,000 seconds immersion and presented in Table 6.1 below. Multi-material corrosion inhibitors for the Al - Cu - CFRP system were identified by tracking their inhibitive effects on each of the dual galvanic couples in the galvanic system on the premise that if an inhibitor or combination of inhibitors is effective on the galvanic constituents of the Al - Cu - CFRP system, it is most likely to be an efficient inhibitor for the multi-material assembly. To aid in the discussion of observed mechanisms, some non-candidate inhibitors and inhibitor combinations were added to Table 6.1. For brevity, the complementary extracted galvanic current densities and potential profiles together with potentiodynamic polarization curves of only the most relevant of these candidate inhibitors from tests on the dual galvanic constituents of the galvanic system; Al - CFRP, Al - Cu, and Cu - CFRP respectively are presented herein. Based on the observations from test results plausible mechanisms for multi-material corrosion and multi-material corrosion inhibition in the Al - Cu - CFRP multi-material system were postulated.

6.1. Overview of the Galvanic Behaviour of Galvanic Couples in 50 mM NaCl

Prior to other tests the galvanic corrosion behaviour of 9 dual galvanic couples (Al - CFRP, Al - Cu, Al - Fe, Cu - CFRP, Fe - CFRP, Zn - Fe, Zn - Al, and Zn - Cu), derived from combinations of the 5 single materials (Al, CFRP, Cu, Fe, and Zn), was determined and ranked using galvanic current density measurements with time employing Gamry potentiostats in zero resistance ammeter (ZRA) mode which are capable of simultaneous potential measurements. The results are presented in Fig. 6.1 (a and b) below which shows the galvanic corrosion activity of the couples based on measured galvanic current densities after 150,000 seconds in 50 mM NaCl decreases in the order: Al - Cu, Zn - Fe, Zn - Cu, Fe - CFRP, Al - Fe, Zn - CFRP, Al - CFRP, Zn - Al, and Cu - CFRP (Fig. 6.1a). From Fig. 6.1b, it is observed that significant fluctuations in the mixed corrosion potential of dual coupled materials were only observed in the galvanic couples containing aluminium (Al - Cu and Al - CFRP), and Fe - CFRP. In Fe - CFRP during the initial 8 hours (28,800 s) the potential dropped from from initial values of about $-320 \text{ mV}_{\text{SCE}}$ to stable values around $-670 \text{ mV}_{\text{SCE}}$.

The potential - time trend observed in Fe - CFRP galvanic couple is consistent with an actively corroding metal (Fig.3.1) [472], suggesting that iron coupled to CFRP undergoes active corrosion in quiescent 50 mM NaCl most probably due to the combination of an increased cathodic area via galvanic coupling with CFRP that supports increased anodic activity and the non-protective nature of the resultant corrosion products. The potential evolution observed for

aluminium containing galvanic couples (Al - Cu and Al - CFRP) is consistent with a metal corroding initially before passivating (Fig.3.1) [472], indicating the effect of the protective nature of the resultant aluminium corrosion products in the test media.

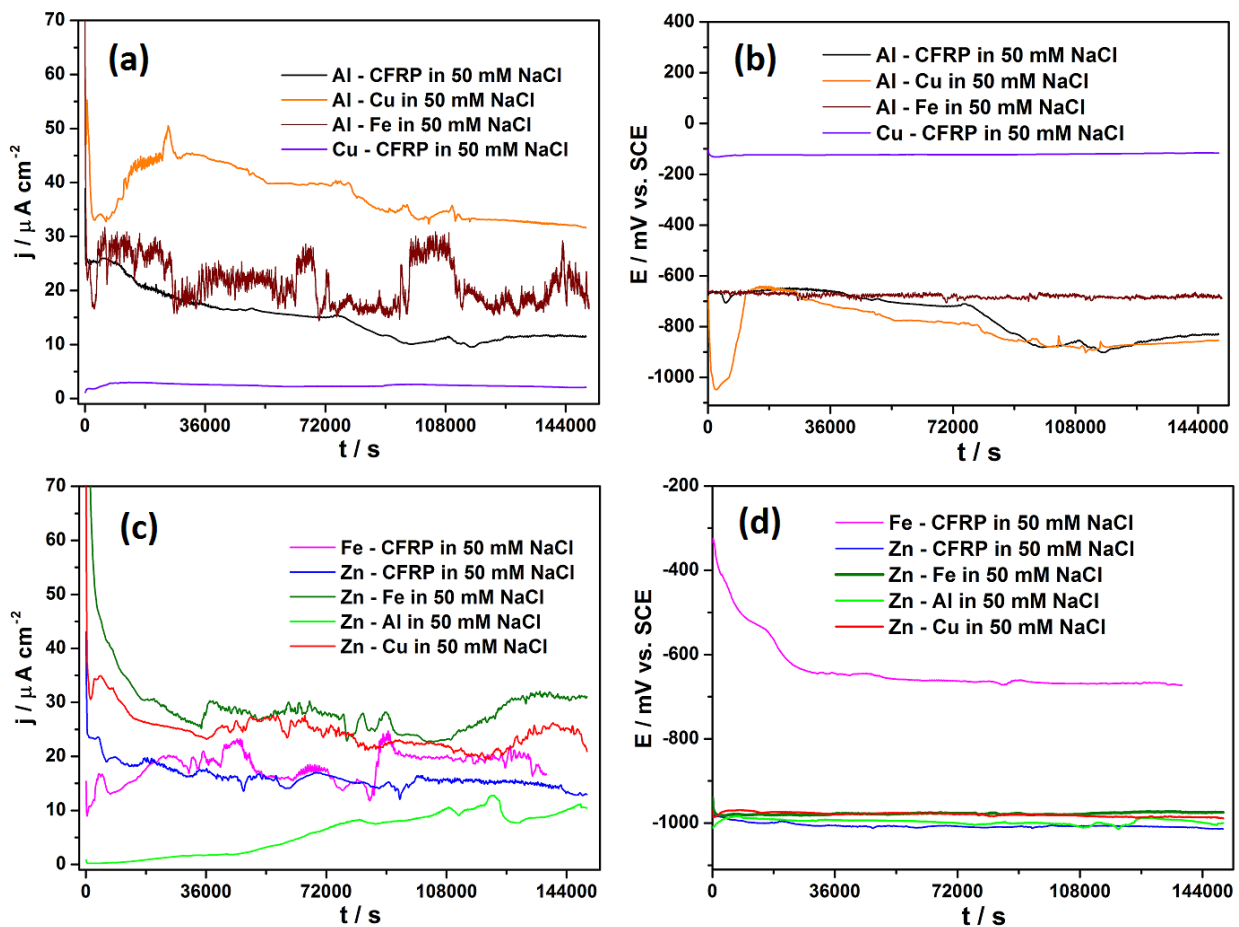


Fig. 6.1. ZRA results for 9 dual galvanic couples in 50 mM NaCl (a and c) galvanic current density evolution with time, and (b and d) potential evolution with time.

Based on observations in Fig. 6.1 (a and b) active aluminium corrosion appears to be intense during the first 3 hours (20,800 s) of immersion and much more intense in Al - Cu compared to Al - CFRP. In all the other galvanic couples involving zinc (Zn - CFRP, Zn - Fe, Zn - Al, and Zn - Cu), the mixed corrosion potential is maintained very close to -1000 mV_{SCE} consistent with the measured corrosion potential of zinc in this work (Figs. 5.1 and 5.2); a property that makes zinc suitable for use as a protective coating for protection of underlying metals.

In order to obtain more mechanistic information on galvanic corrosion of these 9 dual galvanic couples beyond what can be grasped from analysis of ZRA data, cathodic and anodic potentiodynamic polarization scans were made on each of the 9 galvanic couples (with components having equal exposed area) 10 mV from OCP values in the anodic and cathodic directions respectively, and the results presented in Fig. 6.2 below.

From Fig. 6.2 below, the earlier congruence/convergence in the mixed corrosion potentials of galvanic couples containing zinc observed from ZRA data is further confirmed by the potentiodynamic polarization curves. In addition for the zinc containing dual galvanic couples (Zn - CFRP, Zn - Fe, Zn - Al, and Zn - Cu) the cathodic current densities are observed to be highest for Zn - Fe couple, then Zn - Cu, and lowest and similar in Zn - CFRP and Zn - Al. However, anodic behaviour for this ensemble in the active region is almost similar, except for Zn - Al in which some appreciable reduction in anodic current density is observed in the active corrosion region. Generally, the anodic activities in the ensemble of dual galvanic couples containing zinc can be ranked to decrease in the following order; Zn - CFRP, Zn - Fe, Zn - Al, and Zn - Cu. With respect to the entire 9 dual galvanic couples, the highest cathodic current densities are observed in Al - Fe and Fe - CFRP, then lower but similar in Cu - CFRP and Al - Cu, even lower in Zn - Fe and Zn - Cu, then much lower and similar in Zn - CFRP and Zn - Al, and least in Al - CFRP.

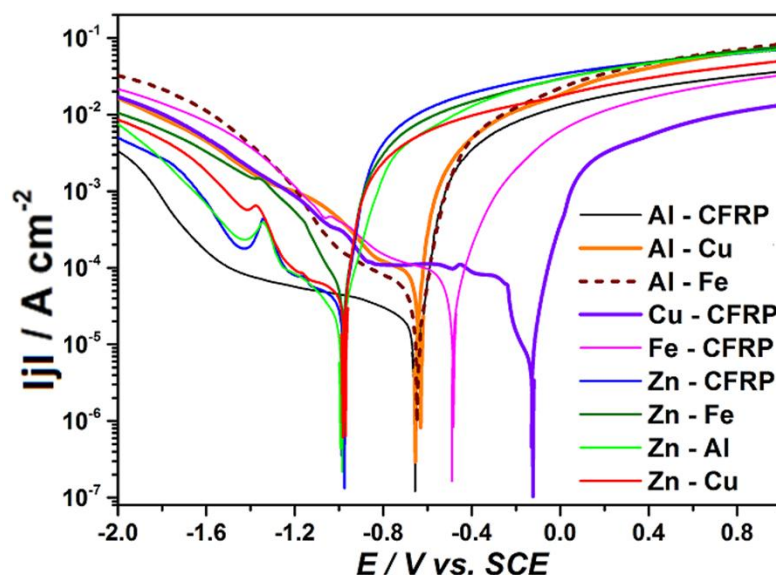


Fig. 6.2. Potentiodynamic polarization scans for 9 dual galvanic couples after 1 hour immersion in 50 mM NaCl.

From the analysis of the potentiodynamic polarization curves for the 9 dual galvanic couples, the enhanced and deleterious cathodic activity observed in Fe - CFRP galvanic couple which is reproducible under service conditions on failure of zinc coatings on steel coupled to CFRP is appreciated. This enhanced cathodic activity in Fe - CFRP galvanic couple is expected on the basis of the ZRA results in this work (Fig. 6.1b) to be most severe during the first 8 hours of immersion as the mixed potential of the Fe - CFRP galvanic couple shifts from the anodic ($\approx -320 \text{ mV}_{\text{SCE}}$) to the more cathodic ($\approx -620 \text{ mV}_{\text{SCE}}$), a potential excursion which from earlier results (sections 5.2.3.3 (Fig. 5.9) and 5.2.4.1. (Fig. 5.26c) have been proven to begin in the

active oxygen diffusion potential range on CFRP in the test media to the oxygen diffusion limited potential range.

The high and deleterious cathodic current densities observed in Al - Cu and Cu - CFRP galvanic couples is appreciated and are likely to emerge from the use of copper containing aluminium alloys (a lot of aeronautical grade aluminium alloys e.g. AA2024) coupled to CFRP. This can be due to substantial quantities of the alloy area being preferentially covered by the more noble copper. The high cathodic current density observed in Zn - Fe galvanic couple is reproducible in compromised galvanized structures or by the presence of intermetallic phases containing both zinc and iron on aluminium alloy surface.

Although, cathodic current densities are lowest in the galvanic couple comprising high purity aluminium and CFRP (Al - CFRP), much lower values are desirable in the aerospace and transport industries, and motivated the extensive research on the use of corrosion inhibitors to mitigate cathodic and galvanic current densities on this couple, the results of which are presented in section 6.2. below. Representative electrochemical impedance spectra acquired from each of the 9 galvanic couples in quiescent 50 mM NaCl after 1 hour immersion are presented in Fig. 6.3 as Nyquist and Bode plots.

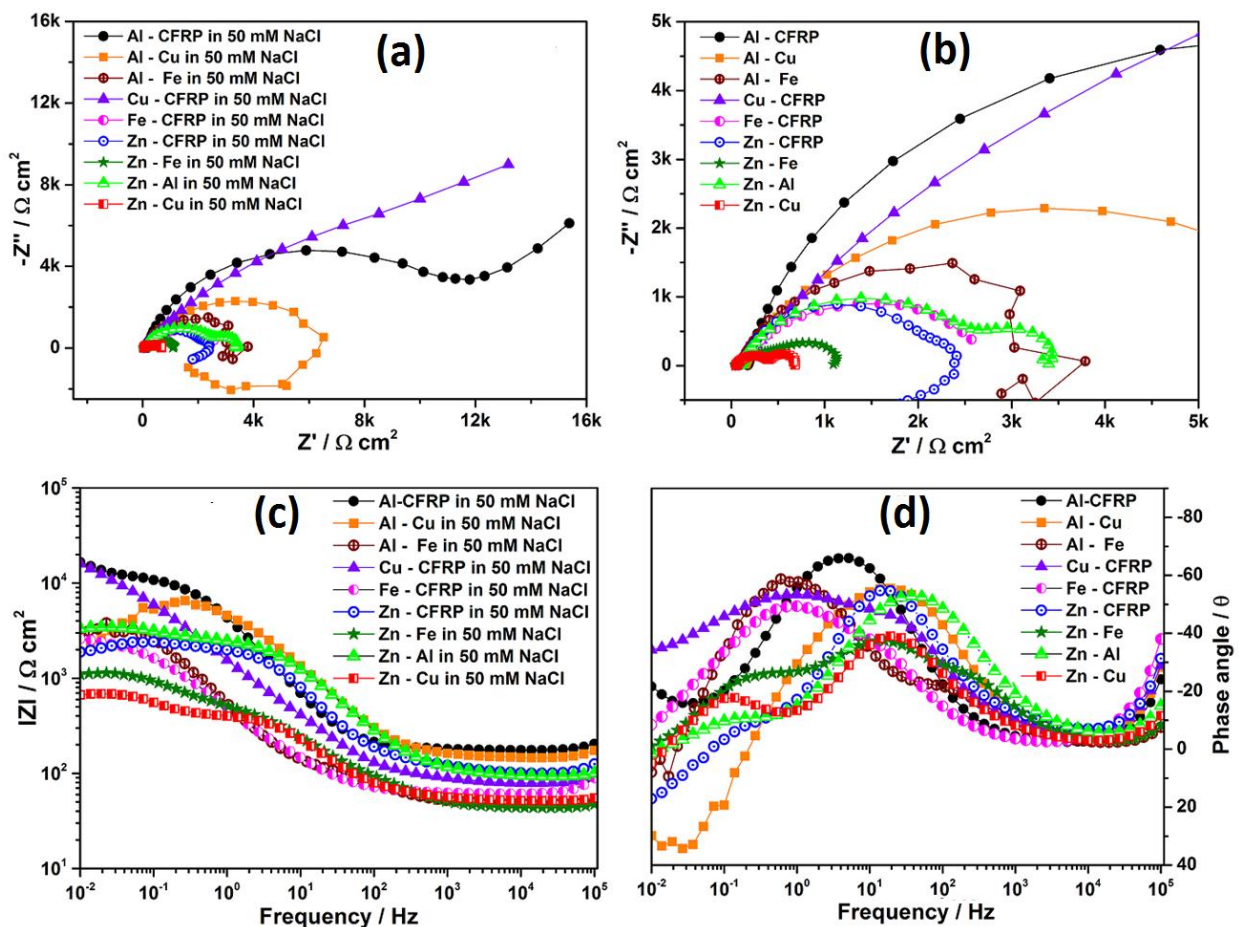


Fig. 6.3. Nyquist and Bode plots for 9 dual galvanic couples after 1 hour immersion in 50 mM NaCl.

6.2. Overview of the Multi-material Corrosion Inhibition in the Al-Cu-CFRP Galvanic System and the Galvanic Behaviour of Galvanic Couples in the System in the Presence of Inhibitors in 50 mM NaCl based Solutions.

The Al - Cu - CFRP triplet material galvanic system is of vital importance to the aerospace industry in which high strength coupled with weight reduction requirements leads to the use of high strength aluminium alloys (such as AA2024, 7075) rich in copper together with carbon fiber reinforced polymers. On the basis of results obtained with inhibition of galvanic corrosion in Al - CFRP, Al - Cu, and Cu - CFRP dual galvanic couples, a shortlist of promising candidate inhibitors and combinations of inhibitors for multi-material inhibition in the Al - Cu - CFRP "triplet" galvanic system was drawn (Table 6.1). The search for multi-material corrosion inhibitors for the Al - Cu - CFRP galvanic system was premised on the assumption that if an inhibitor or combination of inhibitors is good for the component galvanic couples (Al - CFRP, Al - Cu, and Cu - CFRP), it will most probably be effective for the multi-material combinations they are part of. The success of this approach is demonstrated in Table 6.1 below. These dual galvanic couples (Al - CFRP, Al - Cu, and Cu - CFRP dual galvanic couples) that formed the basis for identification of multi-material corrosion inhibitor combinations are respectively of significant technological importance to warrant detailed study of both their corrosion and corrosion inhibition mechanism.

The Al - Cu galvanic system appears to be the most important in the Al - Cu - CFRP multi-material combination as it simulates "self-corrosion" in the high strength copper-rich aluminium alloys commonly used in the aeronautical industry and in a wide range of applications in other industries when high strength to weight ratios are desirable. Hence corrosion inhibitors and inhibitor combinations that are efficient in mitigating galvanic corrosion in the Al - Cu dual galvanic couple are very likely to be good inhibitor solutions for mitigating corrosion in copper-rich aluminium alloys such as AA2024 and AA7075.

The Al - CFRP galvanic system appears to be the most relevant to the aeronautical industry, as the surface of high strength copper-rich aluminium alloys are often clad with a thin layer of purer grades of aluminium alloys (usually of the 1000 series) in order to enhance corrosion resistance without a compromise on strength. With the increasing use of CFRP together with high strength metals/alloys in the aeronautical industry electrical contact between aluminium and CFRP is a possibility which can lead to galvanic corrosion of aluminium and/or potential degradation of CFRP in the presence of an electrolyte. As a consequence information on mitigation of degradative processes on the Al - CFRP dual galvanic couple is of great

importance.

The Cu - CFRP galvanic couple though apparently the least critical in the Al - Cu - CFRP system due to the much lower galvanic current densities involved (usually less than $2.5 \mu\text{A cm}^{-2}$ in 50 mM NaCl) was nevertheless warrants to be studied in the presence and absence of inhibitors due to its relevance to the aeronautical industry. The Cu - CFRP galvanic couple can become operative in modern weight-optimized aircraft structures in which the substitution of metal fuselage with less-conductive carbon fiber composites or non-conductive fiberglass, necessitates the use of a copper mesh in contact with carbon reinforced composites for lightning strike protection (LSP) [686]. Efforts at mitigating galvanic corrosion of the more active dual galvanic couples (Al - CFRP and Al - Cu) or the entire multi-material combination Al - Cu - CFRP by use of inhibitors can lead to drastic increases or reductions in the otherwise low uninhibited galvanic current densities between Cu and CFRP. Since collateral drastic increase in the galvanic current density between Cu and CFRP can occur as observed in this work (Table 6.1) while trying to mitigate corrosion in the more active couples (Al - Cu and Al -CFRP) leading to new challenges, while drastic reductions in the galvanic current density between Cu and CFRP which is desirable from the corrosion mitigation perspective can compromise the desirable conductivity of the interface due to passivation of the Cu - CFRP interface which may sabotage lightning strike protection efforts, information on how the presence of inhibitors affect the Cu - CFRP galvanic couple can be of great importance.

Having established the electrochemical behaviour of the 9 dual galvanic couples that can be formed from the 5 materials of interest in this work (Al, Cu, Zn, Fe, and CFRP), zero resistance ammeter (ZRA) measurements of galvanic currents and galvanic potentials of Al - Cu, Al - CFRP, and Al - Cu - CFRP (Al - Cu electrically connected and measurements made between Al - Cu and CFRP) were measured and the results of the normalized current densities after 150,000 s in the presence of the most relevant inhibitor/inhibitor combinations presented in Table 6.1 below. On the basis of these current densities 150,000 s, the inhibition efficiencies were calculated and used to rank the inhibitors and make a shortlist of candidate potential multi-material corrosion inhibitors for the Al - Cu - CFRP multi-material system.

The results indicate that except for cerium compounds (cerium nitrate and cerium acetate) most of the other single compounds offer little promise as multi-material corrosion inhibitors for the Al - Cu - CFRP multi-material combination. For cerium nitrate (Table 1, row 4),

Table 6.1: Shortlist of potential multi-material corrosion inhibitors for the Al-Cu-CFRP galvanic system on the basis of measured galvanic current densities in $\mu\text{A cm}^{-2}$ after 150,000 seconds immersion (figures in parentheses are calculated inhibition efficiencies).

	Inhibitor	Al-CFRP ($\mu\text{A cm}^{-2}$)	Al-Cu ($\mu\text{A cm}^{-2}$)	Cu-CFRP (nA cm^{-2})	Al-Cu-CFRP ($\mu\text{A cm}^{-2}$)
1.	No inhibitor (in 50 mM NaCl)	18.9	29.9	2070	18
2	5 mM $\text{Ce}(\text{CH}_3\text{COO})_3$	2.75 (85.45%)	10.5 (64.88%)	3600 (-73.91%)	3.33 (81.5%)
3	5 mM CH_3COONa	22.4 (-18.52%)	25.4 (15.05%)	382 (81.55%)	25.1 (-39.44%)
4	5 mM $\text{Ce}(\text{NO}_3)_3$	4.44 (76.51%)	4.28 (85.69%)	2194 (-5.99%)	4.86 (73%)
5	5 mM NaNO_3	22.7 (-20.11%)	28.7 (4.01%)	1,130 (45.41%)	19.4 (-7.78%)
6	5 mM BTA	14.7 (22.22%)	17.6 (41.14%)	0.768 (99.96%)	15.0 (16.67%)
7	2.5 mM ($\text{Ce}(\text{NO}_3)_3$ + BTA)	0.73//3.42 (96.18 - 81.9%)	7.52 (74.85%)	85.64 (95.86%)	1.37 (92.39%)
8	2.5 mM ($\text{La}(\text{NO}_3)_3$ + BTA)	8.42 (55.45%)	6.29 (78.96%)	1.42 (99.93%)	9.64 (46.44%)
9	2.5 mM ($\text{Pr}(\text{NO}_3)_3$ + BTA)	12.7 (32.80%)	20.1 (32.78%)	0.026 (99.999%)	11.3 (37.22%)
10	2.5 mM (NaNO_3 + BTA)	10.6 (43.92%)	21.4 (28.43%)	0.735 (99.96%)	16.2 (10%)
11	2.5 mM ($\text{Ce}(\text{NO}_3)_3$ + BIA)	3.07 (83.76%)	3.77 (87.39%)	169 (91.83%)	2.33 (87.06%)
12	2.5 mM ($\text{Ce}(\text{NO}_3)_3$ + 1,2,3 - triazole)	2.5 & 1.29 (86.77-93.17%)	9.45 & 12.0 (68.39-59.87%)	29.8 (98.56%)	2.83 (84.28%)
13	2.5 mM ($\text{Ce}(\text{CH}_3\text{COO})_3$ + 1,2,3 - triazole)	3.05 (83.86%)	6.86 & 8.43 (77.06-71.81%)	26.2 (98.73%)	2.42 (86.56%)
14	2.5 mM ($\text{Ce}(\text{NO}_3)_3$ + CH_3COONa)	1.61 (91.48%)	4.67 (84.38%)	2870 (-38.65%)	4.29 (76.17%)
15	2.5 mM (NaNO_3 + $\text{Ce}(\text{CH}_3\text{COO})_3$)	4.13 (78.15%)	4.33 (85.52%)	4.05 (99.80%)	3.11 (82.72%)
16	2.5 mM ($\text{Ce}(\text{CH}_3\text{COO})_3$ + BTA)	1.99&3.05 (89.47-83.86%)	5.80 (80.60%)	44.2 (97.86%)	2.78 (84.56%)
17	2.5 mM ($\text{La}(\text{CH}_3\text{COO})_3$ + BTA)	9.33 (50.63%)	5.80 (80.60%)	49.26 (97.62%)	5.51 (69.39%)
18	2.5 mM (CH_3COONa + BTA)	19.7 (-4.23%)	20.2 (32.44%)	2.13 (99.9%)	14.6 (18.89%)
19	2.5 mM ($\text{Ce}(\text{CH}_3\text{COO})_3$ + BIA)	2.60 (86.24)	4.38 (85.35%)	94.9 (95.42%)	3.29 (81.72%)
20	2.5 mM ($\text{La}(\text{CH}_3\text{COO})_3$ + NaNO_3)	15.9 (15.87%)	18.3 (38.79%)		11.6 (35.56%)
21	2.5 mM (CH_3COONa + $\text{La}(\text{NO}_3)_3$)	12.9 (31.75%)	18.3 (38.79%)		12.3 (31.67%)

its effectiveness can be explained by the reported [687] anodic inhibitive ability of the nitrate ion which can allow it act on anodic areas while the cerium precipitates on cathodic areas in the

presence of a high pH. For cerium acetate (Table 1, row 2), its effectiveness is unexplained as NaNO_3 was not effective (Table 1, row 3).

The shortlisted inhibitors for multi-material corrosion inhibition in the Al - Cu - CFRP "triplet" galvanic system are for single inhibitors; cerium nitrate and cerium acetate, and for combination of inhibitors; $(\text{Ce}(\text{NO}_3)_3 + \text{BTA})$, $(\text{Ce}(\text{NO}_3)_3 + \text{BIA})$, $(\text{Ce}(\text{CH}_3\text{COO})_3 + \text{BTA})$, $(\text{Ce}(\text{CH}_3\text{COO})_3 + \text{BIA})$, $\text{Ce}(\text{CH}_3\text{COO})_3 + \text{NaNO}_3$, $(\text{Ce}(\text{NO}_3)_3 + \text{CH}_3\text{COONa})$, $\text{Ce}(\text{NO}_3)_3 + 1,2,3$ triazole, and $(\text{La}(\text{CH}_3\text{COO})_3 + \text{BTA})$. This shortlist is made based on the observation that these combinations of inhibitors efficiently inhibited the galvanic corrosion of all the dual galvanic couples (Al - CFRP, Al - Cu and Cu - CFRP) that constitute the Al - Cu - CFRP multi-material galvanic system and also inhibited galvanic corrosion of the Al-Cu-CFRP galvanic triplet. From this shortlist it is obvious that the combination of rare earth salts (cerium and lanthanum) in the form of nitrates and acetates with azoles (BTA, BIA, and 1,2,3 triazole), and rare earths (cerium and lanthanum) nitrates in the presence of sodium acetates or rare earths (cerium and lanthanum) acetates in the presence of sodium nitrate give the best multi-material corrosion inhibitors for Al - Cu - CFRP "triplet" galvanic system with cerium being much more effective than lanthanum. The presence of other rare earth metal ions; Praseodymium, Samarium, Neodymium alone or in combination with azoles were much less effective in inhibiting multi-material corrosion in the Al - Cu - CFRP "triplet" galvanic system.

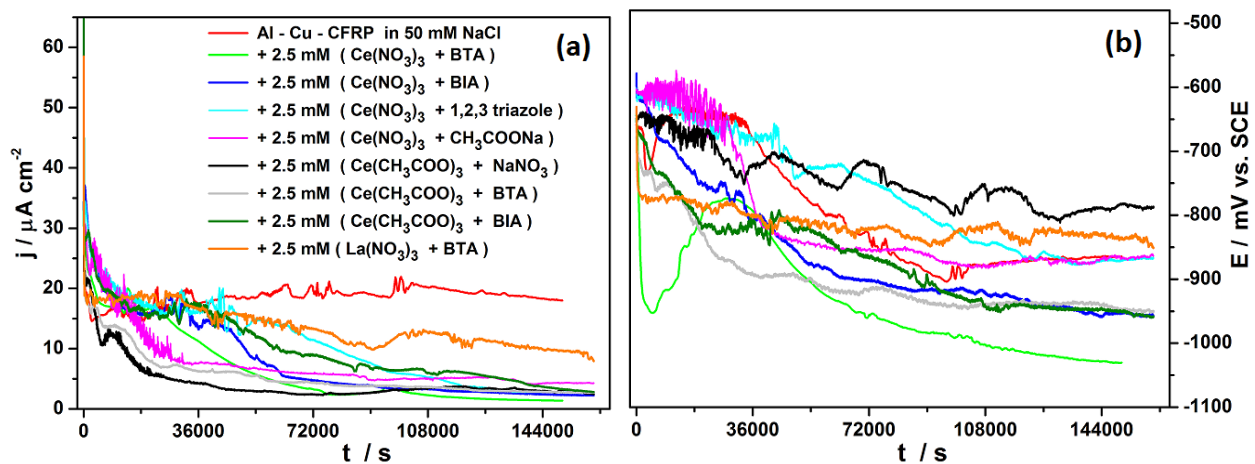


Fig. 6.4. Effect of selected combination of inhibitorson evolution of (a) galvanic current density and (b) for Al - Cu - CFRP galvanic triplet in 50 mM NaCl.

The excellent performance of the selected combination of inhibitors as multi-material corrosion inhibitor for mitigating galvanic corrosion in the multi-material assembly; Al - Cu - CFRP is graphically presented in the time evolution of galvanic current densities (Fig. 6.4a). From Fig. 6.4a it is observed that all the 9 inhibitor combinations exhibited good inhibitive effects with inhibition efficiencies ranging from $> 50\%$ for $\text{La}(\text{NO}_3)_3 + \text{BTA}$ to $> 90\%$ for $\text{Ce}(\text{NO}_3)_3 + \text{BTA}$.

Fig. 6.5 below, presents the potentiodynamic polarization curves for Al - Cu - CFRP in the selected inhibitors from which significant reductions in both cathodic and anodic current densities are observed in the presence of inhibitor combinations that manifested very high inhibition efficiencies.

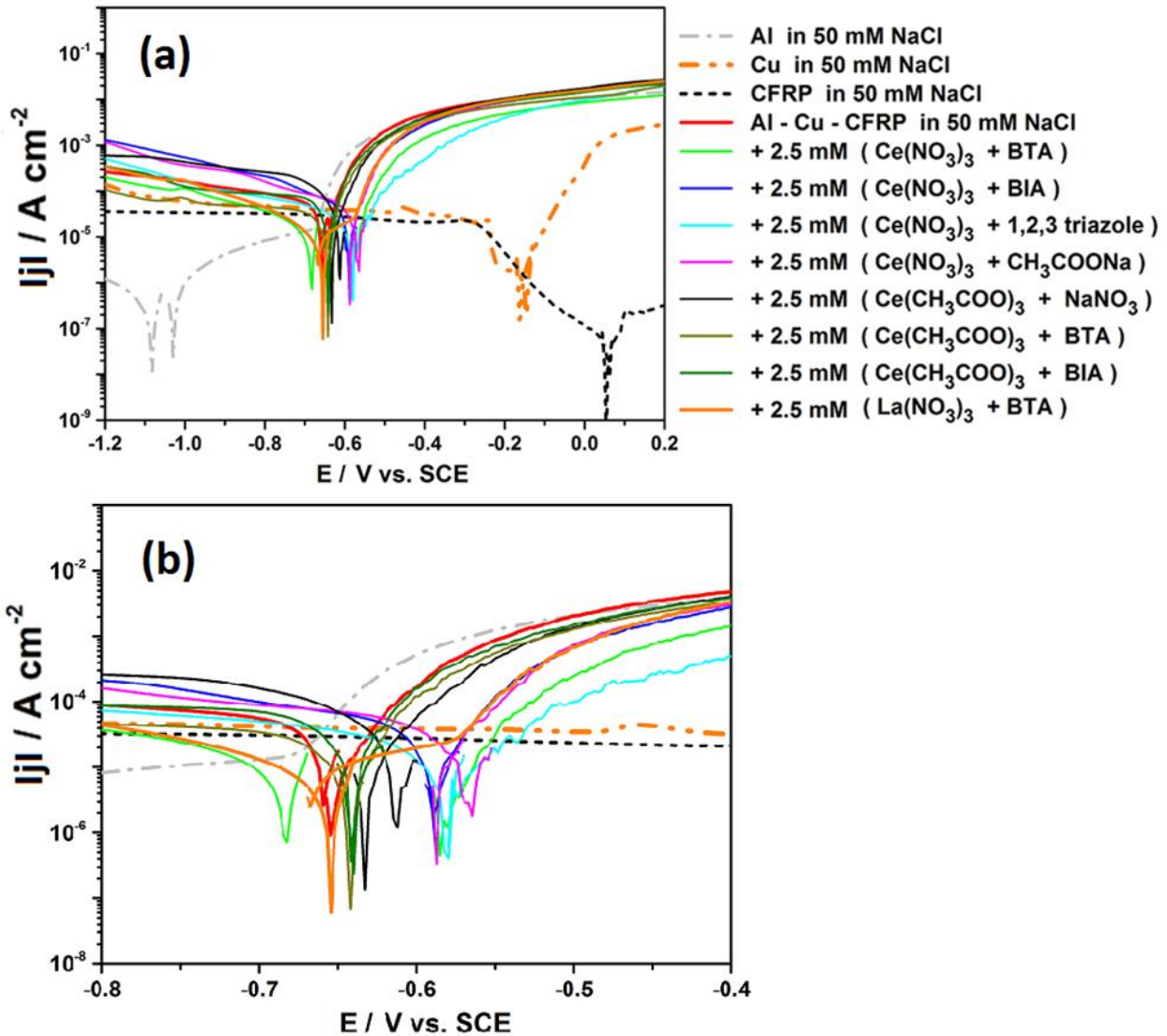


Fig. 6.5. Effect of selected combination of inhibitors on the potentiodynamic polarization curves for Al - Cu - CFRP galvanic triplet in 50 mM NaCl (b) is magnified section of the potentiodynamic curves.

6.2.1. Effect of Selected Combinations of Inhibitors on the Galvanic Corrosion of Al - CFRP, Al - Cu, and Cu - CFRP Galvanic Couples.

Based on the premise that inhibitor selections that are effective for the simpler galvanic components are most likely to be effective for mitigating corrosion in the more complex Al - Cu - CFRP multi-material combination, the excellent performance of the selected combination of inhibitors as multi-material corrosion inhibitor for mitigating galvanic corrosion in the Al - Cu - CFRP multi-material assembly is likely to be linked to their respective effects on the galvanic

corrosion of the dual material galvanic couples (Al - CFRP, Al - Cu, and Cu - CFRP) that form part of the Al - Cu - CFRP multi-material galvanic system. In the light of these, the evolution of galvanic current densities and potentials of these dual material galvanic couples in the presence of these selected inhibitors are presented in Fig. 6.6, and the potentiodynamic polarization curves in Fig. 6.7.

Having demonstrated multi-material corrosion inhibition of Al - Cu - CFRP multi-material combinations, studied the effect of individual inhibitors (under different classifications) on the galvanic corrosion behaviour of Al - CFRP, Al - Cu, and Cu - CFRP galvanic couples and guided by insights obtained from earlier studies with single inhibitors, further studies were made with different combinations of these classes of inhibitors. The evolution of galvanic current densities and potentials of Al - CFRP, Al - Cu, and Cu - CFRP galvanic couples in the presence of these selected inhibitors are presented in Fig 6.6 below.

From the measurements of galvanic current densities and potentials for Al - CFRP in the presence of selected combinations of inhibitors (Fig. 6.6a and b), it is observed that significant inhibition of galvanic corrosion occurs in the presence of all the presented inhibitor combinations with inhibition efficiencies based on measured galvanic corrosion current densities after 150,000 seconds immersion ranging from $\approx 50\%$ in the presence of 2.5 mM ($\text{La}(\text{NO}_3)_3$ + BTA) to $>85\%$ in the presence of 2.5 mM ($\text{Ce}(\text{NO}_3)_3$ + CH_3COONa). On the basis of such calculated inhibition efficiencies the effectiveness of these inhibitor combinations are ranked in the following order; $(\text{Ce}(\text{NO}_3)_3 + \text{CH}_3\text{COONa}) > (\text{Ce}(\text{CH}_3\text{COO})_3 + \text{BTA}) > (\text{Ce}(\text{CH}_3\text{COO})_3 + \text{BIA}) > (\text{Ce}(\text{NO}_3)_3 + \text{BTA}) > (\text{Ce}(\text{CH}_3\text{COO})_3 + \text{NaNO}_3) > (\text{Ce}(\text{NO}_3)_3 + \text{BIA}) > (\text{Ce}(\text{NO}_3)_3 + 1,2,3\text{-triazole}) > (\text{La}(\text{CH}_3\text{COO})_3 + \text{BTA}) > (\text{La}(\text{NO}_3)_3 + \text{BTA})$. From the ranking above it is evident that for Al - CFRP, the best inhibition efficiencies were obtained in the presence of inhibitor combinations comprised of cerium nitrate and an acetate, and cerium nitrates or acetates and an azole.

Based on the observation from tests on galvanic couples with single inhibitors that for the Al - Cu galvanic couple the azoles act predominantly on cathodic processes, while the rare-earth nitrates act on anodic process, selected combinations of inhibitors predominantly comprised of rare-earth nitrates and azoles were tested for possible additive or synergistic corrosion inhibition effects on Al - Cu galvanic couple and results of ZRA measurements of galvanic current densities and potentials presented in Fig. 6.6c-d. From Fig. 6.6c very significant inhibition of Al - Cu galvanic corrosion is recorded for all 9 inhibitor combinations with inhibition efficiencies ranging from $\approx 62\%$ to 88% based on measured galvanic corrosion densities after 150,000 seconds immersion. Based on this criterion the effectiveness of the

tested inhibitor combinations on Al - Cu galvanic corrosion is ranked thus; $(\text{Ce}(\text{NO}_3)_3 + \text{BIA}) > (\text{Ce}(\text{CH}_3\text{COO})_3 + \text{BIA}) > (\text{Ce}(\text{CH}_3\text{COO})_3 + \text{NaNO}_3) > (\text{Ce}(\text{NO}_3)_3 + \text{CH}_3\text{COONa}) > (\text{Ce}(\text{CH}_3\text{COO})_3 + \text{BTA}) > (\text{La}(\text{NO}_3)_3 + \text{BTA}) > (\text{La}(\text{CH}_3\text{COO})_3 + \text{BTA}) > (\text{Ce}(\text{NO}_3)_3 + \text{BTA}) > (\text{Ce}(\text{NO}_3)_3 + 1,2,3\text{-triazole})$.

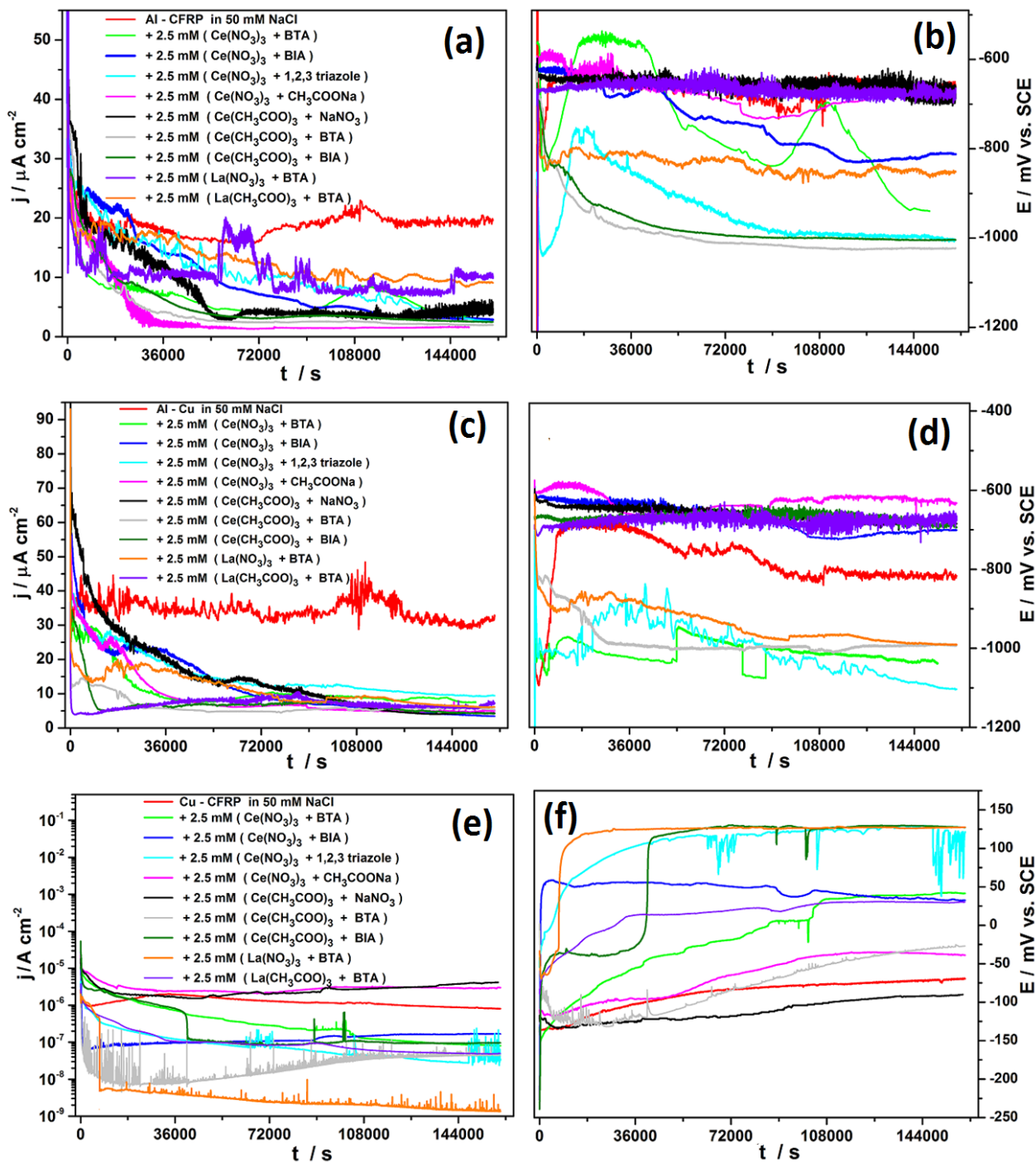


Fig. 6.6. Effect of selected combination of inhibitors on evolution of galvanic current densities and potentials for (a-b) Al - CFRP, (c-d) Al - Cu, and (e-f) Cu - CFRP galvanic couples in 50 mM NaCl based inhibitor solutions.

The results from ZRA measurements using these inhibitor combinations on the Cu - CFRP couple presented in Fig. 6.6c above, show that with the exception of $(\text{Ce}(\text{NO}_3)_3 +$

CH₃COONa) and (Ce(CH₃COO)₃ + NaNO₃) all the other inhibitor combinations manifested significant inhibitive effects on Cu - CFRP galvanic corrosion. The inhibitive performance of the 7 promising inhibitor combinations on galvanic corrosion of Cu - CFRP couple based on measured galvanic current densities after 150,000 seconds immersion is ranked thus; (La(NO₃)₃ + BTA) > (Ce(NO₃)₃ + 1,2,3 - triazole) > (Ce(CH₃COO)₃ + BTA) > (La(CH₃COO)₃ + BTA) > (Ce(NO₃)₃ + BTA) > (Ce(CH₃COO)₃ + BIA) > (Ce(NO₃)₃ + BIA).

In an attempt to obtain more information on the possible mechanism of the significant inhibition efficiencies obtained with the combinations of inhibitors on the galvanic corrosion of dual galvanic galvanic couples, potentiodynamic polarization tests were carried out and the results presented in Fig. 6.7 below. From Fig. 6.7a below, it is observed that the mixed corrosion potential for Al - CFRP galvanic couple is displaced significantly and cathodically only in the presence of the combinations; (Ce(NO₃)₃ + BTA) and (Ce(NO₃)₃ + 1,2,3-triazole) compared to all of the other inhibitor combinations, but not more cathodic than the E_{corr} of aluminium in the blank solution. From Fig. 6.7b for Al - Cu galvanic couple, inhibition of anodic dissolution processes is observed to varying degrees for all the inhibitor combinations evidenced by lower measured anodic current densities in the active corrosion region of the anodic curve. However, significant suppression of cathodic current densities apparently indicative of inhibition of cathodic processes is only observed in the presence of (Ce(NO₃)₃ + BTA), (Ce(CH₃COO)₃ + BTA), (Ce(CH₃COO)₃ + BIA), (Ce(NO₃)₃ + 1,2,3-triazole), and (La(NO₃)₃ + BTA), all of which contain azoles. This observation is in tandem with earlier discussed results with respect to azoles in single inhibitor studies in which their predominant action on cathodic processes in Al - Cu galvanic couple was demonstrated. From these results it is evident that the effectiveness of azoles in suppressing cathodic processes is not suppressed by the addition of rare-earth cations as nitrates or acetates which makes additive and/or synergistic corrosion inhibition a possibility. From the potentiodynamic polarization curves for Cu - CFRP galvanic couple in the presence of selected inhibitor combinations (Fig. 6.7c), it is observed that the desired simultaneous suppression of both cathodic and anodic processes is achieved in the presence of all the inhibitor combinations that exhibited inhibitive effects (i.e. those containing azoles). This trend for Cu - CFRP galvanic couple is attributed to the well known inhibitive action of azoles on copper, and their generally good but marginal effects on cathodic processes on CFRP (section 5.2.8.3).

In analyzing the potentiodynamic polarization curves of galvanically coupled materials cathodic activities are considered to occur solely on the cathodic material (Cu and/or CFRP) and

anodic processes solely on the anodic metal (Al). Hence the cathodic branch of the polarization curve is deemed to give information on processes occurring on the cathode under the test conditions while the anodic branch gives formation on anodic processes on aluminium supported by the corresponding cathode (Cu and or CFRP). Using this convention in the comparison of the cathodic branches of the polarization curves for Al - CFRP (Fig. 6.7a) and that of Al - Cu (Fig. 6.7b), it is observed that whereas only marginal reduction in the cathodic current densities with respect to that measured on CFRP in 50 mM NaCl were observed in all the inhibitor combinations, very significant reductions in cathodic current densities were observed for for Al - Cu with respect to that measured on copper in 50 mM NaCl in the presence of $(\text{Ce}(\text{NO}_3)_3 + \text{BTA})$ and $(\text{Ce}(\text{CH}_3\text{COO})_3 + \text{BTA})$. This highlights the challenges in suppressing cathodic activities on CFRP even with the effective inhibitor combinations. On the basis of trends and differences observed in the inhibitive effects of different azoles on copper corrosion under cathodic and anodic polarizations in chloride solutions at different pH, it is postulated that the effectiveness observed in suppression of cathodic activities on Al - Cu galvanic couples with cerium and BTA based inhibitor combinations is most probably due to the suppression of copper oxide formation on copper under the test conditions which could have enhanced cathodic processes and/or its modification. Since neither of these are possible with CFRP, suppression of cathodic processes on CFRP is much more difficult. In addition, the positive effects of the inhibitor combinations containing azoles in mitigating multi-material corrosion of Al - Cu - CFRP galvanic system is attributed to the ability of these azoles to passivate copper surface and thus reduce the effective cathodic area that supports anodic dissolution of aluminium. This is quite obvious from the anodic branch of the polarization curve for Cu - CFRP (Fig. 6.7c below) and in that of Al - Cu (Fig. 6.7b) albeit less obvious. In these two instances, marked reductions in anodic current densities were distinctively marked in the presence of inhibitor combinations containing azoles. In summary, these results demonstrate that multi-material corrosion inhibition in the Al - Cu - CFRP multimaterial galvanic system is feasible with synergistic inhibitor combinations predominantlt composed of rare-earth (Ce and La) cations and azoles.

Further insight on the possible reasons for the effectiveness of these inhibitor combinations are provided in the next section (section 6.3) that deals with the effect of single inhibitors on the galvanic corrosion of the dual galvanic couples that also incorporates data on the effect of these individual inhibitors that constitute these promising inhibitor combinations on the individual materials that constitute these dual galvanic couples.

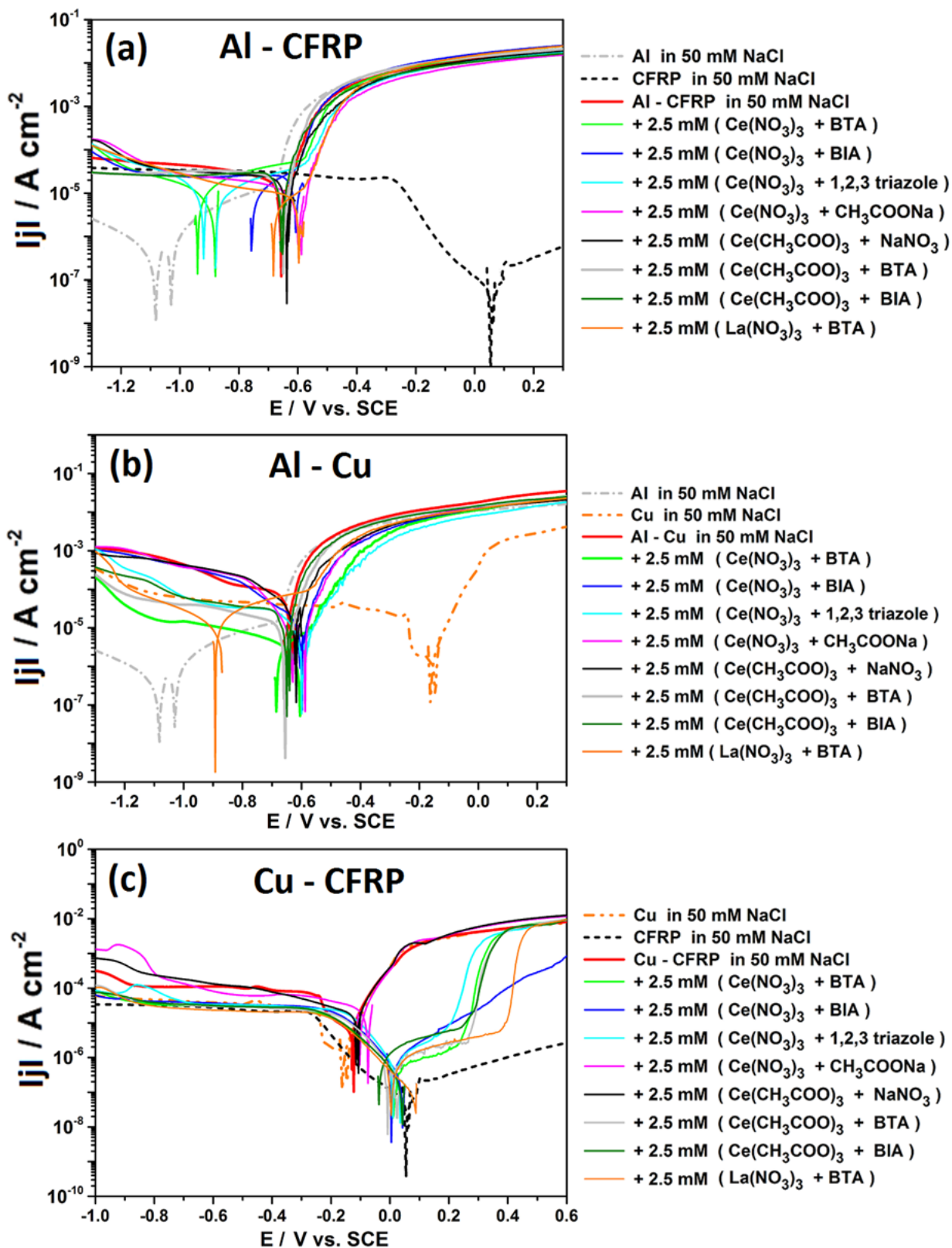


Fig. 6. 7. Effect of selected combination of inhibitors on the potentiodynamic curves of (a) Al - CFRP, (b) Al - Cu, and (c) Cu - CFRP galvanic couples in 50 mM NaCl based inhibitor solutions after 1 hour immersion.

6.3.0. Effect of Selected Single Inhibitors on the Galvanic Corrosion of Al - CFRP, Al - Cu, and Cu - CFRP Galvanic Couples.

To explain the positive effects observed in the preceding section (section 6.2) using combinations of inhibitors to inhibit multi-material corrosion in the Al - Cu - CFRP multi-material combination, and on its possible galvanic components (Al - CFRP, Al - Cu, and Cu - CFRP), earlier tests on these galvanic system with single inhibitors employed in the promising inhibitor combinations are presented and discussed herein. To this end, for Al, Cu, and CFRP the data employed are their respective potentiodynamic polarization curves after 1 hour immersion in 5 mM concentrations of the respective azoles in 50 mM NaCl solution. For the dual galvanic couples (Al - CFRP, Al - Cu, and Cu - CFRP), their respective polarization curves after 1 hour immersion in the respective test media obtained while galvanically coupled, their galvanic current density and galvanic potential evolutions with time were employed. Though arguments can be raised especially with regards to the dual galvanic couples as to the propriety of the use of potentiodynamic polarization curves acquired after such short immersion times in systems observed to display time evolution as manifested in their galvanic current density and potential evolutions, such short term potentiodynamic tests were employed because it gives information on the system before the cathodic and anodic activities are severely suppressed by the inhibitive action of the inhibitors. Understandably, this difference in the time-scale of ZRA measurements and potentiodynamic polarization tests resulted in some instances to subtle differences in the results from these two tests, as the potentiodynamic tests give information that is apparently representative of ZRA measurements up to about 3600 seconds. However the trends from the short term potentiodynamic polarization tests ($t = 3600$ seconds after immersion) and ZRA measurements of galvanic current densities and potentials (up to or greater than 150,000 seconds) were largely in agreement. For ensuing work however, longer term potentiodynamic polarization curves at different immersion times are recommended. The single inhibitors employed are the azoles, nitrates, and acetates

6.3.1. Effect of Azoles (Single Inhibitors) on the Galvanic Corrosion of Al - CFRP, Al - Cu, and Cu - CFRP Galvanic Couples.

The effect of azoles comprising, benzotriazole (BTA), benzimidazole (BIA), 1,2,3-triazole, and 1,2,4-triazole on the corrosion of Al, Cu, and CFRP, and on the galvanic corrosion of Al - CFRP, Al - Cu, and Cu - CFRP dual galvanic couples are presented herein with an aim to unveiling the contribution of azoles to the mechanism(s) of the observed multi-material corrosion

inhibition in the Al - Cu - CFRP multi-material galvanic system. The inhibitors classified as azoles are benzotriazole (BTA), benzimidazole (BIA), 1,2,3 - triazole and 1,2,4 - triazole.

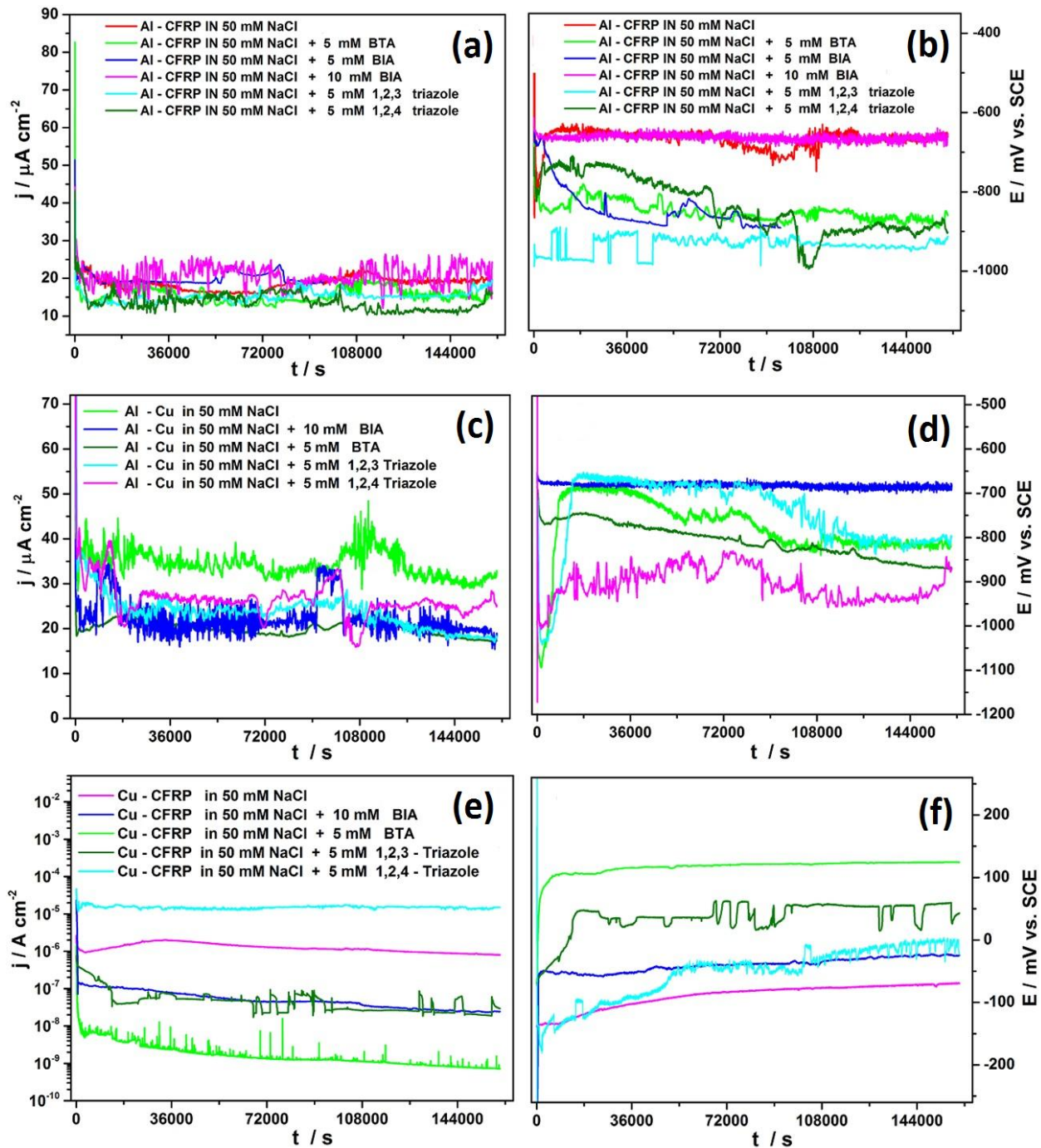


Fig. 6.8. Effect of azole inhibitors on evolution of galvanic current densities and potentials for (a-b) Al - CFRP, (c-d) Al - Cu, and (e-f) Cu - CFRP galvanic couples in 50 mM NaCl based inhibitor solutions.

Fig. 6.8 above presents the ZRA results in the presence and absence of this class of inhibitors, which shows that for Al - CFRP galvanic couple (Fig. 6.8a) mild inhibitive effects manifest after about 24 hours immersion with the best effects in the presence of 1,2,3-triazole and 1,2,4-triazole, and to a smaller extent in benzotriazole. For Al - Cu galvanic couple (Fig. 6.8c), moderate inhibition of galvanic corrosion is recorded in the presence of azoles; the best trend being

observed in the presence of benzotriazole. With the exception of 1,2,4-triazole all the azoles tested on the Cu - CFRP galvanic couple (Fig. 6.8e) were found to exhibit very significant inhibitive effects on the measured galvanic current densities between Cu and CFRP, with benzotriazole suppressing galvanic current densities to values about two orders of magnitude lower than values measured in blank solution.

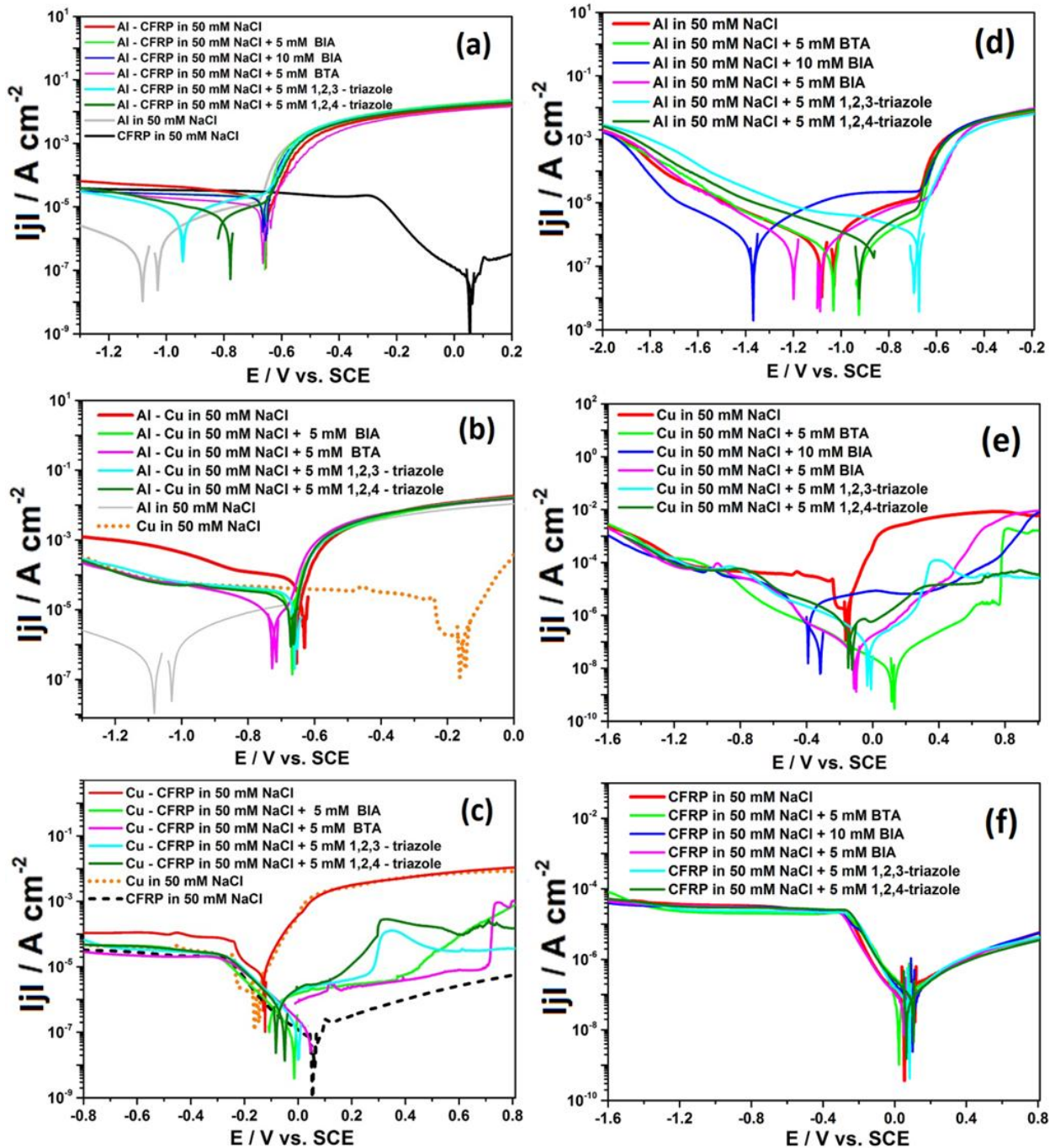


Fig. 6.9. Effect of azole inhibitors on the potentiodynamic curves of (a) Al - CFRP, (b) Al - Cu, and (c) Cu - CFRP galvanic couples, and (d) aluminium, (e) copper, and (f) CFRP in 50 mM NaCl based inhibitor solutions after 1 hour immersion.

From the potentiodynamic polarization curve for Al - CFRP in the presence of azoles (Fig. 6.9a above), it is observed that the superior performances of 1,2,3-triazole and 1,2,4-triazole

correlates with cathodic shifts in their "corrosion potential" away from that of uninhibited Al-CFRP couple tending towards values for aluminium in blank solution.

From the potentiodynamic polarization curves for Al - Cu in the presence of azoles (Fig. 6.9b), it is evident that the azoles act predominantly on cathodic processes. The measured cathodic current densities in the presence of azoles are all much lower than values measured for the couple in blank solution. From the anodic side of the polarization curve (Fig.6.9b), it is evident the azoles are unable to exert inhibiting effects on anodic processes as measured current densities in the active corrosion region are not diminished compared to values in the blank solution.

The potentiodynamic polarization curves of Cu-CFRP galvanic couple (Fig. 6. 9c) sheds more light on the mechanism of the inhibitive action of the azoles on Cu - CFRP galvanic couple. The cathodic part of the polarization curves in the presence of triazoles reveals significant suppression of cathodic processes in the presence of all the azoles studied compared to values measured for Cu - CFRP in blank solution. For benzotriazole which exhibited the best and very significant suppression of galvanic current densities (Fig. 6.9c), the measured cathodic current densities in the diffusion limited potential range is suppressed to values lower than those measured in both un-coupled copper and un-coupled CFRP. Reduced anodic current densities and passivation is observed in the anodic curves, with observed trends consistent with trends earlier observed from galvanic current density measurements.

For the single materials, the presence of 5 mM concentrations of the azoles generally results in shifting the corrosion potentials of both Al (Fig. 6.9d) and Cu (Fig. 6.9e) to more anodic values. In the case of Cu (Fig. 6.9e) the displacement of the corrosion potentials to more anodic values occurs in conjunction with marked decreases in the anodic current densities. This reduction in anodic current densities is most significant in the presence of BTA in which passivation of Cu surface is observed, and inferred to account for the superior performance of inhibitor combinations containing BTA in mitigating multi-material corrosion in all the dual and galvanic triplet of the Al - Cu - CFRP multi-material galvanic system. For CFRP (Fig. 6.9f) no marked differences are observed in its potentiodynamic polarization curves in the presence of any of the azole compounds.

6.3.2. Effect of Rare Earth Cations (Single Inhibitors) on the Galvanic Corrosion of Al - CFRP, Al - Cu, and Cu - CFRP Galvanic Couples.

The effect of introduction of the rare-earth cations in the presence of different conjugate anions (nitrates and acetates) on the corrosion of Al, Cu, and CFRP, and on the galvanic corrosion of Al - CFRP, Al - Cu, and Cu - CFRP dual galvanic couples were studied in an attempt to understand their contribution to the mechanism(s) of the observed multi-material corrosion inhibition in the Al - Cu - CFRP multi-material galvanic system and the results and its discussion presented herein.

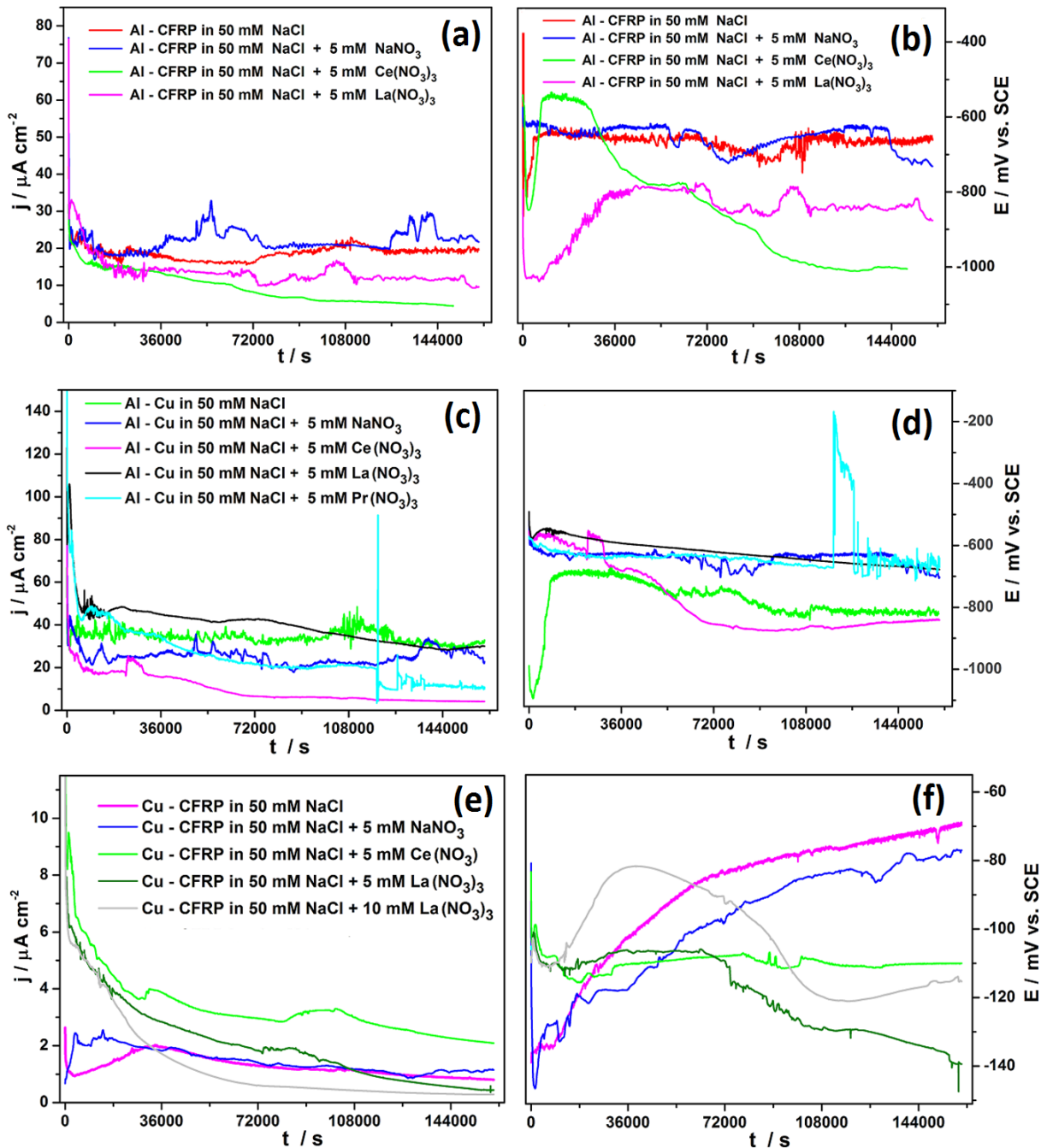


Fig. 6.10. Effect of rare-earth nitrate inhibitors on evolution of galvanic current densities and potentials for (a-b) Al - CFRP, (c-d) Al - Cu, and (e-f) Cu - CFRP galvanic couples in 50 mM NaCl based inhibitor solutions.

Fig 6.10 (a and b) presents the effects of Na, and RE nitrates on the galvanic corrosion of Al-CFRP galvanic couples from which it is observed that inhibitive effects manifest only in the presence of the rare-earth nitrates (Ce and La) but not in the presence of sodium nitrate. On the basis of this observation it is concluded that the inhibitive effects are due to the presence of the rare-earth cations. It is observed that the inhibition kinetics become pronounced after 10 hours of immersion and is much faster in the presence of cerium nitrate. From Fig. 6.10b it is observed that inhibitive effects correlate with shifts in the galvanic potential towards cathodic potentials with the displacement faster and more pronounced in the presence of the more effective cerium nitrate.

From the galvanic current density evolution plots of different nitrates on Al-Cu galvanic couple (Fig. 6.10 (c and d)), differences in effects are obvious. Significant inhibitive effects are for Al - Cu galvanic couple in the presence of cerium nitrate and praeodymium nitrate while enhancement of corrosion processes is observed in the presence of lanthanum nitrate (from immersion till after > 24 hours of immersion). In the presence of sodium nitrate some inhibitive effects are observed but it apparently decreases with increase in immersion time.

From the plots of evolution of galvanic current density and potential for Cu-CFRP in the presence of nitrates (Fig. 6.10 e and f), it is observed that significant inhibition effects are only obtained in the presence of lanthanum nitrate at higher concentration of 10 mM with cerium nitrate exhibiting accelerative effects until after 30 hours of immersion.

From the potentiodynamic polarization curves for Al - CFRP in the presence of nitrates (Fig. 6.11a below), the cathodic potential shifts observed in ZRA data is also manifest for the effective rare earth nitrates (Ce and La). In the presence of Ce and La nitrates changes are observed in the anodic dissolution kinetics of aluminium as evident in the shift towards more anodic potentials and away from the "corrosion potential" of the "pitting/break down potential" compared to observed trends for aluminium and Al - CFRP in the absence of these rare-earth nitrates. Furthermore, enhanced cathodic activities are observed in the presence of all the rare-earth nitrates studied (Ce, La, and Pr), but suppressed in the presence of sodium nitrate below values measured for Al - CFRP couple in the blank solution coupled with the apparent absence of a well-defined oxygen diffusion plateau. It should be noted that the observed increase in the cathodic current densities in the presence of all the nitrates is not due to increase in corrosion related anodic processes, but rather due to electrochemical decomposition of nitrates on the (cathode) CFRP surface as demonstrated earlier in chapter 5 (**section 5.2.6.3.**).

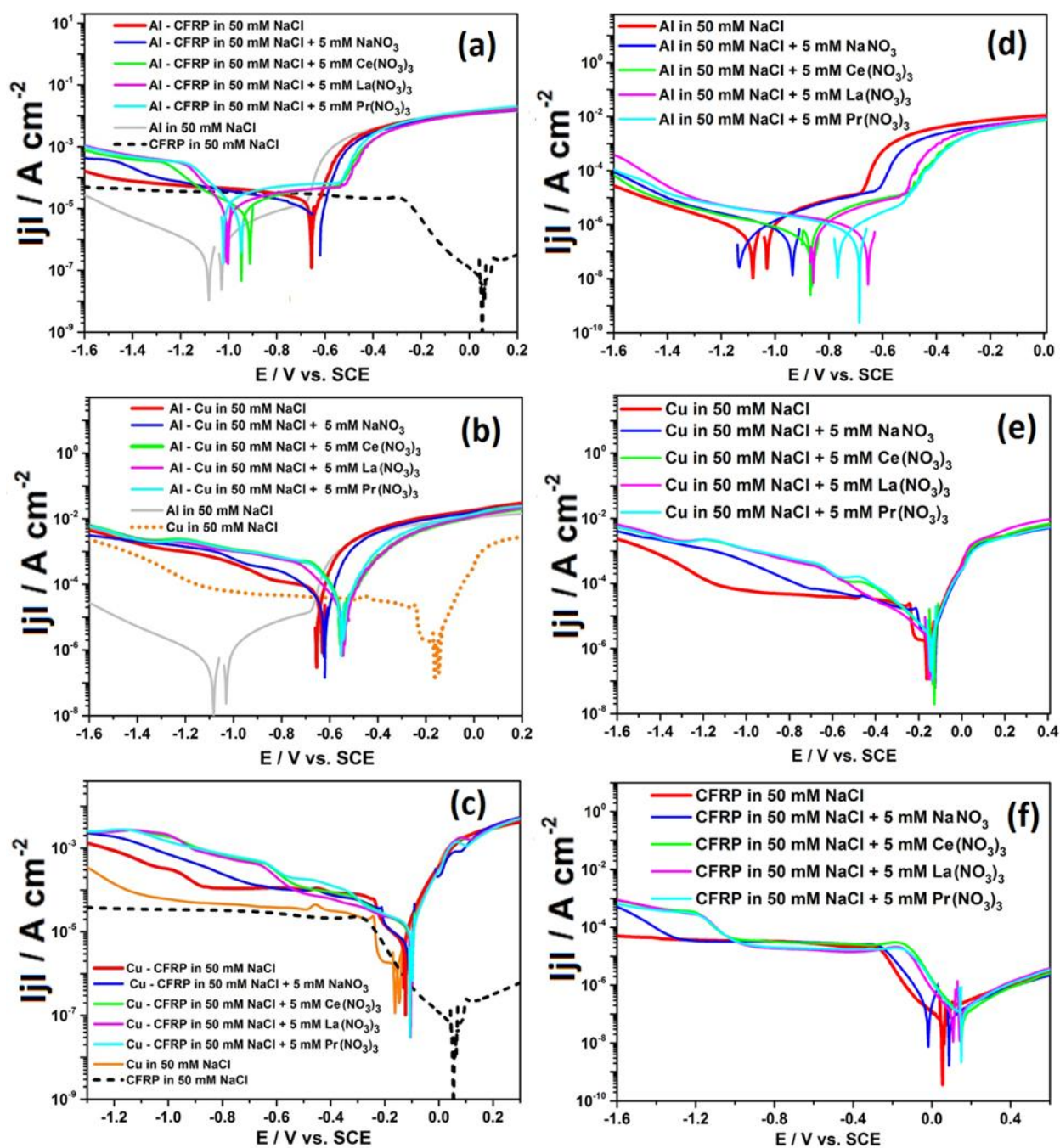


Fig. 6.11. Effect of nitrate inhibitors on the potentiodynamic curves of (a) Al - CFRP, (b) Al - Cu, and (c) Cu - CFRP galvanic couples, and (d) aluminium, (e) copper, and (f) CFRP in 50 mM NaCl based inhibitor solutions after 1 hour immersion.

From the potentiodynamic polarization curves for Al - Cu galvanic couple in the presence of nitrates (Fig. 6.11b), lower measured anodic current densities coupled with shifts of the corrosion potential of the couple towards anodic values is observed in the presence of all the RE nitrates studied. Such reductions in the anodic current densities in the active corrosion region of the curve indicates that RE cations act on Al - Cu couple also by suppression of anodic dissolution processes.

The potentiodynamic polarization curves for Cu - CFRP couple in the presence of nitrates (Fig. 6.11c) shows no significant changes in the measured current densities but cathodic current densities are lowered in the potential range from -0.2 to -0.5 V_{SCE} in the presence of lanthanum nitrate in which inhibitive effects were obtained from ZRA measurements of galvanic current densities (Fig. 6.10 above).

With respect to the single materials, for aluminium (Fig. 6.11d) the presence of nitrate anion either in the absence (as in NaNO₃) or in the presence of rare-earth cations (as in Ce(NO₃)₃, La(NO₃)₃, and Pr(NO₃)₃), generally lead to increased cathodic current densities on the cathodic branch of the potentiodynamic polarization curves, and on the anodic branch shifts in the corrosion potential and pitting potential of aluminium to more anodic values. The effects on the anodic branch are however much enhanced in the presence of both the nitrate anion and rare earth cations. This suggests an additive or synergistic effect of the nitrate anion and rare-earth cations in suppressing anodic activities on aluminium. For copper (Fig. 6.11e) the presence of nitrate anion either in the absence (as in NaNO₃) or in the presence of rare-earth cations (as in Ce(NO₃)₃, La(NO₃)₃, and Pr(NO₃)₃), generally lead to enhancement of cathodic processes evidenced by increased cathodic current densities without any significant changes on anodic processes. Hence it is concluded that the nitrates tend to promote cathodic activities on copper. For CFRP (Fig. 6.11f) with rare-earth nitrates, very marginal reduction in the cathodic current densities were observed in the potential ranges (-0.6 to -0.9 V_{SCE}) it is likely to be polarized to on galvanic coupling to aluminium indicating possibility of some beneficial effects with the use of rare earth nitrates on galvanic system composed of Al and CFRP only. This is confirmed from Table 6.1 in which inhibition efficiency of $\approx 76\%$ was obtained for Al - CFRP dual material galvanic couple after 150,000 seconds immersion in the presence of Ce(NO₃)₃. However, for Al - Cu, in spite of the fact that the results from short term potentiodynamic polarization tests (3600 seconds immersion) which indicated marked inhibitive effects of rare-earth nitrates on anodic processes on aluminium but enhanced cathodic processes on copper in the same time scale (3600 seconds) which could be suggestive of a low probability of significant inhibitive effects on Al - Cu galvanic couple, significant inhibitive effects were obtained (Table 6.1) on long term measurements of galvanic current density (IE = 85% with Ce(NO₃)₃ and $\approx 4\%$ NaNO₃). These discrepancies are attributed to the differences in the time-scales of the two measurements, and in nature of the two test methods.

The effect of introduction of the rare-earth cations as acetates on the corrosion of Al, Cu, and CFRP, and on the galvanic corrosion of Al - CFRP, Al - Cu, and Cu - CFRP dual galvanic couples were studied in an attempt to understand their contributions to the mechanism(s) of the observed multi-material corrosion inhibition in the Al - Cu - CFRP multi-material galvanic system and the results and its discussion presented herein.

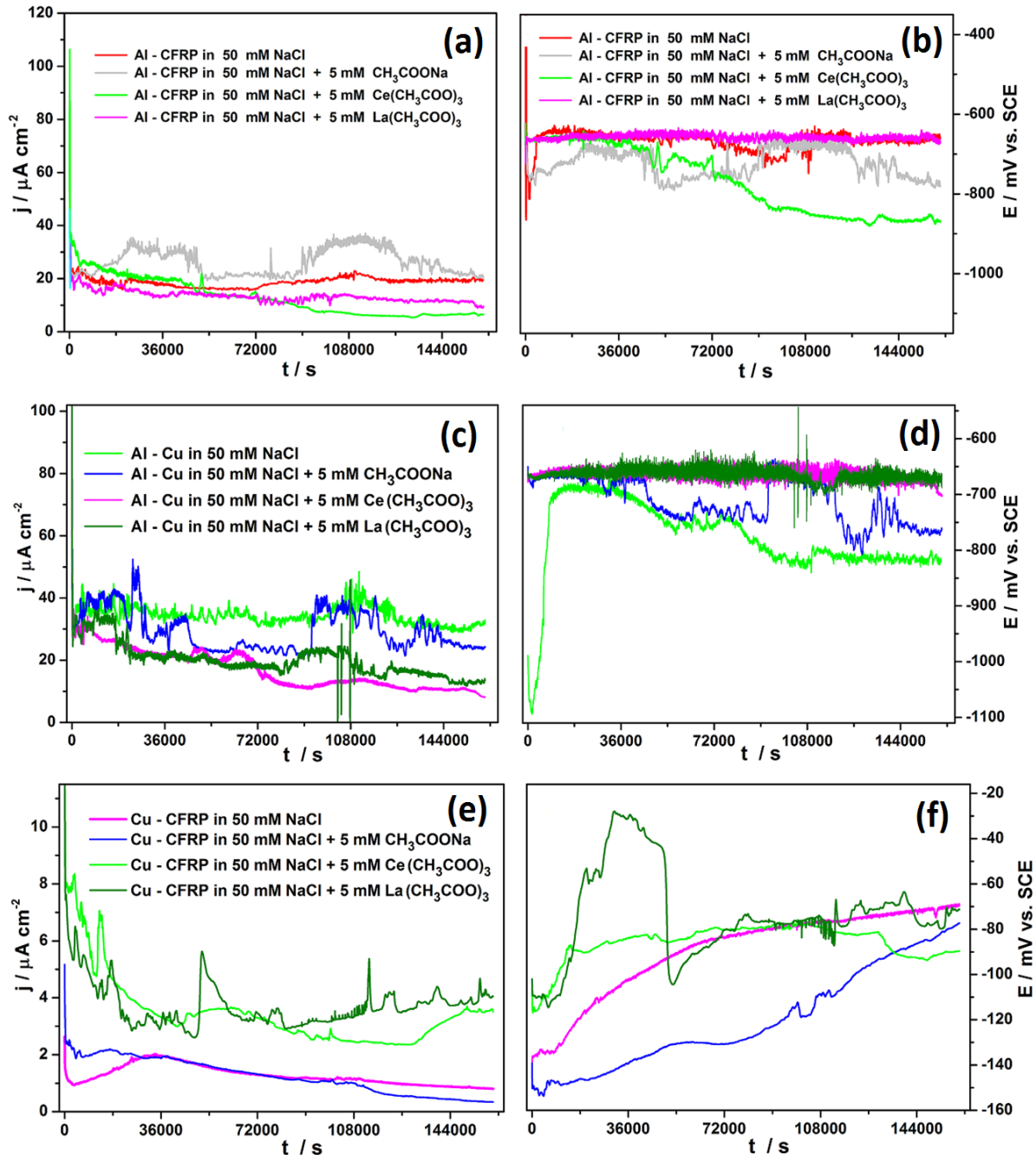


Fig. 6.12. Effect of rare-earth acetate inhibitors on evolution of galvanic current densities and potentials for (a-b) Al - CFRP, (c-d) Al - Cu, and (e-f) Cu - CFRP galvanic couples in 50 mM NaCl based inhibitor solutions.

From Fig. 6.12a above presenting the effect of acetates on the galvanic corrosion of Al-CFRP couple the same trends and ranking observed in nitrates of inhibitive effects only in the presence of rare earth cations is manifested with Ce performing better than La. The observance

of same trends suggests that the effect of the conjugate anion of the rare earth salt (nitrate or acetate) is apparently insignificant in this galvanic couple.

The evolution of galvanic current densities for Cu - CFRP in the presence of acetates (Fig. 6.12b) indicates that the rare-earth acetates markedly enhanced galvanic current densities between Cu and CFRP. In the presence of sodium acetate some inhibitive effects are observed on prolonged immersion after 30 hours.

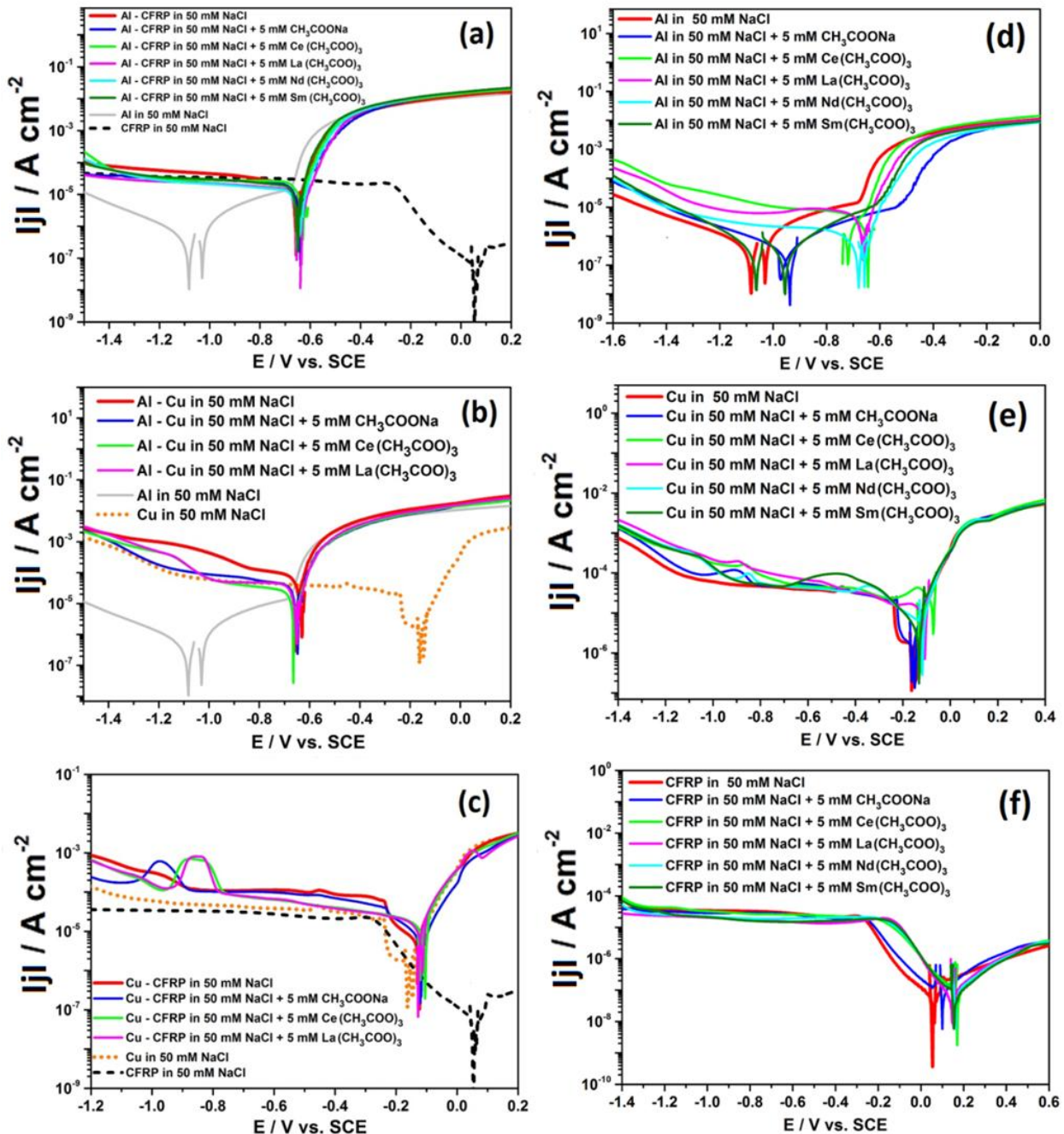


Fig. 6.13. Effect of acetate inhibitors on the potentiodynamic curves of (a) Al - CFRP, (b) Al - Cu, and (c) Cu - CFRP galvanic couples, and (d) aluminium, (e) copper, and (f) CFRP in 50 mM NaCl based inhibitor solutions after 1 hour immersion.

Unlike in nitrates the potentiodynamic polarization curve for Al - CFRP in the presence of

the effective rare-earth cations (Ce and La) in acetates (Fig. 6.13a above) does not exhibit any shifts in the galvanic corrosion potential compared to values in uninhibited couples (red line). Furthermore, the cathodic current densities are lower in the presence of the acetates compared to values in uninhibited galvanic couple supporting the earlier conclusion that increased cathodic current densities in the presence of nitrates arise from non-corrosion related processes of nitrate electro-decomposition on the cathode surface.

In studying the effects of acetates on galvanic corrosion of Al - Cu galvanic couple (Fig. 6.13b), the same trends observed in the case of nitrates (Fig. 6.11b) was observed suggesting that for this couple the inhibitive effects are linked to the presence of the rare-earth cations. However, unlike in nitrates the potentiodynamic polarization curves of Al - Cu galvanic couple in the presence of acetates (Fig. 6.13b) exhibit neither shifts in the corrosion potential nor marked reduction in anodic current densities compared to values measured in blank solution. In contrast to the scenario in nitrates, in the presence of acetates lower cathodic current densities are recorded. Since the lower cathodic current densities are observed even in the absence of rare-earth cations (as in sodium acetate), the suppression of cathodic activity might be attributed to the presence of acetate anions.

In the potentiodynamic polarization curves for Cu - CFRP in the presence of acetates (Fig. 6.13c), marginally lower anodic currents are observed only in the presence of sodium acetate, and though lower cathodic current densities are observed in the presence of the rare-earth acetates (Ce and La) from the mixed corrosion potential of the couple ($\approx 0.1 V_{SCE}$) to $\approx -0.8 V_{SCE}$, inhibitive effects are not observed in the galvanic current density profile (Fig. 6.12c). The cathodic peaks observed in the potentiodynamic polarization curves of Cu - CFRP couple in all the acetates studied (Na, Ce, and La acetates) are inferred to be related to the acetate ion based on the fact that similar peaks are not observed in the presence of nitrates (Fig. 6.13c).

Regarding the single materials (Al, Cu, and CFRP), the trends observed in the potentiodynamic polarization curve for each material were very similar to those obtained for same material in nitrates (Fig. 6.11d-f). In the potentiodynamic polarization curve for aluminium (Fig. 6.13d), the presence of the acetates resulted in enhanced cathodic activities, shifts in corrosion potential of aluminium towards more anodic potentials, lowered anodic current densities in the active corrosion region, and shifts in the pitting potential of aluminium to more anodic values. However, unlike in nitrates, the suppression of anodic processes appear to be most significant in the absence of rare-earth cations (as in CH_3COONa). For copper, its potentiodynamic polarization curve (Fig. 6.13e) indicate enhanced cathodic processes, very

small shifts in corrosion potentials towards more anodic values with no significant effect on anodic processes. The potentiodynamic polarization curve for CFRP (Fig. 6.13f) reveal a shift in "E_{corr} values" in the presence of all the acetates (with and without rare-earth cations), and relatively lower cathodic current densities compared to values in blank solution and in nitrates (Fig. 6.11f) in the potential range (-0.6 to -0.9 V_{SCE}) it is likely to be polarized on galvanic coupling to aluminium.

Since a cathodic peak is observed between -0.7 V to -1.1 V_{SCE} in the potentiodynamic curves of Cu - CFRP in the presence of all the acetates (Fig. 6.13c) was also observed in the presence of copper though less pronounced, but not on any other material or galvanic couple, the peak is attributed to the reduction most probably copper acetate and/or (hydro)oxides. This attribution is supported by the report of Sanders et al. [688] that they obtained oxide-free copper surface by polarizing copper for 30 minutes at -900 mV_{NHE} (-1144 mV_{SCE}) in 0.1 M KOH solution. Besides its ability to act as an alkaline pH buffer, acetates have been reported [689] to be capable of inhibiting copper corrosion in NaCl solutions at pH 8.5 by initially accelerating copper dissolution leading to the formation of a protective complex with copper corrosion products. The presence of cuprous and cupric acetate salts on the surface of corroded copper samples in environments containing acetate have been reported [689,690]. These can partly account for the differences observed in the inhibition profiles of the rare earth cations either alone or in inhibitor combinations, based on the conjugate anion of the rare-earth cations in which slower kinetics were observed in the presence of acetates compared to nitrates. From the results presented above it is concluded that the observed inhibiting effects observed in the presence of rare-earth compoundson galvanic corrosion in the Al - Cu - CFRP system is predominantly associated with the presence of the rare-earth cations; the most effective of these being Ce³⁺ and La³⁺ cations. More detailed insights on the effect of the conjugate anion of the most promising rare-earth cations (Ce³⁺ and La³⁺) on galvanic corrosion in the Al - Cu - CFRP multi-material galvanic system are presented in section 6.3.3 below.

6.3.3. Effect of Conjugate Ions of Rare-earth Metal Cations on the Galvanic Corrosion of Al - CFRP , Al - Cu, and Cu - CFRP Galvanic Couples.

To confirm any effects of the conjugate ion of the rare earth metal ions (NO₃⁻ and CH₃COO⁻) on galvanic corrosion in the Al - Cu - CFRP multi-material galvanic system comparisons of the galvanic current densities and potential evolution of Al - CFRP, Al - Cu, and Cu - CFRP

galvanic couples in the presence of NaNO_3 and CH_3COONa , $\text{Ce}(\text{NO}_3)_3$ and $\text{Ce}(\text{CH}_3\text{COO})_3$, and $\text{La}(\text{NO}_3)_3$ and $\text{La}(\text{CH}_3\text{COO})_3$ respectively were made and presented in Fig. 6.14 below.

From Fig. 6.14(a-b) it observed that for Al - CFRP these effects are insignificant. By comparison of the galvanic current densities and potential evolution of Al - Cu galvanic couple in the presence of NaNO_3 and CH_3COONa , $\text{Ce}(\text{NO}_3)_3$ and $\text{Ce}(\text{CH}_3\text{COO})_3$, and $\text{La}(\text{NO}_3)_3$ and $\text{La}(\text{CH}_3\text{COO})_3$ respectively (Fig. 6.14c-d), a link between the observed inhibitive effect of the rare-earth metal salts and their conjugate anion is established. It is observed that whereas cerium exerts inhibitive effects when added as either cerium nitrate or cerium acetate the magnitude and kinetics of the inhibitive effect are more pronounced when added as a nitrate. With lanthanum, significant inhibition of galvanic corrosion of Al - Cu galvanic couple is observed on addition as acetate while acceleration of corrosion is observed on addition as a nitrate until after about 30 hours of immersion. In the light of the above it is concluded that for Al - Cu galvanic couple the conjugate anion of the rare-earth metal cation affects its inhibitive properties with the actual effects dependent on the particular rare-earth cation (Ce or La). The marked effect of the choice of conjugate anion of the rare-earth metal cation on galvanic corrosion of the Al - Cu galvanic couple is predominantly attributed to the strong interaction of the acetate anion with copper surface (Figs. 6.13c, 6.13e, and 6.15c) resulting in a probable change in the composition of the corrosion products on its surface at the potential range it is polarized to on galvanic coupling with aluminium.

By comparison of the galvanic current densities and potential evolution of Cu - CFRP galvanic couple in the presence of NaNO_3 and CH_3COONa , $\text{Ce}(\text{NO}_3)_3$ and $\text{Ce}(\text{CH}_3\text{COO})_3$, and $\text{La}(\text{NO}_3)_3$ and $\text{La}(\text{CH}_3\text{COO})_3$ respectively (Fig. 6.14e-f), it is observed that except in the case of lanthanum in which some inhibitive effects are observed in the presence of lanthanum nitrate, but accelerative effects in the presence of lanthanum acetate, the conjugate anions (nitrate or acetate) exerts no significant effect on the response of the rare earth metal salts to the galvanic processes in Cu - CFRP couple.

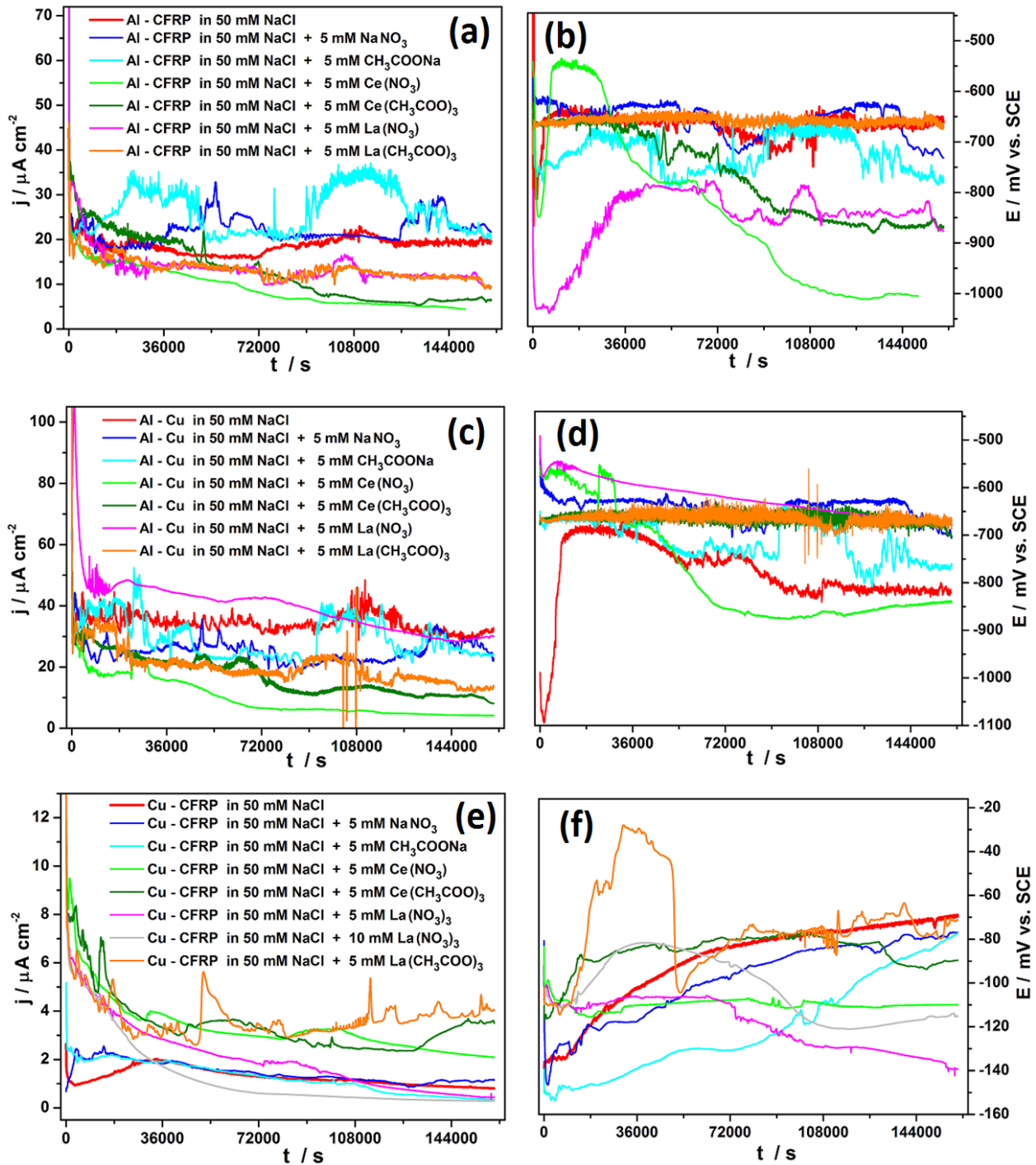


Fig. 6.14. Effect of conjugate anion of rare-earth metal salts on the galvanic current density and (b) potential evolution of (a-b) Al - CFRP, (c-d) Al - Cu, and (e-f) Cu - CFRP galvanic couples in 50 mM NaCl based inhibitor solutions.

By comparison of the potentiodynamic polarization curves of Al - CFRP, Al - Cu, and Cu - CFRP galvanic couples and those of the single materials (Al, Cu, and CFRP) in 50 mM NaCl based inhibitor solutions containing different rare-earth cations with either of nitrate or acetate anions after 1 hour immersion the differences in the effects of the conjugate anions on cathodic and anodic processes in each of these materials and galvanic couples are demonstrated with clarity (Fig. 6.15).

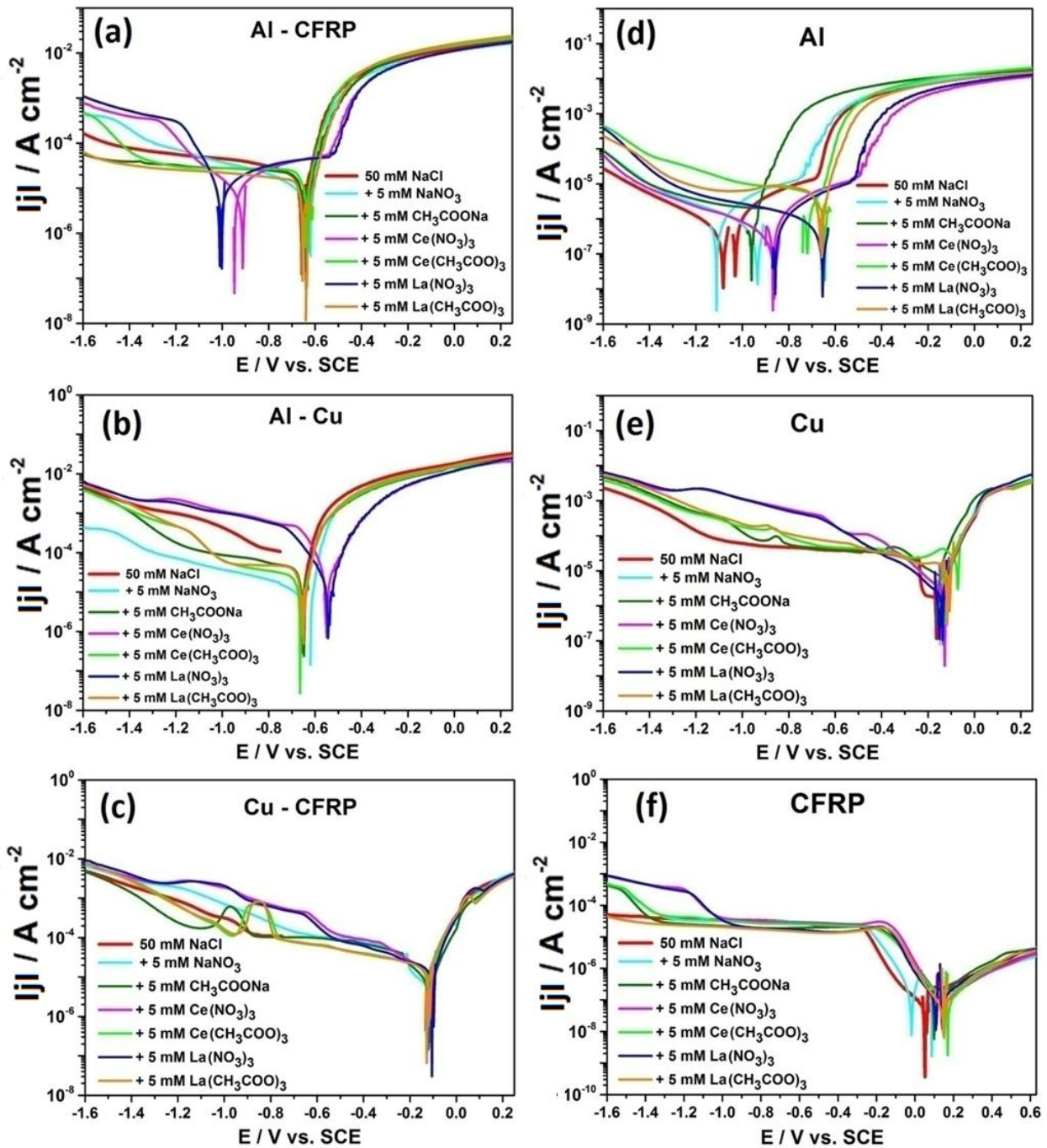


Fig. 6.15. Effect of conjugate anion of rare-earth metal salts on the potentiodynamic polarization curves of (a) Al - CFRP, (b) Al - Cu, and (c) Cu - CFRP, (d) Al, (e) Cu, and (f) CFRP in 50 mM NaCl based inhibitor solutions after 1 hour immersion.

For Al - CFRP dual galvanic couple (Fig. 6.15a), it is observed that on introduction of the rare earth cations (Ce^{3+} and La^{3+}) as nitrates the mixed corrosion potential of Al - CFRP dual galvanic couple is observed to be displaced by over 300 mV towards more cathodic potentials, with the cathodic current densities comparatively lower with respect to values in blank solution up to about $-1100 \text{ mV}_{\text{SCE}}$ which is similar to the corrosion potential of aluminium in blank 50 mM NaCl solution (Fig. 6.15d). Above this potential the cathodic current densities increase steeply above values in blank solution. On the anodic branch of the polarization curve, the

"pitting" potential is displaced towards more anodic potentials in the presence of rare-earth nitrates but not in NaNO_3 . The fact that similar changes in the cathodic and anodic branches of the polarization curves were not observed in the presence of NaNO_3 leads to the conclusion that these effects are due to either the presence of the rare-earth cations or the cooperative action of the rare-earth cations and the nitrate anion on the basis of the absence of similar effects in the presence of rare-earth acetates and sodium acetate (Fig. 6.15a). In contrast, in the polarization curve of aluminium (Fig. 6.15d) only the effects on the anodic branch (marked displacement of the pitting potential) persist in the presence of rare-earth nitrates as the mixed corrosion potential is displaced in the opposite direction (of trends observed in Al - CFRP couple) towards more anodic potentials and the cathodic current densities higher at all potentials compared to values in blank test solution. On the other hand the introduction of rare-earth cations as acetates resulted in reduced cathodic current densities in Al - CFRP couple but opposite effect on aluminium alone (Fig. 6.15d), but less marked effects on anodic processes in both in Al - CFRP couple and Al compared to trends observed with rare-earth nitrates.

For Al - Cu galvanic couple (Fig. 6.15b), the cathodic current densities were observed to be enhanced on introducing rare-earth cations as nitrates, while the mixed corrosion potentials were displaced to more anodic potentials with significantly lower anodic current densities. Similar enhancements in the cathodic current densities were also observed for copper (Fig. 6.15d) in the presence of rare-earth cations particularly as nitrates. By comparing the observed trends in the cathodic and anodic branches of the polarization curves of Al - Cu galvanic couple (Fig. 6.15b) with those of Al (Fig. 6.15d) and Cu (Fig. 6.15e) in the presence of nitrates, the earlier stated position of considering/attributing changes or trends in the cathodic branch of the polarization curve of galvanic couples to the constituent cathodic material(s) of the such couples, and changes in the anodic branch to the anodes in such galvanically coupled arrangements is validated. On introducing the rare-earth cations as acetates or in the presence of both the nitrate anion and rare-earth cations (as in NaNO_3), cathodic processes were suppressed in Al - Cu galvanic couple but enhanced in both Al and Cu. The observed effect of the presence of rare-earth cations as acetates on the polarization curve of Al - Cu galvanic couple but not in Al or Cu is partly attributed to the plausible buffering effect of the acetate anion on the alkaline pH generated near copper surface on coupling to aluminium which probably enhances faster and sustained precipitation of the rare-earth hydro(oxides) onto copper surface leading to suppression of cathodic processes on copper surface.

In the polarization curves for Cu - CFRP (Fig. 6.15c) the presence of nitrate anion without

rare-earth cations (as in NaNO_3) leads to increase in the cathodic current densities above values observed in the blank solution, while introduction of the rare-earth cations as nitrates lead to further increase in the cathodic currents measured in NaNO_3 between ≈ -550 and -1200 mV_{SCE} which were also observed in the polarization curves of copper in the presence of these rare-earth nitrates (Fig. 6.15e). In the presence of acetates with or without the rare-earth cations, the cathodic current densities were generally lower than those measured in blank solution except for cathodic peaks observed in the presence of CH_3COONa between -880 and -1050 mV_{SCE} but between -760 and -920 mV_{SCE} in the presence of the combination the acetate anion and rare-earth cations (in $\text{Ce}(\text{CH}_3\text{COO})_3$ and $\text{Ce}(\text{CH}_3\text{COO})_3$). These peaks are attributed to the reduction of corrosion products on copper that are probably predominantly composed of copper acetate. For Cu - CFRP no significant changes were observed in the mixed corrosion potential and the anodic current densities in response to changes in the conjugate anions (NO_3^- or CH_3COO^-) of the the rare-earth cations.

The polarization curve of CFRP in the presence of acetates and nitrates (Fig. 6.15f) indicate slight reduction of the diffusion limited cathodic currents in the presence of all the acetates with the potential range over which this effect is observed is highest in the presence of lanthanum acetate. Of the rare earth nitrates this reduction of cathodic current densities in the diffusion limited region was only observed in the presence of lanthanum nitrate though the potential range over which effect was persistent was narrower. In the light of these the slight reduction of the cathodic current densities if CFRP in the diffusion limited region is attributed to the co-operative action of the rare-earth cations and acetate anion that probably accelerates the precipitation of metal hydroxides onto CFRP surface in the high pH near its surface due to cathodic process that is apparently buffered by the acetate anions. In the "active region" of the cathodic branch of the polarization curve of CFRP (Fig. 6.15f) higher current densities were measured in the presence of all the inhibitors irrespective of the rare-earth cation or its conjugate anion. In spite of the increased cathodic current densities observed in this region the slope of the polarization curve in this region were generally similar to that in the blank solution which leads to a conclusion that similar processes occurred in this region but the kinetics of these processes were apparently enhanced by the presence of the inhibitors irrespective of the conjugate anion employed. The steep increase in the cathodic current densities observed in the presence of the rare earth nitrates around -1050 mV_{SCE} had been reported earlier in section 5.2.8.4 (Fig. 5.43), and attributed to the electrochemical reduction of nitrates on CFRP surface, as the increase in the measured cathodic current density at potentials more cathodic than $\approx -$

1050 mV_{SCE} was sensitive to changes in the concentration of the nitrates while the onset potential was invariant. Though a similar increase in cathodic current densities were observed in the presence of NaNO₃ at potentials more cathodic than ≈ -1500 mV_{SCE}, in this case it is attributed to hydrogen evolution reactions as the onset potential was much more cathodic and in the potential region where water reduction with hydrogen evolution is favoured. Consequently, by comparison of the cathodic polarization curves of CFRP in the presence of nitrates and acetates, with and without the rare earth cations it is concluded that hydrogen evolution processes are most probably suppressed on CFRP surface in the presence of lanthanum acetate for reasons that are not yet fully clarified.

From the results presented herein it is obvious that the rare-earth cations principally Ce³⁺ and La³⁺ generally exhibit inhibitive effects on the galvanic corrosion of the dual galvanic couples (Al - CFRP, Al - Cu, and Cu - CFRP) in the Al - Cu - CFRP galvanic system irrespective of the conjugate anion. In some instances additive/synergistic inhibition may be achieved by the choice of conjugate anion as with Al - CFRP dual galvanic couple (Fig. 6.15a), in which the introduction of the rare earth cations (Ce³⁺ and La³⁺) as nitrates caused the mixed corrosion potential of Al - CFRP dual galvanic to be displaced by over 300 mV towards more cathodic potentials, with the cathodic current densities comparatively lower with respect to values in blank solution up to about -1100 mV_{SCE}. This effect is attributed to the well known anodic inhibitor effect of the nitrate anion on aluminium. In contrast, a marked but deleterious effect is observed on introduction of rare-earth metal cation as an acetate against galvanic corrosion of the Al - Cu galvanic couple attributed to the strong interaction of the acetate anion with copper surface (Figs. 6.13c, 6.13e, and 6.15c) resulting in a probable change in the composition of the corrosion products on its surface. In the light of these in spite of benefits of employing rare-earth cations as corrosion inhibitors in the Al - Cu - CFRP multi-material system care is advised on the choice of the conjugate anion to maximize inhibitive effects.

6.4.0. Unveiling the Mechanism of Multi-material Corrosion Inhibition in the Al - Cu - CFRP Galvanic system

In order to understand the mechanism of the observed multi-material corrosion and its successful inhibition in the Al -Cu - CFRP "triplet" multi-material galvanic system, further tests were carried out on Al - Cu and Al - CFRP dual galvanic couples and on Al - Cu - CFRP galvanic triplet to establish changes on and near the surface of the material components of these couples on galvanic coupling and changes in the concentration of Cu in known volumes of the test

solution (consistent with electrochemical test conditions) using atomic absorption spectrometry (AAS), as the presence of cations of the cathodic metal (Cu) are known to affect anodic dissolution of the anodic metal (Al) with and without galvanic coupling. The concentration of Al in the test media was not monitored primarily because the AAS facility was not suitable for its measurement and secondly, its presence in solution is expected as it is the anode. Since the pH around the cathodes have been demonstrated to change to alkaline values on galvanic coupling to the anode (Al), the cyclic voltametric response of Cu under quiescent and anoxic conditions were evaluated at different pH values after 1 hour immersion in 50 mM NaCl. Similar analysis for the other cathode in the system (CFRP) was done and already presented in chapter 5 of this work (**section 5.2.8.4 and Fig 5.43**). In addition surface analysis of galvanic couples after exposure to test media (coupled and uncoupled) using x-ray fluorescence spectroscopy (XRF), and localized measurements of pH profile, oxygen profile and ionic currents near the surface of the components of the galvanic couples (coupled and uncoupled), with and without inhibitors using the selective-ion electrode technique (SIET) and scanning vibrating electrode technique (SVET) enabled the determination of the mechanism(s) of multi-material corrosion and multi-material corrosion inhibition in the Al - Cu - CFRP multi-material combination presented herein.

6.4.1. Multimaterial Corrosion Inhibition in the Al - Cu - CFRP Galvanic system: Insight into the Changes in the Local pH around Constituent Materials on Galvanic Coupling.

For a better understanding of the mechanism of action of the candidate multi-material corrosion inhibitors shortlisted above, micro-scale tests were carried out to establish the local environment(s) near un-coupled and coupled multi-material assemblies in the presence and absence of selected inhibitors. Prior to studies with inhibitors on the galvanic corrosion behaviour of this "galvanic triplet", tests were made to obtain information on the local environment around Al, Cu, and CFRP in this "galvanic triplet" on galvanic coupling in 50 mM NaCl.

Having demonstrated in chapter 5 (**sections 5.2.3.1 to 5.2.3.3**) that the local pH above CFRP is very sensitive to the applied polarization, and aware that changes in the local pH affects the mechanism and efficiency of certain inhibitors, using the Al - CFRP dual galvanic couple as a test case the pH profile across CFRP and metal (Al) in quiescent 50 mM NaCl was determined at a height of 12 μm from the surface and presented in Fig. 6.16 (a and b). Furthermore, the pH profile across the surface of the components of the galvanically coupled Al - Cu - CFRP "galvanic triplet" was measured and presented in Fig. 6.16 (c and d) below.

From Fig. 6.16a below (red line), it is observed that in galvanically coupled Al - CFRP in quiescent 50 mM NaCl the local pH at a height of about 12 μm above the CFRP is around 10.5 (with the impressed polarization on CFRP due to galvanic coupling to Al in the test solution determined electrochemically to be around -650 to 700 mV_{SCE} (Fig. 6.1b), while the pH above the coupled aluminium falls below the bulk pH to as low as 5.5. This local acidification above galvanically coupled aluminium is attributed to hydrolysis reactions involving Al^{3+} ions that leads to a local abundance of H^+ . In contrast there are no significant changes in the local pH in the absence of galvanic coupling (black line).

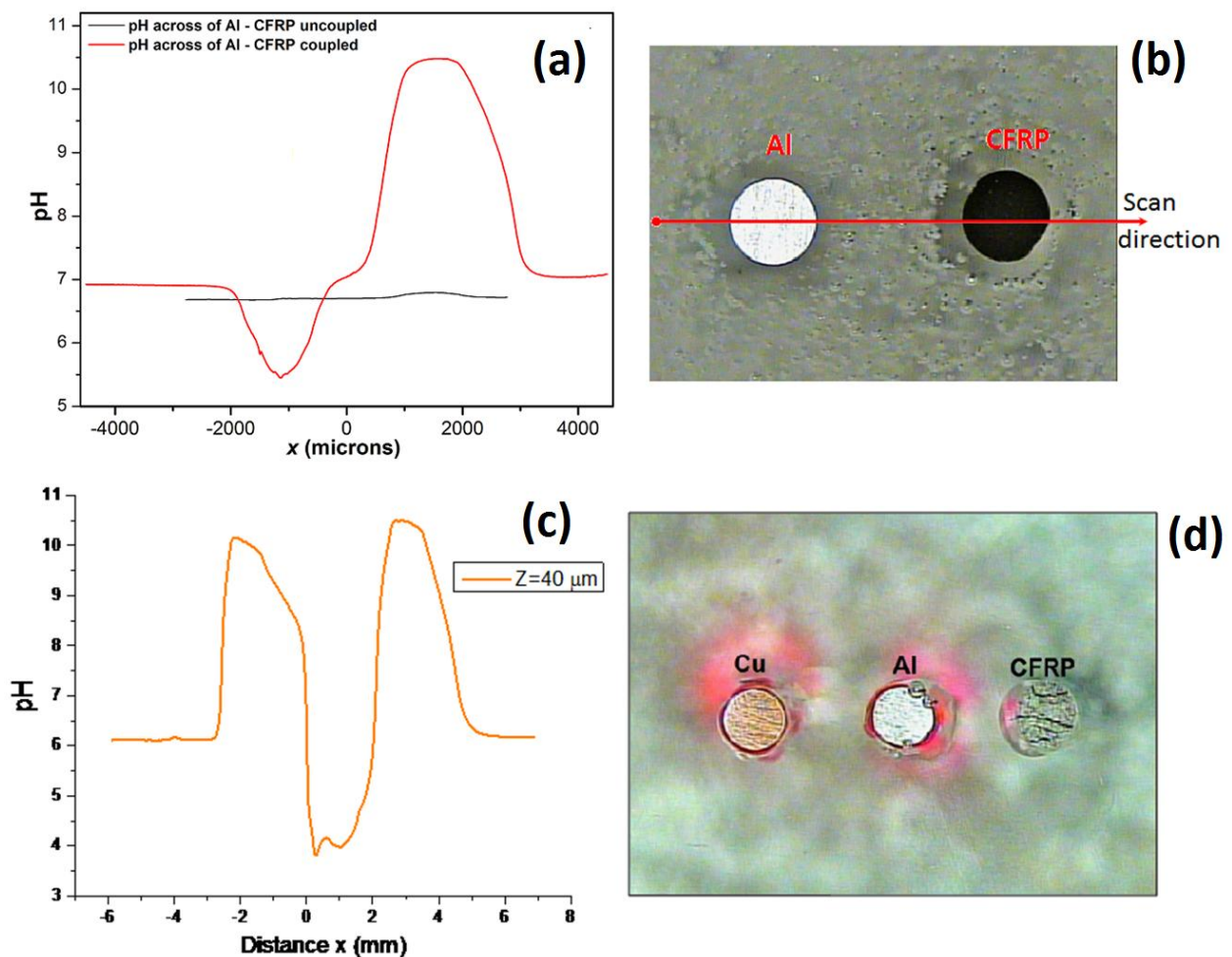


Fig. 6.16. pH profile in 50 mM NaCl 12 μm above (a-b) galvanically coupled and uncoupled Al - CFRP and (c-d) 40 μm above galvanically coupled Al - Cu - CFRP "triplet" couple.

From Fig. 6.16c above, in galvanically coupled Al - Cu - CFRP "triplet" galvanic couple the pH is observed to be above 10 at a height of $\approx 40 \mu\text{m}$ from the surfaces of both cathodes (Cu and CFRP) and as low as 4 above the anode (aluminium). Comparing the pH value above aluminium in this case with the ≈ 5.5 earlier observed in measurements across galvanically coupled Al - CFRP couple (Fig. 6.16a), it is apparent that increase in cathodic area relative to the anodic area, leads to further lowering of the pH above the aluminium due to enhanced anodic

activities. This lowered pH values above the anode in the "galvanic triplet" compared to values measured above the anode in the dual galvanic couple can be explained by the increased rate of aluminium dissolution and hydrolysis reactions due to galvanic coupling to a larger cathode.

6.4.2. Multimaterial Corrosion Inhibition in the Al - Cu - CFRP Galvanic system: Insight into the Electrochemical Response of the Cathodes to Changes in Local pH.

Being aware of the fact that galvanic coupling of Al to the cathodes (Cu and CFRP) causes a change in the pH near these cathodes to alkaline values (Fig. 6.16) between pH 10 and 11, and having established the electrochemical response of one of the cathodes (CFRP) to polarization at different pH (**sections 5.2.3.2 and 5.2.3.3; Figs. 5.9 and 5.10**) using potentiodynamic polarization tests and cyclic voltammetry, cyclic voltammetric tests were carried out on the other cathode (Cu) in 50 mM NaCl adjusted to different pH values with NaOH. These tests on copper were carried out in both quiescent and anoxic conditions, and the voltammograms presented in Fig. 6.17 below.

It is worthy of note that the results of cyclic voltammetric tests on CFRP in quiescent chloride solutions adjusted to pH 1, 3, 7, 10, and 12, over a potential range of -1000 to +500 mV_{SCE} at a scan rate of 50 mV/s earlier presented in chapter 5 (**Fig. 5.10**) indicated a significant and consistent cathodic peak around -250 mV SCE under all test conditions employed, attributed to the 2-electron reduction of oxygen with formation of hydroxyl ions and hydrogen peroxide [672]. Very importantly, significant cathodic current densities in the range $\geq 100 \mu\text{A cm}^{-2}$ was measured on CFRP in quiescent 50 mM NaCl solution adjusted to pH 7,10, and 12, in the potential range of -300 to -1000 mV_{SCE} which lies in the range of potentials CFRP is likely to be polarized to on galvanic coupling to copper.

The voltammograms of copper in quiescent 50 mM NaCl (Fig. 6.17) below shows that very significant cathodic current densities with peak current of $\approx 8 \text{ mA cm}^{-2}$ measured around a potential of -600 mV_{SCE} at pH 7 and pH 10 in both quiescent and anoxic test conditions. At pH of 12 the cathodic current density around this potential drops significantly with the highest measured cathodic peak current densities less than $\approx 2 \text{ mA cm}^{-2}$ and peak position apparently shifted to more cathodic potentials ($\approx -800 \text{ mV}_{\text{SCE}}$) under both quiescent and anoxic conditions coupled with the presence of other cathodic peaks at this pH. It is noteworthy to mention that the magnitude of these peaks might not have much relevance to the long term kinetics of cathodic processes and have been employed for comparison herein.

These results indicate and gives an idea of the apparent magnitudes of the significant

cathodic activities expected on coupling these cathodes (Cu and CFRP) to Al in multi-material assemblies. These results suggest more intense galvanic corrosion in Al - Cu dual galvanic couple compared to Al - CFRP galvanic couple. This position is validated by the analysis of ZRA measurements of galvanic current densities for Al -Cu and Al - CFRP galvanic couples in 50 mM NaCl solution (Table 6.1) based on values after 150,000 seconds immersion which indicated galvanic current densities of $29.9 \mu\text{A cm}^{-2}$ for Al - Cu and $18.9 \mu\text{A cm}^{-2}$ for Al - CFRP.

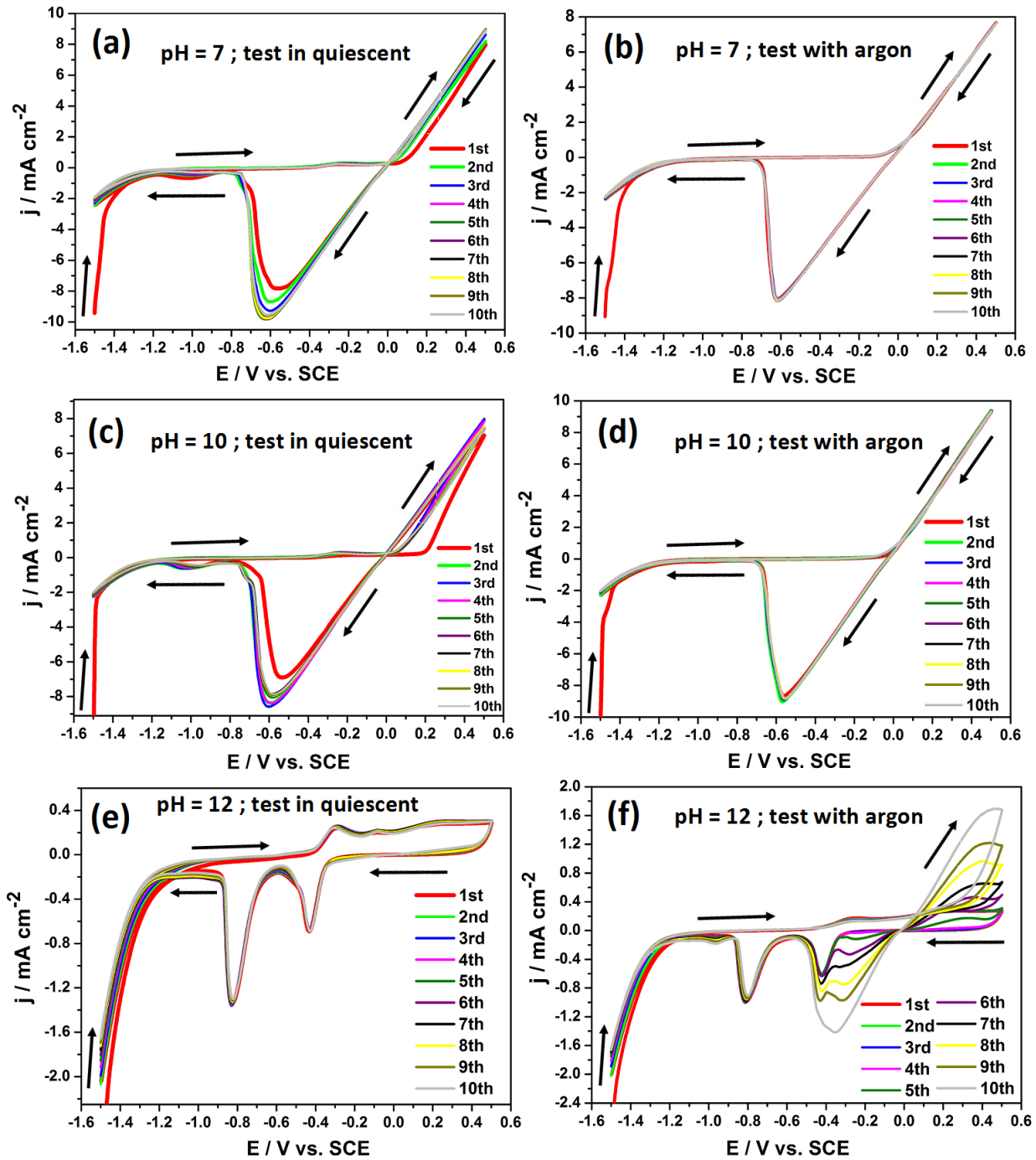


Fig. 6.17. Cyclic voltammogram of copper after 1 hour immersion in quiescent 50 mM NaCl adjusted to different pH and testing under quiescent conditions and anoxic conditions respectively by purging with argon for 15 minutes prior to and during testing.

In the light of these results and the discussions above, it is concluded that from near neutral pH to pH 10 significant multi-material corrosion is quite feasible in the Al - Cu - CFRP galvanic system which is consistent with the range of expected pH transitions near the cathodes in this multi-material system, and that this change in pH can be exploited as a trigger for corrosion inhibition strategies in the Al - Cu - CFRP multi-material galvanic system. Furthermore, on the basis of the observed reduction in the cathodic peaks on Cu at pH 12 in both quiescent and anoxic conditions in the potential ranges (-600 to -800 mV_{SCE}) consistent with the expected polarizations on the cathodes on galvanic coupling to Al, it is postulated but not confirmed that further increase of the local pH to 12 or more might lead to some reduction in the galvanic corrosion of the Al - Cu - CFRP multi-material assembly.

6.4.3. Multimaterial Corrosion Inhibition in the Al - Cu - CFRP Galvanic system: Insight into Significant Changes in Test Solution Composition.

Having thus established the range of the changes in local pH around each of the constituent of the Al - Cu - CFRP multi-material assembly on galvanic coupling, the electrochemical response of the cathodes to changes in bulk pH with respect to the evolution of cathodic processes on them, and aware of the effects the cations of the cathodic metals can have on anodic dissolution of the anode, and by extension on multi-material corrosion in the Al - Cu - CFRP multi-material combination, the time evolution of copper ions in the test solution was monitored on galvanically coupled and uncoupled Al - Cu assembly, and the results presented as Fig. 6.18 below.

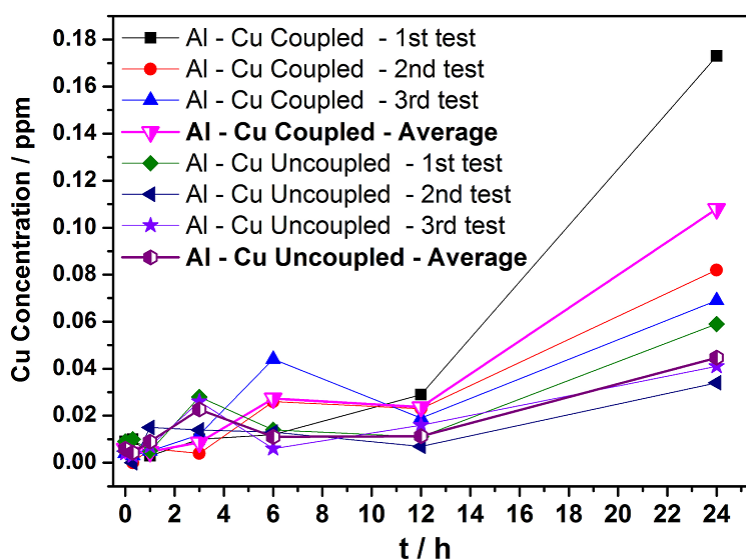


Fig. 6.18. Time evolution of copper concentration in 50 mM NaCl solution for (a) Al - Cu galvanically coupled and uncoupled (surface area of Cu and Al was 0.5 cm² and volume of test solution = 100 ml).

From the triplicate measurements of copper concentrations and the average values from these triplicate measurements in the test media (100 ml) prior to immersion (0 h) and at 1, 3, 6, 12, and 24 hours after immersion in galvanically coupled and uncoupled Al - Cu assembly (Fig. 6.18), the entry of copper into solution is confirmed in both cases but it is observed that in galvanically coupled Al - Cu couple the concentration of copper in the test solution is consistently higher; an effect that becomes very significant after 24 hours immersion. The presence of copper ions in solution coupled in the light of their ability to be electro-deposited onto aluminium surface is very likely to affect the corrosion and corrosion inhibition mechanism in the Al - Cu - CFRP multi-material galvanic system. This confirmed entry of copper into solution in Cu galvanically coupled to Al is inferred to most probably be the major cause of the observed differences (in some cases) in the trends from short term (1 h) potentiodynamic curves and longer term ($\geq 150,000 \text{ s} \approx 44 \text{ h}$) ZRA measurements of galvanic current density and potential. In the light of this, it is advised that in future work on the subject matter, longer term potentiodynamic polarization curves be acquired preferably after immersion for various time intervals ranging from 1 hour to ≥ 24 hours.

In Fig. 6.18, it is observed that in tests conducted on galvanically coupled Al - Cu assembly with (normalized surface area to test solution volume ratio), anode area : cathode area : test solution volume ratios of 1 : 1 : 200, the copper concentration in the test solution rises to concentrations of about 10^{-7} M ($\approx 0.1 \text{ ppm}$) which is in the lower range of concentrations in which the presence of copper and iron cations have been demonstrated [142,456] to still exert significant influences on the dissolution of aluminium, and attributed to be equivalent to about ≥ 0.1 atomic layers of the electro-deposited metal on the assumption that all the ions that enter into the solution adhered to the metal (Al) surface [456]. Furthermore, the presence of electro-deposited copper on aluminium surface is likely to lead to a reduction in the anodic area which in the absence of an appropriate inhibitor accelerate the dissolution of aluminium. However, in the presence of appropriate/certain inhibitor(s) the presence of copper on part of aluminium surface is capable of causing inhibitors that are very sensitive to copper (like the azoles) to interact with aluminium through the electro-deposited copper on its surface with potential effects on self-corrosion of aluminium and multi-material corrosion and multi-material corrosion inhibition in the Al - Cu - CFRP multi-material galvanic system.

6.4.4. Multimaterial Corrosion Inhibition in the Al - Cu - CFRP Galvanic system: Insight into Significant Changes in Oxygen Concentration Near Component Materials.

Aware that the oxygen concentrations around the galvanically coupled components of the Al - Cu - CFRP "galvanic triplet" is bound to change and can be employed to monitor inhibitive effects of added candidate multi-material inhibitor combinations, the oxygen distribution around the Al - Cu - CFRP "galvanic triplet" was evaluated by measurements of the cathodic currents generated by oxygen reduction in 50 mM NaCl solution without inhibitors to obtain a reference profile against which later tests in the presence of inhibitors can be compared. The oxygen distribution was evaluated at a height of $\approx 100 \mu\text{m}$ above components of the Al - Cu - CFRP system and the results presented in Fig. 6.19 below with the observed trends consistent with expected patterns in the cathodes (Cu and CFRP) and the anode (Al).

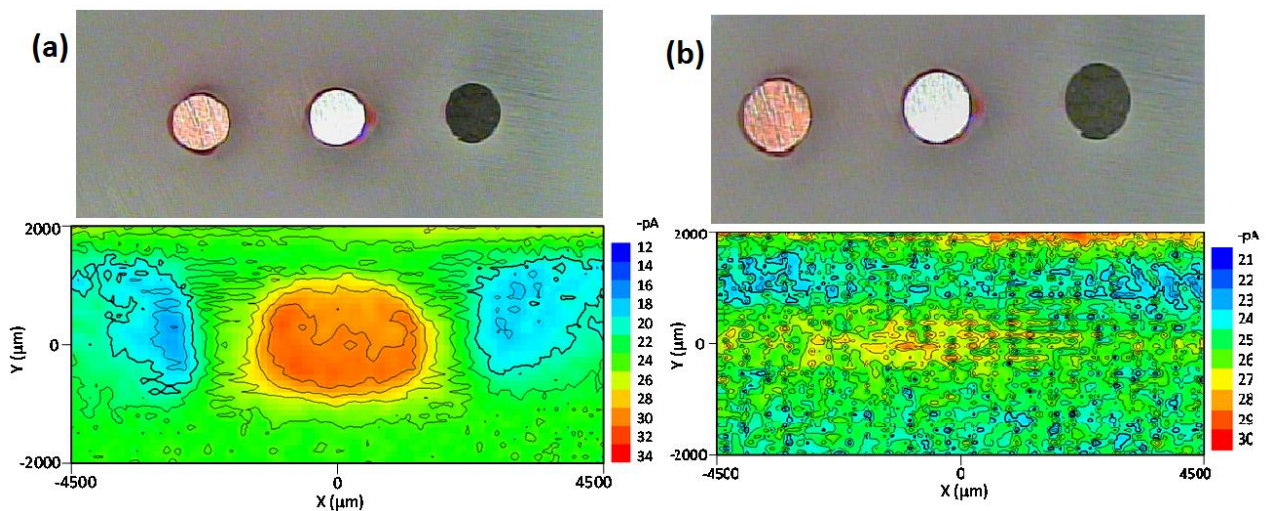


Fig. 6.19. Measured cathodic currents due to oxygen reduction $\approx 100 \mu\text{m}$ above components of the Al-Cu-CFRP system (a) galvanically coupled, and (b) uncoupled indicative of O_2 distribution.

In uncoupled Al - Cu - CFRP triplet assembly (Fig. 6.19b) no significant changes in the oxygen distribution marked by uniform measured current distribution is observed above the components of the multi-material assembly. However, on galvanically coupled components of the Al - Cu - CFRP triplet assembly (Fig. 6.19a), lower currents were measured over the cathodes (Cu and CFRP) which corresponds to depletion of oxygen near the cathodes due to cathodic processes that feeds on the dissolved oxygen near their surfaces. It is obvious that suppression of cathodic processes on the cathodes will result in less depletion of oxygen near them and hence measurement of higher current values near the cathodes. It is on the basis of this that variations in oxygen concentrations around constituent of this multi-material assembly was employed in monitoring inhibitive effects on this galvanic system which is reported in a later sub-section. Over the anode (Al), since the anodic processes occurring on its surface does not

involve the consumption of oxygen currents similar to background values were expected over the the (anode) aluminium but higher current magnitudes were measured over the anodes should otherwise correspond to higher oxygen concentrations. It is deemed important to highlight that the high currents measured over the anode (Al) was neither expected nor can as yet be explained by any possible processes that generate oxygen on the anode (Al). The possibility that this current might be due to the reduction of Al^{3+} cation is negated by the fact that the reduction of Al^{3+} is not thermodynamically feasible in aqueous media. It is also important to mention that the results were presented as a current distribution which is proportional to oxygen concentration. To be able to present the results as oxygen concentrations, calibration of the measured currents with values measured in varied but known dissolved oxygen concentrations is necessary and was not done.

Later in this work the results from attempts made to utilize the oxygen distribution around galvanically couple materials to monitor diminution/cessation of corrosion processes and hence the effectiveness of inhibitors is presented (Figs. 6. 20 and 6.21).

6.4.5. Multi-material Corrosion Inhibition in the Al - Cu - CFRP Galvanic system: Effect of Inhibitor Combinations ($\text{Ce}(\text{NO}_3)_3$ + BTA) on the Al - Cu - CFRP Galvanic Couple.

Having obtained insights from macro-tests on the promising inhibitor combinations and on the changes in the local environment from macro- and micro-tests in the absence of inhibitors, further localized tests (employing SVET and SIET) were carried out in the presence of inhibitor combinations, and results from tests using one of the candidate multi-materials corrosion inhibitor combinations ($\text{Ce}(\text{NO}_3)_3$ + BTA) presented herein to demonstrate the inhibitive effects of inhibitor combinations at micro-scales and from thence establish the mechanism of the observed inhibitive action.

Multi-material corrosion inhibition in the Al - Cu - CFRP galvanic system on a micro-scale with one of the proposed multi-material corrosion inhibitors for the galvanic system; 2.5 mM ($\text{Ce}(\text{NO}_3)_3$ + BTA) showed very significant multi-material corrosion inhibition in the system with this combination. Inhibitive effects were detectable few minutes after introduction of the inhibitor combination in ZRA, SVET measurements of current distribution around galvanic components, and even with the oxygen distribution measurements (Figs. 6. 20 and 6.21).

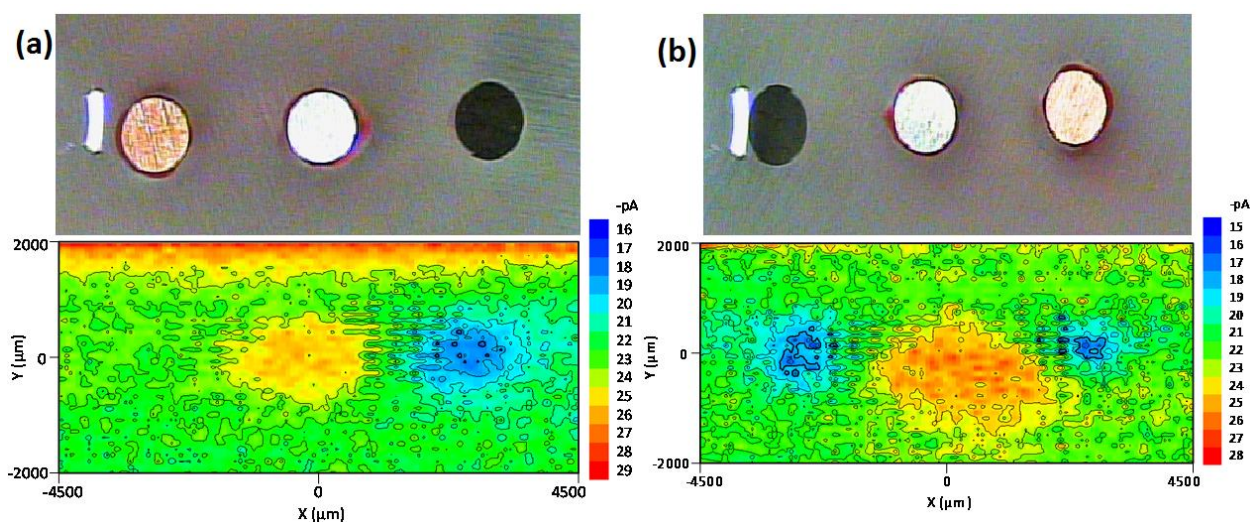


Fig. 6.20. Measured cathodic currents due to O_2 reduction $\approx 100 \mu\text{m}$ above galvanically coupled components of the Al-Cu-CFRP system (a) 30 min after immersion in 50 mM NaCl containing 2.5 mM each of $Ce(NO_3)_3$ and BTA after prior immersion in 50 mM NaCl solution for 150 mins, (b) 30 mins after polishing and immersion in same inhibitor solution indicative of the oxygen distribution.

In Fig. 6.20(a) above, oxygen depletion due to cathodic activity is not observed above copper after removal of the prior 50 mM NaCl solution and addition of inhibitor containing solution, most probably due to passivation of the copper surface. After polishing the sample surface and measuring less than 30 minutes after addition of inhibitor containing solution Fig. 6.20(b), cathodic activity identified by oxygen depletion is observed above the copper surface but much more above the CFRP surface. This illustrates the challenge in combating cathodic activity on CFRP coupled to metals as unlike metals (e.g. Cu) it does not passivate.

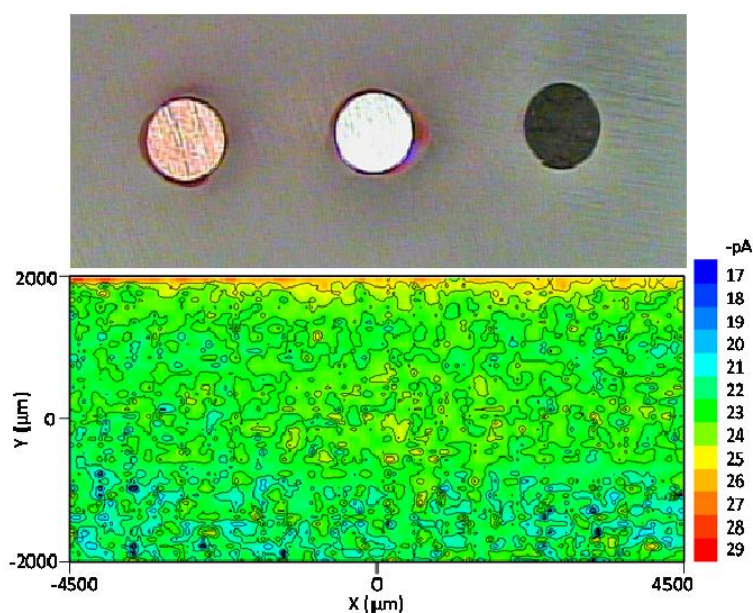


Fig. 6.21. Measured cathodic currents due to O_2 reduction $\approx 100 \mu\text{m}$ above non-galvanically coupled components of the Al-Cu-CFRP system 60 mins after immersion in 50 mM NaCl containing 2.5 mM each of $Ce(NO_3)_3$ and BTA indicative of oxygen distribution.

In Fig. 6.21 above, of oxygen distribution measurements above uncoupled Al - Cu - CFRP components cathodic activity is not detected in the presence of the inhibitors denoting the absence of localized corrosion processes strong enough to change the local oxygen distribution to measurable proportions. It should be noted that in these measurement oxygen distribution is presented in direct terms of the measured currents and not in concentration units; the magnitude of the measured current being proportional to the local oxygen concentration. To present results in oxygen concentrations some calibration is necessary in test solution at different and known oxygen concentrations.

Further studies of the efficient inhibitive action of rare-earth metal salts and azoles on Al - Cu galvanic couple were carried out using cerium nitrate and BTA combinations by using x-ray fluorescence spectroscopy to attempt to establish the metal on which the cerium acts principally on in this galvanic couple. The results of this XRF mapping using a voltage of 40 kV, current of 1000 μ A, collimator size of 0.2 x 0.2 mm, acquisition time of 50 ms per pixel, resulting in a mapping time of 123.5 minutes are presented in Fig. 6.22 below, from which the preferential presence of cerium on the cathode (copper) of the coupled Al - Cu galvanic couple is observed (Fig. 6.22d). It is notable that with the test conditions, the detection of aluminium with Al - k_{α} radiation is limited as evidenced by the low counts and little differences in the aluminium elemental mapping over aluminium and copper surfaces (Fig. 6.21b) after exposure to 50 mM NaCl containing 2.5 mM ($\text{Ce}(\text{NO}_3)_3$ + BTA). In spite of the low counts for aluminium, the higher counts for aluminium compared to the mounting material suggests the re-deposition of aluminium based corrosion products over the copper (cathode) surface.

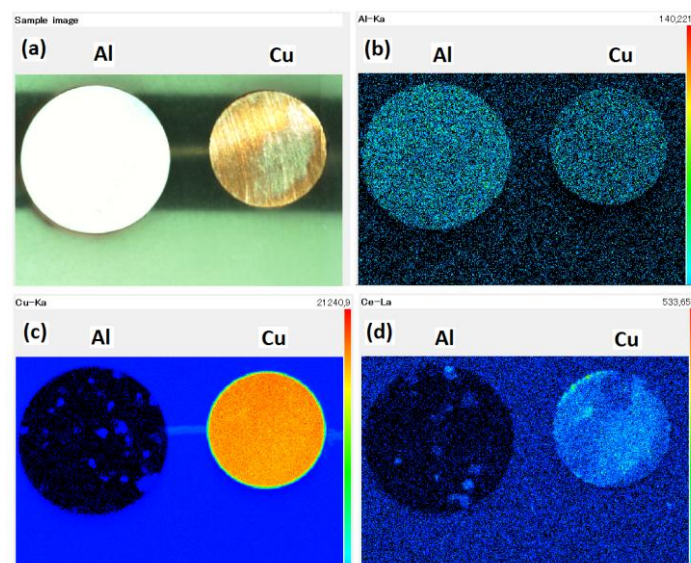


Fig. 6.22. X-ray fluorescence mapping of surfaces of aluminium and copper of coupled Al - Cu galvanic couple after exposure 50 mM NaCl containing 2.5 mM ($\text{Ce}(\text{NO}_3)_3$ + BTA).

6.4.6. Proposed Mechanism(s) of Multi-material Corrosion Inhibition in the Al - Cu - CFRP Galvanic system.

Based on the insights obtained from the survey of literature, macro- and micro-electrochemical tests on Al, Cu, CFRP, and Al - Cu, Al - CFRP, Al - Cu dual galvanic couples, and Al - Cu - CFRP "triplet" galvanic couple under varied test conditions, coupled with solution and surface analysis of coupled and uncoupled multi-material assemblies already presented earlier sub-sections, the plausible mechanism(s) of multi-material corrosion and multi-material corrosion inhibition in Al - Cu - CFRP multimaterial galvanic system are postulated, illustrated, and discussed herein.

In uncoupled Al - Cu -CFRP multi-material assembly (Fig. 6.23b), the constituent materials are bound to interact with the electrolyte almost independently, with cathodic and anodic regions co-existing on each metal's surface except for the plausible effects the entry of the more cathodic cation into the solution exerts on the more anodic metal. For CFRP, being non-metallic material very insignificant if any electrochemical activity is envisaged on its surface without polarization. Under this condition each component "corrodes" at its own rate virtually independent of the other.

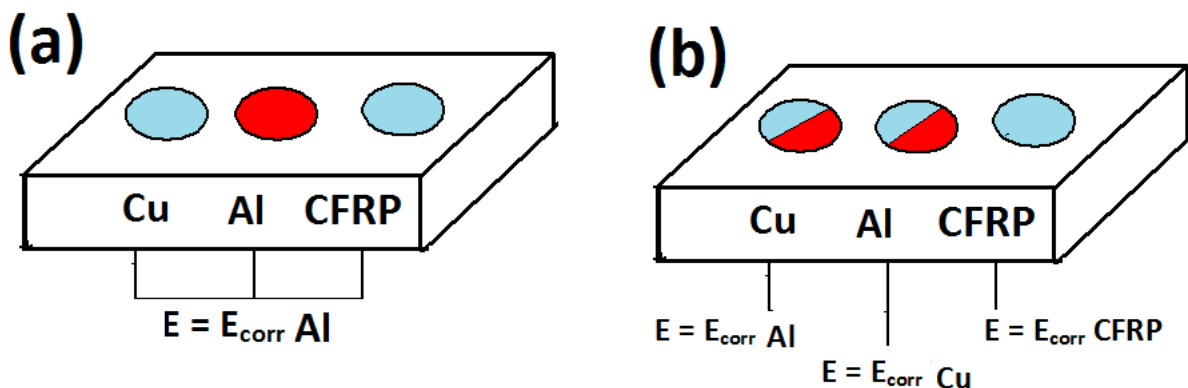


Fig. 6.23. Illustration of plausible mechanism of multi-material corrosion in the Al - Cu - CFRP multi-material galvanic system (red colour denotes anodic areas and blue cathodic areas).

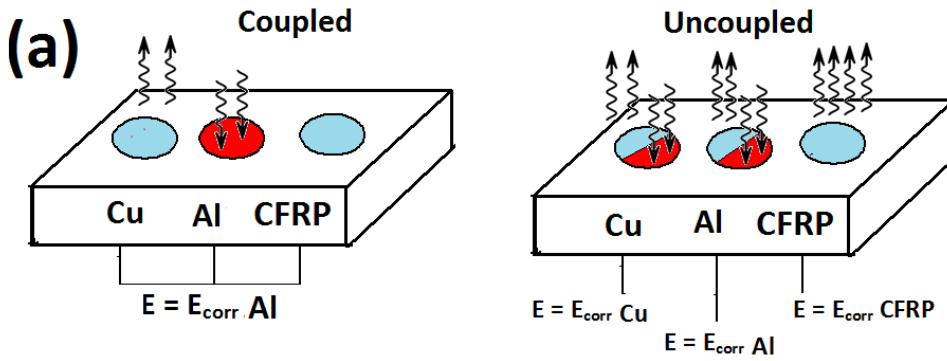
On galvanically coupled Al, Cu, and CFRP in the Al - Cu - CFRP multi-material galvanic system (Fig. 6.23a), the anodic dissolution of Al is enhanced due to the onset and progress of cathodic processes on the cathodes (Cu and CFRP) leading to increase in the local pH near the cathodes. Near the anode (Al) slight acidification of the local pH occurs due to anodic aluminium dissolution and the accompanying hydrolysis reactions that depletes the concentration of OH^- near the corroding aluminium surface and consequent increase in the H^+ concentration in this zone. These changes in local pH occur simultaneously with a change in the localized dissolved oxygen concentrations around each of the three components (Al, Cu, and CFRP) of the

galvanically coupled Al - Cu - CFRP multi-material galvanic system (**Fig. 6.18**). Over and near both cathodes (Cu and CFRP) the dissolved oxygen concentration is reduced due to oxygen consumption in the ongoing cathodic process while the solution. However, with time differences appear in the dissolved oxygen concentrations near both cathodes (Cu and CFRP) with slightly higher oxygen concentration near Cu compared to the oxygen distribution around CFRP. This difference in oxygen concentration near copper surface with time is attributed to the passivation of Cu surface by adherent corrosion products, and reveals the major and significant difference between multi-material corrosion in the Al - Cu - CFRP multi-material galvanic system and the Zn - Fe - CFRP multi-material galvanic system, as unlike as it is in the Al - Cu - CFRP multi-material galvanic system, the surface of the metallic cathode (Fe) is oxide free, its naturally formed surface oxide being stripped off its surface on galvanic coupling to zinc so that it presents an oxide free surface in the multi-material assembly. This occurs because whereas an oxide free surface can be obtained on Cu in alkaline solution at a cathodic polarization of $\approx -900 \text{ mV}_{\text{NHE}}$ ($= -1144 \text{ mV}_{\text{SCE}}$) [688] it is observed to be usually polarized on galvanic coupling to Al to potentials in the range of ≈ -600 to $-900 \text{ mV}_{\text{SCE}}$ in this work which is not cathodic enough to get rid of the oxide/hydroxide layer on copper surface. On the other hand, the naturally formed oxide layer on Fe is reported [691] to be stripped from Fe surface on application of a cathodic potential of $\approx -1050 \text{ mV}_{\text{SCE}}$ in 400 seconds, which is in the range of the potentials ($\approx -1000 \text{ mV}_{\text{SCE}}$) iron has been observed to be usually polarized to on galvanic coupling to zinc in the present work.

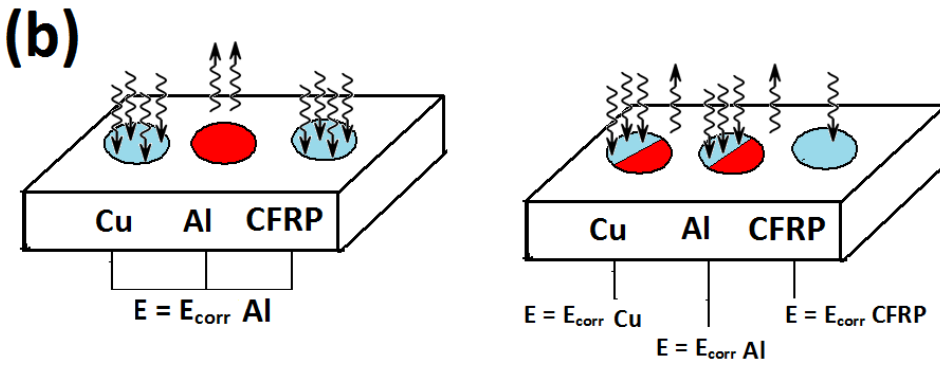
On introduction of corrosion inhibitors or inhibitor combinations, a variety of plausible scenarios might emerge in the corrosion inhibition of the Al - Cu - CFRP depending on the type of inhibitor and composition of the inhibitor combination(s). Fig. 6.24 below, illustrates the most relevant scenarios with respect to this work.

However, at near neutral pH, the effectiveness of an adsorption based inhibitor as a single inhibitor is likely to be influenced more by its ability to adsorb onto both oxide covered surface(s) of the cathode(s) and relatively "oxide free" surface at anodic sites. Hence adsorption based inhibitor interaction occurs predominantly on the anodic sites on both uncoupled and galvanically coupled arrangements of the Al - Cu - CFRP multi-material combination (Fig. 6.24a). In galvanically coupled Al - Cu - CFRP multi-material combination this is likely to result in predominant inhibitive effects on anodic processes with little effects on cathodic processes and thus marginal inhibitive effects on the multi-material corrosion of the "galvanic triple" as observed with BTA on Al - Cu - CFRP "galvanic triplet" (Table 6.1, Row 4; IE = 15%). The challenge in finding a single adsorption based inhibitor that possesses these unique criteria among many

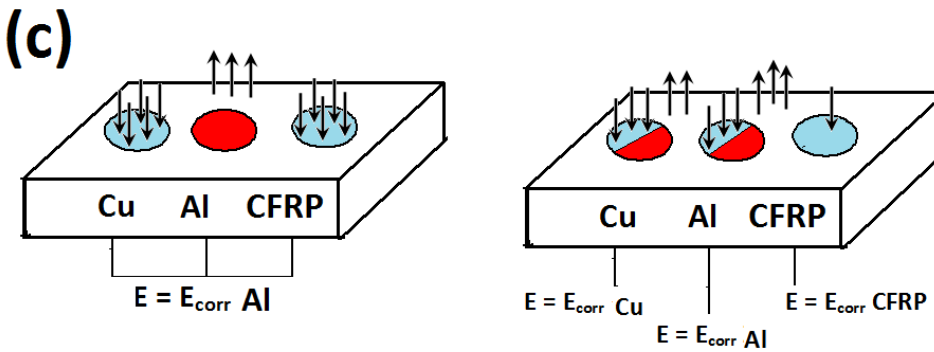
others demands another approach for corrosion inhibition in multi-material combinations : inhibitor combinations.



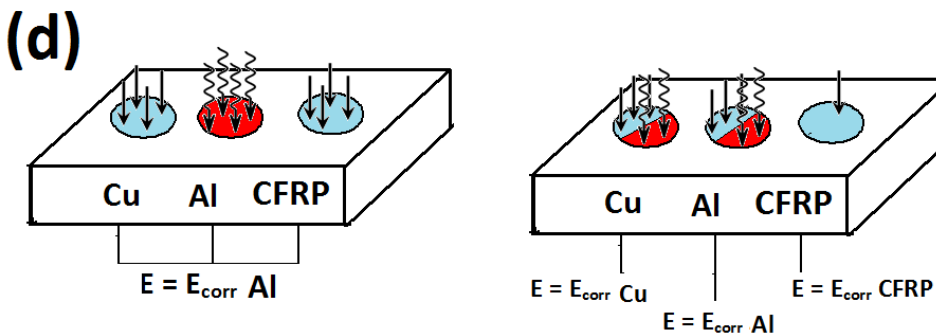
Adsorption based inhibitor that is effective at near neutral pH



Adsorption based inhibitor that is effective at high (alkaline) pH



Precipitation based inhibitor that is sensitive to high pH



Combination of a precipitation based inhibitor sensitive to high pH and adsorption based inhibitor effective at near neutral pH on anodic metal(s)

Fig. 6.24. Illustration of the different plausible scenarios in the mechanism of multi-material corrosion inhibition in the Al - Cu - CFRP multi-material system (Wavy arrows denote adsorption based inhibitors while the straight arrows denote precipitation based inhibitors. Arrows pointing towards surface denote effective interaction while pointing away denote no interaction).

In the presence of an adsorption based inhibitor that is effective at alkaline pH (Fig. 6.24b), adsorption of inhibitor onto metal surface in galvanically coupled Al - Cu - CFRP "galvanic triplet" is likely to be more favourable at the cathodes around which the local pH is increased to alkaline values due to cathodic processes. In this scenario moderate inhibition of multi-material corrosion is feasible as reduction of the active cathodic area due to interaction of the inhibitors with the cathodes is likely to result some reduction in the galvanic dissolution of the anodic metal.

In the presence of a precipitation based inhibitor that is sensitive to alkaline pH (Fig. 6.24c), the scenario is similar to that in an adsorption based inhibitor that is sensitive to high pH, as the onset of cathodic processes on the cathodes and the concomitant increase in pH acts a trigger for precipitation of hydroxides and oxides (of the rare-earth cations) onto the cathodes in galvanically coupled Al - Cu - CFRP "galvanic triplet". If the rare-earth cation is introduced as a salt with a conjugate anion like the NO_3^- anion that is able to inhibit anodic processes, significant inhibition of multi-material corrosion might be feasible with a single inhibitor. This was indeed observed in this work with $\text{Ce}(\text{NO}_3)_3$ (Table 6.1; Row 4) and $\text{Ce}(\text{CH}_3\text{COO})_3$ (Table 6.1; Row 3) that showed inhibition efficiencies of 73% and 87.5% respectively, on multi-material corrosion of Al - Cu - CFRP "galvanic triplet" based on the afore-mentioned criterion.

In the presence of a synergistic or additive combination of an adsorption based inhibitor that is effective at near neutral pH (Fig. 6.24a) and a precipitation based inhibitor that is sensitive to alkaline pH (Fig. 6.24c), the scenario illustrated in Fig. 6.24d emerges in which both anodic and cathodic processes are inhibited in galvanically coupled Al - Cu - CFRP "galvanic triplet" leading to high inhibition efficiencies ($\geq 90\%$). In such combination of inhibitors, The precipitation based inhibitor that is sensitive to the high pH acts on the cathode, precipitating their hydr(oxides) onto the surface of cathodes triggered by the high pH around these cathodes generated by cathodic processes while the adsorption inhibitor acts predominantly on the anode. This accounts for the high inhibition efficiencies obtained with galvanically coupled Al - Cu - CFRP "galvanic triplet" using the candidate multi-material inhibitor combinations; ($\text{Ce}(\text{NO}_3)_3$ + 1,2,3 - triazole), ($\text{Ce}(\text{CH}_3\text{COO})_3$ + BTA), ($\text{Ce}(\text{NO}_3)_3$ + BTA), ($\text{Ce}(\text{CH}_3\text{COO})_3$ + BIA), and ($\text{Ce}(\text{NO}_3)_3$ + BIA).

6.6. Chapter Summary

Multi-material corrosion of the Al - Cu - CFRP galvanic system have been studied and the plausible mechanism(s) of both multi-material corrosion and multi-material corrosion inhibition

postulated and illustrated. The major factors affecting multi-material corrosion in general and in the Al - Cu - CFRP galvanic are; the type of electrolyte, pH, temperature, the potential to which the cathodes are polarized to by the anode on galvanic coupling, the presence or absence of corrosion products on the surface of the cathode(s) under the cathodic potential it/they are polarized to by the anode, and the magnitude of the pH changes near the constituents of the multi-material assembly. Understandably, these same factors affect multi-material corrosion inhibition. Besides these factors other factors affecting material corrosion inhibition are the type of inhibitor and its basis of action, the ability of the inhibitor to interact with the surface of the cathodic metal(s) in the multi-material assembly under both a high pH and cathodic polarization, the conjugate anion of the inhibitor (if it is a salt), the presence in solution of cations of metals that are cathodic to the anode, and for precipitation based inhibitors the onset pH for precipitation of their hydr(oxides), and the solubility products of these oxides and/or hydroxides.

From the results obtained and presented herein for the Al-Cu-CFRP galvanic system, it is concluded that multi-material corrosion inhibition of galvanic corrosion in the system is best achieved with the use of synergistic or at least additive inhibitor combinations comprised of rare-earth metal (preferably Ce) nitrates or acetates and azoles. On the basis of significantly measured high inhibition efficiencies in all the four studied galvanic assemblies (Al - CFRP, Al - Cu, Cu - CFRP, and Al - Cu - CFRP), five inhibitor combinations ((Ce(NO₃)₃ + 1,2,3 - triazole) , (Ce(CH₃COO)₃ + BTA), (Ce(NO₃)₃ + BTA), (Ce(CH₃COO)₃ + BIA) ,and (Ce(NO₃)₃ + BIA)) are proposed for use as efficient multi-material corrosion inhibitors for the Al - Cu - CFRP galvanic system.

For the component dual couples (Al - CFRP, Al - Cu, and Cu - CFRP) that are found in the Al - Cu - CFRP multi-material galvanic system effective galvanic corrosion inhibitors have been identified but some of these have not qualified to be shortlisted as multi-material corrosion inhibitors due to non-observance of significant and simultaneous inhibitive effects on all three dual couples and the multi-material "galvanic triplet" (Al - Cu - CFRP).

The inhibitors identified as effective corrosion inhibitors of Al - CFRP galvanic couple in 50 mM NaCl solution and measured inhibition efficiencies bases on prior stated criterion are Ce(CH₃COO)₃ (85.45%), Ce(NO₃)₃ (76.51%), (Ce(NO₃)₃ + CH₃COONa) (91.48%), (Ce(NO₃)₃ + 1,2,3-triazole) (86.77-93.17%),(Ce(CH₃COO)₃ + 1,2,3-triazole) (83.86%), (Ce(NO₃)₃ + BTA) (81.9-96.2%),(Ce(CH₃COO)₃ + BTA) (83.86-89.47%), (Ce(CH₃COO)₃ + BIA) (86.42%), (Ce(CH₃COO)₃ + NaNO₃) (78.15%),(La(NO₃)₃ + BTA) (55.45%), and (La(CH₃COO)₃ + BTA) (50.63%).

For the galvanic corrosion of Al - Cu galvanic couple the identified effective corrosion

inhibitors and their inhibition efficiencies are; $\text{Ce}(\text{NO}_3)_3$ (85.69%), $\text{Ce}(\text{CH}_3\text{COO})_3$ (64.88%), $(\text{Ce}(\text{NO}_3)_3 + \text{BIA})$ (87.39%), $(\text{Ce}(\text{CH}_3\text{COO})_3 + \text{BIA})$ (85.35%), $(\text{Ce}(\text{NO}_3)_3 + \text{CH}_3\text{COONa})$ (85.52%), $(\text{Ce}(\text{CH}_3\text{COO})_3 + \text{NaNO}_3)$ (84.38%), $(\text{Ce}(\text{CH}_3\text{COO})_3 + \text{BTA})$ (80.60%), $(\text{La}(\text{CH}_3\text{COO})_3 + \text{BTA})$ (80.60%), $(\text{La}(\text{NO}_3)_3 + \text{BTA})$ (78.96%), $(\text{Ce}(\text{NO}_3)_3 + \text{BTA})$ (74.85%), $(\text{Ce}(\text{CH}_3\text{COO})_3 + 1,2,3\text{-triazole})$ (71.81- 77.06%), and $(\text{Ce}(\text{NO}_3)_3 + 1,2,3\text{-triazole})$ (59.87-68.39%).

With respect to the Cu - CFRP galvanic couple the identified effective corrosion inhibitors and their inhibition efficiencies are; CH_3COONa (81.55%), BTA (99.96%), $(\text{Pr}(\text{NO}_3)_3 + \text{BTA})$ (99.999%), $(\text{NaNO}_3 + \text{BTA})$ (99.96%), $(\text{La}(\text{NO}_3)_3 + \text{BTA})$ (99.93%), $(\text{CH}_3\text{COONa} + \text{BTA})$ (99.9%), $(\text{Ce}(\text{CH}_3\text{COO})_3 + \text{NaNO}_3)$ (99.80%), $(\text{Ce}(\text{CH}_3\text{COO})_3 + 1,2,3\text{-triazole})$ (98.73%), $(\text{Ce}(\text{NO}_3)_3 + 1,2,3\text{-triazole})$ (98.56%), $(\text{Ce}(\text{CH}_3\text{COO})_3 + \text{BTA})$ (97.86%), $(\text{La}(\text{CH}_3\text{COO})_3 + \text{BTA})$ (97.62%), $(\text{Ce}(\text{NO}_3)_3 + \text{BTA})$ (95.86%), $(\text{Ce}(\text{CH}_3\text{COO})_3 + \text{BIA})$ (94.9%), and $(\text{Ce}(\text{NO}_3)_3 + \text{BIA})$ (91.83%).

From these results for the Al - Cu - CFRP galvanic system it is obvious that superior inhibitive effects have been generally recorded in the presence of cerium compounds. The azoles in these inhibitor combinations are known to be adsorption based inhibitors. From the results in this work it has been demonstrated that they act predominantly on cathodic processes. The observed generally superior performance of Ce^{3+} cations compared to other rare-earth cations (e.g. La) have been attributed by earlier researchers to the lower solubility of Ce^{3+} hydroxides [63], which can in turn be related to the differences in the sizes of the rare earth cations [692]. An additional factor accounting for the superior performance of Ce^{3+} compared to other rare earth cations may be linked to the demonstrated unique ability of cerium to exist in two redox states; $\text{Ce}^{3+}/\text{Ce}^{4+}$ compared to other REM cations (e.g. La^{3+} and Pr^{3+}) in the presence of oxygen, water, and some ligands [693,694]. According to Böhm et al., [691], freely corroding metal surfaces in aerated aqueous chloride media can be covered by native hydr(oxide) films of thickness in the range of 6 -15 nm, and proposed that rare-earth metal hydr(oxide) deposits produced by metal cation hydrolysis near the metal surface - solution interface due to increased interfacial pH arising from cathodic processes only nucleate efficiently on native hydr(oxide) covered surfaces. Hence the inhibition effects observed in this work in the presence of rare-earth cations can be considered to arise from pH dependent modification of the native hydr(oxide) layer on metal surfaces. Based on observation of significant rdeposition of the more active metal on cathodes it is proposed that this phenomena may be playing a part in the mechanism of the observed additive and synergistic multi-material corrosion inhibition.

CHAPTER 7

Multi-material Corrosion Inhibition in the Zn - Fe - CFRP Galvanic system

7.0. Results of Tests on Galvanic Couples in the Zn - Fe - CFRP Galvanic System

This chapter begins with the presentation of the summary of ZRA tests results carried out on each of the the dual galvanic couples (Fe - CFRP , Zn - CFRP, and Zn - Fe), and the "galvanic triplet" (Zn - Fe - CFRP) of the Zn - Fe - CFRP galvanic system, in quiescent 50 mM NaCl solution with and without the addition of a wide range of inhibitors and combinations of inhibitors based on the measured current densities after 150,000 seconds (Table 7.1).

Tests were conducted using single inhibitors, which can be classified in groups; as azoles, surfactants, phosphates, nitrates, and acetates. Combinations of these inhibitors (azoles + azoles, azoles + nitrates, azoles + acetates, azoles + phosphates, were tested for inhibitive effects in the Zn - Fe - CFRP multi-material system. The most promising results were obtained with inhibitor combinations comprised of azoles + RE cations. For brevity presentation and dicussion of results have been limited to these two inhibitor combinations and their constituents (azoles, nitrates, and acetates). In order to establish the mechanism of observed inhibitive effects on multi-material assemblies, results of tests with each of these three classes of inhibitors on each of the constituent materials (Zn, Fe, and CFRP) are presented.

By analysis of the measured current densities from ZRA measurements after 150,000 seconds immersion for each of the dual galvanic couples (Zn - CFRP, Zn - Fe, and Fe - CFRP) in the system, potential multi-material corrosion inhibitors for the Zn - Fe - CFRP galvanic ensemble were identified, and tested on the "triplet galvanic" system and the results presented herein. In order to establish the corrosion mechanism(s) in this multi-material system (Zn - Fe - CFRP) localized electrochemical measurements (SVET and SIET) on galvanic couples and "galvanic triplets" in the presence and absence of inhibitors were carried out together with potentiodynamic polarization scans. From these results plausible corrosion mechanism(s) operative in this multi-material combination and the mechanism of the corrosion inhibitive effects observed with certain inhibitor combinations were inferred, and presented herein.

7.1.0 Overview of Macro Studies of Multi-material Corrosion Inhibition in the Zn - Fe - CFRP Galvanic system: Effect of Inhibitors on the Zn -Fe - CFRP Galvanic System.

An overview from results of ZRA measurements on Zn - Fe - CFRP (Zn - Fe coupled together with galvanic currents measured between Zn - Fe and CFRP) and each of the dual galvanic couples Zn - Fe , Zn - CFRP, and Fe - CFRP, based on the galvanic current densities after

Table 7.1: Shortlist of potential multi-material corrosion inhibitors for the Zn-Fe-CFRP galvanic system on the basis of measured galvanic current densities in $\mu\text{A cm}^{-2}$ after 150,000 seconds immersion (figures in parentheses are calculated inhibition efficiencies).

	Inhibitors	Zn - CFRP ($\mu\text{A cm}^{-2}$)	Zn - Fe ($\mu\text{A cm}^{-2}$)	Fe - CFRP ($\mu\text{A cm}^{-2}$)	Zn - Fe - CFRP ($\mu\text{A cm}^{-2}$)
1.	No inhibitor (in 50 mM NaCl)	16.2	24.3	19.8	24.17
2	5 mM BTA	5.35 ; 4.79 ; 9.52 (70.43- 41.23%)	8.72 (64.12%)	10.8 (45.45%)	14.88 (38.44%)
3	5 mM BIA	18.3 (-12.96%)	27.12 (-11.6%)	18.5 (6.57%)	9.94 (58.87%)
4	5 mM 1,2,3 - triazole	14.15 (12.65%)	30.4 (-25.1%)	13.9 (29.80%)	11.25 (53.45%)
5	5 mM 1,2,4 - triazole	8.52 (47.41%)	20.0 (17.7%)	11.37 (42.58%)	12.84 (46.88%)
6	5 mM $\text{Ce}(\text{NO}_3)_3$	3.16 ; 3.17 ; 6.28 (61.23%)	78.01 (-221.03%)	3.48 (82.42%)	0.665 (97.25%)
7	5 mM $\text{La}(\text{NO}_3)_3$	9.99 (38.33%)	159.43 (-556.09%)	8.76 (55.76%)	1.38 (94.29%)
8	5 mM $\text{Ce}(\text{CH}_3\text{COO})_3$	3.39 (79.07%)	92.5 (-280.66%)	2.81 (85.81%)	1.53 (93.67%)
9	5 mM $\text{La}(\text{CH}_3\text{COO})_3$	9.27 (42.78%)	85.35 (-251.23%)	11.11 (43.89%)	13.70 (43.32%)
10	2.5 mM ($\text{Ce}(\text{NO}_3)_3$ + BTA)	1.32 ; 2.19 (91.85 -86.48%)	5.47 (77.49%)	9.25 (53.28%)	2.13 (91.19%)
11	2.5 mM ($\text{Ce}(\text{NO}_3)_3$ + BIA)	3.70 (77.10%)	37.68 (-55.06%)	4.03 (77.63%)	1.20 (95.04%)
12	2.5 mM ($\text{La}(\text{NO}_3)_3$ + BTA	5.84 (63.95%)	2.84 (88.31%)	4.61 (76.72%)	1.18 (95.12%)
13	2.5 mM ($\text{Ce}(\text{NO}_3)_3$ + CH_3COONa)	2.53 (84.38%)	70.5 (-190.12%)	1.38 (93.03%)	2.39 (90.11%)
14	2.5 mM ($\text{Ce}(\text{CH}_3\text{COO})_3$ + NaNO_3)	2.61 (83.89%)	61.69 (-153.87%)	1.50 (92.42%)	2.68 (88.91%)
15	2.5 mM ($\text{Ce}(\text{NO}_3)_3$ + 1,2,3 - triazole)	7.14 (55.93%)	123.61 (-412.80%)	5.63 (71.57%)	2.36 (90.24%)
16	2.5 mM ($\text{Ce}(\text{NO}_3)_3$ + 1,2,4 - triazole)	11.6 (28.40%)	79.2 (-225.93%)	4.11 (79.24%)	0.791 (96.73%)
17	2.5 mM ($\text{Ce}(\text{CH}_3\text{COO})_3$ + 1,2,3 - triazole)	9.52 (41.23%)	85.96 (-253.74%)	4.28 (78.38%)	7.74 (67.98%)
18	2.5 mM ($\text{Ce}(\text{CH}_3\text{COO})_3$ + BIA)	1.47 (90.93%)	14.48 (40.41%)	2.93 (85.20%)	1.37 (94.33%)
19	2.5 mM ($\text{Ce}(\text{CH}_3\text{COO})_3$ + BTA)	2.79 (82.78%)	61.13 (-151.56%)	6.06 (69.39%)	3.13 (87.05%)
20	2.5 mM ($\text{La}(\text{CH}_3\text{COO})_3$ + BTA)	3.38 (79.14%)	2.01 (91.73%)	4.52 (77.17%)	1.48 (93.88%)
21	2.5 mM (CH_3COONa + BTA)	14.12 (12.84%)	21.30 (12.35%)	12.59 (36.41%)	15.21 (37.07%)

150,000 seconds immersion (Table 7.1) enables a shortlist of potential multi-material corrosion inhibitors for each of Zn - Fe , Zn - CFRP, and Fe - CFRP dual galvanic couples and ultimately for

the Zn - Fe - CFRP "galvanic triplet" in the Zn - Fe - CFRP multi-material galvanic system. In order to clarify the mechanism of action of shortlisted inhibitor combinations, some inhibitor combinations that were not effective as multi-material inhibitors were included in Table 7.1.

The shortlist of candidate multi-material corrosion inhibitor combinations for the Zn - Fe - CFRP "galvanic triplet" was drawn based on good and simultaneous inhibitive effects of inhibitor combinations on all the 3 dual galvanic couples that can be obtained from the constituents of the Zn - Fe - CFRP multi-material galvanic system. Based on these criteria the shortlisted inhibitors for multi-material corrosion inhibition in the Zn - Fe - CFRP "triplet" galvanic system are $(\text{La}(\text{NO}_3)_3 + \text{BTA})$ and $(\text{Ce}(\text{NO}_3)_3 + \text{BTA})$. This is based on the observation of high inhibition efficiencies of these inhibitor combinations on the galvanic corrosion of all the dual galvanic couples (Zn - CFRP, Fe - CFRP, and Zn - Fe) in the Zn - Fe - CFRP multi-material galvanic system and also on the Zn - Fe - CFRP "triplet" galvanic system. Table 7.1 below presents the measured galvanic current densities for each the galvanic components of the Zn - Fe - CFRP galvanic system in the presence of the shortlisted potential multi-material inhibitors/combinations and their constituents.

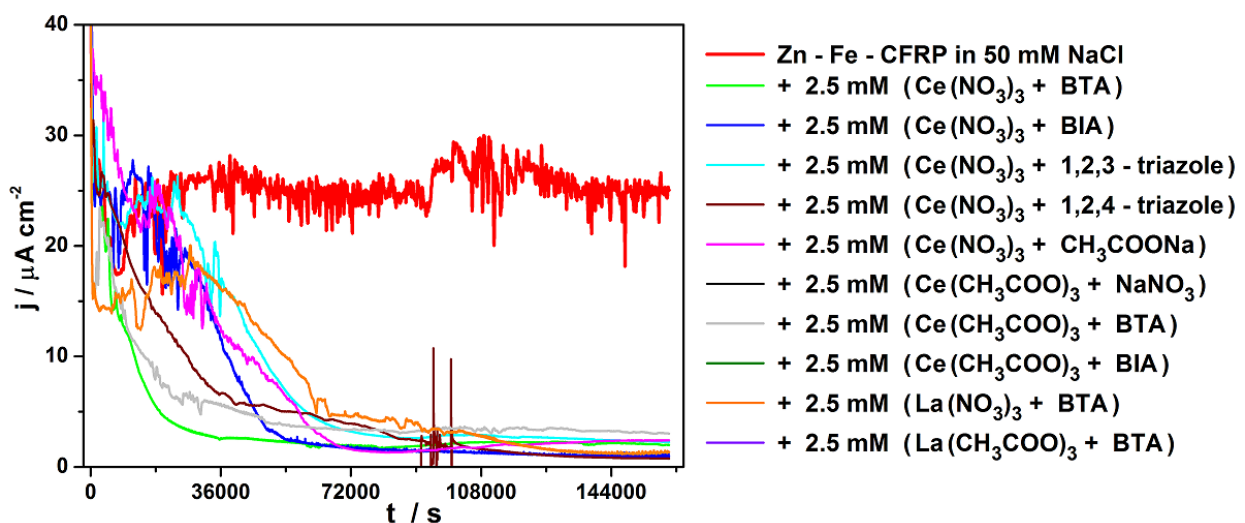


Fig 7.1. Effect of selected inhibitor combinations on the time evolution of galvanic current densities of Zn - Fe - CFRP "galvanic triplet" in 50 mM NaCl (Zn - Fe was coupled together with galvanic currents measured between Zn - Fe and CFRP).

Fig. 7.1. presents the time evolution of galvanic current densities for the Zn - Fe - CFRP "galvanic triplet" in the absence and presence of selected inhibitor combinations, from which it can be observed that generally, marked inhibitive effects in the Zn - Fe - CFRP "galvanic triplet" manifest after immersion times greater than 10 hours (60,000 seconds). Furthermore, in spite of the fact that galvanic current densities were markedly reduced in the presence of all the presented inhibitor combinations (Fig. 7.1), only $\text{La}(\text{NO}_3)_3 + \text{BTA}$ and $(\text{Ce}(\text{NO}_3)_3 + \text{BTA})$ are

recommended as candidate multi-material corrosion inhibitors for the Zn - Fe - CFRP multi-material assembly because they were able to inhibit galvanic corrosion in any galvanic configurations of any two of the constituent materials (Zn, Fe, and CFRP) in the Zn - Fe - CFRP galvanic system. Particularly, for the two shortlisted multi-material corrosion inhibitors for the Zn - Fe - CFRP "galvanic triplet", while inhibitive effects become prominent in the presence of $(\text{Ce}(\text{NO}_3)_3 + \text{BTA})$ after about 5 hours, it takes much longer (about 20 hours) to reach its peak in the presence of $(\text{La}(\text{NO}_3)_3 + \text{BTA})$. Interestingly, inspite of the fact that the inhibitive effects manifested faster in the presence of $(\text{Ce}(\text{NO}_3)_3 + \text{BTA})$ the measured galvanic current densities in the presence of $(\text{La}(\text{NO}_3)_3 + \text{BTA})$ are lower after about 35 hours of immersion. These differences in the time evolution of peak inhibitive effects even with very closely related inhibitor combinations ($(\text{Ce}(\text{NO}_3)_3 + \text{BTA})$ and $(\text{La}(\text{NO}_3)_3 + \text{BTA})$) is attributed to some differences in the kinetics and mechanism of the interaction of the rare earth cations (Ce^{3+} and La^{3+}), the details of which will be unravelled in the succeeding sections of this work.

To get a general overview of the effects of these inhibitor combinations on anodic and cathodic processes in the Zn - Fe - CFRP "triplet" galvanic system potentiodynamic polarization tests were carried out on Zn, Fe and CFRP galvanically coupled together and the polarization curves presented in Fig. 7.2. below.

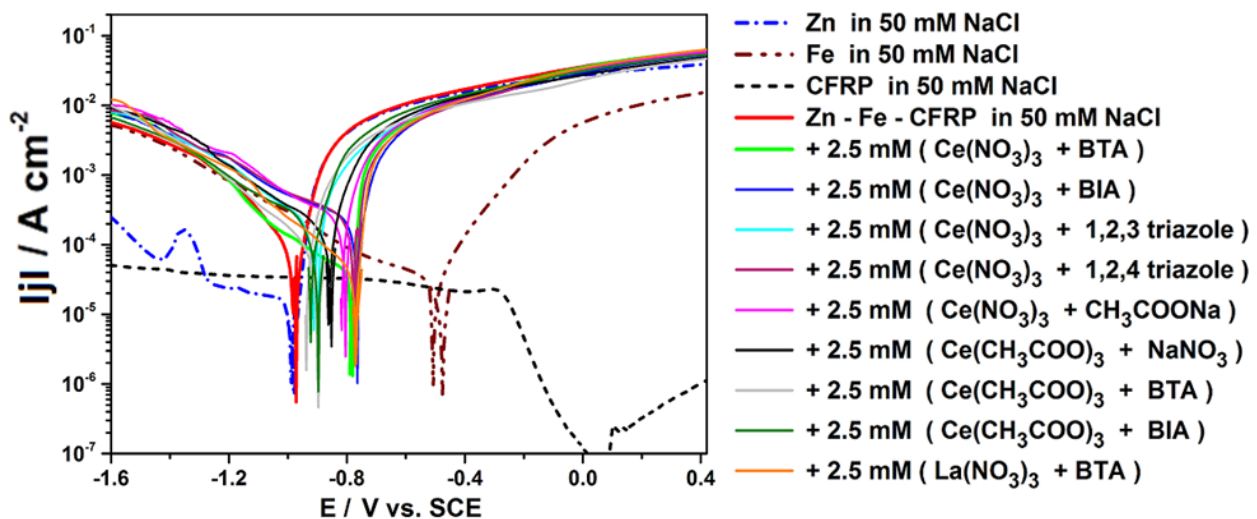


Fig. 7.2. Effect of selected inhibitor combinations on the potentiodynamic polarization curves for Zn - Fe - CFRP "galvanic triplet" in 50 mM NaCl after 1 hour immersion.

The potentiodynamic polarization curves for Zn - Fe - CFRP "galvanic triplet" (Fig. 7.2) gives more insight into the possible mechanism of the observed inhibitive effects in the presence of the inhibitor combinations. In the presence of the inhibitor combinations the "corrosion potential" of the couple is displaced towards more anodic potentials with marked reductions in measured anodic densities in the active corrosion region of the curve. The

reduction in the anodic current densities at similar potentials suggests that the inhibitor combinations exert effects predominantly on the anodic dissolution kinetics of the anode (zinc), and that the observed inhibitive effects are predominantly due to some suppression of the kinetics of anodic processes. Insights on why and how this occurs are provided in ensuing sections of this chapter, particularly in studies on the effects of inhibitor combinations and single inhibitors on component dual galvanic couples (Zn - Fe, Zn - CFRP, Fe - CFRP) and individual component materials (Zn, Fe, CFRP) of the Zn - Fe - CFRP galvanic system (in section 7.3).

7.2.0 Overview of Macro Studies of Multi-material Corrosion Inhibition in the Zn - Fe - CFRP Galvanic system: Effect of Selected Inhibitor Combinations on Galvanic Corrosion of Dual Galvanic Couples in the Zn - Fe - CFRP Galvanic System.

Fig. 7.3 presents the effect of selected inhibitor combinations on the time evolution of galvanic current densities of Zn - Fe, Zn - CFRP, and Fe - CFRP couples of the Zn - Fe - CFRP multi-material galvanic system in 50 mM NaCl. From Fig. 7.3a it can be observed that inhibition of the galvanic corrosion of the most active dual couple (Zn - Fe) is challenging, with inhibitive effects obtained only in the presence of $(\text{Ce}(\text{NO}_3)_3 + \text{BTA})$ and $(\text{La}(\text{NO}_3)_3 + \text{BTA})$ only. With Zn - Fe galvanic couple in these inhibitor combinations inhibitive effects manifested in less than 3 hours.

For Zn - CFRP galvanic couple (Fig. 7.3b) the galvanic current evolution of Zn - CFRP in the presence of the selected combinations of inhibitors show suppression of galvanic current in the presence of all the inhibitor combinations with the inhibitive effects most significant in the presence of $(\text{Ce}(\text{NO}_3)_3 + \text{BTA})$, $(\text{Ce}(\text{CH}_3\text{COO})_3 + \text{BTA})$, $(\text{Ce}(\text{NO}_3)_3 + 1,2,4\text{-triazole})$, $(\text{Ce}(\text{NO}_3)_3 + \text{CH}_3\text{COONa})$, and $(\text{Ce}(\text{NO}_3)_3 + \text{BIA})$.

The galvanic current density evolution of Fe - CFRP galvanic couple in the presence of the selected inhibitors (Fig.7.3c) indicates significant inhibitive effects in the presence of the selected inhibitor combinations with galvanic current densities reduced to values between 5 and $10 \mu\text{A cm}^{-2}$ after about 30 hours immersion.

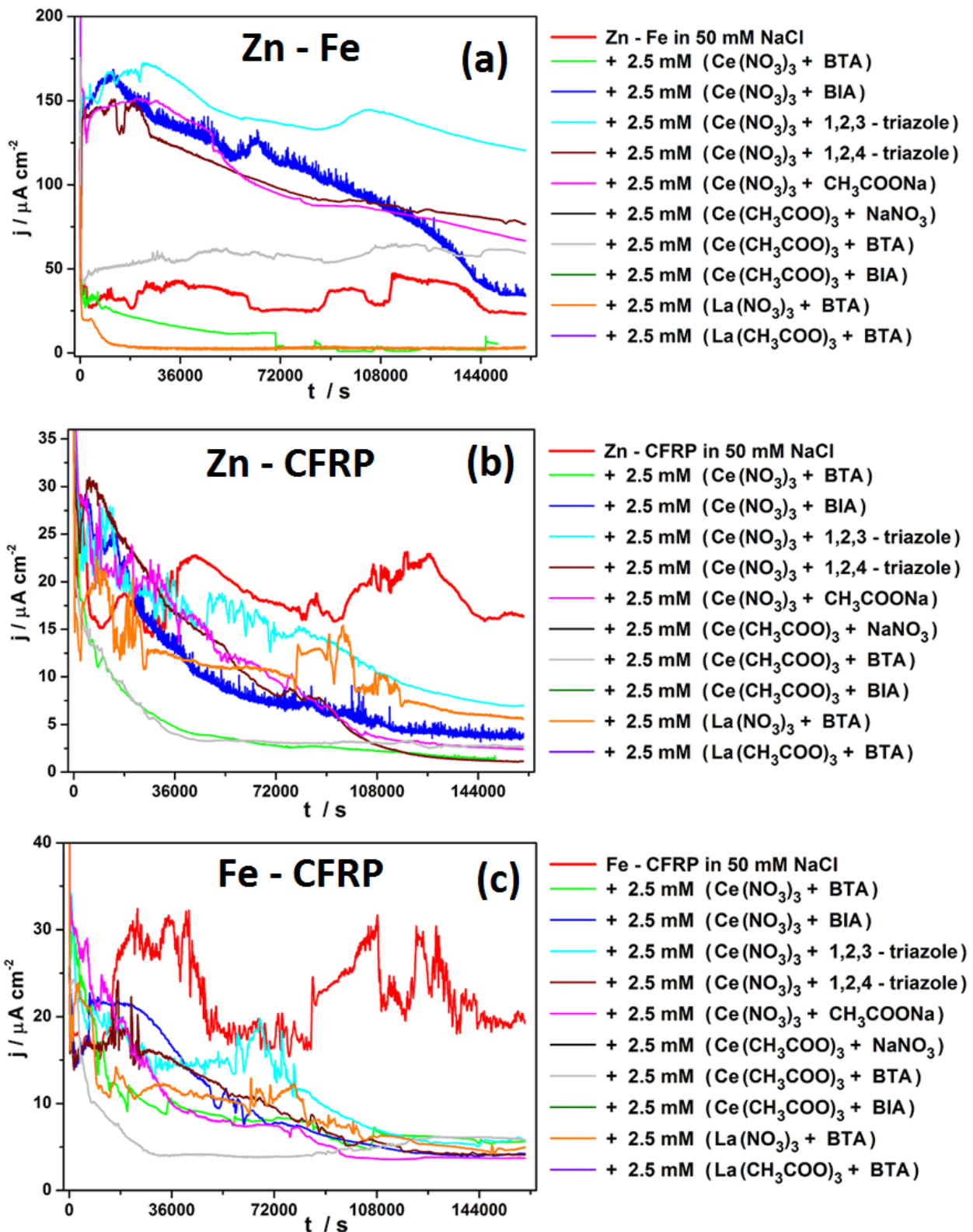


Fig 7.3. Effect of selected inhibitor combinations on the time evolution of galvanic current densities of (a) Zn - Fe, (b) Zn - CFRP, and (c) Fe - CFRP couples of the Zn - Fe - CFRP multi-material galvanic system in 50 mM NaCl.

The potentiodynamic polarization curves of Zn - Fe galvanic couple in the presence of the selected combination of inhibitors (Fig. 7.4a) do not explain the excellent inhibitive effects observed in the presence of (La(NO₃)₃ + BTA) and (Ce(NO₃)₃ + BTA) as similar trends in the

cathodic and anodic current densities were observed in all the inhibitor combinations. The polarization curves in the presence of each of the selected inhibitor combinations were characterized by reduced current densities in the active corrosion region of the anodic part of the curve and undiminished cathodic current densities. The reason for the excellent inhibitive effects observed with Zn - Fe galvanic couple in the presence of $(\text{La}(\text{NO}_3)_3 + \text{BTA})$ and $(\text{Ce}(\text{NO}_3)_3 + \text{BTA})$ are unveiled in section 7.3 in the presentation and discussion of effects of single inhibitors and inhibitor combinations on galvanic corrosion of Zn, Fe, and Zn - Fe galvanic couple.

The potentiodynamic polarization curves of Zn - CFRP in the presence of selected combinations of inhibitors (Fig. 7.4b) show that anodic current densities were lowered in the presence of all 9 inhibitor combinations tested while cathodic currents are suppressed in 4 of the inhibitor combinations comprised of $(\text{Ce}(\text{NO}_3)_3 + \text{BTA})$, $(\text{La}(\text{NO}_3)_3 + \text{BTA})$, $(\text{Ce}(\text{CH}_3\text{COO})_3 + \text{BTA})$, and $(\text{Ce}(\text{CH}_3\text{COO})_3 + \text{BIA})$. Such suppression of both cathodic and anodic current densities in the presence of these 4 inhibitor combinations is suggestive of a high possibility of good inhibition efficiencies for Zn - CFRP galvanic corrosion in test solutions containing them.

The potentiodynamic polarization curve of Fe - CFRP galvanic couple (Fig. 7.4c) in selected combinations of inhibitors reveal interesting details that can give some insight into the mechanism of observed inhibitive effects. From the cathodic curves in Fig. 7.4c reduction in cathodic current densities below that measured on Fe - CFRP couple in blank solution is observed in virtually all the inhibitor combinations at least close to the corrosion potential of the couple. For $(\text{Ce}(\text{NO}_3)_3 + \text{BIA})$, $(\text{Ce}(\text{NO}_3)_3 + 1,2,3\text{-triazole})$, $(\text{Ce}(\text{CH}_3\text{COO})_3 + \text{BTA})$ and $(\text{La}(\text{NO}_3)_3 + \text{BTA})$ the diminution of cathodic current densities is more extensive covering the entire diffusion-controlled range (down to more cathodic potentials $\geq -0.8 V_{\text{SCE}}$) with cathodic current densities even lower than measured values in uncoupled iron in blank solution. In the presence of $(\text{Ce}(\text{NO}_3)_3 + \text{BTA})$, and $(\text{Ce}(\text{NO}_3)_3 + 1,2,4\text{-triazole})$ a similar trend is obtained except that measured cathodic current densities had values similar to that measured on uncoupled iron in the blank solution. On the anodic part of the polarization curve reduced anodic current densities compared to values measured in Fe - CFRP couple in blank solution, are observed in all the inhibitor combinations except $(\text{Ce}(\text{CH}_3\text{COO})_3 + \text{BTA})$, $(\text{Ce}(\text{CH}_3\text{COO})_3 + \text{BIA})$, $(\text{Ce}(\text{CH}_3\text{COO})_3 + \text{NaNO}_3)$, and $(\text{Ce}(\text{NO}_3)_3 + \text{CH}_3\text{COONa})$ in which higher anodic current densities were observed in the active corrosion region of the curve. Characteristic of these four inhibitor combinations in

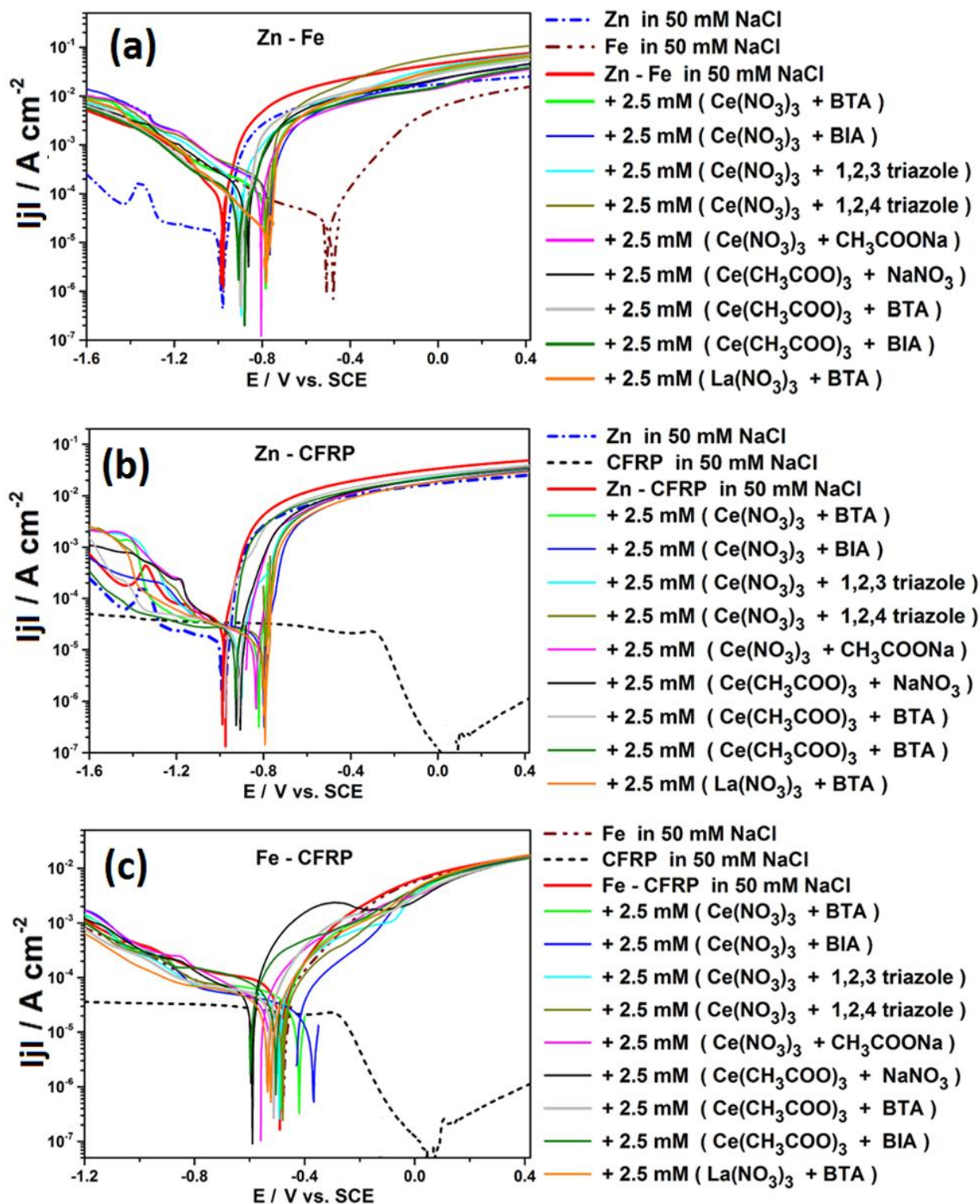


Fig 7.4. Effect of selected inhibitor combinations on potentiodynamic polarization curves of (a) Zn - Fe, (b) Zn - CFRP, and (c) Fe - CFRP couples of the Zn-Fe-CFRP multi-material galvanic system in 50 mM NaCl.

which anodic dissolution is enhanced based on higher anodic current densities in the active corrosion region is the presence of acetate anion. Hence, it is inferred that the presence of acetate anions do not favour inhibition of Fe - CFRP galvanic corrosion even in the presence of cerium cations and azoles.

7.3.0 Effect of Single Inhibitors on the Galvanic Corrosion of Zn- Fe, Zn-CFRP, and Fe-CFRP Dual Material Galvanic Couples

To understand the mechanism of multi-material corrosion in the Zn - Fe - CFRP multi-material galvanic system and of its mitigation using a combination of inhibitors, tests were carried out with single inhibitors (azoles, nitrates, and acetates) that comprise these inhibitor combinations on Zn - Fe, Zn - CFRP, and Fe - CFRP dual galvanic couples. Besides being components of the Zn - Fe - CFRP multi-material galvanic system being studied, mitigation of galvanic corrosion in these couples has important technological implications.

The Zn - Fe galvanic system being of immense technological importance and relevance to the automobile industry, was extensively and systematically studied in the absence and presence of inhibitors and the results presented below. It has been reported that cathodic polarization of Fe to a potential ($-1050 \text{ mV}_{\text{SCE}}$) similar to values it is polarized to on galvanic coupling to Zn led to stripping of the native oxide layer in about 400 seconds [691]. Consequently in the Zn - Fe couple, Fe most likely presents an oxide free surface available for direct interaction with inhibitors.

The Zn - CFRP galvanic system is also very relevant to the transport industry and can become operative when galvanized steel structures come into electrical contact with CFRP in the presence of an electrolyte.

The Fe - CFRP galvanic couple is very relevant to the general transportation industry. This galvanic system can become operative when zinc-rich coatings on for instance galvanized steel coupled to CFRP is compromised, resulting in direct galvanic coupling of the underlying iron to CFRP. Unlike the Cu - CFRP system in which the observed galvanic current densities of the two members cathodic to aluminium in Al - Cu - CFRP multi-material galvanic system were comparatively insignificant, the observed galvanic current densities between Fe and CFRP (both cathodic to Zn) in the Zn - Fe - CFRP triple material galvanic system is quite significant (Fig. 7.5e). Compared to other dual galvanic couples in the Zn - Fe - CFRP galvanic system (Zn - CFRP and Zn - Fe), the Fe - CFRP dual galvanic couple is unique; differing from these by virtue of the fact that the more active component (Fe) is able to polarize the cathode (CFRP) to potentials around which oxygen diffusion effects do not always limit cathodic activity on CFRP (Fig. 5.9), especially in some cases for several hours after immersion. As a consequence, the anodic dissolution of iron which proved a challenge to mitigate with a wide range of inhibitors is favoured in this galvanic couple. After some significant immersion times the cathodic polarization on the CFRP can increase to values in the diffusion limited potential range. In spite

of this, due to the non-protective nature of the iron corrosion products, in the absence of effective inhibitors the measured galvanic current is often not significantly reduced.

7.3.1. Effect of Azoles on the Galvanic Corrosion of Zn - Fe, Zn - CFRP, and Fe - CFRP Galvanic Couples

Results from ZRA measurements of galvanic current density and potential (Fig.7.5a) show that out of the four azole compounds tested only benzotriazole and 1,2,4- triazole manifested appreciable and sustained inhibitive effects on Zn - Fe galvanic corrosion.

With the exception of benzimidazole, all the azoles tested exert some inhibitive effect on the galvanic corrosion of Zn - CFRP couple (Fig. 7.5a and b). From the galvanic current density evolution with time (Fig. 7.5a) it is evident that the most significant inhibitive effect was observed in the presence of benzotriazole.

All the azoles studied exhibited inhibitive effects on the galvanic corrosion of Fe - CFRP couple; the most significant effects being observed in benzotriazole and 1,2,3-triazole (Fig.7.5e). However the potentiodynamic polarization curves for Fe and Fe - CFRP couple respectively in the presence of azoles (Figs. 7.6d and 7.6e), indicate that the observed inhibitive effects are a consequence of the suppression of cathodic process to values significantly lower than those measured on uncoupled iron, as in the presence of all the azoles higher anodic current densities were recorded in the active corrosion range.

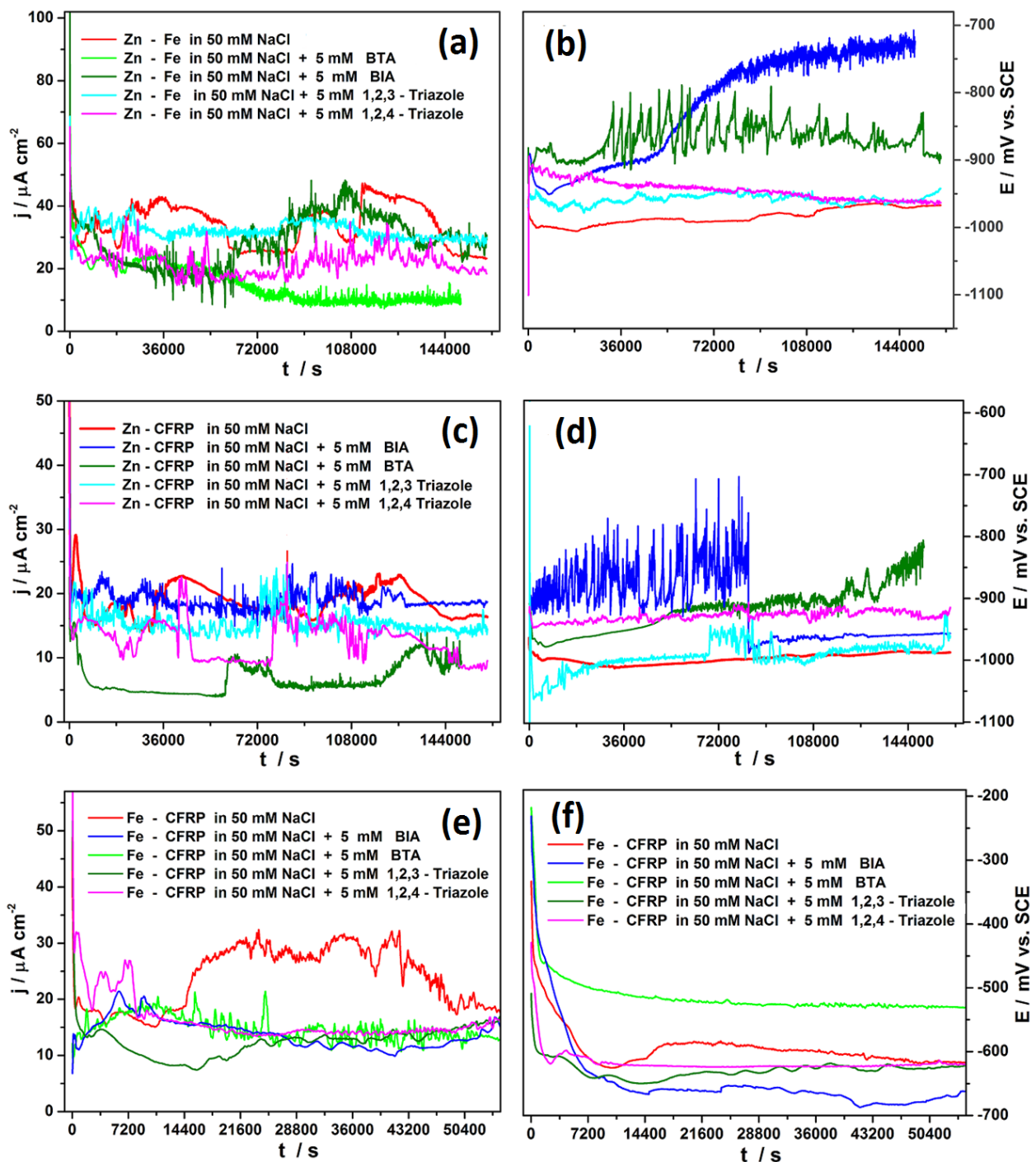


Fig 7.5. Effect of azole inhibitors on the time evolution of galvanic current densities and galvanic potential respectively of (a-b) Zn - Fe, (c-d) Zn - CFRP, and (e-f) Fe - CFRP couples of the Zn-Fe-CFRP multi-material galvanic system in 50 mM NaCl.

The potentiodynamic polarization curves for Zn - Fe couples in the presence of the azoles after 1 hour immersion (Fig.7.6a) show reduction in both cathodic and anodic current densities coupled with slight shifts of the corrosion potential towards anodic potentials. From the potentiodynamic polarization curves it is concluded that the azoles (with the exception of 1,2,3-triazole) act as mixed inhibitors on Zn - Fe galvanic corrosion but with a predominant effect on anodic processes. Among the azoles, suppression of both cathodic and anodic current densities

was most intense in the presence of benzotriazole. This is consistent with superior inhibitive effects observed in the galvanic current density profile in the presence of benzotriazole (Fig.7.5a). In the presence of 1,2,3-triazole cathodic currents are suppressed without significant changes in anodic current densities, thus 1,2,3-triazole is classified as a cathodic inhibitor for Zn - Fe galvanic corrosion.

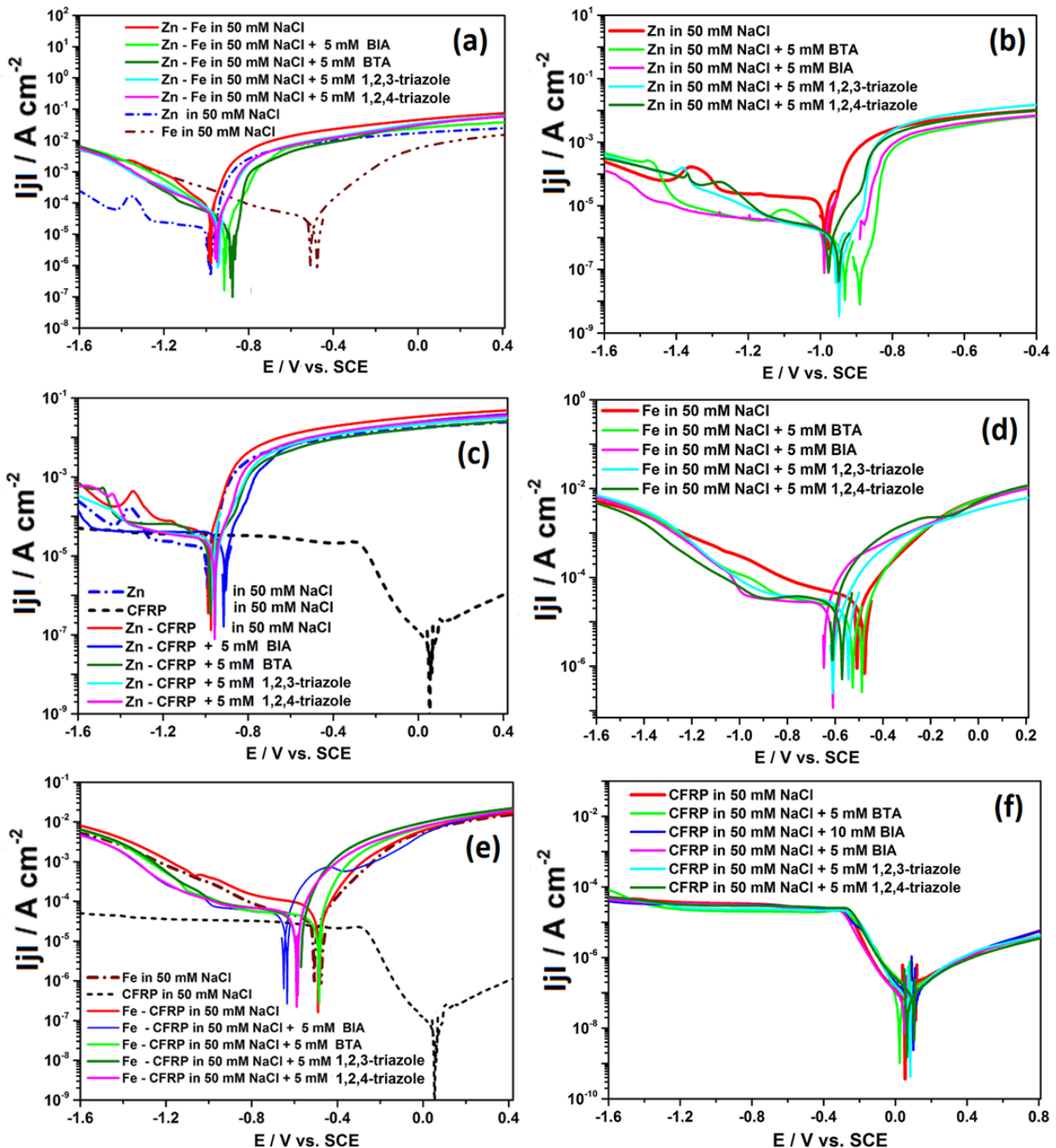


Fig 7.6. Effect of azole inhibitors on the potentiodynamic polarization curves of (a) Zn - Fe, (b) Zn ,(c) Zn - CFRP, (d) Fe, (e) Fe - CFRP, and (f) CFRP after 1 hour immersion in different azoles in 50 mM NaCl.

The potentiodynamic polarization curves of Zn - CFRP in the presence of azoles (Fig.7.6c) indicates reduction in cathodic current densities in the presence of all the azoles indicating

inhibition of cathodic processes. In the presence of benzimidazole the measured cathodic current densities are similar to values measured on uncoupled CFRP in blank solution. The anodic part of the polarization curves show significant reduction of anodic current densities in the presence of all the azoles. On the basis of these results, azoles are adjudged to be mixed corrosion inhibitors of Zn - CFRP galvanic corrosion and candidates for combination with other inhibitors to achieve enhanced inhibition efficiencies.

The potentiodynamic polarization curves of Fe - CFRP in the presence of azoles (Fig.7.6e) indicates that cathodic processes are suppressed in the presence of all the azoles with reference to current densities measured for both Fe - CFRP and Fe in the blank solution. In contrast anodic processes were enhanced in the presence of the azoles. The trends observed in the potentiodynamic curves of Fe - CFRP in the presence of azoles (Fig.7.6e) are consistent with trends observed for iron in the presence of azoles (Fig.7.6d) which can be indicating that galvanic corrosion in the Fe - CFRP galvanic couple is predominantly controlled by anodic dissolution of iron.

7.3.2. Effect of Rare-Earth Cations on the Galvanic Corrosion of Zn - Fe, Zn - CFRP, and Fe - CFRP Galvanic Couples

To understand the effects of rare-earth cations on the galvanic corrosion of the dual galvanic couples (Zn - CFRP, Zn - Fe, and Fe - CFRP) in the Zn - Fe - CFRP galvanic system components results from ZRA measurement and potentiodynamic polarizarion tests in the presence and absence of rare-earth cations as nitrates and acetates are compared.

The results of ZRA measurements of galvanic current densities and potentials of Zn - Fe couple in the presence of nitrates (Fig. 7.7a and b) indicate that in the presence of rare-earth nitrates the galvanic corrosion of Zn - Fe couple is accelerated. Since in the presence of sodium nitrate the galvanic current density of Zn - Fe couple is unchanged, the increase in galvanic current density in the presence of all the tested rare-earth nitrates is concluded to be linked to the presence of the rare-earth cations.

The results of the effect of nitrates on the galvanic corrosion of Zn - CFRP (fig. 7.7c-d) show that the nitrates exert inhibitive effects on the galvanic corrosion of Zn - CFRP with effects manifesting after "incubation times" ranging from a few minutes to about 9 hours after immersion. In the presence of lanthanum nitrate inhibitive effects manifest fastest, but manifests after 9 hours in the presence cerium and praesodymium nitrates. The presence of such incubation times may be suggesstive of the time needed to generate and modify the

corrosion product layer on zinc so it becomes protective enough to diminish anodic metal dissolution kinetics.

In all the nitrates tested on Fe - CFRP some inhibitive effects were observed (Fig. 7.7e) but roughly after the same "incubation time" (≥ 4 hours). Among the rare-earth nitrates significant, stable and sustained inhibitive effects are observed in the presence of lanthanum nitrate and praeosodymium nitrate. The observance of an incubation period prior to manifestation of inhibitive effects in the presence of all the nitrates suggests similarity in operative inhibition mechanisms that very probably involves enhanced initial corrosion rates to generate corrosion product layer(s) that is/are then modified by the nitrates. The observed inhibitive effects of rare-earth nitrates on the galvanic corrosion of Fe-CFRP ranked in the order; La > Ce > Pr.

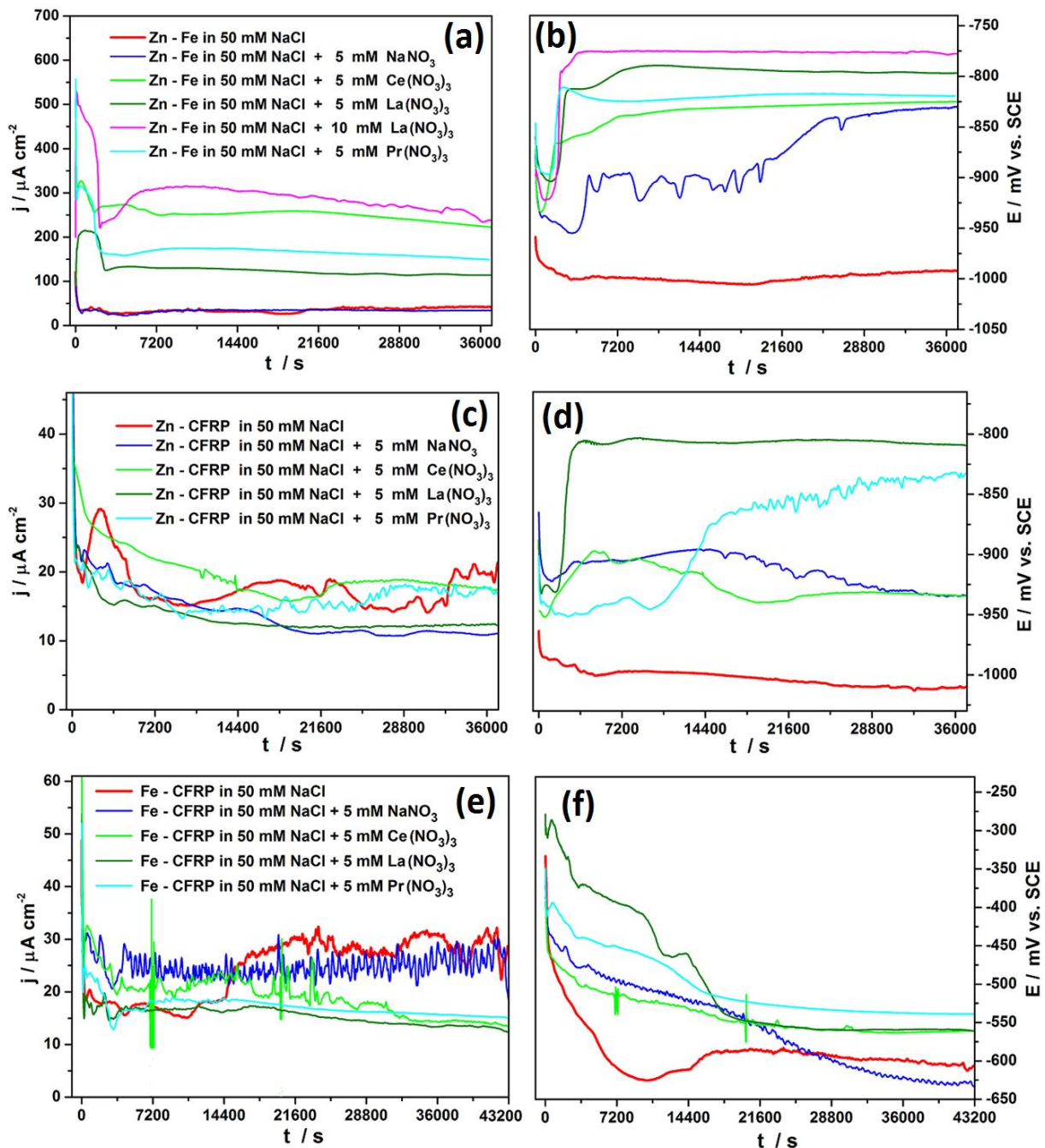


Fig 7.7. Effect of nitrate inhibitors on the time evolution of galvanic current densities and galvanic potential respectively of (a-b) Zn - Fe, (c-d) Zn - CFRP, and (e-f) Fe - CFRP couples of the Zn - Fe - CFRP multi-material galvanic system in 50 mM NaCl.

The potentiodynamic polarization curves for Zn - Fe galvanic couple in the presence of nitrates (Fig.7.8a) indicates that all the nitrates act as anodic corrosion inhibitors on the couple based on the observed shifts in corrosion potential towards more anodic values, increase in cathodic current densities, and reduction in anodic current densities in the presence of the nitrates. However, by comparing the effects of these nitrates on the polarization curves of Zn - Fe dual galvanic couple (Fig.7.8a), and those of its constituent materials; zinc (Fig.7.8b) and iron (Fig. 7.8a) and the galvanic potential evolution for the Zn - Fe couple (Fig.7.7b) which is in the

range -775 to -1000 mV_{SCE}, it appears to be that the galvanic corrosion of Zn - Fe dual galvanic couple is predominantly controlled by the cathodic processes on iron.

The potentiodynamic polarization curves for Zn - CFRP in the presence of nitrates (Fig. 7.8b) show increased cathodic current densities, shifts in corrosion potential of the couple towards anodic values and reduction in anodic current densities. This behaviour suggests that the nitrates act as anodic inhibitors on Zn - CFRP galvanic couple. The potentiodynamic polarization curves of Fe - CFRP couple in the presence of nitrates (Fig.7.8c) yields further information on the mechanism of the observed inhibitive effect and trends. It can be observed that in the presence of nitrate ion but absence of the rare-earth cations (as in NaNO₃) the corrosion potential of the couple is uniquely shifted to more cathodic values, the cathodic current density is suppressed to values lower than those of the uncoupled iron and Fe - CFRP couple in blank solution, but anodic current densities are enhanced in the active corrosion region to values higher than measured values for both uncoupled iron and Fe - CFRP couple in blank solution. However, in the presence of all the rare-earth nitrates with the exception of praeosodymium nitrate suppression of both cathodic and anodic current densities are observed. This scenario suggests that the nitrate ion might be linked to the suppression of cathodic processes on this couple while the suppression of anodic processes is strongly linked to the presence of rare earth cations.

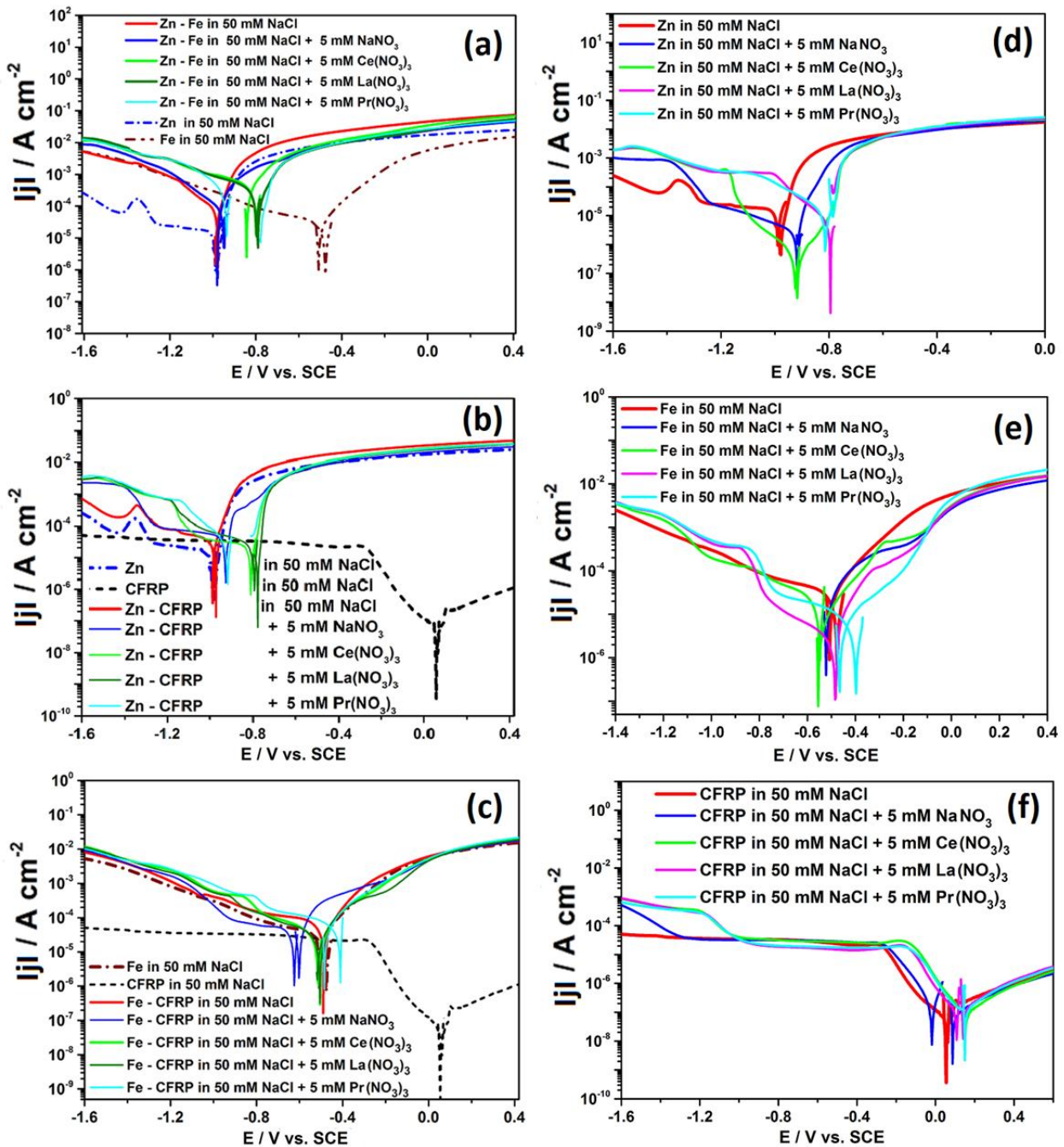


Fig 7.8. Effect of nitrate inhibitors on the potentiodynamic polarization curves of (a) Zn - Fe, (b) Zn, (c) Zn - CFRP, (d) Fe, (e) Fe - CFRP, and (f) CFRP after 1 hour immersion in different azoles in 50 mM NaCl.

Similar to observations presented earlier (Fig. 7.7a) for Zn - Fe couple in the presence of rare-earth nitrates, the measured galvanic current densities for Zn - Fe couple in the presence of acetates (Fig.7.9a) increased in the presence of all the rare-earth acetates while values in the presence of sodium acetate remain largely unchanged compared to values measured in blank solution. In fact a marginal inhibitive effect can be attributed to the presence of sodium acetate after 6 hours immersion. This observation confirms an earlier conclusion in the discussions on nitrates that the presence of rare-earth cations promote galvanic corrosion of Zn - Fe couple.

Furthermore, it is observed that in both nitrates and acetates, the rare-earth cation that is least effective in accelerating galvanic corrosion of Zn - Fe couple is lanthanum.

Tests on acetates as inhibitors for the galvanic corrosion of Zn - CFRP galvanic couple (Figs. 7.9c and 7.10b) show results similar to trends observed with rare-earth nitrates. After varying "incubation times" ranging from almost instantaneous for sodium acetate to about 10 hours for samarium acetate all the acetates tested exhibited inhibitive effects on Zn - CFRP galvanic corrosion. The best inhibitive effects were observed in the presence of sodium and cerium acetates (Fig.7.9c) based on the observed galvanic current density evolution with time.

From Fig.7.9e-f below, it is observed that all the acetates tested exerted some inhibitive effect on the galvanic corrosion of Fe - CFRP except sodium nitrate. Since the other acetates contained rare-earth cations, the observed inhibitive effects must be closely associated with these cations. The observed inhibitive effects of rare-earth acetates on the galvanic corrosion of Fe - CFRP ranked in the order; Ce >> La > Sm > Nd. From Fig.7.9f. it is observed that the galvanic potential of Fe - CFRP galvanic couple tends either towards values measured in blank solution or potentials anodic to values in un-inhibited solution, but tends towards cathodic to values measured in blank solution in the presence of the ineffective sodium acetate.

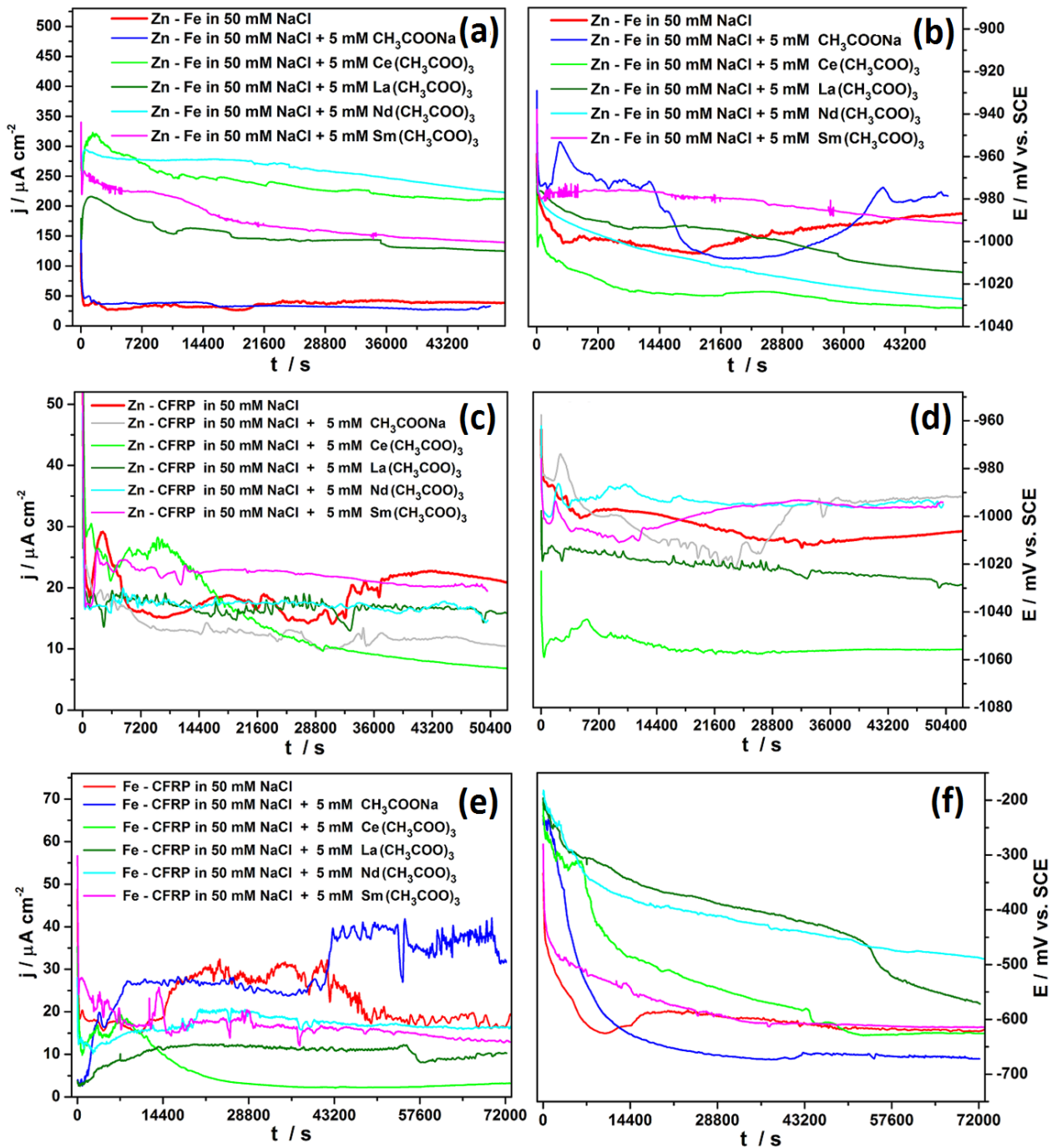


Fig 7.9. Effect of acetate inhibitors on the time evolution of galvanic current densities and galvanic potential respectively of (a-b) Zn - Fe, (c-d) Zn - CFRP, and (e-f) Fe - CFRP couples of the Zn-Fe-CFRP multi-material galvanic system in 50 mM NaCl.

The potentiodynamic polarization curves for Zn- Fe couple in the presence of acetates (Fig.7.10a) shows increased cathodic and anodic current densities in the presence of all the rare-earth acetates. However, in the presence of sodium acetate significant reductions are observed in the cathodic current densities without tangible changes in the anodic current densities. This behaviour indicates that sodium acetate is most likely a cathodic inhibitor of Zn - Fe galvanic corrosion.

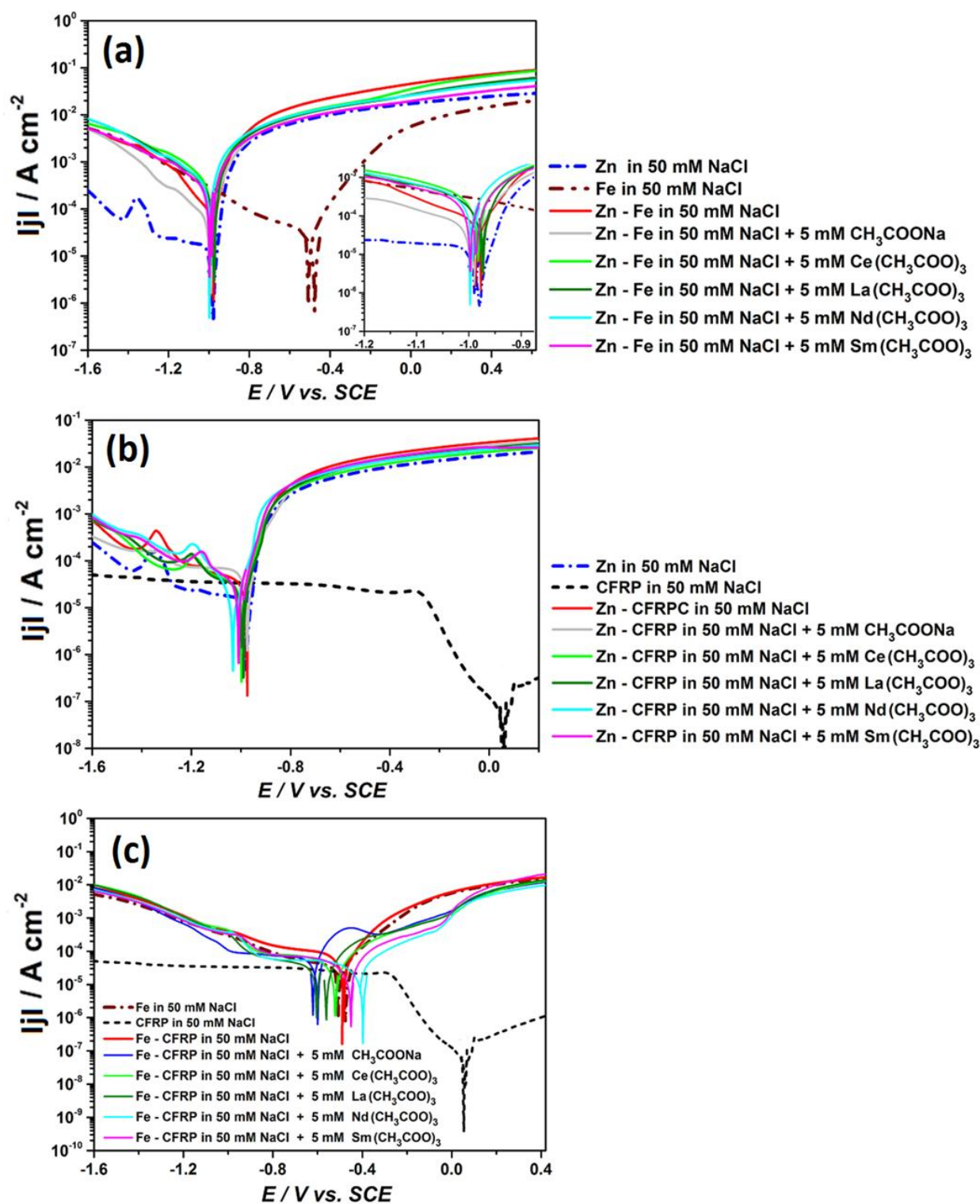


Fig 7.10. Effect of acetate inhibitors on the potentiodynamic polarization curves of (a) Zn - Fe, (b) Zn - CFRP, and (c) Fe - CFRP after 1 hour immersion in different acetates in 50 mM NaCl.

The potentiodynamic polarization curves of Zn - CFRP in the presence of acetates show marginal reduction in anodic current densities in the presence of sodium, cerium, and lanthanum acetates.

The potentiodynamic polarization curves for Fe - CFRP in the presence of acetates (Fig. 7.10c) shows that cathodic current densities are suppressed in the presence of all the acetates

studied. The anodic polarization curves appear to show signs of passivation which is most pronounced in the presence of neodymium acetate and samarium acetate. In the presence of sodium acetate this apparent "passivation effect" is least and only manifest after much higher increases in anodic current densities. This apparently suggests in the absence of rare-earth cations much higher metal loss (or thicker passivation layer) may be required to ensure passivation.

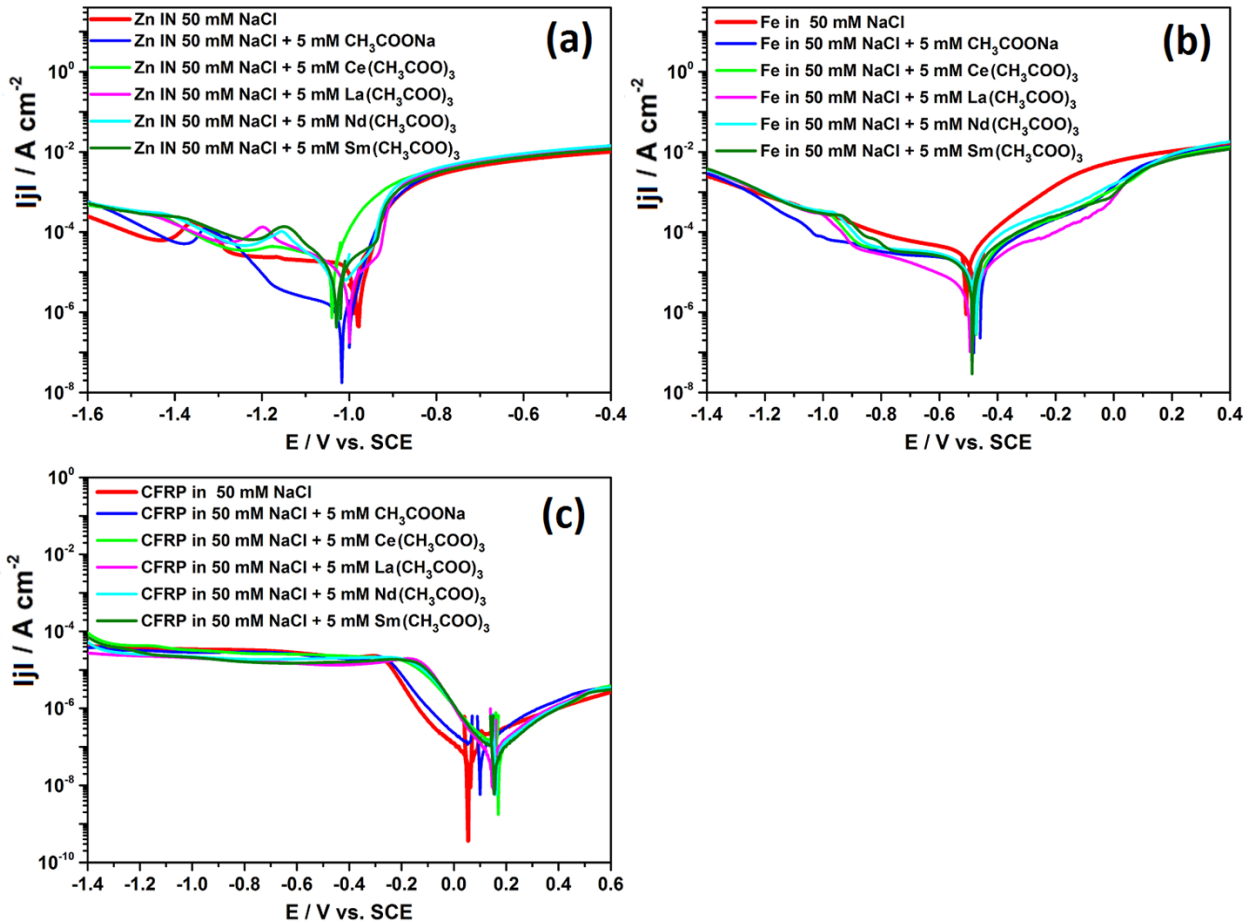


Fig. 7.11. Effect of acetates on the potentiodynamic polarization curves of (a) zinc, (b) iron and (c) CFRP in 50 mM NaCl based solutions after 1 hour immersion.

The potentiodynamic curves of zinc, iron and CFRP in acetates (Fig. 7.11) reveals interesting and varied effects of the acetates on cathodic and anodic processes in each of these three materials. For zinc (Fig. 7.11a) cathodic process appear to be enhanced in acetates containing rare earth cations (Ce, La, Nd, and Sm) but reduced in their absence (but with the presence of acetate anions as) in the presence of sodium acetate. On the other hand anodic processes appear to be enhanced in the presence of cerium acetate, not significantly changed in the presence of other acetates except in the presence of lanthanum acetate in which marginal reduction is observed. For iron (Fig. 7.11b) reductions in both cathodic and anodic processes were observed in the presence of all the acetates with the reductions most significant in the

presence of lanthanum acetate among the rare earth acetates.

In the case of CFRP (Fig. 7.11c), significant increases were observed only in the cathodic branch of the potentiodynamic polarization curves in the presence of rare-earth acetates in the "active region" (non-diffusion limited region) of the cathodic curve. Since the slopes of the cathodic polarization curve is similar to that in the blank solution, the enhanced cathodic currents is attributed to probable enhanced kinetics of cathodic processes rather than changes in mechanism of cathodic processes. In the more relevant diffusion limited region with respect to multi-material corrosion inhibition ($E \geq 600 \text{ mV}_{\text{SCE}}$) to which CFRP can be polarized to in galvanic coupling to more active metals (Al, Zn etc.) marginal reduction in cathodic current densities were observed in all the acetates

In summary, some inhibitive effects were observed on introduction of rare-earth cations as inhibitors of galvanic corrosion in the dual galvanic couples (Zn - CFRP, Fe - CFRP) in the Zn - Fe - CFRP galvanic system, except in the case of Zn - Fe galvanic couple. For the Zn - Fe galvanic couple the presence of rare-earth cations irrespective of the conjugate anion (acetate or nitrate) promoted galvanic corrosion of Zn - Fe couple and that the rare-earth cation that is least effective in accelerating galvanic corrosion of Zn - Fe couple is lanthanum.

7.3.3. Effect of Conjugate ion of Rare earths on the Galvanic Corrosion of Zn-Fe, Zn-CFRP, and Fe - CFRP Galvanic Couples

Since the rare-earth cations have been observed to exert marked accelerative effects on the galvanic corrosion of Zn - Fe couple effort was made to determine any effects the conjugate anion of the rare-earth cation might have on the galvanic corrosion of Zn - Fe, Zn - CFRP, and Fe - CFRP galvanic couples respectively. By comparison of the galvanic current densities of these galvanic couples and their potential evolutions in the presence of NaNO_3 and CH_3COONa , $\text{Ce}(\text{NO}_3)_3$ and $\text{Ce}(\text{CH}_3\text{COO})_3$, and $\text{La}(\text{NO}_3)_3$ and $\text{La}(\text{CH}_3\text{COO})_3$ respectively, any link between the observed accelerative effect of the rare-earth metal salts and their conjugate anion is established.

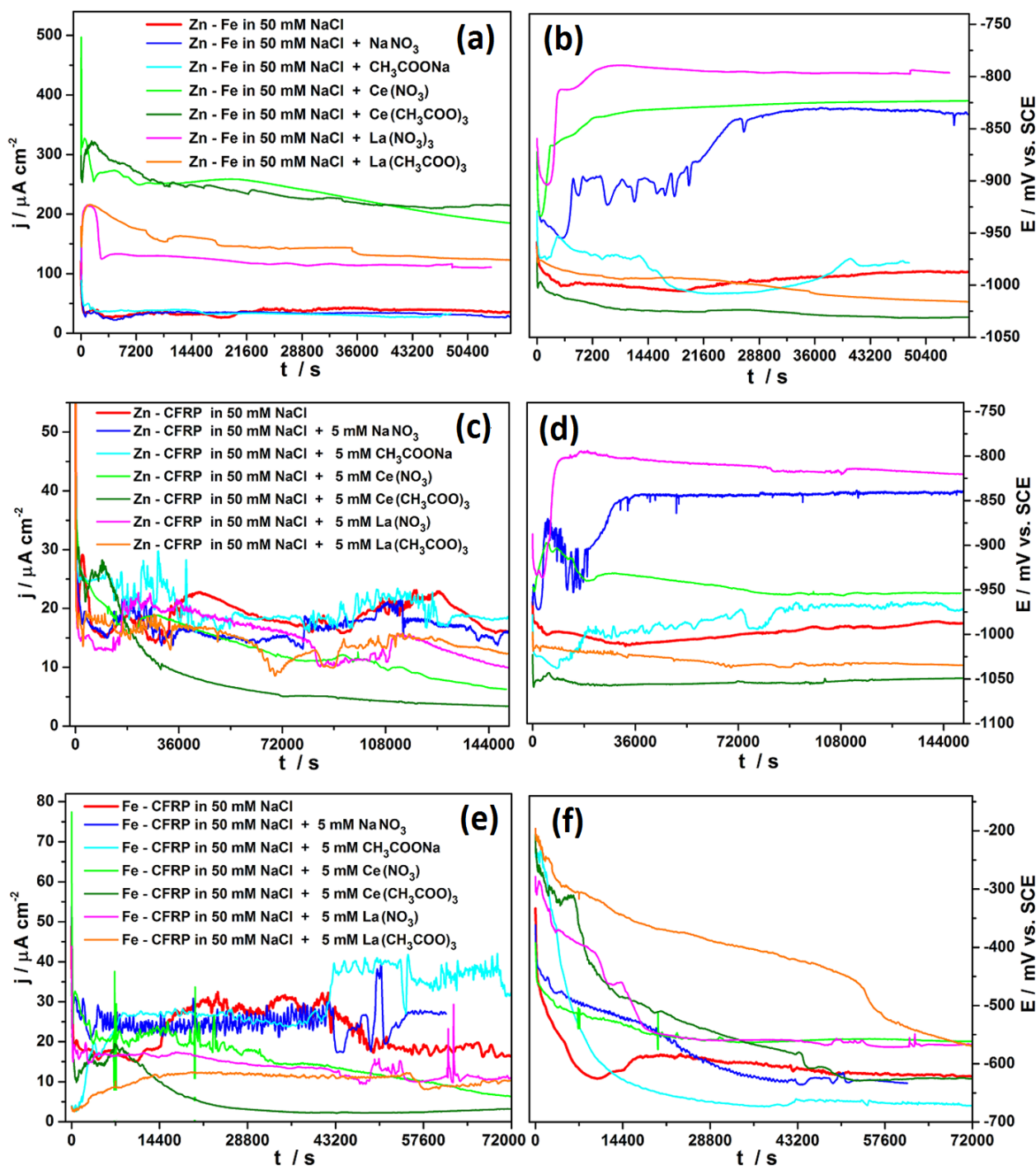


Fig. 7.12. Effect of conjugate anion of rare-earth metal salts on the time evolution of galvanic current densities and galvanic potential respectively of (a-b) Zn - Fe, (c-d) Zn - CFRP, and (e-f) Fe - CFRP couples of the Zn - Fe - CFRP multi-material galvanic system in 50 mM NaCl.

From Fig. 7.12(a) it is observed that the presence of rare-earth metal salts irrespective of the conjugate anion (NO_3^- or CH_3COO^-) lead to increase in the galvanic corrosion kinetics of Zn - Fe couple. The association of the enhanced galvanic corrosion of Zn - Fe couple to the presence of rare earth cations and not the conjugate anions is confirmed by the fact that in the absence of rare earths, but presence of the conjugate anions (NO_3^- or CH_3COO^-) as in NaNO_3 and CH_3COONa , the measured galvanic current density profile is in both cases different from those

measured in the presence of rare-earths but consistent with values measured in blank test solution. Consequently it is concluded that the galvanic corrosion of Zn - Fe couple is enhanced by the presence of rare earth cations but insensitive to the conjugate anion of the rare earth salt employed. From Fig. 7.12(b) it is observed that the galvanic potential of Zn - Fe couple is sensitive to the conjugate anion of the cation with nitrates shifting the potential to more anodic values and acetates to more cathodic values with respect to values measured in blank solution.

To determine if the conjugate anions of the rare earth salts had effect(s) on the inhibitive effects observed, a comparison of the galvanic current densities and potential evolution of Zn - CFRP galvanic couple in the presence of NaNO_3 and CH_3COONa , $\text{Ce}(\text{NO}_3)_3$ and $\text{Ce}(\text{CH}_3\text{COO})_3$, and $\text{La}(\text{NO}_3)_3$ and $\text{La}(\text{CH}_3\text{COO})_3$ respectively was made. From Fig. 7.12 (c and d) obvious differences are observed in the galvanic current densities and potential profiles in the presence of cerium cations depending on the conjugate anion of the rare earth metal used. Though the "incubation times" before the manifestation of inhibitive effects are similar, the kinetics are faster when cerium is introduced as an acetate compared to its introduction as a nitrate. From the plot of galvanic potential evolution with time (Fig. 7.12c), it is observed that right from immersion a wide difference of over $200 \text{ mV}_{\text{SCE}}$ exist between potential values measured in the presence of cerium nitrate and cerium acetate. Whereas measured potentials in the presence of cerium acetate are cathodic with respect to values measured across Zn - CFRP couple in blank solution, the potential profile in the presence of cerium nitrate is shifted but towards more anodic values. These shifts either way are most probably indicative of a change in inhibition mechanism occasioned by the difference in the conjugate anion. The same trend is observed by comparing the galvanic potential evolution in the presence of NaNO_3 and CH_3COONa , and $\text{La}(\text{NO}_3)_3$ and $\text{La}(\text{CH}_3\text{COO})_3$ confirming that in spite of the cation, introduction of the conjugate anion as nitrate ion leads to shifts in the galvanic potential towards anodic values relative to both the values in the blank solution and in the presence of acetates of the corresponding cation. The exact opposite effect is observed on introduction of the conjugate anion as an acetate with galvanic potentials tending to more cathodic values. Consequently it is concluded that in the Zn - CFRP galvanic couple the conjugate anion influences the observed inhibition efficiencies and the potential evolution, while in the presence of La and Na cations only the galvanic potential evolution is affected.

By similar comparisons of the galvanic current densities and potential evolution of Fe - CFRP galvanic couple in the presence of NaNO_3 and CH_3COONa , $\text{Ce}(\text{NO}_3)_3$ and $\text{Ce}(\text{CH}_3\text{COO})_3$, and $\text{La}(\text{NO}_3)_3$ and $\text{La}(\text{CH}_3\text{COO})_3$ respectively, any link(s) between the observed inhibitive effect

of the rare-earth metal salts and their conjugate anion can be established. From Fig. 7.9(e-f) and Fig. 7.7(e-f) and comparing galvanic current density evolution of Fe - CFRP galvanic couple in the presence of NaNO_3 and CH_3COONa (Fig. 7.12 (e- f)), it is observed that in the absence of rare earth cations the effect of the conjugate anions appear to be insignificant. By making similar comparison between $\text{La}(\text{NO}_3)_3$ and $\text{La}(\text{CH}_3\text{COO})_3$, It can be concluded that in the presence of La cation the conjugate anions (nitrate or acetate) apparently do not exert significant effects. However, similar comparison between $\text{Ce}(\text{NO}_3)_3$ and $\text{Ce}(\text{CH}_3\text{COO})_3$ reveal a marked effect of the conjugate anion of cerium cation on the inhibition efficiency with better performance recorded by introducing cerium cations as an acetate compared to as a nitrate. This conclusion is corroborated by the work of Hinton [695] who working with several cerium salts ($\text{CeCl}_3 \cdot 7\text{H}_2\text{O}$, $\text{Ce}_2(\text{SO}_4)_3 \cdot \text{H}_2\text{O}$, $\text{Ce}(\text{ClO}_4)_3$, and $\text{Ce}(\text{CH}_3\text{COO})_3$) on high strength aluminium-zinc-magnesium-copper alloy (AA7075) reported superior inhibitor performance in the presence of cerium acetate

The potentiodynamic polarization curves of Fig. 7.13 illustrates the effects of conjugate anion of rare-earth metal salts on the potentiodynamic polarization curves of (a) Zn - Fe, (b) Zn - CFRP, and (c) Fe - CFRP, (d) Zn, (e) Fe, and (f) CFRP in 50 mM NaCl based inhibitor solutions after 1 hour immersion, which can provide further insight on the mechanism of the observed effects of the conjugate anions of rare-earth cations in the Zn - Fe - CFRP multi-material galvanic system. For Zn - Fe galvanic couple (Fig. 7.13a), enhanced cathodic activity was observed in the presence of all the acetates and nitrates except in the presence of CH_3COONa . Furthermore, the "corrosion potential" of the Zn - Fe galvanic couple was shifted towards more anodic potentials in the presence of the rare-earth nitrates (Ce and La). Similar trends of enhanced cathodic current densities coupled with anodic shifts of the corrosion potential were observed in the potentiodynamic polarization curves of zinc (Fig. 7.13d) in the presence of same rare-earth nitrates.

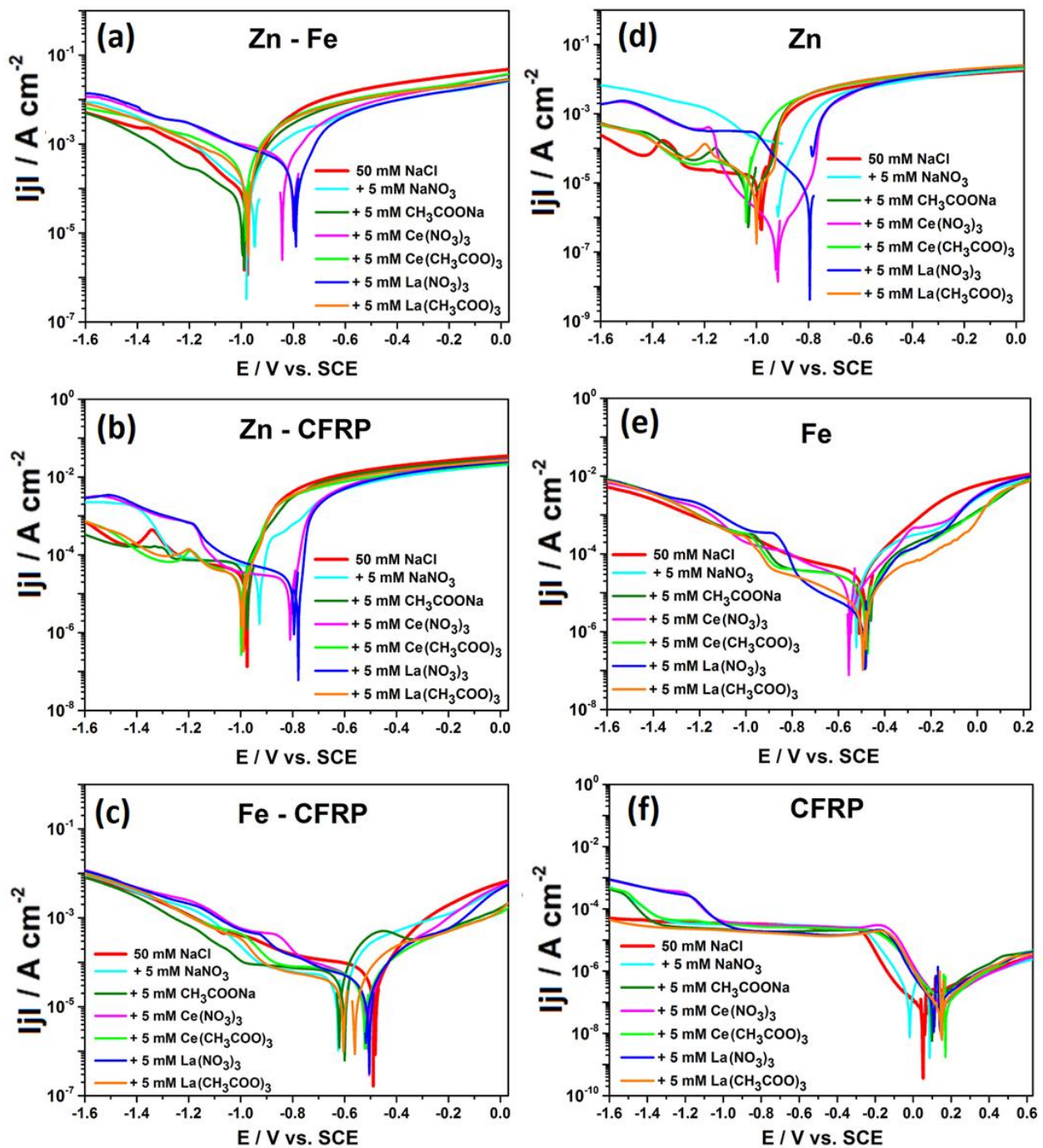


Fig. 7.13. Effect of conjugate anion of rare-earth metal salts on the potentiodynamic polarization curves of (a) Zn - Fe, (b) Zn - CFRP, and (c) Fe - CFRP, (d) Zn, (e) Fe, and (f) CFRP in 50 mM NaCl based inhibitor solutions after 1 hour immersion.

However, in the potentiodynamic polarization curves for iron in the presence of nitrates and acetates (Fig. 7.13e), significant reductions in the cathodic and anodic current densities were observed in the presence of lanthanum acetate, to less extent in the presence of lanthanum nitrate and cerium acetate, even at potentials consistent with the "mixed corrosion potential" of Zn - Fe galvanic couple ($\approx -1000 \text{ mV}_{\text{SCE}}$, Fig. 7.13a) in this study.

This suppression of both cathodic and anodic processes in the presence of lanthanum either as an acetate or as a nitrate is postulated to account for the superior performance of

lanthanum containing inhibitor combinations at mitigating galvanic corrosion of the Zn - Fe galvanic couple, and ultimately the Zn - Fe - CFRP multi-material combination (sections 7.3 and 7.2). This position is supported by the observance of similar reductions in the cathodic and anodic current densities were of the potentiodynamic polarization curves of Fe - CFRP galvanic couple in the presence of lanthanum acetate (Fig. 7.13c) and even in the cathodic curves of CFRP (Fig. 7.13f).

7.4. The Nature and Changes in the Local Environment Near Constituent Materials of the Zn - Fe - CFRP Multi-material Galvanic System.

Since the effect of inhibitors on the Zn-Fe-CFRP multi-material "galvanic triplet" can be affected by the local pH profile around each member of the multi-material assembly, knowledge of the pH profile will aid understanding of the possible mechanisms of the inhibitive effects observed. Hence, the pH profile across the (connected) "triplet" Zn - Fe - CFRP multi-material galvanic couple at a height of 40 μm above the surface was measured and presented in Fig. 7.14 below. From the pH profile across connected Zn - Fe - CFRP multi-material assembly (Fig 7.14), slight acidification is observed above the zinc surface (the anode). This acidification is also observed to be apparently most intense at the centre while decreasing sharply in intensity moving away from the centre. Similar trends are observed above the iron and CFRP surfaces (both cathodes) along with very marked alkalization with the local pH above these cathodes rising to about 8.5 and 9 respectively.

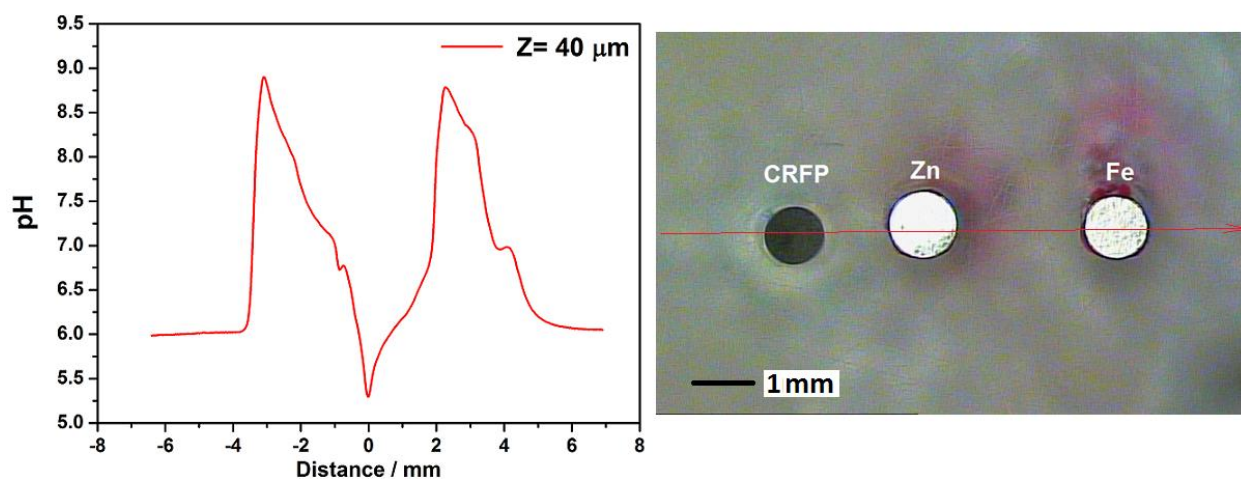


Fig. 7.14. pH profile across connected Zn - Fe - CFRP in 50 mM NaCl solution.

Comparing this pH profile with that obtained across Al - Cu - CFRP under same conditions, it is concluded that alkalization around the cathodes is less severe in Zn - Fe - CFRP "galvanic triplet". The slight acidification observed above zinc surface is attributed to the

consumption of OH^- ions with the formation zinc hydroxy- corrosion products at a rate faster than its diffusion kinetics from the bulk solution, resulting in a local excess of H^+ ions. In the light of the above, it is obvious that the corrosion inhibitors employed interact with the coupled materials in the Zn - Fe - CFRP multi-material combination at local pH values significantly different from the bulk pH.

To confirm the metal on which cerium acts on this couple, and get a better understanding of the mechanism of inhibitive effects observed in the presence of cerium, elemental mapping by x-ray fluorescence spectroscopy was carried out on the surface of coupled Zn - Fe galvanic couple after immersion in 50 mM NaCl containing 2.5 mM ($\text{Ce}(\text{NO}_3)_3 + \text{BTA}$) employing a voltage of 40 kV, current of 1000 μA , collimator size of 0.2 x 0.2 mm, acquisition time of 50 ms per pixel, resulting in a mapping time of 112.1 minutes. The results of the XRF mapping are presented in Fig. 7.15 below.

In the Zn - Fe galvanic couple, zinc is the anode while iron is the cathode. From Fig. 7.15 (b) showing mapping for iron using Fe-K_α , the high surface sensitivity of this surface analysis method is evident in the lower counts for iron on iron surface at sites observed to be rich in corrosion products (green areas in Fig.7.15 (b)). Secondly, and very importantly is the non-detection of iron on the zinc surface. In Fig. 7.15 (c) showing mapping for zinc using Zn-K_α radiations, high counts for zinc above zinc surface (red), and low counts for zinc over iron surface that clearly marks out the iron surface and higher on iron surface at sites consistent with the presence of corrosion products, indicates the re-deposition of zinc on iron surface. From Fig. 7.15 (d) showing mapping for cerium using Ce-L_α radiation it is revealed that the cerium acts principally on the cathode (iron) based on the unique and much higher counts for cerium all over the iron surface, which was even much higher (red colour) at sites on the iron surface deficient in corrosion products and hence deemed to be well protected. The precipitation of cerium on the iron is consistent with the high local pH values measured over iron coupled to zinc (Fig. 7.14.). Due to the less severe local acidification over Zn surface (pH 5.5) and less drastic pH increase above iron (pH 8.5) it is believed that cerium precipitation on Zn might be a possibility in the presence of oxygen most probably as Ce(IV) oxy/hydroxy compounds and as both Ce(III) and Ce(IV) oxy/hydroxy compounds over iron [565]. This can be proved conclusively by x-ray photoelectron spectroscopy (XPS) measurements which had not been done. However, the observance of the presence of cerium around the edges of zinc in Fig. 7.15(d) at which according to the measured pH profile (Fig. 7.14) the acidification effect is most likely to be less severe supports this assertion.

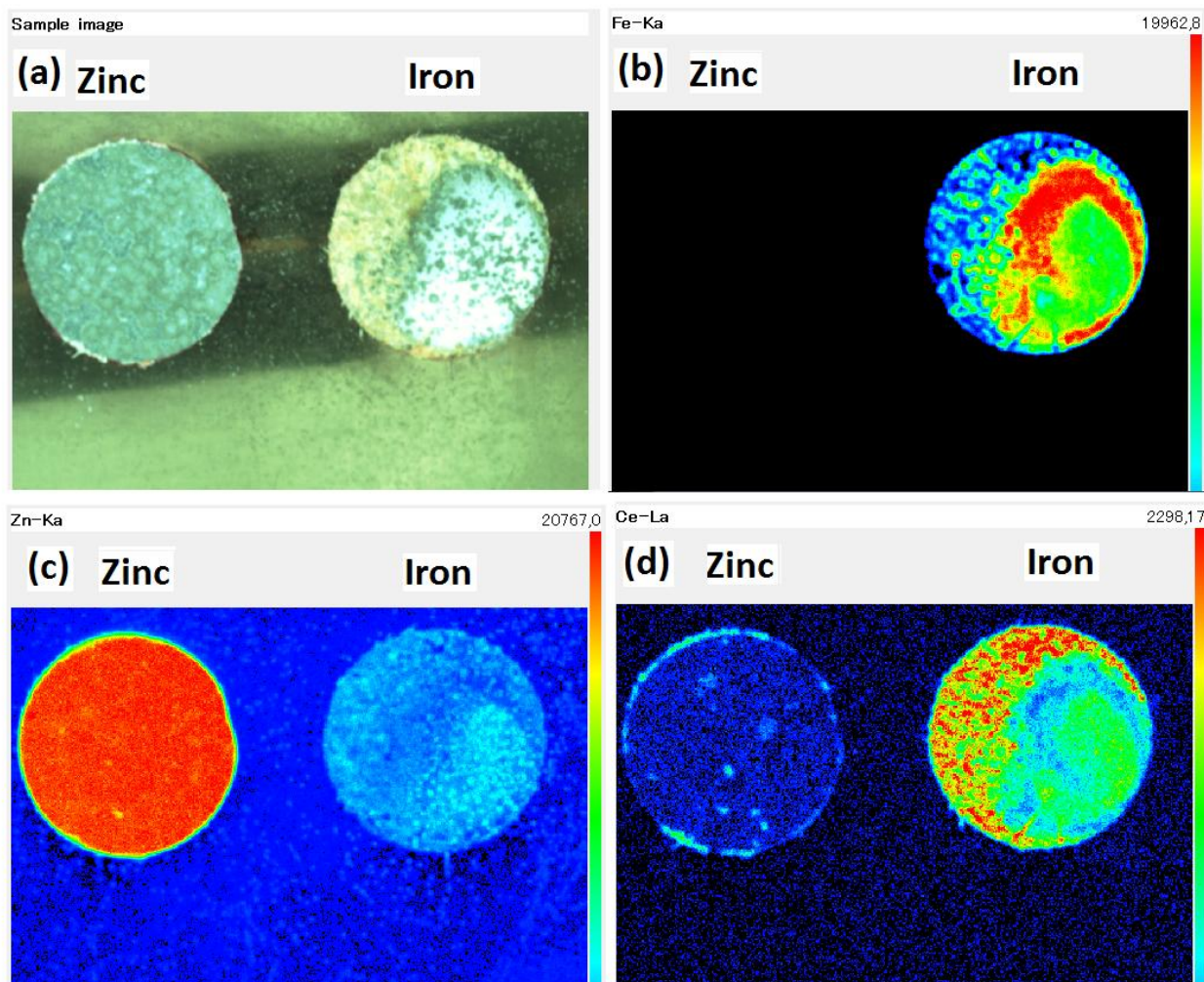


Fig. 7.15. X-ray fluorescence mapping of surfaces of Zinc and Iron of coupled Zn - Fe galvanic couple after exposure 50 mM NaCl containing 2.5 mM (Ce(NO₃)₃ + BTA).

Since in uncoupled metals, the cathodic and anodic areas are bound to be present on each metal, further XRF mapping of uncoupled Zn - Fe galvanic couple after immersion in 50 mM NaCl containing 2.5 mM (Ce(NO₃)₃ + BTA) was done to establish cerium distribution under this condition, and the results presented in Fig. 7.16 below.

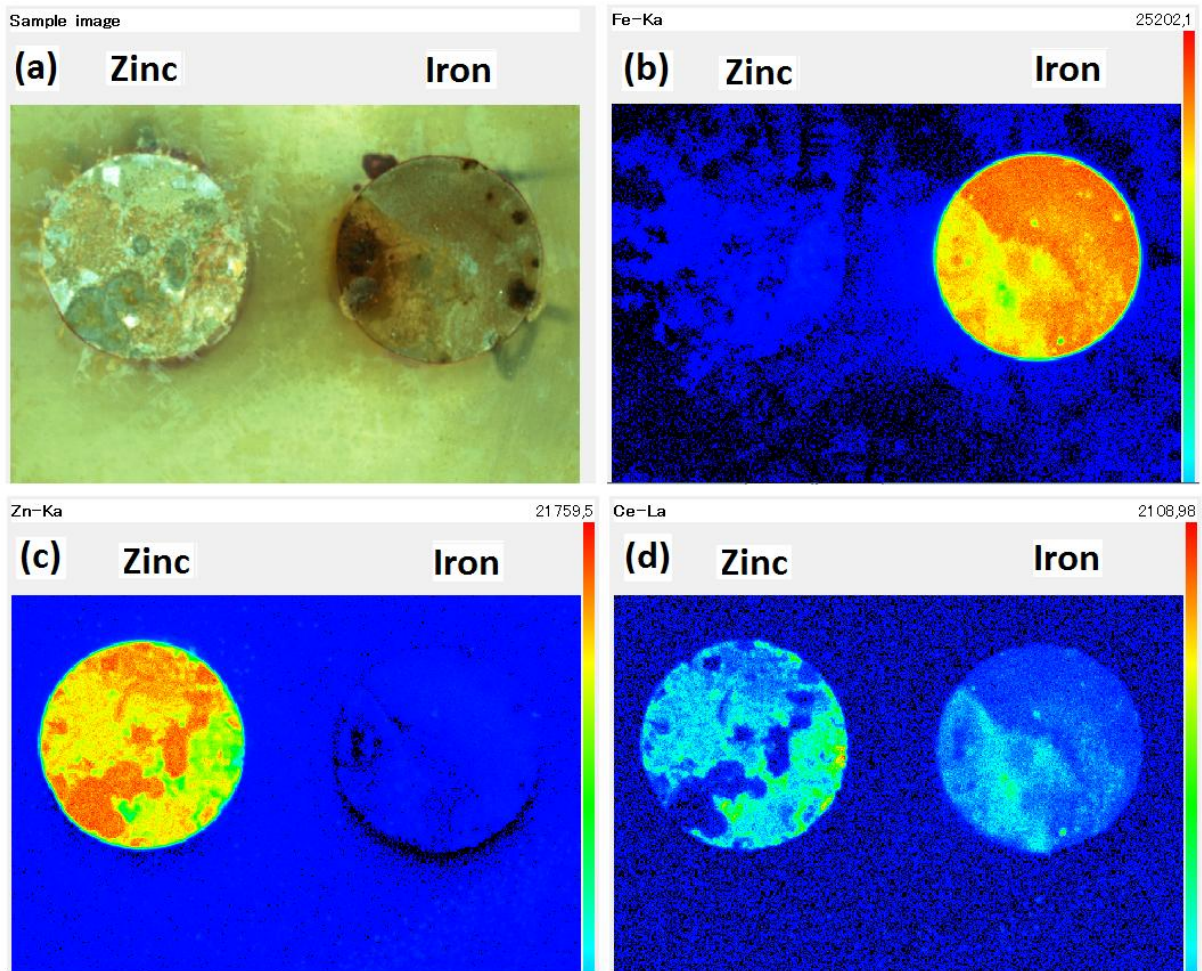


Fig. 7.16. X-ray fluorescence mapping of surfaces of Zinc and Iron of uncoupled Zn - Fe galvanic couple after exposure 50 mM NaCl containing 2.5 mM ($\text{Ce}(\text{NO}_3)_3$ + BTA).

Fig. 7.16 (a) presents the optical image of uncoupled Zn - Fe galvanic couple after exposure 50 mM NaCl containing 2.5 mM ($\text{Ce}(\text{NO}_3)_3$ + BTA) which shows the presence of corrosion products, and also anodic and cathodic areas on each metal. In the mappings for iron (Fig. 7.16 (b)) and zinc (Fig.7.16 (c)) respectively, the surface sensitivity of the XRF mapping is again evident in the discrimination of cathodic areas from anodic areas (red colour) due to apparent absence of corrosion products at anodic areas and hence higher counts for each metal over its own surface. Notable is the non-detection of any re-deposition of either iron or zinc as observed in the coupled condition. From the mapping for cerium (Fig. 7.16 (d)), it is observed clearly that cerium is preferentially deposited/precipitated on cathodic areas of both metals, confirming the cathodic inhibitive action of cerium.

7.5. Proposed Mechanism(s) of Multi-material Corrosion and Multi-material Corrosion Inhibition in the Zn - Fe - CFRP Multi-Material Combination.

Having studied the effect of individual inhibitors (under different classifications) on the galvanic corrosion behaviour of Zn - Fe, Zn - CFRP, and Fe - CFRP dual galvanic couples and on the galvanic corrosion of the Zn - Fe - CFRP multi-material combination, and guided by insights obtained from earlier studies with single inhibitors, plausible mechanism(s) are herein proposed to account for the observed multi-material corrosion in the Zn - Fe - CFRP multi-material galvanic system and the observed inhibiting effects in the presence of inhibitor concentrations comprised of rare-earth nitrates and the azole; benzotriazole, $(\text{La}(\text{NO}_3)_3 + \text{BTA})$ and $(\text{Ce}(\text{NO}_3)_3 + \text{BTA})$.

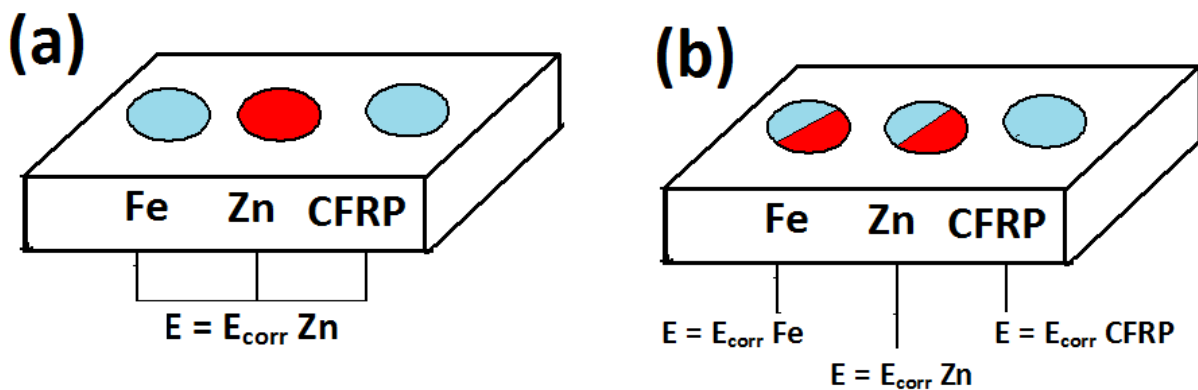


Fig. 7.17. Illustration of the mechanism of multi-material corrosion in the Zn -Fe - CFRP multi-material system (red colour denotes anodic surface and blue cathodic area of surface).

When Zn - Fe - CFRP are uncoupled (Fig. 7.17b) "corrosion" of each of its three component materials proceed under open circuit conditions, with cathodic and anodic processes manifesting on each of the metallic components (Fig. 7.16). The corrosion of the respective materials proceed in line with their respective corrosion behaviours in the test media based on the pH, temperature, oxygen concentration etc. Hence corrosion inhibitors that are known to inhibit each of the material components are able to interact with the surfaces of its target material with expected inhibition efficiencies.

However, on galvanic coupling (Fig. 7.17a) by electrically connecting Zn, Fe, and CFRP together, the surface properties/charges of the cathodic components (Fe and CFRP) are bound to change because they are now polarized by the zinc to cathodic potentials close to the corrosion potential of zinc. In addition to these changes on the the cathodic components of multi-material combinations significant changes in the local pH of the electrolyte near their surface occur and have been demonstrated to rise to pH values in the range of $\approx 8.7 - 9$ (Fig. 7.14). For the more active component (zinc) of the multi-material combination, except for the

enhancement of anodic processes as a result of the increased cathodic area due to galvanic coupling to Fe and/or CFRP no significant changes occur on or near its surface. Hence inhibitors that are known to interact with zinc surface under the test conditions (bulk pH, etc) are very likely to continue to exert inhibitive effects on zinc even in this galvanically coupled multi-material assembly.

For the cathodic components (Fe and CFRP) of the galvanically coupled multi-material assembly the corrosion inhibition scenario is quite different as their surface properties/charges are bound to change on galvanic coupling to zinc with a concomitant rise in the local pH near their surfaces to alkaline values. Hence corrosion inhibitors that have been proven to interact with the surfaces of cathodic components of galvanically coupled material assemblies and inhibit corrosion processes under open circuit conditions might not be effective in combating their corrosion in galvanically coupled material assemblies. This can account for the poor performance of some of the azole inhibitors targeted as inhibitors of cathodic processes on the cathodic material components of multi-material assemblies in selected inhibitor combinations (**section 7.2.0, Figs 7.2, and 7.3**), in spite of their confirmed effectiveness on the target single materials under open circuit conditions (**section 7.3.1, Figs. 7.5 and 7.6**).

In the light of these, it is postulated that the search for multi-material corrosion inhibitor combinations will be better served firstly, by focusing more on identification of adsorption based inhibitors that are able to inhibit the target cathodic materials in a multi-material combination at cathodic polarizations consistent with the expected polarization it is anticipated to be subjected to on galvanic coupling in the multi-material assembly, as the known inhibitors for the more active components (anode(s)) of such multi-material assemblies are more likely to continue to be effective on their targets (anodic component(s)). Secondly, in addition to impressed polarization, the use of solutions at bulk alkaline pH consistent with the pH of the local environment(s) around the galvanically coupled cathode(s) is more likely to enhance the outcome of research efforts at effective adsorption based cathodic inhibitors for inhibitor combinations for mitigating corrosion in multi-material assemblies rather than tests at near-neutral bulk pH. An alternative or complementary route is a search focused on precipitation based inhibitors (or their combinations) whose precipitation onto the surfaces of cathodic components of multi-material assemblies can be tuned to be efficiently triggered by the high pH near their surfaces on the onset of cathodic processes

Another potent factor that can interfere with the mechanism(s) of multi-material corrosion and its inhibition is the effect of the cations of the cathodic metals in the electrolyte

which have been known [142] and demonstrated herein (Fig. 7.15) to redeposit on anodic metal surfaces (by their reduction) in galvanically coupled systems. Such redeposition of cathodic metal cations onto anodic metal surfaces besides its known deleterious effect on the anodic dissolution of the anodes, can in the presence of inhibitor(s) change/interfere with the mechanism(s) of multi-material corrosion inhibition. This can occur for instance, by making it easier for cathodic inhibitors intended to interact with the cathodic metals, to interact also with sections of the anodes covered by electro-deposited cathodic metals thus leading to possible "de-activation" of these sections of the anode surface and a possible improvement of inhibitive effects.

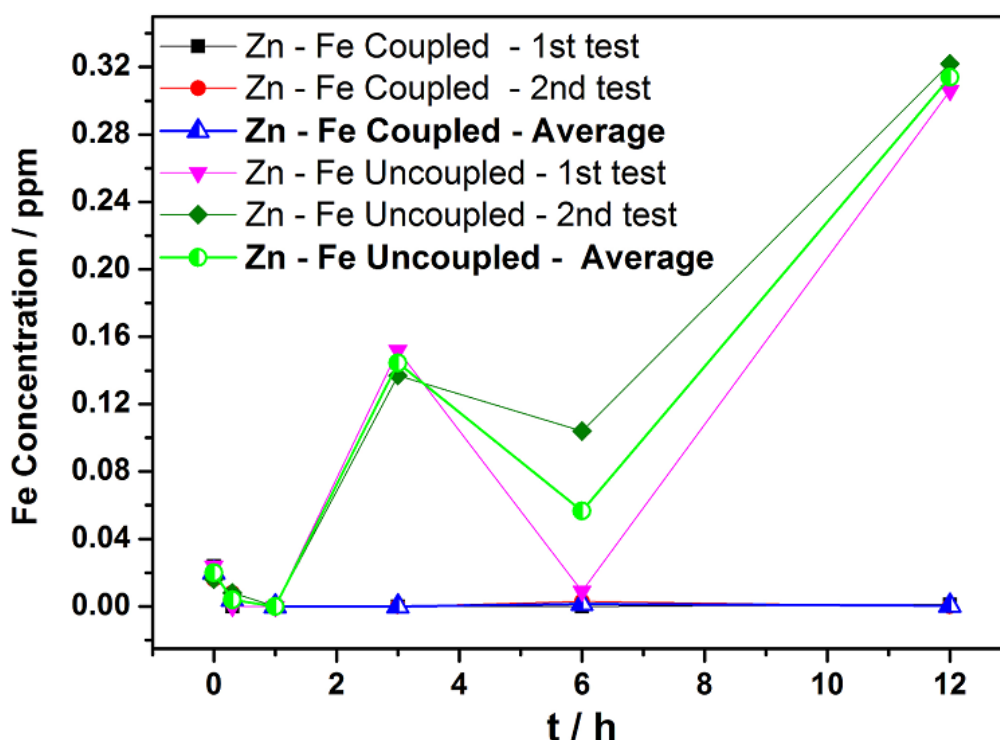
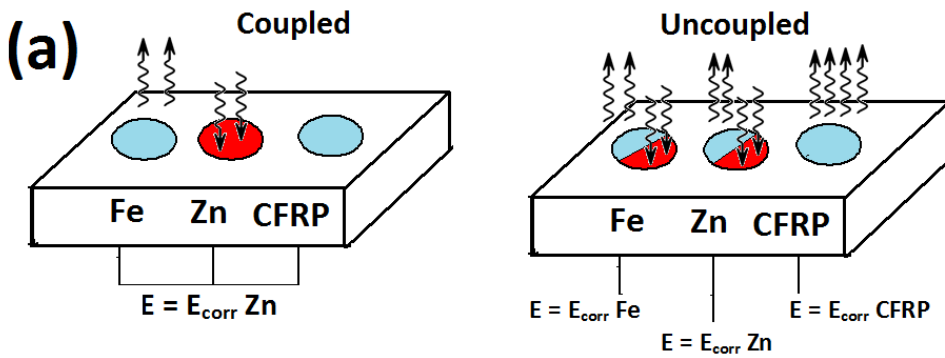


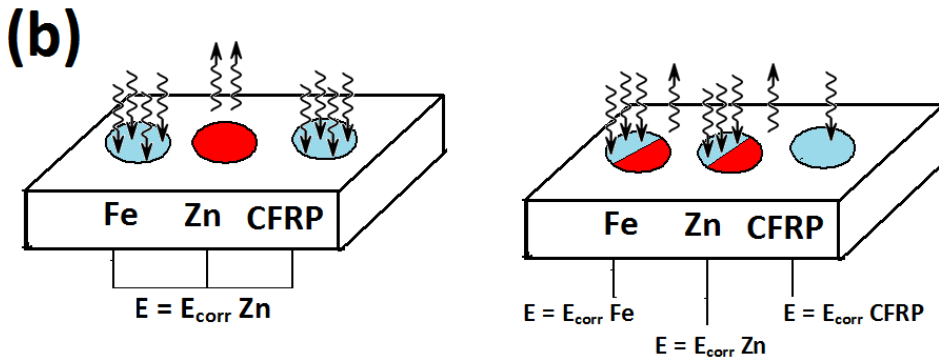
Fig. 7.18. Changes in Fe concentrations in 50 mM NaCl solution as a function of time for galvanically coupled and uncoupled Zn - Fe.

Fig. 7. 18 above gives further confirmation of this possibility as the iron content in bulk 50 mM NaCl solution is observed to be diminished soon after immersion of galvanically coupled Zn - Fe to values lower than the initial values prior to immersion. This sustained decrease in the iron content of the test media in the presence of galvanically coupled Zn - Fe couple is attributed to iron cation removal from solution by their electro-reduction and deposition on zinc surface which has been demonstrated earlier in XRF analysis of Zn - Fe galvanically coupled and uncoupled (Figs. 7.15 and 7.16). However, it is acknowledged that another factor that might account for the observed decrease in the iron content of the test media in the presence of galvanically coupled Zn - Fe couple is the plausible formation of insoluble hydroxides at

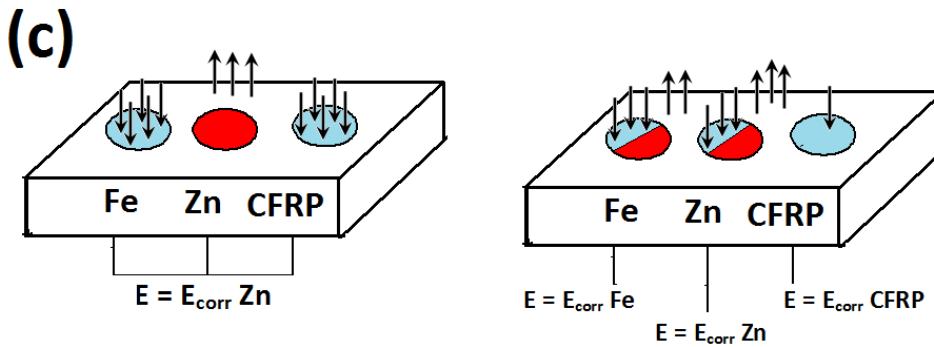
cathodes in galvanically coupled assemblies.



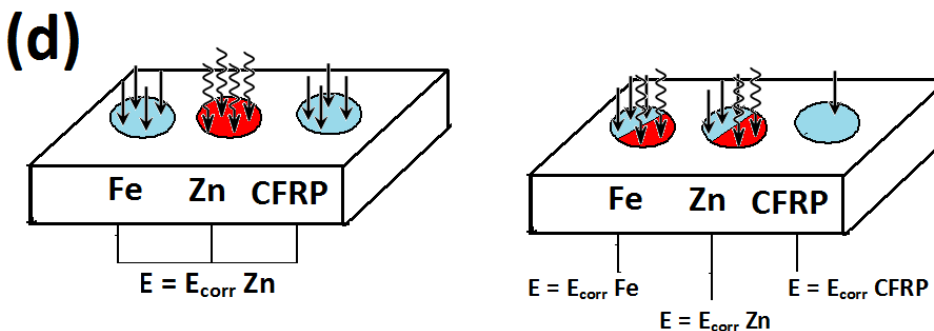
Adsorption based inhibitor that is effective at near neutral pH



Adsorption based inhibitor that is effective at high (alkaline) pH



Precipitation based inhibitor that is sensitive to high pH



Combination of a precipitation based inhibitor sensitive to high pH and adsorption based inhibitor effective at near neutral pH on anodic metal(s)

Fig. 7.19. Illustration of the different plausible scenarios in the mechanism of multi-material corrosion inhibition in the Zn -Fe - CFRP multi-material system (Wavy arrows denote adsorption based inhibitors while the straight arrows denote precipitation based inhibitors.).

Based on the results obtained in this work and the important factors affecting multi-material corrosion and multi-material corrosion inhibition demonstrated and discussed above, the plausible mechanisms/scenarios for/in multi-material corrosion inhibition in the Zn - Fe - CFRP multi-material assembly (galvanically coupled and uncoupled) are illustrated above (Fig. 7.19) in the presence of a variety of inhibitors and inhibitor combinations. The scenarios considered herein are; (a) Zn - Fe - CFRP multi-material assembly corrosion mechanism on galvanic coupling and uncoupled in the absence of inhibitors (already presented in Fig. 7.17 above), (b) in the presence of adsorption based inhibitor that is ineffective at high pH, (c) in the presence of adsorption based inhibitor that is effective at high pH, (d) in the presence of adsorption based inhibitor that is only effective at near-neutral pH, (e) in the presence of a precipitation based inhibitor, and (f) in the presence of the combination a precipitation based inhibitor and an adsorption based inhibitor. In Fig 7.19 above, the wavy arrows denote adsorption based inhibitors while the straight arrows denote precipitation based inhibitors. From Fig 7.19d it is obvious that the most effective corrosion inhibitive effects occur with the combination of a precipitation based inhibitor targeted primarily at the cathodes and an adsorption based inhibitor primarily targeted at the anode(s) which is consistent with the results in this study.

From the results presented in this chapter and their discussion above, it is concluded and illustrated in Fig.7.19d above that the most viable option for multi-material corrosion inhibition in galvanically coupled Zn - Fe - CFRP multi-material combination is the use of a combination of inhibitors composed of at least a precipitation based inhibitor that is sensitive to the high pH around the cathodes (Fe and CFRP) (Figs. 7.15 and 7.16), which has been demonstrated to be in the range of 8.5 to 9 (Fig. 7.14), and an adsorption based inhibitor that is able to interact with surfaces of the anodic metal(s) at near neutral pH to retard its/their anodic dissolution.

This conclusion is in tandem with the two suggested inhibitor combinations for multi-material corrosion inhibition; $(\text{Ce}(\text{NO}_3)_3 + \text{BTA})$ and $(\text{La}(\text{NO}_3)_3 + \text{BTA})$. The cerium has been demonstrated to precipitate onto the surface of the cathodes on coupling (Fig. 7.15), an event triggered by the development of a high pH around the cathodes due to cathodic processes earlier discussed, while the adsorption based azole inhibitor (benzotriazole) most probably adsorbs to the zinc surface. In addition the nitrate ions which have been reported [687] to exert inhibitive effects on anodic processes is inferred to also interact with the anodic zinc surface complementing inhibitive effects on anodic process. This can explain the reason the inhibitor combinations comprised of rare earth nitrates were more effective in mitigating multi-material

corrosion in Zn - Fe - CFRP multi-material assemblies. Hence a search for adsorption based inhibitors for anodic constituents of galvanically coupled multi-material system that are effective at near-neutral pH is thought to be a viable research route. On the other hand, the superior performance of inhibitor combinations containing benzotriazole (among the other azoles) is attributed to its superior interaction with the zinc surface, which can be a subject for further confirmatory studies.

In addition the plausible redeposition of cations of the cathodic metals is inferred to be capable of significantly affecting the corrosion mechanism in the absence of inhibitors (enhanced anodic dissolution) but in the right conditions aid inhibitor interaction with the anode to ensure better inhibitive effects. The confirmation of this postulation can be the subject of further enquiry on multi-material corrosion inhibition

The differences in the effectiveness of inhibitor combinations containing the same azole inhibitor but different rare earth cations in which La and Ce exhibited superior performance is attributed to differences in the solubilities of their respective hydroxides as a function of pH which apparently favours La and Ce among the rare-earth cations employed in this study.

The observed differences in the effectiveness and time evolution of inhibitive effects in inhibitor combinations containing the most promising rare-earth cations (La^{3+} and Ce^{3+}) and other rare earth cations, with respect to the Zn-Fe-CFRP multi-material system can be partially attributed to the differences in the solubility products (K_{sp}) of their various hydroxides [697-699] of the respective cations, which is likely to favour the preferential precipitation of hydroxides of cations that have the lowest solubility products (K_{sp}) values. Hence the presence of a rare-earth cation that forms a hydroxide with a lower solubility product (K_{sp}) is likely to be more protective compared to that with a higher solubility product (K_{sp}) as the hydroxide of the cation with a lower solubility product (K_{sp}) is expected to precipitate faster and with more ease onto the cathodic metal surface. In instances in which the solubility of both hydroxides are low as have been reported in an earlier work [63] on aluminium alloys, the decisive factor in determining superior inhibitive effects can be the compactness (density) and barrier properties; the compactness of the precipitated hydroxides in turn being dependent on its deposition kinetics. Another factor exerting influence can be the anions present in the test media as was demonstrated in the section on effects of conjugate anions (section 7.3.4). This assertion is supported by the work of Moeller and Kremers [700] who had demonstrated in Table 2 of their work with their own data and that from earlier workers, the differences in the precipitation pH values of rare-earth hydroxides from solutions containing their respective cations as a function

of the conjugate anion present in solution. In support of the position in this work on the effects of the conjugate anions, and for clarity and brevity, data for the rare earths used in this study have been extracted from the work of Moeller and Kremers [700] and presented as Table 7.2 below.

Table 7.2: Precipitation pH Values of Rare Earth Hydroxides at Precipitation Incidence [(Extracted from Table 2 of Moeller and Kremers (1944), Ref: 700) (References in Table 7.2 below are references in Ref: 700)].

Rare Earth	Atomic No.	Cation Radius (Å)	NO ₃ ⁻	SO ₄ ²⁻	CH ₃ COO ⁻	Cl ⁻
La	57	1.00	7.82 8.35 (Ref 2) 8.71(Ref 18)	7.41 7.61 (Ref 1)	7.93	8.03 (Ref 1)
Ce	58	0.94	7.60 8.1 (Ref 18)	7.35 7.07 (Ref 1)	7.77	7.41 (Ref 2)
Pr	59	0.91	7.35	7.17	7.66	7.05 (Ref 2)
Nd	60	0.90	7.31 7.00 (Ref 2)	6.95 6.98 (Ref 1)	7.59	7.02 (Ref 2) 7.40 (Ref 1)
Sm	62	0.87	6.92	6.70 6.73 (Ref 1)	7.40	

From the pH values for the onset of precipitation of the hydroxides of the various rare earths employed in this study, extracted from [Ref: 700] and presented in Table 7.2 above, the complex nature of the effects of anions present in this study becomes manifest, as under the test conditions in the present work, at least two anions are always present besides OH⁻ in the test media; Cl⁻ from the supporting electrolyte (NaCl), and either NO₃⁻ or CH₃COO⁻ as the conjugate anion from the rare earth compound. In contrast, the data reproduced in Table 7.2 above were carried out in systems without a similar "multi-anion" composition. In spite of these differences, it is clear that the precipitation of hydroxides of all the rare earth cations employed in this study are favoured in the pH range 8.5 - 9.0 expected around cathodic members of the Zn - Fe - CFRP multi-material assembly when galvanically coupled. The particular or predominant cause of the differences in the effectiveness of La and Ce which can be the subject of a separate study and might be also somehow related to subtle differences in the sizes of the rare earth cations.

With respect to this study and the Zn - Fe - CFRP galvanic multi-material system, the predominant cause of the differences in the effectiveness of La and Ce in manifesting inhibitive effects, and the time evolution of these effects which appear to favour La in a lot of cases, is hinged on the interplay between the expected pH ranges (pH ≈ 8.5 - 9.0) around the cathodes in

the Zn - Fe - CFRP galvanic multi-material system, and the observation from Table 7.2 containing data emanating from diverse sources that in spite of the predominant conjugate anion, the onset pH for precipitation of lanthanum hydroxide is consistently higher than that for cerium. The effect of the combination of these two important observations is most likely to be that that La^{3+} cations stay longer in solution as the pH around the cathode increases from near-neutral values and tends towards pH 9, while the Ce^{3+} cations are able to precipitate as hydroxides with smaller increases in local pH, even before the onset of very intense cathodic activity. Such scenario is likely to ensure that Ce^{3+} are faster in action while La^{3+} cations are likely to be more enduring.

7.5. Chapter Summary

The multi-material corrosion and multi-material corrosion inhibition of the Zn - Fe - CFRP multi-material galvanic system and its component dual material galvanic couples have been studied using single inhibitors and a combination of inhibitors. The mechanism of its multi-material corrosion has been demonstrated and plausible scenarios of the mechanisms of multi-material corrosion inhibition in the the Zn - Fe - CFRP multi-material galvanic system with different types and combination of inhibitors postulated. Inhibitor combinations composed of at least an adsorption based inhibitor targeted primarily at the anode(s) and at least a precipitation based inhibitor that can be triggered to precipitate onto the surfaces of the cathode(s) is advanced as the most promising solution. For more practical and enduring effects, combinations comprised of more than one of these two types of inhibitors might be desirable.

Based on the results obtained in the tests on the Zn - Fe - CFRP multi-material galvanic system, $(\text{La}(\text{NO}_3)_3 + \text{BTA})$ and $(\text{Ce}(\text{NO}_3)_3 + \text{BTA})$ with inhibition efficiencies of 95.12% and 91.19% respectively on the Zn - Fe - CFRP multi-material "galvanic triplet" are identified as multi-material corrosion inhibitors for the multi-material combination. This is based on the observation that these inhibitors also simultaneously inhibit the galvanic corrosion of all the dual galvanic couples (Fe - CFRP, Zn - CFRP, and Zn - Fe) in the Zn - Fe - CFRP galvanic multi-material system.

For Fe - CFRP galvanic couple the identified effective galvanic corrosion inhibitors and their measured inhibition efficiencies based on prior stated criterion are; $\text{Ce}(\text{NO}_3)_3$ (82.42%), $\text{Ce}(\text{CH}_3\text{COO})_3$ (85.81%), $(\text{Ce}(\text{NO}_3)_3 + \text{CH}_3\text{COONa})$ (93.03%), $(\text{Ce}(\text{NO}_3)_3 + 1,2,4\text{-triazole})$ (79.24%), $(\text{Ce}(\text{NO}_3)_3 + \text{BIA})$ (77.63%), $(\text{La}(\text{NO}_3)_3 + \text{BTA})$ (76.72%), and $(\text{Ce}(\text{NO}_3)_3 + \text{BTA})$ (53.28%). For Zn - CFRP galvanic couple the identified effective galvanic corrosion inhibitors and their respective

measured inhibition efficiencies based on prior stated criterion are; $\text{Ce}(\text{NO}_3)_3$ (61.23%), $\text{Ce}(\text{CH}_3\text{COO})_3$ (79.07%), BTA (41.23-70.43%), $(\text{Ce}(\text{NO}_3)_3 + \text{CH}_3\text{COONa})$ (84.38%), $(\text{Ce}(\text{NO}_3)_3 + 1,2,3\text{-triazole})$ (55.93%), $(\text{La}(\text{NO}_3)_3 + \text{BTA})$ (63.95%), and $(\text{Ce}(\text{NO}_3)_3 + \text{BTA})$ (86.48- 91.85%). For Zn - Fe galvanic couple the identified effective galvanic corrosion inhibitors and their respective measured inhibition efficiencies are; BTA (64.12%), $(\text{La}(\text{NO}_3)_3 + \text{BTA})$ (88.31%), and $(\text{Ce}(\text{NO}_3)_3 + \text{BTA})$ (77.49%).

CHAPTER 8

Conclusions and Future Outlook

8.0. Conclusions and Recommendations

This section of the thesis brings the short conclusive remarks from the PhD work and the outlook towards directions of further research. The results of research work aimed at multi-material corrosion inhibition on Al - Cu - CFRP and Zn - Fe - CFRP systems presented in preceding chapters of this thesis demonstrated that the use of inhibitor combinations with their constituents targeted on cathodic and anodic constituents of multi-material assemblies is the most promising strategy in employing inhibitors in mitigating multi-material corrosion. Insights have been provided on the plausible mechanism(s) of multi-material corrosion and multi-material corrosion inhibition in both multi-material systems. It is important to highlight that this work did not aim at full characterization of all the potential inhibition systems under study. The focus was directed towards screening of a number of potential inhibitor candidates and their combinations. Potential candidate inhibitors were selected on the basis of trends observed in their inhibitive effects under varied test conditions. The final expected outcome was to prove that corrosion inhibition approaches can be used to suppress galvanic corrosion rate in complex multi-material assemblies including those with CFRP as one of the cathodic counterparts.

As with most research efforts, questions are usually answered while new questions needing answers arise from the answers of the previous research question. The focus of this research which was to explore the viability of employing corrosion inhibitors in mitigating multi-material corrosion in technologically relevant multi-material systems have led to a better understanding of the mechanism of corrosion and its inhibition in the systems of interest. This better understanding have culminated in the identification of candidate inhibitor combination(s) for each of the systems. In the course of achieving the thesis objectives a variety of questions have been raised which could guide the future outlook on research on development of market-ready inhibitor solutions for multi-material corrosion inhibition. In this regard important conclusions drawn from the analysis of the results obtained in this work are presented in section 8.1, while suggestion on future outlook on further research related to the subject matter are presented in section 8.2 below.

8.1. Conclusions

On the strength of the results and trends observed in this work the following conclusions and

postulations are made;

- a) From the results obtained in this work it is concluded that the most viable option for multi-material corrosion inhibition in the studied multi-material combinations is the use of synergistic combinations of inhibitors comprised of rare-earth cations and azoles.
- b) That the mechanism of CFRP degradation under cathodic polarization is hinged on marked electrochemical activity at cathodic potentials that is observed to be independent of the bulk solution pH and most significant around $-250 \text{ mV}_{\text{SCE}}$.
- c) That the predominant cathodic electrochemical activity on CFRP surface under cathodic polarization is the 2-electron oxygen reduction process which is the favoured mechanism for oxygen reduction on carbon instead of the 4-electron process.
- d) That in contrast to the 4-electron process, the 2-electron oxygen reduction process on CFRP surface leads to the production of the hydroperoxyl radical (HO_2^-) which is able to interact with certain polymer bonds in the matrix and hence lead to epoxy degradation.
- e) That CFRP degradation under cathodic polarization presents predominantly as carbon fiber erosion and interfacial damage.
- f) That though measured success was achieved in the course of this work in suppressing cathodic processes on CFRP subjected to cathodic polarization, the use of inhibitors is considered a very viable approach. In this regard, it is postulated that by leveraging on carbon's well known adsorptive properties, an adsorption based inhibitor might be discovered that adsorbs strongly on the surface of the carbon fibres in CFRP while suppressing the electron transfer process(es) that are necessary for oxygen reduction to occur. An alternative approach can be the use of precipitation based inhibitors that can be triggered by the local increase in the pH near CFRP surface due to the onset of cathodic process to precipitate species onto the surfaces of the carbon fibers and bring about a decrease in the electrochemically active area.
- g) that the most viable strategy for combating multi-material corrosion in the studies system is the use of synergistic or at least additive inhibitor combinations rather than the use of single inhibitors.
- h) Multi-material corrosion inhibition of the Al - Cu - CFRP multi-material combination is possible using any of these five combination of inhibitors comprised of rare-earth metal compound in form of an acetate or nitrate and azoles; $(\text{Ce}(\text{NO}_3)_3 + 1,2,3\text{-triazole})$, $(\text{Ce}(\text{CH}_3\text{COO})_3 + \text{BTA})$, $(\text{Ce}(\text{NO}_3)_3 + \text{BTA})$, $(\text{Ce}(\text{CH}_3\text{COO})_3 + \text{BIA})$, and $(\text{Ce}(\text{NO}_3)_3 + \text{BIA})$.

- i) $(\text{La}(\text{NO}_3)_3 + \text{BTA})$ and $(\text{Ce}(\text{NO}_3)_3 + \text{BTA})$ are proposed as effective multi-material corrosion inhibitors for the Zn - Fe - CFRP multi-material combination.
- j) that the inhibition of multi-material corrosion is apparently easier for the Al - Cu - CFRP system than for the Zn - Fe - CFRP system as evidenced by the higher number of promising inhibitor combinations for the former.
- k) That synergistic effects were obtained with the use of inhibitor combinations comprised of rare-earth cations and azoles for the Al-Cu-CFRP multi-material galvanic systems. In this multi-material combination and with $\text{Ce}(\text{NO}_3)_3 + \text{BTA}$ inhibitor combination, synergistic parameters (s) of $\approx 1.67, 3.61, 2.90$ and 2.96 were obtained based on calculated inhibition efficiencies after 150,000 seconds immersion for Al - CFRP, Al - Cu, Cu - CFRP, and Al - Cu - CFRP, respectively. In the Zn - Fe - CFRP multi-material system synergistic inhibition effects were not observed across all its components (Zn - CFRP, Zn - Fe, Fe - CFRP, and Zn - Fe - CFRP) with any of the inhibitor combinations.
- l) The re-deposition of metal ions (of the cathodic metal in a couple) onto the anode(s) appear to exert some influence on the interaction of inhibitors with the anode surface and hence on the mechanism and inhibitive efficiencies of the inhibitors.
- m) The conjugate anion of the rare-earth metals salts influences the inhibition efficiencies of the rare earth cations with the effects dependent on the galvanic couple/system being studied.
- n) That the major difference in the mechanisms of multi-material corrosion of the Al - Cu - CFRP and Zn - Fe - CFRP multimaterial systems in absence of inhibitors is that whereas multi-material corrosion occurs in the Al - Cu - CFRP with the metallic copper surface covered by a layer of copper oxides and hydroxides in the high pH environment around it under the impressed cathodic polarization, the metallic cathode, iron, Zn - Fe - CFRP multimaterial systems in the is stripped of its naturally formed oxides on galvanic coupling with zinc so that cathodic activities occur on bare iron surface.
- o) That the presence of these oxides/hydroxides on the surface of copper galvanically coupled accounts for the wide difference in the mixed corrosion potential of galvanically coupled Al - Cu dual couple and Al - Cu - CFRP "galvanic triplet" with the mixed potential close to $\approx -650 \text{ mV}_{\text{SCE}}$ compared to $E_{\text{corr}} \approx -980$ to $-1100 \text{ mV}_{\text{SCE}}$ observed on aluminium in quiescent 50 mM NaCl solution, while in the Zn - Fe - CFRP multi-material system with an oxide-free metallic cathode (iron), the mixed corrosion potentials of galvanically coupled

Zn - Fe dual galvanic couple and Zn - Fe - CFRP "triplet" galvanic couples is consistently close to the E_{corr} of zinc $\approx -1000 \text{ mV}_{\text{SCE}}$ in same solution.

- p) That as a consequence of the major difference in the mechanisms of multi-material corrosion of the Al - Cu - CFRP and Zn - Fe - CFRP multi-material systems (expressed in (k) above), multi-material corrosion inhibition occurs in the Al - Cu - CFRP multi-material system with inhibitors interacting with the metallic cathode surface through a layer of oxides/hydroxides while interaction with the metallic cathode in the Zn - Fe - CFRP multi-material system occurs on a relatively oxide free surface.

8.2. Recommendations / Future Outlook

Based on the results obtained and inferences made from the results in this work, the following recommendations are advanced;

- (a) That further work should be carried out to confirm the postulated re-deposition of carbon onto CFRP surface under aqueous immersion conditions and/or cathodic polarization.
- (b) That further studies should be carried out on galvanic systems with the shortlisted multi-material corrosion inhibitors in the presence and absence of cations of the cathodic metal(s) to clearly identify the effect of these on the reported inhibitive effects, and provide a better understanding of the mechanism(s).
- (c) That since the tests employed in this work were done under quiescent conditions, further work be carried out under both oxygen deficient and oxygen enriched conditions to establish any changes in mechanism, and if the reported inhibitive effects are sustained under these conditions.
- (d) From results obtained in this work and observed trends it is recommended that in future work, the use of inhibitor combinations composed of more than one rare-earth cation be studied
- (e) That in future work the experimental approach employed in the present work be combined with modelling of galvanic corrosion in multi-material assemblies.
- (f) That the possibility of a time dependence of the multi-material corrosion mechanism(s) and the multi-material corrosion inhibition mechanism(s) be studied.
- (g) That a systematic study of the influence of inhibitor concentrations both as single inhibitors and in inhibitor combinations on their inhibitive effects in multi-material assemblies be incorporated in upcoming works.

- (h) That a detailed study of the influence of atmospheric conditions such as abundance and deficit of oxygen, nitrogen, carbon dioxide and other relevant atmospheric variables on multi-material corrosion inhibition, not considered in the present work be incorporated in succeeding works.
- (i) Having established the feasibility of multi-material corrosion inhibition with the use of inhibitor combinations, upcoming research efforts can be focused on the development of viable procedures for introducing inhibitors into coating systems without loss of efficacy.

References

1. Shaw, B. A., & Kelly, R. G. (2006). What is corrosion?. *Interface-Electrochemical Society*, 15(1), 24-27.
2. Cicek, V. (2013) Cost of Corrosion. in *Cathodic Protection: Industrial Solutions for Protecting Against Corrosion*, John Wiley & Sons, Inc. Hoboken, New Jersey, and Scrivener Publishing LLC, Salem, Massachusetts pp.127-130.
3. Biezma, M. V., & San Cristobal, J. R. (2005). Methodology to study cost of corrosion. *Corrosion engineering, science and technology*, 40(4), 344-352.
4. Uhlig, H. H. (1950). The Cost of Corrosion to The United States. *Corrosion*, 6(1), 29-33.
5. Kermani, M. B., & Harr, D. (2008, June). The impact of corrosion on oil and gas industry. In *Giornata di studio IGF S. Donato Milanese 1996*.
6. Hale, J. (2006). Boeing 787 from the ground up. *Aero*, 4, 17-24.
7. Marsh, G. (2007). Airbus takes on Boeing with reinforced plastic A350 XWB. *Reinforced plastics*, 51(11), 26-29.
8. Askeland, D. R., & Phulé, P. P. (2003). *The science and engineering of materials*.
9. Chung, D. (2012). *Carbon fiber composites*. Butterworth-Heinemann. pp.10.
10. Buchheit, R. G., Guan, H., Mahajanam, S., & Wong, F. (2003). Active corrosion protection and corrosion sensing in chromate-free organic coatings. *Progress in Organic Coatings*, 47(3), 174-182.
11. Lamaka S.V, Shchukin D.G., Andreeva D.V., Zheludkevich M.L., Mohwald H., Ferreira M.G.S., Sol-Gel /Polyelectrolyte Active Corrosion Protection System. *Advanced Functional Materials*. 18 (2008) 3137-3147.
12. Shchukin D.G., Lamaka S.V., Yasakau K.A., Zheludkevich M.L., Ferreira M.G.S., Mohwald H. Active Corrosion Coatings with Halloysite Containers. *Journal of Physical Chemistry C*, 112 (2008) 958-964.
13. Shchulin D.G., Mohwald H., Ferreira M.G.S., Zheludkevich M.L. Corrosion Inhibiting Pigment Comprising Nanoreservoirs of Corrosion Inhibitor. European Patent No: EP1832629, Publication Date: 12.09.2997, WO2007104457-A1, Publication Date: 20.09.2007 (2007).
14. Kumar, A., & Stephenson, L. D. (2002). Self Healing Coatings. In *CORROSION 2002*. NACE International.
15. Zheludkevich M.L., Shchukin G.G., Yasakau K.A., Mohwald H., Ferreira M.G.S. Anticorrosion Coatings with Self-healing Effect Based on Nanocontainers Impregnated with Corrosion Inhibitor. *Chemistry of Materials*. 19 (2007) 402-411
16. Sauvant-Moynot, V., Gonzalez, S., & Kittel, J. (2008). Self-healing coatings: An alternative route for anticorrosion protection. *Progress in Organic Coatings*, 63(3), 307-315.
17. Park, J. H., & Braun, P. V. (2010). Coaxial Electrospinning of Self-Healing Coatings. *Advanced materials*, 22(4), 496-499.
18. Galio A.F, Lamaka S.V., Zheludkevich M.L., Dick L.F., Muller I.L., Ferreira M.G.S. Evaluation of Corrosion Protection of Sol-Gel Coatings on AZ31B Magnesium Alloy. *Advanced Materials Forum IV*, 587-588 (2008) 390-394.
19. Musa, A. Y., Kadhum, A. A. H., Takriff, M. S., & Mohamad, A. B. (2011). Inhibition of galvanic corrosion by 4-amino-5-phenyl-4H-1, 2, 4-triazole-3-thiol. *International Journal of Surface Science and Engineering*, 5(2-3), 226-231.
20. Mustafa, C. M., & Shahinoor Islam Dulal, S. M. (1996). Molybdate and nitrite as corrosion inhibitors for copper-coupled steel in simulated cooling water. *Corrosion*, 52(1), 16-22.

21. Kallip, S., Bastos, A. C., Yasakau, K. A., Zheludkevich, M. L., & Ferreira, M. G. (2012). Synergistic corrosion inhibition on galvanically coupled metallic materials. *Electrochemistry Communications*, 20, 101-104.
22. Morcos, I., & Yeager, E. (1970). Kinetic studies of the oxygen—peroxide couple on pyrolytic graphite. *Electrochimica Acta*, 15(6), 953-975.
23. Taylor, R. J., & Humffray, A. A. (1975). Electrochemical studies on glassy carbon electrodes: III. Oxygen reduction in solutions of low pH (pH < 10). *Journal of Electroanalytical Chemistry and Interfacial Electrochemistry*, 64(1), 85-94.
24. Taylor, R. J., & Humffray, A. A. (1975). Electrochemical studies on glassy carbon electrodes: II. Oxygen reduction in solutions of high pH (pH > 10). *Journal of Electroanalytical Chemistry and Interfacial Electrochemistry*, 64(1), 63-84.
25. Yeager, E. (1984). Electrocatalysts for O₂ reduction. *Electrochimica Acta*, 29(11), 1527-1537.
26. Zhang, Z. W., Tryk, D. A., & Yeager, E. B. (1984). Effect of surface treatment of glassy carbon on O₂ reduction in alkaline solution. In *Proc. workshop on the electrochemistry of carbon*. The Electrochemical Society, Pennington, New Jersey (pp. 158-178).
27. Paliteiro, C., Hamnett, A., & Goodenough, J. B. (1987). The electroreduction of oxygen on pyrolytic graphite. *Journal of electroanalytical chemistry and interfacial electrochemistry*, 233(1), 147-159.
28. Hossain, M. S., Tryk, D., & Yeager, E. (1989). The electrochemistry of graphite and modified graphite surfaces: the reduction of O₂. *Electrochimica acta*, 34(12), 1733-1737.
29. Chu, X., & Kinoshita, K. (1997). Surface modification of carbons for enhanced electrochemical activity. *Materials Science and Engineering: B*, 49(1), 53-60.
30. Vaik, K., Schiffrin, D. J., & Tammeveski, K. (2004). Electrochemical reduction of oxygen on anodically pre-treated and chemically grafted glassy carbon electrodes in alkaline solutions. *Electrochemistry communications*, 6(1), 1-5.
31. Phil Hart. The Cost of Corrosion. The Oil Drum: Australia and New Zealand http://europe.theoil Drum.com/pdf/theoil Drum_5215.pdf accessed 03.09.2013.
32. Standard Definition of Terms Relating to corrosion and Corrosion Testing, ASTM Designation G15, 1983. Annual book of ASTM Standards. Vol. 3.02.
33. 2004 EUCAR RTD Priorities FO7 Doc. id: 041207 (2004) 1-12.
34. Suitable Production Technologies of Emission Reduced Light Weight Car Concepts: SuperLight-Car Materials, Processes & Manufacturing Program Board – September 24, 2008- EUCAR- Brussels, Belgium.
35. Berger, L., Lesemann, M., Sahr, C., Hart, S., & Taylor, R. (2009). SuperLIGHT-CAR-the Multi-Material Car Body. In 7th European LS-DYNA Conference.
36. Goede, M., Stehlin, M., Rafflenbeul, L., Kopp, G., & Beeh, E. (2009). Super Light Car—lightweight construction thanks to a multi-material design and function integration. *European Transport Research Review*, 1(1), 5-10.
37. Hirsch, J. (2011). Aluminium in innovative light-weight car design. *Materials Transactions*, 52(5), 818-824.
38. Hirsch, J. (2014). Recent development in aluminium for automotive applications. *Transactions of Nonferrous Metals Society of China*, 24(7), 1995-2002.
39. http://ec.europa.eu/research/innovation-union/ic2011/index_en.cfm?pg=project_details&project=superlight_car assessed 22.12.2014.,// <http://www.superlightcar.com/public/docs/SuperLight-Car%20poster%20FINAL.pdf> assessed 23.12.2014.

40. <http://www.nadiaproject.org> assessed 24.05.2015
41. United States Automotive Materials Partnership Report, Magnesium Vision 2020: A North American Automotive Strategic Vision for Magnesium, released 11.01.2006.
42. Airbus A380, Jane's All the World's Aircraft. (2005-2006) 241-246.
43. The New Technology Boeing 787 Dreamliner, Which Makes Extensive Use of Composite Materials, Promises to Revolutionize Commercial Air Travel. Aviation Week & Space Technology, March 14. (2005) S1-S31.,
44. Mecham. M. Evolution and Revolution Aviation Week & Space Technology, March 28. (2005) 46-47.
45. Lesemann M., Bröckerhoff M., and Urban P. "The Prospects of Multi-Material Design for a Compact-Class Front Section" ATZ autotechnology July, 2008 Vol. 8 pp. 16-20.
46. Marsh, G. (2006). Duelling with composites. Reinforced Plastics, 50(6), 18-23.
47. Brown, A. R. G., & Coomber, D. E. (1972). Behaviour of couples of aluminium and plastics reinforced with carbon fibre in aqueous salt solutions. British Corrosion Journal, 7(5), 232-235.
48. Johnston, G. R., Fritzen, J. S., & Weber, K. E. (1973). Galvanic Corrosion Effects Associated with Graphite Composite/Metal Joints (No. LR-26088). LOCKHEED-CALIFORNIA CO BURBANK.
49. Miller Jr, B. A. (1975). The galvanic corrosion of graphite epoxy composite materials coupled with alloys (No. GAE/MC/75D-8). AIR FORCE INST OF TECH WRIGHT-PATTERSON AFB OH SCHOOL OF ENGINEERING.
50. Miller, B. A., & Lee, S. G. (1976). The Effect of Graphite-Epoxy Composites on the Galvanic Corrosion of Aerospace Alloys (No. AFML-TR-76-121). AIR FORCE MATERIALS LAB WRIGHT-PATTERSON AFB OHIO.
51. Fischer, P. and DeLuccia, T.T. :(1974) Effects of Graphite-Epoxy Composite Materials on the Corrosion Behavior of Aircraft Alloys. Naval Air Development Center, paper presented at the Tri-Service Corrosion Conference, Wright-Patterson Air Force Base, Ohio, 1974.
52. Mueller, Y., Tognini, R., Mayer, J., Virtanen, S., (2007) , Anodized Titanium and Stainless Steel in Contact with CFRP: An Electrochemical Approach Considering Galvanic Corrosion., Journal of Biomedical Research. Part A, (82) 936-946.
53. Danford, M. D., & Higgins, R. H. (1983). Galvanic Coupling Between D6AC Steel, 6061-T6 Aluminum, Incone1 718, and Graphite-Epoxy Composite Material: Corrosion Occurrence and Prevention (No. M-427). NATIONAL AERONAUTICS AND SPACE ADMINISTRATION HUNTSVILLE AL GEORGE C MARSHALL SPACE FLIGHT CENTER.
54. Torres-Acosta, A. A. (2002). Galvanic corrosion of steel in contact with carbon-polymer composites. II: Experiments in concrete. Journal of Composites for Construction, 6(2), 116-122.
55. Ambat, R., & Møller, P. (2007). Corrosion investigation of material combinations in a mobile phone dome-key pad system. Corrosion Science, 49(7), 2866-2879.
56. Ambat, R., Jensen, S. G., & Møller, P. (2008). Corrosion reliability of electronic systems. ECS Transactions, 6(24), 17-28.
57. Yasakau, K. A., Zheludkevich, M. L., & Ferreira, M. G. (2008). Study of the corrosion mechanism and corrosion inhibition of 2024 aluminum alloy by SKPFM technique. In Materials Science Forum (Vol. 587, pp. 405-409). Trans Tech Publications.

58. Bastos, A. C., Lamaka, S. V., Zheludkevich, M. L., & Ferreira, M. G. (2008). Extending the Lifetime of Weldable Primers by Means of Chemical Inhibitors. In *Materials Science Forum* (Vol. 587, pp. 1003-1007). Trans Tech Publications.
59. Zheludkevich, M. L., Yasakau, K. A., Poznyak, S. K., & Ferreira, M. G. S. (2005). Triazole and thiazole derivatives as corrosion inhibitors for AA2024 aluminium alloy. *Corrosion Science*, 47(12), 3368-3383.
60. Cabral A.M, Trabelsi W., Serra F., Montemor M.F., Zheludkevich M.L., Ferreira M.G.S. The Corrosion Resistance of Hot dip galvanized Steel and AA2024-T3 Pre-treated with bis-[triethoxysilypropyl] tetrasulfide Solutions Doped with Ce(NO₃)₃. *Corrosion Science*, 48,(2006) 3740-3758.,
61. McMurray, H. N., Powell, S. M., & Worsley, D. A. (2001). Mechanistic changes in cut edge corrosion induced by variation of inhibitor pigmentation in organically coated galvanised steel. *British Corrosion Journal*, 36(1), 42-48.
62. Bastos, A. C., Karavai, O. V., Zheludkevich, M. L., Yasakau, K. A., & Ferreira, M. G. S. (2010). Localised measurements of pH and dissolved oxygen as complements to SVET in the investigation of corrosion at defects in coated aluminum alloy. *Electroanalysis*, 22(17-18), 2009-2016.
63. Yasakau K.A., Zheludkevich M.L., Lamaka S.V., Ferreira M.G.S. (2006) Mechanism of Corrosion Inhibition of AA2024 by Rare-earth Compounds. *Journal of Physical Chemistry B*, 110 pp.5515-5528.
64. Yasakau K.A., Zheludkevich M.L., Ferreira M.G.S. (2008) Lanthanide Salts as Corrosion Inhibitors for AA5083: Mechanism and Efficiency of Corrosion Inhibition. *Journal of the Electrochemical Society*, 155, pp.C169-177
65. Aramaki, K. (2002). Self-healing mechanism of an organosiloxane polymer film containing sodium silicate and cerium (III) nitrate for corrosion of scratched zinc surface in 0.5 M NaCl. *Corrosion Science*, 44(7), 1621-1632.
66. Trabelsi, W., Cecilio, P., Ferreira, M. G. S., & Montemor, M. F. (2005). Electrochemical assessment of the self-healing properties of Ce-doped silane solutions for the pre-treatment of galvanised steel substrates. *Progress in Organic Coatings*, 54(4), 276-284.
67. Muster, T.H., Hughes, A.E., Furman, S.A., Harvey, T., Sherman, N., Hardin, S., Corrigan, P., Lau, D., Scholes, F.H., White, P.A. and Glenn, M., (2009). A rapid screening multi-electrode method for the evaluation of corrosion inhibitors. *Electrochimica Acta*, 54(12), pp.3402-3411.
68. Kallip S. , Bastos A.C., Zheludkevich M.L., Ferreira, M.G.S. A multi-electrode cell for high-throughput SVET screening of corrosion inhibitors. *Corrosion Science* 52 (2010) 3146–3149.
69. ISO 8044-1986 Corrosion of metals and alloys -Terms and definitions.
70. IUPAC: 'Compendium of Chemical Terminology (The "Gold Book")' , 2006; <http://goldbook.iupac.org/C01351.html>, accessed 30.05.2015.
71. Roberge, P. R. (2008). *Corrosion engineering: principles and practice* (pp. 370-375). New York: McGraw-Hill.
72. Eshbach, O. W., Tapley, B. D., & Poston, T. R. (1990). *Eshbach's handbook of engineering fundamentals*. 4th Edition, John Wiley & Sons. pp.14-48 –14-50.
73. Bockris, J.O. & Khan, S.U.M, (1993). *Surface Electrochemistry*, Plenum Press, New York, pp. 319.
74. Scully, J. C. (1990) *The Fundamentals of Corrosion*, Pergamon Press, New York. pp. 143.

75. Aldykewicz, A. J., Isaacs, H. S., & Davenport, A. J. (1995). The Investigation of Cerium as a Cathodic Inhibitor for Aluminum-Copper Alloys. *Journal of the Electrochemical Society*, 142(10), 3342-3350.
76. Aldykewicz, A. J., Davenport, A. J., & Isaacs, H. S. (1996). Studies of the Formation of Cerium-Rich Protective Films Using X-Ray Absorption Near-Edge Spectroscopy and Rotating Disk Electrode Methods. *Journal of the Electrochemical Society*, 143(1), 147-154.
77. Pourbaix, M. (1974). *Atlas of Electrochemical Equilibria in Aqueous Solutions*. National Association of Corrosion Engineers, Houston, TX, USA.
78. Vargel, C. (2004). *Corrosion of Aluminium*. Elsevier.
79. Ref: 71, pp.74-76.
80. McCafferty, E. (2010). *Introduction to corrosion science*. Springer Science & Business Media. pp. 125.
81. Sukiman, N. L., Hughes, A. E., Thompson, G. E., Mol, J. M. C., Birbilis, N., Garcia, S. J., & Zhou, X. (2012). Durability and corrosion of aluminium and its alloys: overview, property space, techniques and developments. INTECH Open Access Publisher.
82. Wagner, C., & Traud, W. (1938). Concerning the evaluation of corrosion reactions by superposition of electrochemical partial reactions and concerning the potential formation on mixed electrodes. *Z. Electrochemical*, 44(391), 52.
83. Kimball, G. E., & Glassner, A. (1940). The Rate of Solution of Metals in Acids as a Function of Overvoltage II. The Solution of Cadmium in Sulfuric Acid. *The Journal of Chemical Physics*, 8(10), 820-827.
84. Petrocelli, J. V. (1950). The Electrochemical Behavior of Aluminum I. In Solutions of Cerium Sulfate in Sulfuric Acid. *Journal of The Electrochemical Society*, 97(1), 10-19.
85. Andersen, T. N., Ghandehari, M. H., & Eyring, H. (1975). A Limitation to the Mixed Potential Concept of Metal Corrosion Copper in Oxygenated Sulfuric Acid Solutions. *Journal of The Electrochemical Society*, 122(12), 1580-1585.
86. Davis, J. R. (Ed.). (2000). *Corrosion: Understanding the basics*. ASM International. pp.89.
87. Baboian, R. (1972). Investigations of Galvanically Induced Localized Corrosion. *Localized Corrosion-Cause of Metal Failure*, ASTM STP516, 145-163.
88. Baboian R. (1976) *Galvanic and Pitting Corrosion-Field and Laboratory Studies* ASTM Inc. pp.8.
89. Roberge, P. (2012). *Handbook of Corrosion Engineering*, 2nd Edition. McGraw Hill Professional.
90. Scully J.R. (2005) *Electrochemical Tests, In Corrosion Tests and Standards, Application and Interpretation*, 2nd edition, Baboian R.(ed). ASM International, Materials Park, OH, pp. 109.
91. ASTM G102-89 (2010). *Standard Practice for Calculation of Corrosion Rates and Related Information from Electrochemical Measurements*. American Society for Testing and Materials.
92. Zhang, X. G. (2013). *Corrosion and electrochemistry of zinc*. Springer Science & Business Media.
93. Fovet, Y., Pourreyron, L., & Gal, J. Y. (2000). Corrosion by galvanic coupling between carbon fiber posts and different alloys. *Dental materials*, 16(5), 364-373.
94. Torres-Acosta, A. A. (2002). Galvanic corrosion of steel in contact with carbon-polymer composites. I: Experiments in mortar. *Journal of Composites for Construction*, 6(2), 112-115.

95. Mansfeld, F., Hengstenberg, D. H., & Kenkel, J. V. (1974). Galvanic Corrosion of Al Alloys I. Effect of Dissimilar Metal. *Corrosion*, 30(10), 343-353.
96. Hatch, G. B. (1952). Inhibition of galvanic attack of steel with phosphate glasses. *Industrial & Engineering Chemistry*, 44(8), 1780-1786.
97. Mansfeld, F., & Parry, E. P. (1973). Galvanic corrosion of bare and coated Al alloys coupled to stainless steel 304 or Ti-6Al-4V. *Corrosion Science*, 13(8), 605-621.
98. Mansfeld, F. (1971). Area relationships in galvanic corrosion. *Corrosion*, 27(10), 436-442.
99. Mansfeld, F. and Parry, E.P., (1971) Galvanic corrosion test for EMP/EMI coatings on Al alloys. Technical Report NRSC, 2 August 1971.
100. Mansfeld, F., & Kenkel, J. V. (1975). Galvanic corrosion of Al alloys—III. The effect of area ratio. *Corrosion Science*, 15(4), 239-250
101. Ref.79, pp.370-375.
102. Mansfeld, F., and Gilman, S. (1970) The effect of several electrode and electrolyte additives on the corrosion and polarization behavior of the alkaline zinc electrode, 1. *Electrochem. Soc.* 117, 1328-1333.
103. Era, A., Takehara, Z., and Yoshizawa, S. (1968) Influence of impurities especially lead contained in manganese dioxide upon the self-discharge of the leclanche dry cell, *Electrochim. Acta* 13. 383-396.
104. Cachet, C., and Wiart, R.(1990) Zinc deposition and passivated hydrogen evolution in highly acidic sulphate electrolytes, depassivation by nickel impurities, *J. Appl. Electrochem.* 20. 1009-1014.
105. Wiart, R., Cachet, C., Bozhkov, C., and Rashkov, S. (1990) On the nature of the "induction period" during the electrowinning of zinc from nickel containing sulphate electrolytes, *J. Appl. Electrochem.* 20, 381-389.
106. Wang, Y., O'Keefe, T. J., and James, W. J. (1980) Voltammetric evaluation of zinc electrowinning solution containing nickel, *J. Electrochem. Soc.* 127,2589-2593.
107. Townsend, H. E. (1994) Continuous hot dip coatings, in *ASM Metals Handbook*, Vol. 5, pp. 339-348, American Society for Metals, Materials Park, Ohio, 1994.
108. Zhang, X. G. (1996). *Corrosion and electrochemistry of zinc*. Springer Science & Business Media. pp.197.
109. Akimov, G.W. (1955) *Electrode Potentials Corrosion* 11, 477t-486t.
110. Vujičić, V., & Lovreček, B. (1985). A Study of the Influence of pH on the Corrosion Rate of Aluminium. *Surface technology*, 25(1), 49-57.
111. Hart, R. K. (1957). The formation of films on aluminium immersed in water. *Transactions of the Faraday Society*, 53, 1020-1027.
112. Jayalakshmi, M., & Muralidharan, V. S. (1997). Inhibitors for aluminium corrosion in aqueous media. *Corrosion Reviews*, 15(3-4), 315-340.
113. Chatalov, A. Y. (1952). Effet du pH sur le comportement électrochimique des métaux et leur résistance à la corrosion. *Dokl. Akad. Naouk SSSR*, 86, 775-777.
114. Deltombe, E., & Pourbaix, M. (1958), The Electrochemical Behavior of Aluminum: Potential pH Diagram of the System Al-H₂O at 25°C. *Corrosion*, 14, 496-500.
115. Nguyen, T. H., & Foley, R. T. (1980). The chemical nature of aluminum corrosion III. The dissolution mechanism of aluminum oxide and aluminum powder in various electrolytes. *Journal of the Electrochemical Society*, 127(12), 2563-2566.
116. Abd-El-Nabey, B. A., Khalil, N., & Khamis, E. (1984). Alkaline corrosion of aluminium in water-organic solvent mixtures. *Surface Technology*, 22(4), 367-376.

117. Keddad, M., Kuntz, C., Takenouti, H., Schustert, D., & Zuili, D. (1997). Exfoliation corrosion of aluminium alloys examined by electrode impedance. *Electrochimica Acta*, 42(1), 87-97.
118. Foley, R. T. (1986). Localized corrosion of aluminum alloys-a review. *Corrosion*, 42(5), 277-288.
119. Kim, S. H., Erb, U., Aust, K. T., & Palumbo, G. (2001). Grain boundary character distribution and intergranular corrosion behavior in high purity aluminum. *Scripta materialia*, 44(5), 835-839.
120. Speidel, M. O. (1975). Stress corrosion cracking of aluminum alloys. *Metallurgical Transactions A*, 6(4), 631-651.
121. Fedrizzi, L., Deflorian, F., Rossi, S., & Bonora, P. L. (1998, August). Study of aluminium filiform corrosion by using electrochemical techniques. In *Materials science forum* (Vol. 289, pp. 485-498).
122. Moshier, W. C., Davis, G. D., & Ahearn, J. S. (1987). The corrosion and passivity of aluminum exposed to dilute sodium sulfate solutions. *Corrosion science*, 27(8), 785-801.
123. Nguyen, T. H., & Foley, R. T. (1982). The Chemical Nature of Aluminum Corrosion II. The Initial Dissolution Step. *Journal of the Electrochemical Society*, 129(1), 27-32.
124. Foley, R. T., & Nguyen, T. H. (1982). The chemical nature of aluminum corrosion v. energy transfer in aluminum dissolution. *Journal of the Electrochemical Society*, 129(3), 464-467.
125. Galvele, J. R. (1976). Transport processes and the mechanism of pitting of metals. *Journal of The Electrochemical Society*, 123(4), 464-474.
126. Bogar, F. D., & Foley, R. T. (1972). The influence of Chloride ion on the Pitting of Aluminum. *Journal of the Electrochemical Society*, 119(4), 462-464.
127. Berrada, S., Elboujdaini, M., & Ghali, E. (1992). Comportement electrochimique des alliages d'aluminium 2024 ET 7075 dans un milieu salin. *Journal of applied electrochemistry*, 22(11), 1065-1071.
128. Lepin, L., & Kadek, V. (1966). Conditions for disruption of the primary film during corrosion of aluminium in neutral solutions. *Corrosion Science*, 6(3), 177-181.
129. McKee, A. B., & Brown, R. H. (1947). Resistance of Aluminum to Corrosion in Solutions Containing Various Anions and Cations. *Corrosion*, 3(12), 595-612.
130. Khairy, E. M., & Hussein, M. K. (1957). The Static Electrode Potential Behavior Of Aluminum and the Anodic Behavior of the Pure Metal And Its Alloys in Chloride Media. *Corrosion*, 13(12), 27-32.
131. Lepin L. K. and VAIVADE .A. Y. (1963), *Latv. PSR Zinat. Acad. Vest. ser. khim.* No. 3, 297.
132. Vaivade A. Y. and Lepin L. K. (1963), *Latv. PSR Zinat. Acad. Vest. ser. khim.* No. 3, 363.
133. Lepin L. K., Oshis Z. F. and Baumanis A. K. (1963), *Latv. PSR Zinat. Acad. Vest. ser. khim.* No. 6, 683.
134. Lepin L. K. (1954), *Dokl. Acad. Nauk. SSSR* 99, 117.
135. Macdonald, D. D., Real, S., Smedley, S. I., & Urquidi-Macdonald, M. (1988). Evaluation of Alloy Anodes for Aluminum-Air Batteries IV. Electrochemical Impedance Analysis of Pure Aluminum in at 25° C. *Journal of The Electrochemical Society*, 135(10), 2410-2414.
136. Pyun, S. I., & Moon, S. M. (2000). Corrosion mechanism of pure aluminium in aqueous alkaline solution. *Journal of Solid State Electrochemistry*, 4(5), 267-272.
137. Adhikari, S., & Hebert, K. R. (2008a). Factors controlling the time evolution of the corrosion potential of aluminum in alkaline solutions. *Corrosion Science*, 50(5), 1414-1421.

138. Adhikari, S., & Hebert, K. R. (2008b). Participation of aluminum hydride in the anodic dissolution of aluminum in alkaline solutions. *Journal of The Electrochemical Society*, 155(5), C189-C195.
139. Adhikari, Saikat, Jinju Lee, and Kurt R. Hebert. "Formation of aluminum hydride during alkaline dissolution of aluminum." *Journal of The Electrochemical Society* 155, no. 1 (2008): C16-C21.
140. Adhikari, S., Ai, J., Hebert, K. R., Ho, K. M., & Wang, C. Z. (2010). Hydrogen in aluminum during alkaline corrosion. *Electrochimica Acta*, 55(19), 5326-5331.
141. Zhang, J., Klasky, M., & Letellier, B. C. (2009). The aluminum chemistry and corrosion in alkaline solutions. *Journal of Nuclear Materials*, 384(2), 175-189.
142. Streicher, M. A. (1949). The dissolution of aluminum in sodium hydroxide solutions. II. *Journal of The Electrochemical Society*, 96(3), 170-194.
143. Muylder J.V., Zoubov N. and Pourbaix M. (1962), *Rapp. Tech. 101*, (Centre Belge D'etude de la corrosion (CEBELCOR), Bruxelles)
144. Feitknecht W., and Schultze W. (1955), *Revue de Metallurgie*, Vol. 52, p. 327.
145. Kato, C., Ateya, B. G., Castle, J. E., & Pickering, H. W. (1980). On the Mechanism of Corrosion of Cu-9.4 Ni-1.7 Fe Alloy in Air Saturated Aqueous NaCl Solution I. Kinetic Investigations. *Journal of the Electrochemical Society*, 127(9), 1890-1896.
146. Kato, C., & Pickering, H. W. (1984). A Rotating Disk Study of the Corrosion Behavior of Cu-9.4 Ni-1.7 Fe Alloy in Air-Saturated Aqueous NaCl Solution. *Journal of the Electrochemical Society*, 131(6), 1219-1224.
147. Drogowska, M., Brossard, L., & Menard, H. (1987). Anodic Copper Dissolution in the Presence of Cl⁻ Ions at pH 12. *Corrosion*, 43(9), 549-552.25.
148. King, F. (2010). Critical review of the literature on the corrosion of copper by water. Svensk Kärnbränslehantering AB, Swedish Nuclear Fuel and Waste Management Company.
149. Hurlen, T. (1961). Electrochemical behavior of copper in acid chloride solution. *Acta Chemica Scandinavica*, 15, 1231-1238.
150. Bacarella, A. L., & Griess, J. C. (1973). The anodic dissolution of copper in flowing sodium chloride solutions between 25 and 175°C. *Journal of the Electrochemical Society*, 120(4), 459-465.
151. Braun, M., & Nobe, K. (1979). Electrodeposition kinetics of copper in acidic chloride solutions. *Journal of the Electrochemical Society*, 126(10), 1666-1671.
152. Lee, H. P., & Nobe, K. (1986). Kinetics and mechanisms of Cu electrodeposition in chloride media. *Journal of the Electrochemical Society*, 133(10), 2035-2043.
153. Crousier, J., Pardessus, L., & Crousier, J. P. (1988). Voltammetry study of copper in chloride solution. *Electrochimica acta*, 33(8), 1039-1042.
154. Pearlstein, A. J., Lee, H. P., & Nobe, K. (1985). Film formation and current oscillations in the electrodeposition of copper in acidic chloride media II. Mathematical model. *Journal of The Electrochemical Society*, 132(9), 2159-2165.
155. Deslouis, C., Tribollet, B., Mengoli, G., & Musiani, M. M. (1988a). Electrochemical behaviour of copper in neutral aerated chloride solution. I. Steady-state investigation. *Journal of applied electrochemistry*, 18(3), 374-383.
156. Deslouis, C., Tribollet, B., Mengoli, G., & Musiani, M. M. (1988b). Electrochemical behaviour of copper in neutral aerated chloride solution. II. Impedance investigation. *Journal of applied electrochemistry*, 18(3), 384-393.

157. Deslouis, C., Mattos, O. R., Musiani, M. M., & Tribollet, B. (1993). Comments on mechanisms of copper electro-dissolution in chloride media. *Electrochimica acta*, 38(18), 2781-2783.
158. Starosvetsky, D., Khaselev, O., Auinat, M., & Ein-Eli, Y. (2006). Initiation of copper dissolution in sodium chloride electrolytes. *Electrochimica acta*, 51(26), 5660-5668.
159. Moreau, A. (1981a.) Etude du mecanisme d'oxydo-reduction du cuivre dans les solutions chlorurees acides-I. Systeme Cu-. *Electrochimica Acta* 26, 497-504.
160. Moreau, A. (1981b.) Etude du mecanisme d'oxydo-reduction du cuivre dans les solutions chlorurees acides-II. Systemes Cu-CuCl- et Cu-Cu₂(OH)₃Cl-CuCl+ Cu²⁺. *Electrochimica Acta* 26, 1609-1616.
161. Millet, B., Fiaud, C., Hinnen, C., & Sutter, E. M. M. (1995). A correlation between electrochemical behaviour, composition and semiconducting properties of naturally grown oxide films on copper. *Corrosion science*, 37(12), 1903-1918.
162. King F, Lilja C, Pedersen K, Pikänen P, Vähänen M, (2010) An update of the state-of-the-art report on the corrosion of copper under expected conditions in a deep geologic repository. SKB TR-10-67, Svensk Kärnbränslehantering AB.
163. Christina Lilja, (2013) Influence of high chloride concentration on copper corrosion. SKB Memo <http://www.skb.se/9999c2d7-c13b-4345-bb1c-9595a4b3d7c7.fodoc> accessed 07.05.2015.
164. Lal, H., & Thirsk, H. R. (1953). 538. The anodic behaviour of copper in neutral and alkaline chloride solutions. *Journal of the Chemical Society (Resumed)*, 2638-2644.
165. Bjorndahl, W. D., & Nobe, K. (1984). Copper corrosion in chloride media. Effect of oxygen. *Corrosion*, 40(2), 82-87.
166. Dhar, H. P., White, R. E., Burnell, G., Cornwell, L. R., Griffin, R. B., & Darby, R. (1985). Corrosion of Cu and Cu-Ni alloys in 0.5 M NaCl and in synthetic seawater. *Corrosion*, 41(6), 317-323.
167. De Sanchez, S. R., & Schiffrin, D. J. (1982). The flow corrosion mechanism of copper base alloys in sea water in the presence of sulphide contamination. *Corrosion Science*, 22(6), 585-607.
168. Wood, R. J. K., Hutton, S. P., & Schiffrin, D. J. (1990). Mass transfer effects of non-cavitating seawater on the corrosion of Cu and 70Cu-30Ni. *Corrosion Science*, 30(12), 1177-1201.
169. Balakrishnan, K., & Venkatesan, V. K. (1979). Cathodic reduction of oxygen on copper and brass. *Electrochimica Acta*, 24(2), 131-138.
170. Tourky, A. R., & El Wakkad, S. E. S. (1948). 147. Studies on some metal electrodes. Part II. The behaviour of the copper electrode in dilute copper sulphate solutions. *Journal of the Chemical Society (Resumed)*, 749-752.
171. Feng, Y., Teo, W. K., Siow, K. S., Tan, K. L., & Hsieh, A. K. (1996). The corrosion behaviour of copper in neutral tap water. Part I: Corrosion mechanisms. *Corrosion Science*, 38(3), 369-385.
172. Tromans, D., & Sun, R. H. (1992). Anodic behavior of copper in weakly alkaline solutions. *Journal of the Electrochemical Society*, 139(7), 1945-1951.
173. Tromans, D., & Sun, R. H. (1991). Anodic polarization behavior of copper in aqueous chloride/benzotriazole solutions. *Journal of the Electrochemical Society*, 138(11), 3235-3244.

174. Otmačić, H., Telegdi, J., Papp, K., & Stupnišek-Lisac, E. (2004). Protective properties of an inhibitor layer formed on copper in neutral chloride solution. *Journal of applied electrochemistry*, 34(5), 545-550.
175. De Chialvo, M. G., Marchiano, S. L., & Arvia, A. J. (1984). The mechanism of oxidation of copper in alkaline solutions. *Journal of applied electrochemistry*, 14(2), 165-175.
176. Becerra, J. G., Salvarezza, R. C., & Arvia, A. J. (1988). The influence of slow Cu(OH)₂ phase formation on the electrochemical behaviour of copper in alkaline solutions. *Electrochimica acta*, 33(5), 613-621.
177. Burke, L. D., & Ryan, T. G. (1990). The participation of interfacial hydrous oxide species in some anodic reactions at copper electrodes in base. *Journal of the Electrochemical Society*, 137(5), 1358-1364.
178. Blundy, R. G., & Pryor, M. J. (1972). The potential dependence of reaction product composition on copper-nickel alloys. *Corrosion Science*, 12(1), 65-75.
179. Kato, C., Castle, J. E., Ateya, B. G., & Pickering, H. W. (1980). On the Mechanism of Corrosion of Cu-9.4 Ni-1.7 Fe Alloy in Air Saturated Aqueous NaCl Solution II. Composition of the Protective Surface Layer. *Journal of the Electrochemical Society*, 127(9), 1897-1903.
180. King, F., Quinn, M. J., & Litke, C. D. (1995). Oxygen reduction on copper in neutral NaCl solution. *Journal of Electroanalytical Chemistry*, 385(1), 45-55.
181. Brisard, G., Bertrand, N., Ross, P. N., & Marković, N. M. (2000). Oxygen reduction and hydrogen evolution–oxidation reactions on Cu (hkl) surfaces. *Journal of Electroanalytical Chemistry*, 480(1), 219-224.
182. Jiang, T., & Brisard, G. M. (2007). Determination of the kinetic parameters of oxygen reduction on copper using a rotating ring single crystal disk assembly (RRD Cu (h k l) E). *Electrochimica acta*, 52(13), 4487-4496.
183. Tromans, D., & Silva, J. C. (1997). Anodic behavior of copper in chloride/tolytriazole and chloride/benzotriazole solutions. *Corrosion*, 53(1), 16-25.
184. Miller, B. (1969). Split-ring disk study of the anodic processes at a copper electrode in alkaline solution. *Journal of the Electrochemical Society*, 116(12), 1675-1680.
185. Ambrose, J., Barradas, R. G., & Shoesmith, D. W. (1973). Investigations of copper in aqueous alkaline solutions by cyclic voltammetry. *Journal of Electroanalytical Chemistry and Interfacial Electrochemistry*, 47(1), 47-64.
186. Ashworth, Y., & Fairhurst, D. (1977). The Anodic Formation of Cu₂ O in Alkaline Solutions. *Journal of The Electrochemical Society*, 124(4), 506-517.
187. Wilhelm, S. M., Tanizawa, Y., Liu, C. Y., & Hackerman, N. (1982). A photo-electrochemical investigation of semiconducting oxide films on copper. *Corrosion Science*, 22(8), 791-805.
188. De Chialvo, M. G., Zerbino, J. O., Marchiano, S. L., & Arvia, A. J. (1986). Correlation of electrochemical and ellipsometric data in relation to the kinetics and mechanism of Cu₂O electroformation in alkaline solutions. *Journal of Applied Electrochemistry*, 16(4), 517-526.
189. Droog, J. M., Alderliesten, C. A., Alderliesten, P. T., & Bootsma, G. A. (1980). Initial stages of anodic oxidation of polycrystalline copper electrodes in alkaline solution. *Journal of Electroanalytical Chemistry and Interfacial Electrochemistry*, 111(1), 61-70.
190. Burke, L. D., Ahern, M. J. G., & Ryan, T. G. (1990). An investigation of the anodic behavior of copper and its anodically produced oxides in aqueous solutions of high pH. *Journal of the Electrochemical Society*, 137(2), 553-561.
191. Zaafarany, I., & Boller, H. (2009). Electrochemical behavior of copper electrode in sodium hydroxide solutions. *Current World Environment*, 4(2), 8.

192. Lohrengel, M. M., Schultze, J. W., Speckmann, H. D., & Strehblow, H. H. (1987). Growth, corrosion and capacity of copper oxide films investigated by pulse techniques. *Electrochimica acta*, 32(5), 733-742.
193. Antonijevic, M. M., Alagic, S. C., Petrovic, M. B., Radovanovic, M. B., & Stamenkovic, A. T. (2009). The influence of pH on electrochemical behavior of copper in presence of chloride ions. *International Journal of Electrochemical Science*, 4, 516-524.
194. Chin, R. J., & Nobe, K. (1972). Electrodeposition kinetics of iron in chloride solutions III. Acidic solutions. *Journal of the Electrochemical Society*, 119(11), 1457-1461.
195. Todt, F., Ed. (1961). *Korrosion und Korrosionsschutz (Corrosion and corrosion protection)*, 2nd ed., de Gruyter, Berlin, pp. 1422.
196. Forrest, H. O., Roetheli, B. E., & Brown, R. H. (1931). Products of Corrosion of Steel Factors Determining Their Composition and Its Influence on Rate of Corrosion in Oxygenated Water. *Industrial & Engineering Chemistry*, 23(6), 650-653.
197. Bockris, J. M., Drazic, D., & Despic, A. R. (1961). The electrode kinetics of the deposition and dissolution of iron. *Electrochimica Acta*, 4(2), 325-361.
198. Kesavan, S., Mozhi, T. A., & Wilde, B. E. (1989). Technical Note: Potential-pH Diagrams for the Fe-Cl-H₂O System at 25 to 150°C. *Corrosion*, 45(3), 213-215.
199. Stratmann, M., & Müller, J. (1994). The mechanism of the oxygen reduction on rust-covered metal substrates. *Corrosion Science*, 36(2), 327-359.
200. Craig, B. D. (1991) *Fundamental Aspects of Corrosion Films in Corrosion Science*, Plenum Press, New York.
201. Jovancicevic, V., & Bockris, J. M. (1986). The mechanism of oxygen reduction on iron in neutral solutions. *Journal of The Electrochemical Society*, 133(9), 1797-1807.
202. You, D., Pebere, N., & Dabosi, F. (1993). An investigation of the corrosion of pure iron by electrochemical techniques and in situ observations. *Corrosion science*, 34(1), 5-15.
203. Bonnel, A., Dabosi, F., Deslouis, C., Duprat, M., Keddou, M., & Tribollet, B. (1983). Corrosion study of a carbon steel in neutral chloride solutions by impedance techniques. *Journal of the Electrochemical Society*, 130(4), 753-761.
204. Duprat, M., Bui, N., & Dabosi, F. (1978). Sur le choix d'un critère de détermination de la vitesse de corrosion d'un acier au carbone dans une solution à 3% de chlorure de sodium aérée et agitée. *Journal of Applied Electrochemistry*, 8(5), 455-465.
205. Shepherd, C. M., & Schuldiner, S. (1968). Potentiostatic Current-Potential Measurements on Iron and Platinum Electrodes in High-Purity Closed Alkaline Systems. *Journal of The Electrochemical Society*, 115(11), 1124-1130.
206. Asakura, S., & Nobe, K. (1971). Electrodeposition Kinetics of Iron in Chloride Solutions Part II. Alkaline Solutions. *Journal of The Electrochemical Society*, 118(1), 19-22.
207. Schragar, B. (1929) Das amphotere Eisenhydroxid. *Chem. News* 138 pp.354.
208. Kabanov, B., Burstein, R., & Frumkin, A. (1947). Kinetics of electrode processes on the iron electrode. *Discussions of the Faraday Society*, 1, 259-269.
209. Guzman, R. S., Vilche, J. R., & Arvia, A. J. (1979). The potentiodynamic behaviour of iron in alkaline solutions. *Electrochimica Acta*, 24(4), 395-403.
210. Zou, J. Y., & Chin, D. T. (1988). Anodic behaviour of carbon steel in concentrated NaOH solutions. *Electrochimica Acta*, 33(4), 477-485.
211. Maja, M., Penazzi, N., Fratesi, R., and Roventi, G. (1982) Zinc electrocrystallization from impurity-containing sulfate baths, *J. Electrochem. Soc.* 129, 2695-2700.

212. Brodd, R. J., and Leger, V. E. (1976) Zinc, in Encyclopedia of Electrochemistry of the Elements, Vol. V, A. 1. Bard (ed.), pp. 2-60, Marcel Dekker, New York, 1976.
213. Graedel, T. E. (1989) Corrosion mechanisms for zinc exposed to the atmosphere. 1. Electrochem. Soc. 136, 193-203.
214. Uhlig, H. H., and Revie, R. W. (1985) Corrosion and Corrosion Control-An Introduction to Corrosion Science and Engineering, 3rd ed., John Wiley & Sons, New York.
215. Delahay, P., Pourbaix, M., and Van Rysselberghe, P. (1951) Potential-pH diagram of zinc and its applications to the study of zinc corrosion. J. Electrochem. Soc. 98, 101- 105.
216. Thomas, S., Birbilis, N., Venkatraman, M. S., & Cole, I. S. (2012). Corrosion of zinc as a function of pH. Corrosion, The Journal of Science and Engineering, 68(1), 015009-1 — 015009-9.
217. Belisle, S., and DuFresne, R. (1986). Corrosion resistance of ZA alloys. Int. Symp. Zinc-Aluminium Casting Alloys, Toronto, Canadian Institute of Mining and Metallurgy, Montreal, pp. 109-126.
218. GAV (1967). (Cost analysis for galvanizing of fabricated parts.) Translated by ZDA, London.
219. Porter, F. C. (1994). Corrosion resistance of zinc and zinc alloys. CRC Press. pp. 270-271.
220. Feitknecht, W. (1955) Die festen Korrosionsprodukte als korrosionslenkende Faktoren (Influence of adhering corrosion products on corrosion behavior). Werkst. Korros. 6, 15-26, (in German).
221. Roetheli, B. E., Cox, G. L., and Littreal, W. B. (1932) Effect of pH on the corrosion products and corrosion rate of zinc in oxygenated aqueous solutions, Met. Alloys 3(3), 73-76.
222. Baugh, L. M. (1979). Corrosion and polarization characteristics of zinc in neutral—acid media—I. Pure zinc in solutions of various sodium salts. Electrochimica Acta, 24(6), 657-667.
223. Bota, K. G., and Williams, L. F. G. (1977) Rotating disc electrode studies of zinc corrosion, J. Electroanal. Chem. 77.
224. Ref. 108, pp.179.
225. Macias. A and Andrade. C. (1987) Corrosion of galvanized steel reinforcements in alkaline solutions. Part II. SEM study and identification of corrosion products, Br. Corros. J. 22. 129.
226. Lorking. K. E (1967) The corrosion of zinc, Department of Supply, Australian Defence Scientific Service, Metallurgy Report No. 67, Melbourne, Australia, May 1967.
227. Mokaddem, M., Volovitch, P., & Ogle, K. (2010). The anodic dissolution of zinc and zinc alloys in alkaline solution. I. Oxide formation on electrogalvanized steel. Electrochimica Acta, 55(27), 7867-7875.
228. Baugh, L. M., and Lee. J. A. (1973) Differential capacitance of polycrystalline zinc. Part I. Effect of pH and ammonium ions, Electroana/. Chem. Interfacial Electrochem. 48,55-61.
229. TrabANELLI, G., Zucchi, F., Brunoro, G., & Gilli, G. (1975). Characterization of the corrosion or anodic oxidation products on zinc. Electrodeposition and Surface Treatment, 3(2), 129-138.
230. Kannangara, D. C. W., and Conway, B. E.: Zinc oxidation and redeposition processes in aqueous alkali and carbonate solutions, 1. Electrochem. Soc. 134,894-918,1987.
231. Batrakov, Y Y, Bogdanov, N. Y, and Kocherov, A. V. (1984) The application of alternating current method for adsorption and corrosion measurement on iron and zinc, Proceedings of the International Congress on Metallic Corrosion, Toronto, Ontario, June 3-7,1984, Vol. I, pp. 287-290.

232. Caswell, P., Hampson, N. A., and Larkin, D. (1969) The differential capacitance of zinc in aqueous solution—a further note, *J. Electroanal. Chem.* 20, 335-338.
233. Fedrizzi, L., Ciaghi, L., Bonora, P. L., Fratesi, R., and Roventi, G. (1992) Corrosion behaviour of electrogalvanized steel in sodium chloride and ammonium sulphate solutions, a study by E.I.S. *J. Appl. Electrochem.* 22, 247-254.
234. Ref. 108, pp.27.
235. Bockris, J. O. M., Nagy, Z., and Danjanovic, A. (1972) On the deposition and dissolution of zinc in alkaline solutions, *J. Electrochem. Soc.* 119, 285-295.
236. Cachet, C., Stroder, U., and Wiart, R. (1982) The kinetics of zinc electrode in alkaline zincate electrolytes, *Electrochim. Acta* 27, 903-908.
237. Armstrong, R. D., & Bell, M. F. (1974). The active dissolution of zinc in alkaline solution. *Journal of Electroanalytical Chemistry and Interfacial Electrochemistry*, 55(2), 201-211.
238. Mouanga, M., Berçot, P., & Rauch, J. Y. (2010). Comparison of corrosion behaviour of zinc in NaCl and in NaOH solutions. Part I: Corrosion layer characterization. *Corrosion Science*, 52(12), 3984-3992.
239. Qu, Q., Li, L., Bai, W., Yan, C., & Cao, C. N. (2005). Effects of NaCl and NH₄Cl on the initial atmospheric corrosion of zinc. *Corrosion science*, 47(11), 2832-2840.
240. Kalinauskas, P., Valsiūnas, I., & Juzeliūnas, E. (2001). Zinc photo-corrosion in neutral solutions. *Corrosion science*, 43(11), 2083-2092.
241. Chen, Z. Y., Persson, D., & Leygraf, C. (2008). Initial NaCl-particle induced atmospheric corrosion of zinc—Effect of CO₂ and SO₂. *Corrosion Science*, 50(1), 111-123.
242. Youssef, K. M., Koch, C. C., & Fedkiw, P. S. (2004). Improved corrosion behavior of nanocrystalline zinc produced by pulse-current electrodeposition. *Corrosion Science*, 46(1), 51-64.
243. Sloan, F. E., & Talbot, J. B. (1992a). Corrosion of graphite-fiber-reinforced composites I—galvanic coupling damage. *Corrosion*, 48(10), 830-838.
244. McCreery, R. L. (2008). Advanced carbon electrode materials for molecular electrochemistry. *Chem. Rev.* 108(7), 2646-2687.
245. Boehm, H. P., Diehl, E., Heck, W., & Sappok, R. (1964). Surface oxides of carbon. *Angewandte Chemie International Edition in English*, 3(10), 669-677.
246. Boehm, H. P. (1994). Some aspects of the surface chemistry of carbon blacks and other carbons. *Carbon*, 32(5), 759-769.
247. Moreno-Castilla, C., Lopez-Ramon, M. V., & Carrasco-Marin, F. (2000). Changes in surface chemistry of activated carbons by wet oxidation. *Carbon*, 38(14), 1995-2001.
248. Figueiredo, J. L., & Pereira, M. F. R. (2010). The role of surface chemistry in catalysis with carbons. *Catalysis Today*, 150(1), 2-7.
249. Bismarck, A., Wuertz, C., & Springer, J. (1999). Basic surface oxides on carbon fibers. *Carbon*, 37(7), 1019-1027.
250. Barton, S. S., Boulton, G. L., & Harrison, B. H. (1972). Surface studies on graphite: Acidic surface oxides. *Carbon*, 10(4), 395-400.
251. Dastgheib, S. A., Karanfil, T., & Cheng, W. (2004). Tailoring activated carbons for enhanced removal of natural organic matter from natural waters. *Carbon*, 42(3), 547-557.
252. Evans, M. J. B., Halliop, E., & MacDonald, J. A. F. (1999). The production of chemically-activated carbon. *Carbon*, 37(2), 269-274. 24-27

253. Shen, W., Li, Z., & Liu, Y. (2008). Surface chemical functional groups modification of porous carbon. *Recent Patents on Chemical Engineering*, 1(1), 27-40.
254. Figueiredo, J. L., Pereira, M. F. R., Freitas, M. M. A., & Orfao, J. J. M. (1999). Modification of the surface chemistry of activated carbons. *Carbon*, 37(9), 1379-1389.
255. Jannakoudakis, A. D., Jannakoudakis, P. D., Theodoridou, E., & Besenhard, J. O. (1990). Electrochemical oxidation of carbon fibres in aqueous solutions and analysis of the surface oxides. *Journal of Applied Electrochemistry*, 20(4), 619-624.
256. Boehm, H. P. (1966). Functional groups on the surfaces of solids. *Angewandte Chemie International Edition in English*, 5(6), 533-544.
257. Besenhard, J. O., & Fritz, H. P. (1983). The electrochemistry of black carbons. *Angewandte Chemie International Edition in English*, 22(12), 950-975.
258. Besenhard, J.O., Jakob, J., Krebber, U., Moeller, P., Sauter, R.F., Kurtze, A., Kanani, N., Meyer, H., Hoerber, J.K.H. and Jannakoudakis, A.D., (1989). Anodische Oberflächen- und Volumenoxidation graphitischer Materialien in neutralen und alkalischen wäßrigen Lösungen/Anodic Surface and Bulk Oxidation of Graphitic Materials in Neutral and Basic Aqueous Solutions. *Zeitschrift für Naturforschung B*, 44(7), pp.729-735.
259. Zuleta, M., Björnbom, P., & Lundblad, A. (2006). Characterization of the electrochemical and ion-transport properties of a nanoporous carbon at negative polarization by the single-particle method. *Journal of the Electrochemical Society*, 153(1), A48-A57.
260. Ruiz, V., Blanco, C., Raymundo-Piñero, E., Khomenko, V., Béguin, F., & Santamaría, R. (2007). Effects of thermal treatment of activated carbon on the electrochemical behaviour in supercapacitors. *Electrochimica Acta*, 52(15), 4969-4973.
261. Ruiz, V., Malmberg, H., Blanco, C., Lundblad, A., Björnbom, P., & Santamaría, R. (2008). A study of Faradaic phenomena in activated carbon by means of macroelectrodes and single particle electrodes. *Journal of Electroanalytical Chemistry*, 618(1), 33-38.
262. Béguin, F., Kierzek, K., Friebe, M., Jankowska, A., Machnikowski, J., Jurewicz, K., & Frackowiak, E. (2006). Effect of various porous nanotextures on the reversible electrochemical sorption of hydrogen in activated carbons. *Electrochimica acta*, 51(11), 2161-2167.
263. Yeager E. J., Molla J. A., and Gupta S. (1984), in "The Electrochemistry of Carbon," S. Sarangapani, J. R. Akridge, and B. Schumm, Editors, PV 84-5, p. 123, The Electrochemical Society Softbound Proceedings Series, Pennington, NJ.
264. Kalnin I., Carbon '76, Int. Carbon Conf., 94 (1976).
265. Kalnin I. (1979), Ext. Abstr. Program-Bienn. Conf. Carbon, 14, 218.
266. Weinberg N. (1984), in "The Electrochemistry of Carbon," S. Sarangapani, J. R. Akridge, and B. Schumm, Editors, PV 84-5, p. 463, The Electrochemical Society Softbound Proceedings Series, Pennington, NJ.
267. Allred, C. D., & McCreery, R. L. (1992). Adsorption of catechols on fractured glassy carbon electrode surfaces. *Analytical Chemistry*, 64(4), 444-448.
268. Chen, P., & McCreery, R. L. (1996). Control of electron transfer kinetics at glassy carbon electrodes by specific surface modification. *Analytical Chemistry*, 68(22), 3958-3965.
269. Chen, P., Fryling, M. A., & McCreery, R. L. (1995). Electron transfer kinetics at modified carbon electrode surfaces: the role of specific surface sites. *Analytical Chemistry*, 67(18), 3115-3122.
270. Kelly, R. S., Weiss, D. J., Chong, S. H., & Kuwana, T. (1999). Charge-selective electrochemistry at high-surface-area carbon fibers. *Analytical Chemistry*, 71(2), 413-418.

271. Kelly, R. S., Coleman, B. D., Huang, T., Inkaew, P., & Kuwana, T. (2002). Electrochemical flow injection analysis study of ion partitioning at high surface area carbon fiber electrodes. *Analytical chemistry*, 74(24), 6364-6369.
272. Weiss, D. J., Kelly, R. S., Cumararatunge, M., & Kuwana, T. (1999). Computer simulation of charge-selective electrochemistry of catechols at high-surface-area carbon fibers. *Analytical chemistry*, 71(17), 3712-3720.
273. Gotch, A. J., Kelly, R. S., & Kuwana, T. (2003). Characterization and modeling of the nonfaradaic response of ultrahigh surface area carbon fibers by electrochemical flow injection analysis. *The Journal of Physical Chemistry B*, 107(4), 935-941.
274. Kinoshita K., Chu X. (1996), Carbon for supercapacitors, in: F. Delnick, M. Tomkiewicz (eds.), *Proc. Symp. on Electrochemical Capacitors*, vol. 95-29, The Electrochemical Society, Pennington, NJ, 1996, pp.171.
275. Randin, J. P., & Yeager, E. (1971). Differential capacitance study of stress-annealed pyrolytic graphite electrodes. *Journal of the Electrochemical Society*, 118(5), 711-714.
276. Maldonado, S., & Stevenson, K. J. (2005). Influence of nitrogen doping on oxygen reduction electrocatalysis at carbon nanofiber electrodes. *The Journal of Physical Chemistry B*, 109(10), 4707-4716.
277. Maldonado, S., & Stevenson, K. J. (2004). Direct preparation of carbon nanofiber electrodes via pyrolysis of iron (II) phthalocyanine: electrocatalytic aspects for oxygen reduction. *The Journal of Physical Chemistry B*, 108(31), 11375-11383
278. Vijayaraghavan, G., & Stevenson, K. J. (2007). Synergistic assembly of dendrimer-templated platinum catalysts on nitrogen-doped carbon nanotube electrodes for oxygen reduction. *Langmuir*, 23(10), 5279-5282.
279. Fischer, P., & Heitbaum, J. (1980). Mechanistic aspects of cathodic oxygen reduction. *Journal of Electroanalytical Chemistry and Interfacial Electrochemistry*, 112(2), 231-238.
280. Kinoshita, K. (1988). *Carbon: electrochemical and physicochemical properties.*; John Wiley and Sons: New York, pp. 360-372.
281. Mrha, J. (1967). Study of catalysts for fuel cell electrodes. IV. Active carbon electrodes for oxygen in alkaline electrolyte. *Collection of Czechoslovak Chemical Communications*, 32(2), 708-719.
282. Xu, J., Huang, W., & McCreery, R. L. (1996). Isotope and surface preparation effects on alkaline dioxygen reduction at carbon electrodes. *Journal of Electroanalytical Chemistry*, 410(2), 235-242.
283. Yang, H. H., & McCreery, R. L. (2000). Elucidation of the Mechanism of Dioxygen Reduction on Metal-Free Carbon Electrodes. *Journal of the Electrochemical Society*, 147(9), 3420-3428.
284. Yuan, W., Zhou, Y., Li, Y., Li, C., Peng, H., Zhang, J., Liu, Z., Dai, L. and Shi, G. (2013). The edge-and basal-plane-specific electrochemistry of a single-layer graphene sheet. *Scientific reports*, 3.
285. Shen, A., Zou, Y., Wang, Q., Dryfe, R.A., Huang, X., Dou, S., Dai, L. and Wang, S., (2014). Oxygen reduction reaction in a droplet on graphite: Direct evidence that the edge is more active than the basal plane. *Angewandte Chemie*, 126(40), 10980-10984.
286. Ji, X., Banks, C. E., Xi, W., Wilkins, S. J., & Compton, R. G. (2006). Edge plane sites on highly ordered pyrolytic graphite as templates for making palladium nanowires via electrochemical decoration. *The Journal of Physical Chemistry B*, 110(45), 22306-22309.

287. Rao, C. V., Cabrera, C. R., & Ishikawa, Y. (2010). In search of the active site in nitrogen-doped carbon nanotube electrodes for the oxygen reduction reaction. *The Journal of Physical Chemistry Letters*, 1(18), 2622-2627.
288. Wiggins-Camacho, J. D., & Stevenson, K. J. (2011). Mechanistic discussion of the oxygen reduction reaction at nitrogen-doped carbon nanotubes. *The Journal of Physical Chemistry C*, 115(40), 20002-20010.
289. Uvarov, N. F., Mateyshina, Y. G., Ulihin, A. S., Yusin, S. I., Varentsova, V. I., & Varentsov, V. K. (2010). Surface Electrochemical Treatment of Carbon Materials for Supercapacitors. *ECS Transactions*, 25(21), 11-16.
290. Song, C., & Zhang, J. (2008). Electrocatalytic oxygen reduction reaction. In *PEM fuel cell electrocatalysts and catalyst layers* (pp. 89-134). Springer London.
291. Deslouis, C., Duprat, M., and Tuiet-Tournillon, C. (1984), The cathodic mass transport process during zinc corrosion in neutral aerated sodium sulphate solutions, *J. Electroanal. Chem.* 181.
292. Tarasevich, M. R., Sadkowsky, A., and Yeager, E. (1983) Oxygen electrochemistry, in *Comprehensive Treatise of Electrochemistry*, Vol. 7, B. E. Conway et al. (eds.), Plenum Press, New York, pp. 301-398.
293. Tucker, W. C., Brown, R., & Russell, L. (1990). Corrosion between a graphite/polymer composite and metals. *Journal of Composite Materials*, 24(1), 92-102.
294. Sloan, F. E. (1992). Chemical attack of graphite/epoxy by hydrogen peroxide. *Applied spectroscopy*, 46(3), 524-528.
295. Schirmann, J. P., & Delavarenne, S. Y. (1979). *Hydrogen peroxide in organic chemistry*. Edition et documentation industrielle, Paris.
296. Sloan, F. E., & Talbot, J. B. (1997). Evolution of perhydroxyl ions on graphite/epoxy cathodes. *Journal of The Electrochemical Society*, 144(12), 4146-4151.
297. Taylor, S. R., Wall, F. D., & Cahen, G. L. (1996). The detection and analysis of electrochemical damage in bismaleimide/graphite fiber composites. *Journal of The Electrochemical Society*, 143(2), 449-458.
298. De Levie, R. (1963). On porous electrodes in electrolyte solutions: I. Capacitance effects. *Electrochimica Acta*, 8(10), 751-780.
299. De Levie, R. (1964). On porous electrodes in electrolyte solutions—IV. *Electrochimica acta*, 9(9), 1231-12
300. De Levie, R. (1965). The influence of surface roughness of solid electrodes on electrochemical measurements. *Electrochimica Acta*, 10(2), 113-130.
301. Taylor, S. R. (1994). A nondestructive electrochemical method to detect and quantify graphite fiber/polymer matrix disbondment in aqueous and cathodically polarized conditions. *Composite Interfaces*, 2(6), 403-417.
302. Pauly, C. C., Taylor, S. R., & Gomez, J. P. (2002). FINAL REPORT ENVIRONMENTAL DURABILITY OF GRAPHITE/EPOXY COMPOSITES: THE COMBINED EFFECTS OF MOISTURE, CATHODIC POLARIZATION, AND STRESS (No. FHWA/VTRC 02-R13).
303. Taylor, S. R., & Cahen Jr, G. L. (1995). The Detection and Analysis of Galvanic Damage in BMI/Graphite Fiber Composites. *Corrosion Detection and Management of Advanced Airframe Materials*. pp,6-1 —6-11.
304. Kawai F. (1992), in *Biodegradable Polymers and Plastics*, M. Vert, J. Feijen, A. Albertsson, G. Scott, and F. Chiellini, Editors, pp. 20-29, The Royal Society of Chemistry, Redwood Press, Wiltshire, England.

305. Tang, Y., Hartt, W., Granata, R., Yu, H., & Farooq, M. U. (2012). Degradation of carbon/vinyl ester composites under cathodic polarization in seawater. *Journal of Composite Materials*, 46(25), 3115-3120.
306. Sloan, F. E., & Talbot, J. B. (1992b). Corrosion of Graphite-Fiber-Reinforced Composites II-Anodic Polarization Damage. *Corrosion*, 48(12), 1020-1026.
307. Stafford, G. R., Cahen, G. L., & Stoner, G. E. (1991). Graphite Fiber-Polymer Matrix Composites as Electrolysis Electrodes. *Journal of the Electrochemical Society*, 138(2), 425-430.
308. Bismarck, A., Kumru, M. E., Springer, J., & Simitzis, J. (1999). Surface properties of PAN-based carbon fibers tuned by anodic oxidation in different alkaline electrolyte systems. *Applied surface science*, 143(1), 45-55.
309. Gulyás, J., Földes, E., Lázár, A., & Pukánszky, B. (2001). Electrochemical oxidation of carbon fibres: surface chemistry and adhesion. *Composites Part A: Applied Science and Manufacturing*, 32(3), 353-360.
310. Basova, Y. V., Hatori, H., Yamada, Y., & Miyashita, K. (1999). Effect of oxidation-reduction surface treatment on the electrochemical behavior of PAN-based carbon fibers. *Electrochemistry communications*, 1(11), 540-544.
311. Riggs Jr O.L., (1973) *Corrosion Inhibitors* (2nd ed.), Nathan C.C. (Ed.), NACE, Houston, TX , pp. 43.
312. TrabANELLI G.in "Chemical Industries: Corrosion Mechanism", Chap. 3: Corrosion Inhibitors 28, 120 (Edited by Florian Mansfeld). Marcel Dekker, New York (1987) , pp. 120 - 163.
313. Papavinasam, S.(2000) "Corrosion Inhibitors," in Uhlig's *Corrosion Handbook*, ed. R.W Revie , John Wiley and Sons Inc. New York, pp. 1089-1106.
314. Noack, M. G. (1982). Evaluation of Catalyzed Hydrazine as an Oxygen. *Materials Performance*, 21(3), 26-30.
315. Noack, M.G. (1989), *Oxygen Scavengers*, Corrosion'89, Paper no. 436, The National Association of Corrosion Engineers (NACE), Houston, TX.
316. Revie, R. W. (2008). *Corrosion and corrosion control*. 4th Edition. John Wiley & Sons. pp.303
317. Murakawa, T., Nagaura, S., & Hackerman, N. (1967). Coverage of iron surface by organic compounds and anions in acid solutions. *Corrosion Science*, 7(2), 79-89.
318. Hoar, T. P. (1958). Nitrite Inhibition of Corrosion: Some Practical Cases. *Corrosion*, 14(2), 63-64.
319. Matsuda, S., & Uhlig, H. H. (1964). Effect of pH, sulfates, and chlorides on behavior of sodium chromate and nitrite as passivators for steel. *Journal of the electrochemical society*, 111(2), 156-161.
320. Bird, C. E., & Evans, U. R. (1956). Corrosion of Aluminium in Proximity with Iron. *Anti-Corrosion Methods and Materials*, 3(9), 279-281.
321. Arnott, D. R., Hinton, B. R. W., & Ryan, N. E. (1989). Cationic-film-forming inhibitors for the protection of the AA 7075 aluminum alloy against corrosion in aqueous chloride solution. *Corrosion*, 45(1), 12-18.
322. Ref. 80, pp. 358 -359.

323. Fischer, H. (1972a). Modes of inhibiting electrode processes (corrosion included) and their experimental discrimination. I. Definition, nomenclature and classification of modes of inhibition in electrochemical electrode reactions. *Materials and Corrosion*, 23(6), 445-452.
324. Fischer, H. (1972b). Modes of inhibiting electrode processes (corrosion included) and their experimental discrimination II. Methodology for the investigation of the different modes of inhibition. *Materials and Corrosion*, 23(6), 453-465.
325. Lorenz, W. J., & Mansfeld, F. (1986). Interface and interphase corrosion inhibition. *Electrochimica Acta*, 31(4), 467-476.
326. Grahame, D. C., & Soderberg, B. A. (1954). Ionic components of charge in the electrical double layer. *The Journal of Chemical Physics*, 22(3), 449-460.
327. Grahame, D. C. (1954). Differential capacity of mercury in aqueous sodium fluoride solutions. I. Effect of concentration at 25. *Journal of the American Chemical Society*, 76(19), 4819-4823.
328. Kastening B. (1965) Die Rolle der Adsorption bei elektrochemischen Vorgängen an Quecksilberelektroden, Habilitationsschrift Bamberg 1965, p. 32-34, 100/02.
329. TrabANELLI G., and Carassiti V.: Mechanism and Phenomenology of Organic Inhibitors, *Advances in Corrosion Science and Technology*, Vol. 1, Ed. by M. G. Fontana and R. W. Staehle, Plenum Press, New York/London 1970, p. 147-228.
330. Fischer, H. (1960). Wirkungen der Inhibitoren bei der elektrokristallisation: Übersicht über den gegenwärtigen Stand der Forschung. *Electrochimica Acta*, 2(1), 50-91.
331. Fischer H. (1944) *Koll. Z.* 106, 50.
332. Vetter, K. J., & Arnold, K. (1960). Korrosion und Sauerstoffüberspannung des passiven Nickels in Schwefelsäure. *Zeitschrift für Elektrochemie, Berichte der Bunsengesellschaft für physikalische Chemie*, 64(2), 244-251.
333. Mansfeld, F., Kendig, M. W., & Lorenz, W. J. (1985). Corrosion inhibition in neutral, aerated media. *Journal of the Electrochemical Society*, 132(2), 290-296
334. Lorbeer, P., & Lorenz, W. J. (1980). The kinetics of iron dissolution and passivation in solutions containing oxygen. *Electrochimica Acta*, 25(4), 375-381.
335. Hausler, R. H. (1988). Corrosion inhibition: proceedings of the International Conference on Corrosion Inhibition, May 16-20, 1983, Dallas, Texas. National Association of Corrosion Engineers, Paper 19
336. Fischer, H. (1964). Wirkung sorbierter Fremdstoffe auf die elektrolytische Abscheidung und Auflösung von Metallen. *Chemie Ingenieur Technik*, 36(6), 581-588.
337. Fischer H. (1967) *J. Electrochem. Soc. Japan* 35, 169.
338. Baukloh, W., & Zimmermann, G. (1936). Wasserstoffdurchlässigkeit von Stahl beim elektrolytischen Beizen. *Arch. Eisenhüttenwes.*, 9, 459-465.
339. Ibl, N. (1954). Zur Kenntnis der elektrolytischen Abscheidung von Metallpulvern: Die quantitativen Zusammenhänge mit den Transportvorgängen bei natürlicher Konvektion. *Helvetica Chimica Acta*, 37(4), 1149-1163.
340. Evans U.R. (1965) Einführung in die Korrosion der Metalle (An Introduction to Metallic Corrosion. Translated and revised by E. Heitz, Verlag Chemie GmbH., Weinheim/ Bergstr., p. 159-186.
341. Fischer, H., Knaack, M., & Volk, O. (1957). Einfluß von Inhibitoren auf die kathodische Abscheidung von Wasserstoff im Grenzstromdichtebereich. I. *Zeitschrift für Elektrochemie, Berichte der Bunsengesellschaft für physikalische Chemie*, 61(1), 123-134.

342. Fischer, H., Schaaf, E., & Thoresen, G. (1959). Zum Mechanismus der Inhibitionswirkung organischer Verbindungen im System Eisen/Säure, I. Zeitschrift für Elektrochemie, Berichte der Bunsengesellschaft für physikalische Chemie, 63(3), 427-440.
343. Fisher H. (1961) C. R. du Symposium Européen sur les Inhibiteurs de Corrosion, Annali dell' Universith. di Ferrara, N. S. Sec. V, 1.
344. Yamaoka, H., & Fischer, H. (1965). Zum mechanismus der inhibitionswirkung organischer verbindungen im system eisen/säure—III. Reaktive fremdstoffbelegungen. Electrochimica Acta, 10(7), 679-711.
345. Horner L. and Rottger F. (1963) Über Inhibitoren der Korrosion, Korrosion 16, Verlag Chemie, Weinheim/Bergstr., p. 55/70.
346. Antropov, L. I. (1967). A correlation between kinetics of corrosion and the mechanism of inhibition by organic compounds. Corrosion Science, 7(9), 607-620.
347. Sanyal, B. (1981). Organic compounds as corrosion inhibitors in different environments—a review. Progress in Organic Coatings, 9(2), 165-236.
348. Riggs JR, O. L., & Every, R. L. (1962). Study of Organic Inhibitors for Hydrochloric Acid Attack on Iron. Corrosion, 18(7), 262t-26t.
349. Hackerman, N., & Schmidt, H. R. (1949). The Role of Adsorption from Solution In Corrosion Inhibitor Action Corrosion, 5(7), 237-243.
350. Hackerman, N., & Makrides, A. C. (1954). Action of polar organic inhibitors in acid dissolution of metals. Industrial & Engineering Chemistry, 46(3), 523-527.
351. Hoar, T. P., & Holliday, R. D. (1953). The inhibition by quinolines and thioureas of the acid dissolution of mild steel. Journal of Applied Chemistry, 3(11), 502-513.
352. Ofoegbu, S. U., Galvão, T. L., Gomes, J. R., Tedim, J., Nogueira, H. I., Ferreira, M. G. S., & Zheludkevich, M. L. (2017). Corrosion inhibition of copper in aqueous chloride solution by 1 H-1, 2, 3-triazole and 1, 2, 4-triazole and their combinations: electrochemical, Raman and theoretical studies. Physical Chemistry Chemical Physics, 19(8), 6113-6129.
353. Riggs Jr, O. L., Morrison, K. L., & Brunzell, D. A. (1979). Inhibitor development for titanium corrosion. Corrosion, 35(8), 356-360.
354. Schweitzer, P. A. (2009). Fundamentals of corrosion: mechanisms, causes, and preventative methods. CRC Press, pp. 309-326.
355. Hackerman, N., & Hurd, R. M. (1962). in Proceedings First International Congress . on Metallic Corrosion, Butterworths, London, pp.166.
356. Zecher, D. C. (1976). Corrosion inhibition by surface-active chelants. Materials Performance 15 (4): 33-37.
357. Antropov, L. I., (1962) in Proceedings First International Congress . on Metallic Corrosion, Butterworths, London, pp.147.
358. Antropov, L. I., & King, C. V. (1961). Kinetics of electrode processes and null points of metals. Journal of The Electrochemical Society, 108(9), 219C-219C.
359. Iofa, Z. A., Batrakov, V. V. and Cho-Ngok-Ba (1964). Influence of anion adsorption on the action of inhibitors on the acid corrosion of iron and cobalt. Electrochimica Acta, 9(12), 1645-1653.
360. Frumkin A.N. (1952) Vestnik Mosk. Univ., p. 37 No. 9
361. Antropov L.I, (1951), Zh. Fiz Khim., V25, P1494
362. Iofa Z. A. (1958), Vestnik Mosk. Univ. No. 2, 139.

363. Banerjee, G., & Malhotra, S. N. (1992). Contribution to adsorption of aromatic amines on mild steel surface from HCl solutions by impedance, UV, and Raman spectroscopy. *Corrosion*, 48(1), 10-15.
364. Frignani .A., TrabANELLI G., Zucchi F., and Zucchini M. (1980), Proceedings of 5th European Symposium of. Corrosion Inhibitors, University of Ferrara N S sez V, Suppl No 7, Ferrara, Italy,. (1980) 1185
365. Brasher D.M. (1960) "Corrosion Inhibition and the Zero Charge Potential of Metals." *Nature* 185, 838 - 839.
366. De C. P. (1957). A Unified Theory of the Mechanism of Inhibition of Corrosion of Iron in Acid and Neutral Media based on the Electro-capillary Behaviour of Ions.
367. Antropov, L. I., Grigor'ev, V. P., & Petrenko, A. T. (1958). Utilization of the data of electrocapillary measurements in the investigation of inhibitors of acid corrosion of metals. *Zh. Prikl. Khim*, 31, 1497-1503.
368. Tripkovic, D. V., Strmcnik, D., Van Der Vliet, D., Stamenkovic, V., & Markovic, N. M. (2009). The role of anions in surface electrochemistry. *Faraday discussions*, 140, 25-40.
369. Huang, J. C., Ogrady, W. E., & Yeager, E. (1977). The effects of cations and anions on hydrogen chemisorption at Pt. *J. Electrochem. Soc.;*(United States),124.
370. Maxted, E. B. (1949). 422. Studies on the nature of chemisorptive bonds. Part I. Some observed regularities. *Journal of the Chemical Society (Resumed)*, 1987-1991.
371. Maxted, E. B., & Moon, K. L. (1949). 463. Studies on the nature of chemisorptive bonds. Part II. The catalytic toxicity of organometallic compounds. *Journal of the Chemical Society (Resumed)*, 2171-2174.
372. Maxted, E. B., & Walker, A. G. (1948). 217. Studies in the detoxication of catalyst poisons. Part VII. The self-poisoning effect in the hydrogenation of pyridine. *Journal of the Chemical Society (Resumed)*, 1093-1097.
373. Maxted, E. B., & Biggs, M. S. (1957). 764. The catalytic toxicity of nitrogen compounds. Part I. Toxicity of ammonia and of amines. *Journal of the Chemical Society (Resumed)*, 3844-3847.
374. Dilke, M. H., Eley, D. D., & Maxted, E. B. (1948). Catalytic Poisons and Magnetic Susceptibility. *Nature*, 161, 804.
375. Lukovits, I., Kalman, E., & Zucchi, F. (2001). Corrosion inhibitors-correlation between electronic structure and efficiency. *Corrosion*, 57(1), 3-8.
376. Aramaki, K., & Hackerman, N. (1968). Structure Effects of Many-Membered Polymethyleneimine on Corrosion Inhibition. *Journal of the Electrochemical Society*, 115(10), 1007-1013.
377. Vasseghi, S., & Nobe, K. (1979). The Effect of Substituted Purines on the Corrosion Behavior of Iron. *Corrosion*, 35(7), 300-303.
378. Skrypnik, Y. G., & Doroshenko, T. F. (1998). Substituted azines as inhibitors of acid corrosion of steel; correlation'structure- anti-corrosional activities'. In *Netherlands Corrosion Centre, EUROCORR'98 Book of Abstracts(Netherlands)*, pp. 38).
379. Heusler, K. E. (1989). The influence of electrolyte composition on the formation and dissolution of passivating films. *Corrosion science*, 29(2), 131-147.
380. Landolt, D. (2007). *Corrosion and surface chemistry of metals*. CRC Press. pp.227
381. McBee, C. L., & Kruger, J. (1972). Nature of passive films on iron-chromium alloys. *Electrochimica Acta*, 17(8), 1337-1341.

382. Kruger, J. (1989). The nature of the passive film on iron and ferrous alloys. *Corrosion science*, 29(2), 149-162.
383. Haupt, S., & Strehblow, H. H. (1989). Combined electrochemical and surface analytical investigations of the formation of passive layers. *Corrosion science*, 29(2), 163-182.
384. Olsson, C. O., & Landolt, D. (2003). Passive films on stainless steels—chemistry, structure and growth. *Electrochimica acta*, 48(9), 1093-1104.
385. Schmutz, P., & Landolt, D. (1999). In-situ microgravimetric studies of passive alloys: potential sweep and potential step experiments with Fe–25Cr and Fe–17Cr–33Mo in acid and alkaline solution. *Corrosion Science*, 41(11), 2143-2163.
386. Leygraf, C., Hultquist, G., Olefjord, I., Elfström, B. O., Knyazheva, V. M., Plaskeyev, A. V., & Kolotyркиn, Y. M. (1979). Selective dissolution and surface enrichment of alloy components of passivated Fe18Cr and Fe18Cr3Mo single crystals. *Corrosion Science*, 19(5), 343-357.
387. Maurice, V., & Marcus, P. (2012). Passive films at the nanoscale. *Electrochimica Acta*, 84, 129-138.
388. Stern, M. (1958). The Mechanism of Passivating-Type Inhibitors. *Journal of the Electrochemical Society*, 105(11), 638-647
389. Pourbaix, M., & Van Rysselberghe, P. (1950). An Electrochemical Mechanism Of Corrosion Inhibition by Chromates, Nitrites and Other Oxidants. *Corrosion*, 6(9), 313-315.
390. Evans, U. R. (1927). CXL.—The passivity of metals. Part I. The isolation of the protective film. *Journal of the Chemical Society (Resumed)*, 1020-1040.
391. Hoar, T. P., & Evans, U. R. (1932). 366. The passivity of metals. Part VII. The specific function of chromates. *Journal of the Chemical Society (Resumed)*, 2476-2481.
392. Evans U. R. (1946), "Metallic Corrosion, Passivity and Protection," 2nd Ed., , Edward Arnold, London, pp. 542-546.
393. Robertson, W. D. (1951). Molybdate and tungstate as corrosion inhibitors and the mechanism of inhibition. *Journal of the electrochemical Society*, 98(3), 94-100.
394. Cartledge, G. H. (1962). Recent Studies of the Action of Inorganic Inhibitors. *Corrosion*, 18(9), 316t-322t
395. Slaiman, Q. J. M., & Davies, D. E. (1971). Mechanism of the corrosion inhibition of Fe by sodium benzoate—II. The inhibitive properties of sodium benzoate in de-aerated and air-saturated solutions. *Corrosion Science*, 11(10), 683-692.
396. Uhlig, H. H. (1947). The Mechanism of the Action of Corrosion Inhibitors. *Metaux et Corrosion*, 22, 204-10.
397. Uhlig, H. H., Triadis, D. N., & Stern, M. (1955). Effect of oxygen, chlorides, and calcium ion on corrosion inhibition of iron by polyphosphates. *Journal of the Electrochemical Society*, 102(2), 59-66.
398. Pryor, M. J., & Cohen, M. (1953). The inhibition of the corrosion of iron by some anodic inhibitors. *Journal of the Electrochemical Society*, 100(5), 203-215.
399. Latimer, W. M. (1938). Oxidation states of the elements and their potentials in aqueous solutions., Prentice-Hall, New York, p. 235-237
400. Robertson, W. D. (1951). Molybdate and tungstate as corrosion inhibitors and the mechanism of inhibition. *Journal of the electrochemical Society*, 98(3), 94-100.
401. Gilroy, D., & Mayne, J. E. O. (1965). The breakdown of the air-formed oxide film on iron upon immersion in solutions of pH 6–13. *British Corrosion Journal*, 1(3), 102-106.
402. Davies, D. E., & Slaiman, Q. J. M. (1973). Mechanism of the corrosion inhibition of iron by sodium benzoate—III. The role of oxygen. *Corrosion Science*, 13(11), 891-905.

403. Pryor, M. J., & Cohen, M. (1951). The mechanism of the inhibition of the corrosion of iron by solutions of sodium orthophosphate. *Journal of the Electrochemical Society*, 98(7), 263-272.
404. Wormwell, F., & Mercer, A. D. (1952). Sodium benzoate and other metal benzoates as corrosion-inhibitors in water and in aqueous solutions. *Journal of Applied Chemistry*, 2(3), 150-160.
405. Davies, D. E., & Slaiman, Q. J. M. (1971). Mechanism of the corrosion inhibition of Fe by sodium benzoate—I. The influence of concentration and pH in air-saturated solutions of sodium benzoate. *Corrosion Science*, 11(10), 671-682.
406. Wachter, A. (1945). Sodium Nitrite as Corrosion Inhibitor for Water. *Industrial & Engineering Chemistry*, 37(8), 749-751.
407. Legault, R. A., & Walker, M. S. (1964). Sodium nitrite as a corrosion inhibitor for mild steel. *Corrosion*, 20(9), 282t-288t.
408. Mayne, J. E. O., & Ramshaw, E. H. (1960). Inhibitors of the corrosion of iron. II. Efficiency of the sodium, calcium and lead salts of long chain fatty acids. *Journal of Applied Chemistry*, 10(10), 419-422.
409. Brasher, D. M., Beynon, J. G., Rajagopalan, K. S., & Thomas, J. G. N. (1970). Passivity of Iron In Chromic Acid Solutions. *British Corrosion Journal*, 5(6), 264-269.
410. Shreir L.L. (Ed.), *Corrosion, Vol. 2, Corrosion Control* (2nd edn.) Newnes-Butterworths, London (1976), pp. 18-44 –18-49.
411. Mayne, J. E. O., & Menter, J. W. (1954). The mechanism of inhibition of the corrosion of iron by solutions of sodium phosphate, borate, and carbonate. *Journal of the Chemical Society (Resumed)*, 103-107.
412. Koudelka, M., Sanchez, J., & Augustyński, J. (1982). On the nature of surface films formed on iron in aggressive and inhibiting polyphosphate solutions. *Journal of the Electrochemical Society*, 129(6), 1186-1191.
413. McCafferty, E., Bennett, M. K., & Murday, J. S. (1988). An XPS study of passive film formation on iron in chromate solutions. *Corrosion science*, 28(6), 559-576.
414. Thomas, J. G. N. (1966). The adsorption of anions on iron during anodic passivation in neutral solution. *British Corrosion Journal*, 1(4), 156-160.
415. Sato, N., Kudo, K., & Nishimura, R. (1976). Depth analysis of passive films on iron in neutral borate solution. *Journal of the Electrochemical Society*, 123(10), 1419-1423.
416. Sieber, I. V., Hildebrand, H., Virtanen, S., & Schmuki, P. (2006). Investigations on the passivity of iron in borate and phosphate buffers, pH 8.4. *Corrosion science*, 48(11), 3472-3488.
417. Kozłowski, W., & Flis, J. (1991). An ellipsometric study of the effect of phosphate anions in borate solution on anodic films grown on iron. *Corrosion science*, 32(8), 861-875.
418. Nishimura, R., Kudo, K., & Sato, N. (1980). Intensity-following ellipsometry of passive films on iron. *Surface Science*, 96(1), 413-425.
419. Nishimura, R., & Sato, N. (1984, June). Potential-p H Diagram of Composition/Structure of Passive Film on Iron. In *International Congress on Metallic Corrosion*, (Vol. 1), pp. 96-101.
420. Evans, U. R. (1927). CXL.—The passivity of metals. Part I. The isolation of the protective film. *Journal of the Chemical Society (Resumed)*, 1020-1040.
421. Khamis, E., Ameer, M. A., & Al-Senani, G. (2007) "Influence of Phosphoric Acid Produced by Wet Process on Corrosion Behaviour of Steel: Effect of TSC and its Derivatives

- on the Corrosion Behavior of Steel.", in Prevention of metal corrosion: new research. Nunez, M. (Ed.), Nova Publishers Inc. pp.1-59. (6-10).
422. Popov, B. N. (2015). Corrosion Engineering: Principles and Solved Problems. Elsevier. pp. 586.
423. Costello, M.T. (2009) "Corrosion Inhibitors and Rust Preservatives" in Lubricant additives: chemistry and applications. Rudnick, L. R. (Ed.). CRC Press. pp.425.
424. Snaveley, E. S., & Blount, F. E. (1969). Rates of reaction of dissolved oxygen with scavengers in sweet and sour brines. *Corrosion*, 25(10), 397-404.
425. Roberge, P. R. (2007). Corrosion inspection and monitoring (Vol. 2). John Wiley & Sons. pp.4-10
426. Ellis, D.M., Cuisia, D.G. and Thompson, H.W (1987). "The Oxidation and Degradation Products of Volatile Oxygen Scavengers and their Relevance in Plant Applications," *Corrosion* , pp.432.
427. Kasinecz F.(2001) Diethylhydroxylamine (DEHA): A Volatile Oxygen Scavenger for Boiler System Treatment. *The Analyst*. <https://www.awt.org/pub/014E996C-FA59-3BFF-67C3-FCD3627F94C7> accessed 1/10/2015.
428. Harder, Scott R. "Method of scavenging oxygen from boiler waters with substituted quinolines." U.S. Patent 5,167,835, issued December 1, 1992
429. Ellis, D. M. (1988). The oxidation and degradation products of volatile oxygen scavengers and their relevance in plant applications, *Corrosion* 87/432, NACE, Houston, TX.
430. Revie, R. W., & Uhlig, H. H. (2011). *Uhlig's corrosion handbook* (Vol. 51). John Wiley & Sons.
431. Ma, H., Chen, S., Yin, B., Zhao, S., & Liu, X. (2003). Impedance spectroscopic study of corrosion inhibition of copper by surfactants in the acidic solutions. *Corrosion Science*, 45(5), 867-882.
432. Khaled, K. F., & Hackerman, N. (2003). Investigation of the inhibitive effect of ortho-substituted anilines on corrosion of iron in 1 M HCl solutions. *Electrochimica Acta*, 48(19), 2715-2723.
433. El Rehim, A. (1999). Corrosion inhibition and adsorption behaviour of 4-aminoantipyrine on mild steel in H₂SO₄. *Corrosion Prevention and Control*, 46(6), 157-62.
434. Szklarska-Smialowska Z., Kaminsky M. (1974), in: *Proceedings of 5th International Congress on Metallic Corrosion*, NACE, Houston, p. 555.
435. Patel N. and Mehta G.(2011). "New Era of Eco-friendly Corrosion Inhibitors" in *Green corrosion chemistry and engineering: opportunities and challenges*. Sharma S. K. (Ed.). John Wiley & Sons. pp.125.
436. Evans, U. R. (1924). The Action of Salt Solution on Iron and Steel In The Presence of Oxygen. *Journal of the Society of Chemical Industry Transactions*, 43, pp.315.
437. Ai, J. Z., Guo, X. P., & Chen, Z. Y. (2006). The adsorption behavior and corrosion inhibition mechanism of anionic inhibitor on galvanic electrode in 1% NaCl solution. *Applied Surface Science*, 253(2), 683-688.
438. Ai, J. Z., Guo, X. P., Qu, J. E., Chen, Z. Y., & Zheng, J. S. (2006). Adsorption behavior and synergistic mechanism of a cationic inhibitor and KI on the galvanic electrode. *Colloids and Surfaces A: Physicochemical and Engineering Aspects*, 281(1), 147-155.
439. Vosta, J., Eliasek, J., & Knizek, P. (1976). A quantum-chemical study of the corrosion inhibition of iron by means of aniline derivatives in hydrochloric acid. *Corrosion*, 32(5), 183-187.

440. Aramaki, K. (1978). POLARIZATION STUDY ON INHIBITION OF IRON CORROSION BY MEANS OF PHENYLALKYL AMINES IN ACID-SOLUTION. *Denki Kagaku*, 46(2), 86-91.
441. Uehara, J., Nishihara, H., & Aramaki, K. (1990). An Investigation of Adsorption and Orientation of Some Nitrogen Compounds at Iron Surface in an Acid Solution by Surface-Enhanced Raman Scattering Spectroscopy. *Journal of the Electrochemical Society*, 137(9), 2677-2683.
442. Demuth, J. E., Christmann, K., & Sanda, P. N. (1980). The vibrations and structure of pyridine chemisorbed on Ag (111): the occurrence of a compressional phase transformation. *Chemical Physics Letters*, 76(2), 201-206.
443. Soriaga, M. P., White, J. H., & Hubbard, A. T. (1983). Orientation of aromatic compounds adsorbed on platinum electrodes. The effect of temperature. *The Journal of Physical Chemistry*, 87(16), 3048-3054.
444. Vashi, R., & Desai, K. (2013) Aniline as Corrosion Inhibitor for Zinc in Hydrochloric Acid. *Chemical Science Transactions*. Vol. 2(2), pp.670-676.
445. Campanella, L. (1970). Zero charge potential of metals. *Journal of Electroanalytical Chemistry and Interfacial Electrochemistry*, 28(1), 228-232.
446. Holze, R. (2007). 3 Electrode potentials of zero charge. In *Electrochemical Thermodynamics and Kinetics* (pp. 207-222). Springer Berlin Heidelberg.
447. Trasatti, S., & Lust, E. (1999). The potential of zero charge. In *Modern aspects of electrochemistry* (pp. 1-215). Springer US.
448. Telegdi, J., Kalman, E., & Karman, F. H. (1992). Corrosion and scale inhibitors with systematically changed structure. *Corrosion science*, 33(7), 1099-1103.
449. Zhang, D. Q., Gao, L. X., & Zhou, G. D. (2003). Synergistic effect of 2-mercapto benzimidazole and KI on copper corrosion inhibition in aerated sulfuric acid solution. *Journal of applied electrochemistry*, 33(5), 361-366.
450. Kalman, E., Lukovits, I., & Palinkas, G. (1993). A simple model of synergism of corrosion inhibitors. *ACH Models in Chemistry(Hungary)*, 132(4), 527-537.
451. Lazarides, C., Allen, P. D., Hampson, N. A., Marshall, A., & Willars, M. (1979). Synergism in corrosion inhibition. *Surface technology*, 9(3), 159-169.
452. Makrides, A. C., & Stern, M. (1960). Inhibition of Metal Dissolution by Ferric Sulfate. *Journal of The Electrochemical Society*, 107(11), 877-883.
453. Evans, U. R. "An Introduction to Metallic Corrosion," Edward Arnold, Ltd., London (1948).
454. Hackerman, N., Snavely, E. S., & Payne, J. S. (1966). Effects of anions on corrosion inhibition by organic compounds. *Journal of the Electrochemical Society*, 113(7), 677-681.
455. Hosseini, M., Mertens, S. F., & Arshadi, M. R. (2003). Synergism and antagonism in mild steel corrosion inhibition by sodium dodecylbenzenesulphonate and hexamethylenetetramine. *Corrosion Science*, 45(7), 1473-1489.
456. Buck III, W. R., & Leidheiser Jr, H. (1958). The Activation and Inhibition of Corrosion of Metals by Metallic Cations. *Corrosion*, 14(7), 22-26.
457. Oguzie, E. E., Li, Y., & Wang, F. H. (2007). Corrosion inhibition and adsorption behavior of methionine on mild steel in sulfuric acid and synergistic effect of iodide ion. *Journal of colloid and interface science*, 310(1), 90-98
458. Wu, Y. C., Zhang, P., Pickering, H. W., & Allara, D. L. (1993). Effect of KI on improving copper corrosion inhibition efficiency of benzotriazole in sulfuric acid electrolytes. *Journal of the Electrochemical Society*, 140(10), 2791-2800.

459. Forsyth, M., Forsyth, C. M., Wilson, K., Behrsing, T., & Deacon, G. B. (2002). ATR characterisation of synergistic corrosion inhibition of mild steel surfaces by cerium salicylate. *Corrosion science*, 44(11), 2651-2656.
460. Aramaki, K. (2002a). Synergistic inhibition of zinc corrosion in 0.5 M NaCl by combination of cerium (III) chloride and sodium silicate. *Corrosion science*, 44(4), 871-886.
461. Aramaki, K. (2002b). Cerium (III) chloride and sodium octylthiopropionate as an effective inhibitor mixture for zinc corrosion in 0.5 M NaCl. *Corrosion science*, 44(6), 1361-1374.
462. Ramji, K., Cairns, D. R., & Rajeswari, S. (2008). Synergistic inhibition effect of 2-mercaptobenzothiazole and Tween-80 on the corrosion of brass in NaCl solution. *Applied Surface Science*, 254(15), 4483-4493.
463. Aballe, A., Bethencourt, M., Botana, F. J., & Marcos, M. (2001). CeCl₃ and LaCl₃ binary solutions as environment-friendly corrosion inhibitors of AA5083 Al-Mg alloy in NaCl solutions. *Journal of Alloys and Compounds*, 323, 855-858.
464. Yazdzad, A. R., Shahrabi, T., & Hosseini, M. G. (2008). Inhibition of 3003 aluminum alloy corrosion by propargyl alcohol and tartrate ion and their synergistic effects in 0.5% NaCl solution. *Materials Chemistry and physics*, 109(2), 199-205.
465. Okafor, P. C., Liu, C. B., Liu, X., Zheng, Y. G., Wang, F., & Liu, C. Y. (2010). Corrosion inhibition and adsorption behavior of imidazoline salt on N80 carbon steel in CO₂-saturated solutions and its synergism with thiourea. *Journal of Solid State Electrochemistry*, 14(8), 1367-1376.
466. Mu, G. N., Zhao, T. P., Liu, M., & Gu, T. (1996). Effect of metallic cations on corrosion inhibition of an anionic surfactant for mild steel. *Corrosion*, 52(11), 853-856.
467. Li, X., Deng, S., Mu, G., & Qu, Q. (2007). The synergistic inhibition effect of rare earth cerium (IV) ion and iso-vanillin on the corrosion of cold rolled steel in 1.0M H₂SO₄ solution. *Materials Letters*, 61(11), 2514-2517.
468. Aramaki, K. (2002c). Synergistic inhibition of zinc corrosion in 0.5 M NaCl by combination of cerium (III) chloride and sodium silicate. *Corrosion science*, 44(4), 871-886.
469. Ramji, K., Cairns, D. R., & Rajeswari, S. (2008). Synergistic inhibition effect of 2-mercaptobenzothiazole and Tween-80 on the corrosion of brass in NaCl solution. *Applied Surface Science*, 254(15), 4483-4493.
470. Musa, A. Y., Muhamad, N., Tien, L. T., & Chee, E. P. (2011). Synergistic Effect of Iodide Ion and 1-(2H)-Phthalazinone on Galvanic Corrosion of Aluminum and Mild Steel in 1.0 M HCl. *Int. J. Electrochem. Sci*, 6, 5298-5304.
471. Aramaki, K., & Hackerman, N. (1969). Inhibition mechanism of medium-sized polymethyleneimine. *Journal of the Electrochemical Society*, 116(5), 568-574.
472. Ref: 80, pp. 94-95.
473. Barbier, B., Pinson, J., Desarmot, G., & Sanchez, M. (1990). Electrochemical bonding of amines to carbon fiber surfaces toward improved carbon-epoxy composites. *Journal of the Electrochemical Society*, 137(6), 1757-1764.
474. Adenier, A., Chehimi, M. M., Gallardo, I., Pinson, J., & Vila, N. (2004). Electrochemical oxidation of aliphatic amines and their attachment to carbon and metal surfaces. *Langmuir*, 20(19), 8243-8253.
475. Andrieux, C. P., Gonzalez, F., & Savéant, J. M. (1997). Derivatization of carbon surfaces by anodic oxidation of arylacetates. Electrochemical manipulation of the grafted films. *Journal of the American Chemical Society*, 119(18), 4292-4300.

476. Delamar, M., Hitmi, R., Pinson, J., & Saveant, J. M. (1992). Covalent modification of carbon surfaces by grafting of functionalized aryl radicals produced from electrochemical reduction of diazonium salts. *Journal of the American Chemical Society*, 114(14), 5883-5884.
477. Delamar, M., Desarmot, G., Fagebaume, O., Hitmi, R., Pinson, J., & Savéant, J. M. (1997). Modification of carbon fiber surfaces by electrochemical reduction of aryl diazonium salts: Application to carbon epoxy composites. *Carbon*, 35(6), 801-807.
478. Allongue, P., Delamar, M., Desbat, B., Fagebaume, O., Hitmi, R., Pinson, J., & Savéant, J. M. (1997). Covalent modification of carbon surfaces by aryl radicals generated from the electrochemical reduction of diazonium salts. *Journal of the American Chemical Society*, 119(1), 201-207.
479. Hoekstra, K. J., & Bein, T. (1996). Adsorption of Zirconium– Phosphonate Multilayers onto Phosphate-Derivatized Glassy Carbon Substrates. *Chemistry of materials*, 8(8), 1865-1870.
480. Saby, C., Ortiz, B., Champagne, G. Y., & Bélanger, D. (1997). Electrochemical modification of glassy carbon electrode using aromatic diazonium salts. 1. Blocking effect of 4-nitrophenyl and 4-carboxyphenyl groups. *Langmuir*, 13(25), 6805-6813.
481. Ortiz, B., Saby, C., Champagne, G. Y., & Bélanger, D. (1998). Electrochemical modification of a carbon electrode using aromatic diazonium salts. 2. Electrochemistry of 4-nitrophenyl modified glassy carbon electrodes in aqueous media. *Journal of Electroanalytical Chemistry*, 455(1), 75-81.
482. Mansfeld, F. (2003) *Electrochemical Methods of Corrosion Testing, Corrosion: Fundamentals, Testing, and Protection, Vol 13A, ASM Handbook*, ASM International, pp. 446–462.
483. Popov, B. N. (2015). *Corrosion Engineering: Principles and Solved Problems*. Elsevier. pp.207.
484. Enos, D. G., & Scribner, L. L. (1997). The potentiodynamic polarization scan. Solartron Instruments, Hampshire, UK, Technical Report, (33). <http://www.solartronanalytical.com/download/Technote-33-The-Potentiodynamic-Polarization-Scan.pdf> accessed 10/06/2015.
485. Virtanen S. (2011) Corrosion and Passivity of Metals and Coatings, In *Tribocorrosion of passive metals and coatings*, Landolt, D., & Mischler, S. (Eds.). Elsevier. pp.1-14.
486. McCafferty, E. (2005). Validation of corrosion rates measured by the Tafel extrapolation method. *Corrosion science*, 47(12), pp.3202-3215.
487. Bandy, R. (1980). The simultaneous determination of tafel constants and corrosion rate—a new method. *Corrosion Science*, 20(8), 1017-1028.
488. Stern, M., & Geary, A. L. (1957). Electrochemical polarization I. A theoretical analysis of the shape of polarization curves. *Journal of the electrochemical society*, 104(1), 56-63.
489. Stern, M. (1958). A method for determining corrosion rates from linear polarization data. *Corrosion*, 14(9), 60-64.
490. Heinze, J. (1984). Cyclic voltammetry—“electrochemical spectroscopy”. *New analytical methods* (25). *Angewandte Chemie International Edition in English*, 23(11), 831-847.
491. Kissinger P.T., Heineman W.R., (1983) Cyclic voltammetry. *Journal of Chemical Education* 60(9): 702.
492. Kounaves, S. P. (1997). *Voltammetric Techniques*. in *Handbook of instrumental techniques for analytical chemistry*, Ed, Settle F.A, Prentice Hall, 709-726.

493. Mansfeld, F. (1990). Electrochemical impedance spectroscopy (EIS) as a new tool for investigating methods of corrosion protection. *Electrochimica Acta*, 35(10), 1533-1544.
494. Ref. 108, pp.55.
495. Amirudin, A., & Thieny, D. (1995). Application of electrochemical impedance spectroscopy to study the degradation of polymer-coated metals. *Progress in organic coatings*, 26(1), 1-28.
496. Macdonald, D. D. (2009). Why electrochemical impedance spectroscopy is the ultimate tool in mechanistic analysis. *ECS Transactions*, 19(20), 55-79.
497. Westing, E.P.M. van, (1992) Determination of coating performance with impedance measurements, Ph.D. Thesis, Delft University of Technology.
498. Pirnát, A., Mészáros, L., & Lengyel, B. (1990). Study of the formation of chromate layer on zinc by impedance technique. *Electrochimica Acta*, 35(2), 515-522.
499. Bonora, P. L., Deflorian, F., & Fedrizzi, L. (1996). Electrochemical impedance spectroscopy as a tool for investigating underpaint corrosion. *Electrochimica Acta*, 41(7), 1073-1082.
500. De Wit, H. J., Wijenberg, C., & Crevecoeur, C. (1979). Impedance measurements during anodization of aluminum. *Journal of the Electrochemical Society*, 126(5), 779-785.
501. Anik, M., & Celikten, G. (2007). Analysis of the electrochemical reaction behavior of alloy AZ91 by EIS technique in H₃PO₄/KOH buffered K₂SO₄ solutions. *Corrosion Science*, 49(4), 1878-1894.
502. Srinivasan, A., Blawert, C., Huang, Y., Mendis, C. L., Kainer, K. U., & Hort, N. (2014). Corrosion behavior of Mg–Gd–Zn based alloys in aqueous NaCl solution. *Journal of Magnesium and Alloys*, 2(3), 245-256.
503. Jorcin, J. B., Orazem, M. E., Pébère, N., & Tribollet, B. (2006). CPE analysis by local electrochemical impedance spectroscopy. *Electrochimica Acta*, 51(8), 1473-1479.
504. Macdonald, J. R., & Brachman, M. K. (1956). Linear-system integral transform relations. *Reviews of modern physics*, 28(4), 393.
505. Schrama J. (1957) On the Phenomenological Theory of Linear Relaxation Processes, Ph.D. thesis, University of Leiden, Netherlands.
506. Macdonald, D. D., & Urquidi-Macdonald, M. (1990). Kramers-Kronig Transformation of Constant Phase Impedances. *Journal of The Electrochemical Society*, 137(2), 515-517.
507. Warburg, E. (1901). Ueber die polarisationscapacität des platins. *Annalen der Physik*, 311(9), 125-135.
508. Mansfeld, F. (1988). Technical note: concerning the display of impedance data. *Corrosion*, 44(8), 558-559.
509. Macdonald, D. D., & Urquidi-Macdonald, M. (1985). Application of Kramers-Kronig Transforms in the Analysis of Electrochemical Systems I. Polarization Resistance. *Journal of the Electrochemical Society*, 132(10), 2316-2319.
510. Urquidi-Macdonald, M., Real, S., & Macdonald, D. D. (1986). Application of Kramers-Kronig Transforms in the Analysis of Electrochemical Impedance Data II. Transformations in the Complex Plane. *Journal of the Electrochemical Society*, 133(10), 2018-2024.
511. Van Meirhaeghe, R. L., Dutoit, E. C., Cardon, F., & Gomes, W. P. (1976). On the application of the Kramers-Kronig relations to problems concerning the frequency dependence of electrode impedance. *Electrochimica Acta*, 21(1), 39-43.

512. Dougherty, B. J., & Smedley, S. I. (1993). Validation of Experimental Data from High Impedance Systems Using the Kramers-Kronig Transforms, in *Electrochemical Impedance: Analysis and Interpretation*, ASTM SPECIAL TECHNICAL PUBLICATION1188, J.R. Scully, D.C. Silverman, and M.W. Kendig, Eds., American Society for Testing Materials, Philadelphia, 1993, pp. 154-170.
513. Kramers, H. A. (1929). Die dispersion und absorption von Röntgenstrahlen. *Phys. Z*, 30, 522.]
514. Kronig, R. D. (1926). On the theory of dispersion of x-rays. *JOSA*, 12(6), 547-556.
515. Cahan, B. D., & Chen, C. T. (1982). The Nature of the Passive Film on Iron II. A-C Impedance Studies. *Journal of the Electrochemical Society*, 129(3), 474-480.
516. Bode H. W., "Network Analysis and Feedback Amplifier Design," Van Nostrand, New York (1945).
517. Amirudin A., (1994) Application of electrochemical impedance spectroscopy to study the degradation of polymer-coated metals , (Ph.D. Thesis)The Royal Institute of Technology, Stockholm, Sweden, p. 59.
518. Lamaka, S. V., Karavai, O. V., Bastos, A. C., Zheludkevich, M. L., & Ferreira, M. G. S. (2008). Monitoring local spatial distribution of Mg²⁺, pH and ionic currents. *Electrochemistry Communications*, 10(2), 259-262.
519. Deshpande, K. B. (2010). Experimental investigation of galvanic corrosion: Comparison between SVET and immersion techniques. *Corrosion Science*, 52(9), 2819-2826.
520. Souto, R. M., Izquierdo, J., Santana, J. J., & González, S. (2013). SCANNING MICROELECTROCHEMICAL TECHNIQUES A HIGHLY SENSITIVE ROUTE TO EVALUATE DEGRADATION REACTIONS AND PROTECTION METHODS WITH CHEMICAL SELECTIVITY. *European Journal of Science and Theology*, 9(2), 71-89.
521. Isaacs, H. S. (1990). Limitations of in situ current density mapping for vibrating electrodes close to metal surfaces. *Corrosion*, 46(8), 677-679.
522. Khobaib, M., Buchanan, A., & Donley, M. (2004). Scanning Vibrating Electrode Technique as a Benchmark for NDE of Corrosion. In *Nondestructive Materials Characterization* (pp. 286-293). Springer Berlin Heidelberg.
523. Jaffe, L. F., & Nuccitelli, R. (1974). An ultrasensitive vibrating probe for measuring steady extracellular currents. *The Journal of cell biology*, 63(2), 614-628.
524. Mackenzie, D. (1982). The electricity that shapes our ends. *New Scientist*, 93(1290), 217-220.
525. Isaacs, H. S. and Ishikawa, Y. (1986) (Application of the vibrating probe to localized current measurements) in *Electrochemical Techniques for Corrosion Engineering* (R. Baboian, ed.), National Association of Corrosion Engineers, Houston, Texas, USA, p. 17.
526. Isaacs, H. S. (1988). The measurement of the galvanic corrosion of soldered copper using the scanning vibrating electrode technique. *Corrosion science*, 28(6), 547-558.
527. Scheffey, C. (1988). Two approaches to construction of vibrating probes for electrical current measurement in solution. *Review of scientific instruments*, 59(5), 787-792.
528. Freeman, J. A., & Wikswo, J. P. (1982). DEVELOPMENT OF A CIRCULARLY VIBRATING MICRO-PROBE FOR MEASURING STEADY CURRENTS FROM LIVING TISSUE. In *BIOPHYSICAL JOURNAL* (Vol. 37, No. 2, pp. A79-A79). 9650 ROCKVILLE PIKE, BETHESDA, MD 20814-3998: BIOPHYSICAL SOCIETY.
529. Reid, B., Nuccitelli, R., & Zhao, M. (2007). Non-invasive measurement of bioelectric currents with a vibrating probe. *Nature protocols*, 2(3), 661-669.

530. Ferrier, J., & Lucas, W. J. (1986). Ion transport and the vibrating probe. *Biophysical journal*, 49(4), 803.
531. Bastos, A. C., Dias, S. A. S., & Diamantino, T. C. (2013). Uma introdução à técnica svet. *Corrosão e Protecção de Materiais*, 32(2), 50-57.
532. Scheffey C. (1986), (Electric fields and the vibrating probe, for the uninitiated) in *ionic Currents in Development* (R. Nuccitelli, ed.), a. r. Liss inc., New York, USA, p. xxv (1986).
533. Akid, R., & Garma, M. (2004). Scanning vibrating reference electrode technique: a calibration study to evaluate the optimum operating parameters for maximum signal detection of point source activity. *Electrochimica acta*, 49(17), 2871-2879.
534. Ishikawa Y. and Isaacs H. S., Brookhaven National Laboratory Report BNL 33095 (1983).
535. Freeman, J. A., Manis, P. B., Snipes, G. J., Mayes, B. N., Samson, P. C., Wikswo, J. P., & Freeman, D. B. (1985). Steady growth cone currents revealed by a novel circularly vibrating probe: a possible mechanism underlying neurite growth. *Journal of neuroscience research*, 13(1-2), 257-283.
536. Crowe, C. R. (1985a). Localized Corrosion Currents from Graphite/Aluminum and Welded SiC/Al Metal Matrix Composites (No. NRL-MR-5415). NAVAL RESEARCH LAB WASHINGTON DC.
537. Crowe, C. R. (1985b). Localized Ionic Currents from a Corroding Iron-Copper Galvanic Couple (No. NRL-MR-5416). NAVAL RESEARCH LAB WASHINGTON DC.
538. Crowe, C. R., & Kasper, R. G. (1986). Ionic Current Densities in the Nearfield of a Corroding Iron-Copper Galvanic Couple. *Journal of the Electrochemical Society*, 133(5), 879-887.
539. Pieretti, E. F., Manhabosco, S. M., Dick, L. F., & Costa, I. Use of Scanning Vibrating Electrode Technique to Localized Corrosion Evaluation of ASTM F139 Stainless Steel Marked by Laser.
540. Williams, G., & McMurray, H. N. (2008). Localized corrosion of magnesium in chloride-containing electrolyte studied by a scanning vibrating electrode technique. *Journal of the electrochemical Society*, 155(7), C340-C349.
541. Williams, G., ap Llwyd Dafydd, H., & Grace, R. (2013). The localised corrosion of Mg alloy AZ31 in chloride containing electrolyte studied by a scanning vibrating electrode technique. *Electrochimica Acta*, 109, 489-501.
542. Simões, A. M., Bastos, A. C., Ferreira, M. G., González-García, Y., González, S., & Souto, R. M. (2007). Use of SVET and SECM to study the galvanic corrosion of an iron-zinc cell. *Corrosion Science*, 49(2), 726-739.
543. Souto, R. M., Gonzalez-Garcia, Y., Bastos, A. C., & Simoes, A. M. (2007). Investigating corrosion processes in the micrometric range: a SVET study of the galvanic corrosion of zinc coupled with iron. *Corrosion Science*, 49(12), 4568-4580.
544. Shinohara, T., Ozaki, K., & Tsujidawa, S. (1990). Scanning Vibrating Electrode Technique for Detecting Intergranular Corrosion Current. *Corrosion Engineering(Japan)(USA)*, 39(12), 755-768.
545. Uchida, H., Yamashita, M., Inoue, S., & Koterazawa, K. (2001). In-situ observations of crack nucleation and growth during stress corrosion by scanning vibrating electrode technique. *Materials Science and Engineering: A*, 319, 496-500.
546. Bastos, A. C., Ferreira, M. G., & Simões, A. M. (2006). Corrosion inhibition by chromate and phosphate extracts for iron substrates studied by EIS and SVET. *Corrosion Science*, 48(6), 1500-1512.

547. Ogle, K., Morel, S., & Jacquet, D. (2006). Observation of self-healing functions on the cut edge of galvanized steel using SVET and pH microscopy. *Journal of The Electrochemical Society*, 153(1), B1-B5.
548. Thébault, F., Vuillemin, B., Oltra, R., Ogle, K., & Allely, C. (2008). Investigation of self-healing mechanism on galvanized steels cut edges by coupling SVET and numerical modeling. *Electrochimica Acta*, 53(16), 5226-5234.
549. Isaacs, H. S. (1987). The use of the scanning vibrating electrode technique for detecting defects in ion vapor-deposited aluminum on steel. *Corrosion*, 43(10), 594-596.
550. Isaacs, H. S. and Jackson, R. (1984) *Fundamental Aspects of Corrosion Protection by Surface Modification*, McCafferty, E., Clayton, C. R., and Oudar, J., Eds., Electrochemical Society, Pennington, New Jersey, pp. 339.
551. Bastos A.C., Zheludkevich M.L., Ferreira M.G.S. (2008) Concerning the Efficiency of Corrosion Inhibitors as Given by SVET. *Portugaliae Electrochimica Acta* Vol. 26 pp. 47-54.
552. Kallip, S., Bastos, A. C., Zheludkevich, M. L., & Ferreira, M. G. S. (2010). A multi-electrode cell for high-throughput SVET screening of corrosion inhibitors. *Corrosion Science*, 52(9), 3146-3149.
553. Issacs, H.S., and Vyas, B., in: Mansfield, F., and Bertocci, U. (Eds.), *Electrochemical Corrosion Testing*, ASTM STP 727, 1981, pp. 3.
554. Bastos, A. C., Taryba, M. G., Karavai, O. V., Zheludkevich, M. L., Lamaka, S. V., & Ferreira, M. G. S. (2010). Micropotentiometric mapping of local distributions of Zn²⁺ relevant to corrosion studies. *Electrochemistry Communications*, 12(3), 394-397.
555. Klusmann, E., & Schultze, J. W. (1997). pH-microscopy—theoretical and experimental investigations. *Electrochimica acta*, 42(20), 3123-3134.
556. Klusmann, E., & Schultze, J. W. (2003). pH-Microscopy: technical application in phosphating solutions. *Electrochimica acta*, 48(20), 3325-3332.
557. Etienne, M., Dierkes, P., Erichsen, T., Schuhmann, W., & Fritsch, I. (2007). Constant-Distance Mode Scanning Potentiometry. High Resolution pH Measurements in Three-Dimensions. *Electroanalysis*, 19(2-3), 318-323.
558. Thomas R. C. (1978) *Ion-Sensitive Intracellular Microelectrodes. How to make and use them*. Academic Press, London, New York, San Francisco (1978).
559. Horrocks, B. R., Mirkin, M. V., Pierce, D. T., Bard, A. J., Nagy, G., & Toth, K. (1993). Scanning electrochemical microscopy. 19. Ion-selective potentiometric microscopy. *Analytical Chemistry*, 65(9), 1213-1224.
560. Thompson, F. C., & Brudevold, F. (1954). A micro-antimony electrode designed for intraoral pH measurements in man and small experimental animals. *Journal of dental research*, 33(6), 849-853.
561. Oyama, N., Hirokawa, T., Yamaguchi, S., Ushizawa, N., & Shimomura, T. (1987). Hydrogen ion selective microelectrode prepared by modifying an electrode with polymers. *Analytical Chemistry*, 59(2), 258-262.
562. Głab, S., Hulanicki, A., Edwall, G., & Ingman, F. (1989). Metal-metal oxide and metal oxide electrodes as pH sensors. *Critical Reviews in Analytical Chemistry*, 21(1), 29-47.
563. Wipf, D. O., Ge, F., Spaine, T. W., & Baur, J. E. (2000). Microscopic measurement of pH with iridium oxide microelectrodes. *Analytical chemistry*, 72(20), 4921-4927.
564. Roetheli, B. E., Cox, G. L., & Littreal, W. B. (1932). Effect of pH on the corrosion products and corrosion rate of zinc in oxygenated aqueous solutions. *Metals and Alloys*, 3, 73-76.

565. Ambat, R., & Dwarakadasa, E. S. (1994). Studies on the influence of chloride ion and pH on the electrochemical behaviour of aluminium alloys 8090 and 2014. *Journal of applied electrochemistry*, 24(9), 911-916.
566. Whitman, G. W., Russell, R. P., & Altieri, V. J. (1924). Effect of Hydrogen-Ion Concentration on the Submerged Corrosion of Steel. *Industrial & Engineering Chemistry*, 16(7), 665-670.
567. Nagayama, M., & Cohen, M. (1963). The Anodic Oxidation of Iron in a Neutral Solution II. Effect of Ferrous Ion and pH on the Behavior of Passive Iron. *Journal of the Electrochemical Society*, 110(6), 670-680.
568. Bala, H. (1984). The corrosion of iron in sulphate solutions at pH= 0–2. *Electrochimica Acta*, 29(1), 119-129.
569. Ammar, I. A., & Riad, S. (1958). Effect of pH on Corrosion Potentials. *The Journal of Physical Chemistry*, 62(2), 150-154.
570. Silverman, D. C., Kalota, D. J., & Stover, F. S. (1995). Effect of pH on corrosion inhibition of steel by polyaspartic acid. *Corrosion*, 51(11), 818-825.
571. Schaschl, E., & Marsh, G. A. (1957). The Effect of Dissolved Oxygen on Corrosion of Steel And on Current Required for Cathodic Protection. *Corrosion*, 13(4), 35-43.
572. Tromans, D. (2000). Modeling oxygen solubility in water and electrolyte solutions. *Industrial & engineering chemistry research*, 39(3), 805-812.
573. Montgomery, H., Thom, N. S., & Cockburn, A. (1964). Determination of dissolved oxygen by the Winkler method and the solubility of oxygen in pure water and sea water. *Journal of Applied Chemistry*, 14(7), 280-296.
574. Narita, E., Lawson, F., & Han, K. N. (1983). Solubility of oxygen in aqueous electrolyte solutions. *Hydrometallurgy*, 10(1), 21-37.
575. Weiss, R. F. (1970). The solubility of nitrogen, oxygen and argon in water and seawater. In *Deep Sea Research and Oceanographic Abstracts* (Vol. 17, No. 4, pp. 721-735). Elsevier.
576. Murray, C. N., & Riley, J. P. (1969, June). The solubility of gases in distilled water and sea water—II. Oxygen. In *Deep Sea Research and Oceanographic Abstracts* (Vol. 16, No. 3, pp. 311-320). Elsevier.
577. Battino, R., Rettich, T. R., & Tominaga, T. (1983). The solubility of oxygen and ozone in liquids. *Journal of physical and chemical reference data*, 12(2), 163-178.
578. Tromans, D. (1998). Temperature and pressure dependent solubility of oxygen in water: a thermodynamic analysis. *Hydrometallurgy*, 48(3), 327-342.
579. Preidel, W., Rao, J. R., Mund, K., Schunck, O., & David, E. (1995). A new principle for an electrochemical oxygen sensor. *Sensors and Actuators B: Chemical*, 28(1), 71-74.
580. McAleer, J., & Ackland, M. (1999). "Electrochemical oxygen sensor." U.S. Patent 5,876,577, issued March 2, 1999
581. Kitazawa, N. (2008) "Electrochemical oxygen sensor." U.S. Patent Application 12/734,714, filed November 28, 2008.
582. Stevens, B. (1971) "Instrument for determining oxygen quantities by measuring oxygen quenching of fluorescent radiation." U.S. Patent 3,612,866, issued October 12, 1971.
583. Hasumoto, H., Imazu, T., Miura, T., & Kogure, K. (2006). Use of an optical oxygen sensor to measure dissolved oxygen in seawater. *Journal of oceanography*, 62(1), 99-103.
584. Gouin, J. F., Baros, F., Birot, D., & Andre, J. C. (1997). A fibre-optic oxygen sensor for oceanography. *Sensors and Actuators B: Chemical*, 39(1), 401-406.

585. Glazer, B. T., Marsh, A. G., Stierhoff, K., & Luther, G. W. (2004). The dynamic response of optical oxygen sensors and voltammetric electrodes to temporal changes in dissolved oxygen concentrations. *Analytica chimica acta*, 518(1), 93-100.
586. Silva, E., Bastos, A. C., Miguel, N., Fernandes, A.J, Silva, R., Mário Guerreiro Silva Ferreira, M.G.S., Zheludkevich, M., and Oliveira, F. (2014). New fluorinated diamond microelectrodes for localized detection of dissolved oxygen. *Sensors and Actuators B: Chemical*, 204, 544-551
587. Silva, E. L., Gouvêa, C. P., Quevedo, M. C., Neto, M. A., Archanjo, B. S., Fernandes, A. J., Achete, C.A., Silva, R.F., Zheludkevich, M.L., and Oliveira, F.J. (2015). All-Diamond Microelectrodes as Solid State Probes for Localized Electrochemical Sensing. *Analytical chemistry*, 87(13), 6487-6492.
588. Keresztury G. (2002), Raman spectroscopy theory. In: *Handbook of vibrational spectroscopy*, eds. Chalmers J. and Griffiths P. R. (eds.), John Wiley & Sons Inc., Chichester, Vol. 1, p. 76.
589. Gardiner, D. J., Graves, P. R., & Bowley, H. J. (1989). *Practical Raman Spectroscopy* (Vol. 21). Berlin: Springer-Verlag.
590. Ahlawat, N. (2014). Raman Spectroscopy: A Review. *International Journal of Computer Science and Mobile Computing*, Vol.3 (11), pp. 680-685.
591. Placzek G, *Rayleigh-Streuung und Raman-Effekt*, Handbuch der Radiologie, Marx E Ed., Akademie Verlag, Leipzig; VI: 205-374
592. Atkins .W.(1970) *Molecular Quantum Mechanics: An Introduction to Quantum Chemistry*, Clarendon Press: Oxford.
593. Long D.A. (1977) *Raman Spectroscopy*, McGraw-Hill Ed., UK, London, 4: 74-110. 61.
594. Baranska, M. (2013). *Optical Spectroscopy and Computational Methods in Biology and Medicine* (Vol. 14). Springer Science & Business Media. pp.30-32.
595. Garrell, R. L. (1989). Surface-enhanced Raman spectroscopy. *Anal. Chem*, 61(6), 401A-411A.
596. Dieing, T., Hollricher, O., & Toporski, J. (2011). *Confocal raman microscopy* (Vol. 158). Springer Science & Business Media. pp.27-55.
597. Raman, C. V. (1928). A new radiation. *Indian Journal of physics*, 2, 387-398.
598. Raman, C. V. and Krishnan K. (1928). A new class of spectra due to secondary radiation Part I. *Indian Journal of physics*, 2, 399-419.
599. Fleischmann, M., Hendra, P. J., & McQuillan, A. J. (1974). Raman spectra of pyridine adsorbed at a silver electrode. *Chemical Physics Letters*, 26(2), 163-166.
600. Albrecht, M. G., & Creighton, J. A. (1977). Anomalously intense Raman spectra of pyridine at a silver electrode. *Journal of the American Chemical Society*, 99(15), 5215-5217.
601. Temperini, M. L. A., Chagas, H. C., & Sala, O. (1981). Raman spectra of pyridine adsorbed on a copper electrode. *Chemical Physics Letters*, 79(1), 75-78.
602. Campion, A., Brown, J. K., & Grizzle, V. M. (1982). Surface Raman spectroscopy without enhancement: Nitrobenzene on Ni (111). *Surface Science Letters*, 115(3), L153-L158.
603. Creighton, J. A. (1983). Surface Raman electromagnetic enhancement factors for molecules at the surface of small isolated metal spheres: The determination of adsorbate orientation from SERS relative intensities. *Surface Science*, 124(1), 209-219.
604. Schadler, L. S., & Galiotis, C. (1995). Fundamentals and applications of micro Raman spectroscopy to strain measurements in fibre reinforced composites. *International Materials Reviews*, 40(3), 116-134.

605. Mohiuddin, T.M.G., Lombardo, A., Nair, R.R., Bonetti, A., Savini, G., Jalil, R., Bonini, N., Basko, D.M., Galiotis, C., Marzari, N., Novoselov, K.S., Gein, A.K., & Ferrari, A. C. (2009). Uniaxial strain in graphene by Raman spectroscopy: G peak splitting, Grüneisen parameters, and sample orientation. *Physical Review B*, 79(20), 205433.
606. Loechelt, G. H., Cave, N. G., & Menendez, J. (1999). Polarized off-axis Raman spectroscopy: A technique for measuring stress tensors in semiconductors. *Journal of Applied Physics*, 86(11), 6164-6180.
607. Kip, B. J., Van Eijk, M. C., & Meier, R. J. (1991). Molecular deformation of high-modulus polyethylene fibers studied by micro-Raman spectroscopy. *Journal of Polymer Science Part B: Polymer Physics*, 29(1), 99-108.
608. Cheong, Y. M., Marcus, H. L., & Aclar, F. (1987). Raman microprobe measurements of residual strains at the interfaces of Si on quartz. *Journal of Materials Research*, 2(06), 902-909.
609. Remy, C., Reynard, B., & Madon, M. (1997). Raman Spectroscopic Investigations of Dicalcium Silicate: Polymorphs and High-Temperature Phase Transformations. *Journal of the American Ceramic Society*, 80(2), 413-423.
610. Zinn, A. S., Schiferl, D., & Nicol, M. F. (1987). Raman spectroscopy and melting of nitrogen between 290 and 900 K and 2.3 and 18 GPa. *The Journal of chemical physics*, 87(2), 1267-1271.
611. Kalampounias, A. G., Andrikopoulos, K. S., & Yannopoulos, S. N. (2003). Probing the sulfur polymerization transition in situ with Raman spectroscopy. *The Journal of chemical physics*, 118(18), 8460-8467.
612. Kester, J. J., Furtak, T. E., & Bevolo, A. J. (1982). Surface enhanced Raman scattering in corrosion science: benzotriazole on copper. *Journal of The Electrochemical Society*, 129(8), 1716-1719.
613. Ref: 615, pp. 2
614. Sheppard, C. J. R., & Wilson, T. (1978). Depth of field in the scanning microscope. *Optics Letters*, 3(3), 115-117.
615. Tabaksblat, R., Meier, R. J., & Kip, B. J. (1992). Confocal Raman microspectroscopy: theory and application to thin polymer samples. *Applied spectroscopy*, 46(1), 60-68.
616. Brakenhoff, G. J., Blom, P., & Barends, P. (1979). Confocal scanning light microscopy with high aperture immersion lenses. *Journal of Microscopy (Oxford)*, 117(2), 219-232.
617. Thierry, D., & Leygraf, C. (1985). Simultaneous Raman spectroscopy and electrochemical studies of corrosion inhibiting molecules on copper. *Journal of The Electrochemical Society*, 132(5), 1009-1014.
618. Payling, R., Barnett, N. W., & Nelis, T. (2002). *Glow Discharge Optical Emission Spectroscopy: A Practical Guide*. Royal Society of Chemistry.
619. Broekaert J. A. C. (2003) "Optical Emission Spectrometry with Glow Discharges" In *Glow Discharge Plasmas in Analytical Spectroscopy*, eds by Marcus R.K. and Broekaert J.A.C. John Wiley & Sons, Ltd. 15-69.
620. Nelis, T., & Pallosi, J. (2006). Glow discharge as a tool for surface and interface analysis. *Applied Spectroscopy Reviews*, 41(3), 227-258.
621. Sánchez, P., Fernández, B., Menéndez, A., Orejas, J., Pereiro, R., & Sanz-Medel, A. (2011). Quantitative depth profile analysis of metallic coatings by pulsed radiofrequency glow discharge optical emission spectrometry. *Analytica chimica acta*, 684(1), 47-53.

622. Kiryukhantsev-Korneev, P. V. (2012). Elemental analysis of coatings by high-frequency glow discharge optical emission spectroscopy. *Protection of Metals and Physical Chemistry of Surfaces*, 48(5), 585-590.
623. Payling R. (1998). Glow discharge optical emission spectrometry Spectroscopy Spectroscopy Vol.13, 36-44.
624. Wolpers, M., & Angeli, J. (2001). Activation of galvanized steel surfaces before zinc phosphating—XPS and GDOES investigations. *Applied Surface Science*, 179(1), 281-291.
625. Suzuki, S., & Suzuki, K. (1991). AES/GDS characterization of thin oxide films on Fe-Cr sheet steels. *Surface and interface analysis*, 17(8), 551-555.
626. Beck, U., Reiners, G., Wirth, T., Hoffmann, V., & Präbller, F. (1996). Multilayer reference coatings for depth profile standards. *Thin solid films*, 290, 57-62.
627. Thobor, A., Rousselot, C., & Mikhailov, S. (2003). Depth profiles study of n (TiN+ AlN) bilayers systems by GDOES and RBS techniques. *Surface and Coatings Technology*, 174, 351-359.
628. Galindo, R. E., Gago, R., Forniés, E., Muñoz-Martín, A., Font, A. C., & Albella, J. M. (2006). Nanometric resolution in glow discharge optical emission spectroscopy and Rutherford backscattering spectrometry depth profiling of metal (Cr, Al) nitride multilayers. *Spectrochimica Acta Part B: Atomic Spectroscopy*, 61(5), 545-553.
629. Galindo, R. E., Gago, R., Albella, J. M., & Lousa, A. (2009). Comparative depth-profiling analysis of nanometer-metal multilayers by ion-probing techniques. *TrAC Trends in Analytical Chemistry*, 28(4), 494-505.
630. Galindo, R. E., Gago, R., Duday, D., & Palacio, C. (2010). Towards nanometric resolution in multilayer depth profiling: a comparative study of RBS, SIMS, XPS and GDOES. *Analytical and bioanalytical chemistry*, 396(8), 2725-2740.
631. Pisonero, J. (2006). Glow discharge spectroscopy for depth profile analysis: from micrometer to sub-nanometer layers. *Analytical and bioanalytical chemistry*, 384(1), 47-49.
632. Shimizu, K., Payling, R., Habazaki, H., Skeldon, P., & Thompson, G. E. (2004). Rf-GDOES depth profiling analysis of a monolayer of thiourea adsorbed on copper. *Journal of Analytical Atomic Spectrometry*, 19(5), 692-695.
633. Shimizu, K., Brown, G. M., Habazaki, H., Kobayashi, K., Skeldon, P., Thompson, G. E., & Wood, G. C. (1999). Influence of surface roughness on the depth resolution of GDOES depth profiling analysis. *Surface and interface analysis*, 27(3), 153-156.
634. Shimizu, K., Habazaki, H., Skeldon, P., Thompson, G. E., & Wood, G. C. (2000). Influence of argon pressure on the depth resolution during GDOES depth profiling analysis of thin films. *Surface and interface analysis*, 29(2), 155-159.
635. Shimizu, K., Habazaki, H., Skeldon, P., Thompson, G. E., & Marcus, R. K. (2001). Influence of interfacial depth on depth resolution during GDOES depth profiling analysis of thin alumina films. *Surface and interface analysis*, 31(9), 869-873.
636. Bogaerts, A., & Gijbels, R. (1998). Fundamental aspects and applications of glow discharge spectrometric techniques. *Spectrochimica Acta Part B: Atomic Spectroscopy*, 53(1), 1-42.
637. Steiner, R.E., Barshick, C.M., and Bogaerts, A. (2009). Glow Discharge Optical Spectroscopy and Mass Spectrometry. in R.A Meyers (Ed.) *Encyclopedia of Analytical Chemistry*. , John Wiley & Sons Ltd., pp. 11-28.
638. Jacobs, H. O., Leuchtman, P., Homan, O. J., & Stemmer, A. (1998). Resolution and contrast in Kelvin probe force microscopy. *Journal of Applied Physics*, 84(3), 1168-1173.

639. Guillaumin, V., Schmutz, P., & Frankel, G. S. (2001). Characterization of corrosion interfaces by the scanning Kelvin probe force microscopy technique. *Journal of the Electrochemical Society*, 148(5), B163-B173.
640. Kolasinski, K. K., & Kolasinski, K. W. (2012). *Surface science: foundations of catalysis and nanoscience*. 3rd Edition, John Wiley & Sons. pp.258.
641. Druffner, C., Schumaker, E., Sathish, S., Frankel, G. S., & Leblanc, P. (2004). Scanning Probe Microscopy: Ultrasonic Force and Scanning Kelvin Probe Force Microscopy. In *Nondestructive Materials Characterization*, Springer Berlin Heidelberg. pp. 323-355.
642. Sathirachinda N. (2010), Relative nobility of precipitated phases in stainless steels - Evaluation with a combination of local probing techniques, Doctoral thesis, KTH, Stockholm
643. Craig, P. P., & Radeka, V. (1970). Stress dependence of contact potential: The AC Kelvin method. *Review of Scientific Instruments*, 41(2), 258-264.
644. Ertl G., Kippers J., (1974) *Low Energy Electrons and Surface Chemistry*, Monographs in Modern Chemistry 4 Verlag Chemie, Weinheim.
645. Nonnenmacher, M., o'Boyle, M. P., & Wickramasinghe, H. K. (1991). Kelvin probe force microscopy. *Applied physics letters*, 58(25), 2921-2923.
646. Sadewasser, S., & Glatzel, T. (Eds.). (2011). *Kelvin probe force microscopy: measuring and compensating electrostatic forces* (Vol. 48). Springer Science & Business Media. pp.1-3.
647. Weaver, J. M. R., & Abraham, D. W. (1991). High resolution atomic force microscopy potentiometry. *Journal of Vacuum Science & Technology B*, 9(3), 1559-1561.
648. Krok, F., Sajewicz, K., Konior, J., Goryl, M., Piatkowski, P., & Szymonski, M. (2008). Lateral resolution and potential sensitivity in Kelvin probe force microscopy: Towards understanding of the sub-nanometer resolution. *Physical Review B Condensed Matter And Materials Physics*, 77(23), 235-427.
649. Liscio, A., Palermo, V., & Samorì, P. (2010). Nanoscale quantitative measurement of the potential of charged nanostructures by electrostatic and Kelvin probe force microscopy: unraveling electronic processes in complex materials. *Accounts of chemical research*, 43(4), 541-550.
650. Nony, L., Bocquet, F., Loppacher, C., & Glatzel, T. (2009). On the relevance of the atomic-scale contact potential difference by amplitude-modulation and frequency-modulation Kelvin probe force microscopy. *Nanotechnology*, 20(26), 264014.
651. Campiglio, P., Campione, M., & Sassella, A. (2009). Kelvin probe force microscopy characterization of self-assembled monolayers on metals deposited with dip-pen nanolithography. *The Journal of Physical Chemistry C*, 113(19), 8329-8335.
652. Tanem, B. S., Svenningsen, G., & Mårdalen, J. (2005). Relations between sample preparation and SKPFM Volta potential maps on an EN AW-6005 aluminium alloy. *Corrosion science*, 47(6), 1506-1519.
653. Aveyard, R., & Haydon, D. A. (1973). *An introduction to the principles of surface chemistry*. Cambridge University Press, Cambridge.
654. Buchheit, R. G., Grant, R. P., Hlava, P. F., McKenzie, B., & Zender, G. L. (1997). Local Dissolution Phenomena Associated with S Phase (Al₂CuMg) Particles in Aluminum Alloy 2024-T3. *Journal of the Electrochemical Society*, 144(8), 2621-2628.
655. Schmutz, P., & Frankel, G. S. (2001). CHARACTERIZATION OF POTENTIAL INHOMOGENEITIES ON PASSIVE SURFACES BY SCANNING KELVIN PROBE FORCE

- MICROSCOPY. Passivity of Metals and Semiconductors, Ives M.B., Luo J.L., and Rodda J. R., eds., The Electrochemical Society Proceedings,99(42), 537.
656. Melitz, W., Shen, J., Kummel, A. C., & Lee, S. (2011). Kelvin probe force microscopy and its application. *Surface Science Reports*, 66(1), 1-27.
657. Haugstad, G. (2012). *Atomic force microscopy: understanding basic modes and advanced applications*. John Wiley & Sons.
658. Guillaumin, V., Schmutz, P., & Frankel, G. S. (2001). Characterization of corrosion interfaces by the scanning Kelvin probe force microscopy technique. *Journal of the Electrochemical Society*, 148(5), B163-B173.
659. Magonov, S., & Alexander, J. (2010) Compositional mapping of materials with single-pass Kelvin force microscopy. (Application note), Agilent Technologies, USA. <http://cp.literature.agilent.com/litweb/pdf/5990-5480EN.pdf> accessed 01/09/2015.
660. Magonov S., Alexander J., and Wu S., (2011) Advancing characterization of materials with atomic force microscopy-based electric techniques scanning probe microscopy of functional materials, in: A. Gruverman, S.V. Kalinin (Eds.), *Scanning Probe Microscopy of Functional Materials*, Springer, New York pp. 233-300.
661. Magonov, S., & Alexander, J. (2011). Single-pass Kelvin force microscopy and dC/dZ measurements in the intermittent contact: applications to polymer materials. *Beilstein journal of nanotechnology*, 2(1), 15-27.
662. Sababi, M., Ejnermark, S., Andersson, J., Claesson, P. M., & Pan, J. (2013). Microstructure influence on corrosion behavior of a Fe–Cr–V–N tool alloy studied by SEM/EDS, scanning Kelvin force microscopy and electrochemical measurement. *Corrosion Science*, 66, 153-159.
663. Bettini, E., Kivisäkk, U., Leygraf, C., & Pan, J. (2013). Study of corrosion behavior of a 22% Cr duplex stainless steel: Influence of nano-sized chromium nitrides and exposure temperature. *Electrochimica Acta*, 113, 280-289.
664. Schmutz, P., & Frankel, G. S. (1998a). Characterization of AA2024-T3 by scanning Kelvin probe force microscopy. *Journal of the Electrochemical Society*, 145(7), 2285-2295.
665. Schmutz, P., & Frankel, G. S. (1998b). Corrosion Study of AA2024-T3 by Scanning Kelvin Probe Force Microscopy and In Situ Atomic Force Microscopy Scratching. *Journal of the Electrochemical Society*, 145(7), 2295-2306.
666. Schmutz, P., & Frankel, G. S. (2001). CHARACTERIZATION OF POTENTIAL INHOMOGENEITIES ON PASSIVE SURFACES BY SCANNING KELVIN PROBE FORCE MICROSCOPY. Passivity of Metals and Semiconductors, Ives M.B., Luo J.L., and Rodda J. R., eds., The Electrochemical Society Proceedings,99(42), 537.
667. Leblanc, P., & Frankel, G. S. (2002). A study of corrosion and pitting initiation of AA2024-T3 using atomic force microscopy. *Journal of the Electrochemical Society*, 149(6), B239-B247.
668. Stratmann, M. (1987). The investigation of the corrosion properties of metals, covered with adsorbed electrolyte layers—A new experimental technique. *Corrosion Science*, 27(8), 869-872.
669. Brug, G. J., Van Den Eeden, A. L. G., Sluyters-Rehbach, M., & Sluyters, J. H. (1984). The analysis of electrode impedances complicated by the presence of a constant phase element. *Journal of electroanalytical chemistry and interfacial electrochemistry*, 176(1), 275-295.
670. Hassan, H. H. (2001). Corrosion behaviour of zinc in sodium perchlorate solutions. *Applied surface science*, 174(3), 201-209.

671. Hurley, B. L., Ralston, K. D., & Buchheit, R. G. (2014). Corrosion Inhibition of Zinc by Aqueous Vanadate Species. *Journal of The Electrochemical Society*, 161(10), C471-C475.
672. Alias, M. N., & Brown, R. (1992). Damage to composites from electrochemical processes. *Corrosion*, 48(5), 373-378.
673. Borup, R., Meyers, J., Pivovar, B., Kim, Y.S., Mukundan, R., Garland, N., Myers, D., Wilson, M., Garzon, F., Wood, D. and Zelenay, P., (2007) Scientific aspects of polymer electrolyte fuel cell durability and degradation. *Chemical reviews*, 107(10), pp.3904-3951.
674. Su-Il, P., Young-Gyoon, R. and Soo-Hyun, C., (1994a). Corrosion behaviour of platinum-catalyzed carbon in phosphoric acid solution. *Carbon*, 32(1), pp.161-164.
675. Su-Il, P., Eung-Jo, L., Tae-Young, K., Seo-Jae, L., Young-Gyoon, R. and Chang-Soo, K., (1994b). Role of surface oxides in corrosion of carbon black in phosphoric acid solution at elevated temperature. *Carbon*, 32(1), pp.155-159.
676. Vivian, J. E., & King, C. J. (1964). Diffusivities of slightly soluble gases in water. *AIChE Journal*, 10(2), 220-221
677. St-Denis, C. E., & Fell, C. J. D. (1971). Diffusivity of oxygen in water. *The Canadian Journal of Chemical Engineering*, 49(6), 885-885.
678. Tse, F.C & Sandall, O.C. (1979) Diffusion Coefficients for Oxygen and Carbon Dioxide in Water at 25°C by Unsteady State Desorption from a Quiescent Liquid. *Chemical Engineering Communications*, 3(3), 147-153..
679. Gerasimov, V. V., & Rozenfeld, I. L. (1956). Effect of temperature on the diffusion current and the thickness of the diffusion layer. *Russian Chemical Bulletin*, 5(7), 797-801.
680. Moreno-Castilla, C. (2004). Adsorption of organic molecules from aqueous solutions on carbon materials. *Carbon*, 42(1), 83-94.
681. Kaneko, Y., Abe, M., & Ogino, K. (1989). Adsorption characteristics of organic compounds dissolved in water on surface-improved activated carbon fibres. *Colloids and Surfaces*, 37, 211-222.
682. Hanzlík P., Jehlička J., Weishauptová Z., Šebek. O. (2004) Adsorption of copper, cadmium and silver from aqueous solutions onto natural carbonaceous materials. *Plant Soil Environment*, 50(6): 257–264
683. Abe I, Iwasaki S., Tokimoto T., Kawasaki N., Nakamura T., and Tanada S. (2004) Adsorption of fluoride ions onto carbonaceous materials. *Journal of Colloid and Interface Science* 275 (2004) 35–39.
684. De, D., Kalu, E. E., Tarjan, P. P., & Englehardt, J. D. (2004). Kinetic Studies of the Electrochemical Treatment of Nitrate and Nitrite Ions on Iridium-Modified Carbon Fiber Electrodes. *Chemical engineering & technology*, 27(1), 56-64
685. Reyter, D., Bélanger, D., & Roué, L. (2008). Study of the electroreduction of nitrate on copper in alkaline solution. *Electrochimica Acta*, 53(20), 5977-5984.
686. Black, S. (2013). Lightning strike protection strategies for composite aircraft. *High-Performance Composites*, (5-1).
687. Fujioka, E., Nishihara, H., & Aramaki, K. (1996). The inhibition of pit nucleation and growth on the passive surface of iron in a borate buffer solution containing Cl⁻ by oxidizing inhibitors. *Corrosion science*, 38(11), 1915-1933
688. Sander, U., Strehblow, H. H., & Dohrmann, J. K. (1981). In situ photoacoustic spectroscopy of thin oxide layers on metal electrodes. Copper in alkaline solution. *The Journal of Physical Chemistry*, 85(4), 447-450.

689. Kiliñçeker, G., & Galip, H. (2008). The effects of acetate ions (CH_3COO^-) on electrochemical behavior of copper in chloride solutions. *Materials Chemistry and Physics*, 110(2), 380-386.
690. Cano, E., Bastidas, J. M., Polo, J. L., & Mora, N. (2001). Study of the effect of acetic acid vapor on copper corrosion at 40 and 80% relative humidity. *Journal of the electrochemical society*, 148(11), B431-B437.
691. Böhm, S., Greef, R., McMurray, H. N., Powell, S. M., & Worsley, D. A. (2000). Kinetic and Mechanistic Studies of Rare Earth-Rich Protective Film Formation Using In Situ Ellipsometry. *Journal of the Electrochemical Society*, 147(9), 3286-3293.
692. Seter, M., Girard, G. M., Lee, W. W., Deacon, G., Junk, P., Hinton, B., & Forsyth, M. (2015). The influence of organic structure and rare earth metal cation on the corrosion efficiency observed on AS1020 steel compared with $\text{La}(\text{4OHcin})_3$. *AIMS Materials Science [E]*, 2(1), 1-15.
693. Behrsing, T., Bond, A. M., Deacon, G. B., Forsyth, C. M., Forsyth, M., Kamble, K. J., Skelton, B.W. & White, A. H. (2003). Cerium acetylacetonates—new aspects, including the lamellar clathrate $[\text{Ce}(\text{acac})_4] \cdot 10\text{H}_2\text{O}$. *Inorganica chimica acta*, 352, 229-237.
694. Barrett, S. D., & Dhesi, S. S. (2001). The structure of rare-earth metal surfaces. *World Scientific*. pp.11.
695. Hinton, B. R. W. (1992). Corrosion inhibition with rare earth metal salts. *Journal of Alloys and Compounds*, 180(1), 15-25.
696. Bouchaud, B., Balmain, J., Bonnet, G., & Pedraza, F. (2012). pH-distribution of cerium species in aqueous systems. *Journal of Rare Earths*, 30(6), 559-562.
697. Meloche, C. C., & Vrátný, F. (1959). Solubility product relations in the rare earth hydrous hydroxides. *Analytica Chimica Acta*, 20, 415-418.
698. Dean, J.A. (Ed), *Lang's Handbook of Chemistry*, 12th edition, McGraw-Hill, New York, 1979, pp.5-7.
699. Lide, D.R. (Ed.) *CRC Handbook of Chemistry and Physics*, 80th edition, CRC Press, Boca Raton, 1999, pp. 8-111.
700. Moeller, T., & Kremers, H. E. (1944). Observations on the Rare Earths. LI. An Electrometric Study of the Precipitation of Trivalent Hydrous Rare Earth Oxides or Hydroxides. *The Journal of Physical Chemistry*, 48(6), 395-406.